Weak Lensing Mass Determination *of* Eight X-ray Selected Galaxy Clusters from the *400d* Survey

DISSERTATION

zur
Erlangung des Doktorgrades (Dr. rer. nat)
der
Mathematisch–Naturwissenschaftlichen Fakultät
der
Rheinischen Friedrich–Wilhelms–Universität Bonn

vorgelegt von

HOLGER ISRAEL
aus
Göttingen

BONN, 2010

Angefertigt mit Genehmigung der
Mathematisch–Naturwissenschaftlichen Fakultät der
Rheinischen Friedrich–Wilhelms–Universität Bonn

1. Referent: Prof. Dr. Thomas H. Reiprich

2. Referent: Prof. Dr. Peter Schneider

Tag der Promotion: 17. Dezember 2010

Erscheinungsjahr: 2011

Abstract

Evolution in the mass function of galaxy clusters sensitively traces both the expansion history of the Universe and cosmological structure formation. Hence, measuring the number density of galaxy clusters as a function of redshift provides constraints to cosmological parameters, independent of other methods. Current results from these probes, including clusters of galaxies, are found to agree on a cosmological model dominated by Dark Energy and Cold Dark Matter. Investigating the unknown physical nature of Dark Energy ranks among the foremost questions in current cosmology. In particular, the presence or absence of evolution in Dark Energy density is expressed by the equation-of-state parameter.

This thesis presents the first results from the *400d* Galaxy Cluster Survey Weak Lensing Programme, in which optical follow-up observations for a sample of relatively distant ($0.35 < z < 0.90$) X-ray selected galaxy clusters are analysed and presented. Mass determination by weak gravitational lensing uses minute distortions in the images of *background* galaxies, caused by the relativistic curvature of space-time, to infer the mass of the intervening cluster. The weak lensing follow-up project aims at measuring reliable weak lensing masses for 36 clusters, for which a mass function and resulting cosmological constraints using CHANDRA X-ray observations have been published. Determining cluster masses by weak lensing makes possible a cross-calibration of the assumptions and systematics related to both the X-ray and weak lensing methods.

As the initial phase of the *400d* weak lensing programme project, observations of eight clusters were obtained with the MEGACAM instrument at the 6.5 m MMT telescope, which we demonstrated to be well-suited for weak lensing. In this thesis, the successful weak lensing detections of these eight clusters are reported, leading to weak lensing mass estimates which then are compared to X-ray masses. For the pilot object, CL 0030+2618, the data analysis is described in great detail, focussing in particular on the construction of a catalogue of lensed background galaxies by using photometry in three passbands. In a synopsis involving several optical and X-ray methods, the identity of the brightest cluster galaxy is established and found to be consistent with both X-ray and weak lensing cluster centres for CL 0030+2618. Cluster masses are obtained by fitting the tangential weak lensing shear measured as a function of separation from the cluster centre with a profile function derived from the Navarro-Frenk-White Dark Matter density profile.

Performing a similar analysis for the seven further clusters and investigating the spatial distribution of the lensing signal, multiple shear peaks and/or clusters are detected in three cases. In a comparison between the weak lensing and hydrostatic X-ray mass estimates for the eight clusters, good agreement and a power-law relation with remarkably small scatter are found. Preliminary scaling relations between the weak lensing masses and published X-ray observables of the eight clusters indicate the potential of the weak lensing survey, once observations are available for the complete 36 cluster sample. The completion of the *400d* weak lensing survey is concluded to be feasible and promising in terms of improved cosmological constraints from galaxy clusters.

"We have no need of other worlds. We need mirrors.
We don't know what to do with other worlds."

Stanisław Lem, ***Solaris***

Contents

Chapter 0

Introduction

For the past decade, the first time in the history of physical cosmology, a consistent "standard" model of cosmology has emerged in which cosmological parameters inferred with various techniques agree within their uncertainties. Meanwhile, these uncertainties continue to decrease because of new observing instruments, improved simulations, and analytical methods. The emerging picture is often referred to as "Concordance Cosmology" or ΛCDM cosmology, for its two main ingredients: Dark Energy ("Λ") and Cold Dark Matter (CDM). The combined energy densities of these two components amount to ~ 95 % of the total energy in the Universe; only the small rest consists of the particles known to physics today.

Concerning Cold Dark Matter, viable particle physics models (e.g. stable supersymmetric particles) exist, and current experiments (e.g. at the Large Hadron Collider) are expected to be able to test and constrain these models. Astrophysical constraints on the properties of CDM can already be inferred from the study of merging *galaxy clusters*: Clowe et al. (2006a), mapping the mass in a system of two merging galaxy clusters with the technique of *weak gravitational lensing*, found its centre of mass to coincide with the centre of the – collisionless – galaxy distribution. The majority of the known, baryonic cluster mass, however, lies in the hot *intracluster medium* (ICM). Observations of its X-ray emission in the system studied by Clowe et al. (2006a) not only reveal that the ICM is affected by merger shocks but, more important, its centre of mass to differ from the one inferred from weak lensing. Clowe et al. (2006a) conclude that most of the cluster mass is dark and collisionless, giving one of the most compelling pieces of evidence for the existence of non-baryonic CDM.

Much less we know about Dark Energy (DE). Riess et al. (1998) and Perlmutter et al. (1999) surprisingly discovered that the expansion of the Universe does not decelerate, as was usually assumed, but accelerates. Subsequently, the accelerated expansion was confirmed with various methods (e.g., Vikhlinin et al. 2009b; Schrabback et al. 2009; Larson et al. 2010), but theories about its source, Dark Energy, have so far remained speculative. An important question to which astrophysicists hope to find an answer in the not-too-distant future is whether DE is an invariable "Cosmological Constant" or evolves with time. This question is parametrised in the DE *equation-of-state parameter*, $w_{\rm DE}$.

Among the several probes contributing to the progress in cosmology, galaxy clusters are of particular interest, offering insights into both the expansion history of the Universe and the formation of structures out of a homogeneous initial state. Being the largest virialised structures – i.e. stable under their own gravity – their mass distribution allows us to infer the interplay of gravitative attraction and cosmic expansion. Put more quantitatively, the *cluster mass function* enables us to constrain cosmological parameters, e.g. $w_{\rm DE}$.

In this thesis, we present the first results from the *400d* Galaxy Cluster Survey Weak Lensing Programme, in which we perform and analyse optical follow-up observations for a sample of relatively distant ($0.35 < z < 0.90$) X-ray selected galaxy clusters. The *400d* sample consists of galaxy clusters serendipitously detected in all suitable observations obtained with the ROSAT *PSPC* instrument (Burenin et al. 2007). The subsample of 36 clusters we consider for cosmology was defined by Vikhlinin et al. (2009a), who measured the cluster mass function from CHANDRA X-ray observations of these clusters and inferred cosmological parameters (Vikhlinin et al. 2009b).

Gravitational lensing arises from the curvature of space-time in the presence of gravitating mass, predicted by Einstein's theory of General Relativity. Light bundles emitted by a background source and passing by a massive deflector, e.g. a cluster of galaxies become distorted on their way to the observer. In the case of weak lensing (WL) where the distortion is not obvious to the observer, detailed statistical analyses are necessary to infer the lens properties. Determining cluster masses by weak lensing, we obtain an independent test of the X-ray analyses for the *400d* clusters. In particular, the WL follow-up allows us to cross-calibrate the different assumptions going into and systematic effects influencing both the X-ray and WL mass measurements. Thus, we plan to contribute to the study of *scaling relations* between cluster observables; an important field of research for improving the accuracy of cluster cosmology.

In this work, we present the analyses for the first eight clusters we studied as part of the *400d* WL survey, resulting in WL mass estimates which we compare to X-ray masses. We observed these clusters with the MEGACAM instrument at the 6.5 m MMT telescope, which we demonstrate to be well-suited for weak lensing. This thesis is organised as follows: In Chapter 1, we introduce the current status of cosmological models to which the work here aims to contribute ultimately. We focus in particular on the cosmological parameters determining the expansion history of the Universe and the formation of structures in this expanding Universe, which can be tested using the mass function of galaxy clusters. How the cluster mass function enables us to constrain cosmological parameters, for instance $w_{\rm DE}$, we discuss in Chapter 2, after a brief overview on the basic properties of clusters and their detection in several astronomical wavelength regimes. We further introduce the most important scaling relations considered for the cosmological application of cluster data. Chapter 3 presents the basic concepts of gravitational lens theory relevant to our analysis, i.e. focussing on weak lensing by clusters and methods to infer the cluster mass from the shapes of lensed background sources.

In Chapter 4, we review the X-ray selection of the *400d* sample clusters as well as the cosmological results from the CHANDRA analyses. We give a detailed motivation of the weak lensing follow-up survey and present the status of observations, in particular the dedicated MEGACAM imaging of eight clusters, conducted by our team, on which this thesis is built. Data reduction with the `THELI` pipeline, specially designed to deal with wide-field, multi-chip optical data is discussed in Chapter 5, as well as the photometric calibration. We analyse the point spread function of MEGACAM and, selecting usable frames, conclude that the instrument serves well for weak lensing.

We analysed the cluster CL 0030+2618 in a pilot study, which we published in Israel et al. (2010), and present, with some revisions in Chapter 6. There, we describe our methods for background selection and estimation of the source redshift distribution. We discuss the mass map of CL 0030+2618 before describing how the cluster mass is determined by fits to the shear signal. With a few modifications, we apply the same methods in the analyses of seven further *400d* clusters. These new results are given in Chapter 7. Investigating the spatial distribution of the lensing signal, we detect multiple shear peaks and/or clusters in three cases. We adopt our fitting technique in order to account for two cluster components. The shear detections are discussed and the analysis is reviewed based on the experience with the peculiarities of eight cluster fields in Chapter 8. We compare the lensing masses to hydrostatic masses based on CHANDRA X-ray observations. After giving an outlook on future analyses. we summarise our results and conclusions in Chapter 9.

Chapter 1

Concepts of Cosmology

How can we even begin to describe the Universe as a whole? Perhaps the most important decision is what to tell and what to leave out. Therefore, as this thesis aims at presenting results of cosmological studies of galaxy clusters with weak gravitational lensing, I will focus on the context for this work in the current state of cosmology. Inspiration was drawn from the reviews of cosmology by Liddle (2003), Schneider (2006a,b), and Tereno (2006).

1.1 The Concordance Model of Cosmology

1.1.1 Expansion and Big Bang, H_0 and CMB

The most important observation in modern cosmology is Hubble's 1929 measurement of a *recession velocity v* of galaxies proportional to their distance *D*. The coefficient of this proportionality is called the *Hubble parameter*, H_0. Hubble's discovery laid the groundwork for the *Big Bang* model in which the recession of galaxies is interpreted as an expansion of the Universe as a whole, from a very dense state at a time given by $\sim H_0^{-1}$ before present. Although heavily contested, the Big Bang model of an expanding universe has succeeded in producing correct predictions for several decades. During most of this time, however, the value of the Hubble parameter was strongly disputed, with different measurements and factions of cosmologists favouring either $H_0 \approx 50\,\mathrm{km\,s^{-1}\,Mpc^{-1}}$ or $H_0 \approx 100\,\mathrm{km\,s^{-1}\,Mpc^{-1}}$. In the past ~ 10 years, owing to improved observational capabilities, a consensus has emerged, contributing to the development of the "concordance cosmology" model.

One influential recent study of the Hubble parameter using the period–luminosity relation of Cepheids in combination with several other distance measures as part of a cosmological distance ladder is the *Hubble Key Project*. Monitoring Cepheids in nearby galaxies with the Hubble Space Telescope (HST) wide field cameras, (Freedman et al. 2001) inferred:

$$H_0 = 72 \pm 8\,\mathrm{km\,s^{-1}\,Mpc^{-1}} \quad . \tag{1.1}$$

The tests used by Freedman et al. (2001) include Cepheids, luminosities of supernovae, the Tully & Fisher (1977) relation linking the maximum rotational velocity of a spiral galaxy to its total luminosity, the fundamental plane spanned by elliptical galaxies, and the surface brightness fluctuation method. Gravitational lensing offers an independent probe of H_0 via the time-delays observed for brightness variations in different images of multiply-imaged quasars. Observing Cepheids in galaxies whose distances are known from type Ia supernovae (SN Ia) measurements (and from a MASER source in one case), Riess et al. (2009) obtain $H_0 = 74.2 \pm 3.6\,\mathrm{km\,s^{-1}\,Mpc^{-1}}$. Suyu et al. (2010), fixing the values for the other relevant cosmological parameters, determine the Hubble parameter to $H_0 = 70.6 \pm 3.1\,\mathrm{km\,s^{-1}\,Mpc^{-1}}$. Combining X-ray

and Sunyaev-Zel'dovich effect observations (Sect. 2) of galaxy clusters, Bonamente et al. (2006) constrain $H_0 = 70.6^{+3.9+10.0}_{-3.4-8.0}$, km s^{-1} Mpc^{-1} independent of all other distance scales.

The crucial successful prediction made by Big Bang cosmology is the *Cosmic Microwave Background* (CMB), the afterglow of the hot early phase of the Universe, which was first observed by Penzias & Wilson in 1964. Since then, it has become a very versatile tool for cosmology. The CMB offers insights into the epoch of (re-)combination, when the temperature in the expanding and therefore cooling universe dropped beneath the threshold below which electrons and nuclei can bind to form atoms. During the (re-)combination epoch, the CMB radiation field decoupled from the (baryonic) matter, leaving a "fossil imprint" of the matter properties at that time which is preserved by the adiabatic cooling of the CMB due to the expansion.

Another important ingredient to modern cosmology is the *Big Bang Nucleosynthesis*, predicting particle interactions in the hot and dense medium of the early universe and leading to powerful constraints on the abundances of the lightest complex nuclei (i.e., D, He, Li) in the primordial gas before any processing by stars.

1.1.2 Friedmann Equation and Energy Densities

Physical cosmology is based on the principle that, from a grand perspective, there is no point in the Universe that is preferred, meaning the fundamental laws of physics are the same everywhere in the cosmos. Although this "cosmological principle" can be contested (e.g., Wiltshire 2007; Leith et al. 2008), there is no convincing evidence known to the author that disfavours a model of the Universe that is homogeneous and isotropic on sufficiently large scales.

The geometry of an expanding universe which is homogeneous and isotropic is given by the Robertson–Walker metric, expressed by a time coordinate t and spatial coordinates $\vec{r}(t) = a(t)\vec{x}$. The time-independent *comoving* coordinate vector $\vec{x}$ is expressed by spherical coordinates (χ, θ, ϕ) for the three space-like dimensions:

$$\mathrm{d}s^2 = c^2\mathrm{d}t^2 - a^2(t)\left[\mathrm{d}\chi^2 + f_K^2(\chi)\left(\mathrm{d}\theta^2 + \sin^2\theta\,\mathrm{d}\phi^2\right)\right] \quad . \tag{1.2}$$

The *scale factor* $a(t)$, normalised to unity at the present epoch t_0, describes any possible expansion or contraction of the Universe. An observer at the arbitrarily chosen point $\vec{x} = 0$ will see every other point in the Universe receding at velocity $v(t) = H(t)a(t)\chi$, where $H(t) = \dot{a}/a$ is the *Hubble parameter*. Its present value $H(t = t_0)$ is the Hubble constant, yielding a recession velocity $v = H_0\chi$.

In Eq. (1.2), $f_K(\chi)$ denotes a family of functions determined by the parameter K, a measure for the overall *curvature* of space:

$$f_K(\chi) = \begin{cases} \sin(\chi\sqrt{K})/\sqrt{K} & K > 0 \\ \chi & K = 0 \\ \sinh(\chi\sqrt{-K})/\sqrt{-K} & K < 0 \end{cases} \quad . \tag{1.3}$$

The two free parameters, a and K, in the purely geometrical description (Eq. 1.2) are determined by the material (energetic) content of the Universe. Geometry on the one hand and energy on the other are linked in General Relativity (GR) by the *Einstein field equations*:

$$G_{\mu\nu} = \frac{8\pi G_\mathrm{N}}{c^4} T_{\mu\nu} - \Lambda g_{\mu\nu} \quad . \tag{1.4}$$

Here, the Einstein tensor $G_{\mu\nu}$ and metric $g_{\mu\nu}$ represent functions of geometrical quantities only, while the energy-momentum tensor $T_{\mu\nu}$ encompasses the properties of the different forms of energy and matter, namely its density ρ and pressure p. With G_N, we denote the gravitational constant. An additional degree of freedom to the solutions of Eq. (1.4) is introduced by adding the *Cosmological Constant* Λ.

Inserting the Robertson-Walker metric (1.2) into the Einstein equations (1.4), two equations governing the expansion of the Universe can be deduced. In the following, we will motivate the first, the Friedmann equation, from purely Newtonian concepts. Considering an expanding sphere homogeneously filled with gravitating matter of density ρ, the total energy of a test mass m at radius $r(t) = a(t)\chi$ is given by

$$E = E_{\mathrm{kin}} + E_{\mathrm{pot}} = \frac{m\dot{r}^2}{2} - \frac{4}{3}\pi G_{\mathrm{N}}\rho m r^2 = \frac{ma^2\chi^2}{2}\left[\left(\frac{\dot{a}^2}{a^2}\right) - \frac{8\pi}{3}G_{\mathrm{N}}\rho\right] \quad . \tag{1.5}$$

Introducing $\tilde{K} = -2E/(mc^2\chi^2)$ then gives the "Newtonian Friedmann equation":

$$\left(\frac{\dot{a}}{a}\right)^2 = \frac{8\pi}{3}G_{\mathrm{N}}\rho - \frac{\tilde{K}c^2}{a^2} \quad . \tag{1.6}$$

For the transition to the relativistic result, we identify the two constants $\tilde{K}$ and K. Comparing the relativistic Friedmann equation

$$H^2(t) = \left(\frac{\dot{a}}{a}\right)^2 = \frac{8\pi}{3}G_{\mathrm{N}}\rho - \frac{Kc^2}{a^2} + \frac{\Lambda c^2}{3} \tag{1.7}$$

with Eq. (1.6) allows the Cosmological Constant to be interpreted as a choice fixing the absolute energy scale. Relativistically, K can be understood as the curvature of the space-like subspace of space-time given by (χ, θ, ϕ), which is induced by gravitating energy. The three cases in Eq. (1.3) are three fundamental geometries of the universe: $K > 0$ describes a *closed* universe, e.g., a 3-sphere[1], $K < 0$ gives a hyperbolic, *open* universe, and the *flat*, limiting case of $K = 0$ implies the usual Euclidean geometry without large-scale curvature.

Which are the matter components determining the expansion of the Universe and how do their densities evolve with increasing scale factor $a(t)$? The first law of thermodynamics – the conservation of energy – can be expressed as

$$\frac{\mathrm{d}}{\mathrm{d}t}\left[a^3(t)\rho_i(t)c^2\right] + p_i(t)\frac{\mathrm{d}a^3(t)}{\mathrm{d}t} = 0 \quad . \tag{1.8}$$

This fluid or Raychaudhuri equation is like the Friedmann equation derived from Eqs. (1.2) and (1.4) and can be similarly motivated by classical physics, considering an adiabatically expanding fluid. In reality, in the Universe there are not only one, but several interacting fluids. The important role the pressure term plays becomes clearer when we combine the Friedmann (1.7) and fluid (1.8) equations, forming the *acceleration equation*:

$$\frac{\ddot{a}}{a} = -\frac{4\pi G_{\mathrm{N}}}{3}\sum_i\left(\rho_i + \frac{3p_i}{c^2}\right) + \frac{\Lambda c^2}{3} \quad . \tag{1.9}$$

In writing Eq. (1.9), we have taken into account the existence of several fluids with densities ρ_i and pressures p_i. Pressure $p_i > 0$ acts like gravitating mass and decelerates the expansion, while a cosmological constant $\Lambda > 0$ accelerates it. The pressure p_i of a fluid is significant for the expansion if it is not small compared to $\rho_i c^2$. This relation between pressure and density is given by the *equation-of-state parameter*

$$w_i := \frac{p_i}{\rho_i c^2} \quad . \tag{1.10}$$

[1]The value of K does not yet determine the actual *topology* of the Universe. Neither does it in the general case determine its fate at $t \to \infty$. Current knowledge suggests a flat ($K = 0$) cosmos which will forever continue to accelerate its expansion.

Introducing it, the following solution for the evolution of the density with $\rho_{i,0} := \rho_i(a=1)$ can be deduced

$$\rho_i(t) = \rho_{i,0}\, a(t)^{-3}\, \exp\left(-3\int_0^{a(t)} w_i(a')\, a'^{-1} \mathrm{d}a'\right) \quad . \tag{1.11}$$

In the case of a time-independent equation-of-state parameter ($\dot{w}_i = 0$), this expression reduces to:

$$\rho_i(t) = \rho_{i,0}\, a(t)^{-3(1+w_i)} \quad . \tag{1.12}$$

First, there is non-relativistic matter whose pressure can be neglected because of $p_\mathrm{m} \ll \rho_\mathrm{m} c^2$. Fixing $p_\mathrm{m} = 0$, Eq. (1.12) yields

$$\rho_\mathrm{m}(t) = \rho_{\mathrm{m},0}\, a(t)^{-3} \quad , \tag{1.13}$$

which can be interpreted as the dilution of a constant number of particles in an expanding space.

Second, relativistic particles ("radiation") exert non-negligible pressure which is linked to their density by $p_\mathrm{r} = \rho_\mathrm{r} c^2/3$ or $w_\mathrm{r} = 1/3$. Using Eq. (1.12), one finds that the evolution of radiation density is governed by

$$\rho_\mathrm{r}(t) = \rho_{\mathrm{r},0}\, a(t)^{-4} \quad , \tag{1.14}$$

where the additional factor of a^{-1} corresponds to the energy loss experienced by photons due to their cosmological redshift.

Lastly, the cosmological constant can be regarded as a fluid whose density $\rho_\Lambda = \Lambda c^2/(8\pi G_\mathrm{N})$ follows directly from the Friedmann equation (1.7) and is a constant function of time. Inserting this condition $\dot{\rho}_\Lambda = 0$ into the fluid equation (1.8) then, immediately, implies $\rho_\Lambda + p_\Lambda/c^2 = 0$ or

$$w_\Lambda = p_\Lambda/(\rho_\Lambda c^2) = -1 \quad . \tag{1.15}$$

In a flat ($K = 0$) universe without cosmological constant ($\Lambda = 0$), a (time-dependent) natural density scale is defined by the Hubble parameter by:

$$\rho_\mathrm{c} = \frac{3H^2(t)}{8\pi G_\mathrm{N}} \quad . \tag{1.16}$$

For the current epoch, this *critical density* is as low as $\rho_\mathrm{c} = 1.0 \times 10^{-26}\,\mathrm{kg\,m^{-3}}$. The individual density constituents of the Universe are commonly expressed in units of the critical density:

$$\Omega_\mathrm{r}(t) = \frac{\rho_{\mathrm{r},0}}{\rho_\mathrm{c}(t)}, \quad \Omega_\mathrm{m}(t) = \frac{\rho_{\mathrm{m},0}}{\rho_\mathrm{c}(t)}, \quad \Omega_\Lambda(t) = \frac{\rho_\Lambda}{\rho_\mathrm{c}(t)} = \frac{\Lambda c^2}{3H^2(t)} \quad . \tag{1.17}$$

The total density of the Universe is then defined as:

$$\Omega_0 = \Omega_\mathrm{r} + \Omega_\mathrm{m} + \Omega_\Lambda \quad \text{resp.} \quad \Omega_0 = \Omega_\mathrm{r} + \Omega_\mathrm{m} + \Omega_\mathrm{DE} \quad \text{with} \quad \Omega_\mathrm{DE} = \rho_\mathrm{DE}/\rho_\mathrm{c} \quad . \tag{1.18}$$

We will subsequently prefer the more general case of a time-dependent (Eq. 1.11) *Dark Energy* component whose negative w_DE not necessarily equals $w_\Lambda = -1$, because this thesis is motivated by constraining w_DE. These definitions allow us to rewrite the Friedmann eq. (1.7) as

$$H^2(a) = H_0^2\left(\frac{\Omega_\mathrm{r}}{a^4} + \frac{\Omega_\mathrm{m}}{a^3} + \frac{1-\Omega_0}{a^2} + \Omega_\mathrm{DE}\exp\left[-3\int_0^a w_i(a')\, a'^{-1}\mathrm{d}a'\right]\right) \quad , \tag{1.19}$$

which implies how and when the different densities affect the expansion. Furthermore, inserting $a = 1$, we established the relation $K = H_0^2(\Omega_0 - 1)/c^2$ between the contents and the curvature In particular, a flat universe is equivalent to $\Omega_0 = 1$, i.e. the total density equals the critical density.

In the early phases of the Universe ($0 < a \ll 1$), because of its a^{-4}-dependence, Ω_r was the most important contribution, whereas it is negligibly small at the current epoch. At a certain a_eq, this radiation-dominated era was superseded by the matter-dominated era. Rather recently[2] on the cosmological timescale, Ω_DE became the dominant term in the composition of Ω_0. Finally, Eq. (1.19), via $H = \frac{1}{a}\frac{\mathrm{d}a}{\mathrm{d}t}$, leads to the relation between time and scale factor (here, for the cosmological constant case $w = -1$):

$$t(a) = \int_0^a \frac{\mathrm{d}a'}{a' H(a')} = \frac{1}{H_0}\int_0^a \mathrm{d}a' \left(\frac{\Omega_\mathrm{r}}{a'^2} + \frac{\Omega_\mathrm{m}}{a'} + (1-\Omega_0) + \Omega_\Lambda a'^2\right)^{-1/2} \quad . \tag{1.20}$$

The scale of the observable universe inside which events can be causally connected to the observer is given by the time-dependent comoving *horizon*

$$R_\mathrm{h} = \int_0^a \frac{c}{a'^2 H(a')}\mathrm{d}a' \quad . \tag{1.21}$$

1.1.3 Redshift and Distance Measures

For observational astronomers, the most tangible consequence of cosmic expansion is the resulting *redshift* of sources: owing to the expanding space during the time of its travel, light emitted at a wavelength λ_1 and time t_1 is observed with $\lambda_0 > \lambda_1$ at $t_0 > t_1$. Therefore, observing a redshifted spectral feature allows a simple determination of the scale factor at the time the light was emitted:

$$(1+z) := \frac{\lambda_0}{\lambda_1} = \frac{a(t_0)}{a(t_1)} = \frac{1}{a(t_1)} \quad . \tag{1.22}$$

Due to the non-Euclidean geometry of the curved space-time, there is no unique, unambiguous notion of "distance" between objects at cosmologically relevant scales. Observationally, the two most commonly used distance measures are the *angular diameter distance* $D_\mathrm{A}(z) = D/\vartheta = a(z) f_K(\chi)$, relating the angular size ϑ of a source to its (small) physical diameter D, and the *luminosity distance* $D_\mathrm{L}(z) = \sqrt{L/(4\pi S)}$, relating the flux S of a source to its intrinsic luminosity L. The two distances are connected by the following equation:

$$D_\mathrm{L}(z) = (1+z)^2 D_\mathrm{A}(z) = (1+z) f_K(\chi) \quad . \tag{1.23}$$

In the context of gravitational lensing, the angular diameter distance *between* a source at z_2 and a deflection point at z_1 with $z_2 > z_1 > 0$ will be of special importance:

$$D_\mathrm{A}(z_1, z_2) = a(z_2) f_K(\chi(z_2) - \chi(z_1)). \tag{1.24}$$

Because of the prefactor $a(z) = 1/(z+1)$, the angular diameter distance is not additive – $D_\mathrm{A}(z_1, z_2) \neq D_\mathrm{A}(z_2) - D_\mathrm{A}(z_1)$ – even in the flat case $f_K(\chi) = \chi$.

1.1.4 Dark Matter

One of the most intriguing features of the current "Concordance Cosmology" model is its prediction of ~ 80 % of its matter density Ω_m to be contributed by an unknown non-baryonic component not interacting with the electromagnetic field. The existence of this "Dark Matter" (DM) can be inferred from the several independent probes. As we will see in Sect. 1.3.1, the value of Ω_m can be inferred from the CMB (e.g., Larson et al. 2010), while Big Bang Nucleosynthesis predicts a significantly smaller cosmic density Ω_b of baryons (e.g., Tytler et al. 2000).

[2] This result has spawned philosophical debate as the *coincidence problem* of Dark Energy.

Dark Matter was first postulated by Zwicky (1933) who discovered that the Coma galaxy cluster could not form a gravitationally bound system if only consisting of the visible stellar matter. Also, rotation curves of spiral galaxies can be explained most easily if their DM halos contain an additional matter component which does not emit any electromagnetic radiation. In principle, these observations can be interpreted as a deviation of gravity from its Newtonian r^{-1} potential (e.g., Milgrom 1983; Bekenstein 2004). However, the eponymous concordance of cosmological probes testing different physics (e.g., Kowalski et al. 2008; Vikhlinin et al. 2009b; Komatsu et al. 2010) favours the simplest explanation of a universe dominated by non-baryonic *Cold Dark Matter* (CDM). Moreover, combined weak-lensing and X-ray observations of merging galaxy clusters (e.g., Clowe et al. 2006a; Mahdavi et al. 2007; Bradač et al. 2008b,a) strongly suggest that most of their matter content is collisionless, seriously challenging models relying on all or most gravitating mass being baryons.

1.2 Structure Formation

The observed foam-like cosmic web of voids and pronounced galaxy clusters connected by filaments has – according to the current model – evolved from a very homogeneous primordial state. Figure 1.1 depicts the result of a numerical simulation of this structure. Observational evidence is provided by the CMB which shows that the strongest anisotropies in the baryon density differed by only $\sim 10^{-5}$ at $z \approx 1100$. Driven by the DM anisotropies – already larger than $\sim 10^{-5}$ at $z \approx 1100$ – the primordial perturbations grew through gravitational instability by accreting matter from neighbouring regions experiencing a net gravitational attraction towards the overdense regions. The quantitative description of structure formation provides the basis for inferring cosmological parameters from the study of galaxy clusters.

1.2.1 Growth of Inhomogeneities

The suggested origin of primordial density perturbations is quantum mechanical fluctuations, which were strongly amplified during *inflation*, a period of very rapid expansion of the early Universe. Inflation was postulated to explain the overall homogeneity and apparent flatness of the Universe and is supported by indirect observational tests, e.g. from the CMB. It is convenient to describe the primordial perturbations by a *random density field* $\rho(t, \vec{x})$ in comoving coordinates (Sect. 1.1.2), following a Gaussian (or approximately Gaussian) statistic. Another useful quantity is the *density contrast* $\delta(t, \vec{x})$, i.e. the relative overdensity with respect to the mean density $\bar{\rho}(t)$:

$$\delta(t, \vec{x}) = \frac{\rho(t, \vec{x}) - \bar{\rho}(t)}{\bar{\rho}(t)}. \tag{1.25}$$

Neglecting pressure, and first considering perturbations on scales smaller than the the horizon R_h (Eq. 1.21), the motion of matter as a self-gravitating fluid is determined by the following three equations, the continuity, Euler, and Poisson equations:

$$\frac{\partial \delta(t, \vec{x})}{\partial t} + \frac{1}{a(t)} \vec{\nabla} \cdot [1 + \delta(t, \vec{x})] \vec{v}(t, \vec{x}) = 0 \quad , \tag{1.26}$$

$$\frac{\partial \vec{v}(t, \vec{x})}{\partial t} + \frac{\dot{a}(t)}{a(t)} \vec{v}(t, \vec{x}) + \frac{1}{a(t)} \left(\vec{v}(t, \vec{x}) \cdot \vec{\nabla} \right) \vec{v}(t, \vec{x}) = -\frac{1}{a(t)} \vec{\nabla} \Phi(t, \vec{x}) \quad , \tag{1.27}$$

$$\vec{\nabla}^2 \Phi(t, \vec{x}) = \frac{3 H_0^2 \Omega_\mathrm{m}}{2 a(t)} \delta(t, \vec{x}) \quad , \tag{1.28}$$

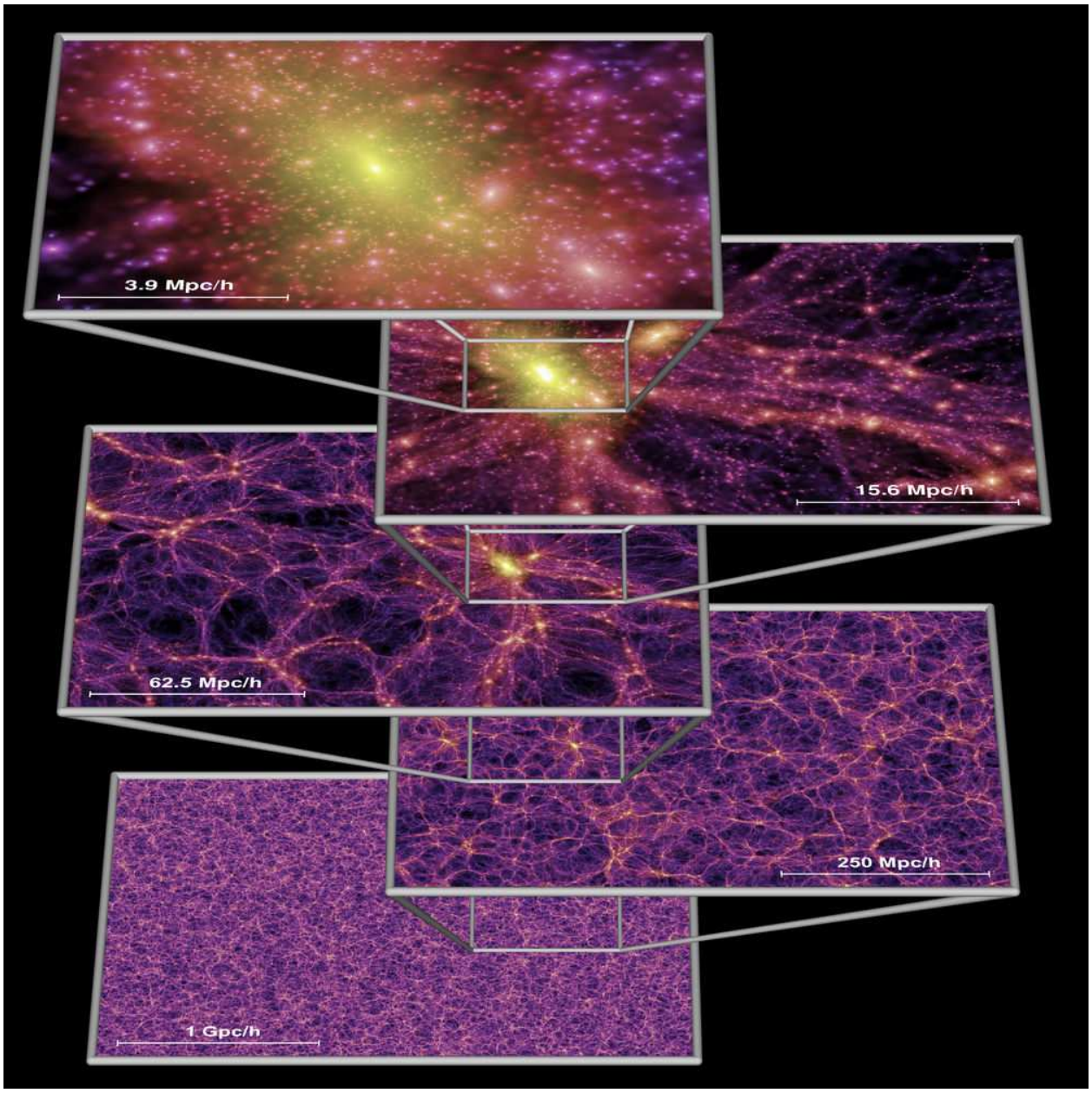

Figure 1.1: Structure formation resulting from a numerical simulation (Springel et al. 2005). From bottom to top a sequence of zoomed images is depicted, showing the transition from the isotropic, stochastic Dark Matter distribution on large scales to the concentrated halo of a galaxy cluster, forming impressive structure at the highest peaks of the matter distribution on smaller scales. Figure from Springel et al. (2005).

where the *peculiar velocity* $\vec{v}(t,\vec{x}) = 0$ vanishes for a comoving observer and the $\vec{\nabla}$ operator is defined with respect to comoving coordinates. Finally, $\Phi(t,\vec{x})$ denotes the gravitational potential in comoving coordinates. For the case of small overdensities $\delta(t,\vec{x})$ and velocities $\vec{v}(t,\vec{x})$, an analytic solution can be found by replacing Eqs. (1.26) and (1.27) by the linearised equations

$$\frac{\partial\delta(t,\vec{x})}{\partial t} + \frac{1}{a(t)}\vec{\nabla}\cdot\vec{v}(t,\vec{x}) = 0\,, \qquad \frac{\partial\vec{v}(t,\vec{x})}{\partial t} + \frac{\dot{a}(t)}{a(t)}\vec{v}(t,\vec{x}) = -\frac{1}{a(t)}\vec{\nabla}\Phi(t,\vec{x}) \quad , \tag{1.29}$$

and differentiating and rearranging the system of three differential equations gives:

$$\frac{\partial^2\delta(t,\vec{x})}{\partial t^2} + \frac{2\dot{a}(t)}{a(t)}\frac{\partial\delta(t,\vec{x})}{\partial t} - \frac{3H_0^2\,\Omega_\mathrm{m}}{2a^3(t)}\delta(t,\vec{x}) = 0 \quad . \tag{1.30}$$

Because the dependence on $\vec{x}$ in Eq. (1.30) is only implicit, each of the two independent solutions of Eq. (1.30) separate into a spatial and a temporal factor:

$$\delta(t,\vec{x}) = D_+(t)\Delta_+(\vec{x}) + D_-(t)\Delta_-(\vec{x}) \quad . \tag{1.31}$$

Via $a(t)$ and H(t), the exact form of the solutions $D_\pm(t)$, in which we are interested, depends on the cosmological model. However, as a general feature, only one temporal solution, $D_+(t)$, grows, while the other, $D_-(t)$, decays. In the absence of pressure, one can show that the *growth factor*

$$D_+(t) \propto H(t)H_0^2\int_0^a \frac{\mathrm{d}t'}{a^2(t')H^2(t')} \quad \Rightarrow \tag{1.32}$$

$$D_+(a) \propto \frac{H(t)}{H_0}\int_0^a \left(\Omega_\mathrm{r}a'^{-2} + \Omega_\mathrm{m}a'^{-1} + (1-\Omega_0) + \Omega_\Lambda a'^2\right)^{-3/2}\mathrm{d}a' \tag{1.33}$$

(here for $w_\mathrm{DE} = -1$) describes the growth of small-scale, small-amplitude density perturbations, such that

$$\delta(t,\vec{x}) = D_+(t)\,\delta(t=0,\vec{x}) \quad . \tag{1.34}$$

An homogeneous, isotropic Gaussian density field is completely defined by its *power spectrum*

$$P(k) = \langle|\tilde{\delta}(t,\vec{k})|^2\rangle \quad , \tag{1.35}$$

where $\tilde{\delta}(t,\vec{k})$ is the Fourier transform of $\delta(t,\vec{x})$ with the comoving wavevector $\vec{k}$. Thus, with $P_0(k) := P(t=0, k=|\vec{k}|)$, its evolution follows as:

$$P(t,k) = D_+^2(t)\,P_0(k) \quad . \tag{1.36}$$

The power spectrum is usually modelled as $P(k) \propto k^{n_\mathrm{s}}$. The *spectral index* n_s is measured to be close to the scale-invariant (Harrison-Zel'dovich) case of $n_\mathrm{s} = 1$, but slightly lower (e.g., Larson et al. 2010), confirming the prediction of inflation theory.

In a more realistic model, perturbations in the radiation, baryon, and CDM fluids can be calculated taking into account the respective pressure terms. In particular, the growth rate of perturbations depends on their scale length. Considering modes whose scale is comparable or larger than the horizon R_h (Eq. 1.21), relativistic effects have to be taken into account. Given the expansion of the Universe, for each length scale there exists an a_enter at which it will become smaller and "enter" the horizon. Perturbations of the radiation, DM, and baryon density fields experience different growth factors $D_+(t)$, determined by whether they enter the horizon in the radiation, matter, or Dark Energy dominated eras. The effect of the departures from the simple model outlined here on the power spectrum is expressed by introducing the *transfer function* $T(k)$, such that $P(t,k) \propto T^2(k)D_+^2(t)k^{n_\mathrm{s}}$. A particular consequence of coupling between overdensities in baryons and Dark Matter is baryonic acoustic oscillations.

1.2.2 Spherical Collapse and Halo Mass Function

Leaving the linear regime, structure formation cannot, in general, be calculated analytically, but instead requires extensive numerical simulations. The toy model of a spherical overdensity of constant mass M inside a radius $r(t)$, however, is analytically solvable, describing expansion to a maximal radius, followed by a collapse into a singularity. This spherical collapse model serves well for interpreting numerical results.

The spherical collapse model gives rise to two useful quantities: First, the overdensity $\delta_{\mathrm{c},0}$ for which, given linear growth of structure, a spherical perturbation would have collapsed at the present epoch. In a $\Omega_\mathrm{m}=1$, $\Omega_\mathrm{DE}=0$ (Einstein–de Sitter) universe, this value is $\delta_{\mathrm{c},0}=1.686$.

An even slightly asymmetric, realistic overdensity will not collapse into a single point but reach virial equilibrium with a finite orbital radius $r_\mathrm{vir}=G_\mathrm{N}M/(2E_\mathrm{kin})$ of its particles, where E_kin is the kinetic energy of the overdensity. This process is called violent relaxation. Thus, we can calculate the overdensity Δ_c (with respect to the critical density ρ_c) inside such a sphere where *virialisation* has taken place. The value of Δ_c depends on the cosmological parameters, and can be approximated for a flat universe by (Bryan & Norman 1998):

$$\Delta_\mathrm{c} = 18\pi^2 + 82(\Omega_\mathrm{m}-1) - 39(\Omega_\mathrm{m}-1)^2. \tag{1.37}$$

In turn, the matter within an overdensity exceeding Δ_c can be considered virialised, which we will use to define the extent of a galaxy cluster.[3]

The spherical collapse model can be applied to describe the properties of *Dark Matter halos*, often conceived as the building blocks of the cosmological matter distribution. Structure formation can then be parametrised by the evolving number density of virialised halos as a function of their mass M – the *halo mass function*. Generally, at all epochs low-mass halos are more abundant than massive ones, while all halos grow more massive with time. Based on the probability that, for a Gaussian random density field, a point lies within a region that will collapse into a virialised structure at a redshift $z(t)$, Press & Schechter (1974) derived an analytic expression for the halo mass function from the spherical collapse model. For its derivation we refer to, e.g., Voit (2005). The halo mass function commonly (e.g., Pillepich et al. 2010) takes the following form

$$\frac{\mathrm{d}n(M,z)}{\mathrm{d}M} = f(\sigma(M,z))\frac{\bar{\rho}_\mathrm{m}(z=0)}{M}\frac{\mathrm{d}\ln(\sigma^{-1}(M,z))}{\mathrm{d}M} \quad , \tag{1.38}$$

where $\bar{\rho}_\mathrm{m}(z=0)$ is the mean matter density in the Universe today. The quantity $\sigma(M,z)$ denotes the standard deviation of the underlying density field whose variance is related to the initial power spectrum by

$$\sigma^2(M,z) = \frac{D_+^2(z)}{2\pi^2}\int_0^\infty k^2 P_0(k)\tilde{W}(k,M)\,\mathrm{d}k \quad . \tag{1.39}$$

Here, $\tilde{W}(k,M)$ is the Fourier transform of a mass-dependent smoothing function with which the density field is filtered. Equation (1.39) is used to measure the normalisation of the power spectrum, which is a cosmological parameter not constrained *a priori* by theoretical models, via the quantity

$$\sigma_8 := \sigma(M_8, z=0) \quad , \tag{1.40}$$

where M_8 is the mass contained in a spherical volume using a smoothing length of $8h^{-1}\,\mathrm{Mpc}$. Here, the notation $h=H_0/(100\,\mathrm{km\,s^{-1}\,Mpc^{-1}})\approx 0.72$ has been introduced. Constraints on σ_8 can be derived from, e.g. the combination of *cosmic shear* (weak gravitational lensing by large-scale

[3] This is an order-of-magnitude definition. Commonly used values for virialised overdensities are $18\pi^2\approx 180$ or 200, whereas $\Omega_\mathrm{m}=0.3$ yields $\Delta_\mathrm{c}=100$.

structure) and CMB measurements (Fu et al. 2008; Schrabback et al. 2009) or the mass function of galaxy clusters (Vikhlinin et al. 2009b; Mantz et al. 2009b). For σ_8, too, recent determinations with different probes are in better agreement than measurements from a few years ago, measuring e.g. $\sigma_8 = 0.802^{+0.028}_{-0.029}$ (Schrabback et al. 2009).

The mass function is expressed in terms of the function $f(\sigma(M,z))$ in Eq. (1.38), for which the Press & Schechter (1974) ansatz yields:

$$f_{\mathrm{PS}}\left(\sigma(M,z)\right) = \sqrt{\frac{2}{\pi}}\frac{\delta_{\mathrm{c}}}{\sigma(M,z)}\exp\left(-\frac{\delta_{\mathrm{c}}^2}{2\sigma^2(M,z)}\right) \quad . \tag{1.41}$$

In addition to the analytical results by Press & Schechter (1974), the halo mass function has been investigated numerically, and fitting functions to the mass functions found in numerical simulations have been devised. The Sheth & Tormen (1999) mass function derives from a modified Press & Schechter (1974) formula, which in the notation by Pillepich et al. (2010) reads:

$$f_{\mathrm{ST}}\left(\sigma(M,z)\right) = A_{\mathrm{ST}}\sqrt{\frac{2a_{\mathrm{ST}}}{\pi}}\frac{\delta_{\mathrm{c}}}{\sigma(M,z)}\exp\left(-\frac{a_{\mathrm{ST}}\delta_{\mathrm{c}}^2}{2\sigma^2(M,z)}\right)\left[1+\left(\frac{\sigma^2(M,z)}{a_{\mathrm{ST}}\delta_{\mathrm{c}}^2}\right)^{p_{\mathrm{ST}}}\right] \quad , \tag{1.42}$$

with the parameters $A_{\mathrm{ST}} = 0.322$, $a_{\mathrm{ST}} = 0.707$, and $p_{\mathrm{ST}} = 0.3$. Jenkins et al. (2001) find a simpler empirical fit to their simulations:

$$f_{\mathrm{J}}\left(\sigma(M,z)\right) = A_{\mathrm{J}}\exp\left(-\left|\ln\sigma(M,z)^{-1} + B_{\mathrm{J}}\right|^{p_{\mathrm{J}}}\right) \quad , \tag{1.43}$$

whose parameters are $A_{\mathrm{J}} = 0.315$, $B_{\mathrm{J}} = 0.61$, and $p_{\mathrm{J}} = 3.8$. Recently, Tinker et al. (2008) proposed the following fit to the empirical mass function:

$$f_{\mathrm{T}}\left(\sigma(M,z)\right) = A_{\mathrm{T}}\left[1+\left(\frac{\sigma(M,z)}{b_{\mathrm{T}}}\right)^{a_{\mathrm{T}}}\right]\exp\left(-\frac{c_{\mathrm{T}}}{\sigma(M,z)}\right) \quad , \tag{1.44}$$

where the parameters, A_{T}, a_{T}, b_{T}, c_{T} are functions of the overdensity Δ and redshift z.

Via the dependence of the growth factor on cosmology (Eqs. 1.39 and 1.32), the halo mass function sensitively depends on cosmological parameters. This forms the basis for probing cosmology with the *galaxy cluster mass function* discussed in detail in Sect. 2.2, because galaxy clusters evolve out of the most pronounced peaks in the density fluctuation field as has been well established in numerical simulations (e.g. Springel et al. 2005).

1.2.3 Galaxy Formation

Structure formation as discussed hitherto is mainly driven by Dark Matter, whose purely gravitational interaction can be modelled relatively easily in numerical simulations. From an observational astrophysicist's perspective, the question how galaxies form and evolve (passively by accretion and by merging) in the framework of hierarchical structure is of equal importance. Describing the multitude of baryonic effects that have to be taken into account empirically and modelled semi-analytically is beyond the scope of this thesis.

1.3 The ΛCDM Universe

1.3.1 Values of the Density Parameters

We will now present current status of knowledge on the values of the density parameters, in the framework of "Concordance Cosmology". The most recent CMB results on cosmological parameters, after seven years of integration with the *WMAP* satellite, are presented by Larson et al.

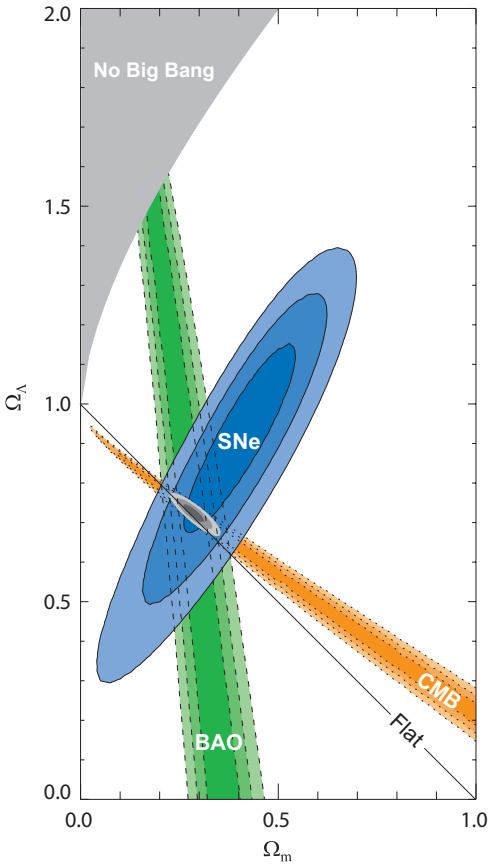

Figure 1.2: The cosmological parameter space spanned by Ω_m and Ω_Λ. Flat cosmologies and those without a Big Bang (ruled out by observations) are indicated. Contours give the 3σ, 2σ, and 1σ confidence levels obtained from the CMB (orange, Dunkley et al. 2009), baryonic acoustic oscillations (BAOs, green, Eisenstein et al. 2005), and supernovae (blue, Kowalski et al. 2008), assuming $w = -1$ for Dark Energy. Note that *all three* independent probes intersect with each other giving the grey, combined contours around $\Omega_m \approx 0.3$ and $\Omega_\Lambda \approx 0.7$, consistent with a flat universe. Figure from Kowalski et al. (2008).

(2010) and Komatsu et al. (2010). Cosmological constraints are drawn from the *power spectrum* of CMB temperature fluctuations which due to the physics of structure formation (Sect. 1.2) exhibits a clear series of peaks, i.e. preferred distance scales on which perturbations are present. The positions and amplitudes of these peaks are sensitive to changes in the cosmological parameters (e.g. Hu & Dodelson 2002).

The measured CMB power spectrum is in good agreement with a *flat universe*. Thus, most models assume $\Omega_0 = 1$ from the beginning. CMB data clearly suggest the dominant component to be $\Omega_\Lambda = 0.734 \pm 0.029$ (Larson et al. 2010). We will discuss *Dark Energy* in Sect. 1.3.2. The CMB peaks allow us to distinguish between baryonic matter (atoms in galaxies) and *Cold Dark Matter* (CDM), interacting with baryonic matter only via gravitation. Larson et al. (2010) find $\Omega_b = 0.045 \pm 0.003$ for baryons and $\Omega_c = 0.222 \pm 0.026$ for Dark Matter, where $\Omega_m = \Omega_b + \Omega_c$. Due to its rapid decay with a, Ω_r is negligibly small in the current universe.

As mentioned before, the current cosmological model, termed ΛCDM for its two main components, the Cosmological Constant and Cold Dark Matter, is supported by *independent* probes. Thus, combining the results of these probes leads to more accurate determinations of cosmological parameters. Figure 1.2 shows how constraints on Ω_m and Ω_Λ from the CMB (Dunkley et al. 2009), SNe Ia (Kowalski et al. 2008, Sec. 1.3.2), and *baryonic acoustic oscillations* (BAOs, Eisenstein et al. 2005) complement each other. BAOs are the remnants of sound waves caused by a preferred length-scale in structure formation (Sect. 1.2). From the combination shown in Fig. 1.2, Kowalski et al. (2008) determine $\Omega_\Lambda = 0.713^{+0.024+0.036}_{-0.029-0.039}$ and $\Omega_m = 0.274^{+0.016+0.013}_{-0.016-0.012}$, where the first error is the statistical one and the second the systematic error.

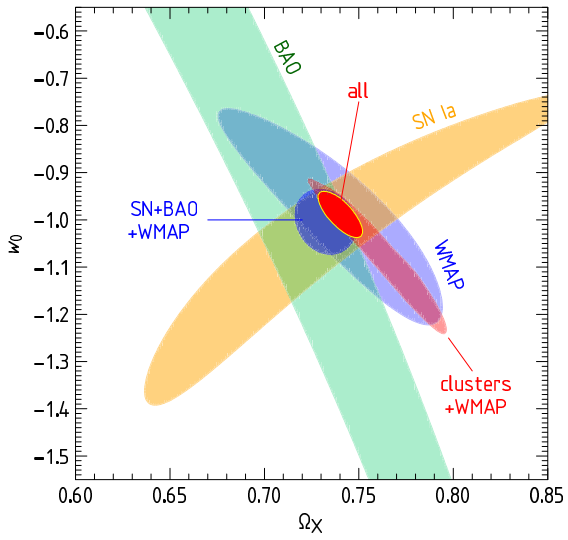

Figure 1.3: Constraints (1σ confidence contours) on the Dark Energy parameters $\Omega_X = \Omega_{DE}$ and w_0, from different probes by assuming a flat universe: SN Ia (Davis et al. 2007), BAOs (Percival et al. 2007), and the CMB (Komatsu et al. 2009). The red area shows the combined contours including constraints from the cluster mass function (Vikhlinin et al. 2009b). Figure from Vikhlinin et al. (2009b).

1.3.2 The Case for Dark Energy

Having been discarded by Einstein shortly after its introduction when Hubble discovered the expanding universe, the term Λ in the Friedmann Eq. (1.7), re-entered the stage of cosmology by another revolutionary discovery: Riess et al. (1998) and Perlmutter et al. (1999) independently found evidence for an *accelerating expansion* of the Universe from the observations of type Ia supernovae. This class of supernovae is commonly interpreted as being caused by exploding white dwarfs which, accreting material from a companion star, increase their mass beyond the critical Chandrasekhar limit for a degenerate plasma. This mass limit, only weakly dependent on factors like element abundance ratios, allows the use of SNe Ia as *standard candles*, i.e. sources of intrinsically constant luminosity. Although their maximum luminosity does vary to some degree, SNe Ia can indeed be used for cosmological distance measurements to redshifts $z \gtrsim 1$.

The accelerated expansion has since then been confirmed in subsequent studies using various cosmological probes (e.g., Kowalski et al. 2008; Vikhlinin et al. 2009b; Schrabback et al. 2009; Komatsu et al. 2010, cf. Figs. 1.2 and 1.3). The nature of Dark Energy is still unknown, nevertheless numerous ideas have been put forward based on various theoretical concepts (vacuum energy, cosmological scalar fields, etc.). The first question to answer is whether we actually observe the time-invariant Einsteinian cosmological constant with $w_\Lambda = -1$ or an evolving Dark Energy whose equation of state $-\frac{1}{3} > w(a=1)$ changes with time. Interestingly, currently the best constraints are consistent with the cosmological constant case[4]: Komatsu et al. (2010), combining *WMAP* data with BAO measurements (Percival et al. 2010), and H_0 determined by Riess et al. (2009), arrive at $w = -1.10 \pm 0.14$. Vikhlinin et al. (2009b), combining their measurements of the cluster mass function, yielding $w = -1.14 \pm 0.21$ alone, with *WMAP*, BAO, and SN Ia data, constrain Dark Energy to $w = -0.991 \pm 0.045 \pm 0.04$ (Fig. 1.3). Using a slightly different approach relying on the mass function of galaxy clusters (Sect. 2.2.1) measured via their gas mass fraction (Sect. 2.2.2), Mantz et al. (2009b) found $w = -1.01 \pm 0.20$. Frieman et al. (2008) provide an overview on the discovery history of Dark Energy and the different probes currently being used to constrain Ω_{DE} and w. Considered as one of the most important open questions of modern cosmology, numerous experiments are planned to further constrain Dark Energy parameters. With a special regard to satellite missions, the potentials of the various techniques are discussed and compared by Peacock et al. (2006) and Albrecht et al. (2006).

[4]Therefore, we use Ω_Λ to describe the corresponding energy density, e.g. in Sect. 1.3.1.

Chapter 2

Clusters of Galaxies

2.1 Clusters from Abell to Zwicky and far Beyond

Galaxies are not distributed randomly in the Universe, but form a "sponge-like" structure of clusters, filaments, and voids, observed in the three-dimensional galaxy distribution, e.g. from the Two Degree Redshift Survey (Peacock et al. 2001) or the Sloan Digital Sky Survey (SDSS, Tegmark et al. 2004; Gott et al. 2005). This clustering is a natural consequence of structure formation (Sect. 1.2). The first observation of a galaxy cluster even predates the modern concept of a galaxy: The Virgo cluster, the most nearby cluster, contains many bright galaxies which already were listed by Messier who in the late 18^{th} century noted a high density of "nebulæ" ("clouds") in Virgo.

The earliest method of identifying galaxy clusters as overdensities in the projected density distribution on the sky continues to be productive and has yielded the important catalogues of Abell (1958) on the northern and Abell et al. (1989) on the southern hemisphere. Although galaxies in clusters account for only a small fraction of the total matter, they are numerous and impressive objects themselves, in particular the brightest cluster galaxies (BCGs) often located near the centre of the potential well of the cluster.

In addition to galaxies, clusters contain luminous matter in the form of stars not bound to any of the galaxies but only to the cluster potential which emit the "intracluster light". The majority of cluster baryons, however, compose the diffuse ($n \lesssim 0.1$ particles cm^{-3}) and hot ($T \approx 10^7$–10^8 K) *intracluster medium* (ICM). Owing to its temperature, the ICM is a strong emitter of thermal X-ray bremsstrahlung, so that clusters are regularly detected as extended X-ray sources.

Approximately tracing the cosmic baryon fraction (Sect. 2.2.2), 80–90 % of the mass in galaxy clusters is contributed by their Dark Matter halo, formed from a primordial overdensity in the Dark Matter distribution and continuously growing by accretion and merger processes with neighbouring halos in the large-scale structure (LSS). Cluster masses in the local universe range between $10^{14}\,\mathrm{M}_\odot$ and $10^{15}\,\mathrm{M}_\odot$, with a mass function increasing towards lower masses where objects $\approx 10^{13}\,\mathrm{M}_\odot$ are considered *galaxy groups*. In the remainder of this section, we will give a brief overview of the most important properties of galaxy clusters in the optical, X-ray, and radio wavelength regimes, partly based on Reiprich (2009a,b). Gravitational lensing techniques are discussed separately in Chapter 3.

2.1.1 Optical Cluster Detection

The classical method of optical cluster detection applied by Abell (1958) and Abell et al. (1989) is based on counting galaxies inside a certain aperture radius on the sky and magnitude bin and defining a "richness" criterion for a cluster of galaxies. The resulting cluster catalogues continue to be an important reference for nearby ($z \lesssim 0.2$) clusters. However, projections of physically

unrelated LSS pose a severe contamination problem in projected galaxy count techniques, and methods have been devised to overcome that problem. Matched filters suppress chance alignments by taking into account additional information such as the typical radial distribution of galaxies in clusters and the galaxy luminosity function (e.g., Postman et al. 1996). *Distance information* from spectra or galaxy colours is an important ingredient in optical cluster detection which many of the recent detection techniques (e.g., Miller et al. 2005; Koester et al. 2007; Milkeraitis et al. 2009) incorporate.

There are numerous effects related to galaxy cluster colours and, closely connected, morphology. The ratio of spheroidal to spiral galaxies increases with galaxy density in the environment (morphology–density relation). Not only are clusters populated preferentially by galaxy types with on average redder colours, also the colours of cluster late-type galaxies are redder than those in the field. These observations can be explained by ram-pressure stripping whereby gas is stripped from the galaxies and falls into the cluster potential cutting off the gas supply for further star formation. Dominated by old, red stellar populations (e.g., Bower et al. 1992), cluster galaxies represent the reddest galaxies observed at a given redshift. They are considered to be the most gas-depleted systems showing very similar colours over a large range in magnitude (Gladders et al. 1998). Observationally, this *cluster red sequence* currently is one of the most prolific methods in identifying clusters of galaxies in the optical band (e.g., Gladders & Yee 2000, 2005). Red sequence techniques are restricted to a redshift range $z < 1$, where the above statements on galaxy colours hold. At intermediate to high redshifts, intrinsic galaxy colours are observed to become more gas-rich and blue (Butcher & Oemler 1978). This Butcher-Oemler effect can be related to the significant increase with z of the fraction of clusters undergoing a merger, as it is observed in simulations (e.g., Cohn & White 2005). It can be interpreted as the gas depletion resulting in red intrinsic colours not being completed in cluster galaxies at higher redshifts.

Finally, optical spectroscopy provides insight into the velocity distribution of galaxies in clusters. Investigating the dynamics of cluster galaxies can be used to confirm the presence of an optically detected cluster, and furthermore to determine cluster masses (e.g., Rines et al. 2007).

2.1.2 The X-ray View on Clusters

The X-ray emission from the ICM was discovered early in the history of X-ray astronomy; a historic overview on X-ray cluster astronomy is given by Edge (2004). Today, many X-ray selected cluster samples are in use, most of them ultimately based on data obtained with the ROSAT satellite (e.g., Ebeling et al. 2000, 2010; Böhringer et al. 2000, 2004). The X-ray selected *400d* catalogue from which the clusters analysed in this thesis are selected, will be introduced in more detail in Chapter 4. Detecting clusters by their X-ray emission takes the advantage of the ICM effectively tracing the presence of a potential well to which it is bound. X-ray detection is to good approximation free of false detections due to projection effects, because the bolometric bremsstrahlung emissivity is proportional to the square of the electron and hence the gas density:

$$\epsilon_{\mathrm{bol}}^{\mathrm{ff}} \propto \sqrt{T_{\mathrm{e}}}\, n_{\mathrm{e}}^2. \tag{2.1}$$

The free-free process dominates the X-ray emissivity for ICM with temperatures $k_{\mathrm{B}} T_{\mathrm{e}} \gtrsim 2\,\mathrm{keV}$ which is the case for massive clusters discussed in this thesis. For the emissivity in the 0.1–2.4 keV energy band, the temperature dependence in Eq. (2.1) is negligible.

Current X-ray observatories such as XMM-NEWTON, CHANDRA, or SUZAKU allow us to study the ICM in great detail. For fitting the ICM density profile $\rho_{\mathrm{g}}(r)$, usually spherical symmetry and often so-called β-models (Cavaliere & Fusco-Femiano 1978) are assumed:

$$\rho_{\mathrm{g}}(r) = \rho_{\mathrm{g},0} \left(r^2 / r_{\mathrm{c}}^2 + 1 \right)^{-3\beta/2} \quad , \tag{2.2}$$

where $\rho_{g,0}$ is the central density, r_c a core radius, and the exponent β is related to the ratio of the specific kinetic energies of galaxies and ICM. In addition, X-ray spectra yield the ICM temperature (and temperature profile $T_X(r)$ for nearby clusters) and its elemental composition.

An important application of X-ray data is the determination of the total cluster mass via ICM thermodynamics (e.g., Sarazin 1988). Assuming spherical symmetry and the absence of magnetic or other external fields besides gravity, the ICM rests in *hydrostatic equilibrium* in the gravitational potential Φ. In this case, the Euler equation reduces to a purely radial dependence and yields

$$\frac{1}{\rho_g}\frac{dP}{dr} = -\frac{d\Phi}{dr} = -\frac{G_N M(<r)}{r^2} \quad , \tag{2.3}$$

where on the right-hand side the Poisson equation $\vec{\nabla}^2\Phi = 4\pi G_N \rho_{tot}$ relating Φ and total mass density ρ_{tot} as well as Gauss's divergence theorem have been applied. The term $M(<r)$ in Eq. (2.3) denotes the mass inside the radius r. Assuming an ideal gas of mean molecular weight μ, its pressure is given by $P = \rho_g k_B T_g/(\mu m_p)$, where m_p denotes the proton mass and T_g the gas temperature. Introducing the final assumption that μ and thus the elemental composition is independent of r, we insert this relation into Eq. (2.3) and obtain the expression

$$M(<r) = \frac{-k_B T_g(r) r}{\mu m_p G_N}\left(\frac{d\ln\rho_g}{d\ln r} + \frac{d\ln T_g}{d\ln r}\right) \tag{2.4}$$

for the hydrostatic mass $M(<r)$, indicating its dependence on both the density and temperature profiles which can be determined from X-ray data. Limitations and extensions to this idealised model for X-ray mass determination are discussed in Chapter 8.

2.1.3 The Sunyaev-Zel'dovich Effect

Clusters of galaxies are visible in radio wavelengths for several reasons: First, their central galaxies often host active galactic nuclei (AGN) which are powerful radio emitters and are likely to play an important role in re-heating the ICM in the cluster centres, balancing the depletion of the ICM by cooling flows (e.g., Sijacki et al. 2008; Mittal et al. 2009; Hudson et al. 2010).

The second important process is the Sunyaev-Zel'dovich effect (SZE, Sunyaev & Zel'dovich 1970), which is inverse Compton scattering of CMB photons by thermal ICM electrons in galaxy clusters along the line-of-sight, modifying the CMB spectrum. For the observationally relevant Rayleigh-Jeans regime of the CMB blackbody spectrum, the relative temperature change is given by

$$\frac{\Delta T_{SZE}}{T_{CMB}} = -2y_C = -2\int n_e \frac{k_B T_e}{m_e c^2}\sigma_T \, d\ell, \tag{2.5}$$

where $\sigma_T = 8\pi e^4/(3m_e^2c^4)$ is the electron's Thomson cross-section, and the integration over ℓ runs along the line-of-sight. The important fact is that y_C is proportional to both the temperature T_e and density n_e, but independent of the cluster redshift z. For frequencies $< 218\,\mathrm{GHz}$, the wavelength dependence of the SZE signal results in a decrement, i.e. a reduction in CMB intensity, as the signature of a SZE cluster, while for higher frequencies an increment is detected. The related signal observed with a mm-radiation telescope is then proportional to the SZE cross-section $Y_{SZ} = D_d^{-2}\int y_C \, dA$, where A is the area on the sky covered by the cluster.

The SZ effect was first observed by Gull & Northover (1976), but only later detailed cluster studies became feasible (e.g., Birkinshaw et al. 1991; Rephaeli 1995; Carlstrom et al. 2001), and cosmological studies of samples (e.g., Grego et al. 2001; Halverson et al. 2009; Nord et al. 2009) became feasible. Staniszewski et al. (2009) reported the first SZE-selected cluster which was confirmed later (McInnes et al. 2009) with other methods. Vanderlinde et al. (2010) detected further SZE clusters and use their cluster catalogue to constrain cosmological parameters. Detailed reviews of the SZE are provided by, e.g. Birkinshaw (1999) and Carlstrom et al. (2002).

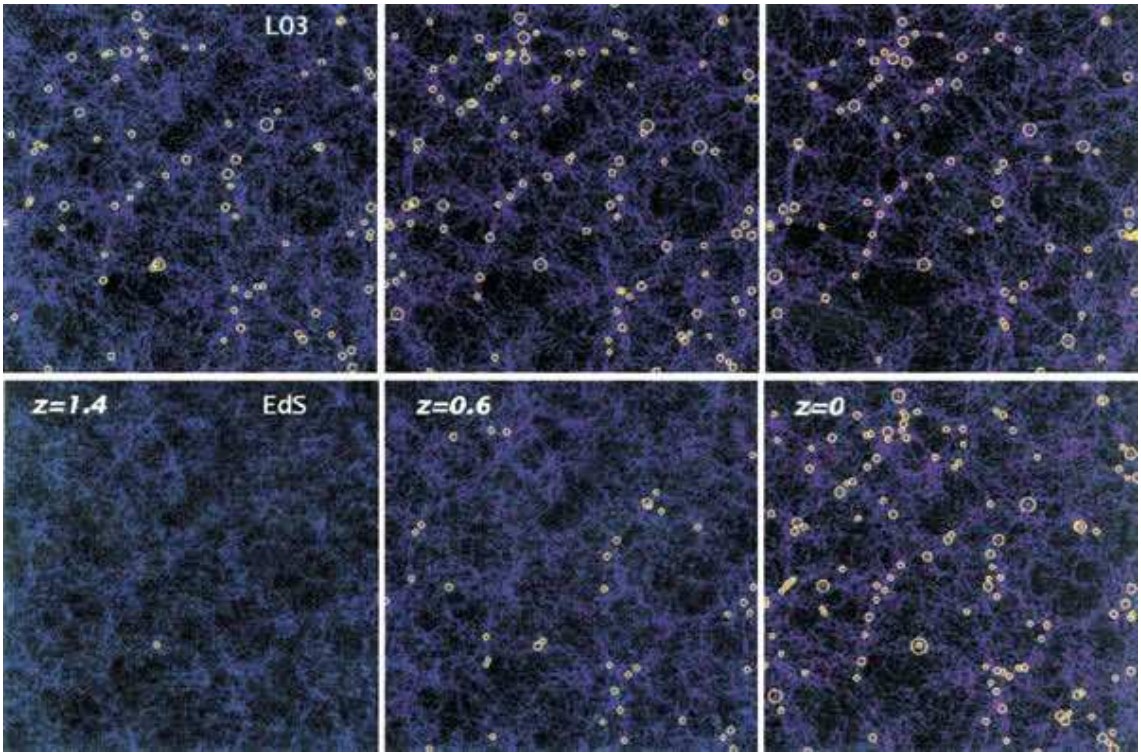

Figure 2.1: The evolution of galaxy clusters for two different cosmologies: Concordance model ($\Omega_{\rm DE} = 0.7$, $\Omega_{\rm m} = 0.3$; upper panels) and Einstein–de Sitter ($\Omega_{\rm DE} = 0.0$, $\Omega_{\rm m} = 1.0$; lower panels). In a simulation of structure formation (Borgani & Guzzo 2001), clusters have been identified (yellow circles) at $z = 1.4$, $z = 0.6$, and $z = 0.0$ (from left to right). At high z, the number of clusters is significantly larger in (more realistic) cosmologies with smaller $\Omega_{\rm m}$, e.g., the Concordance model. Figure from Borgani & Guzzo (2001).

2.2 Clusters as Cosmological Probes

2.2.1 The Cluster Mass Function

As already outlined in Sect. 1.2, clusters of galaxies are the largest virialised overdensities resulting from cosmological structure formation, and provide important questions and answers to cosmology. The cluster mass function $n(M, z)$ sensitively depends on both cosmic expansion and the evolution of structure by gravitational collapse (cf. e.g., Rosati et al. 2002; Voit 2005; Schuecker 2005, for detailed reviews). Therefore, mass functions derived from representative cluster samples are frequently used to determine cosmological parameters such as $\Omega_{\rm m}$, $\Omega_{\rm DE}$, or σ_8. In addition, measurements of the mass function at different redshifts constrain the value and possible evolution in the Dark Energy equation-of-state $w_{\rm DE}$ (Sect. 1.3.2).

The effects of $\Omega_{\rm m}$ and $\Omega_{\rm DE}$ on the evolution of the cluster mass function compared to the present epoch is counter-intuitive and thus notable (Eke et al. 1996): At higher matter densities, structures develop more quickly, leading to stronger evolution in the mass function at a given epoch. Therefore, in a universe with higher $\Omega_{\rm m}$, e.g. in an Einstein–de Sitter cosmology, we expect fewer high-redshift clusters than in a universe with low $\Omega_{\rm m}$ (Figs. 2.1 and 2.2). This results from the normalisation to the same statistical properties of the LSS today, which is the fixed standard against which observations are calibrated. Hence, the same setup is reproduced in the simulations (Borgani & Guzzo 2001) shown in Fig. 2.1 (right panels).

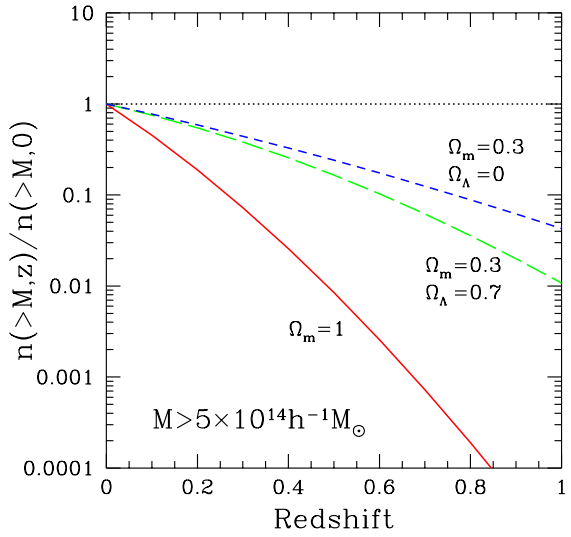

Figure 2.2: The number density of massive ($M > 5 \times 10^{14}\,h^{-1}\,\mathrm{M}_\odot$) galaxy clusters for different cosmologies, normalised to unity at the current epoch. In the Concordance Cosmology (green long-dashed line), structure formation is slower than in Einstein–de Sitter (red solid line, also cf. Fig. 2.1) but faster than in an open universe with $\Omega_\mathrm{m} = 0.3$, $\Omega_\mathrm{DE} = 0.0$ (blue short-dashed line). Furthermore, $\sigma_8 = 0.5$ has been chosen for the Einstein–de Sitter model and $\sigma_8 = 0.8$ for the other two cases. Note that the dependence of the number density of massive clusters on cosmology is stronger at higher redshifts. Figure from Rosati et al. (2002).

Indeed, the existence of rather massive galaxy clusters that were observed out to $z \approx 1.4$ (e.g., Stanford et al. 2006; Rosati et al. 2009) already puts tight constraints on Ω_m, ruling out high values. Observations of X-ray clusters contributed important evidence resulting in the paradigm shift from favouring the Einstein–de Sitter to the concordance model including Dark Energy. Reiprich (2006) noted the sensitivity of the measured cluster mass function to discriminate between relatively small changes in Ω_m and σ_8 from an update of the best-fit *WMAP* model.

Similarly, the fact that, given the same Ω_m, a Universe with higher Ω_DE exhibits a stronger evolution in the mass function, i.e. *less* massive galaxy clusters at a given $z > 0$ (Fig. 2.2) can be explained by the normalisation to the amount of structure we observe today. The underlying reason is the different recent expansion history of the Universe influencing $\Omega_\mathrm{m}(z)$: Because the greater expansion in a universe with larger Ω_DE or more negative w_DE counteracts structure formation, structures had to grow faster in the past to arrive at the same present level. This dependence is illustrated in Fig. 2.3 which shows the redshift evolution in Ω_m and Ω_DE for four different cosmologies, highlighting how Ω_m begins to decrease at slightly different redshifts for models with a different DE equation-of-state w_DE, which leads to a deceleration in the growth of structure.

2.2.2 Mass Proxies and Scaling Relations

Definition of Cluster Mass Almost all cosmological applications of clusters require the total mass to be known very accurately. There exists no *a priori* "true" mass of a galaxy cluster, because no unambiguous cluster boundary can be defined, as both observations and numerical simulations show (e.g., White 2001). Virialisation (Sect. 1.2.2) in principle provides a criterion of how to distinguish the cluster interior from its surroundings. But virialisation, in particular of unknown Dark Matter particles, cannot easily be inferred directly from observables, nor does it define a simple (e.g. spherical) cluster surface. In practice, *overdensity radii* with respect to a measured or assumed density profile are used. The radius r_Δ is defined such that $M_\Delta := M(< r_\Delta)$, the enclosed mass, satisfies

$$\frac{3M_\Delta}{4\pi r_\Delta^3} = \Delta\rho_\mathrm{c} \quad , \tag{2.6}$$

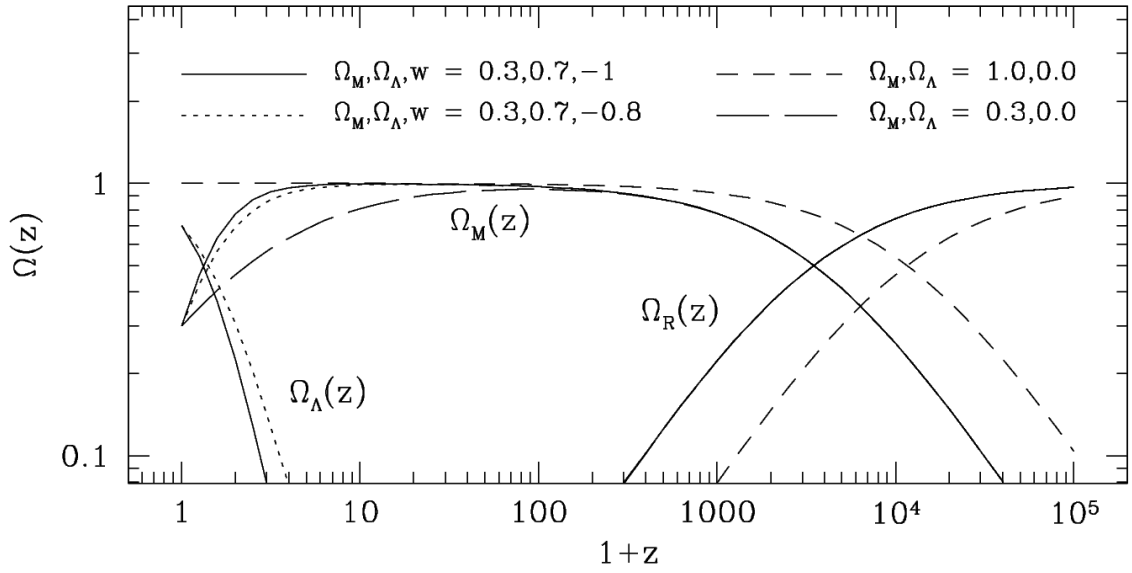

Figure 2.3: Evolution of the radiation, matter, and Dark Energy densities $\Omega_r(z)$, $\Omega_m(z)$, and $\Omega_{DE}(z)$ – termed Ω_Λ – with redshift for different cosmologies defined by the present-day values for Ω_m, Ω_{DE}, and w_{DE}. Note the logarithmic scales on both axes. This figure illustrates the relation between $\Omega_m(z)$ and the DE parameters at late times, when larger Ω_{DE} or more negative w_{DE} today imply a higher Ω_m in the past and, thus, more rapid structure formation. Figure from Voit (2005).

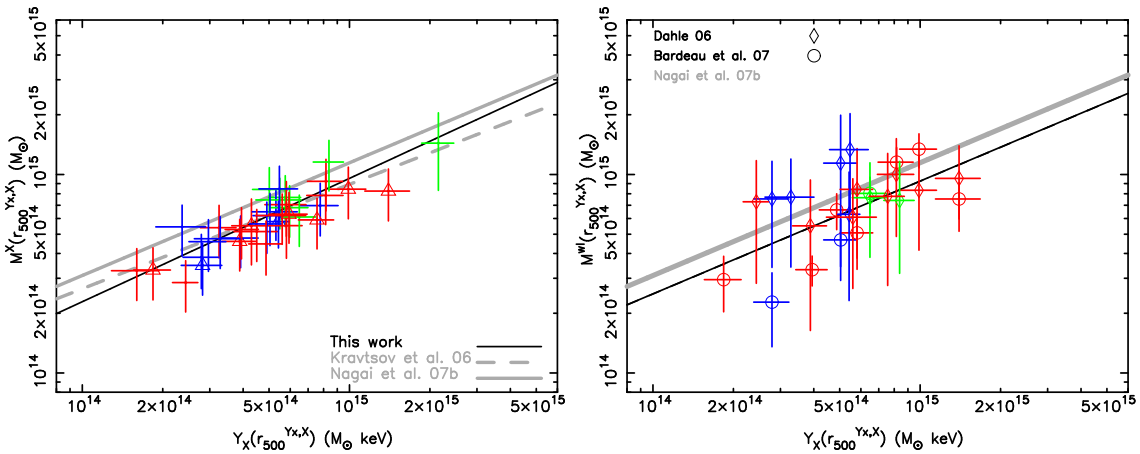

Figure 2.4: Example for a scaling relation, showing the relation between Y_X, measured within r_{500}, and $M(r_{500})$ as measured from X-ray (left panel) and weak lensing data (right panel). The coloured data points correspond to measurements from a sample of X-ray luminous $0.15 < z < 0.3$ clusters which is unbiased with respect to cluster morphology. Clusters are sorted in morphology bins denoted by the different colours, while triangles in the left panel indicate the presence of a cool core. Weak lensing clusters analysed by Dahle (2006) and Bardeau et al. (2007) are indicated in the right panel. The best-fit scaling relations by Zhang et al. (2008) (thin solid black line) and Kravtsov et al. (2006) (thick solid grey line) using X-ray masses are compared to the one by Nagai et al. (2007a) (thick dashed grey line), using weak-lensing masses. In the right panel, slopes are fixed to simulation results. Figure adapted from parts of Fig. 9 in Zhang et al. (2008).

where Δ is the overdensity factor with respect to the critical density ρ_c, whose choice in practice depends on the mass observable and application. See e.g., Vikhlinin et al. (2009a) for X-ray observables and Okabe et al. (2009) for a detailed study on the optimal range of Δ for several weak-lensing mass determination techniques.

Scaling Relations We will now focus on how cluster masses are inferred from the accessible observables, in particular X-ray observables, which are most commonly used. Direct application of Eq. (2.4) requires a sufficiently large number of detected X-ray photons to obtain a density and, if possible, also temperature profile by spectral fitting. For large samples of high-redshift ($z \gtrsim 0.5$) X-ray clusters, it is currently not possible to carry out deep enough follow-ups with high enough resolution. *Scaling relations* between an observable which can be measured to a good accuracy even with only a small number of photons and the total cluster mass come to the rescue and serve as a proxy. Because using scaling relations allows us to draw cosmological conclusions from large statistical samples, most cosmological constraints from X-ray clusters involve scaling relations. Despite its great advantage, this indirect method comes at the cost of having to assume how the respective scaling relations evolve with z. These evolutionary effects have not been well tested yet. The relations involving low scatter proxies, such as the gas mass $M_{\rm gas}$ or $Y_{\rm X} = T_{\rm X} M_{\rm gas}$, are of particular interest to high-precision cluster cosmology. Figure 2.4 shows examples for scaling relations analysed by Zhang et al. (2008).

Self-Similar Scaling Both observed and simulated scaling relations are well-fitted by power laws in most cases. This behaviour is expected from the simple model of *self-similar* scaling, postulating that "all clusters should look the same" when properly re-scaled for their mass. From $M_{\rm tot} \propto R^3$ with a characteristic cluster radius R and the virial equilibrium $T_{\rm X} \propto M_{\rm tot}/R$, the prediction for the relation between the global temperature and mass $T_{\rm X}$–$M_{\rm tot}$ follows automatically as

$$M_{\rm tot} \propto T_{\rm X}^{3/2} \quad . \tag{2.7}$$

Further reasoning along these lines yields the expected power-law slopes $L_{\rm bol} \propto M_{\rm tot}^{4/3}$ for the bolometric and $L_{\rm X} \propto M_{\rm tot}$ for the X-ray luminosity in the 0.1–2.4 keV "ROSAT" energy band. Self-similar scaling provides a sensible starting point for more complex models of observed clusters.

X-ray Luminosity and ICM Temperature The cluster *X-ray luminosity* $L_{\rm X}$, measured by counting photons in the ROSAT band, was inferred by e.g., Reiprich & Böhringer (2002), and used to calculate the mass function and constrain cosmological parameters (e.g., Schuecker et al. 2003; Mantz et al. 2008). Conversely, Stanek et al. (2006) inferred $L_{\rm X}(M_{\rm tot})$ given the cosmology.

The $M_{\rm tot}$–$T_{\rm X}$ relation shows relatively low scatter for relaxed clusters, but is sensitive to mergers (e.g., Vikhlinin et al. 2006; Zhang et al. 2008). Dependencies of the resulting mass on different temperature estimators (Rasia et al. 2005) and the choice of the radial range (Vikhlinin et al. 2009a) need to be considered. Thus, the low-scatter proxies are becoming more important.

The Gas Mass Fraction Because of the sensitive dependence of X-ray emissivity on the squared electron number density $n_{\rm e}^2$, compared to its weak dependence on $T_{\rm X}$, (Eq. 2.1) cluster density profiles can be inferred accurately, and hence, the total mass $M_{\rm gas}$ in the ICM. The *gas mass fraction*

$$f_{\rm gas} = \frac{M_{\rm gas}}{M_{\rm tot}} \approx \frac{\Omega_{\rm b}}{\Omega_{\rm m}} \approx \frac{1}{6} \tag{2.8}$$

is found to vary little from cluster to cluster in simulations, rendering $M_{\rm gas}$ a good proxy for the total cluster mass. Given the strong BBN constraints on $\Omega_{\rm b}$, $f_{\rm gas}$ measurements provided important

evidence for $\Omega_m \ll 1$ (White et al. 1993). However, the baryon fraction in clusters is reduced significantly compared to the cosmic average probed by the CMB, as confirmed by measurements both from X-ray emission and the SZE (e.g., LaRoque et al. 2006). The nature of this depletion is still unclear. the "missing baryons" problem rests to be solved. Furthermore, the observed trend for a higher baryon fraction in more massive clusters (e.g., Vikhlinin et al. 2006) should be taken into account before f_{gas} can be used to constrain cosmological parameters (Vikhlinin et al. 2009a). To this end, we note that M_{gas} and Y_X are considered to be the most promising total mass proxies.

The Y_X Estimator The quantity $Y_X = T_X M_{gas}$ has been suggested to construct an observable similar to Y_{SZ} (Sect. 2.1.3) from X-ray data to facilitate comparisons with the SZE. Simulations by Nagai et al. (2007b) show a tight correlation between this new proxy and the total mass (Kravtsov et al. 2006). The 7.1 % scatter in the M_{tot}–Y_X relation is smaller than the scatter Kravtsov et al. (2006) found for the scaling relations of its components, 19.5 % for M_{tot}–T_X and 10.7 % for M_{tot}–M_{gas}, evaluated at $\Delta = 500$. Subsequently, the small scatter in the M_{tot}–Y_X relation was also confirmed observationally (e.g., Arnaud et al. 2007; Vikhlinin et al. 2009a).

Scatter and Evolution The scatter in scaling relations is, besides to cool cores, attributed partially to the different merger histories of the clusters and the resulting substructure. Merger events cause deviations from hydrostatic equilibrium and shift cluster parameters from the "virial" values (e.g., Chen et al. 2007; Jeltema et al. 2008; Ventimiglia et al. 2008; Zhang et al. 2010). Furthermore, they are also connected to the behaviour of a cluster's "central engine", i.e. the supposedly AGN-driven heating mechanism of cluster core gas. In recent years, studies of the departures from hydrostatic equilibrium have become feasible because the improved possibilities of the current generation of X-ray satellites (e.g., XMM-Newton, Chandra, Suzaku) are small enough and will be even smaller for the next generation, providing the precision required for future constraints on cosmological parameters, e.g., the Dark Energy w parameter.

Structure formation also manifests a considerable evolution in scaling relations (esp. M–L_X), being a crucial source of uncertainties in constraints on w (Vikhlinin et al. 2009b). Usually, the self-similar prediction invoking the evolution function $E(z) = H(z)/H_0$, a re-written form of Eq. (1.19), is applied in observational studies. Although the evolution of scaling relations has already been studied in simulations (e.g., Nagai et al. 2007b), it still awaits observational constraints.

"Self-calibration", the consistent treatment of mutual dependencies of scaling relation and cosmological parameters has been suggested by e.g., Mohr (2005). A simultaneous constraint of cosmological parameters and X-ray scaling relations was carried out by Mantz et al. (2009a).

X-ray – Lensing Comparisons To study the departures from the assumptions typically made in X-ray analyses, the independent total mass estimates inferred from weak gravitational lensing (WL, Chapts. 3 and 8) provide useful insights. Several studies have been undertaken in which X-ray and weak lensing cluster observables have been compared: Dahle (2006) found the weak lensing mass M_{wl} to scale with X-ray luminosity as $L_X^{1.04\pm0.46}$ and constrained a combination of Ω_m and σ_8. Hoekstra (2007) established a proportionality between M_{wl} within the radius r_{2500}, and T_X^{α}, which has an exponent $\alpha = 1.34^{+0.30}_{-0.28}$. For the same radius, Mahdavi et al. (2008) quoted a ratio $M_X/M_{wl} = 1.03 \pm 0.07$ that decreases towards larger radii. Zhang et al. (2008, see Fig. 2.4 for an example) determined a ratio of weak lensing to X-ray mass $M_{wl}/M_X = 1.09 \pm 0.08$, at a radius r_{500}, and confirmed this value and the trend with radius (Zhang et al. 2010). Corless & King (2009) investigated how the choice of mass estimators affects the systematics of the WL mass function, while Meneghetti et al. (2009) performed detailed comparisons of mock cluster X-ray and WL observations. X-ray and SZ properties of clusters were compared by e.g., Pace et al. (2008).

Chapter 3

Gravitational Lensing

3.1 Concepts of Lensing Theory

Gravitational lensing describes the phenomenon that gravitational fields affect the propagation of electromagnetic radiation by the curvature of space-time predicted from General Relativity. Notions of light being bent in the presence of a massive body already existed in the era of classical physics: e.g. Soldner in 1804 calculated the angle by which a ray of light would be deflected passing the Sun, assuming light to consist of massive particles to which classical physics could be applied.[1] Despite its interesting pre-relativistic history (e.g., Schneider et al. 1992), gravitational lensing has to be treated relativistically, and the first observation of a lensing effect, the small apparent displacements of stars observed during a solar eclipse by Eddington in 1919, was a crucial, successful observational test of General Relativity. This Chapter provides the theoretical background for gravitational lensing in observational cosmology, along the lines of Schneider (2006b,c) and focussing on weak lensing by galaxy clusters.

3.1.1 Deflection Angle and Lens Equation

According to General Relativity, the trajectories along which light propagates are the null geodesics given by the local metric and depend on the matter distribution through the Einstein equation (1.4). For the purposes of this thesis, a simplified description assuming the weakness of gravitational fields ($\Phi/c^2 \ll 1$) suffices; more general contexts are discussed in, e.g., Schneider et al. (1992). In analogy to the Born approximation in quantum mechanics, the *geometrically thin lens* deflects an otherwise straight light ray in a single point. (Still, a photon can encounter several such thin lenses along its trajectory.)

Figure 3.1 shows a sketch of the thin lens geometry: light emitted from the source at angular diameter distance D_s from the observer gets deflected by an intervening mass at distance D_d, while the angular diameter distance between source and deflector is denoted D_ds. Lensing causes the observed image of the source to be observed at position $\boldsymbol{\theta} = \boldsymbol{\xi}/D_\mathrm{d}$ instead of $\boldsymbol{\beta} = \boldsymbol{\eta}/D_\mathrm{s}$. Here, $\boldsymbol{\eta}$ and $\boldsymbol{\xi}$ refer to 2-vectors in the *source plane* and *lens plane*, respectively, where we assume smallness of all relevant angles such that these planes can be considered perpendicular to the optical axis and at fixed (angular diameter) distances to the observer. On the other hand, $\boldsymbol{\beta}$ and $\boldsymbol{\theta}$ are the corresponding celestial positions with respect to a fiducial line-of-sight. The difference between

[1] Soldner's result differs from the general relativistic solution for this case, given by Eq. (3.4), by a factor of 2.

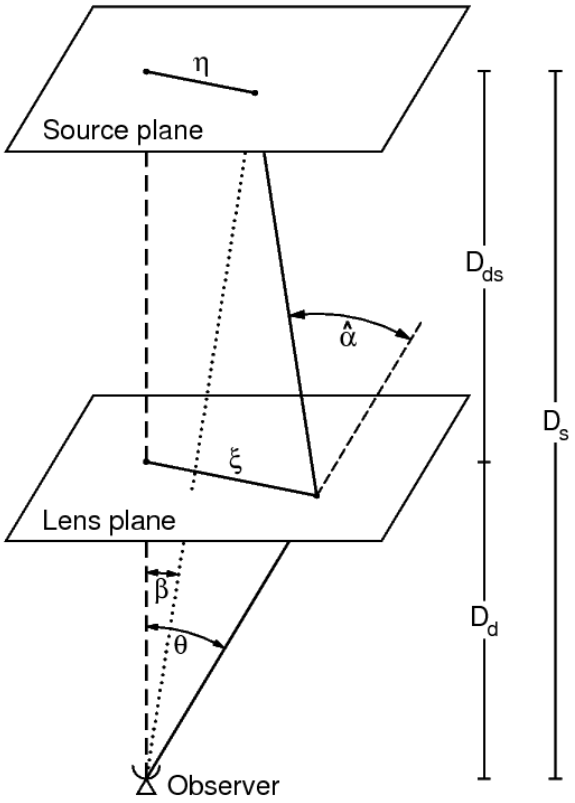

Figure 3.1: Sketch of gravitational lensing in the geometrically thin lens scenario. Light from a source at an angular diameter distance D_s from the observer and at perpendicular separation $\boldsymbol{\eta}$ from the optical axis defined by the observer and the deflecting mass at distance D_d passes the lens plane with an impact parameter $\boldsymbol{\xi}$, changing direction by the deflection angle $\hat{\boldsymbol{\alpha}}$. Consequently, the source is observed at celestial coordinates $\boldsymbol{\theta}$ instead of its unlensed position $\boldsymbol{\beta}$, related to $\hat{\boldsymbol{\alpha}}$ by Eq. (3.1). Figure from Schneider (2006b).

the unlensed celestial position $\boldsymbol{\beta}$ and the actually observable lensed coordinates $\boldsymbol{\theta}$ is given by the *deflection angle* $\hat{\boldsymbol{\alpha}}(D_\mathrm{d}\boldsymbol{\theta})$, for which, in the limit of small $\hat{\boldsymbol{\alpha}}$, the geometric configuration yields:

$$\boldsymbol{\beta} = \boldsymbol{\theta} - \frac{D_\mathrm{ds}}{D_\mathrm{s}}\hat{\boldsymbol{\alpha}}(D_\mathrm{d}\boldsymbol{\theta}) \quad . \tag{3.1}$$

Introducing the *scaled deflection angle* $\boldsymbol{\alpha}(\boldsymbol{\theta}) := \frac{D_\mathrm{ds}}{D_\mathrm{s}}\hat{\boldsymbol{\alpha}}(D_\mathrm{d}\boldsymbol{\theta})$, the *lens equation* can be written more concisely as:

$$\boldsymbol{\beta} = \boldsymbol{\theta} - \boldsymbol{\alpha}(\boldsymbol{\theta}) \quad . \tag{3.2}$$

Next, we have to specify this general relation by determining the deflection angle $\hat{\boldsymbol{\alpha}}(\boldsymbol{\theta})$ for a given mass distribution and angular separation $\boldsymbol{\theta}$. We consider an arbitrary, thin-sheet mass distribution $\rho(\xi_1, \xi_2, \ell)$, where the spatial coordinates ξ_1 and ξ_2 span the lens plane and ℓ runs along the optical axis. A general relativistic calculation in the Born approximation shows that the deflection caused by $\rho(\xi_1, \xi_2, \ell)$ can be expressed as

$$\hat{\boldsymbol{\alpha}}(\boldsymbol{\theta}) = \frac{4G_\mathrm{N}}{c^2}\int \Sigma(\boldsymbol{\xi}')\frac{\boldsymbol{\xi}-\boldsymbol{\xi}'}{\left|\boldsymbol{\xi}-\boldsymbol{\xi}'\right|^2}\,\mathrm{d}\boldsymbol{\xi}' \tag{3.3}$$

in terms of the *surface mass density* $\Sigma(\boldsymbol{\xi}) := \int \rho(\xi_1, \xi_2, \ell)\,\mathrm{d}\ell$.

In the important special case of light being deflected by a spherically symmetric mass distribution of total mass M, with an *impact parameter* $|\boldsymbol{\xi}| =: \xi \gg R_\mathrm{S} = 2G_\mathrm{N}M/c^2$ much larger than its Schwarzschild radius, i.e. its *exterior* field, the deflection angle (Eq. 3.3) simplifies to:

$$\hat{\alpha} = \frac{4G_\mathrm{N}M}{c^2\xi} = \frac{2R_\mathrm{S}}{\xi} \quad . \tag{3.4}$$

This deflection by a point mass lens is the relevant case for Eddington's solar eclipse experiment as well as for *microlensing* by compact objects.[2]

Depending on the nature of the mass distribution, there can be several vectors $\boldsymbol{\theta}$ satisfying the lens equation (3.2). For these lenses, a source at a suitable position will appear *multiply imaged* on the sky. More thorough analysis of the lens equation (e.g., Schneider 2006b) leads to the conclusion that multiple images can – to first order – be produced if the surface mass density exceeds a critical value

$$\Sigma_{\rm cr} = \frac{c^2}{4\pi G_{\rm N}} \frac{D_{\rm s}}{D_{\rm d} D_{\rm ds}} \tag{3.5}$$

somewhere in the lens plane. Therefore, the dimensionless *convergence*

$$\kappa(\boldsymbol{\theta}) := \Sigma(D_{\rm d}\boldsymbol{\theta})/\Sigma_{\rm cr} \tag{3.6}$$

establishes a useful natural scale to discriminate between *strong lenses* with $\kappa(\boldsymbol{\theta}) > 1$ locally, which are capable of producing multiple images, and *weak lenses* with only one solution to Eq. (3.2), describing one distorted image of the source. In case of an axially symmetric mass distributions, $\Sigma(\boldsymbol{\xi}) = \Sigma(|\boldsymbol{\xi}|)$, the mean surface mass density equals the $\Sigma_{\rm cr}$ inside the circle given by the *Einstein radius*:

$$\theta_{\rm E} = \left(\frac{4G_{\rm N} M(<\theta_{\rm E})}{c^2} \frac{D_{\rm ds}}{D_{\rm d} D_{\rm s}} \right)^{1/2} \quad , \tag{3.7}$$

where $M(<\theta_{\rm E})$ is the mass enclosed inside the Einstein radius. The sensitive dependence of multiple image positions on the mass distribution of a strong gravitational lens can be exploited to obtain precise mass estimates for lenses like galaxy clusters or groups (e.g., Kochanek 2006; Halkola et al. 2008; Limousin et al. 2009). Furthermore, the *time delay* between the light travel times for different images of a multiple image system provides a tool for precise measurements of the Hubble parameter (e.g., Vuissoz et al. 2008; Suyu et al. 2010).

Noticing the similarity between Eq. (3.3) and the relation between mass density and gravitational force in three dimensions, it can be shown that a two-dimensional analogue of the gravitational potential $\Phi(\vec{r})$, the *lensing potential* $\psi(\boldsymbol{\theta})$ can be defined as

$$\psi(\boldsymbol{\theta}) = \frac{1}{\pi} \int \kappa(\boldsymbol{\theta}') \, \ln \left| \boldsymbol{\theta} - \boldsymbol{\theta}' \right| \, {\rm d}\boldsymbol{\theta}' \tag{3.8}$$

such that

$$\boldsymbol{\nabla}\psi(\boldsymbol{\theta}) = \boldsymbol{\alpha}(\boldsymbol{\theta}) \quad \text{and} \quad \boldsymbol{\nabla}^2\psi(\boldsymbol{\theta}) = 2\kappa(\boldsymbol{\theta}) \tag{3.9}$$

are the corresponding analogues of Newton's Second Law and the Poisson equation.

3.1.2 Gravitational Shear

Depending on both the mass distribution and the projected impact parameter, Eq. (3.3) yields the amplitude and direction of lensing deflection. Observables, analysis techniques, and astrophysical applications differ substantially for the different regimes of lensing, for which the typical mass and distance scales of the lens and effects on the source image are summarised in Fig. 3.2. We will focus here on weak lensing, the subtle apparent distortion of the source image by a tidal gravitational field. One important class of weak lenses are halos of galaxy clusters, (Sect. 3.2.2) which are usually modelled as smooth, slowly varying density fields on the length scales relevant

[2]Microlensing is interesting in two major fields of astronomy (Wambsganss 2006): galactic microlensing putting tight constraints on the existence of massive cold halo objects provides additional evidence for non-baryonic DM (e.g., Alcock et al. 2000; Afonso et al. 2003). Furthermore, microlensing gives rise to a productive technique for the detection of low-mass, possibly terrestrial extrasolar planets (e.g., Bond et al. 2004; Bennett et al. 2008).

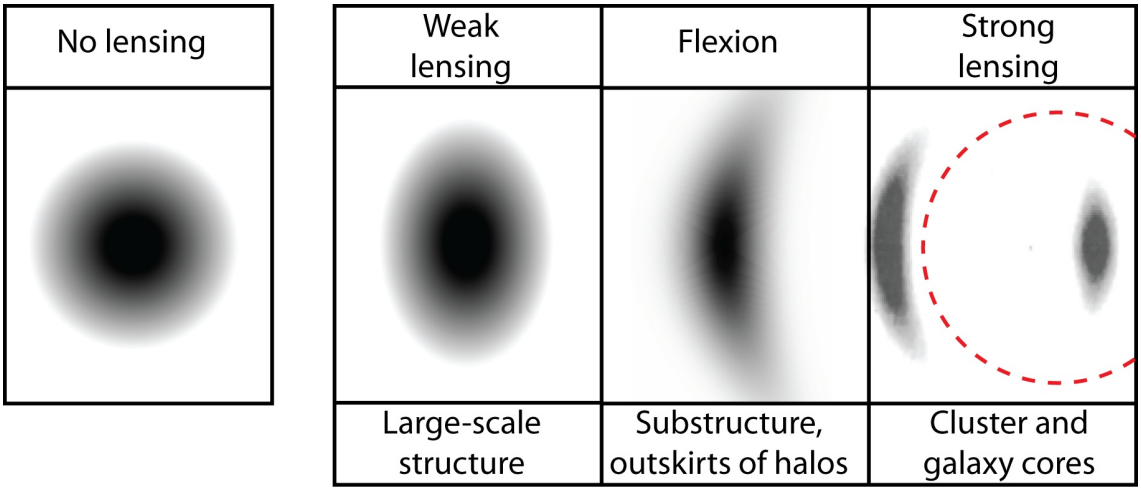

Figure 3.2: The effect of lensing in its different regimes. The image of a source with intrinsically circular isophotes (leftmost panel) gets distorted by an increasingly strong (from left to right) gravitational field, deforming its isophotes first into ellipses (weak lensing). Next, in the case of flexion, higher order terms in the lens equation need to be considered. Finally, in the strong lensing regime, multiple images form. The dashed line denotes the Einstein radius of the lens (Eq. 3.7). At the bottom of the three panels to the right, typical lenses for the different regimes are indicated. Figure from Massey et al. (2010).

for lensing. Further, weak lensing is caused by the large scale structure (LSS) density field as a whole: *cosmic shear* analyses (e.g., Hetterscheidt et al. 2007; Fu et al. 2008; Schrabback et al. 2009) contribute significantly to the determination of cosmological parameters (Sect. 1.3.1) such as Ω_m and σ_8.

In the weak lensing regime, we can assume the lens properties (characterised by the second derivatives of ψ) to vary insignificantly over the size of the image of a typical source. Thus, the linearised lens equation

$$\boldsymbol{\beta}-\boldsymbol{\beta}_0 = \mathcal{A}(\boldsymbol{\theta}_0)\cdot(\boldsymbol{\theta}-\boldsymbol{\theta}_0) \tag{3.10}$$

derived from a first-order Taylor expansion of Eq. (3.2) around a pivot point $\boldsymbol{\beta}_0 = \boldsymbol{\beta}(\boldsymbol{\theta}_0)$ provides a sufficiently accurate description of the lensing effects. The Jacobian matrix $\mathcal{A}(\boldsymbol{\theta}_0)$ of the lens mapping can be expressed as follows:

$$\mathcal{A}(\boldsymbol{\theta}) = \frac{\partial\boldsymbol{\beta}}{\partial\boldsymbol{\theta}} = \left(\delta_{ij}-\frac{\partial^2\psi(\boldsymbol{\theta})}{\partial\theta_i\partial\theta_j}\right) = \begin{pmatrix}1-\kappa-\gamma_1 & -\gamma_2\\ -\gamma_2 & 1-\kappa+\gamma_1\end{pmatrix} \quad . \tag{3.11}$$

Using the notation $\psi_{,i} := \partial\psi/\partial\theta_i$, the scalar $\kappa = (\psi_{,11}+\psi_{,22})/2$ is the convergence introduced in Eq. (3.6), and the components of the complex shear

$$\gamma := \gamma_1 + \mathrm{i}\gamma_2 = |\gamma|\mathrm{e}^{2\mathrm{i}\varphi} \tag{3.12}$$

are as well defined by second order derivatives of the lensing potential:

$$\gamma_1 = (\psi_{,11}-\psi_{,22})/2\,, \quad \gamma_2 = \psi_{,12} \quad . \tag{3.13}$$

The next highest order in $\boldsymbol{\theta}$ after Eq. (3.10) in the expansion of Eq. (3.2), *gravitational flexion* (e.g., Schneider & Er 2008), becomes relevant in the transition from weak to strong lensing.

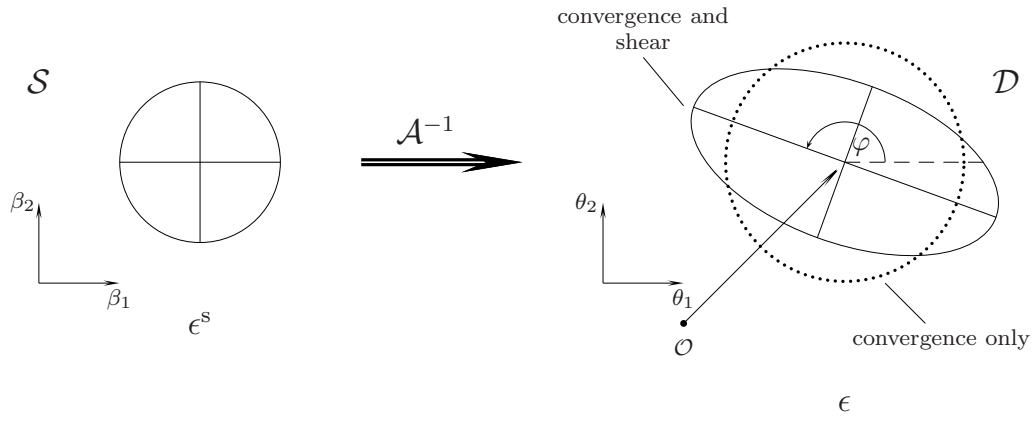

Figure 3.3: The transformation of a circular source in the source plane ($\mathcal{S}$) by the magnification tensor $\mathcal{A}^{-1}$ into the lens plane ($\mathcal{D}$). While pure convergence scales the image isotropically, shear results in an anisotropic distortion, mapping a unit circle into an ellipse with semi-axes $1/[(1-\kappa)(1\pm|g|)]$ and inducing a rotation by φ. More generally, an intrinsic ellipticity $\epsilon^{(\rm s)}$ is transformed into an observed ellipticity ϵ. Figure from Schneider (2006c) after an idea by Maruša Bradač.

Because lensing entails neither emission nor absorption of photons, Liouville's theorem[3] states that – at each frequency ν – the surface brightness $I_\nu = S_\nu/\mathrm{d}\omega = S_\nu^{(\rm s)}/\mathrm{d}\omega^{(\rm s)}$ is conserved under Eqs. (3.2) and (3.10). Here, S_ν denotes the flux at frequency ν and ω the solid angle subtended by the source; the superscript "s" for "source plane" indicates quantities that would be measured in the absence of lensing. Hence, as surface brightness is conserved, lensing modifies[4] the *shape* of the source's image, according to

$$I_\nu(\boldsymbol{\theta}) = I_\nu^{(\rm s)}[\boldsymbol{\beta}(\boldsymbol{\theta})] = I_\nu^{(\rm s)}[\boldsymbol{\beta}_0 + \mathcal{A}(\boldsymbol{\theta}_0)\cdot(\boldsymbol{\theta}-\boldsymbol{\theta}_0)] \quad , \tag{3.14}$$

where Eq. (3.10) was inserted. A suitable isophote can be understood to define the "shape" of an image. We discuss shape measurement in Sect. 3.2. From the form of Eq. (3.14), we conclude immediately that circular isophotes will be transformed into ellipses in the general case. Re-writing Eq. (3.11), it becomes clearer that convergence corresponds to an isotropic stretching or shrinking of the image, while the trace-free factor of $\mathcal{A}$ contains the anisotropic transformation, which turns a circle into an ellipse:

$$\mathcal{A}(\boldsymbol{\theta}) = (1-\kappa(\boldsymbol{\theta}))\begin{pmatrix} 1-g_1(\boldsymbol{\theta}) & -g_2(\boldsymbol{\theta}) \\ -g_2(\boldsymbol{\theta}) & 1+g_1(\boldsymbol{\theta}) \end{pmatrix} \quad , \tag{3.15}$$

where

$$g(\boldsymbol{\theta}) = \frac{\gamma(\boldsymbol{\theta})}{1-\kappa(\boldsymbol{\theta})} \quad \text{with} \quad g = g_1 + \mathrm{i}g_2 = |g|\mathrm{e}^{2\mathrm{i}\varphi} \tag{3.16}$$

denotes the *reduced shear* which is, because of the decomposition Eq. (3.15), the actual observable in weak lensing. A unit circle, mapped by the (locally defined) *magnification tensor* $\mathcal{M} = \mathcal{A}^{-1}$ from the source to the image plane results in an ellipse with semi-axes $1/[(1-\kappa)(1\pm|g|)]$ and an angle φ between the positive θ_1-axis and its major axis (Fig. 3.3). Therefore, the axis ratio of such an ellipse resulting from weak lensing of a circular source is $0 \le r = (1-|g|)/(1+|g|) \le 1$, given $|g| < 1$. An ellipse, under a rotation by π, maps onto itself, which is the significance of the factors of 2 in

[3] i.e., Liouville's theorem on the invariance of phase-space density for closed systems in Hamiltonian mechanics.

[4] This also holds for strong lensing, where an image not only is distorted but split into multiple images for which the surface brightness summed over all components is invariant.

Eqs. (3.12) and (3.16). Consequently, the shear γ and reduced shear g are not vectors but *polars*, "spin 2"-quantities in particle physics' parlance.

Before we take a closer look on how shear influences the shape of galaxies, we note that due to the conservation of surface brightness, the flux of the image changes by a *magnification factor*

$$|\mu| = S_\nu / S_\nu^{(\mathrm{s})} = \mathrm{d}\omega^{(\mathrm{s})}/\mathrm{d}\omega\,, \quad \text{where} \quad \mu = \det \mathcal{M} = 1/[(1-\kappa)^2 - |\gamma|^2] = 1/(1-|g|^2) \quad . \tag{3.17}$$

Both μ and $g(\boldsymbol{\theta})$ diverge at *critical curves*, where $\det \mathcal{A} = (1-\kappa)^2 - |\gamma|^2 = 0$ is satisfied. Hence, weak lensing assumptions do not apply for this case, where indeed the highly distorted and magnified giant arcs typical of strong lensing can be observed.[5]

3.2 Weak Lensing Observables

Although sources with circular isophotes serve well in a *gedankenexperiment* such as Fig. 3.3, real galaxies exhibit intrinsic ellipticity. Moreover, the observed isophotes of astronomical sources don't follow any simple, concentric curves. Quantifying "shape" thus is a subtle problem and *shear measurement* hence the central task in weak lensing: to disentangle the small distortion by which weak gravitational lensing manifests from the – by far dominant – intrinsic contribution. In this Section, we discuss ellipticity estimators and the expected shear signal from a galaxy cluster; shear measurement techniques are the topic of Sect. 5.4.

3.2.1 Shear, Shape, and Ellipticity

Because the isophotes of galaxies cannot be described by ellipses or another simple *a priori* function, we adopt the common approach to express the light distribution of a galaxy by its *moments*. The first two moments of the two-dimensional brightness distribution $I(\boldsymbol{\theta})$ are given by:

$$I_{(1)} := \bar{\boldsymbol{\theta}} = \frac{\int \boldsymbol{\theta}\, W(I(\boldsymbol{\theta}))\, I(\boldsymbol{\theta})\, \mathrm{d}^2\boldsymbol{\theta}}{\int W(I(\boldsymbol{\theta}))\, I(\boldsymbol{\theta})\, \mathrm{d}^2\boldsymbol{\theta}}\,, \quad I_{(2)} := Q = Q_{ij} = \frac{\int \left(\theta_i - \bar{\theta_i}\right)\left(\theta_j - \bar{\theta_j}\right) W(I(\boldsymbol{\theta}))\, I(\boldsymbol{\theta})\, \mathrm{d}^2\boldsymbol{\theta}}{\int W(I(\boldsymbol{\theta}))\, I(\boldsymbol{\theta})\, \mathrm{d}^2\boldsymbol{\theta}} \quad , \tag{3.18}$$

where $W(I(\boldsymbol{\theta}))$ denotes a suitable weight function (Sect. 5.3.1). We express the centroid, describing the image centre, as a vector with Cartesian components $\bar{\boldsymbol{\theta}} = \left(\bar{\theta_1}, \bar{\theta_2}\right)$. The second brightness moment takes the form of a tensor of rank 2 with $i, j \in \{1, 2\}$. In the Kaiser et al. (1995, KSB) algorithm (Sect. 5.4.1), also higher moments of $I(\boldsymbol{\theta})$ are used. In complete analogy, moments of the unlensed brightness distribution are defined with $\boldsymbol{\beta}$ replacing $\boldsymbol{\theta}$.

There exist two concurrent definitions of "ellipticity" in lensing theory. In case of elliptical isophotes and a minor-to-major axis ratio of $0 \leq r = b/a \leq 1$, the arguments of these polars expressed as complex quantities by $\epsilon = |\epsilon| \exp(2\mathrm{i}\varphi)$ and $\chi = |\chi| \exp(2\mathrm{i}\varphi)$ correspond to:

$$|\epsilon| = \frac{1-r}{1+r} \quad , \qquad |\chi| = \frac{1-r^2}{1+r^2} \quad . \tag{3.19}$$

Both estimators can be expressed easily by second-order brightness moments and, as they exhibit the same invariance under rotations by π, the only difference arises from the normalisations:

$$\epsilon := \frac{Q_{11} - Q_{22} + 2\mathrm{i}Q_{12}}{Q_{11} + Q_{22} + 2\sqrt{Q_{11}Q_{22} - Q_{12}^2}}\,, \quad \chi := \frac{Q_{11} - Q_{22} + 2\mathrm{i}Q_{12}}{Q_{11} + Q_{22}} \quad . \tag{3.20}$$

[5] Stability theory predicts that at *critical curves*, the system experiences a transition between two qualitatively different regimes. In lensing, a change in the number of images occurs at *caustics*, i.e. the mappings of critical curves into the source plane via Eq. (3.2).

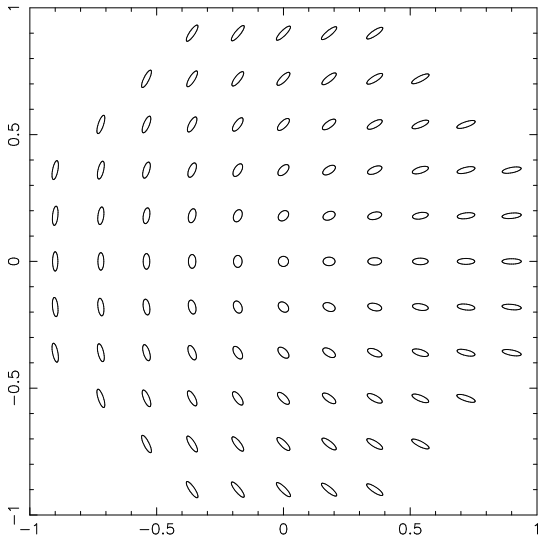

Figure 3.4: The "shape space" for ellipses spanned by the components χ_1 (abscissa) and χ_2 (ordinate) of the complex ellipticity χ. While a source with circular isophotes has $\chi_1 = 0$, $\chi_2 = 0$, the limiting case $\chi = 1$ corresponds to infinite straight lines. The ϵ ellipticity estimator shows the same $\exp(2i\varphi)$ rotational symmetry that can be seen in this plot. Figure from Schneider (2006c) after an idea by Douglas Clowe.

Figure 3.4 illustrates the orientation and axis ratio for ellipses corresponding to different values of χ_1 and χ_2. A similar plot for ϵ_1 and ϵ_2 would exhibit the same rotational symmetry.

Calculating the functional determinant of the lensing mapping, it can be shown that the second-order brightness moments transform under shear as $Q^{(s)} = \mathcal{A}Q\mathcal{A}$, which, for a reduced shear g, yields the following transformations for the ellipticity estimators:

$$\epsilon = \frac{\epsilon^{(s)} + g}{1 + g^* \epsilon^{(s)}} \quad \text{for } |g| \le 1\,, \quad \epsilon = \frac{1 + g\epsilon^{(s)*}}{\epsilon^{(s)*} + g^*} \quad \text{for } |g| > 1 \quad \text{resp.} \quad \chi = \frac{\chi^{(s)} + 2g + g^2 \chi^{(s)*}}{1 + |g|^2 + 2\mathcal{R}e(g\chi^{(s)*})}\,, \quad (3.21)$$

where the asterisk denotes complex conjugation. For the individual galaxy, the two cases in the left hand side of Eq. (3.21) are indistinguishable, but in cluster lensing data the case $|g| > 1$ only occurs for a small number of sources well inside the critical curve.

The central assumption in weak lensing states the random intrinsic orientation of arbitrarily selected galaxies, corresponding to a vanishing expectation value:[6]

$$\mathcal{E}(\chi^{(s)}) = \mathcal{E}(\epsilon^{(s)}) = 0 \quad . \quad (3.22)$$

Inserting Eq. (3.22) into Eq. (3.21), Seitz & Schneider (1997) could show that

$$\mathcal{E}(\epsilon) = \begin{cases} g & \text{for } |g| \le 1 \\ 1/g^* & \text{for } |g| > 1 \end{cases}\,, \quad (3.23)$$

i.e, that for a set of lensed galaxies where Eq. (3.22) holds, the ellipticity ϵ measured for each of these sources gives an unbiased, but very noisy, estimate of the shear g at its position. The expectation value for χ, though, depends on the intrinsic ellipticity distribution and does not have a simple form like Eq. (3.23). Therefore, ϵ is preferred in theoretical studies. For the purpose of numerical calculations, however, using χ is favoured because no case distinction has to be applied. Furthermore, the KSB algorithm we use (Sect. 5.4.1) was invented before the relations for ϵ in Eq. (3.21) were found and is thus defined in terms of χ.

Due to the very noisy shear signal from an individual source galaxy – the intrinsic ellipticity exceeds the typical shear by a factor of $\gtrsim 10$ – weak lensing studies can only be of statistical nature.

[6] However, the correlation $\mathcal{E}(\chi_i, \chi_j)$ between the *observed* ellipticity for two galaxy does not vanish in general. In anticipation of the high accuracy to be achieved in future cosmic shear satellite experiments, these *intrinsic alignments* detected by e.g., Mandelbaum et al. (2006) have become an active field of research (e.g., Joachimi & Schneider 2009).

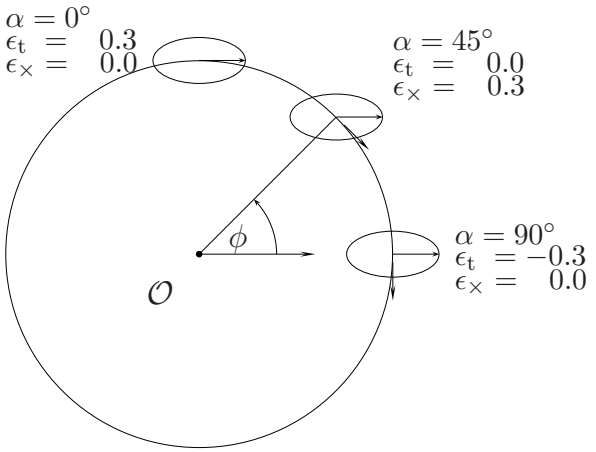

Figure 3.5: The tangential and cross component of the same ellipticity $|\epsilon| = 0.3$ for three different position angles with respect to a reference point O. Here, $\alpha = \pi - \phi$ denotes the orientation of the tangential vector for a source with phase angle ϕ in the (arbitrary) reference coordinate system. Figure from Schneider (2006c) after an idea by Maruša Bradač.

Deep and wide observations are needed to obtain an accurate (local) average of the shear signal for a typical cluster lens. In case of mass-poor clusters and galaxy groups, even stacking of the lenses is applied (Sheldon et al. 2009) such that statistical properties of the lens population can be derived.

3.2.2 Tangential Shear Around Galaxy Clusters

What signature do we expect from the shear field of a galaxy cluster? Starting with the simplest model, an axially symmetric mass distribution, deflection has to be radial for reasons of symmetry. The lensing equation (Eq. 3.2) takes the one-dimensional form $\beta = \theta - \alpha(\theta) = \theta[1 - \overline{\kappa}(\theta)]$, where $\overline{\kappa}(\theta)$ denotes the mean convergence inside a circle of radius θ. By deriving the corresponding Jacobian (Eq. 3.11), an expression for the shear in terms of the convergence can be found:

$$\gamma(\boldsymbol{\theta}) = [\kappa(\theta) - \overline{\kappa}(\theta)]\mathrm{e}^{2\mathrm{i}\tilde{\varphi}} \quad , \tag{3.24}$$

where $\tilde{\varphi}$ is the phase angle in the complex representation of $\boldsymbol{\theta}$ as $\theta\mathrm{e}^{\mathrm{i}\tilde{\varphi}}$. Solving the eigenvalue problem of the Jacobian $\mathcal{A}(\boldsymbol{\theta})$, we find (for $\det\mathcal{A} > 0$) that the image of a source on the θ_1-axis gets elongated along the θ_2-axis. Because of the axial symmetry we conclude that the shear acts tangentially to the source's radius vector.[7] The shear can be decomposed into a tangential and cross component with respect to the phase angle φ of a polar coordinate system by:

$$\gamma_\mathrm{t} = -\mathrm{Re}(\gamma\,\mathrm{e}^{-2\mathrm{i}\varphi}) \,, \quad \gamma_\times = -\mathrm{Im}(\gamma\,\mathrm{e}^{-2\mathrm{i}\varphi}) \quad . \tag{3.25}$$

Analogous definitions apply for the tangential and cross components of g, χ, and ϵ. The minus in Eq. (3.25) assures that a tangentially stretched source indeed has $\gamma_\mathrm{t} > 0$, while a radial orientation to the centre implies $\gamma_\mathrm{t} < 0$ (Fig. 3.5). Because the shear is a polar, $\gamma_\times = 0$ holds in both cases. Vanishing tangential shear and $\gamma_\times \neq 0$ correspond to a rotation by $\pi/4$ w.r.t. the tangential direction. For axisymmetric lenses, the shear field thus is free of cross components, i.e., purely tangential in the sense of Eq. (3.25).[8]

Bartelmann (1995) showed that the relation Eq. (3.24) can be generalised to arbitrary mass distributions when averaging shear and convergence on circles of radius θ:

$$\langle\gamma_\mathrm{t}\rangle = \overline{\kappa} - \langle\kappa\rangle \quad , \tag{3.26}$$

[7] This results holds outside the Einstein radius; for $\theta < \theta_\mathrm{E}$ radial alignment of the shear can be shown.

[8] In cosmic shear, the closely related notions of the curl-free E-modes and source-free B-modes of the shear field are of special importance, named in analogy to electric and magnetic fields. Lensing can only produce E-modes, thus the separation of these modes (e.g., Schneider et al. 2010) provides a crucial test for possible systematics.

where $\bar{\kappa}$ is the average inside the circle. Thus, the notion of tangential shear is very useful also in the investigation of cluster lenses beyond simple axisymmetric models. Clusters of galaxies can be detected by the tangential shear around their centres. The *aperture mass* (Schneider 1996), a filtered estimate of the tangential shear around a point $\boldsymbol{\theta}_\mathrm{c}$, has proven to be prolific in both the recovery of the shear by previously known clusters and the discovery of shear peaks at positions where clusters could be confirmed later by other methods (e.g., Schirmer et al. 2007; Dietrich et al. 2007):

$$M_\mathrm{ap}(\boldsymbol{\theta}_\mathrm{c}) = \int \gamma_\mathrm{t}(\boldsymbol{\theta}-\boldsymbol{\theta}_\mathrm{c}) Q(|\boldsymbol{\theta}-\boldsymbol{\theta}_\mathrm{c}|)\,\mathrm{d}\boldsymbol{\theta} = \int \kappa(\boldsymbol{\theta}) U(|\boldsymbol{\theta}-\boldsymbol{\theta}_\mathrm{c}|)\,\mathrm{d}\boldsymbol{\theta} \quad , \tag{3.27}$$

where the filter functions $U(\theta)$ and $Q(\theta)$ have been chosen to satisfy the conditions:

$$Q(\theta) = \frac{2}{\theta^2}\int_0^\theta \theta'\, U(\theta')\,\mathrm{d}\theta' - U(\theta)\,, \qquad \int_0^\theta \theta'\, U(\theta')\,\mathrm{d}\theta' = 0 \quad . \tag{3.28}$$

The most interesting quantity concerning cluster detection is the aperture mass signal-to-noise ratio, or S-statistics, which, replacing the weighted shear by a weighted sum over the tangential ellipticities of all source galaxies within a circular aperture of radius θ_out, can be written analytically as (Schneider 1996):

$$S_{\theta_\mathrm{out}}(\boldsymbol{\theta}_\mathrm{c}) = \frac{\sqrt{2}}{\sigma_\varepsilon} \frac{\sum_i \varepsilon_{\mathrm{t},i}\, Q_i(|\boldsymbol{\theta}_\mathrm{i}-\boldsymbol{\theta}_\mathrm{c}|)}{\sqrt{\sum_i Q_i^2(|\boldsymbol{\theta}_\mathrm{i}-\boldsymbol{\theta}_\mathrm{c}|)}} \quad . \tag{3.29}$$

Here $\varepsilon_{\mathrm{t},i}$ denotes the measured ellipticity component tangential with respect to the centre for the galaxy at position $\boldsymbol{\theta}_\mathrm{i}$. As a noise term, the S-statistics includes the intrinsic source ellipticity, calculated from the data galaxies as $\sigma_\varepsilon = \langle \varepsilon_1^2 + \varepsilon_2^2 \rangle^{1/2}$ with typical values $0.3 \leq \sigma_\epsilon \leq 0.4$. We discuss the efficiency of the S-statistics as a method for cluster detection and the relation between shear peaks and mass peaks in Sect. 8.1.2.

The amount by which background sources get sheared due to a cluster, i.e. the strength of the shear signal, depends on the angular diameter distances between source, lens, and observer, as Eq. (3.5) shows. In reality, the fact that accurate weak lensing measurements demand averaging over large samples of sources implies that the distance ratio $D_\mathrm{ds}/D_\mathrm{s}$ – between source and lens and source and observer – needs to be replaced. If no spectroscopic or photometric redshift of the individual source is known, an average $\langle D_\mathrm{ds}/D_\mathrm{s} \rangle$ over the typical broad redshift distribution, which deep optical observations yield, offers the second-best solution. The influence of the source redshift distribution can be expressed by the monotonic function

$$Z(z_\mathrm{s}) = \frac{D_\mathrm{ds}/D_\mathrm{s}}{\lim_{z_\mathrm{s}\to\infty} D_\mathrm{ds}/D_\mathrm{s}} \Theta_\mathrm{H}(z_\mathrm{s}-z_\mathrm{d}) \quad , \tag{3.30}$$

where $\Theta_\mathrm{H}(z)$ is the Heaviside step function. As Bartelmann & Schneider (2001) illustrate for different cosmologies, the more distant a source, the larger is, in principle, the shear signal it carries. For a given realistic source redshift distribution with a steep decrease towards high z_s (exposure time, observational setup). However, for a fixed lens surface mass Σ, the strongest lensing signal is expected for $D_\mathrm{d} \sim \langle D_\mathrm{s} \rangle/2$. At small z_d, the signal will be low because of the small D_d in Eq. (3.5), while with increasing $z_\mathrm{d}/\langle z_\mathrm{s} \rangle$ the number of lensed background sources drops steeply (cf. Fig. 8.1).

3.2.3 Mass Reconstruction of Galaxy Clusters

Shape measurement results in local estimates for the reduced shear g, which is, through Eqs. (3.8), (3.12), and (3.16) defined by second derivatives of ψ and thus linked to the (projected) matter

distribution. Ultimately, we want to infer the lens mass from the ellipticities it imposes on images of background galaxies. There are two fundamental approaches to this problem: direct *mass reconstruction* on the one hand and *fitting techniques* based on the shear predicted for an assumed family of mass distributions on the other hand.

Galaxy clusters exhibit detailed interior substructure in their baryonic component and, as simulations show, even more so in the DM component. Nevertheless, Navarro et al. (1997) showed that the density profiles of relaxed clusters can, to first order, universally be described by a rather simple radial function over a wide range of scales within the virial radius. For the mass determinations providing the main results of this Thesis (Sect. 6.4), we rely on fitting the shear profile corresponding to this *NFW density profile* (Sect. 6.4.2) to the observed shear estimates.

However, one of the most important advantages of weak lensing mass estimates is their *a priori* independence of assumptions on the lens geometry. Therefore, we use direct mass reconstruction to probe the validity of the spherically symmetric NFW model for our clusters, i.e., to test if their projected mass distribution appears sufficiently regular to justify radial fitting.

The logical intermediate step when attempting direct mass reconstruction is to relate the reduced shear g to the convergence κ. The expression for the shear field given by an arbitrary matter distribution with convergence $\kappa(\boldsymbol{\theta})$ reads:

$$\gamma(\boldsymbol{\theta}) = \frac{1}{\pi}\int_{\mathbb{R}} \mathcal{D}(\boldsymbol{\theta}-\boldsymbol{\theta}')\,\kappa(\boldsymbol{\theta}')\,\mathrm{d}\boldsymbol{\theta}' \,, \quad \mathcal{D}(\boldsymbol{\theta}) = \frac{-1}{(\theta_1-\mathrm{i}\theta_2)^2} \quad , \tag{3.31}$$

which can be inverted using Fourier transforms to yield (Kaiser & Squires 1993):

$$\kappa(\boldsymbol{\theta}) = \kappa_0 + \frac{1}{\pi}\int_{\mathbb{R}} \mathcal{R}e[\mathcal{D}^*(\boldsymbol{\theta}-\boldsymbol{\theta}')\gamma(\boldsymbol{\theta}')]\,\mathrm{d}\boldsymbol{\theta}' \quad . \tag{3.32}$$

The Kaiser-Squires inversion suffers from several practical problems typical for direct deconvolutions, e.g., its definition assumes an infinite and infinitely well sampled shear field. The integration constant κ_0 in Eq. (3.32) indicates the second problem: unfortunately, the observed reduced shear field $g(\boldsymbol{\theta})$ rests invariant under all transformations

$$\gamma \to \lambda\gamma \,, \quad (1-\kappa) \to \lambda(1-\kappa) \quad , \tag{3.33}$$

where λ is a scalar factor. Thus, no unambiguous solution exists, unless the *mass-sheet degeneracy* can be overcome by additional information, e.g., from measured magnifications, individual source redshifts (Schneider 2006c), or by combining weak lensing with strong lensing constraints (Bradač et al. 2005; Limousin et al. 2007; Merten et al. 2009).

The Kaiser & Squires (1993) inversion has been refined and superseded by finite-field inversion techniques. The particular algorithm we apply in Sect. 6.3.1 (Seitz & Schneider 1996, 2001) expresses the problem in terms of $K(\boldsymbol{\theta}) := \ln[1-\kappa(\boldsymbol{\theta})]$ as a von Neumann problem on the data field $\mathcal{U}$ defined by the condition on its value on the boundary $\partial\mathcal{U}$, to which $\boldsymbol{n}$ is a normal vector:

$$\boldsymbol{\nabla}^2 K = \boldsymbol{\nabla}\boldsymbol{u}_\mathrm{g} \quad \text{where} \quad \boldsymbol{n}\cdot\boldsymbol{\nabla}K|_{\partial\mathcal{U}} = \boldsymbol{n}\cdot\boldsymbol{u}_\mathrm{g} \quad , \tag{3.34}$$

where $\boldsymbol{u}_\mathrm{g} = \boldsymbol{\nabla}K$ is a vector field defined by the components of the reduced shear as:

$$\boldsymbol{u}_\mathrm{g} = \frac{-1}{1-g_1^2-g_2^2}\begin{pmatrix} 1-g_1 & -g_2 \\ -g_2 & 1+g_1 \end{pmatrix}\begin{pmatrix} g_{1,1}+g_{2,2} \\ g_{2,1}-g_{1,2} \end{pmatrix} \quad . \tag{3.35}$$

The von Neumann problem can be solved numerically with, e.g., the algorithms described by Press et al. (1992). In Sect. 6, we apply both profile fitting and mass reconstruction to observational data.

Chapter 4

The *400d* Weak Lensing Survey

The analyses presented in this thesis introduce the weak lensing follow-up of the *400d cosmological sample*, a carefully selected subsample of high-redshift and X-ray luminous *400d* clusters. In this chapter, the underlying 400 square degree (*400d*) galaxy cluster survey (Burenin et al. 2007) is introduced and the selection of the *400d* cosmological sample (Vikhlinin et al. 2009a) is detailed. Furthermore, we discuss the observational setup and status of the weak lensing follow-up survey.

4.1 The *400d* Survey and the Chandra Cosmology Project

4.1.1 The ROSAT–Based *400d* Sample

Samples of galaxy clusters selected by their X-ray properties play an important role in cosmology, as mentioned in Sect. 2.1.2. The combination of its wide field-of-view (even counting only the centre, where the resolution is good) and the long, completed lifetime of the mission render ROSAT the most productive satellite observatory for the purpose of detecting distant galaxy clusters until recently. (The continuing XMM-NEWTON mission is taking over this rank.) Making use of all suitable pointed ROSAT PSPC observations, the *400d* survey comprises all clusters of galaxies detected serendipitously in a consistent re-analysis of this data set (Burenin et al. 2007). The survey's name is derived from the total area of 397 deg^2 on the sky covered by these pointings.

Cluster detection was performed on the central patch of $17\farcm5$ radius of each pointing, applying the algorithm developed for the *160d* survey (Vikhlinin et al. 1998; Mullis et al. 2003), the precursor to the *400d* survey. On the resulting catalogue of extended X-ray sources, a flux limit of

$$f_{\mathrm{ROSAT,min}} = 1.4 \times 10^{-13}\,\mathrm{erg\,s^{-1}\,cm^{-2}} \tag{4.1}$$

is applied to select sources for further investigations. In the ΛCDM cosmology with $h = 0.72$, $\Omega_{\mathrm{m}} = 0.30$ and $\Omega_\Lambda = 0.70$ this corresponds to a minimum luminosity of $1.1 \times 10^{44}\,\mathrm{erg\,s^{-1}}$ in the rest frame 0.5 keV–2.0 keV band for a $z = 0.5$ cluster. Hence, a representative population of fairly massive $0.3 < z < 0.8$ clusters is sampled by the *400d* survey.

The detected extended X-ray sources were re-observed with (medium-sized) optical telescopes to confirm the presence of a cluster at the ROSAT coordinates and to obtain spectroscopic redshifts for those sources for which none existed so far. The final *400d* catalogue lists all 242 serendipitous cluster detections, spanning a redshift range $0.0032 < z < 0.888$. Non-serendipitous cluster detections, i.e. clusters targeted originally with ROSAT, are listed separately by Burenin et al. (2007). The *400d* catalogue provides the basis for subsequent studies of low-mass nearby groups and clusters (e.g., Voevodkin et al. 2010; Rines & Diaferio 2010). Its main scientific driver, however, are cosmological parameter constraints using the distant, more X-ray luminous sources in the context of the *Chandra Cluster Cosmology Project*, which we introduce in the next section.

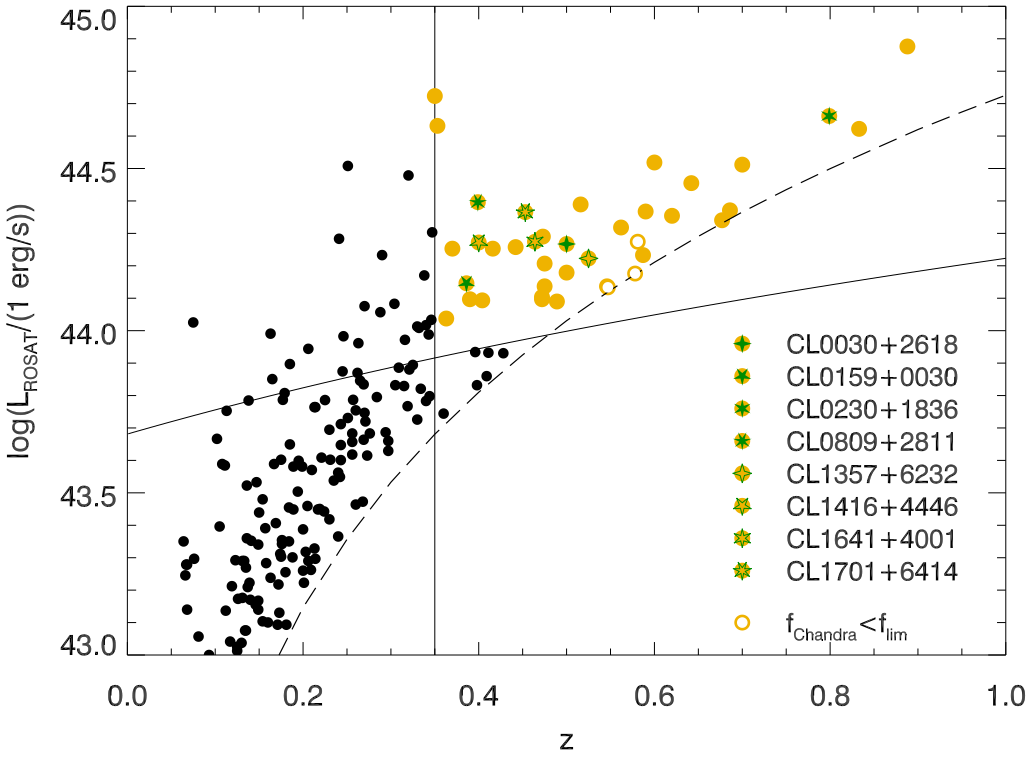

Figure 4.1: Selection of the *400d cosmological sample*: Plotted are the ROSAT luminosities for the more luminous objects in the serendipitous *400d* survey (dots) as a function of redshift z. The luminosity corresponding to the flux limit Eq. (4.1) (dashed line) is valid for an APEC emission model with $kT_X = 5\,\mathrm{keV}$ and metallicity $Z = 0.3\,Z_\odot$. The flux–luminosity relations for the individual clusters are slightly different because of variation in T_X and the elemental composition. The luminosity limit Eq. (4.2) and redshift cut $z_{min} = 0.35$ (solid lines), together with the flux limit, define the cosmological sample. Cosmological sample clusters are displayed with big yellow symbols, and the eight clusters discussed in this thesis are marked by star symbols. Ring symbols denote clusters that have been removed from the cosmological sample because a flux $f_{\mathrm{Chandra}} < f_{\mathrm{lim}}$ was found in the CHANDRA analysis.

4.1.2 The Chandra Cluster Cosmology Project and Subsample

The Chandra Cluster Cosmology Project (CCCP) is a collaborative effort to determine the values of cosmological parameters, in particular w, the Dark Energy equation-of-state, by detailed CHANDRA/X-ray analysis for a subsample of distant *400d* clusters, drawing from the strong evolution of the cluster mass function between a distant and a local sample (Sect. 2.2.1). This primary goal has been achieved, with the cluster masses inferred from X-ray proxies by Vikhlinin et al. (2009a) and the cosmological parameter constraints by Vikhlinin et al. (2009b).[1]

The cosmological or high-redshift subsample was drawn from the *400d* catalogue by selecting all clusters with redshift $z \geq 0.350$, as given in Burenin et al. (2007), and with a *ROSAT* luminosity exceeding

$$L_{\mathrm{ROSAT,min}} = 4.8 \times 10^{43} (1+z)^{1.8}\,\mathrm{erg\,s^{-1}} \quad . \tag{4.2}$$

[1]These publications are titled “Paper II” and “Paper III” of the CCCP, counting Burenin et al. (2007) as “Paper I”.

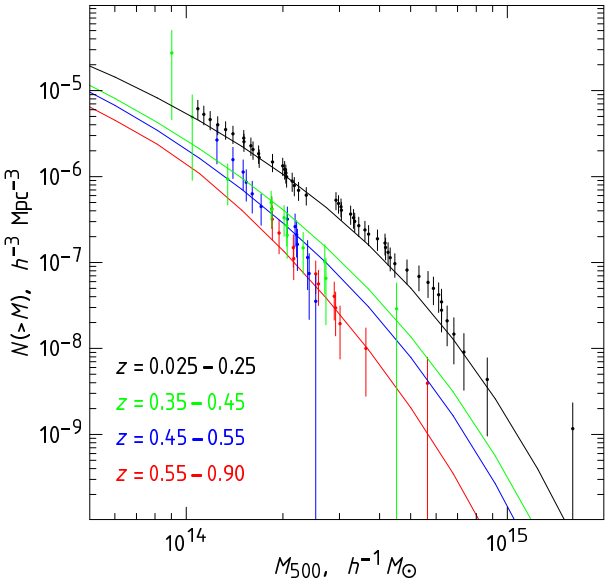

Figure 4.2: The cluster mass functions of the Vikhlinin et al. (2009a) local ($0.025 < z < 0.25$) (black symbols) and distant (*400d*) cluster samples. The latter is shown here divided into three subsamples $0.35 < z < 0.45$ (green symbols), $0.45 < z < 0.55$ (blue symbols), and $0.55 < z < 0.90$ (red symbols). The mass function models (lines) were obtained by fitting σ_8 to the data while keeping $h = 0.72$, $\Omega_\mathrm{m} = 0.3$ and $\Omega_\mathrm{DE} = 0.7$ fixed at their fiducial values. Within the respective redshift bins, the evolution in the mass function has been taken into account by weighting the model number densities. Figure by Vikhlinin et al. (2009b).

Table 4.1 presents the final cluster selection for the cosmological subsample, as published in Vikhlinin et al. (2009a, Table 1), comprising 36 clusters. The cluster redshifts and X-ray properties given in Table 4.1 are quoted directly from Vikhlinin et al. (2009a). Figure 4.1 depicts the selection of the CCCP sample clusters by their redshifts as well as their ROSAT luminosities and fluxes. Noticing the dependence of the f_X–L_X relation on the ICM temperature and metallicity, the dashed line in Fig. 4.1 shows the flux limit for a simple X-ray emission model. The luminosity limit Eq. (4.2) is chosen to remove six lower-redshift, low-luminosity clusters from the sample. Note that the luminosity threshold is only effective in the $0.35 < z < 0.473$ redshift range, while for $z > 0.473$ the *400d* flux limit (Eq. 4.1) corresponds to a luminosity $L > L_\mathrm{ROSAT,min}$.

In its original state, the cosmological sample consisted of 39 clusters. Vikhlinin et al. (2009a), re-analysed all clusters in this preliminary cosmological sample with CHANDRA, exploiting its higher accuracy compared to ROSAT for the determination of the cluster mass function using T_X, the total gas mas M_gas and Y_X as mass proxies (Sect. 2.2.2). The scaling relations were calibrated based on a subsample of relaxed clusters drawn from the sample of 49 low-z clusters. The nearby sample itself is basically a subsample of the *HIFLUCGS* ROSAT sample (Reiprich & Böhringer 2002; Hudson et al. 2010). The Vikhlinin et al. (2009a) CHANDRA analysis pipeline was tested and calibrated using mock cluster observations. In Sect. 8, we discuss the best-fit ICM models for the eight *400d* cosmological sample clusters analysed in this thesis and compare X-ray and weak lensing surface mass profiles.

During the course of their analysis, Vikhlinin et al. (2009a) found the more precise CHANDRA fluxes of the clusters CL 0216−1747 at $z = 0.58$, CL 0521−2530 at $z = 0.58$, and CL 1117+1744 at $z = 0.55$ to be significantly below f_lim and thus removed them from the sample.[2] We note that these three clusters show ROSAT fluxes only slightly above the flux limit (rings in Fig. 4.1). The observed differences between CHANDRA and ROSAT fluxes are in excellent agreement with the expectations based on the *400d* selection function calculated by Burenin et al. (2007). Selection effects due to both the X-ray detection and redshift estimation are controlled via the survey volumes discussed extensively by Burenin et al. (2007) and Vikhlinin et al. (2009a).

Nevertheless, we caution that the quality of the redshift estimates in Table 4.1 might be quite heterogeneous and thus values like $z = 0.5000$ for CL 0030+2618 are inferred from a very small

[2]Because the weak lensing survey (Sect. 4.2) was started well before the publication by Vikhlinin et al. (2009a), using the preliminary sample provided by A. Vikhlinin, there exist partial data sets of CL 0216−1747 and CL 0521−2530 obtained with IMACS/Magellan (see also Fig. 4.3).

Table 4.1: The *400d* Cosmology Sample. Designations (first column) of clusters analysed in this thesis are set in boldface. The cluster redshifts (z), CHANDRA luminosities (L_X), and CHANDRA fluxes (f_X), and the merger flags (columns 2, 3, 6, and 7) are quoted from Vikhlinin et al. (2009a). Luminosities are given in the 0.5–2.0 keV object frame; fluxes in the 0.5–2.0 keV observer frame. Right ascensions and declinations are determined from the ROSAT data (Burenin et al. 2007). The eighth column gives the telescopes with which weak lensing data, if existing, have been obtained. Entries in parentheses denote data sets deemed insufficient for weak lensing analysis while those in italics mark archival data, i.e. not taken by our team. Horizontal lines separate the $0.35 \leq z < 0.45$, $0.45 \leq z < 0.55$, and $0.55 \leq z < 0.90$ redshift bins. Adapted from Vikhlinin et al. (2009a).

Cluster Name	z	L_X erg s^{-1}	α_{J2000}	δ_{J2000}	$f_X \times 10^{13}$ erg s^{-1} cm^{-2}	Merger	WL Obs.
CL 0302−0423	0.3501	5.24×10^{44}	$03^h02^m21^s.3$	−04°23′29″	15.9 ± 1.9	...	WFI
CL 1212+2733	0.3533	3.61×10^{44}	$12^h12^m19^s.2$	+27°33′13″	12.5 ± 1.7	✓	
CL 0350−3801	0.3631	6.80×10^{43}	$03^h50^m43^s.9$	−38°01′25″	2.9 ± 0.8	✓	WFI
CL 0318−0302	0.3700	1.82×10^{44}	$03^h18^m33^s.4$	−03°02′56″	4.6 ± 0.5	✓	(WFI)
CL 0159+0030	0.3860	1.42×10^{44}	$01^h59^m18^s.2$	+00°30′09″	3.3 ± 0.4	...	MMT
CL 0958+4702	0.3900	1.04×10^{44}	$09^h58^m19^s.3$	+47°02′17″	2.8 ± 0.6	...	(MMT)
CL 0809+2811	0.3990	2.50×10^{44}	$08^h09^m41^s.0$	+28°11′58″	5.5 ± 0.8	✓	MMT
CL 1416+4446	0.4000	1.94×10^{44}	$14^h16^m28^s.1$	+44°46′38″	4.0 ± 0.5	...	MMT
CL 1312+3900	0.4037	1.37×10^{44}	$13^h12^m19^s.4$	+39°00′58″	2.6 ± 0.4	✓	
CL 1003+3253	0.4161	1.53×10^{44}	$10^h03^m04^s.5$	+32°53′36″	3.5 ± 0.4	...	*(CFHT)*
CL 0141−3034	0.4423	1.32×10^{44}	$01^h41^m32^s.3$	−30°34′42″	3.1 ± 0.9	✓	WFI
CL 1701+6414	0.4530	2.39×10^{44}	$17^h01^m22^s.5$	+64°14′08″	3.9 ± 0.4	...	MMT
CL 1641+4001	0.4640	9.46×10^{43}	$16^h41^m52^s.3$	+40°01′27″	2.9 ± 0.8	...	MMT
CL 0522−3624	0.4720	1.04×10^{44}	$05^h22^m13^s.8$	−36°24′49″	1.8 ± 0.3	✓	WFI
CL 1222+2709	0.4720	9.88×10^{43}	$12^h22^m01^s.9$	+27°09′19″	1.9 ± 0.4	...	
CL 0355−3741	0.4730	1.76×10^{44}	$03^h55^m59^s.3$	−37°41′46″	2.9 ± 0.7	...	WFI
CL 0853+5759	0.4750	8.43×10^{43}	$08^h53^m13^s.4$	+57°59′44″	2.0 ± 0.5	✓	(MMT)
CL 0333−2456	0.4751	9.79×10^{43}	$03^h33^m10^s.3$	−24°56′40″	2.4 ± 0.5	✓	Magellan
CL 0926+1242	0.4890	1.50×10^{44}	$09^h26^m36^s.6$	+12°42′59″	1.7 ± 0.3	✓	*(VLT)*
CL 0030+2618	0.5000	1.57×10^{44}	$00^h30^m33^s.6$	+26°18′16″	2.4 ± 0.3	✓	MMT
CL 1002+6858	0.5000	1.71×10^{44}	$10^h02^m07^s.6$	+68°58′49″	2.0 ± 0.4	✓	
CL 1524+0957	0.5160	2.07×10^{44}	$15^h24^m40^s.2$	+09°57′35″	3.0 ± 0.4	✓	*(CFHT)*
CL 1357+6232	0.5250	1.63×10^{44}	$13^h57^m19^s.4$	+62°32′42″	2.0 ± 0.3	...	MMT
CL 1354−0221	0.5460	1.40×10^{44}	$13^h54^m16^s.7$	−02°21′46″	1.5 ± 0.2	✓	*(VLT)*
CL 1120+2326	0.5620	1.79×10^{44}	$11^h20^m58^s.3$	+23°26′34″	2.1 ± 0.4	✓	
CL 0956+4107	0.5870	1.85×10^{44}	$09^h56^m02^s.8$	+41°07′08″	1.6 ± 0.3	✓	
CL 0328−2140	0.5901	2.30×10^{44}	$03^h28^m36^s.1$	−21°40′04″	2.1 ± 0.6	...	(Magellan)
CL 1120+4318	0.6000	3.75×10^{44}	$11^h20^m07^s.6$	+43°18′07″	3.0 ± 0.3	...	*CFHT*
CL 1334+5031	0.6200	2.22×10^{44}	$13^h34^m20^s.3$	+50°31′05″	1.8 ± 0.3	✓	
CL 0542−4100	0.6420	2.91×10^{44}	$05^h42^m50^s.8$	−41°00′01″	2.2 ± 0.3	✓	(Magellan)
CL 1202+5751	0.6775	2.22×10^{44}	$12^h02^m13^s.7$	+57°51′53″	1.5 ± 0.4	✓	
CL 0405−4100	0.6861	2.23×10^{44}	$04^h05^m24^s.3$	−41°00′15″	1.5 ± 0.4	✓	Magellan
CL 1221+4918	0.7000	3.35×10^{44}	$12^h21^m25^s.0$	+49°18′07″	2.1 ± 0.5	✓	
CL 0230+1836	0.7990	2.55×10^{44}	$02^h30^m26^s.6$	+18°36′22″	2.2 ± 0.6	✓	MMT
CL 0152−1358	0.8325	5.46×10^{44}	$01^h52^m41^s.3$	−13°58′13″	1.8 ± 0.3	✓	*e.g. HST*
CL 1226+3332	0.8880	8.42×10^{44}	$12^h26^m57^s.7$	+33°32′50″	2.9 ± 0.3	✓	*e.g. HST*

number of sources for which spectra were taken. For our purposes, we round all redshifts to two significant digits, which is sufficiently accurate for the analyses presented in this thesis.

The main conclusions of the CCCP so far are: Vikhlinin et al. (2009a) measured evolution in the $M(Y_X)$–L_X relation – assuming self-similar evolution in the M–Y_X relation – and arrive at a significant evolution of the mass function between their local clusters and the distant *400d*/CCCP sample (but see also the results by Maughan 2007). We show the measured mass functions in Fig. 4.2. Vikhlinin et al. (2009b) find the mass function at $\langle z \rangle \approx 0.5$ to be inconsistent with a flat, decelerating universe and measure $\sigma_8(\Omega_m/0.25)^{0.47} = 0.813 \pm 0.013 \pm 0.024$ (where the first is the statistical and the second the systematic error) from the cluster mass function alone, $w = -1.14 \pm 0.21 \pm 0.13$ from clusters with a prior on the Hubble parameter, and $w = -0.991 \pm 0.045 \pm 0.040$ combining the cluster masses with other probes (see Fig. 1.3, Sect. 1.3.2).

4.2 The Weak Lensing Survey

4.2.1 Motivation

What can be gained from the project this thesis presents, i.e. following up a sample of galaxy clusters whose masses have been measured using state-of-the-art X-ray instruments and techniques with weak gravitational lensing? Weak lensing offers an alternative avenue towards determining cluster masses which is completely independent of the assumptions of hydrostatic equilibrium, elemental composition, and, to a large extent, spherical symmetry, which underlie the X-ray analysis (Vikhlinin et al. 2009a, and Sect. 8). Weak lensing allows us to directly map the (projected) distribution of all matter, Dark and luminous, in a cluster. This provides additional information helpful to detect possible mergers which affect the X-ray observables, compared to identifying mergers based on the morphology of the extended X-ray emission (presented in Table 4.1) alone.

Considering the total energy involved, cluster mergers represent the most energetic processes since the Big Bang. Merging clusters deviate strongly from thermal and hydrostatic equilibrium, with a significant amount of the internal energy being present as kinetic energy of bulk motions or turbulent processes, e.g. merger shocks. Given the typical relaxation timescales of a few Gy, a merging event will keep the ICM in an *unrelaxed* state for a long time. The merger states inferred from X-ray morphology of *400d* clusters (Table 4.1) agree with simulations (e.g., Cohn & White 2005) indicating that a disturbed ICM is more common at $z > 0.5$ than a relaxed one. During the period it takes for hydrostatic equilibrium to re-establish by heat dissipation, the increased mass of the merged system will be at opposition to the low T_X which still has to adapt, biasing low the M-T_X relation. Mergers also increase the local gas density in the shocked regions, causing an overestimation of M_{gas} if hydrostatic equilibrium is assumed (Kravtsov et al. 2006). The anti-correlation between these two effects, seen in some simulations (e.g., Kravtsov et al. 2006; Nagai et al. 2007a) is claimed responsible for the smaller influence of mergers on Y_X (Sect. 2.2.2), giving rise to the small scatter in this estimator (see also Stanek et al. 2010, for simulations showing a *correlation*). Most importantly, bulk motions induce non-thermal pressure, supporting particles against gravity, thus leading the hydrostatic mass to *underestimate* the true mass by 5–20 % even in *relaxed* clusters (Rasia et al. 2006; Nagai et al. 2007b; Meneghetti et al. 2009). Laganá et al. (2010) discuss the roles of non-thermal pressure by magnetic fields and cosmic rays.

Therefore, studying scaling relations of X-ray observables with weak lensing masses has become an important ingredient in refining cluster masses from X-rays (e.g., Meneghetti et al. 2009; Zhang et al. 2010, and the results cited in Sect. 2.2.2). Determining accurate weak lensing masses for the most distant clusters in the *400d* sample furthermore opens the way to observationally test the assumptions Vikhlinin et al. (2009a,b) make for the scaling relation evolution. Put briefly, the weak lensing follow-up of the *400d* cosmological sample clusters provides us with a control

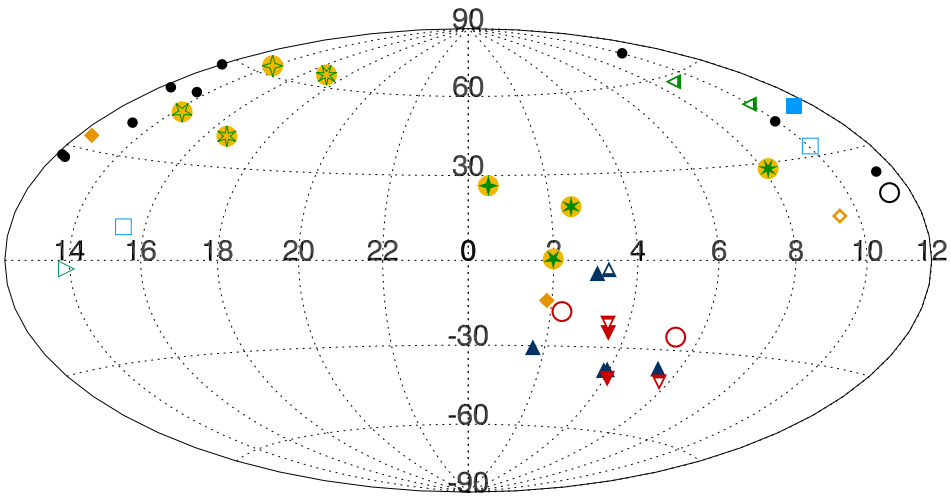

Figure 4.3: Celestial distribution of the *400d cosmological sample* clusters. The map is a Hammer–Aitoff projection centred on right ascension $\alpha = 0^{\rm h}$ and declination $\delta = 0°$. The telescopes with which clusters are observed are marked by symbols and colours (Table 4.1). The eight clusters observed with MEGACAM and discussed in this Thesis are denoted by the same green star symbols in a filled yellow circle as in Fig. 4.1. Green left-facing triangles stand for MEGACAM at MMT; dark-blue upward-facing triangles for WFI/ESO 2.2m; red downward-facing triangles for IMACS/Magellan; orange diamonds for ACS/HST; blue squares for MegaCam/CFHT; and the mint right-facing triangle for FORS/VLT. Half-filled symbols mark incomplete data sets; open symbols mark archival data of questionable depth or field-of-view. Unobserved clusters are denoted by black dots. Ring symbols, as in Fig. 4.1 denote the clusters removed from the sample.

experiment for the mass function presented in Fig. 4.2. We note that the relative uncertainties of the individual WL cluster masses are higher than those from X-rays, largely due to the intrinsic shape noise (Sect. 3.2). Again, the power of weak lensing comes through the statistical analysis of $M_{\rm wl}/M_{\rm X}$ for the whole sample, under the assumption that WL mass estimates are, on average, unbiased. The other way round, statistical comparisons to X-ray masses (e.g., Meneghetti et al. 2009) help us to investigate WL systematic uncertainties, i.e. triaxiality (Corless & King 2009) and projection of unrelated LSS (Hoekstra 2003) to which X-ray observables are far less sensitive.

4.2.2 Data Acquisition

To obtain a mass determination of high accuracy, weak lensing observations of galaxy clusters require deep, wide-field imaging out to at least the (estimated) virial radius of the cluster. Thus, only a few telescopes worldwide and in the orbit can be used for our purposes. Until now (June 2010), not less than 14 observing runs were conducted in which *400d* clusters were observed by our WL survey team; one further run is in preparation. For a number of clusters in the sample, the necessary observations already exist in the public archives. The final column of Table 4.1 lists the

instrument with which data relevant for the WL follow-up, if existing, were observed. Figure 4.3 shows the distribution[3] of the *400d* cosmological sample clusters on the sky and denotes with different symbols clusters for which WL data have been taken with different instruments. Black dots mark the nine unobserved objects, while incomplete or probably insufficient observations are denoted by half-filled symbols in Fig. 4.3 and set in parentheses in Table 4.1. The three clusters cut from the sample by Vikhlinin et al. (2009a) are shown as rings.

Public Archival Data The two most distant objects in our sample, CL 0152−1358 at $z = 0.83$ and CL 1226+3332 at $z = 0.89$, have been observed with the *Advanced Camera for Surveys* (ACS) on board the *Hubble Space Telescope* (HST). With its superb *spatial resolution* and well-known *point spread function* (PSF), ACS has been used extensively for WL (e.g., Schrabback et al. 2007, 2009, and references therein), in particular also for mass modelling of distant ($z \sim 0.9$) galaxy clusters (e.g., Margoniner et al. 2005). Weak lensing analyses of CL 0152−1358 and CL 1226+3332 were already performed by Jee et al. (2005) and Jee & Tyson (2009), resp., identifying these two clusters as outstanding objects, ranking among the hottest, most X-ray luminous, and most massive clusters at high redshift. We note that these two clusters have also been observed with ground-based telescopes and cameras usable for WL. Additionally, several further clusters have short "snap-shot" ACS observations. In Fig. 4.3, the HST/ACS targets are indicated by orange diamonds.[4]

Three of the sample clusters (blue squares in Fig. 4.3) have been observed with the MEGACAM instrument at the *Canada–France Hawaii Telescope* (CFHT) before observations for the *400d* WL programme began, with significant exposure times from a WL perspective. One object, CL 1701+6414, was targeted with CFHT after our MMT/MEGACAM observations (see below) were taken. So far, none of these four clusters has a published WL study. Finally, imaging of CL 1354−0221 with the *Very Large Telescope* (VLT) *Focal Reducer and Low Dispersion Spectrograph 1* (FORS1) exists and might be used for the WL follow-up (mint-green triangle facing to the right in Fig. 4.3).[5] We plan to re-analyse all publicly available data sets consistent with the rest of our sample at a later stage of the follow-up survey.

Dedicated Observations At present, 14 dedicated *observing runs* have been conducted by our team for the *400d* WL follow-up survey, using these telescopes and cameras: Distant ($z \geq 0.48$) southern (declination $\delta < -3°$) clusters were targeted with the *Inamori Magellan Areal Camera and Spectrograph* (IMACS) at the 6.5 m Magellan–Baade telescope (Las Campanas Observatory, Chile). Observations of CL 0333−2456 and CL 0405−4100 are complete, CL 0328−2140 and CL 0542−4100 await completion (filled and half-filled red, downward-facing triangles in Fig. 4.3).

For the six low-redshift ($0.35 \leq z \leq 0.47$) clusters in the sample, dedicated imaging was obtained with the *Wide Field Imager* (WFI) at the 2.2 m *European Southern Observatory* (ESO)/ *Max-Planck-Gesellschaft* (MPG) telescope in La Silla, Chile (dark-blue upward-facing triangles in Fig. 4.3). Five of the six clusters (CL 0302−0423, CL 0350−3801, CL 0141−3034, CL 0522−3624, and CL 0355−3741) have complete data sets, only one object (CL 0318−0302) is in a partial status.

This thesis focusses on observations of sample clusters in the northern celestial hemisphere, performed using the MEGACAM camera at the 6.5 m MMT telescope, located at Fred Lawrence

[3]The inhomogeneity of this distribution reflects the selection of the pointed ROSAT/PSPC observations on which the *400d* survey is based: To ensure a low X-ray absorption, only observations with Galactic latitude $|b| > 25°$, separation $\theta > 10°$ from the Large and Small Magellanic Cloud, Galactic absorption $N_H < 10^{21}$ cm^{-2} and exposure time $T_{exp} > 1000$ s were considered (Burenin et al. 2007). As an unfortunate consequence for the optical, ground-based observer, sample clusters on both hemispheres are preferentially visible in the shorter summer nights.

[4]We include CL 0926+1242, the one "snap-shot" target not observed from the ground with a long enough exposure.

[5]We note that, given the relatively small field-of-view, this data set might not have the radial coverage needed for an accurate WL mass measurement.

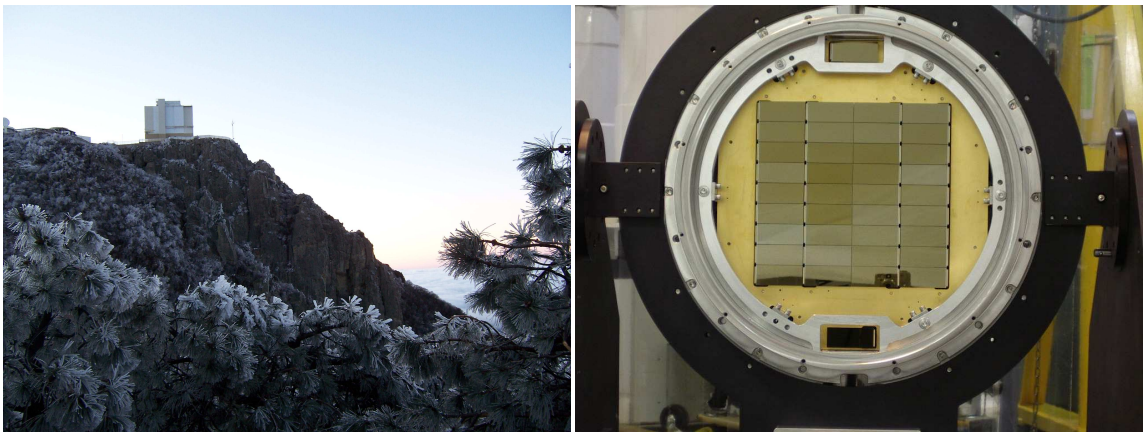

Figure 4.4: *Left:* The 6.5 m MMT telescope dome on the summit of Mt. Hopkins, Arizona. Photography taken by the author before sunrise of January 8, 2008, during *"Run J"*. Note the mountain rising out of a cloud cover. *Right:* The MEGACAM detector array. Photography by Brian McLeod, `http://www.cfa.harvard.edu/~bmcleod/MegacamCCDInstallation/Imgp0622.htm`.

Whipple Observatory (Mt. Hopkins, Arizona; Fig. 4.4). In the remainder of this work, we will discuss the data reduction and analysis for the eight $\delta > 0^\circ$ galaxy clusters with right ascensions $0^\mathrm{h} < \alpha < 8^\mathrm{h}30^\mathrm{m}$ and $13^\mathrm{h}30^\mathrm{m} < \alpha < 24^\mathrm{h}$ for which observations in the lensing band (Sect. 4.2.3) have been completed. These objects are highlighted with bold face in Table 4.1 and individual symbols in Figs. 4.1 and 4.3. The data sets, presented in Sect. 4.2.4, have been reduced completely (Sect. 5). In addition, two further clusters, CL 0853+5759 and CL 0958+4702, were observed with MEGACAM but have not been completed yet (green, half-filled left-facing triangles in Fig. 4.3).

Before turning to the analysis of the existing data, we note that for 27 out of the 36 sample clusters data sets relevant for the WL survey exist. Until now, we consider dedicated observations completed for 15 clusters, which had not previously been observed with large optical telescopes. In the future, we plan to complete observations for the currently 5 unfinished clusters as well as the 9 unobserved objects.

4.2.3 Observing Strategy

MEGACAM is a wide-field, 36-chip, imaging instrument with a field-of-view of $\sim 24' \times 24'$, resulting from a mosaic of 4×9 CCDs, each consisting of 2048×4608 pixels, which corresponds to a very small pixel size of $0.08''$ px^{-1} (McLeod et al. 2000, 2006). Each chip has two read-out circuits and amplifiers, each reading out half a chip. The gaps between the chips measure $6''$ in the direction corresponding to declination using the default derotation. In the direction associated with right ascension, three gaps of $33''$, $5''$, and $33''$ exist. The right panel of Fig. 4.4 shows how the CCDs are arranged in the focal plane. We use MEGACAM in the default 2×2 binning mode.

A system of $u'g'r'i'z'$ filters, similar to but subtly different from their namesakes in the Sloan Digital Sky Survey (Fukugita et al. 1996), is used for MEGACAM. The relations between the MEGACAM and SDSS filter systems are described in detail in Sect. 5.2.1 and visualised in Fig. 5.3.

In principle, the small distortions of background sources which we want to measure are achromatic. In practice, however, the optimal passband for weak lensing observations is determined by the signal-to-noise ratio which can be obtained in a given amount of time and depends on seeing and instrumental throughput. To maximise the number of high signal-to-noise background galaxies whose shapes can be determined reliably for a given exposure time, we choose the r'-band as the default lensing band. Aiming at a limiting magnitude of $r'_\mathrm{lim} \approx 26$ for $T_\mathrm{exp} \approx 3\,\mathrm{h}$, we obtain

a sufficient number of high-quality shape sources ($n_{\rm gal} > 10$–$15\,{\rm arcmin}^{-2}$) in the final catalogue. Conforming with Hildebrandt et al. (2005), we compute the limiting magnitudes in the coadded images for a 5σ-detection in a $2''$ aperture as

$$m_{\rm lim} = Z_f - 2.5 \log\left(5\sqrt{N_{\rm pix}}\sigma_{\rm sky}\right) \quad , \tag{4.3}$$

where Z_f is the photometric zeropoint in the filter f, $N_{\rm pix}$ the number of pixels within the $2''$ aperture, and $\sigma_{\rm sky}$ the RMS sky-background variation measured from the image. We list the limiting magnitudes for each filter and band in Table 4.2.

As mentioned in Sect. 3.2.2, lensing effects depend on the relative distance between source and deflector. Ideally, we would like to determine a *photometric redshift* estimate for each galaxy in our lensing catalogue (e.g.: Benítez 2000; Bolzonella et al. 2000; Wolf et al. 2001; Ilbert et al. 2006; Hildebrandt et al. 2008). However, this is observationally expensive as deep imaging in $\gtrsim 5$ passbands is necessary to obtain accurate photometric redshifts (e.g. Piel et al., in prep.).

On the other hand, using only one filter (the lensing band) and a simple magnitude cut for a rough separation of background from foreground galaxies needs a minimum of observing time but neglects the galaxies' intrinsic distribution in magnitude. We are following an intermediary approach here, using three filters from which we construct colour-colour-diagrams of the detected galaxies and use this information to achieve a more accurate background selection than using the simplistic magnitude cut. This method has been successfully applied to weak-lensing galaxy cluster data by e.g. Clowe & Schneider (2002); Bradač et al. (2005); Kausch et al. (2007). MEGACAM's g' and i' passbands straddle the Balmer break, the most distinctive feature in an elliptical galaxy's optical spectrum at a redshift $z \approx 0.5$, in which we are interested. Therefore, we use the $g'r'i'$ filters with nominal exposure times of $T^{\rm nom}_{g'} = 6000\,{\rm s}$, $T^{\rm nom}_{r'} = 7500\,{\rm s}$, and $T^{\rm nom}_{i'} = 4500\,{\rm s}$ to identify foreground and cluster objects in our catalogues. We extensively discuss the background selection in Sects. 6.1.2, 7.1.2, and 8.1.1.

In order to obtain a high level of homogeneity in data quality over the field-of-view despite the gaps between MEGACAM's chips, we stack dithered exposures. Our dither pattern consists of 5×5 positions in a square array with $40''$ distance between neighbouring points, inclined by 10° with respect to the right ascension axis on which the chips normally are aligned. We find this pattern to be robust against missing frames (exposures which could not be used in the final stack).

None of the previous studies with MEGACAM (e.g.: Hartman et al. 2008; Walsh et al. 2008) is related to gravitational lensing or relying on wide-field imaging. Thus, in Israel et al. (2010) we showed, for the first time, that MEGACAM indeed is suitable for WL analyses (Sect. 5.4.4).

4.2.4 MEGACAM Data Analysed for the *400d* Survey

Hitherto, six observing runs for the *400d* WL survey have been conducted with MEGACAM at the MMT. During five of them, weather conditions permitted usable observations to be performed during parts of or the complete scheduled time. The *400d* clusters mentioned in Sect. 4.2.2 were targeted during runs in October 2004 ("*Run B*"), June 2005 ("*Run C*"), October/November 2005 ("*Run E*"), and January 2008 ("*Run J*").[6] Appendix A gives detailed lists of when the individual objects were observed in which filters.

The four clusters CL 0030+2618, CL 0159+0030, CL 0230+1836, and CL 0809+2811, have completed observations in the $g'r'i'$ filters (*Runs B, E, J*), while due to scheduling constraints, only the r'-imaging could be completed for CL 1357+6232, CL 1416+4446, CL 1641+4001, and

[6] The first MMT observing run, "*Run A*" took place in July 2004, before the *400d* selection criteria were finalised. The $z = 0.53$ cluster RX J2146.0+0423 observed in *Run A* was selected from the *160d* survey (Mullis et al. 2003) but is not part of the *400d* sample due to its flux $f_{\rm ROSAT} = 1.38 \times 10^{-13}\,{\rm erg\,s^{-1}\,cm^{-2}}$ closely missing the flux limit (Eq. 4.1).

Table 4.2: Specifications of the data sets analysed in this thesis. For each cluster and filter, the total MEGACAM exposure time $T_{\rm exp}^{\rm ini}$, usable final exposure time $T_{\rm exp}^{\rm fin}$, seeing, and limiting magnitude (Eq. 4.3) for the final image stack are given. Finally, we indicate whether the photometric calibration (PhC, Sect. 5.2) was performed directly (D) or indirectly (I).

Cluster	Filter	Observation Dates	$T_{\rm exp}^{\rm ini}[s]$	$T_{\rm exp}^{\rm fin}[s]$	Seeing	$m_{\rm lim}$	PhC
CL 0030+2618	r'	2004-10-06/07	15300	6600	$0\farcs82$	25.9	I
	g'	2005-10-30/31,11-01	9150	7950	$0\farcs87$	26.8	D
	i'	2005-10-31	6000	5700	$1\farcs03$	25.1	D
CL 0159+0030	r'	2005-10-30/31,11-01	9900	3600	$0\farcs85$	25.7	D
	g'	2005-11-01,	6000	4800	$1\farcs05$	27.7	D
	i'	2005-10-31,11-01	8100	5700	$1\farcs14$	25.0	D
CL 0230+1836	r'	2004-10-06/07; 2005-11-08	9600	2700	$0\farcs68$	25.1	I
	g'	2005-11-08	6000	4200	$0\farcs80$	27.2	I
	i'	2005-10-31,11-01/08	9600	3600	$0\farcs98$	24.7	D
CL 0809+2811	r'	2005-11-08; 2008-01-09	9300	3000	$0\farcs72$	25.4	D
	g'	2005-10-31/11-08	6000	3600	$1\farcs04$	26.3	D
	i'	2005-10-31/11-01	7500	5700	$0\farcs82$	26.1	D
CL 1357+6232	r'	2005-06-07	7200	2700	$0\farcs90$	25.4	D
CL 1416+4446	r'	2005-06-08	7500	4200	$0\farcs81$	25.8	D
CL 1641+4001	r'	2005-06-07	8100	6900	$0\farcs91$	26.0	D
CL 1701+6414	r'	2005-06-08	7500	6000	$0\farcs89$	25.8	D

CL 1701+6414 (in *Run C*). Therefore, a different strategy has to be adopted for parts of the data reduction (Sect. 5.4.1) and the background source selection in these fields (Sect. 7.1.2).

In the following Sect. 5, we will discuss in detail the data reduction and photometric calibration leading to the final stacked "coadded" images for each cluster and filter. Table 4.2 summarises the main properties of the data set resulting from this process. As indicated by the observation dates, some clusters were observed in the same filter in more than one observing run. The implications for the photometric calibration are detailed in Sect. 5.2 (see Table 4.2 for the flags indicating the calibration method).

The most striking fact to note in Table 4.2 are the drastic reductions in exposure time, comparing the total $T_{\rm exp}^{\rm ini}$ for the raw data to the net usable exposure time $T_{\rm exp}^{\rm fin}$ of the coadded images. In a number of cases, the required seeing $\lesssim 1''$ in the lensing band and $\lesssim 1\farcs2$ in the other bands could only be achieved by removing images such that the resulting $T_{\rm exp}^{\rm fin} < T^{\rm nom}$, where $T^{\rm nom}$ stands for the nominal exposure time given in Sect. 4.2.3. As this inevitably reduces the limiting magnitude (Eq. 4.3), the final stacks represent a compromise between seeing and depth, aiming at an optimal WL signal. A further effect necessitating a strict *frame selection* is discussed in Sect. 5.4. In the remainder of the thesis, the ramifications of the heterogeneous data quality and the shallow exposure times, by which the good overall seeing in the r'-band could be obtained, will be addressed at several occasions.

Chapter 5

Data Reduction and Analysis

5.1 Data Reduction for MMT/Megacam

The data reduction performed for the MMT/MEGACAM observations of *400d* clusters relies on the THELI pipeline originally designed and tested on observations obtained using the *Wide Field Imager* (WFI) mounted on the ESO/MPG 2.2 m telescope (Erben et al. 2005). The reduction follows, in general, the procedure detailed in Erben et al. (2005), some important changes having been made to adapt the THELI pipeline to work on MMT MEGACAM data. Because MMT MEGACAM is a "new" camera with a small field-of-view per chip ($325'' \times 164''$ instead of, e.g., $853'' \times 379''$ for MegaPrime at CFHT, or a factor $1/6$ in field-of-view, or even a factor $1/9$ compared to WFI), using a larger telescope, in the following, special emphasis is given to those developments.

The THELI pipeline distinguishes two stages of data reduction called run processing and set processing. During *run processing*, the first phase, all frames taken during an observation run in a particular filter are treated in the same way. Run processing comprises the removal of instrumental signatures, e.g., de-biasing and flatfielding. In *set processing*, the data are re-ordered according to their celestial coordinates rather than their date of observation. Astrometric and photometric calibration produce a "coadded" (stacked) image for each set.

5.1.1 The `THELI` "Run Processing" Stage

Chips and Amplifiers The MEGACAM control software offers a number of options for the CCD readout. As already mentioned in Sect. 4.2.3, there are 36 physical CCD chips. Each of them is equipped with two output amplifiers, giving a readout of 1024×4608 (unbinned) pixels per amplifier. For our programme, we have chosen to use all 72 amplifiers, each reading out half a chip, thus reducing readout time by a factor of two. As a result, MEGACAM raw images are multi-extension `fits` files with 72 extensions.

Owing to this, all run processing tasks are performed on the 72 subframes individually. Files from the two amplifiers of a chip are joined at the end of the run processing prior to the astrometric calibration to increase the usable surface for the astrometric procedures.

De-Biasing By stacking all bias frames taken within a suitable time interval around the date of science observations, a *master bias image* is constructed and subtracted from all other frames.

Flatfielding `THELI` applies a two-step process. First, science frames are divided by a master sky flatfield frame. In the second step, the median for each pixel of all science frames is calculated, discarding the positions at which objects have been detected by *SExtractor* (Bertin & Arnouts

Table 5.1: The three bright stars exacerbating the analysis of the CL 0159+0030, CL 0230+1836, and CL 0809+2811 fields, identified by their BD and HD designations. We cite SIMBAD (`http://simbad.u-strasbg.fr/simbad/`) for stellar positions, V magnitudes and spectral types (Spec.). By θ we denote the separations between the resp. ROSAT cluster centre and star.

BD	HD	α_{J2000}	δ_{J2000}	Separation θ	m_V	Spec.
−00 301	12134	01:59:10.337	+00:30:24.90	1.94′	8.28	F0
+18 315	15551	02:30:30.146	+18:39:51.64	3.59′	8.25	K0
+28 1562	67543	08:09:34.273	+28:11:46.80	1.51′	8.60	F0

1996). Because of the dithering, *for every pixel* in the field-of-view, these "superflats" contain signal from the sky background *from slightly different positions on the sky*. Thus, the superflat provides a means of comparing the response of different pixels.

Selecting the frames that contribute to the superflat to achieve the optimal flatness of the background is the most time-consuming and work-intensive step in run processing, as inhomogeneities in individual frames will have a significant effect on the superflat. Imperfect photometric conditions and variable instrumental gains are two common reasons for science frames to be removed from the calculation of the superflat.

Very bright stars near target clusters exacerbate the situation in the fields of CL 0159+0030, CL 0230+1836, and CL 0809+2811. The V magnitudes and separation of the stars from the respective clusters are listed in Table 5.1. Because of their position close to the cluster and hence the frame centre, and the coincidence that imaging of those three fields is to a large extent identical to *Run E*, the resulting uncorrected superflat is affected by an additive background component near the frame centre. Involving many iterations of the – manual – frame selection process, our superflatfielding is effective in reducing the relative background variation over the field in the superflatfielded exposures to < 1.5 %, and to < 1.0 % for most exposures.

In the superflatfielding stage, the different sensitivities of the amplifiers are determined and equalised, taking into account all exposures within the `THELI` *run*. This we can do, because the relative sensitivities of most of the amplifiers are constant most of the time. Gain equalisation is achieved by scaling each amplifier with an appropriate factor detailed in Erben et al. (2005, Sect. 4.7). Some amplifiers, however, experience gain fluctuation on short timescales of the order of days. In these situations, the same superflatfield frame can no longer provide the same quality of flattening to all exposures; we therefore had to process separately the g'-band data taken on Nov. 8, 2005 and the remaining exposures taken on Oct. 30, 2005 and Nov. 1, 2005. Because of the small number of frames observed on Nov. 8, 2005, we found the superflat calculated with the rest of the *Run E* g'-band data to provide the better correction. To this end we used a modification of the `THELI` code which allows to feed a (sub-)*run* with a list of additional frames for superflatfielding.

De-Fringing Interference of incident light between the CCD Si layer surfaces (separated by $\sim 1\,\mu$m) causes a spatially variable background in red filters. When necessary – in our case for all i'-band data – this *fringing pattern* can be isolated from the high spatial frequencies of the superflat and subtracted from the science frames. In addition, we divide by the superflat containing the lower spatial frequencies that carry information about the (multiplicative) "flatfield" effects.

Satellite Tracks Light reflected by artificial Earth satellites that move rapidly across the field-of-view produces bright, linear streaks in some of the frames. We identify satellite tracks by visual

inspection when assessing frames for superflat construction and mask pixels that are affected in the given exposure. Masked pixels (stored as a DS9 region file) are set to zero when constructing the weight images.

Weight Images Taking into account bad pixel information from the bias, flatfield, and superflatfield frames we construct a weight image, i.e. noise map, for each individual amplifier and exposure in the *run*. Our algorithm is not only sensitive to cold and hot pixels but also to charge "bleeding" in the vicinity of grossly overexposed stars. It should be noted that the use of dark frames is not necessary for running THELI.

5.1.2 The THELI "Set Processing" Stage

Astrometry We perform the astrometric calibration of our data using the best available catalogue as a reference. In case of overlap with SDSS Data Release Six (Adelman-McCarthy et al. 2008) we adopt the SDSS catalogue; otherwise we employ the shallower USNO B1 catalogue (Monet et al. 2003), as it is the densest all sky astrometric catalogue. The astrometric calibration is carried out by the TERAPIX software *Scamp* (Bertin 2006), replacing the *Astrometrix* programme earlier used within THELI. We find *Scamp* to be more robust than *Astrometrix* when working on chips with a small field-of-view on the sky, as for MEGACAM. Compared to the otherwise similar design of MegaPrime/MegaCam at the Canada-France-Hawaii Telescope, the MMT/MEGACAM chips cover $\sim 1/6$ of the solid angle on the sky, reducing the number of usable sources for astrometry by a similar factor leading to less accurate and robust astrometric solutions when these are calculated on a chip-to-chip basis.

The most important innovation is, that while *Astrometrix* determines an astrometric solution for each chip individually, *Scamp* recognises that the amplifiers of one exposure belong together and can take into account information about the array configuration, drastically reducing the effort to be invested into this task. We provide these additional constraints by defining a template for the same instrument configuration and filter. This template is drawn from the observation of a dense field, i.e., a star cluster. This template guarantees a sensible solution even with few ($\lesssim 20$) astrometric standard stars per chip, a condition frequently met with MEGACAM in fields at high Galactic latitudes.

Furthermore, by running *Scamp* on all frames in all filters for a given target cluster with only one software call, we ensure consistency between the astrometric solutions among the THELI *sets* corresponding to the resulting stacks in different passbands. For the combined CL 0030+2618 data set, we achieve an accurate calibration with a 1σ intrinsic accuracy of $0\farcs04$ for the sources detected with MEGACAM and $0\farcs27$ (statistical uncertainties) with respect to the astrometric standard catalogue USNO B1.

Relative Photometry In addition to the astrometric calibration, the relative photometric zeropoints of the frames are established by *Scamp*. In the first part of this two-step process, relative zeropoints are determined only from the differences in flux found for the astrometric reference stars in different exposures. These are independent of the absolute photometric calibration detailed in Sect. 5.2.

In this first step, the fluxes of the same object in different exposures are compared. Because images with high absorption basically only contribute noise to the coadded image resulting from stacking, they should not be considered. We decide to include only images that have a relative zeropoint $Z_{\rm rel}$ less than 0.1 magnitudes from the median zeropoint:

$$|Z_{\rm rel} - \mathrm{median}(Z_{\rm rel})| < 0.1 \quad . \tag{5.1}$$

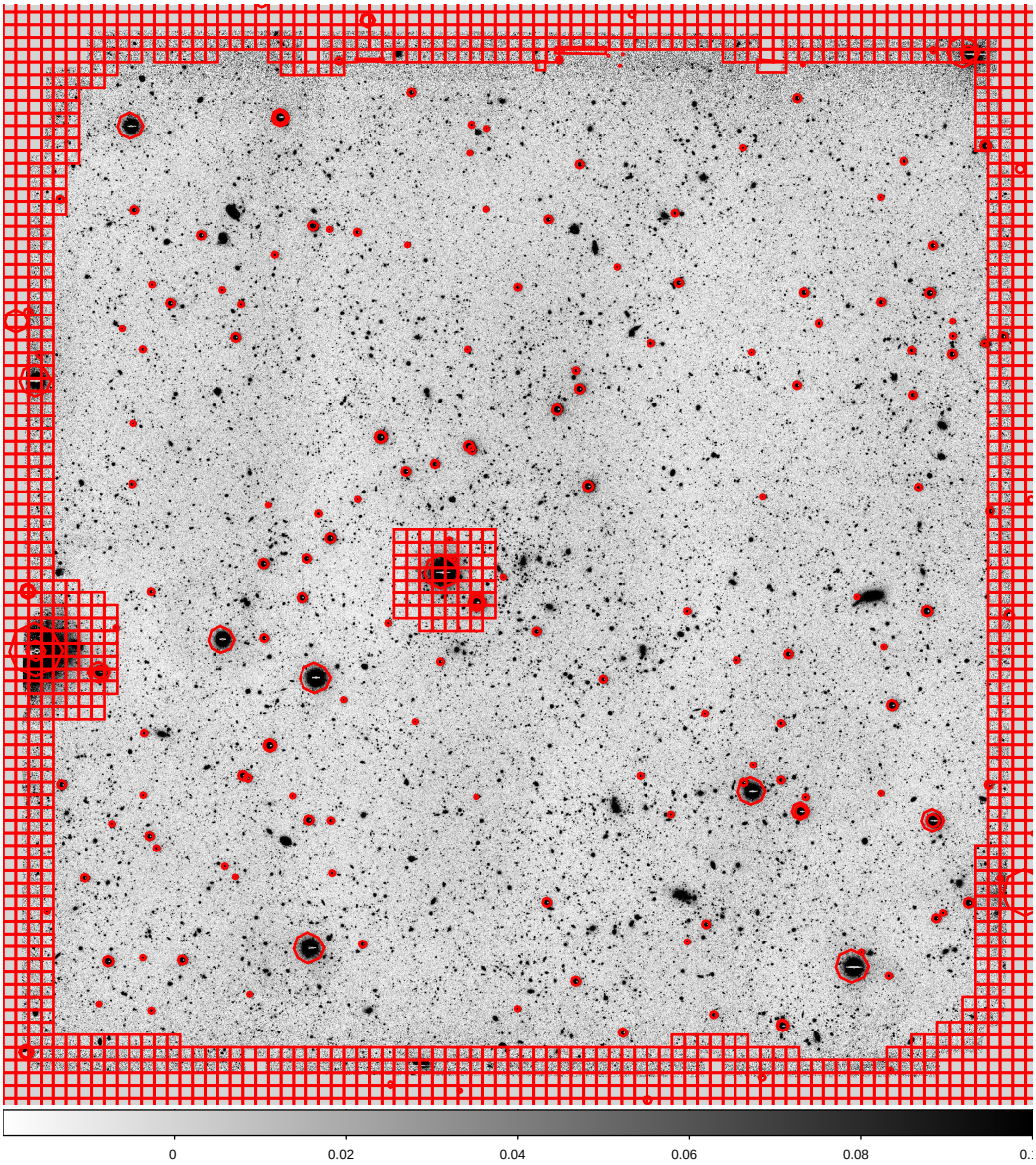

Figure 5.1: The coadded r'-band image of CL 1416+4446 and, superimposed, its final masks. The target cluster is located at the frame centre. Small square masks cover regions masked because of their source counts strongly deviating from the average in the field. The small octagonal masks are saturated stars found using the `USNO B1` catalogue.

In the second step, if the *absolute* photometric calibration (Sect. 5.2) has been applied already, we compute the *corrected zeropoints* defined in Hildebrandt et al. (2006, Eq. (2)) of those individual frames we consider to be taken under photometric conditions. As detailed in Hildebrandt et al. (2006), corrected zeropoints are a useful consistency check, as they need to be consistent for exposures obtained in photometric conditions.

Coaddition Conforming with `THELI` standard, *SWarp* is used to stack ("coadd") images. This, together with the *Scamp* astrometry, also removes optical distortions, yielding a constant pixel scale in the coadded image. The final products of the *set* stage are the coadded image (Fig. 5.1) and the corresponding weight image (Fig. 5.2). Taking into account the seeing distributions for the

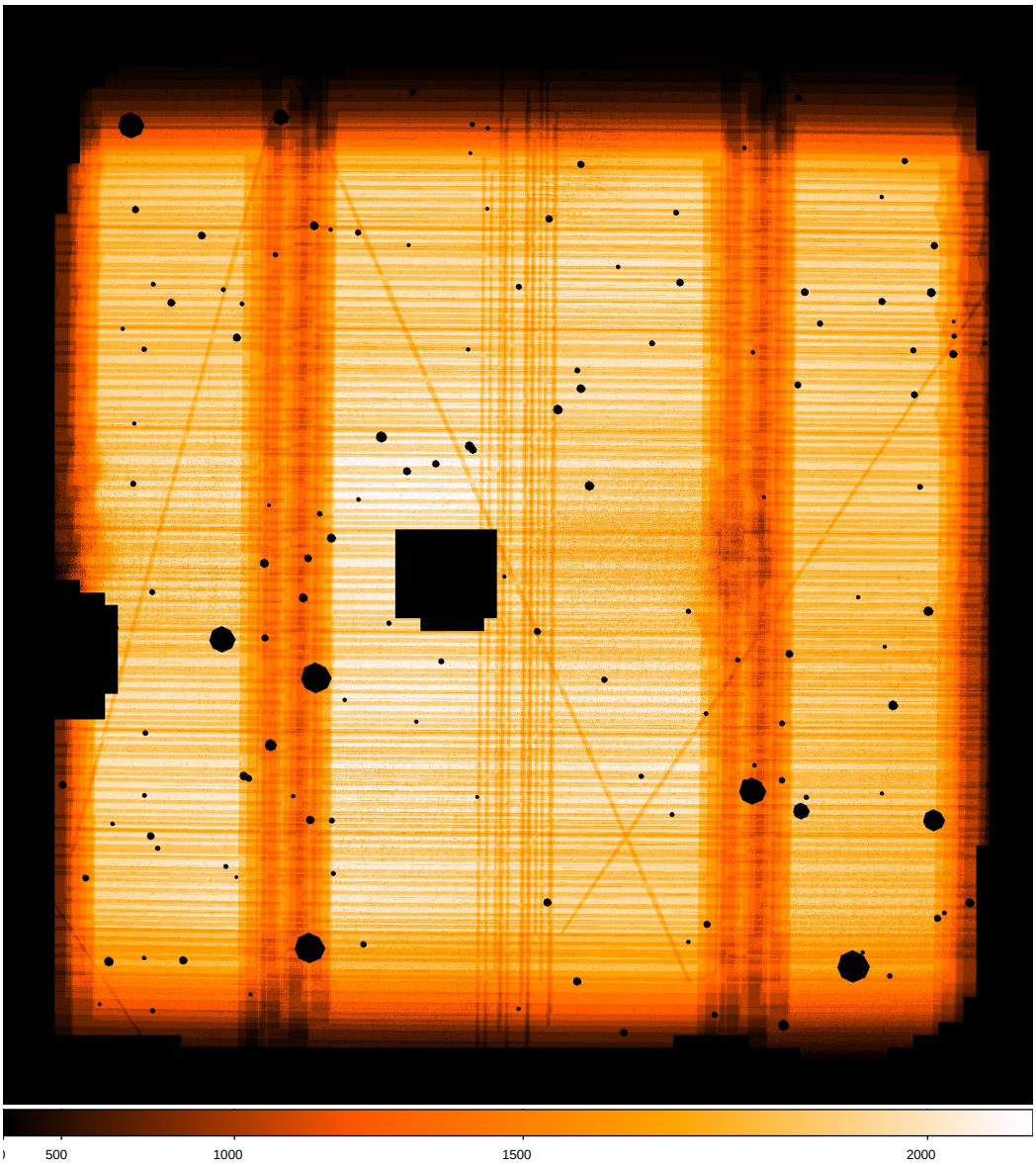

Figure 5.2: The r'-band weight image of CL 1416+4446. The lightness of the colour coding is proportional to the weight squared. Areas covered by the chips in all exposures have significantly higher weights than those that fall on an intra-chip gap in some of the dithered exposures.

different fields and filters, we relax the nominal seeing constraints of $s \leq 1.0''$ in the r' and $s \leq 1.2''$ in the g'- and i'-bands (Sect. 4.2.4) in some cases. For the r'-band, we consider frames based on the following seeing cuts: $s \leq 1.00$ for CL 0030+2618 and CL 0809+2811; $s \leq 1.01$ for CL 1641+4001 and CL 1701+6414; $s \leq 1.05$ for CL 0159+0030, CL 0230+1836, and CL 1357+6232; and $s \leq 1.10$ for CL 1416+4446. We provide further detail on the frame selection for coaddition in Sect. 5.3.

5.1.3 Coaddition Post Production

The final stage of the data reduction is to mask problematic regions in the coadded images by applying the methods presented in Dietrich et al. (2007). By subdividing the image into grid cells of a suitable size and counting *SExtractor* detections within those, we identify regions whose

source density strongly deviate from the average as well as those with large gradients in source density. This method not only detects the image borders but also masks, effectively, zones of higher background close to bright stars, galaxies, or defects (Fig. 5.2).

In a similar way, we mask bright and possibly saturated stars, which are likely to introduce spurious objects into catalogues created with *SExtractor*. We place a mask at each position of these sources as drawn from the `USNO B1` catalogue. The method in which the size of the mask is scaled according to the star's magnitude was described in some detail in Erben et al. (2009). A small number of objects per field that are missing from the `USNO B1` catalogue have to be masked manually, while masks around catalogue positions where no source can be found are removed.[1]

To obtain accurate colours for objects from CCD images, aperture effects have to be taken into account, in addition to the photometric calibration (see Sect. 5.2). Our approach is to measure *SExtractor* isophotal (`ISO`) magnitudes – the *SExtractor* aperture definition providing the most accurate colours – from seeing-equalised images in our three bands. We perform a simplistic PSF matching based on the assumption of Gaussian PSFs described in Hildebrandt et al. (2007). The width of the filter with which to convolve the *k*-th image is given as

$$\sigma_{\mathrm{filter,k}} = \sqrt{\sigma^2_{\mathrm{worst}} - \sigma^2_{\mathrm{k}}}, \tag{5.2}$$

where σ_{k} and σ_{worst} are the widths of the best-fitting Gaussians to the PSFs measured from the *k*-th and the poorest seeing image.

5.2 Photometric Calibration

5.2.1 The Calibration Technique

The photometric calibration of our data is largely based on the method developed by Hildebrandt et al. (2006) but using AB magnitudes, SDSS-like filters, and the SDSS Data Release Six (Adelman-McCarthy et al. 2008, DR6) as our calibration catalogue. To determine the photometric solution, we use *SExtractor* to draw catalogues from all science and standard frames with SDSS overlap. Using the Hildebrandt et al. (2006) pipeline, we then match these catalogues with a photometric catalogue assembled from the SDSS archives, which serve as indirect photometric standards.

The MMT/MEGACAM filter system is based on that of the SDSS but is not identical (see Fig. 5.3). Therefore, relations between instrumental magnitudes and calibrated magnitudes in the SDSS system have to take colour terms into account. To establish the transformation between MMT and SDSS measurements, we need to know the transmissivities of both instruments in great detail. For MEGACAM, the instrument website[2] offers detailed laboratory transmission curves of the actual filters and a few data points that indicate the CCD quantum efficiency. We average the tabulated quantum efficiency values over the 36 MEGACAM chips. The SDSS collaboration provides data on the combined sensitivity of its camera/filter system[3]. Assuming the atmospheric absorption to behave similarly at both sites, we can directly compare the responses of the two instruments, as visualised in Fig. 5.3.

[1] This last manual step can be largely avoided also by automatically masking objects drawn from the Hubble Space Telescope Guide Star Catalog, as demonstrated by Erben et al. (2009).

[2] Overview: `http://www.cfa.harvard.edu/mmti/megacam.html`;
filter data: `http://www.cfa.harvard.edu/~bmcleod/Megacam/Filters/`

[3] `http://www.sdss.org/dr7/instruments/imager/`

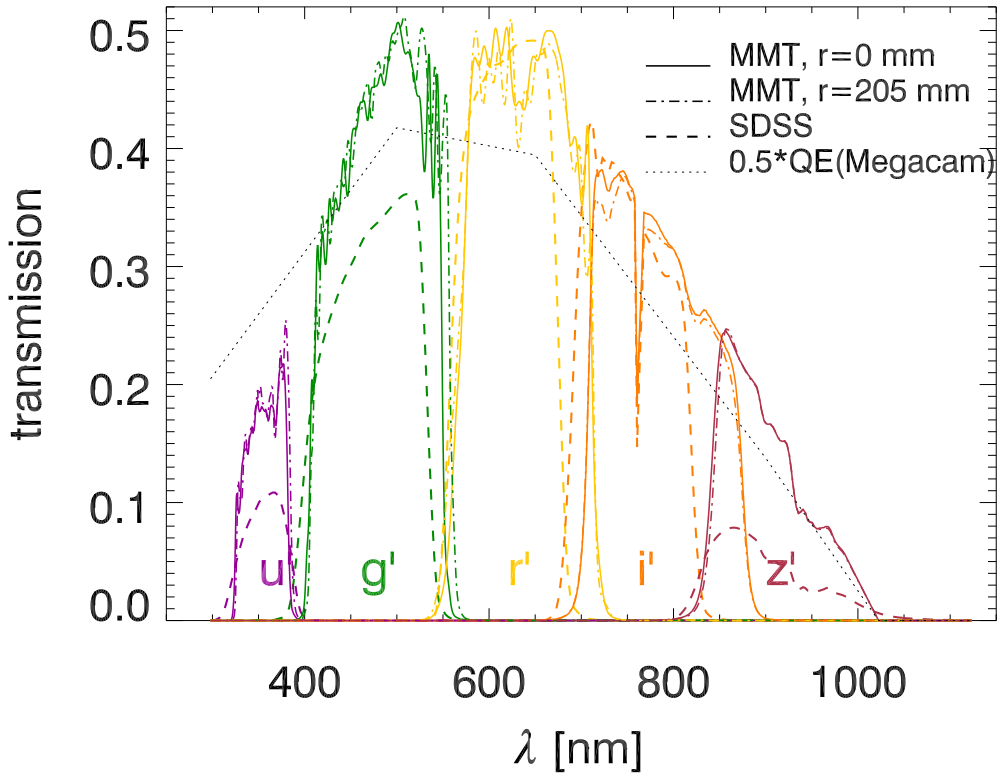

Figure 5.3: Comparison of the SDSS and MEGACAM filter systems. The plot shows the complete transmission curves for the $u'g'r'i'z'$ filters of both systems as a function of wavelength, including the atmospheric transmissivity (as given for the SDSS site), the CCD quantum efficiency, and the actual effect of the filter, as measured in the laboratory. The solid lines give sensitivities of MEGACAM filters for photons incident on the optical axis while the dash-dotted lines show the same quantity near the corner of the MEGACAM array. Over-plotted as dashed lines are the transmission curves defining the SDSS bandpass system. The black, dotted curve shows the MEGACAM quantum efficiency that we derive from the instrument specifications, scaled by one half to show it conveniently on the plot. Note that we need to interpolate its values from only five points in the range $300\ \mathrm{nm} < \lambda < 1000\ \mathrm{nm}$ and have to extrapolate outside this interval.

The relation between MEGACAM instrumental magnitudes m_{inst} and catalogue magnitudes m_{SDSS} for a filter f can be fitted simultaneously as a linear function of airmass a and a first-order expansion with respect to the colour index,

$$m_{\mathrm{f,inst}} - m_{\mathrm{f,SDSS}} = \beta_{\mathrm{f}} c_{\mathrm{SDSS}} + \gamma_{\mathrm{f}} a + Z_{\mathrm{f}} \quad , \tag{5.3}$$

where c_{SDSS} is a colour index defined by two SDSS filters, β_{f} the corresponding colour term, and Z_{f} the photometric zeropoint in which we are mainly interested. For the fit, we select objects of intermediate magnitude that are neither saturated nor exhibit a too large scatter in m_{inst} given a certain m_{SDSS}. Following the model of Hildebrandt et al. (2006), we account for the variable photometric quality of our data by fitting β_{f}, γ_{f}, and Z_{f} simultaneously in optimal conditions, fixing γ_{f} in intermediate, and fixing γ_{f} and β_{f} in even poorer conditions.

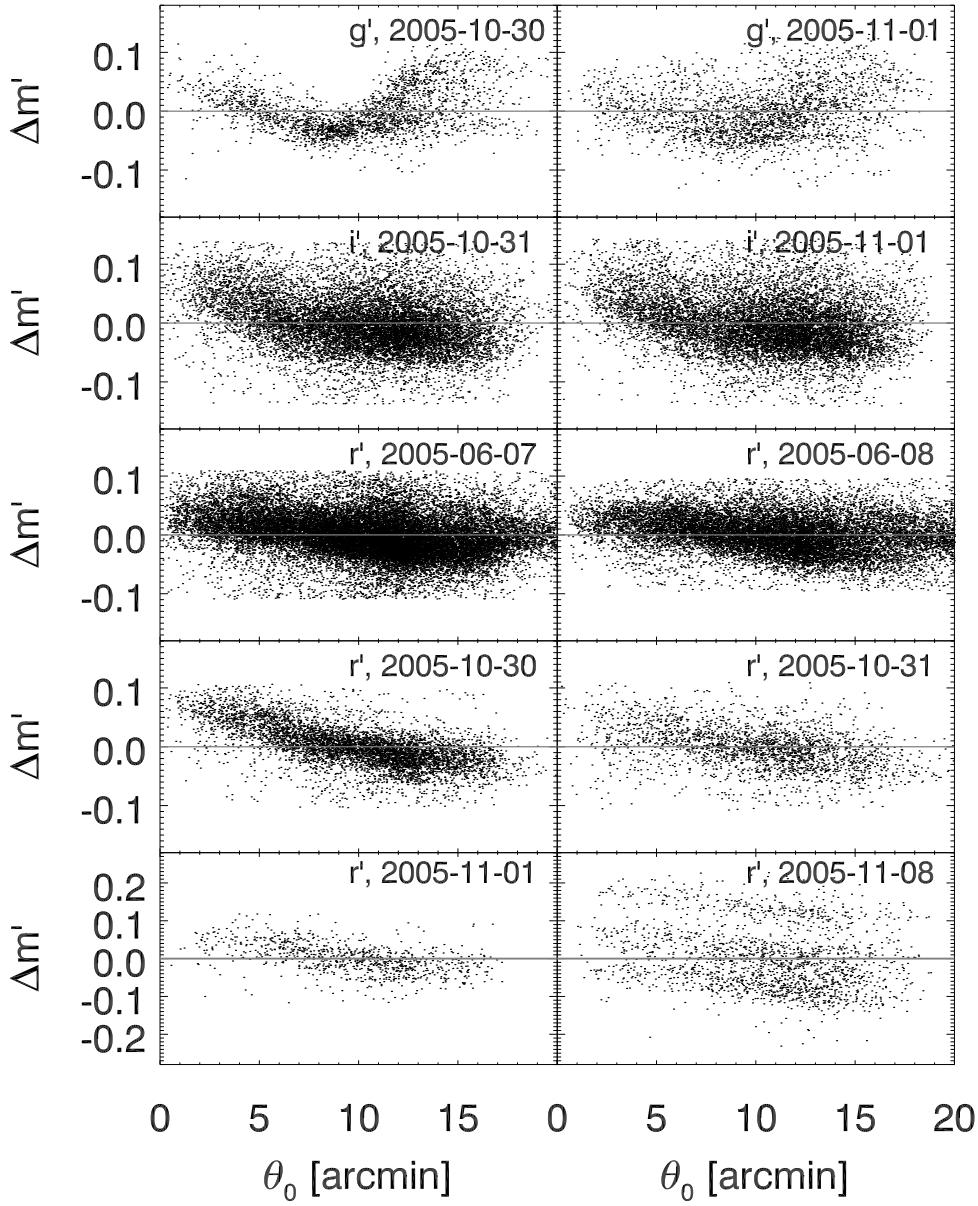

Figure 5.4: Accuracy of the photometric calibration: For the different combinations of filters and nights used to calibrate the data sets discussed in this thesis, the scatter $\Delta m'$ around the best-fit solution (solid line) is shown. Each point corresponds to an SDSS standard source for which the abscissae give the separation θ_0 in arc minutes from the centre of the pointing. Note that for each panel a maximum $\Delta m'$ has been determined by iterative 3σ-clipping.

Table 5.2: Coefficients of photometric calibration defined by Eq. (5.3) for all photometric nights in which *400d* clusters have been observed with MMT/MEGACAM. Note that nearly all *Run C* and *Run E* data are photometric, while there were no photometric nights in neither *Run B* nor *Run J*.

Filter	Obs. Date	$Z_{\rm f}^{\dagger}$	$\beta_{\rm f}$	$c_{\rm SDSS}$	$\gamma_{\rm f}$	$n_{\rm par}^{\ddagger}$
g'	2005-10-30	27.277 ± 0.005	0.106 ± 0.007	$g'-r'$	$(-0.15)^{\S}$	2
	2005-11-01	27.286 ± 0.005	0.116 ± 0.005	$g'-r'$	$(-0.15)^{\S}$	2
i'	2005-10-31	26.426 ± 0.002	0.124 ± 0.002	$r'-i'$	$(-0.05)^{\S}$	2
	2005-11-01	27.408 ± 0.009	0.119 ± 0.002	$r'-i'$	-0.03 ± 0.01	3
r'	2005-06-07	26.819 ± 0.001	0.040 ± 0.001	$g'-i'$	$(-0.10)^{\S}$	2
	2005-06-08	26.834 ± 0.008	0.048 ± 0.001	$g'-i'$	-0.12 ± 0.01	3
	2005-10-30	26.950 ± 0.018	0.046 ± 0.002	$g'-i'$	-0.10 ± 0.02	3
	2005-10-31	26.959 ± 0.004	0.042 ± 0.003	$g'-i'$	$(-0.10)^{\S}$	2
	2005-11-01	26.960 ± 0.008	0.048 ± 0.004	$g'-i'$	$(-0.10)^{\S}$	2
	2005-11-08	26.807 ± 0.005	0.046 ± 0.003	$g'-i'$	$(-0.10)^{\S}$	2

† Normalised to an exposure time of 1s and an airmass $a = 0$.
‡ Number of parameters used in the fit.
§ Fixed to default value.

For each filter, we chose a colour index $c_{\rm SDSS}$ in Eq. (5.3) that has been proven to provide a reliable transformation during calibration of the Canada-France-Hawaii Telescope Legacy Survey (CFHTLS) data, which also uses a similar filter system[4]. These colour indices are given in Table 5.2, which shows the results for the fit parameters $Z_{\rm f}$, $\beta_{\rm f}$, and $\gamma_{\rm f}$ for the photometric nights in which MEGACAM observations of *400d* clusters were performed.[5] We note that while nearly all data in *Run C* and *Run E* were taken in photometric conditions, all zeropoints obtained from observations in *Run B* and *Run J* are significantly smaller, indicative of non-photometric conditions.

We find the zeropoints $Z_{\rm f}$ of the photometric nights to agree among the $g'r'i'$ filters, with a largest deviation of ≈ 0.15 mag. The scatter $\Delta m' = m_{\rm f,inst} - m_{\rm f,SDSS} + \beta_{\rm f} c_{\rm SDSS} + \gamma_{\rm f} a + Z_{\rm f}$ of the individual SDSS standards about the best-fit solution (Fig. 5.4) has a comparable amplitude. The error of $Z_{\rm f}$ given in Table 5.2 is the formal fitting error. Figure 5.4 presents the data from which the parameters $Z_{\rm f}$, $\beta_{\rm f}$, and $\gamma_{\rm f}$ have been determined, applying an iterative 3σ-clipping fit of Eq. (5.3).[6]

Comparing the colour terms $\beta_{\rm f}$ for the different nights, we find considerable agreement within the values for each of the three bands, although the formal errors underestimate the true uncertainties. In previous MEGACAM studies, Hartman et al. (2008, Table 5) quote $\beta_{\rm g} = 0.122 \pm 0.002$ and $\beta_{\rm i} = 0.137 \pm 0.002$, the first in agreement with our results, the latter significantly higher than our value. Furthermore, Walsh et al. (2008) find $\beta_{\rm g} = 0.091 \pm 0.068$, consistent with our values given the large error. We suggest that the large span in values of $\beta_{\rm g}$ might be caused by the known dependence of the filter throughput on the distance to the optical axis, which is most pronounced in this band (Fig. 5.3). Plotting the scatter $\Delta m'$ as a function of the separation θ_0 of the source from the optical axis of MEGACAM (Fig. 5.4), given by the pointing position in the `fits` header, we can confirm trends of $\Delta m'(\theta_0)$ in all filters, most pronounced for the g' band data taken on 2005

[4] `http://www3.cadc-ccda.hia-iha.nrc-cnrc.gc.ca/megapipe/docs/filters.html`

[5] Note that photometric solutions given for *Run E* in Table 5.2 are corrected w.r.t. Table A.1 in Israel et al. (2010). The amount of these corrections is of the order of, and in most cases smaller than, the scatter observed in Fig. 5.4.

[6] The number of initial photometric data points for each night and filter strongly depends on whether the observed clusters lie within the SDSS "footprint".

October 30. Further investigation is needed to conclude about this issue, requiring full propagation of errors on instrumental magnitude. Because the radial dependence observed in Fig. 5.4 does not exceed the residual scatter for sources at the same θ_0, the global photometric fits (Eq. 5.3) fulfil the requirements of our analysis.

5.2.2 Photometric Calibration of CL 0809+2811

The situation for CL 0809+2811 is a peculiar case. This cluster has been targeted in the r'-band both in *Run E* and in *Run J*. Imaging acquired on 2005 November 08 turned out to be photometric – albeit with a large scatter around the photometric solution – while the majority of frames taken on 2008 January 09 was not. Inspection of the PSF anisotropy on the individual frames, however, revealed that all frames taken under photometric conditions had to be removed from the coaddition because of their extremely anisotropic PSF ($|e| > 0.10$). Nevertheless, because the *relative zero-points* that had already been established for the `THELI` *set* of CL 0809+2811 in the r'-band are not affected by the choice of frames for coaddition, the coadded r'-band image for CL0809+2811, consisting entirely of exposures taken on 2008 January 09, is photometrically calibrated through the cluster data acquired on 2005 November 08.

5.2.3 Indirect Photometric Calibration of CL 0030+2618

Comparing the zeropoints for different nights and fields, we conclude that the nights on which the r'-band observations of CL 0030+2618 were performed were not entirely photometric but showed a thin, uniform cirrus. Therefore, in the absence of SDSS data in the field, an indirect calibration method is needed. To this end, we fitted the position in the $r'-i'$ versus $g'-r'$ colour-colour-diagram of the stars identified in the CL 0030+2618 field to those found in two other, fully calibrated, galaxy cluster fields, CL 0159+0030 and CL 0809+2811. In the left panel of Fig. 5.5, we compare the $g'-r'$ versus $r'-i'$ colours of stars identified in these two fields with those for theoretical spectra of main-sequence stars from the Pickles (1998) spectral library, finding good agreement between both of the two observed sequences and the predicted stellar colours.

Since we have attained reliable absolute photometric calibrations for the g'- and i'-bands of CL 0030+2618, the location of the stellar main sequence for this field is determined up to a shift along the main diagonal of the $g'-r'$ versus $r'-i'$ diagram, corresponding to the r' zeropoint. We fix this parameter by shifting the main sequence of CL 0030+2618 on top of the other observed main sequences as well as the Pickles (1998) sequence. We go in steps of 0.05 magnitudes, assuming this to be the highest achievable accuracy when adopting this rather qualitative method, and settle for the best-fit test value (see Table 4.2). The dots in Fig. 5.5 show the closest match with the CL 0159+0030 and CL 0809+2811 stellar colours obtained by the indirect calibration of the CL 0030+2618 r'-band.

After the photometric calibration, we became aware of a field observed in the SEGUE project (Newberg & Sloan Digital Sky Survey Collaboration 2003) using the SDSS telescope and filter system that became publicly available with the Sixth Data Release of SDSS (Adelman-McCarthy et al. 2008) and has partial overlaps with the CL 0030+2618 MEGACAM observations. Thus, we are able to directly validate the indirect calibration by comparing the colours of stars in the overlapping region. The right panel of Fig. 5.5 shows the good agreement between the two independent photometric measurements and the Pickles (1998) templates from which we conclude that our calibration holds to a high accuracy.

For comparison we also calibrated the r'-band of CL 0030+2618 by comparing its source counts to those in the CL 0159+0030 and CL 0809+2811 fields for the same filter, but discard this

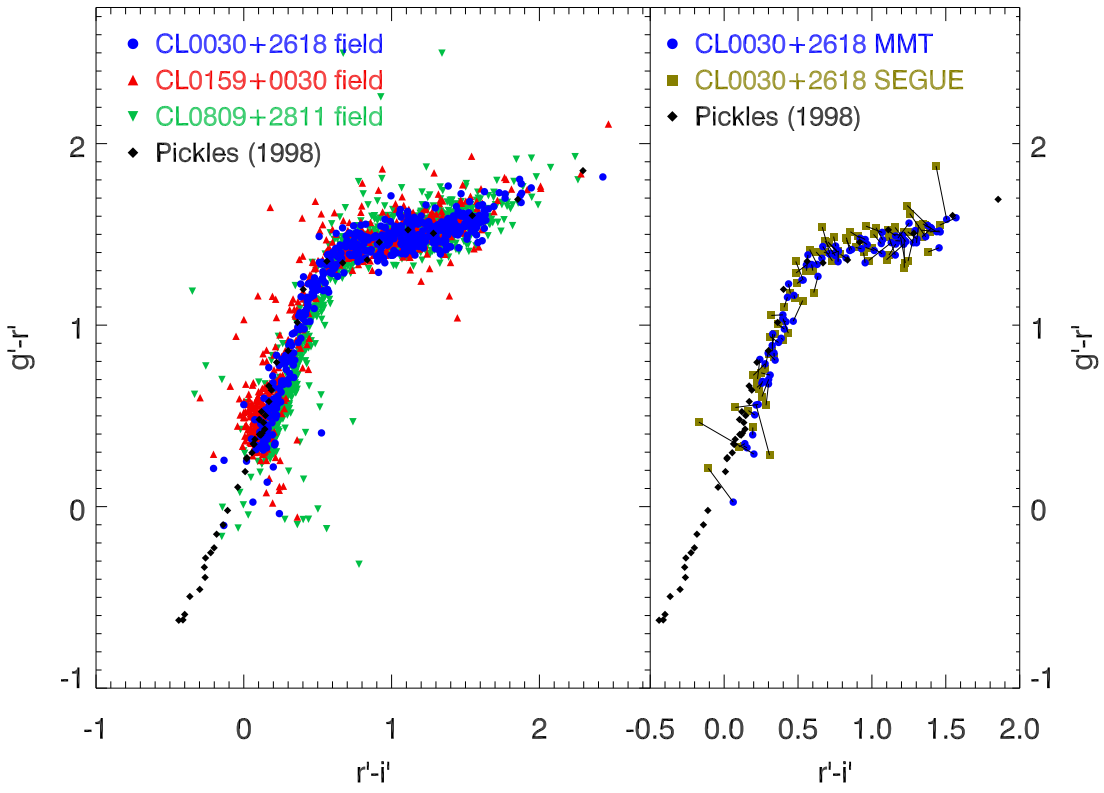

Figure 5.5: Indirect photometric calibration by stellar colours: *Left panel:* plotted here are the $g'-r'$ vs. $r'-i'$ colours of sources identified as stars in three galaxy cluster fields observed with MEGACAM. For two of these fields, CL 0159+0030 (upward triangles) and CL 0809+2811 (downward triangles), absolute photometric calibration with SDSS standards could be performed. For CL 0030+2618, r'-band magnitudes based on the indirect calibration are shown (dots; details see main text). The colours in all three fields agree with the colours of main sequence stars from the Pickles (1998) spectral library (diamonds). *Right panel:* The $g'-r'$ vs. $r'-i'$ colours of stars in the MEGACAM images of CL 0030+2618 (dots) which could also be identified in the partially overlapping SEGUE strip (Newberg & Sloan Digital Sky Survey Collaboration 2003) and shown here as squares are both consistent with each other as well as with the Pickles (1998) colours (diamonds). Each pair of measurements of one individual source is connected with a line.

calibration as we find a discrepancy of the resulting main sequence in $g'-r'$ versus $r'-i'$ with the theoretical Pickles (1998) models mentioned earlier.

5.2.4 Indirect Photometric Calibration of CL 0230+1836

Based on the experiences with the CL 0030+2618 r'-band, we perform the photometric calibration of CL 0230+1836, for which both the r'- and the g'-band were observed in non-photometric conditions, and no SDSS data of the field are available. Because the stellar sequence in $g'-r'$ versus $r'-i'$ colours consists of two "legs" joined at a distinct "knee" where its slope changes, this poses only a slightly more complicated problem. First, we fix $Z_{g'}$ for CL 0230+1836 by shifting the corresponding sequence such that one of the two coordinates of the turning point coincides with the Pickles (1998) templates. Second, we can then determine $Z_{r'}$ in the same way we did for

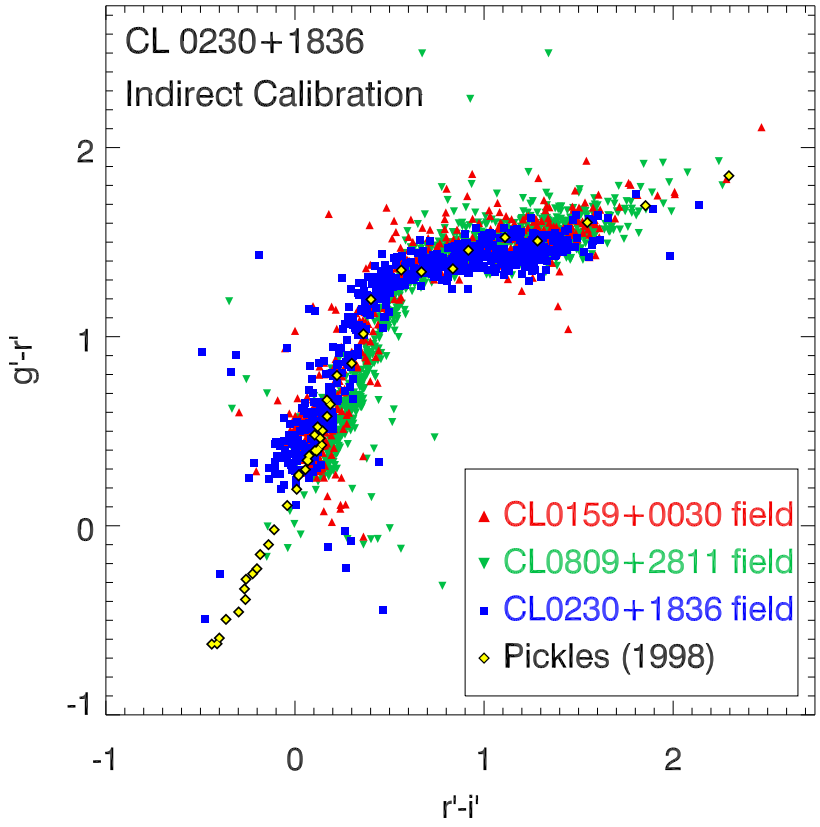

Figure 5.6: Indirect photometric calibration by stellar colours: Same as the left panel of Fig. 5.5, but for CL 0230+1836 (blue squares).

CL 0030+2618. Figure 5.6 shows that a consistent stellar sequence with the CL 0159+0030 and CL 0809+2811 fields is also achieved for the CL 0230+1836 zeropoints.

5.3 Frame Selection

The success of a lensing analysis depends crucially on the data quality. Because we follow the usual approach in weak lensing to rebin the frames to a common image coordinate system and stack them, the stacking process is a potential source of biases to the shape information. It is evident that the decision which frames should contribute to the shape measurement is of great importance. Apart from seeing and photometric quality, which can be easily assessed while the observation takes place, PSF anisotropy is a key factor as it can only be corrected up to a certain degree.

5.3.1 Measuring the PSF Anisotropy

In the following, we describe how star catalogues that allow us to investigate the PSF anisotropy are created from the individual exposures. To this end, we apply modified versions of the catalogue creation routines in our KSB pipeline we describe in Sect. 5.4.

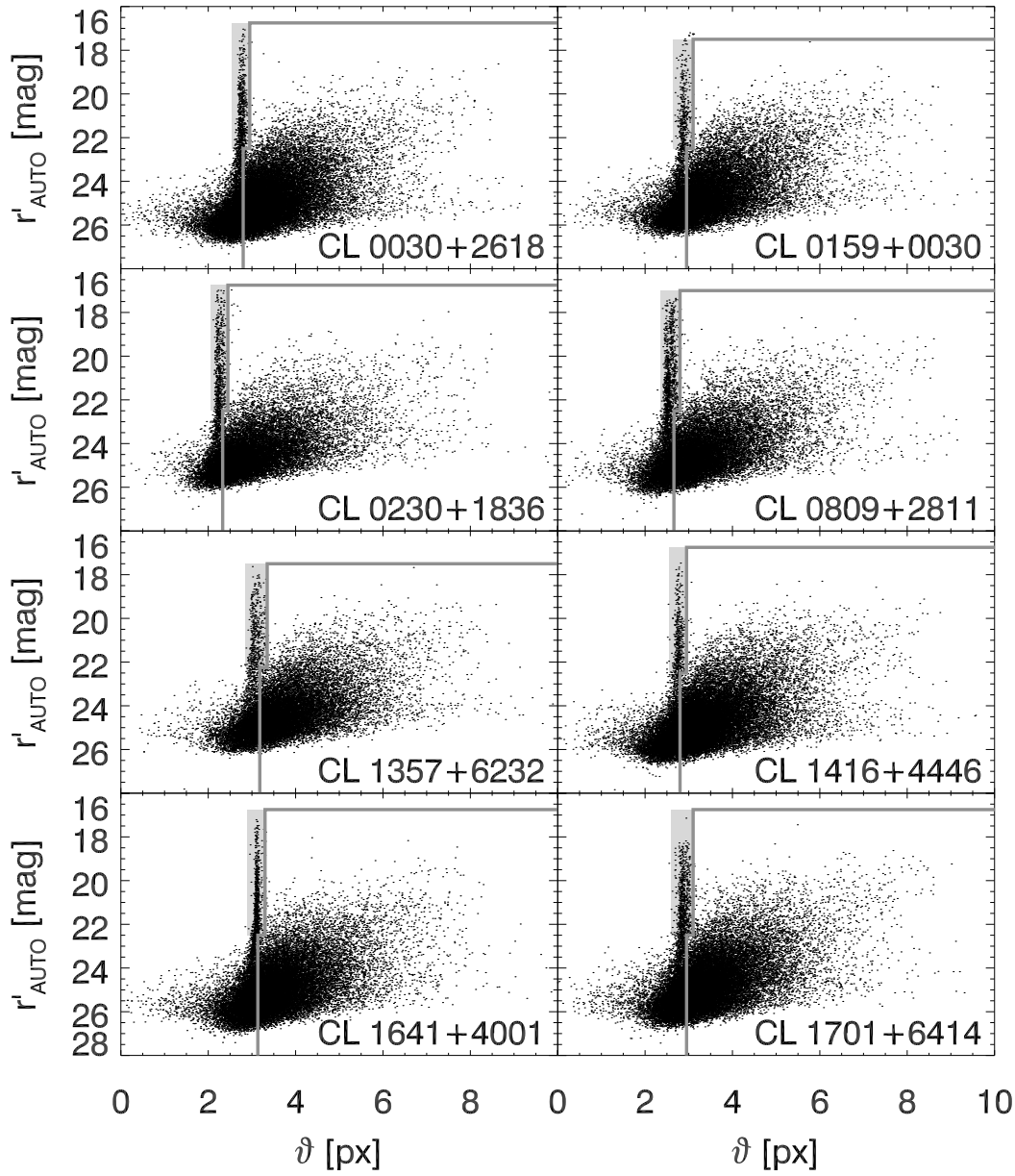

Figure 5.7: The distribution of sources in apparent size – magnitude – space in the eight MEGACAM *400d* cluster fields. Plotted are *SExtractor* magnitudes $r'_{\rm AUTO}$ against half-light radii ϑ of all sources in the respective KSB catalogues. The stellar loci are prominent. We categorise as stars all sources within the light-grey shaded areas defined by $\vartheta^*_{\rm min} < \vartheta < \vartheta^*_{\rm max}$ and $r'^*_{\rm min} < r'_{\rm AUTO} < r'^*_{\rm max}$. All sources to the right and lower sides of the thick grey lines, i.e. those with $\vartheta > \vartheta^*_{\rm max}$ for $r'^*_{\rm min} < r'_{\rm AUTO} < r'^*_{\rm max}$ and $\vartheta > \vartheta^{\rm ana}_{\rm min}$ for $r'_{\rm AUTO} > r'^*_{\rm max}$ are categorised as unsaturated galaxies. The values of $\vartheta^*_{\rm min}$, $\vartheta^{\rm ana}_{\rm min}$, $\vartheta^*_{\rm max}$, $r'^*_{\rm min}$, and $r'^*_{\rm max}$ for the individual fields are listed in Table 5.3.

Using the background-subtracted exposures produced by `THELI` directly before the coaddition as input to *SExtractor* and the corresponding weight files as noise maps, we draw a catalogue of detected sources for each chip in all frames having passed the seeing and relative zeropoint selection criteria. In the source detection, our default criteria `DETECT_MINAREA`= 4 and `DETECT_THRESH`= 1.5 are applied. Next, extended sources exceeding a flux radius of $\vartheta_\mathrm{g} = 10\,\mathrm{px}$ and sources that are flagged by *SExtractor* are removed from the catalogue because the shape measurement does not work reliably in these cases. The main reasons for a source getting flagged are *blending* with another detection and missing data points, e.g., near the image borders.

For the sources in the resulting "pre-KSB" catalogue, we determine the second-order brightness moments Q_{ij}, defined in Eq. (3.18), within an aperture with radius $\ell_\mathrm{SIL} \times \vartheta_\mathrm{g}$ and using a Gaussian window function $W_\mathrm{G}(\theta)$ with standard deviation $\sigma_\mathrm{g} = \vartheta_\mathrm{g}$. Here, we apply the default aperture radius of $\ell_\mathrm{SIL} = 3$ flux radii. The *KSB catalogue* consists of all sources for which the routine `analyseldac` (Erben et al. 2001) returns a successful shape measurement.

By analysing the distribution of the KSB catalogue sources in the space spanned by their r'_AUTO magnitude[7] measured by *SExtractor* and the half-light radius ϑ resulting from `analyseldac`, we now select the unsaturated stars which we will use as PSF tracers. Apart from containing far fewer sources, the resulting diagrams look very similar to the ϑ–r'_AUTO–distributions for the final coadded images presented in Fig. 5.7. The half-light radius of an unsaturated star observed in a CCD image does not depend on its magnitude, its brightness distribution being determined by the PSF scaled by a magnitude-dependent amplitude and the photon noise. We observe a *stellar locus* of small extent in ϑ, blending into the "cloud" of extended sources for faint $r'_\mathrm{AUTO} \approx 22.5$ magnitudes, while saturated stars appear larger than the PSF.[8] The prominent stellar locus enables us to define a sample of stars by applying thresholds $\vartheta^*_\mathrm{min} < \vartheta < \vartheta^*_\mathrm{max}$ and $r'^*_\mathrm{min} < r'_\mathrm{AUTO} < r'^*_\mathrm{max}$ defined for the individual frame (by concatenating the catalogues of all 36 chips). Affected by neither intrinsic ellipticity nor lensing shear, the stars as tracers of the PSF play an eminent role in the KSB algorithm (Sect. 5.4).

Thus having defined a sample of 500–1000 sources probing the PSF at different positions of the MEGACAM array, we repeat the shape measurement for these stars, now with a Gaussian window function of $\sigma_\mathrm{g} = 2.6\,\mathrm{px}$, i.e. similar to the half-light radius ϑ of a star observed with MEGACAM under typical seeing conditions. Calculating the ellipticity components $e_{1,2} := \chi_{1,2}$ of each star by applying Eq. (3.19), we obtain a list of PSF anisotropy measurements for each exposure.

5.3.2 Selection for the *400d* Cluster Fields

Although, generally, the MEGACAM PSF is quite isotropic such that isophotes of stars can to a good degree be considered as circles, there are some frames in our data set that show a highly anisotropic PSF. These images appear in all runs and filters and have not necessarily been taken in the poorest seeing conditions. Figure 5.8 shows the spatial distribution of the anisotropy in stellar images for a typical frame with high (top panel) and low (bottom panel) *average* PSF anisotropy $|\langle e \rangle|$, both of them r'-band observations of CL 0030+2618. In contrast to other telescope–camera systems, there is no stable pattern of low and high anisotropy as a function of position in the focal plane of MEGACAM, but the place where the most circular PSF is found can change significantly in a short

[7] The index "`AUTO`" refers to the default aperture applied by *SExtractor*, for which an elliptical aperture is fitted to the source brightness distribution. To measure colours, we use the preferred isophotal "`ISO`" apertures instead – including all pixels within a given isophote – but find the differences between both to be usually small.

[8] Note that saturated stars are absent from Fig. 5.7 because they are masked out during the "coaddition post production" stage (Sect. 5.1.3).

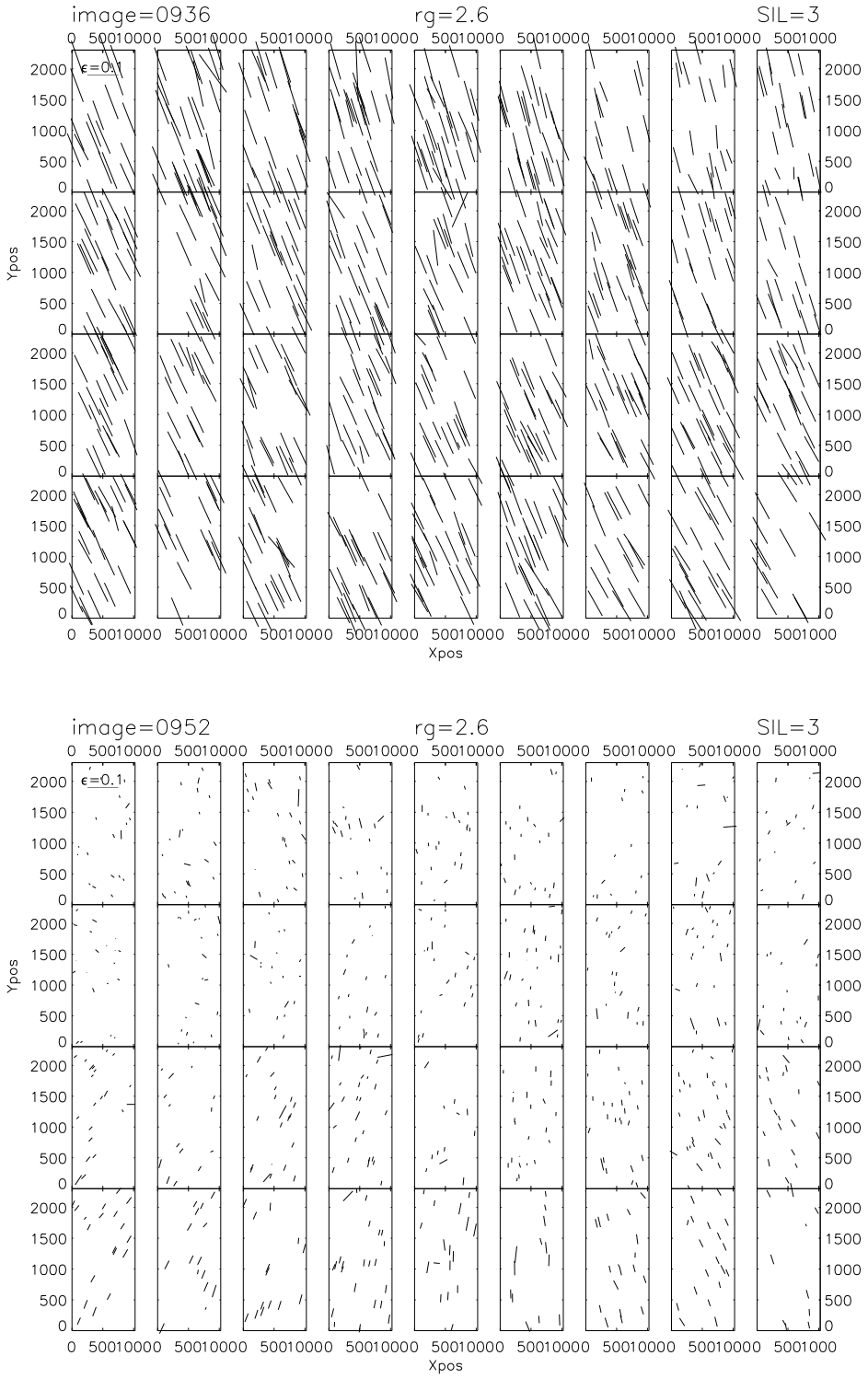

Figure 5.8: Spatial distribution of stellar anisotropies for an example exposure of high overall PSF anisotropy. Shown are the magnitudes and orientations of the raw ellipticity *e* for stars identified in the MMT/MEGACAM exposures of CL 0030+2618 labelled `0936` (*upper panel*) and `0952` (*lower panel*) in Fig. 5.9. While within each chip the *x* and *y* axes are to scale, the array layout is only schematic. Note that, due to the 2×2-binning (Sect. 4.2.3), each chip has 1024×2304 image pixels.

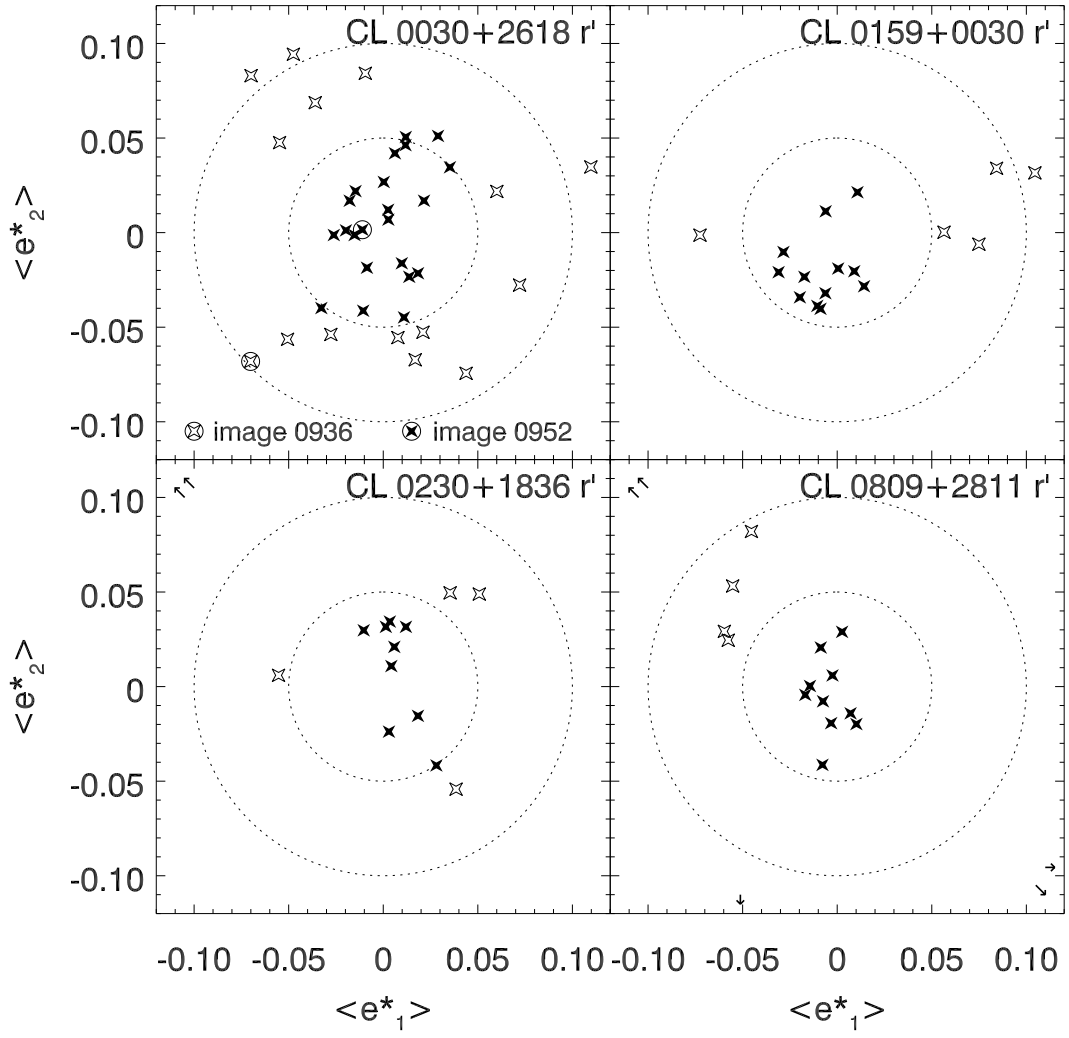

Figure 5.9: Anisotropy of stellar images in the MEGACAM cluster fields. Shown are the average ellipticity components $\langle e_1^* \rangle$ and $\langle e_2^* \rangle$ in the frames considered suitable for coaddition after the data reduction has otherwise been completed. Each symbol corresponds to a r'-band frame observed in the CL 0030+2618, CL 0159+0030, CL 0230+1836, or CL 0809+2811 fields (four panels from top left to bottom right). Frames marked with filled symbols contribute to the final stacked image while open symbols denote frames that were rejected for their highly anisotropic PSFs. The positions of a few extreme outliers far outside the plotting range are indicated by arrows. Special plotting symbols highlight the two cases shown in Fig. 5.8. As a visual aid, dotted circles indicate average anisotropies of $|\langle e \rangle| = 0.05$ and $|\langle e \rangle| = 0.10$.

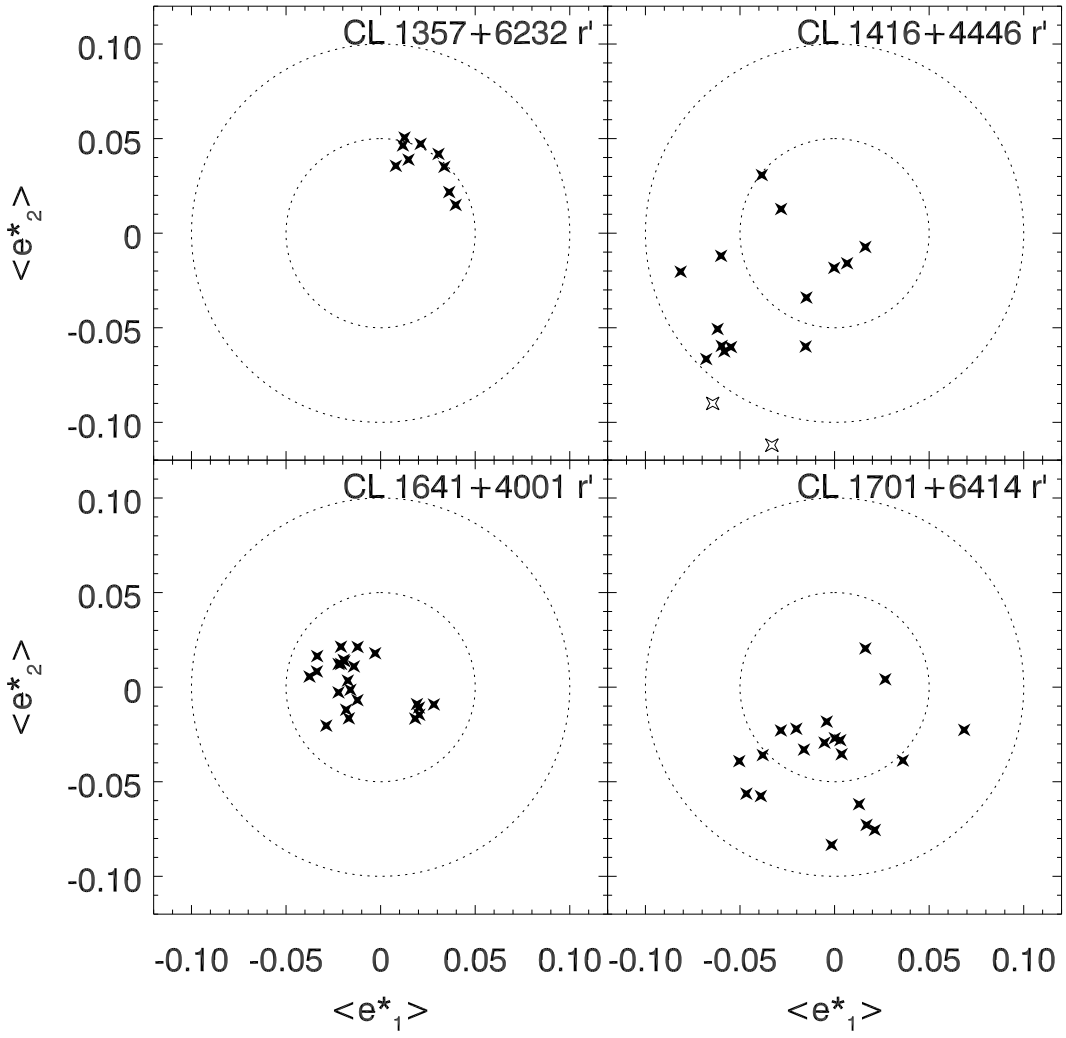

Figure 5.10: Anisotropy of stellar images in the MEGACAM cluster fields. The same as Fig. 5.9, but for the CL 1357+6232, CL 1416+4446, CL 1641+4001, and CL 1701+6414 fields.

time.[9] Most likely, the cases of an anisotropic PSF in the whole field-of-view can be attributed to problems with either the *tracking* or the *focussing* of the telescope.

As we elaborate in Sect. 5.4.1, the KSB algorithm needs to correct for PSF anisotropy which mimics and superposes the shear signal. This correction performs best in terms of recovered shear if the PSF is close to circular in the first place. Consequently, because the PSF anisotropy in every individual frame propagates into the stacked image via resampling with *SWarp*, we reject the frames showing the largest $|\langle e \rangle|$ from the coaddition.

We show the average anisotropies $|\langle e \rangle|$ for the lensing band frames of all eight clusters, which we otherwise consider usable for coaddition, in Figs. 5.9 and 5.10. Each plotting symbol denotes a 300 s r'-band exposure where filled symbols mark frames used in the final coaddition and open

[9] Dietrich et al. (2009) show a corresponding diagram for WFI for which the largest anisotropies were consistently observed at the same edge of the array with a given setup. Gavazzi & Soucail (2007) present very similar stellar anisotropy patterns for the four CHFTLS *Deep* fields.

symbols stand for rejected frames. The frames with the most anisotropic PSFs, far outside the plotting range, are indicated by arrows. In all cases, we include frames with average anisotropies $|\langle e\rangle| \leq 0.05$ and always exclude exposures with $|\langle e\rangle| > 0.10$ (inner and outer circles in Figs. 5.9 and 5.10). We note that only for CL 1641+4001, all analysed r'-frames fulfil $|\langle e\rangle| \leq 0.05$. Concerning the intermediately anisotropic ($0.05 < |\langle e\rangle| \leq 0.10$) PSFs, our approach depends on their distributions in the $\langle e_1\rangle - \langle e_2\rangle$–plane and the number of available frames with $\langle |e|\rangle \leq 0.05$.

If there is almost no (CL 1357+6232) or a significant gap (CL 0809+2811) in the $\langle |e|\rangle$-distribution around 0.05, the decision is relatively easy. For CL 0030+2618, with a large total number of frames, exposures in the $0.05 < |\langle e\rangle| < 0.06$ interval were included in a case-to-case decision based on the inspection of diagrams analogous to Fig. 5.8. We then included frames in which a place in the focal area exists where the PSF is almost circular, i.e. the "tracking error-like" anisotropy does not dominate. We conclude that a more quantitative selection scheme would be desirable in terms of consistency, but we stress that our frame selection is motivated by the few available data with both good seeing and small PSF anisotropy.

5.4 KSB Analysis

The *shape measurement* analysis (cf. Sect. 3.2) we apply is based on the Kaiser et al. (1995, KSB) algorithm, following the ideas introduced in Erben et al. (2001). Our reduction pipeline was adapted from the "TS" implementation presented in Heymans et al. (2006) and explored in Schrabback et al. (2007) and Hartlap et al. (2009).

5.4.1 The KSB Algorithm

The KSB algorithm confronts the problem of reconstructing the shear signal from measured galactic ellipticities by separating the reduced shear g from both the intrinsic ellipticities of the galaxies and PSF effects. The effects of shear dilution by the PSF and the convolution of the intrinsic ellipticity of the detected galaxies with the anisotropic PSF component can be isolated by measuring the PSF from the stars, as already mentioned.

Under realistic circumstances, measuring the second-order brightness moments Q (Eq. 3.18) from discretised images, applying a filter function $W(\boldsymbol{\theta})$ that explicitly depends on pixel position, the relations Eq. (3.21) break down in the sense that the transformation $Q^{(\mathrm{s})} \rightarrow Q$ between unlensed and lensed moments can in general no longer be written as a matrix multiplication. For small reduced shears g and PSF anisotropies q, however, their effects can be assumed to be linear. Hence, the observed ellipticity e of a lensed image and its intrinsic ellipticity $e^{(\mathrm{s})}$ are related by:

$$e_\beta = e_\beta^{(\mathrm{s})} + \mathcal{P}^{\mathrm{g}}_{\beta\alpha} g_\alpha + \mathcal{P}^{\mathrm{sm}}_{\beta\alpha} q^*_\alpha \quad . \tag{5.4}$$

Here, small Greek indices denote either of the two components of the complex ellipticity, and the Einstein summation convention has been applied. The 2×2 matrices $\mathcal{P}^{\mathrm{g}}$ and $\mathcal{P}^{\mathrm{sm}}$, termed *pre-seeing shear polarisability* and *smear polarisability*, provide the transformation of ellipticities under the influences of gravitational shear fields and an (anisotropic) PSF, respectively. Again, asterisks denote quantities measured from stellar sources.

The shear measurement algorithm devised by Kaiser et al. (1995) inverts the relation Eq. 5.4 and infers a direct shear estimator ε from the measured ellipticity e_β of each galaxy:

$$\varepsilon_\alpha = (\mathcal{P}^{\mathrm{g}})^{-1}_{\alpha\beta}\, e^{\mathrm{ani}}_\beta = (\mathcal{P}^{\mathrm{g}})^{-1}_{\alpha\beta} \left[e_\beta - \mathcal{P}^{\mathrm{sm}}_{\beta\gamma} q^*_\gamma \right] \quad , \tag{5.5}$$

where $e^{\mathrm{ani}}_\alpha = e_\alpha - \mathcal{P}^{\mathrm{sm}}_{\alpha\beta} q^*_\beta$ is the *anisotropy-corrected ellipticity* of a measured source. Deriving Eq. (5.5), we employed the usual assumption for weak lensing that intrinsic source ellipticities

cancel out when averaging over a sufficiently large ensemble: $\langle e^{(\mathrm{s})} \rangle = 0$. Hence, the respective term drops out in Eq. (5.5) such that averaging over ε directly yields the reduced shear g and, assuming a convergence $\kappa \ll 1$, the shear γ:

$$\langle \varepsilon \rangle = g \approx \gamma \quad . \tag{5.6}$$

The next step is to insert the observed PSF anisotropy, which can be expressed as $q_\gamma = (\mathcal{P}^{\mathrm{sm}*})^{-1}_{\gamma\delta}\, e^*_\delta$ using the observed stellar ellipticities e^*_δ and applying Eq. (5.4) for $g = 0$ and $e^{(\mathrm{s})*}_\delta = 0$. Thus we arrive at the complete correction, which provides an estimate of the (reduced) shear g exerted on a galaxy in our catalogue:

$$\varepsilon_\alpha = (\mathcal{P}^{\mathrm{g}})^{-1}_{\alpha\beta} \left[e_\beta - \mathcal{P}^{\mathrm{sm}}_{\beta\gamma} \left((\mathcal{P}^{\mathrm{sm}*})^{-1}_{\gamma\delta}\, e^*_\delta \right) \right] \quad . \tag{5.7}$$

Our description so far leaves open how the polarisability matrices are computed. We remark that because in reality, the isotropic part of the PSF can never be avoided for a sheared image, $\mathcal{P}^{\mathrm{g}}$ itself is not a "fundamental" quantity, but is expressed internally as

$$\mathcal{P}^{\mathrm{g}}_{\beta\alpha} = \mathcal{P}^{\mathrm{sh}}_{\beta\alpha} - \mathcal{P}^{\mathrm{sm}}_{\beta\epsilon} \left[(\mathcal{P}^{\mathrm{sm}*})^{-1}_{\epsilon\zeta}\, \mathcal{P}^{\mathrm{sh}*}_{\zeta\alpha} \right] \quad . \tag{5.8}$$

For the details of the involved calculation of the *shear polarisability tensor* $\mathcal{P}^{\mathrm{sh}}$ and $\mathcal{P}^{\mathrm{sm}}$ from fourth-order brightness moments, we refer to Bartelmann & Schneider (2001).

To reduce uncertainties arising from division by a very noisy measured tensor in Eq. (5.8), we approximate the term in brackets by a smoothly varying quantity. Furthermore, we reduce the noise for small galaxies by approximating $\mathcal{P}^{\mathrm{g}}$ by half its trace for the division in Eq. (5.7), noticing its off-diagonal elements to be small compared to the diagonal elements (Heymans et al. 2006):

$$(\mathcal{P}^{\mathrm{sm}*})^{-1}_{\epsilon\zeta}\, \mathcal{P}^{\mathrm{sh}*}_{\zeta\alpha} \rightarrow \frac{\mathrm{tr}\,(\mathcal{P}^{\mathrm{sh}*})}{\mathrm{tr}\,(\mathcal{P}^{\mathrm{sm}*})} \delta_{\epsilon\alpha} =: T^* \delta_{\epsilon\alpha} \quad , \qquad (\mathcal{P}^{\mathrm{g}})^{-1}_{\alpha\beta} \rightarrow \frac{2}{\mathrm{tr}\,(\mathcal{P}^{\mathrm{g}})} \delta_{\alpha\beta} \quad , \tag{5.9}$$

where $\delta_{\alpha\beta}$ denotes the Kronecker symbol. Thus, our pipeline evaluates for each galaxy:

$$\varepsilon_\alpha = \frac{2\delta_{\alpha\beta}}{\mathrm{tr}\left(\mathcal{P}^{\mathrm{sh}}_{\beta\alpha} - T^* \mathcal{P}^{\mathrm{sh}}_{\beta\epsilon} \delta_{\epsilon\alpha} \right)} \left[e_\beta - \mathcal{P}^{\mathrm{sm}}_{\beta\gamma} q^*_\gamma \right] \quad . \tag{5.10}$$

which contains no more matrix inversions. The quantity T^* and the anisotropy kernel q^* are determined as functions of the image coordinates x and y by fitting polynomial functions to the values measured from stars. For $T^*(x, y)$, we generally use a quadratic function; the highest degree d_{ani} for fitting $q^*(x, y)$ is adjusted to the amount of anisotropy in the respective image (Sect. 5.4.4). Based on an observation by Hoekstra et al. (1998) that these quantities depend on the angular extent ϑ_{g} of the source, the "TS" implementation performs these fits for several Gaussian smoothing scales σ_{g} and chooses $q^*(x, y)$ and $T^*(x, y)$ from the appropriate bin in σ_{g}. Before we now proceed to outline the practical implementation of the pipeline, along the lines of Erben et al. (2001), we discuss the performance of our method in the context of the state-of-the-art of shape measurement.

5.4.2 Measuring Shear from Cluster Lenses

Shear measurement remains the pivotal problem in weak lensing and an active field of research. The "TS" shear measurement pipeline we use, based on the original KSB (Kaiser et al. 1995) algorithm and improvements by Erben et al. (2001) was subject to extensive tests based on mock images realistically simulating ground-based cosmic shear surveys as part of the *Shear Testing Programme* (*STEP*, Heymans et al. 2006; Massey et al. 2007). A shear calibration factor, discussed in greater detail in Sect. 6.1.4), was introduced based on the results of Heymans et al. (2006).

There are different families of shape measurement algorithms which are presented by Massey et al. (2007) and Bridle et al. (2010). Following the Massey et al. (2007) classification, methods are sorted based on whether they correct for the PSF by subtraction or deconvolution and whether they reconstruct the sheared image "passively" from basic components or by "actively" shearing a basic image. The "TS" pipeline, amongst other KSB implementations, is listed as a passive method and as a subtraction method by Massey et al. (2007).

Shear measurement techniques based on fitting a set of suited basis function to the sheared galaxy image, e.g. *shapelets* based on Hermite polynomials (e.g., Bernstein & Jarvis 2002; Refregier 2003; Refregier & Bacon 2003) address the problem from a different perspective. Recent results (Melchior et al. 2010; Voigt & Bridle 2010), however, show the fundamental limitations of the shapelet approach in WL. Finding the best-fit representation for the brightness distribution of each galaxy from a set of basic brightness distributions by Bayesian inference, the *Lensfit* method (Miller et al. 2007; Kitching et al. 2008) deserves particular mentioning. In the context of cluster WL, it has successfully been applied in a regime of high stellar anisotropy (Dietrich et al. 2009).

Evolving out of the *STEP* project, in the *GREAT08* challenge (Bridle et al. 2010), shear measurement techniques were tested and compared on improved simulations, aiming at the higher accuracy needed for future space-based cosmic shear surveys. In the publicly announced project, a wider community participated, introducing successful new algorithms, e.g. those stacking galaxy images before the actual shear measurement. Rowe (2010) revisits the problem of PSF modelling for weak lensing and deals with spatial variation of the PSF.

Up to now, no dedicated comparison of shear measurement techniques has been performed that specially addresses their relative performance in a cluster WL situation where, on average and especially in the cluster centres, the shear is higher than the largest input shear $\gamma = 0.1$ used in *STEP* or *GREAT08*. Methods involving stacking of galaxies before shear measurement are likely less useful in cluster lensing. We point out that performing detailed simulations of cluster lenses and improving shear measurement methods using these remain worthwhile tasks for the study of galaxy clusters. In the meantime, KSB offers a relatively well-known WL technique for clusters.

An important difference in WL pipelines is whether and how they apply *weighting* of shear estimates (see Table 4 of Massey et al. 2007). In the "TS" implementation we use, each galaxy is weighted equally.[10] Weighting of galaxies takes into account the different quality of shear estimates based on the signal-to-noise ratio of the galaxy from which the shear is measured, the error in the shear estimator itself, or variations in the intrinsic ellipticities for galaxies of different magnitude and size ϑ in the image. Hoekstra et al. (2000) devised a widely used weighting technique based on an estimate of the error in the KSB algorithm. Clowe et al. (2006b), in their study of clusters from the *ESO Distant Cluster Survey* use a weighting scheme built on the detection significances of the source galaxies. Erben et al. (2001) introduced the weighting factor

$$w_i = \left(\sigma^2_{\mathrm{e,NN}} + \bar{\sigma}^2\right)^{-1} \quad , \tag{5.11}$$

where $\sigma^2_{\mathrm{e,NN}}$ denotes the variance of the shear estimated for the $N = 12$ nearest neighbours in half-light radius–magnitude space and $\bar{\sigma}^2$ the variance of ellipticities in the whole sample. The underlying idea is that Eq. 5.11 provides a weight to the *i*-th galaxy by comparing its intrinsic ellipticity to that of the total (unlensed) galaxy population. Hetterscheidt et al. (2007) found the weighting (Eq. 5.11) to provide an effectively similar weighting as the Hoekstra et al. (2000) scheme. We plan to introduce the Erben et al. (2001) weighting into our lensing analysis as a future improvement.[11]

[10] We note that Table A1 of Heymans et al. (2006) lists a weighting scheme based on Erben et al. (2001) for the "TS" pipeline. The version used for our analyses, however, derives from the Massey et al. (2007) variant which doesn't include weighting.

[11] A test of the weighting (Eq. 5.11) gave inconclusive results in a very early version of our CL 0030+2618 analysis.

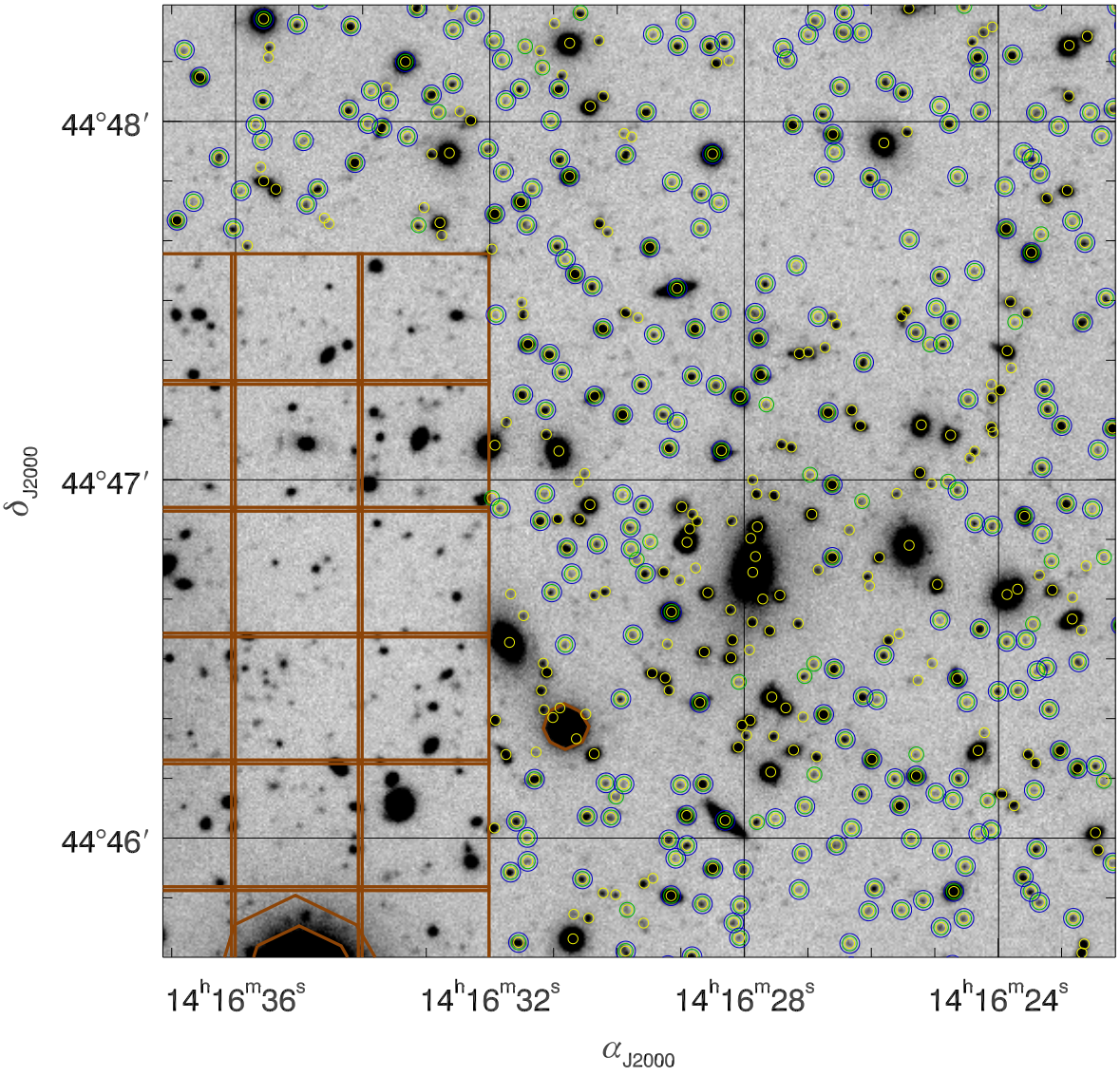

Figure 5.11: Illustration of the object selection in the KSB pipeline. Shown is the central area of the CL 1416+4446 r'-band field, with detection masks overlaid in red (cf. Fig. 5.1). Coloured circles mark sources contained in different catalogues. All initial *SExtractor* detections have one circle. Sources passing the criteria for the "pre-KSB" catalogue show (at least) two circles. KSB catalogue sources with successful shape measurement are marked by three circles.

5.4.3 The KSB Catalogue and Galaxy Shape Catalogue

In the following, we describe how shear estimates are distilled from input images. An outline of the initial KSB pipeline routines was already given in Sect. 5.3.1, such that we now focus on the features that are different in the main pipeline. For the clusters that were observed in three bands, catalogues are created from the images using the *SExtractor double detection mode* in which sources are identified in the lensing band image at its original seeing. Photometric quantities (fluxes, magnitudes) are determined at these coordinates from the measurement images in the three bands $g'r'i'$ convolved to the poorest seeing (cf. Table 4.2). This common procedure ensures that the aperture has the same size compared to the PSF in all filters and thus meaningful colour

Table 5.3: Parameters defining the galaxy shape catalogues. It is $N_{\rm KSB}$ the number of sources in the KSB catalogue, while the galaxy shape catalogue counts $N_{\rm gal}$ sources and a number density of $n_{\rm gal}$. The parameters $\vartheta^*_{\rm min}$, $\vartheta^*_{\rm max}$, $r'^*_{\rm min}$, and $r'^*_{\rm max}$ delineate the stellar locus (Fig. 5.7). The galaxy shape catalogue considers sources $\vartheta > \vartheta^*_{\rm max}$ for $r'^*_{\rm min} < r'_{\rm AUTO} < r'^*_{\rm max}$ and $\vartheta > \vartheta^{\rm ana}_{\rm min}$ for $r'_{\rm AUTO} \geq r'^*_{\rm max}$. Also given is the degree $d_{\rm ani}$ of the polynomial for PSF anisotropy correction and the stellar integration limit $\ell_{\rm SIL}$ in units of stellar flux radii.

Cluster field	$N_{\rm KSB}$	$\vartheta^*_{\rm min}$ [px]	$\vartheta^{\rm ana}_{\rm min}$ [px]	$\vartheta^*_{\rm max}$ [px]	$r'^*_{\rm min}$ [mag]	$r'^*_{\rm max}$ [mag]	$N_{\rm gal}$	$n_{\rm gal}$ [arcmin^{-2}]	$d_{\rm ani}$	$\ell_{\rm SIL}$
CL 0030+2618	31173	2.55	2.80	2.95	16.75	22.5	15760	22.6	5	3
CL 0159+0030	21541	2.65	2.95	3.10	17.5	22.5	10927	18.9	3	3
CL 0230+1836	18714	2.05	2.33	2.45	16.75	22.5	8449	13.2	4	4
CL 0809+2811	20889	2.35	2.66	2.80	17.0	22.5	10358	16.6	2	3
CL 1357+6232	19186	2.85	3.18	3.35	17.5	22.25	9253	14.2	5	3
CL 1416+4446	29375	2.55	2.80	2.95	16.75	22.5	14865	21.0	5	3
CL 1641+4001	25639	2.90	3.135	3.30	16.75	22.5	12569	19.6	3	3
CL 1701+6414	27710	2.60	2.95	3.10	16.75	22.5	14102	20.7	4	4

indices can be measured. Here, we also apply the flag images created for the coadded images (Sect. 5.1.3) to *SExtractor*. Sources centred within a flagged region are treated similar to those with missing data and cut from the catalogue together with the blended sources (Sect. 5.3.1).

The photometric properties determined from the three bands are merged into one catalogue that is primarily based on the detection image. For consistency, the double detection mode is also used for the clusters where only r'-band images exist. The detection image is then identical to the measurement image.

From the resulting "*SExtractor*" catalogues, problematic sources are removed. Figure 5.11 illustrates how the cuts (cf. Sect. 5.3.1) work that result in the "pre-KSB" catalogue of sources for which shape measurement is attempted. Objects marked with only one ring in Fig. 5.11 are affected by the cuts on $\vartheta_{\rm g} < 10$ px and flagged objects. We note that prominent cluster galaxies, e.g. the BCG of CL 1416+4446 to the right and below the centre of Fig. 5.11, typically consist of several blended *SExtractor* peaks and also are extended objects (i.e. larger than 10 px).

We note that the *KSB catalogue* presented in Fig. 5.7 and all catalogues discussed hereafter only contain objects for which a half-light radius ϑ could be successfully determined by `analyseldac`. Objects for which the measurements in the (noisy) data yield negative fluxes, semi-major axes, or second-order brightness moments, or which lie close to the image border are removed from the catalogue, reducing its size by a few percent. This can also be seen from Fig. 5.11 where the vast majority of sources that pass the first filter are present in the KSB catalogue (marked by three rings).

Figure 5.7 shows the distribution of these sources in the apparent radius – magnitude space. The prominent stellar locus enables us to define a sample of stars by applying the thresholds $\vartheta^*_{\rm min} < \vartheta < \vartheta^*_{\rm max}$ and $r'^*_{\rm min} < r'_{\rm AUTO} < r'^*_{\rm max}$ (the shaded areas in Fig. 5.7) from which the PSF anisotropy e^*_δ in Eq. (5.7) is determined.

In creating the *galaxy shape catalogue*, we regard as unsaturated galaxies all objects $r'_{\rm AUTO} > r'^*_{\rm min}$ (i.e., fainter than the brightest unsaturated point sources) and more extended than $\vartheta > \vartheta^*_{\rm max}$ for $r'_{\rm AUTO} < r'^*_{\rm max}$ and $\vartheta > \vartheta^{\rm ana}_{\rm min}$ for $r'_{\rm AUTO} \geq r'^*_{\rm max}$, respectively. The latter is justifiable because although for bright sources it is easy to distinguish galaxies from point sources, there is a significant population

of faint galaxies for which a very small radius is measured by the *SExtractor* algorithm. Thus, we relax the radius criterion by 5 % for sources fainter than $r'^{*}_{\rm max}$.

However, among those small objects there is a population of faint stars that can not be distinguished from poorly resolved galaxies using an apparent size – magnitude diagram alone that cause a dilution of the lensing signal relative to a perfect star – galaxy distinction. Our decision to nevertheless include these small sources in our catalogue is based on the resulting higher cluster weak lensing signal compared to that produced by a more conservative criterion (e.g., $\vartheta/\vartheta^{*}_{\rm max} \geq 1.10$ for the galaxies fainter than $r'^{*}_{\rm max}$). We call "galaxy shape catalogue" the list of objects that pass both this galaxy selection and the cuts for signal quality discussed in Sect. 6.1.4. This important catalogue yields the final "lensing catalogue" by means of the *background selection* discussed in Sect. 6.1.1. Applying these cuts, the source numbers in the galaxy shape catalogues for our eight cluster fields correspond to galaxy densities of 13–23 galaxies/arcmin^2 (Table 5.3). The drastic reduction in source counts compared to the KSB catalogue (usually by ~ 50 %) can be attributed mainly to the small and faint objects whose nature cannot be determined from the ϑ–$r'_{\rm AUTO}$–plots.

5.4.4 The PSF Properties of MMT/MEGACAM

As mentioned in Sect. 5.4.1, the PSF anisotropy kernel $q_\gamma = (\mathcal{P}^{\rm sm*})^{-1}_{\gamma\delta}\, e^*_\delta$ in Eq. (5.10) is determined by a polynomial fit. This is practically equivalent to fitting a model $e^{\rm cor,*}(x,y)$ of the pixel coordinates x and y to the measured ellipticities e^* of stars such that the residual anisotropies $e^{\rm ani,*} = e^* - e^{\rm cor,*}$ of stellar images should effectively be zero. The measurement of e^*_δ and fit are performed for several Gaussian filter scales $\sigma_{\rm g}$. In the following presentation, we restrict ourselves to the case $\sigma_{\rm g} = 2.6$ px, but monitor the results of the fit also for larger $\sigma_{\rm g}$.

Figure 5.12 shows the effect of one such anisotropy correction for CL 0030+2618. The raw ellipticities of the stars presented in the left two panels are modelled by a polynomial $e^{\rm cor} = \sum_k \sum_\ell p_{k\ell} x^k y^\ell$ with $0 \leq k \leq d_{\rm ani}$ and $0 \leq \ell \leq d_{\rm ani} - k$, defined globally over the entire field-of-view. The best-fit solution in the case $d_{\rm ani} = 5$ we adopt here is shown in the middle panels of Fig. 5.12, while the residual ellipticities of the stars $e^{\rm ani}$ are displayed in the panels to the right. We chose the aperture *stellar integration radius* $\ell_{\rm SIL}$ (measured in units of $\vartheta_{\rm g}$) such that the PSF is sufficiently covered out to its wings, i.e. increasing $\ell_{\rm SIL}$ does not result in a larger measured e^*_δ.

We aim to reduce both the mean $\langle e^{\rm ani,*}_\delta \rangle$ of the residual ellipticities and their dispersions. $\sigma(e^{\rm ani,*}_\delta)$. We find that a polynomial order as high as $d_{\rm ani} = 5$ is necessary to effectively correct for the distinctive quadrupolar pattern in the spatial distribution of the "raw" stellar ellipticities (see lower left and middle panels of Fig. 5.12). There is no obvious relation between the zones of preferred orientation of the PSF ellipticity in Fig. 5.12 and the 4×9 chip detector layout of MEGACAM. Some of the PSF ellipticity patterns are qualitatively similar to the one found for CL 0030+2618, whereas others show the same preferred orientation of the PSF ellipticity over the whole area. Two of thses cases are presented in Fig. 5.13, for a field with large PSF anisotropy (CL 1357+6232) and with low PSF anisotropy (CL 1641+4001), respectively. The corresponding plots for the remaining clusters are shown in Figs. B.1 to B.5 in Appendix B.1. Table 5.3 lists the values of $d_{\rm ani}$ and $\ell_{\rm SIL}$ adopted in these cases. Comparing the anisotropy patterns in all eight cluster fields, we conclude that these patterns are variable and not congruent with the chip boundaries. Although Fig. 5.13 demonstrates that the residuals of anisotropy correction increase with higher initial anisotropy, this anisotropy is still removed effectively in the most extreme case of CL 1416+4446. In the following discussion, we will focus on CL 0030+2618, a more typical case in terms of initial PSF anisotropy.

By stacking images in which the PSF anisotropy is different in magnitude and orientation (cf. Figs. 5.8 to 5.10), we already reduce the ellipticity caused by the imaging system before any correction is applied. The total amount of PSF anisotropy present in our MEGACAM coadded images is small. Before correction, we measure $\langle e_1 \rangle = 1.77 \times 10^{-5}$, $\langle e_2 \rangle = -4.03 \times 10^{-3}$, $\sigma(e_1) =$

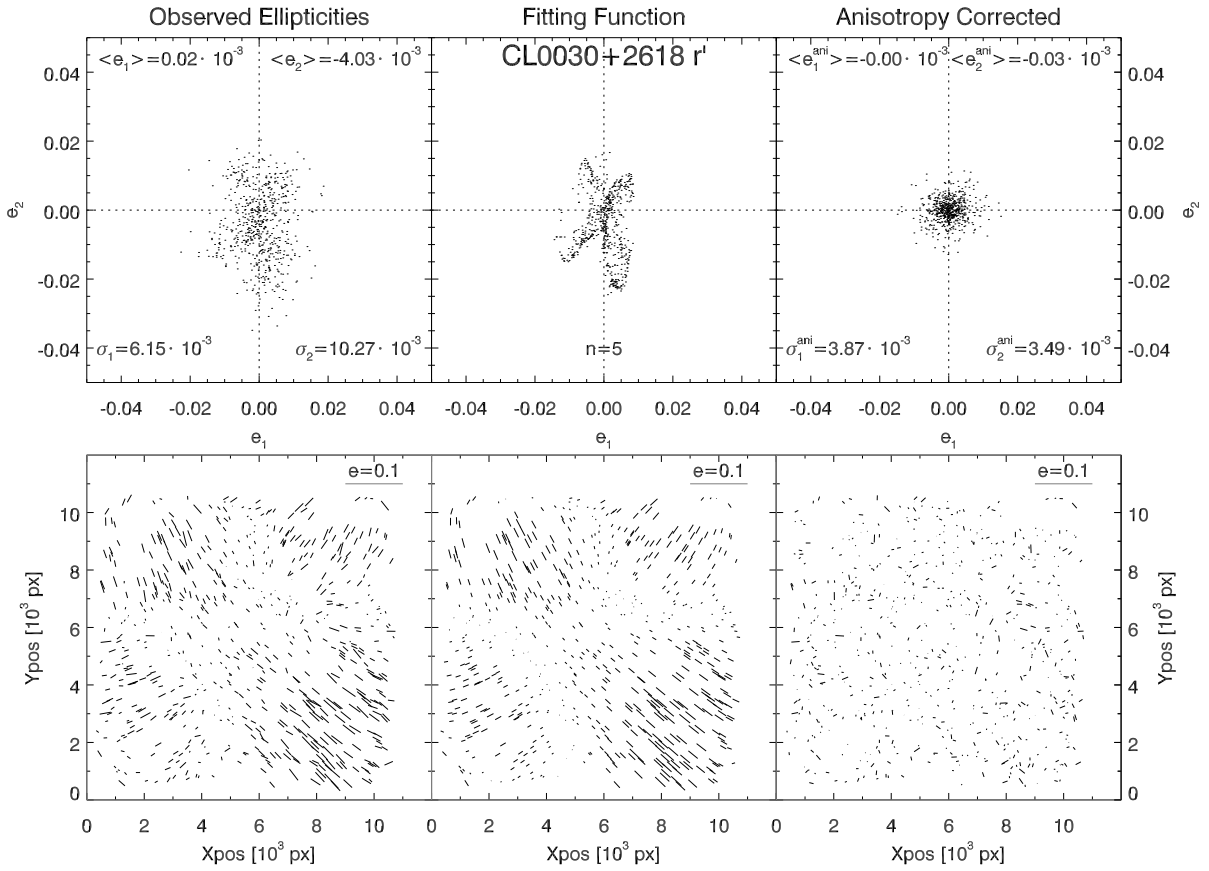

Figure 5.12: Correction of PSF anisotropy of the CL 0030+2618 r' band used in the analysis. The upper panel shows the distribution of the ellipticity components $e_{1,2}$ of the stars identified in the field, and the numerical values of their dispersions $\sigma_{1,2} := \sigma(e_{1,2})$. The "whisker plots" in the lower panel show how the size and orientation of PSF anisotropy vary as a function of the spatial coordinates x and y. On the left, the situation before correction, i.e., the ellipticities as measured in the stars are depicted. The middle two plots give the fit by a global fifth order polynomial in x and y. Residuals after this correction is applied are presented in the plots on the right.

6.15×10^{-3}, $\sigma(e_2) = 1.03 \times 10^{-2}$, and $\sigma(|e|) = 6.19 \times 10^{-3}$, which decrease after the correction to $\langle e_1^{\rm ani}\rangle = -5.60 \times 10^{-7}$, $\langle e_2^{\rm ani}\rangle = -2.60 \times 10^{-5}$, $\sigma(e_1^{\rm ani}) = 3.87 \times 10^{-3}$, $\sigma(e_2^{\rm ani}) = 3.49 \times 10^{-3}$, and $\sigma(|e^{\rm ani}|) = 2.90 \times 10^{-3}$, respectively. We note that the very small average for the individual components *before correction* is caused by the partial cancellation of anisotropies from different parts of the field-of-view. Thus, MMT/MEGACAM shows a similar degree of PSF anisotropy as other instruments from which lensing signals were measured successfully, e.g., MEGAPRIME/MEGACAM on CFHT (Semboloni et al. 2006) or Subaru's SUPRIMECAM (Okabe & Umetsu 2008). The latter authors measured larger values for the anisotropy components before correction: $\langle e_1\rangle = 1.41\times10^{-2}$, $\langle e_2\rangle = 1.63 \times 10^{-2}$, and $\sigma(|e|) = 2.32 \times 10^{-2}$, as an RMS average of seven galaxy cluster fields. However, Okabe & Umetsu (2008) find a simple spatial pattern for SUPRIMECAM.

We further assess the performance of the correction polynomial by analysing the anisotropy-corrected ellipticities $e^{\rm ani}_{{\rm gal},\delta}$ of galaxies as a function of the amount of correction $e^{\rm cor}_\delta$ applied to them by the polynomial fit. Theoretically, the expected positive correlation between the *uncorrected* ellipticities and the correcting polynomial should be removed and $e^{\rm ani}_{\rm gal}(e^{\rm cor})$ thus have a scatter

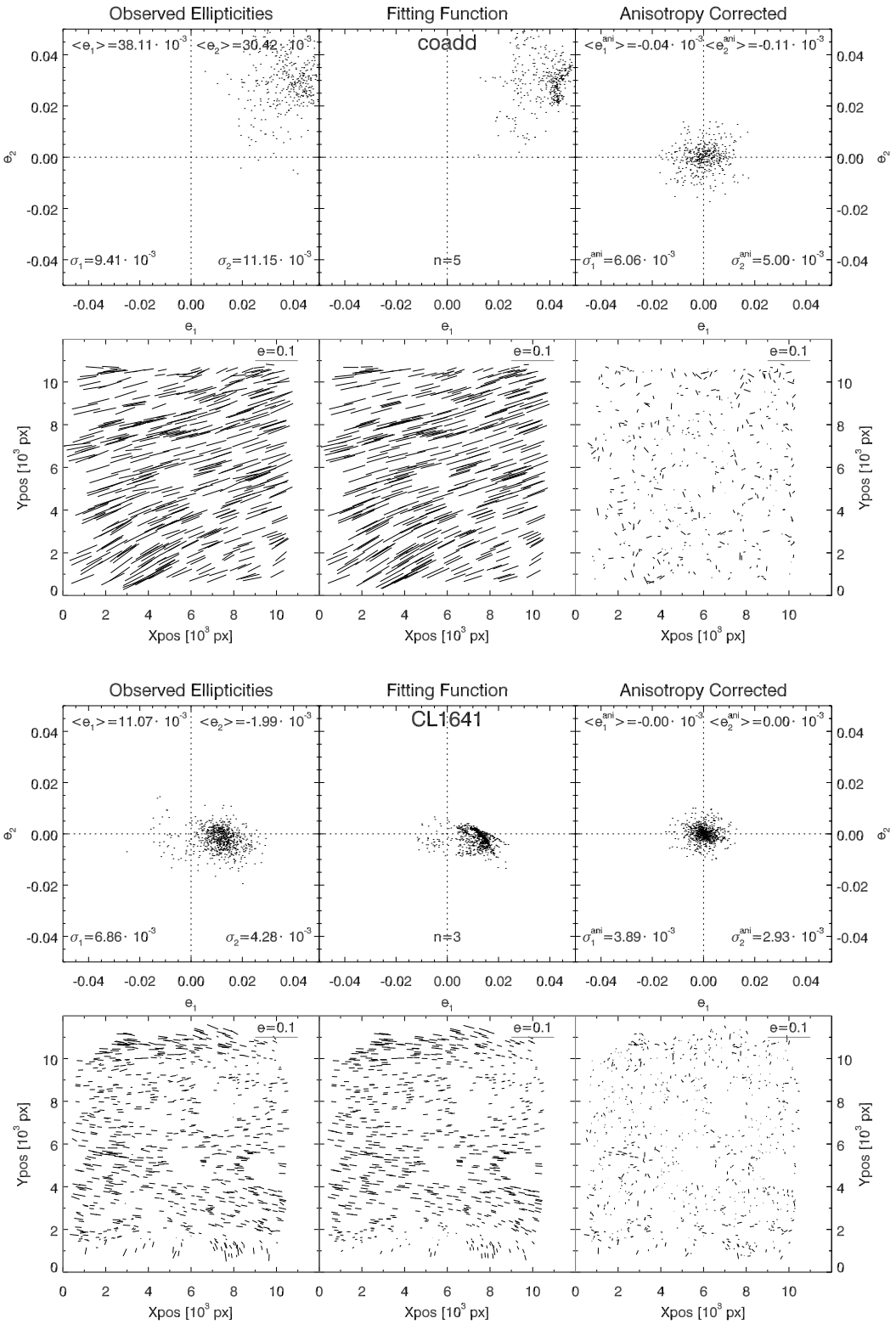

Figure 5.13: Same as Fig. 5.12, but for the r'-bands of CL 1416+4446 (upper plot) and CL 1641+4001 (lower plots). These fields show the correction for a high (CL 1416+4446) and low (CL 1641+4001) level of initial PSF anisotropy.

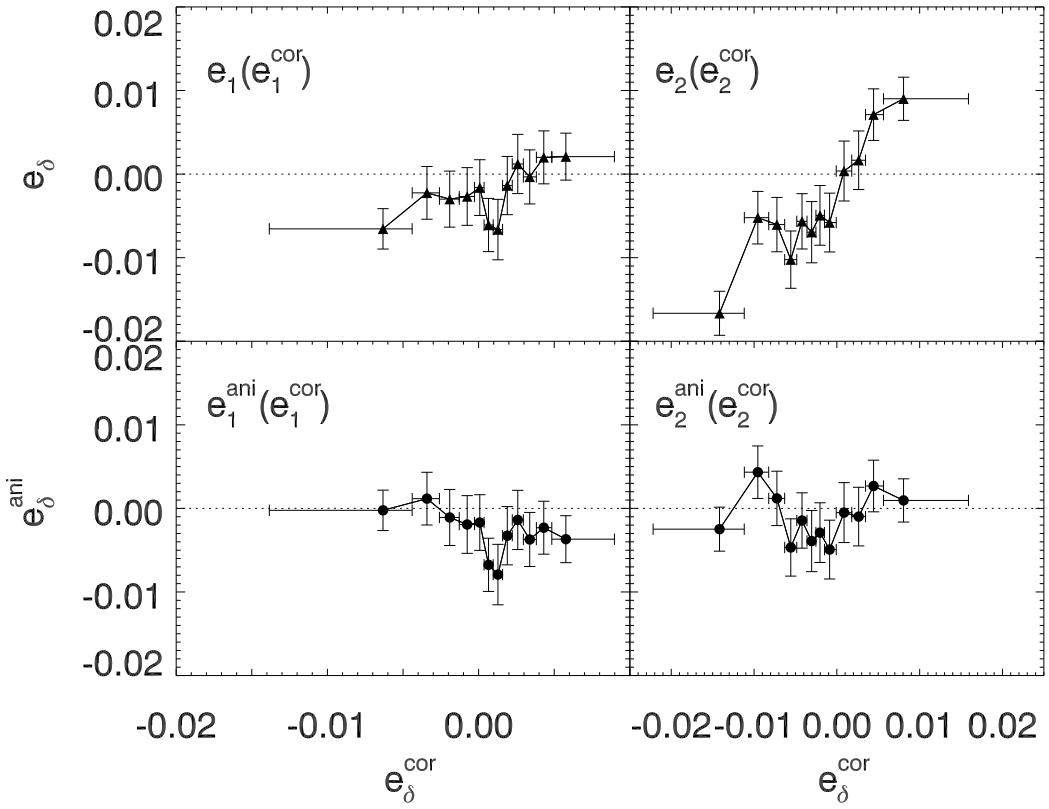

Figure 5.14: The effect of the polynomial correction for the PSF anisotropy on the ellipticities of galaxies averaged in equally populated bins. As a function of the amount of correction $e^{\rm cor}$ applied to the components $\delta = 1$ (left panels) and $\delta = 2$ (right panels), we show the raw ellipticities *before* correction in the upper panels and the PSF-corrected ellipticities ε in the lower panels. The bars in the abscissa and ordinate denote the range of the bin and the standard deviation in the ellipticity in this bin, respectively. The plot shows the CL 0030+2618 field.

around zero. We note that most of the anisotropy is present in the $\delta = 2$ component from the beginning (Fig. 5.14). This is removed in the corrected ellipticities, with $\langle e^{\rm ani}_{\rm gal,2}\rangle = -0.0010 \pm 0.0010$ being marginally consistent with zero in the standard deviation. In the $\delta = 1$ component, we measure a residual anisotropy of $\langle e^{\rm ani}_{\rm gal,1}\rangle = -0.0026 \pm 0.0010$, which is one order of magnitude smaller than the lensing signal we are about to measure.

As an alternative to the n=5 polynomial correction to the entire image, we consider a piecewise solution based on the pattern of preferred orientation in Fig. 5.12. Dividing the field into four regions at $y = 6100$ px and at $x = 4300$ px for $y < 6100$ px and $x = 5800$ px for $y > 6100$ px with a polynomial degree up to $n = 5$ we do not find a significant improvement in $\langle e^{\rm ani,*}\rangle$, $\sigma(e^{\rm ani,*})$, or $e^{\rm ani}_{\rm gal}(e^{\rm cor})$ over the simpler model defined over the whole field.

We conclude that, although we find small-scale changes in the PSF ellipticity that have to be modelled by a polynomial of relatively high order, the more important point is that the PSF anisotropy varies smoothly as a function of the position on the detector surface in every *individual* exposure, showing a simpler pattern than Fig. 5.12. Consequently, it *can* be modelled by a smooth function, which is a necessary prerequisite for using the instrument with the current weak lensing analysis pipelines. Thus, we have shown that weak lensing work is feasible using MMT MEGACAM.

Chapter 6

CL 0030+2618: The Pilot Study

We introduced the *400d Galaxy Cluster Survey Weak Lensing Programme* by focussing on one particular object, CL 0030+2618, which, as we see below, represents an exceptionally interesting case. The contents of this Section will be published in a very similar form by Israel et al. (2010). We describe in detail the methods that we use for data reduction and analysis because this is the first weak lensing study performed using MEGACAM at MMT.

The cluster CL 0030+2618 is reported to have a redshift of $z = 0.500$ in both Burenin et al. (2007) (its designation being BVH 002) and in the precursor of the *400d*, the *160d survey* (Vikhlinin et al. 1998), as VMF 001. Its X-ray emission as detected by ROSAT is centred at $\alpha_{\rm J2000} = 00^{\rm h}30^{\rm m}33\overset{\rm s}{.}6$, $\delta_{\rm J2000} = +26^\circ18'16''$. It was first identified as a cluster of galaxies by Boyle et al. (1997) who conducted a spectroscopic follow-up to ROSAT observations in the visual wavelength range. These authors assigned the designation CRSS J0030.5+2618 and measured a redshift of $z = 0.516$. Brandt et al. (2000) observed the field of CL 0030+2618 with CHANDRA during its calibration phase, by studying faint hard X-ray sources in the vicinity of the cluster. Horner et al. (2008) found a redshift of $z = 0.500$ for the cluster with their designation WARP J0030.5+2618 in their X-ray selected survey of *ROSAT* clusters, but point out a possible contamination of the X-ray signal by a line-of-sight structure at the lower redshift of $z \approx 0.27$.

Additional CHANDRA observations were conducted as part of the CCCP (Vikhlinin et al. 2009a,b). The analysis of CHANDRA data by Vikhlinin et al. (2009a) inferred a luminosity in the 0.5–2.0 keV-band of $L_{\rm X} = 1.57 \times 10^{44}$ erg s^{-1} and an ICM temperature of $k_{\rm B}T_{\rm X} = (5.63 \pm 1.13)$ keV . Based on its X-ray morphology, CL 0030+2618 was classified as a possible merger by Vikhlinin et al. (2009a). The 16.1 ks CCCP CHANDRA data set was analysed independently by Maughan et al. (2008), as part of their study of X-ray morphologies and metal abundances of CHANDRA clusters, which includes 17 out of the 36 *Cosmological Sample* objects. Maughan et al. (2008) find the metallicity of CL 0030+2618 to be $Z = 1.02^{+0.74}_{-0.56}\,{\rm Z}_\odot$, unusually high for a $z = 0.50$ cluster, albeit with large uncertainties.

We (Israel et al. 2010) present the first study of CL 0030+2618 with a large optical telescope, noting that the SEGUE observations used in Sect. 5.2.2 for cross-calibration have some overlap with our MEGACAM imaging south of CL 0030+2618, but do not contain this object itself. Figure 6.1 shows a three-colour composite image prepared from the stacked MEGACAM $g'r'i'$ observations of CL 0030+2618 (cf. Table 4.2).

6.1 Aperture Mass Detection of CL 0030+2618

In this section, we describe the detection of the shear signal of CL 0030+2618 with the aperture mass technique and the consistency checks applied on the shear catalogue.

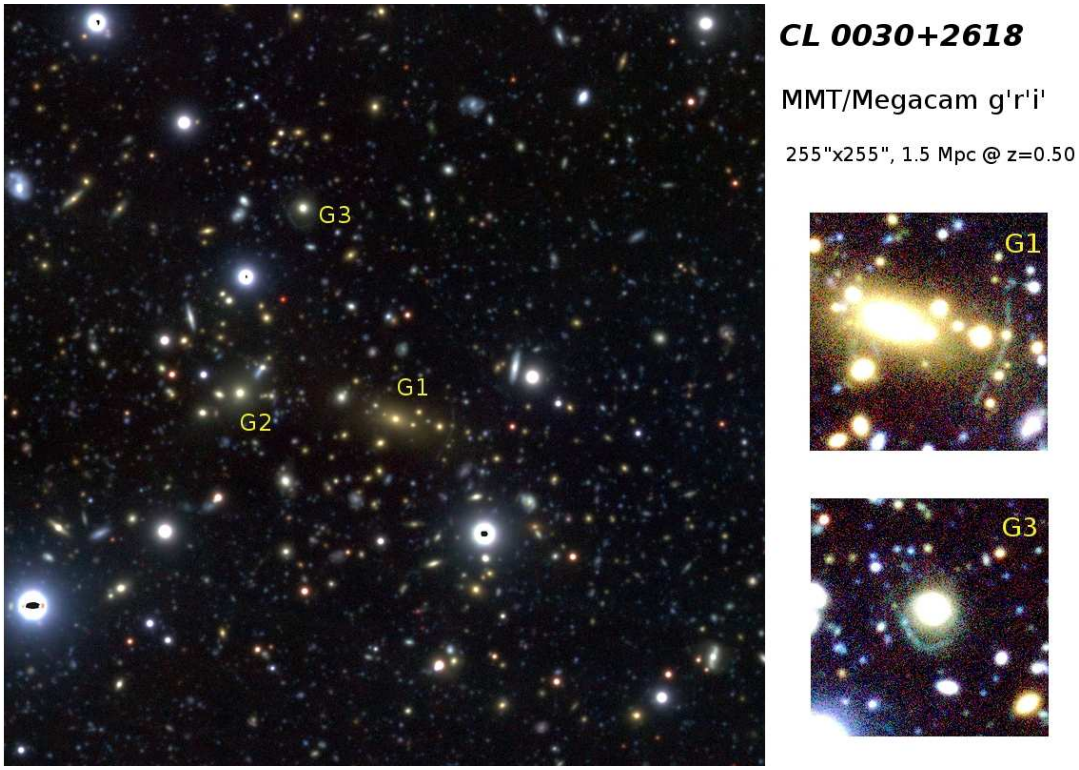

Figure 6.1: Three-colour composite of CL 0030+2618, prepared from the MEGACAM $g'r'i'$ coadded images. The main image shows a cut-out of the central region of CL 0030+2618, with an edge length of $\approx 255''$ (1600 px), i.e. the cluster is covered to about half the virial radius of ≈ 1.5 Mpc. North is up and east is to the left. The tentative luminous arcs near the galaxies G1 and G3 (Table 6.1 and Sect. 6.3.3) are emphasised in the two smaller, zoomed ($40'' \times 40''$) images.

Table 6.1: Notable galaxies in the field of CL 0030+2618. The designations G1 to G3 are also used in Fig. 6.1, while G4 is shown in Fig. 6.10. Redshifts were taken from Boyle et al. (1997).

Galaxy	α_{J2000}	δ_{J2000}	$r'^{\mathrm{MMT}}_{\mathrm{AUTO}}$	$g'^{\mathrm{MMT}}_{\mathrm{AUTO}}$	$i'^{\mathrm{MMT}}_{\mathrm{AUTO}}$	z	Note
G1	$00^{\mathrm{h}}30^{\mathrm{m}}34\overset{\mathrm{s}}{.}0$	$26°18'09''$	19.20	21.14	18.31	0.516	BCG of CL 0030+2618
G2	$00^{\mathrm{h}}30^{\mathrm{m}}37\overset{\mathrm{s}}{.}9$	$26°18'18''$	18.82	20.23	18.27	n.a.	BCG of fg group
G3	$00^{\mathrm{h}}30^{\mathrm{m}}36\overset{\mathrm{s}}{.}3$	$26°19'20''$	19.46	20.76	18.95	n.a.	SL feature
G4	$00^{\mathrm{h}}30^{\mathrm{m}}39\overset{\mathrm{s}}{.}5$	$26°20'56''$	17.23	17.98	16.94	0.493	QSO

6.1.1 Outline of Background Selection

We now introduce the *background selection* based on the galaxy shape catalogue and resulting in the "lensing catalogue" of objects we classify as background galaxies w.r.t. the lensing cluster. While unlensed objects remaining in the catalogue dilute the shear signal, rejection of true background galaxies reduce it as well. A sensible foreground removal is especially important for relatively distant objects such as the *400d* cosmology sample clusters.

Our background selection is based on the $g'r'i'$ photometry of the sources. We introduce two free parameters in our analysis: the magnitude limit m_{faint} below which all fainter galaxies

Table 6.2: Tested regions in colour-colour space inside which galaxies with $m_{\rm bright} < r' < m_{\rm faint}$ are excised from the lensing catalogue. These selection polygons are defined in terms of $g'-r'$, $r'-i'$, and the second-order colour index $s := \frac{8}{3}r' - \frac{5}{3}i' - g'$.

Polygon	$\min(r'-i')$	$\max(r'-i')$	$\min(g'-r')$	$\max(g'-r')$	$\min(s)$	$\max(s)$
large	0	1.25	0.25	2.25	−1.0	0.583
small	0.1	1.2	0.4	2.0	−0.733	0.1

are included in the shear catalogue, regardless of their $g'-r'$ and $r'-i'$ colour indices, and the magnitude $m_{\rm bright}$ above which all brighter galaxies will be considered foreground objects and discarded. Only in the intermediate interval $m_{\rm bright} < r' < m_{\rm faint}$ does the selection of galaxies based on their position in the colour-colour-diagram take place. In these terms, a simple magnitude cut would correspond to $m_{\rm bright} = m_{\rm faint}$. For example, we vary these parameters to optimise the detection of CL 0030+2618 and find $m_{\rm bright} = 20.0$ and $m_{\rm faint} = 22.5$. We present the details of the colour-colour-diagram method in Sect. 6.1.2. The photometric cuts reduce the catalogue size by 6.0 %, leaving us with a lensing catalogue of $N_{\rm cat} = 14\,813$ objects, corresponding to a galaxy surface density of $n_{\rm cat} = 21.2\,{\rm arcmin}^{-2}$.

6.1.2 Background Selection by Galaxy Colours

The selection of background galaxies is based on $r'-i'$ versus $g'-r'$ colour-colour-diagrams for galaxies of intermediate magnitude and works as follows. We identify the region in the colour-colour-diagram populated by the brightest galaxies, a sample we assume to be dominated by cluster ellipticals. As the cluster red sequence shows, the colour of early-type systems in a cluster of galaxies varies little with magnitude. As can be seen from Fig. 6.2, the bright galaxies observed in the CL 0030+2618 field show a well-defined relation between their $r'-i'$ and $g'-r'$ colours. Assuming that the fainter cluster members that fall into the $m_{\rm bright} < r' < m_{\rm faint}$ interval on average show the same colours as their brighter companions, we exclude those intermediately bright galaxies *with colours similar to those of the brighter objects* while keeping those that are inconsistent with the colours of the bright sample.

Following a method introduced by Bradač et al. (2005) and Kausch et al. (2007), we empirically define two polygonal regions in the colour-colour diagram, a "small", rather inclusive polygon and a "large" polygon for a more conservative selection (thick and thin lines in Fig. 6.2, respectively). We test the influence of the colour-colour selection on the lensing signal for those two cases. Table 6.2 gives the respective limits in $g'-r'$, $r'-i'$, and the second-order colour index $s := \frac{8}{3}r' - \frac{5}{3}i' - g'$ chosen to be parallel to the locus of the bright galaxies in Fig. 6.2.

Figure 6.3 (upper panel) shows the effect of the background galaxy selection on the S-statistics if the "small" polygon defined in Table 6.2 is used for the intermediate bright galaxies. Here, the solid line denotes a pure magnitude cut at $m_{\rm bright} = m_{\rm faint}$ while the different line styles show cases in which the colour-colour criterion acts in different intervals of $m_{\rm faint} - m_{\rm bright}$. We first note that the S-statistics depend more sensitively on $m_{\rm faint}$ than on $m_{\rm bright}$, with its maximum occurring in the range $22.0 < m_{\rm faint} < 22.5$, irrespective of $m_{\rm bright}$. The greater relative importance of $m_{\rm faint}$ does not come as a surprise as, in the $r' < 25$ magnitude range we study here, source counts are rising steeply towards fainter magnitudes (Fig. 6.6).

Secondly, we notice that the improvement in the S-statistics upon using the best value of $m_{\rm faint} = 22.5$, which we now adopt, over the case of not applying photometric criteria to our catalogue (corresponding to $m_{\rm faint} = 17.6$) is small: $S = 5.73$ for $m_{\rm bright} = m_{\rm faint}$ as compared

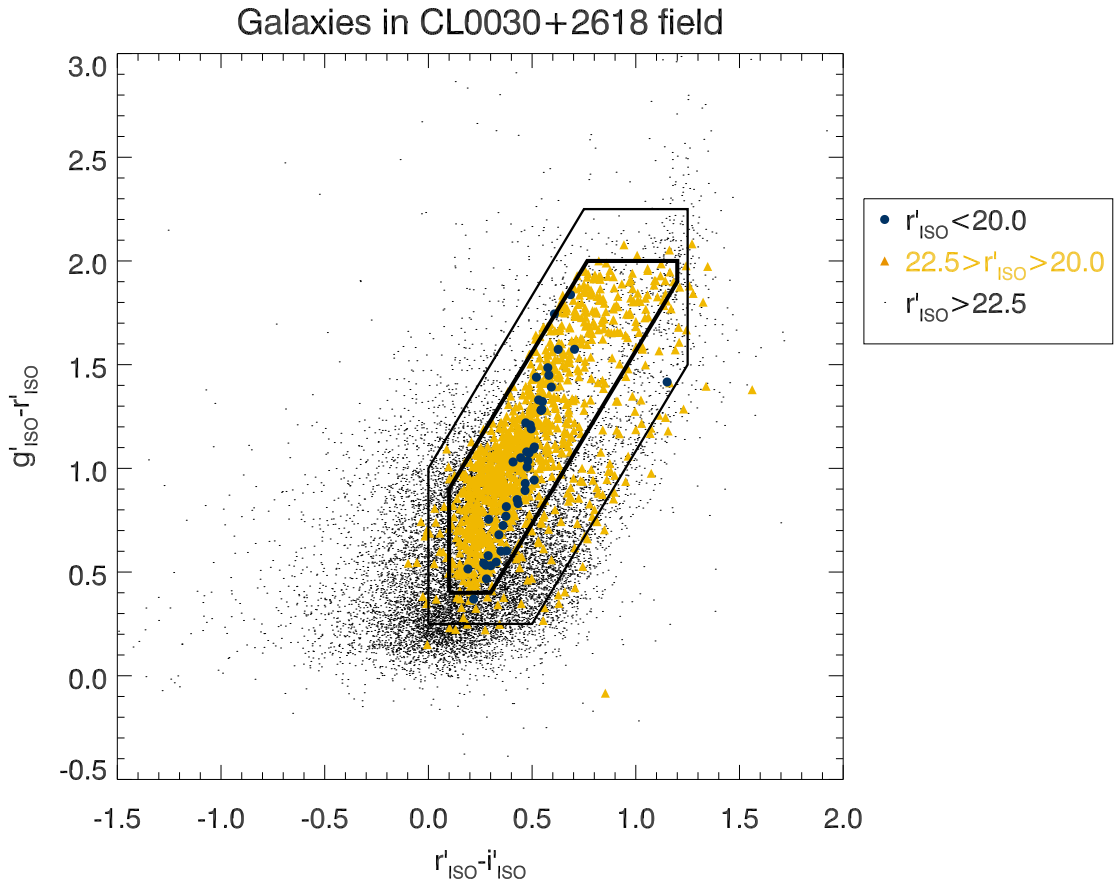

Figure 6.2: Colour-colour selection of the lensing catalogue: plotted are the $g'-r'$ vs. $r'-i'$ colours of the objects in the *galaxy shape catalogue* (with cuts on $\min(\mathrm{tr}\,\mathcal{P}^g)$, $\min(\nu_{\rm gal})$, and $\max(|(\varepsilon|)$ already applied). The galaxy sample is divided into three magnitude bins by the $m_{\rm bright}$ and $m_{\rm faint}$ parameters. All sources brighter than $m_{\rm bright}$ (largest dots) are removed in producing the final lensing catalogue, while all sources fainter than $m_{\rm faint}$ (smallest dots) are kept. Intermediately bright galaxies with $m_{\rm bright} < r' < m_{\rm faint}$ (medium-sized dots) mark the transition between these two regimes. Only in this magnitude interval, the selection into the final galaxy catalogue by colour indices applies: sources outside the thick polygon bounding the region in which we find the brighter galaxies and likely cluster members are included in the final catalogue. See Table 6.2 for the definition of the polygon tracing the locus of bright galaxies.

to $S = 5.46$. This may partly be explained by the small number of catalogue objects affected by background selection. As can be seen by comparing the number of objects in the lensing catalogue as a function of $m_{\rm faint}$ and $m_{\rm bright}$ in the lower panel of Fig. 6.3 with the S-statistics, as selection starts removing (signal-diluting foreground) galaxies from the catalogue at $m_{\rm faint} \gtrsim 21.5$, the S-statistics begins to increase around the same point. For instance, with a magnitude cut at $m_{\rm faint} = 22.5$, the remaining 92.5 % of the sources yield a $S = 5.73$, while for a $m_{\rm faint} = 21.5$ magnitude cut, the remaining 97.3 % of the catalogue give $S = 5.53$.

The strong decrease in detection significance for $m_{\rm faint} \gtrsim 22.7$ – most pronounced for the $m_{\rm bright} = m_{\rm faint}$ case – can also be attributed to a cut at faint magnitudes rejecting an increasingly large number of signal-carrying background galaxies. For the various $m_{\rm bright} < m_{\rm faint}$ cases, the

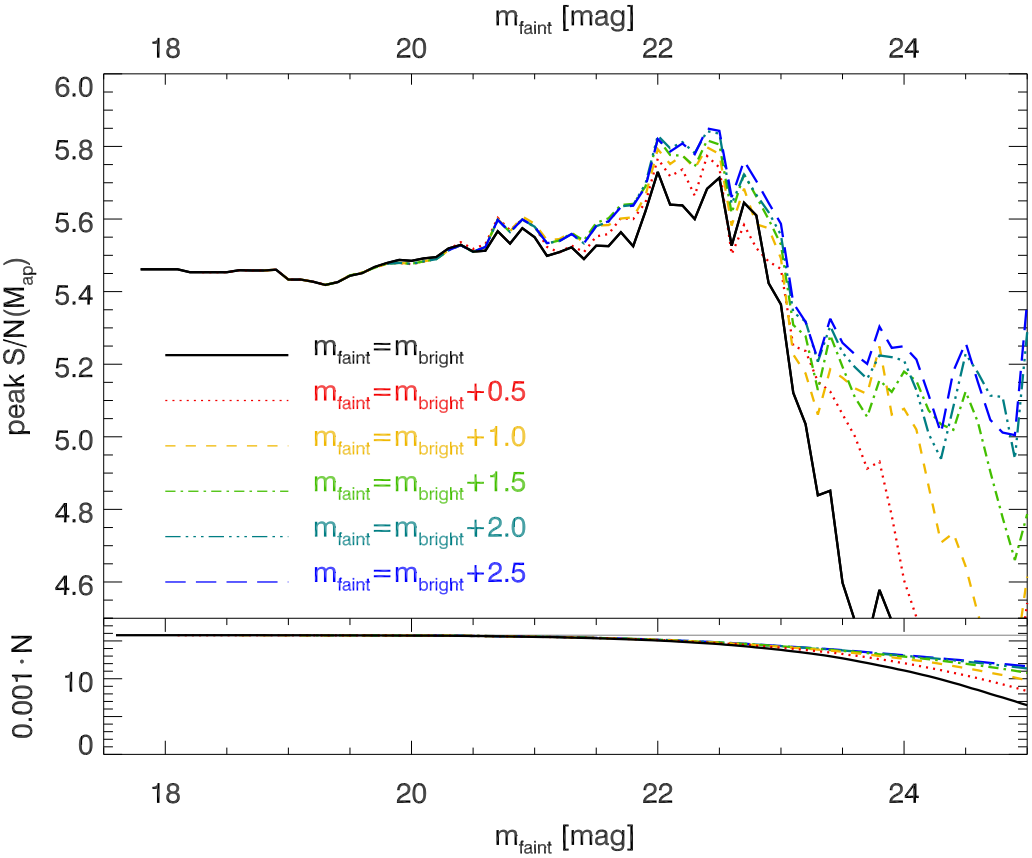

Figure 6.3: *Upper panel:* The maximum $M_{\rm ap}$ signal-to-noise ratio found in the vicinity of CL 0030+2618 as a function of the background selection introduced by $m_{\rm faint}$ and $m_{\rm bright}$. The solid line corresponds to a magnitude cut $m_{\rm bright} = m_{\rm faint}$ while the dotted, dashed, dot-dashed, triple dot-dashed, and long-dashed lines denote background selections by galaxy colours in increasingly wide intervals of $m_{\rm faint} - m_{\rm bright} = \{0.5, 1.0, 1.5, 2.0, 2.5\}$ respectively. Here, the smaller polygon in Fig. 6.2 is used, assuming a well-defined locus of cluster galaxies in colour-colour-space and, in turn, for a rather inclusive selection of galaxies. *Lower panel:* The number N of galaxies in the shear catalogue as a function of $m_{\rm bright}$ and $m_{\rm faint}$. The horizontal line gives $N \approx 16000$ before applying any background selection for comparison. The colours and line-styles denote the same cases as in the upper panel.

higher signals for a given $m_{\rm faint}$ demonstrate that galaxies of intermediate magnitude with colours inconsistent with cluster ellipticals are kept in the catalogue and contribute to the signal.

Repeating this analysis with the "large" polygon defined in Table 6.2, we find that the dependence of S on $m_{\rm bright}$ for a given $m_{\rm faint}$ can be largely reduced. This can be explained by the restrictive choice of the "large" compared to the "small" polygon, leaving only a few galaxies of intermediate magnitude in the catalogue.

In the following analyses, we choose the "small" polygon and the parameter combination $m_{\rm faint} = 22.5$, $m_{\rm bright} = 20.0$, yielding the near-optimal[1] overall detection of the cluster: $S = 5.84$. We also tested catalogues with $m_{\rm faint} - m_{\rm bright} > 2.5$, but did not find any further increase in the

[1]We prefer $m_{\rm faint} = 22.5$ over the slightly better $m_{\rm faint} = 22.4$ because of the greater robustness of the $m_{\rm faint} = 22.5$ cases with respect to changes in $m_{\rm bright}$.

S-statistics. We remark that the selection criteria found here are purely empiric. A comparison to a photo-z catalogue is performed in Sect. 6.2.3.

6.1.3 Detection of the Shear Signal

The weak lensing analysis that we conduct is a two-step process. First, we confirm the presence of a cluster signal by constructing *aperture mass* maps of the field, which determine the position of the cluster centre and the corresponding significance. In the second step, building on this position for CL 0030+2618, the tangential shear profile can be determined and fitted, leading to the determination of the cluster mass.

More precisely, we use the S-statistics, defined in Eq. (3.29). For the filter function $Q(x := |\boldsymbol{\theta}_\mathrm{i} - \boldsymbol{\theta}_\mathrm{c}|/\theta_\mathrm{out})$, we choose the hyperbolic tangent filter introduced by Schirmer et al. (2007):

$$Q_\mathrm{TANH}(x) = \frac{1}{1 + \mathrm{e}^{a-bx} + \mathrm{e}^{c+dx}} \frac{\tanh(x/x_\mathrm{c})}{x/x_\mathrm{c}} \quad , \tag{6.1}$$

where the width of the filter is given by $x_\mathrm{c} = 0.15$ and the shape of its exponential cut-offs for small and large x is given by the default values $\{a, b, c, d\} = \{6, 150, 47, 50\}$.

The value of θ_out in Eq. (3.29) is also fixed such that it maximises $S_{\theta_\mathrm{out}}(\boldsymbol{\theta}_\mathrm{c})$, which strongly depends on the filter size used. Exploring the parameter space spanned by θ_out and the photometric parameters m_bright and m_faint, we find, independent of the latter two, the highest S-values with $14' < \theta_\mathrm{out} < 15'$. The behaviour of S as a function of θ_out (at a fixed $\boldsymbol{\theta}_\mathrm{c}$) is in good general agreement with the results of Schirmer et al. (2007) for the same filter $Q_\mathrm{TANH}(x)$. Thus, we fix $\theta_\mathrm{out} = 14\farcm5$ in the following analysis, noting this number's agreement with the size of our MEGACAM images (cf. Fig. 6.9). We also tested the influence of varying the parameter x_c in the Q_TANH filter and find that, when all other parameters remain fixed, the maximum S-value in the $0.15 \leq x_\mathrm{c} \leq 0.6$ interval changes by < 0.5 % but decreases more steeply for smaller values of x_c.

Applying these parameters and measuring S on a reference grid of $60''$ mesh size, we detect CL 0030+2618 at the 5.8σ level in a grid cell whose central distance of $34''$ from the *ROSAT* position at $\alpha_\mathrm{J2000} = 00^\mathrm{h}30^\mathrm{m}33\fs6, \delta_\mathrm{J2000} = 26°18'16''$ is smaller than the mesh size. We investigate the cluster position in more detail in Sect. 6.3.1.

6.1.4 Verification of the Shear Signal

Maximum Shear Because of the inversion of the noisy matrix $\mathcal{P}^\mathrm{g}$ in Eq. (5.7), the resulting values of the estimator $|\varepsilon|$ are not bound from above, while ellipticities are confined to $0 \leq e \leq 1$. Thus, when attempting to measure weak lensing using the KSB method, we need to define an upper limit $\max(|\varepsilon|)$ of the shear estimates we consider reliable. We evaluate the influence of the choice of $\max(|\varepsilon|)$ on the S-statistics (Eq. 3.29) by varying it while keeping the other parameters fixed, such as $\min(\mathrm{tr}\,\mathcal{P}^\mathrm{g})$, the minimum $\min(\nu)$ of the signal-to-noise ratio ν of the individual galaxy detection determined by the KSB code, and the photometric parameters m_bright and m_faint defined in Sect. 6.1.2. In the range $0.6 \lesssim \max(|\varepsilon|) \lesssim 0.8$, we find a higher shear signal due to the higher number of galaxies in the catalogues when using less restrictive cuts (Fig. 6.4). For $\max(|\varepsilon|) \gtrsim 0.8$, we see a sharp decline in the lensing signal, which we attribute to galaxies entering the catalogue, whose ellipticity estimate is dominated by noise. We fix $\max(|\varepsilon|) = 0.8$, $\min(\mathrm{tr}\,\mathcal{P}^\mathrm{g}) = 0.1$, and $\min(\nu) = 4.5$ simultaneously to their respective values. While nearly optimising the S-statistics, this might bias the mass estimate because a cut in $\max(|\varepsilon|) = 0.8$ directly affects the averaging process yielding the shear.

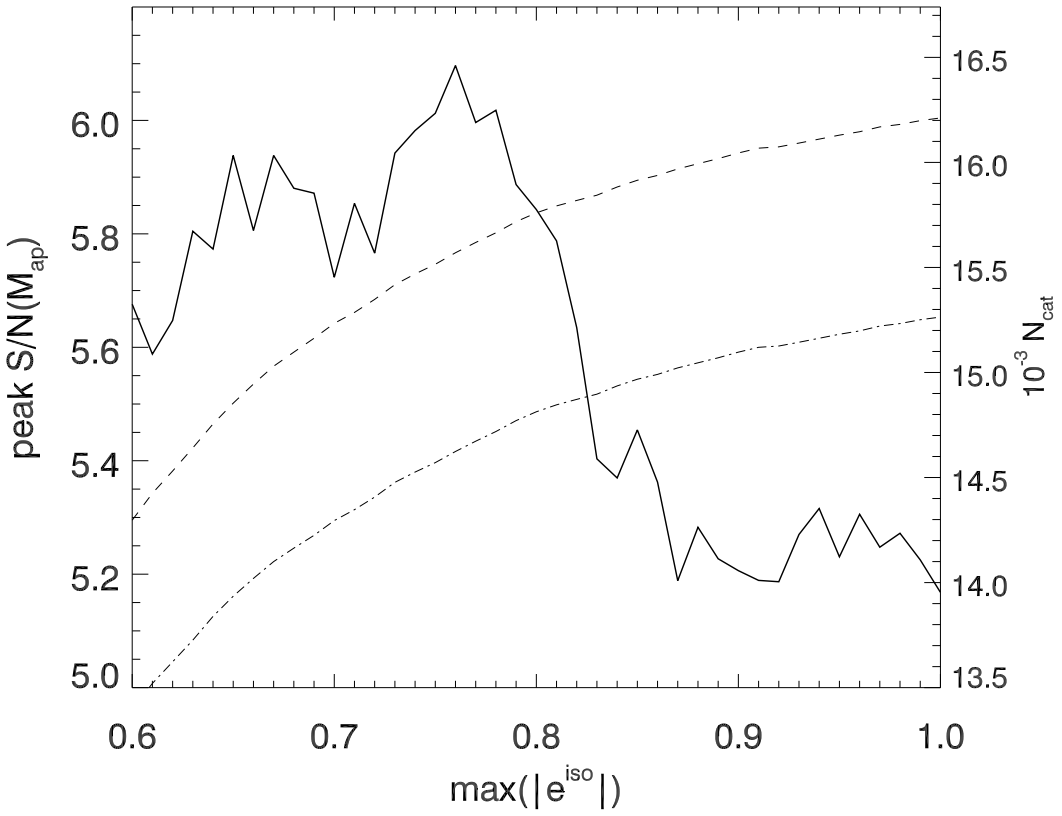

Figure 6.4: The S-statistics (solid line) as a function of the maximum value of the ellipticity estimator ε that we include in the galaxy shape catalogue. The dashed and dash-dotted lines show the sizes of the resulting catalogue before and after background selection (see Sect. 6.1.2).

Shear Calibration We can account for this bias by scaling the shear estimates with a *shear calibration factor* f such that $\varepsilon \rightarrow f_0\varepsilon$ to balance biases such as the effect of $\max(|\varepsilon|)$. The question of how gravitational shear can be measured unbiased and precisely has been identified as the crucial challenge in future weak lensing experiments (see e.g., Heymans et al. 2006; Massey et al. 2007; Bridle et al. 2010). The "TS" KSB method employed here has been studied extensively and is well understood in many aspects. To correct for the biased shear measurements, found by testing the KSB pipeline with the simulated data in Heymans et al. (2006), the shear calibration factor was introduced and studied subsequently (Schrabback et al. 2007; Hartlap et al. 2009). As pointed out by these authors, the calibration bias depends on both the strength of the shear signal being inspected, as well as on the details of the implementation and galaxy selection for the shear catalogue. In the absence of detailed shape measurement simulations under cluster lensing conditions, we chose a fiducial $f_0 = 1.08$ from Hartlap et al. (2009) and assign an error of $\sigma_{f_0} = 0.05$ to it, covering a significant part of the discussed interval.

Complementary Catalogue We check the efficacy of the set of parameters we adopted for the photometric cuts by reversing the selection of galaxies and calculating the S-statistics from those galaxies excluded in our normal procedure. By reversing the background selection, i.e., keeping only those galaxies regarded as cluster or foreground sources, we find that 10^5 bootstrap realisations of the complementary catalogue infer an aperture mass significance of $S = -0.83 \pm 1.06$. From the consistency with zero, we conclude that these cuts effectively select the signal-carrying

Table 6.3: Colours of prominent galaxies observed in the CL 0030+2618 field compared to colours computed from CWW80 elliptical templates at $z = 0.50$ and $z = 0.25$.

Galaxy	z	$g'-i'$	$g'-r'$	$r'-i'$
G1	0.516	2.83	1.94	0.89
G2	n.a.	1.96	1.41	0.55
CWW80 Ell $z = 0.50$	0.50	2.83	1.90	0.93
CWW80 Ell $z = 0.25$	0.25	2.14	1.59	0.55

galaxies. As the background selection removes $f_{\rm ph} = N_{\rm complem}/N_{\rm cat} = 6.0$ % of the sources in the catalogue, we expect the bias $\approx f_{\rm ph} S_{\rm complem}/S_{\rm cat} \approx -0.8$ % caused by it to be small.

6.2 Photometric Analysis

6.2.1 The Red Sequence

We consider the $(g'-i')$ versus i' colour-magnitude diagram of the galaxies in the galaxy shape catalogue (i.e., before applying cuts to select sources on the basis of their lensing signal) close to the coordinates of CL 0030+2618 to identify the red sequence of this $z = 0.5$ cluster, because the observed g' and i' passbands are on different sides of the Balmer break at the cluster redshift.

Having removed the most extended galaxies early-on in the KSB pipeline, we do not expect to find the most prominent cluster members in the catalogue for which shear estimates are determined. The upper panel of Fig. 6.5 shows a rather broad distribution in $g'-i'$ colour of the galaxies at $\theta < 4'$ from the ROSAT cluster centre.[2] Nevertheless, we find an enhancement in the number of galaxies extending from around $(g'-i') \approx 2.8$ for the $i' \approx 21$ to $(g'-i') \approx 2.3$ for the $i' \approx 27$ sources in our catalogue. This enhancement is caused in particular by a high number of galaxies very close ($\theta < 2'$) to the cluster centre.

The CWW80 template for an elliptical $z = 0.50$ galaxy predicts $(g'-i') \approx 2.8$ shown as a solid line and large dot at $i' = 20$ in the upper figure of Fig. 6.5. This is in good agreement with the bright end of our observed cluster red sequence, indicating that we indeed detect the red sequence of CL 0030+2618.[3] At $z = 0.25$, the tentative redshift of the foreground structure found by Horner et al. (2008, see also Sect. 6.2.5), the same template yields $(g'-i') \approx 2.1$, shown by the dashed line and large dot at $i' = 20$ in the upper plot of Fig. 6.5. The broad distributions in $g'-i'$ colours and the weak red sequence of CL 0030+2618 are consistent with the presence of a foreground group.

In the lower panel of Fig. 6.5, we show the $g'-r'$ colours of the same central region galaxies as a function of their $r'-i'$ colours (compare also Fig. 6.2). In addition to the main clump, there is a population of galaxies with both red $g'-r'$ and $r'-i'$ colours that follow the locus of the bright galaxies in Fig. 6.2. As expected, the CWW80 templates for $z \approx 0.25$ and $z \approx 0.50$ belong

[2] Figure 6.5 is a modified and corrected version of Fig. B1 in Israel et al. (2010). The catalogue now consists of all KSB catalogue sources matching the "galaxy" criteria given in Table 5.3. Note that the resulting change in the catalogue is mainly due to sources with small half-light radii ϑ and unclear star/galaxy distinction, which are now excluded. In addition, errors in the plotting routine have been corrected. Both changes result in a more prominent sequence of cluster galaxies, in particular in the lower panel of Figure 6.5, but neither entail further modifications "downstream" in the analysis.

[3] For this argument, we can neglect the known slope of the red sequence due to the lower metallicity of the many dwarf galaxies among the fainter cluster members (Gladders et al. 1998).

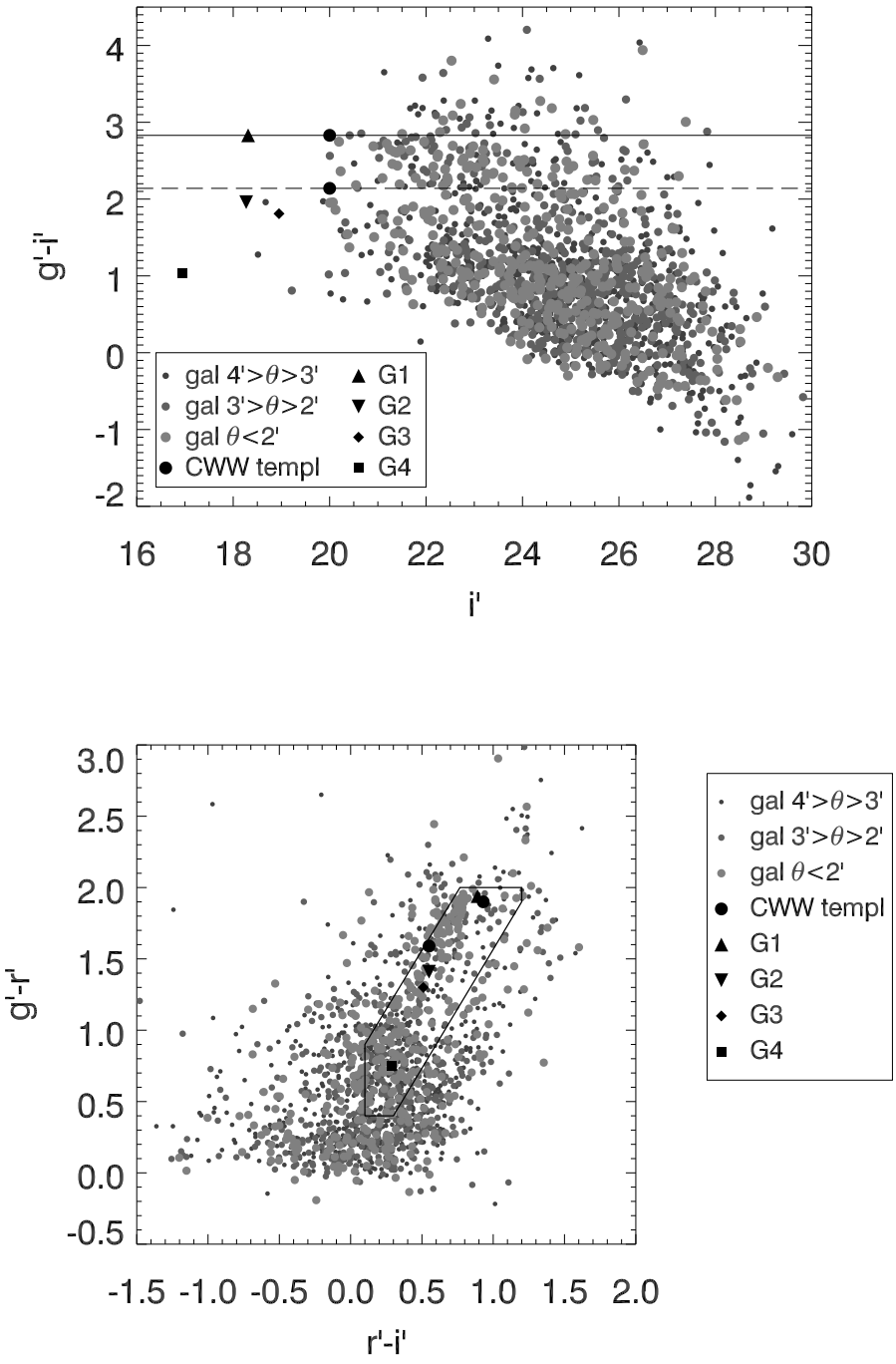

Figure 6.5: *Upper plot*: Colour-magnitude diagram of all galaxies in the KSB catalogue with a radial distance $\theta < 4'$ from the centre of CL 0030+2618. Symbol sizes and shades of grey denote galaxies from the galaxy shape catalogue in different cluster-centric radial bins. The $g'-i'$ colours of Coleman et al. (1980, CWW) template galaxies at $z = 0.5$ (solid line and large dot at $i' = 20$) and $z = 0.25$ (dashed line and large dot) are shown for comparison, as well as four notable bright galaxies detailed in Table 6.1. *Lower plot*: Colour-colour diagram with the same objects. The polygonal region delineating the locus of bright galaxies (cf. Fig. 6.2) is given for comparison.

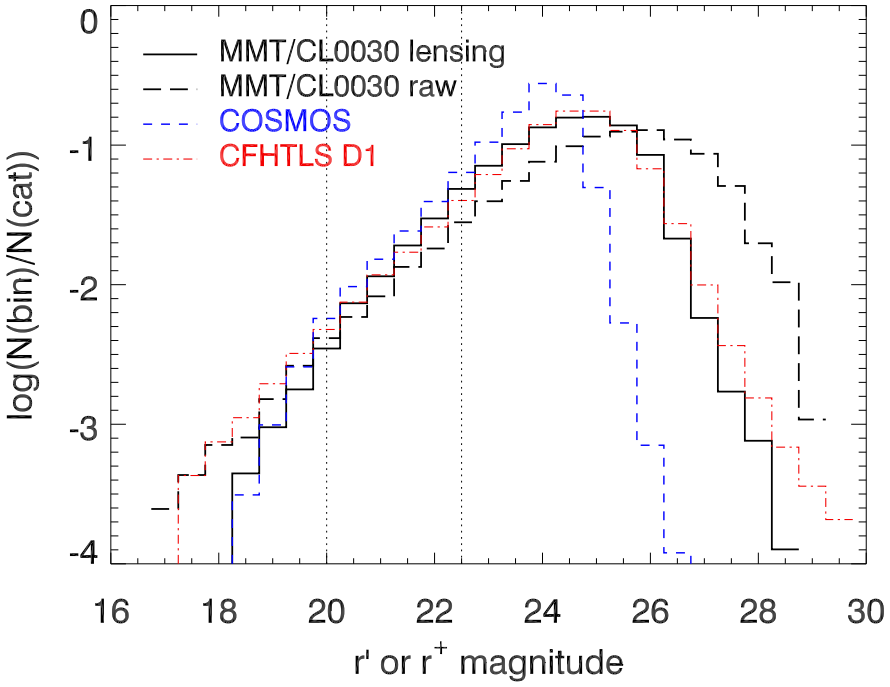

Figure 6.6: Source number counts in the CL 0030+2618 and exemplary photometric redshift fields. Given are the numbers of sources as fractions of the total number of objects in the catalogue in the r' band for the MMT Megacam CL 0030+2618 raw (long-dashed curve) and lensing (before background selection; solid curve) catalogues as well as for the CFHTLS D1 field (dash-dotted curve). The dashed curve denotes the COSMOS r^+-band number counts. Vertical dotted lines indicate $m_{\rm bright}$ and $m_{\rm faint}$.

to the redder population, and for $m < m_{\rm faint}$ would be excluded from the lensing catalogue by the background selection (Sect. 6.1.2).

6.2.2 Comparison to Photometric Redshift Surveys

To check the significance of the optimal values empirically found for $m_{\rm bright}$ and $m_{\rm faint}$ – i.e., to determine whether they provide an effective distinction between galaxies at redshift $z \leq 0.5$ and $z > 0.5$ – and to estimate the geometric factor $\langle D_{\rm ds}/D_{\rm s}\rangle$ needed to convert lensing shear into a mass estimate, we compare our data to two catalogues with known photometric redshift distributions, the CFHTLS Deep 1 field (Ilbert et al. 2006) and the COSMOS survey (Ilbert et al. 2009).

In Fig. 6.6, we compare the source number counts as a function of magnitude observed in the CL 0030+2618 field with MMT/Megacam (before and after selection of high-quality shape objects, i.e., the unflagged `SExtractor` objects compared to the galaxy shape catalogue) to the CFHTLS D1 (MegaCam at CFHT, SDSS filter system) and COSMOS photo-z sources. For the latter, the Subaru $g^+r^+i^+$ magnitudes similar to the SDSS filters are used. From the CFHTLS, we use all unflagged sources classified as galaxies, detected in all five bands ($u^*g'r'i'z'$) and with a photo-z derived from at least three bands whose 1σ error margin $\Delta z_{\rm ph}$ satisfies $\Delta z_{\rm ph}/(1+z_{\rm ph}) < 0.25$. Likewise, we use all unflagged sources classified as galaxies having an unflagged photo-z estimate in the COSMOS catalogue that are detected in the Subaru $g^+r^+i^+$ and CFHT i' passbands.

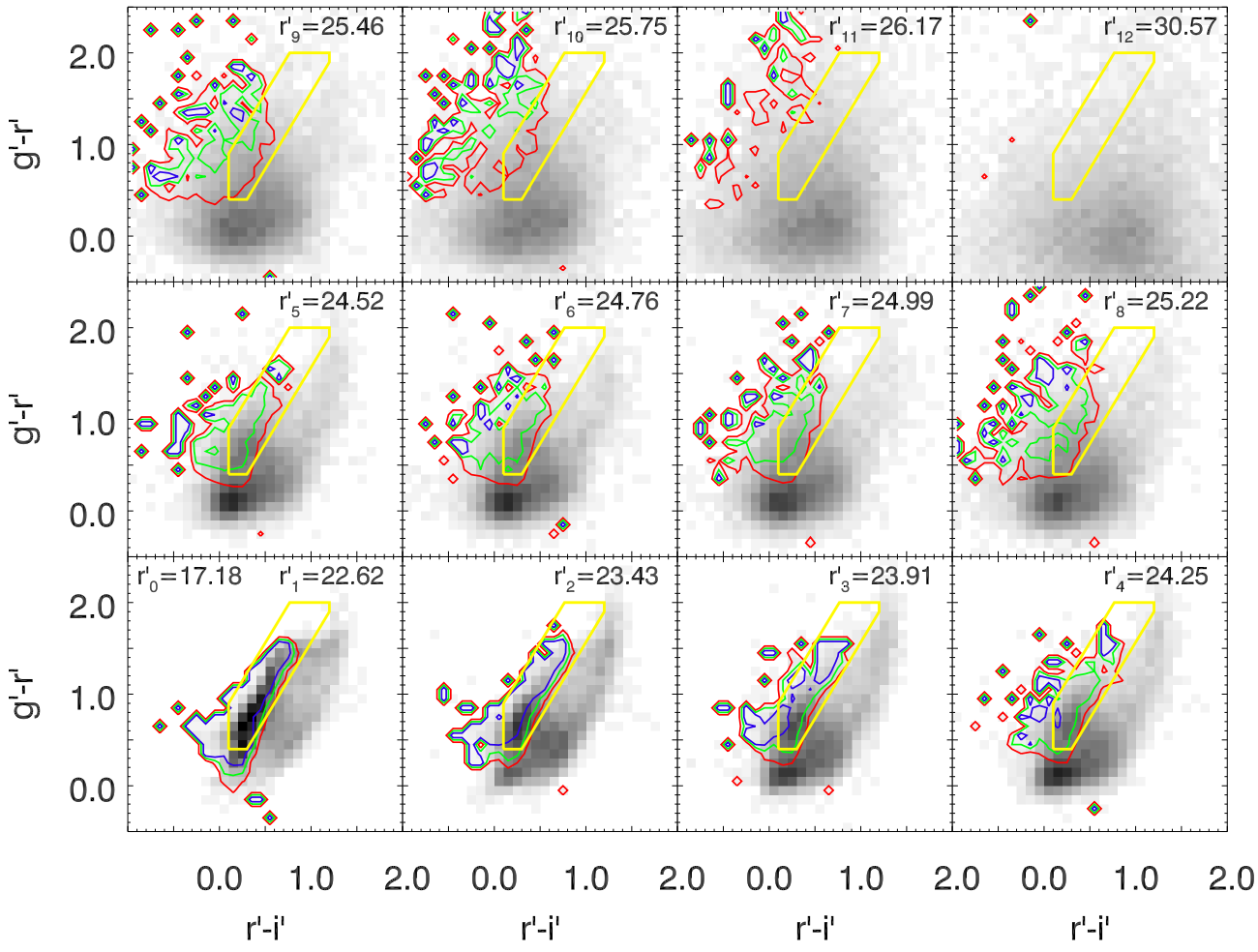

Figure 6.7: Fraction of $z_{\rm ph} \leq 0.50$ galaxies in the CFHTLS D1 field as a function of their $g'-r'$ and $r'-i'$ colours and r' magnitude. Each panel shows a dodecile of the photo-z catalogue, i.e. one of twelve equally populated magnitude bins, where the k-th dodecile includes all galaxies $r'_{k-1} \leq r' < r'_k$. In each panel, the number N_{ij} of galaxies within cells of mesh size $\Delta(g'-r') = \Delta(r'-i') = 0.1$ is plotted, using the same grey scale $\propto \sqrt{N_{ij}}$. White grid cells are empty. The red, green, and blue contours enclose regions in which 25 % (50 %, 75 %) of galaxies have a $z_{\rm ph} \leq 0.50$. The foreground excision polygon we defined *empirically* from the CL 0030+2618 data is overplotted in yellow.

Figure 6.6 illustrates how the various cuts in the KSB pipeline remove faint galaxies from the catalogue, shifting the maximum $r'_{\rm mh}$ of the histogram from $r'_{\rm mh} = 26.0 \pm 0.5$ to $r'_{\rm mh} = 25.0 \pm 0.5$. We note that the CFHTLS D1 shows a very similar histogram over most of the relevant magnitude range $20.5 < r' < 27.0$, also peaking at $r'_{\rm mh} = 25.0 \pm 0.5$. The other fields of the CFHTLS deep survey, D2 to D4, show a behaviour similar to D1 and are omitted from Fig. 6.6 for the sake of clarity. The COSMOS photo-z catalogue, on the other hand, is shallower, with $r^+_{\rm mh} = 24.0 \pm 0.5$, but its number count function is similar to the one in the CL 0030+2618 data at the bright end. Therefore, we use CFHTLS as a reference survey, estimating the relations between galaxy colours and photometric redshift in the CL 0030+2618 data from the D1 field and using all fields to derive the redshift distribution.

6.2.3 Photometric Properties

We investigate the effect of the photometric cuts, applied to optimise the aperture mass detection, on the redshift distribution of the CFHTLS D1 catalogue. Also with the photometric cuts applied, the number counts of the CL 0030+2618 and CFHTLS D1 catalogues still agree well.

In Fig. 6.7, we compare the r'–i' and g'–r' colours of CFHTLS D1 galaxies with photometric redshift to the background excision polygon we defined to contain all bright ($r' < 20.0$) and most of the intermediate ($20.0 < r' < 22.5$) galaxies in the CL 0030+2618 field (Fig. 6.2). Figure 6.7 presents the galaxy numbers and the fraction of $z_{\rm ph} \leq 0.50$ sources in the CFHTLS D1 photo-z catalogue in dependence of the r' magnitude and $g'-r'$ and $r'-i'$ colours. First, the catalogue is divided into its dodeciles in r', i.e. twelve magnitude bins of equal population are defined where the k-th bin consists of the galaxies $r'_{k-1} \leq r' < r'_k$. By r'_k, we denote the magnitude of a source such there is fraction of $k/12$ of brighter galaxies in the catalogue. Second, for each dodecile, we show the number N_{ij} of galaxies falling into grid cells of mesh size $\Delta(g'-r') = \Delta(r'-i') = 0.1$, using a grey scale. Figure 6.7 highlights that at bright r', only a narrow strip in the colour–colour space spanned by $g'-r'$ and $r'-i'$ is populated, while the locus of galaxies becomes much more diffuse towards fainter r', similar to our findings in Fig. 6.2. Third, for each grid cell, we determine the fraction of galaxies we define as foreground sources, i.e. the sources with a redshift estimate $z_{\rm ph} \leq 0.50$. The red, green, and blue contours in Fig. 6.7 mark regions of the colour–colour space populated by increasing fractions $f_{\rm fg}$ of foreground galaxies compared to CL 0030+2618.

We find that the brighter foreground ($z_{\rm ph} \leq 0.5$) galaxies indeed populate a similar region in the colour-colour diagram as their MEGACAM counterparts, albeit being slightly shifted towards bluer $g'-r'$ colours. Thus, given its simplicity, our background selection is quite efficient for the $r' < 22.5$ foreground galaxies, removing 85 % of them from the CFHTLS D1 catalogue. On the other hand, we note the number of bright ($r' < 20.0$) background ($z_{\rm ph} > 0.5$) galaxies to be negligible. Only 28 % of the $20.0 \leq r' \leq 22.5$ CFHTLS D1 *background* galaxies, redder in $r'-i'$ than the foreground sources but not in $g'-r'$, are removed by the selection criteria.

Concerning the faint galaxy population, we first observe that, despite the similar source counts (Fig. 6.6), the colour distributions of faint sources in the CFHTLS D1 and CL 0030+2618 fields differ qualitatively. Further investigations will be needed to relate this observation to a possible cause in the data reduction pipeline. This difference in the colour distributions affects the impact of the background selection: in contrast to the 6.0 % sources removed as foregrounds from the CL 0030+2618 catalogue, the size of the CFHTLS D1 catalogue is reduced by only 0.8 %. The rates differ little for the D2 to D4 fields.

Second, we note the existence of a significant fraction of $z_{\rm ph} \leq 0.5$ galaxies *even to very faint magnitudes*: we find 15 % of the $r' > 22.5$ sources and 8 % of the $r' > 25.0$ sources to be in the foreground to CL 0030+2618, judging from their photo-zs. Our standard background selection cannot identify these sources, leading to a contamination of the lensing catalogue and a dilution of

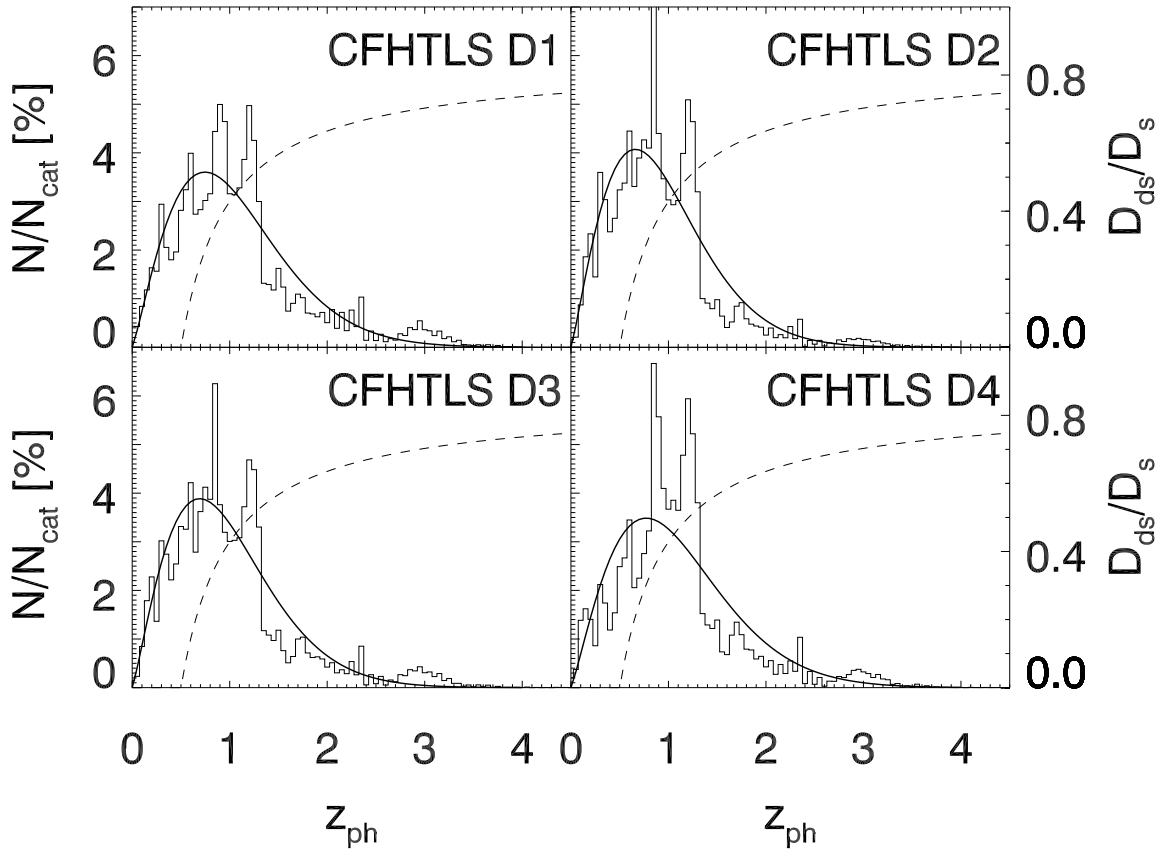

Figure 6.8: Photometric redshift distributions of the CFHTLS D1 to D4 fields after application of the photometric cuts defined in Sect. 6.1.2 (histograms) and van Waerbeke et al. (2001) best fits to the individual fields (solid lines). The function $D_{\rm ds}(z_{\rm s}; z_{\rm d} = 0.5)/D_{\rm s}(z_{\rm s})$ is denoted by dashed lines.

the lensing signal. Ilbert et al. (2006, their Fig. 16) and Ilbert et al. (2009, their Fig. 14) confirm the existence of this population of faint galaxies at low $z_{\rm ph}$. Although *catastrophic outliers*, to which a $z_{\rm ph} \leq 0.5$ has been assigned erroneously, certainly contribute, a comparison with spectroscopic redshifts (Ilbert et al. 2006, their Fig. 12) indicates that most are indeed faint nearby galaxies.

Hence, applying our standard background selection to the whole CFHTLS D1 catalogue, the rate of $z_{\rm ph} \leq 0.5$ galaxies only drops from 18.2 % to 14.8 %. This indicates a similar level of residual contamination to the CL 0030+2618 background catalogue (Sect. 6.4.1), assuming that its redshift distribution follows the one in CFHTLS D1. We account for the shear dilution caused by foreground galaxies as a source of systematic uncertainty. To this end, we measure 15.2 % galaxies at $z_{\rm ph} \leq 0.5$ in the background-selected CFHTLS D1 catalogue, once the $2.2 < g' - i' < 3.0$ sources, already covered in the correction factor for *cluster* galaxies (Sect. 6.4.1) are excised. We consider this 15.2 % uncertainty[4] derived from shear calibration effects in Sect. 6.5.3.

6.2.4 Redshift Distribution

We use the redshift distribution in the CFHTLS Deep Fields to estimate $\langle D_{\rm ds}/D_{\rm s} \rangle$, the catalogue average of the ratio of angular diameter distances between deflector and source, and source and observer. In the absence of (spectroscopic or photometric) redshifts of the individual galaxies, this quantity has to be determined from fields with a known redshift distribution.

[4]Note that due to the correction of an error, this value differs slightly from the 18.0 % given in Israel et al. (2010).

Table 6.4: Best fit parameters z_0 and median redshifts from the fit of Eq. (6.2) to the CFHTLS D1 to D4 redshift distributions. The parameters A and B in Eq. (6.2) are fixed in the fits from which $\langle D_{ds}/D_s\rangle$ is computed for the redshifts of the clusters observed with MEGACAM. Also shown are the averages and standard deviations of the values obtained in the four fields.

Field	z_0	med(z_{ph})	$\langle D_{ds}/D_s\rangle$ $z_d=0.50$	$\langle D_{ds}/D_s\rangle$ $z_d=0.39$	$\langle D_{ds}/D_s\rangle$ $z_d=0.40$	$\langle D_{ds}/D_s\rangle$ $z_d=0.46$	$\langle D_{ds}/D_s\rangle$ $z_d=0.53$	$\langle D_{ds}/D_s\rangle$ $z_d=0.80$
D1	0.91	0.95	0.362	0.460	0.451	0.395	0.338	0.180
D2	0.81	0.84	0.320	0.421	0.411	0.354	0.297	0.145
D3	0.84	0.88	0.336	0.436	0.426	0.370	0.313	0.158
D4	0.94	0.99	0.373	0.471	0.461	0.406	0.349	0.190
$\langle X\rangle$	0.88	0.92	0.348	0.447	0.437	0.381	0.324	0.168
$\sigma(X)$	0.06	0.07	0.024	0.023	0.023	0.024	0.024	0.020

In Fig. 6.8, we show the binned photometric redshift distributions we find for the CFHTLS D1 to D4 fields after having applied the same photometric cuts as to the CL 0030+2618 data. The apparent spikes seen at certain redshifts in all the four fields are artifacts caused by the photo-z determination. Because of those, we prefer calculating $\langle D_{ds}/D_s\rangle$ using a fit to the z_{ph}-distribution. We choose a functional form introduced by van Waerbeke et al. (2001)

$$p_z(z_{ph}) = \frac{B}{z_0\Gamma\left(\frac{1+A}{B}\right)}\left(\frac{z_{ph}}{z_0}\right)^A \exp\left(-\left(\frac{z_{ph}}{z_0}\right)^B\right), \tag{6.2}$$

where z_0 is the typical redshift of the sources, and A and B are shape parameters governing the low-redshift regime and the exponential drop-off at high redshifts. The prefactor including the Gamma function renders $p_z(z_{ph})$ a normalised probability distribution. We fit the binned redshift distributions in the range $0 \le z_{ph} \le 4$, fixing $B = 1.5$ for reasons of robustness to the default value suggested by van Waerbeke et al. (2001). Next, $A = 1.15$ is fixed too, to the value preferred for three of the four fields. The final results are summarised in Table 6.4. For all tested z_d, we note that $D_{ds}(z_s, z_d)/D_s(z_s)$ varies substantially over the range spanned by the median redshifts of the fits to D1 to D4 (see Fig. 6.8). We now calculate the average distance ratio for each field by integrating this function with the redshift distribution over all redshifts larger than $z_d = 0.5$:

$$\left\langle \frac{D_{ds}}{D_s}\right\rangle = \int_{z_d}^{\infty} p_z(z)\frac{D_{ds}(z;z_d)}{D_s(z)}\mathrm{d}z. \tag{6.3}$$

For the mass estimation of CL 0030+2618, we use the average and standard deviation $\langle D_{ds}/D_s\rangle = 0.348 \pm 0.024$ of the distance ratios obtained for the four CFHTLS fields (see Table 6.4) as fiducial value and uncertainty margin, respectively. These values are consistent with the results for $\langle D_{ds}/D_s\rangle$ computed directly from the histograms in Fig. 6.8. We improved the precision of our fitting method, giving rise to the differences between the $\langle D_{ds}/D_s\rangle = 0.348 \pm 0.024$ for CL 0030+2618 we obtain here and the $\langle D_{ds}/D_s\rangle = 0.33 \pm 0.03$ we used in Israel et al. (2010). This is one of the two reasons for the change in the mass estimate (Table 6.7) for CL 0030+2618 w.r.t. Israel et al. (2010).

6.2.5 Identifying the BCG of CL 0030+2618

Figure 6.1 shows two candidates for the brightest cluster galaxy of CL 0030+2618, galaxies with extended cD-like haloes and similar i'-magnitudes (Table 6.1). The galaxy G1, closer to the ROSAT and CHANDRA centres of CL 0030+2618, was attributed to a cluster by Boyle et al. (1997), measuring a spectroscopic redshift of $z_{\rm G1} = 0.516$. We note that three of their six spectro-zs are $z \approx 0.25$.

We note that G1 and G2 show different colours in Fig. 6.1, each being similar to their fainter immediate neighbours. As very extended sources, G1 and G2 are flagged early-on in the pipeline but *are* included in the raw *SExtractor* catalogues. Aware of their larger uncertainties, we use these magnitudes[5] for G1, G2, and two other interesting extended galaxies (Table 6.1).

The observed $g'-r'$, $r'-i'$, and $g'-i'$ colours are compared to the ones predicted for a typical BCG at $z = 0.50$ and $z = 0.25$, using the Coleman et al. (1980, CWW80) elliptical galaxy template (Table 6.3). Nicely consistent with its spectroscopic redshift, we find the colours of G1 to be similar to the $z = 0.50$ template, while G2's bluer colours resemble the CWW template at $z = 0.25$. We conclude that G1, located close to the X-ray centres, is a member of CL 0030+2618, and indeed its BCG. On the other hand, G2 can be considered the brightest member of a *foreground group* at $z \approx 0.25$. The existence of such foreground structure is corroborated by the broad $g'-i'$ distribution (Fig. 6.5). Its implications are discussed in Sect. 6.3.1 and 6.4.3.

6.3 The Multi-Wavelength View of CL 0030+2618

6.3.1 Comparing Centres of CL 0030+2618

The S-Statistics Lensing Centre We determine the centre of the CL 0030+2618 lensing signal and its accuracy by bootstrap resampling of the galaxy catalogue of $N_{\rm cat}$ galaxies used in the measurements of the S-statistics. Choosing S instead of $M_{\rm ap}$ corresponds to considering a significance-weighted centre. From the basic catalogue we draw 10^5 realisations each containing $N_{\rm cat}$ sources. For each realisation, we determine the S-statistics in the central region of $3' \times 3'$ side length (~1Mpc) using a grid size of $15''$ and record the highest S-value found on the grid and the grid cell in which it occurs.

Weak Lensing Mass Reconstruction In order to get an impression of the (total) mass distribution in CL 0030+2618, we perform a finite field mass reconstruction (Seitz & Schneider 2001, Sect. 3.2.3). This method directly aims at the two-dimensional mass distribution $\kappa(\boldsymbol{\theta})$ and breaks the *mass-sheet degeneracy*, by assuming $\langle\kappa\rangle = 0$ on the boundary of the field.

The resulting mass map, derived by smoothing the shear field with a scale of $2'$, is shown in Fig. 6.9, and a zoomed version displaying the central region of CL 0030+2618 as Fig. 6.10. The thick contours give the surface mass density.[6] Beside the clear main peak of CL 0030+2618, we find a number of smaller additional peaks whose significance we are going to discuss in the following section.

CHANDRA and XMM-NEWTON We compare these lensing results to detections by two X-ray observatories, CHANDRA and XMM-NEWTON. For CHANDRA, we use a surface brightness map produced from the 58 ks ACIS exposure (medium-thick, blue lines in Figs. 6.9 and 6.10). Using the

[5] Here, we use *SExtractor* `AUTO` instead of `ISO` magnitudes, known to be more robust at the expense of less accurate colour measurements. Nevertheless, we find only small differences between the two apertures, allowing for cautious direct comparison.

[6] In contrast to the fact that CL 0030+2618 likely has strong lensing arcs (see Sect. 6.3.3), hinting at $\kappa \gtrsim 1$ locally, we measure much smaller surface mass densities. This effect is due to smoothing.

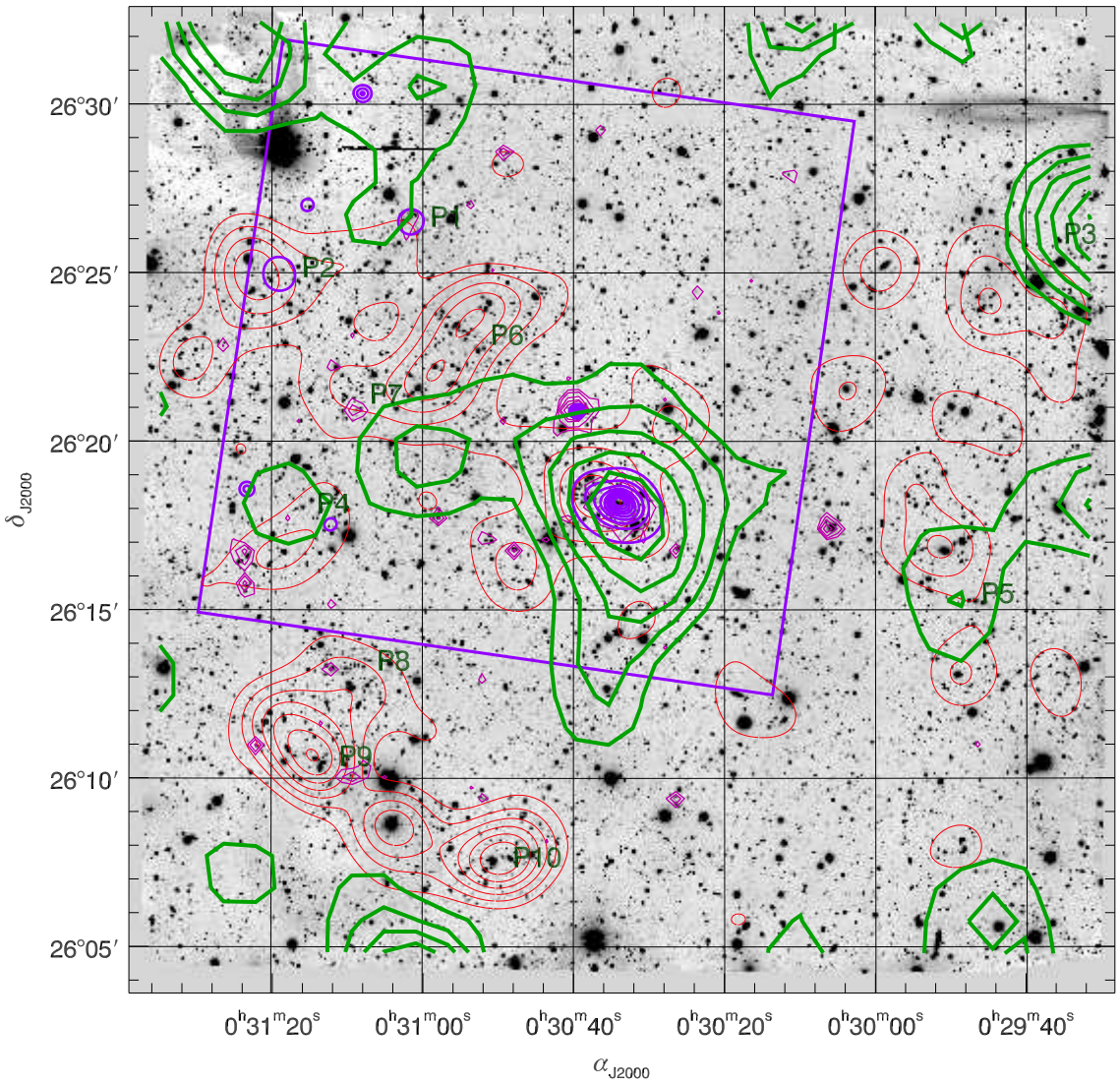

Figure 6.9: The r'-band image of CL 0030+2618, overlaid with r'-band galaxy light (thin, red), CHANDRA (medium-thick, bluish; within the smaller square footprint), and XMM-NEWTON (medium-thin, magenta), and lensing surface mass density contours (thick, green). We show CHANDRA surface brightness levels in multiples of 5×10^{-9}cts cm^{-2}s^{-1}arcmin^{-2} in the 0.5 . . . 2. keV band. The r'-band flux density contours (thin red lines) start from 0.015 flux units per pixel, in intervals of 0.005 flux units. Lensing convergence contour levels were obtained smoothing the shear field $\gamma(\boldsymbol{\theta})$ with a Gaussian filter of 2′ width and are linearly spaced in intervals of $\Delta\kappa = 0.01$, starting at $\kappa = 0.01$. XMM-NEWTON contours show MOS2 counts smoothed by an adaptive Gaussian kernel in logarithmic spacing. The labels "P1" to "P10" designate the peaks discussed in Sect. 6.3.2.

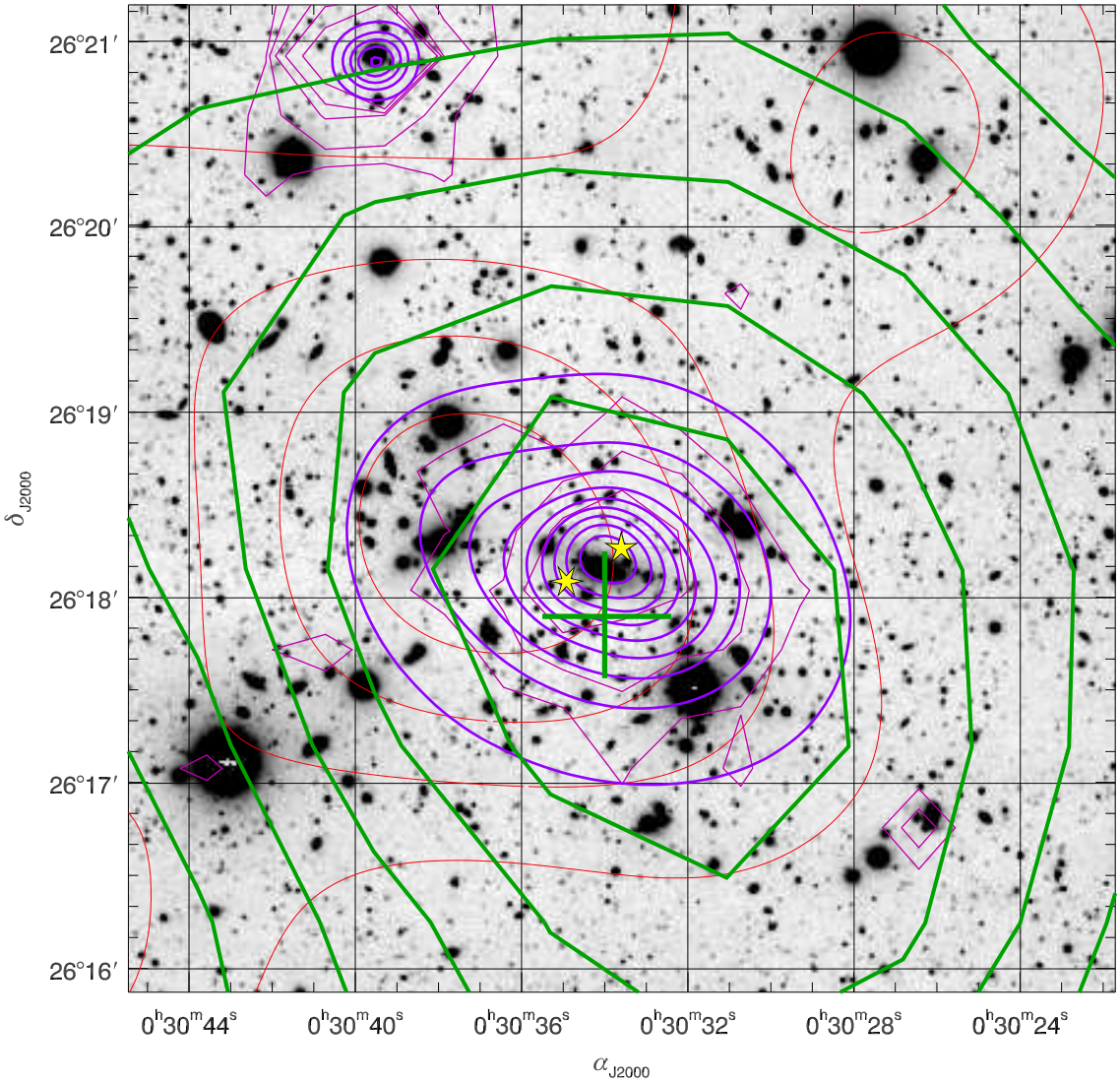

Figure 6.10: Zoomed version of Fig. 6.9, showing only the central region of CL 0030+2618.The cross gives the position and 1σ uncertainty of the centre position of the S-peak obtained by bootstrapping (cf. Sect. 6.3.1) while the star symbols with five and six points denote the X-ray centres found with ROSAT and CHANDRA, respectively. The source on the northern edge on which strong X-ray emission is centred is named G4 in Table 6.1.

Table 6.5: The additional shear, X-ray, and optical flux peaks discussed in Sect. 6.3.2. Given are designations, J2000 epoch celestial coordinates and detection methods.

Peak	α_{J2000}	δ_{J2000}	detected by
P1	$00^{\mathrm{h}}31^{\mathrm{m}}02^{\mathrm{s}}$	$26°26'30''$	X-ray, optical
P2	$00^{\mathrm{h}}31^{\mathrm{m}}19^{\mathrm{s}}$	$26°25'0''$	X-ray, optical
P3	$00^{\mathrm{h}}29^{\mathrm{m}}31^{\mathrm{s}}$	$26°26'$	shear
P4	$00^{\mathrm{h}}31^{\mathrm{m}}17^{\mathrm{s}}$	$26°18'$	shear
P5	$00^{\mathrm{h}}29^{\mathrm{m}}49^{\mathrm{s}}$	$26°15'20''$	shear
P6	$00^{\mathrm{h}}30^{\mathrm{m}}54^{\mathrm{s}}$	$26°23'$	optical
P7	$00^{\mathrm{h}}31^{\mathrm{m}}10^{\mathrm{s}}$	$26°21'15''$	optical
P8	$00^{\mathrm{h}}31^{\mathrm{m}}09^{\mathrm{s}}$	$26°13'20''$	optical
P9	$00^{\mathrm{h}}31^{\mathrm{m}}14^{\mathrm{s}}$	$26°10'30''$	optical
P10	$00^{\mathrm{h}}30^{\mathrm{m}}51^{\mathrm{s}}$	$26°07'30''$	optical

Zhang et al. (2010) method, we find the flux-weighted CHANDRA centre – obtained by weighting each pixel in CHANDRA's field-of-view with its flux – at $00^{\mathrm{h}}30^{\mathrm{m}}34\overset{\mathrm{s}}{.}9$, $26°18'05''$, slightly ($14\overset{''}{.}5$) off the flux peak at $00^{\mathrm{h}}30^{\mathrm{m}}34\overset{\mathrm{s}}{.}0$, $26°18'13''$.

For XMM-NEWTON, we show detections in the EPIC-MOS2 chip, binned in 64×64 pixels and smoothed with an adaptive 6σ Gaussian kernel. The respective contours in Figs. 6.9 and 6.10 are less smoothed than those from CHANDRA and therefore appear more jagged.

Lensing and X-ray Centres As can be seen from the cross in Fig. 6.10, the cluster centre determined with the aperture mass technique falls within the most significant ($\kappa > 0.05$) convergence contour and is, within its 1σ error ellipse of $24'' \times 21''$, in good agreement with the flux-weighted CHANDRA centre of CL 0030+2618, separated by $17''$. Similarly, it is consistent with the ROSAT centre just outside the confidence ellipse and the XMM-NEWTON contours (6.10). All of these cluster centres are, in turn, within $< 20''$ distance from G1, the BCG.

Optical Galaxy Light In addition, we determine the distribution of r'-band light from galaxies by adding the fluxes of all unflagged sources in the *SExtractor* catalogue whose magnitudes and flux radii are consistent with the criteria defined for the galaxy catalogue in Sect. 5.4.3 and Fig. 5.7.[7] We do so for each pixel of an auxiliary grid, then smoothing it with a Gaussian of $60''$ full-width half-maximum. In Figs. 6.9 and 6.10, the r'-band flux density is given in isophotal flux units per MEGACAM pixel, with a flux of one corresponding to an $r' = 25.8$ galaxy falling into that pixel (thin red contours). There is, amongst others, a discernible r'-band flux peak centred between the galaxies G1 and G2 (Fig. 6.10).

6.3.2 Secondary Peaks

The shear peak clearly associated with CL 0030+2618 is the most significant signal in the MEGACAM field-of-view, in the lensing κ-map as well as in the X-rays, which can be seen from the XMM-

[7] In absence of a usable half-light radius ϑ for the more extended galaxies, we have to substitute flux radii ϑ_{g} here. Using the observed relation between ϑ and ϑ_{g} in our dataset, we consider as galaxies objects with $\vartheta_{\mathrm{g}} > 3.5\,\mathrm{px}$ at $16.75 < r'_{\mathrm{AUTO}} < 22.75$ and $\vartheta_{\mathrm{g}} > 3.2\,\mathrm{px}$ at $r'_{\mathrm{AUTO}} > 22.75$.

NEWTON count distribution. In the smoothed r'-band light distribution, CL 0030+2618 shows up as a significant but not the most prominent peak. We have to caution that the background selection based on $m_{\rm bright}$ and $m_{\rm faint}$ optimises the lensing signal for CL 0030+2618, with the likely effect that cluster signals at other z and hence with different photometric properties will be suppressed. Nevertheless, we expect this suppression to be small in the relevant z range. Keeping this in mind, we compare secondary peaks in the κ-map to apparent galaxy overdensities, as indicated by the smoothed distribution of r'-band light, and to the X-ray detections.

The galaxy listed as G4 in Table 6.1, a strong X-ray emitter detected with a high signal by both CHANDRA and XMM-NEWTON, is identified as a QSO at redshift $z = 0.493$ by Boyle et al. (1997) and confirmed to be at $z = 0.492$ by Cappi et al. (2001) who found a significant overdensity of $0.5 \ldots 2$ keV CHANDRA sources in the vicinity of CL 0030+2618. Regarding its redshift, it is thus a likely member of CL 0030+2618.

The CHANDRA analysis finds two additional sources of extended X-ray emission at low surface brightness. One of them, "P1" in Fig. 6.9, (see Table 6.5 for coordinates of this and all following peaks) is also detected by XMM-NEWTON and has been identified as a probable high-redshift galaxy cluster by Boschin (2002, his candidate #1 at $\alpha_{\rm J2000} = 00^{\rm h}31^{\rm m}01\overset{\rm s}{.}3$, $\delta_{\rm J2000} = 26^\circ 26' 39''$) in a deep survey for galaxy clusters using pointed CHANDRA observations. In the κ map, contours near the north-eastern corner of MEGACAM's field-of-view extend close to the position of this cluster, but their significance near this corner and close to the bright star BD+25 65 is doubtful. The MEGACAM images show a small grouping[8] of $r' \approx 21$ galaxies with similar colour in the three-colour composite at the position of "P1".

The other CHANDRA peak, "P2" is located near a prominent peak in the r'-band light, but with a strong contribution from a single bright galaxy within its $60''$ smoothing radius. It does not correspond to a tabulated source in either NED[9] or SIMBAD. We do not notice a significant surface mass density from lensing at this position, but have to stress again that a possible signal might have been downweighted by the catalogue selection process.

Most peaks in the κ map, apart from the one associated with CL 0030+2618, are located at a distance smaller than the $2'$ smoothing scale from the edges of the field, likely due to noise amplification by missing information. Amongst them, only the second strongest κ peak, "P3" seems possibly associated with an overdensity of galaxies, but the coverage is insufficient to draw further conclusions. For a shear peak "P4" close to several CHANDRA and XMM-NEWTON peaks, there also is an enhancement in r'-band flux, without galaxies appearing to be concentrated. Likewise, the high flux density close to a possible shear peak "P5" seems to be caused by a single, bright galaxy.

On the other hand, we notice agglomerations of galaxies ("P6" to "P8") with a cluster-like or group-like appearance that show neither X-ray nor lensing signal. For "P7", the nearby XMM-NEWTON signal is the distant quasar named I3 by Brandt et al. (2000). The two strong r'-band flux overdensities "P9" and "P10" in the south-east corner of the MEGACAM image appear to be poor, nearby groups of galaxies.

6.3.3 Arc-Like Features in CL 0030+2618

We note that, being a massive cluster of galaxies, CL 0030+2618 is a probable strong gravitational lens, leading to the formation of giant arcs. Indeed, we identify two tentative strong lensing features in our deep MEGACAM exposures. The first is a very prominent, highly elongated arc $\sim 20''$ west from the BCG (Fig. 6.1). Its centre is at $\alpha_{\rm J2000} = 00^{\rm h}30^{\rm m}32\overset{\rm s}{.}7$ and $\delta_{\rm J2000} = 26^\circ 18' 05''$; its length is $> 20''$. The giant arc is not circular but apparently bent around a nearby galaxy.

[8] Not visible in Fig. 6.9 due to its binning.

[9] NASA-IPAC Extragalatic Database: `http://nedwww.ipac.caltech.edu/`

The second feature possibly due to strong lensing is located near galaxy G3 which appears to be an elliptical. With the centre of the tentative arc at $\alpha_{J2000} = 00^h30^m36^s.5$ and $\delta_{J2000} = 26°19'14''$, it is bent around the centre of the galaxy, forming the segment of a circle with $\sim 6''$ radius. Thus, an alternative explanation might be that the arc-like feature corresponds to a spiral arm of the close-by galaxy. However, this seems less likely given its appearance in the MEGACAM images. If this arc is due to gravitational lensing it is likely to be strongly influenced by the gravitational field of the aforementioned galaxy as it is opening to the opposite side of the cluster centre.

Whether these two candidate arcs are indeed strong lensing features in CL 0030+2618 will have to be confirmed by spectroscopy.

6.4 Mass Determination

We analyse the tangential shear profile $\langle \varepsilon_t(\theta) \rangle$, i.e., the averaged tangential component of ε with respect to the weak lensing centre of CL 0030+2618 found in Sect. 6.3.1 as a function of the separation θ to this centre. At this point, we also introduce the shear calibration factor, $f_0 = 1.08$, an empirical correction to the shear recovery by our KSB method and catalogue selection (Sect. 6.1.4), and the contamination correction factor $f_1(\theta)$ we will specify in Sect. 6.4.1, thus replacing ε by $f_0 f_1(\theta)\varepsilon$.

6.4.1 Contamination by Cluster Galaxies

In addition to the background selection based on $g'-r'$ and $r'-i'$ colours we estimate the remaining fraction of cluster galaxies in the catalogue using the $g'-i'$ index. We will use this to devise a correction factor accounting for the shear dilution by (unsheared) cluster members. As discussed in Sect. 6.2.1, the colour-magnitude diagramme of the CL 0030+2618 field (Fig. 6.5) does not show a clear-cut cluster red sequence, but a broad distribution in $g'-i'$, indicating two redshift components. We therefore define a wide region $2.2 < g'-i' < 3.0$ of *possible* red sequence sources, including galaxies with colours similar to the $z = 0.50$ CWW elliptical template but redder than the $z = 0.25$ one (cf. Table 6.3). As this definition of "red sequence-like" galaxies is meant to encompass all early-type cluster members, it will also contain background systems, giving an *upper limit* for the actual contamination by cluster galaxies in the catalogue.

Figure 6.11 shows the fraction $f_{cg}(\theta)$ of sources with $2.2 < g'-i' < 3.0$ out of all sources in the galaxy catalogue before (open symbols) and after (filled symbols) the final cut based on m_{bright} and m_{faint} has been applied as a function of distance to the centre of CL 0030+2618 as determined by lensing (Sect. 6.3.1). For visualisation purposes, we present $f_{cg}(\theta)$ in bins of $1'$ width, for which the error bars show the measured standard error. We note a strong increase of the number of "red sequence-like" systems compared to the overall number of galaxies towards the cluster centre, indicating that a significant fraction of those are indeed cluster members. Most intriguingly, the background selection seems to remove only few of these tentative cluster members, with the fractions before and after selection consistent within their mutual uncertainties at all radii. This finding can be explained to a large extent by galaxies too faint to be removed by the background selection criterion: If background selection is extended to the faintest magnitudes ($m_{faint} = 29$), no significant overdensity of "red sequence-like" galaxies at the position of CL 0030+2618 is detected – but also the cluster detection in the S-statistics decreases. Although using a different selection method, this modest effect of background selection is in agreement with Hoekstra (2007).

By repeating this analysis centred on several random positions in our field and not finding a significant increase of the "red sequence-like" fraction towards these positions, we show that the peak around the position of CL 0030+2618 is indeed caused by concentration of these galax-

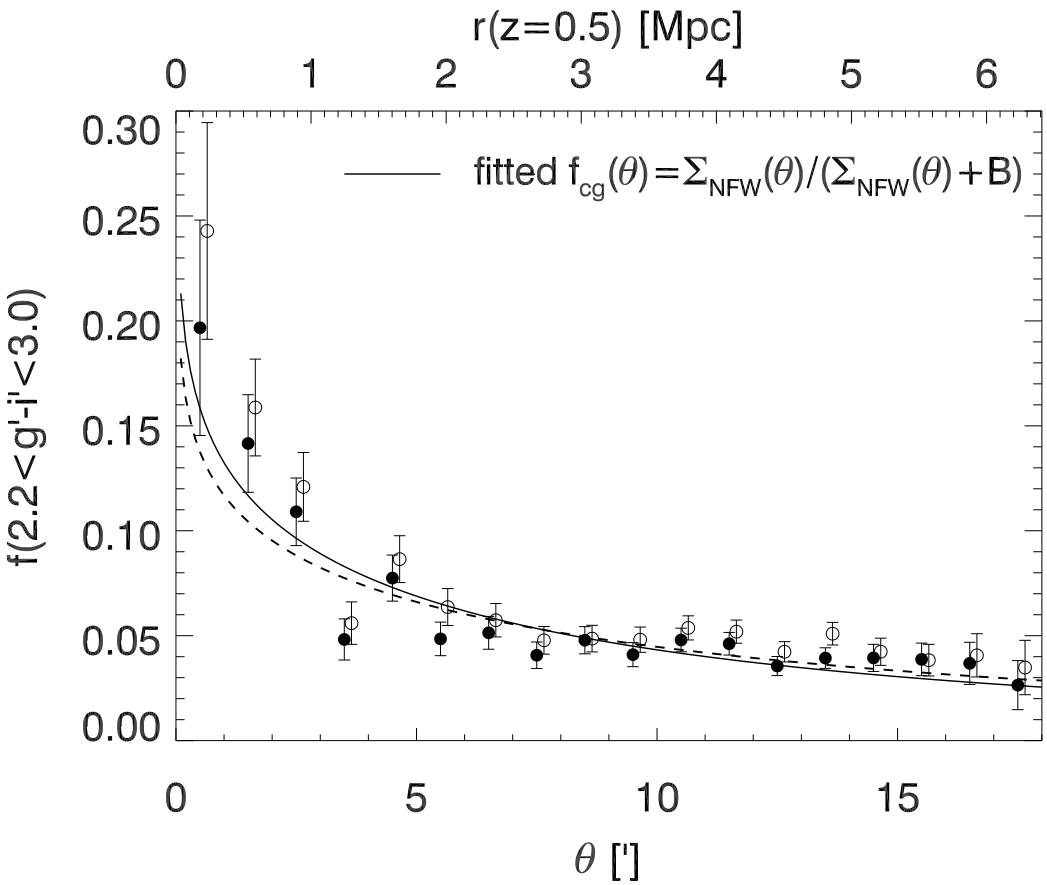

Figure 6.11: The fraction of "red sequence-like" galaxies $2.2 < g' - i' < 3.0$ as a function of clustercentric distance before (open symbols) and after (filled symbols) background selection. The solid and dashed lines denotes the best-fitting sum $f_{\rm cg}$ of an NFW surface mass profile and a constant to the latter, obtained from a χ^2 fit and a maximum likelihood method assuming Poisson statistics. In this figure, we used the ROSAT centre of CL 0030+2618. We apply $f_1 = f_{\rm cg} + 1$ as a correction factor for cluster contamination in Sect. 6.4.

ies towards the cluster centre. We find the residual contamination to be well represented by the function

$$f_{\rm cg}(\theta) = \frac{\Sigma_{\rm NFW}(\theta)}{\Sigma_{\rm NFW}(\theta) + B} \quad , \tag{6.4}$$

the ratio of a NFW surface mass profile $\Sigma_{\rm NFW}(\theta)$ and the sum of the same profile and a constant background component B. Because $f_{\rm cg}$ is obtained by counting galaxies inside and outside the "red sequence-like" range, Poissonian statistics applies for this problem. However, we find the "first-guess" χ^2 minimisation implicitly assuming a Gaussian likelihood function (solid curve in Fig. 6.11) to be in good agreement with the best-fit curve from considering the Poissonian likelihood function. For simplicity, we use the Gaussian fit.[10]

We follow the approach of Hoekstra (2007) and define a radially dependent factor $f_1(\theta) = f_{\rm cg}(\theta) + 1$ correcting for the residual contamination. This correction factor scales up the shear

[10] We expect the difference in the resulting best-fit cluster parameters to be small compared to their statistical errors, and note that the impact of the cluster member correction is generally small (Table 6.7). Nevertheless, we plan to apply the Poissonian method in future analyses. Note that the binning in Fig. 6.11 is for visualisation only; independent of the fitting method, we evaluate for each galaxy whether it falls into the "red sequence-like" range ($d_i = 1$) or not ($d_i = 0$) and fit Eq. (6.4) to the resulting vector. The Poissonian likelihood function is given by $\log \mathcal{L}_{\rm P} = \log \sum_i g_i$ with $g_i = f_{\rm cg}(\theta)$ for $d_i = 1$ and $g_i = 1 - f_{\rm cg}(\theta)$ otherwise.

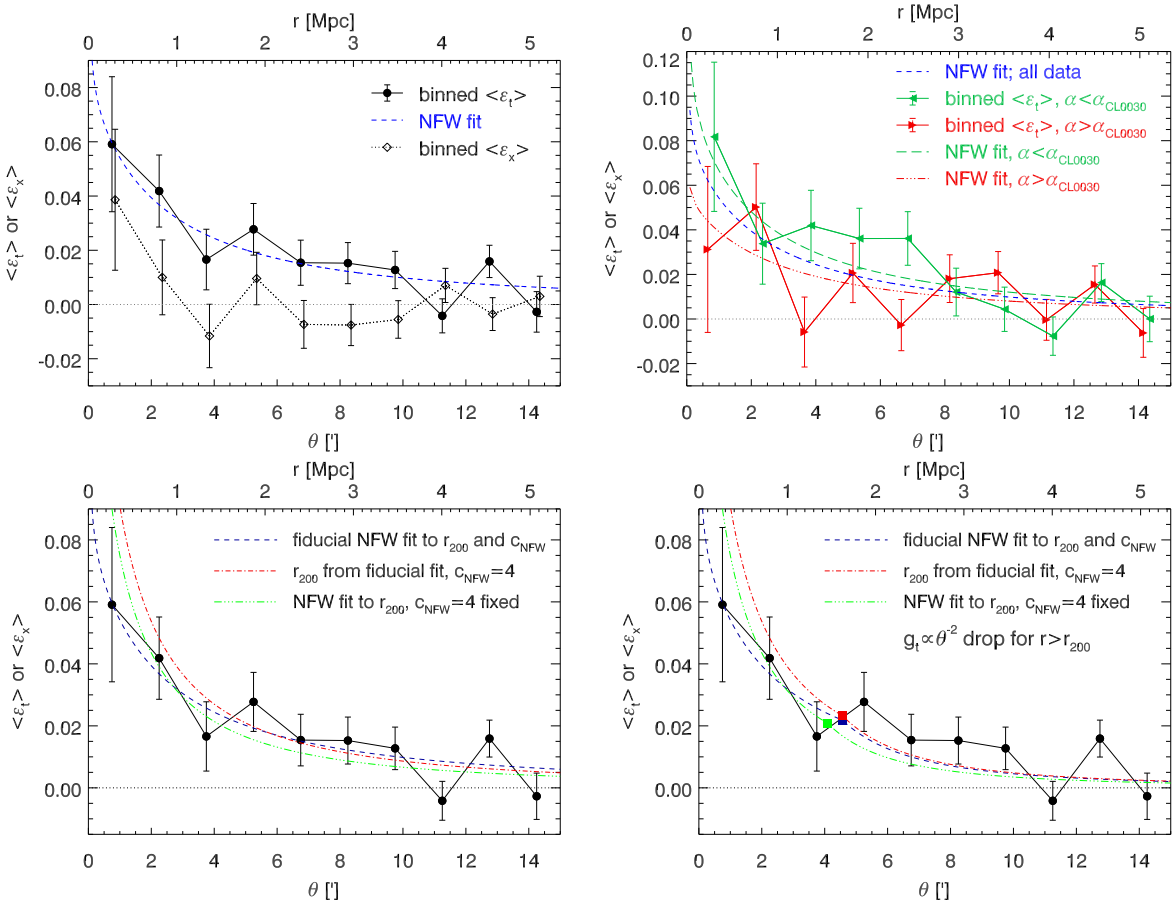

Figure 6.12: The tangential shear profile of CL 0030+2618, averaged in bins of 90″ width (solid line with dots). *Upper left:* The best fitting NFW model in the default case (see text; dashed line) and the binned cross-component $\langle\varepsilon_\times\rangle$ of the measured shear (dotted line with diamonds). Error bars give the standard deviation of measured values in the respective bin. *Upper right:* Shear profiles computed from sources East ($\alpha_{J2000} > \alpha_{CL0030}$; right-facing triangles and triple-dot dashed line) and West ($\alpha_{J2000} < \alpha_{CL0030}$; left-facing triangles and long-dashed line) of CL 0030+2618 are compared to the default fit (dashed line). *Lower left:* NFW models with r_{200} from the default fit with concentration *set* to $c_{NFW} = 4.0$ (dot-dashed line), and from fitting to r_{200}, keeping $c_{NFW} = 4.0$ fixed (triple dot-dashed line), compared to the default fit (dashed line). *Lower right:* The same models as in the lower left panel, but all truncated at r_{200}, with a $g_t \propto \theta^{-2}$ drop-off at larger radii.

estimates close to the cluster centre, counterweighting the dilution by the larger number of cluster members there. Note that we use a different model for $f_{cg}(\theta)$ than in Israel et al. (2010), leading, together with the changed $\langle D_{ds}/D_s\rangle$, to a change in the mass estimate for CL 0030+2618 from $7.2\times10^{14}M_\odot$ to $6.8\times10^{14}M_\odot$ (Table 6.7), well within the statistical error margin.

6.4.2 The NFW Model

Navarro et al. (1995, 1996, 1997) found the following *density profile* to provide a good representation of Dark Matter halos in numerical simulations, out to the virial radius:

$$\rho_{NWF}(r) = \frac{\delta_c \rho_c}{(r/r_s)(1+r/r_s)^2} \quad . \tag{6.5}$$

Table 6.6: Properties of the default model combining the parameter values and assumptions going into the NFW modelling. Parameters above the vertical line determine the galaxy catalogue, while parameters below it influence how the NFW profile is fitted to the data.

Parameter	Value	see Sect.
$\max(\lvert\varepsilon\rvert)$	0.8	6.1.4
$\min(\nu)$	4.5	6.1.4
$\min(\mathrm{tr}\,\mathcal{P}^{\mathrm{g}})$	0.1	6.1.4
m_{bright}	20.0	6.1.2
m_{faint}	22.5	6.1.2
centre	from S-statistics	6.3.1
radial fit range	$0' < \theta < 15'$	6.4.3
f_0	1.08 ± 0.05	6.1.4
$f_1(\theta)$	$f_{\mathrm{cg}}^{\mathrm{NFW}}(\theta) + 1$	6.4.1
$\langle D_{\mathrm{ds}}/D_{\mathrm{s}}\rangle$	0.33 ± 0.03	6.2.4

The NFW *density* profile has two free parameters,[11], combined in the *scale radius* $r_{\mathrm{s}} = r_{200}/c_{\mathrm{NFW}}$: the radius r_{200}, inside which the mean density of matter equals 200 times the critical mass density ρ_{c} (Eq. 1.16), and the concentration parameter c_{NFW}. The concentration parameter is related to the characteristic overdensity δ_{c} in Eq. (6.5) by:

$$\delta_{\mathrm{c}} = \frac{200}{3}\frac{c_{\mathrm{NFW}}^3}{\ln(c_{\mathrm{NFW}}+1) - c_{\mathrm{NFW}}/(c_{\mathrm{NFW}}+1)} \quad . \tag{6.6}$$

The overdensity radius r_{200} is an estimator of the cluster's virial radius, and we define as the mass of the cluster the mass enclosed within r_{200}, which is given by:

$$M_{200} = 200\frac{4\pi}{3}\rho_{\mathrm{c}} r_{200}^3 \quad . \tag{6.7}$$

To estimate for the mass of CL 0030+2618 from the weak lensing data, we fit the tangential shear profile $g_{\mathrm{t}}(\theta)$ with a NFW *shear* profile (e.g., Bartelmann 1996; Wright & Brainerd 2000). The corresponding reduced shear observable,

$$g_{\mathrm{NFW}}(u) = \frac{\gamma_{\mathrm{NFW}}(u)}{1 - \kappa_{\mathrm{NFW}}(u)} \quad , \tag{6.8}$$

can be expressed as a function of the dimensionless radial distance $u = c_{\mathrm{NFW}} D_{\mathrm{d}} \theta r_{200}^{-1}$ containing the angular separation θ and the angular diameter distance D_{d} between lens and observer. The convergence – $\kappa_{\mathrm{NFW}}(u)$ – and shear – $\gamma_{\mathrm{NFW}}(u)$ – profiles are given by (Wright & Brainerd 2000):

$$\kappa_{\mathrm{NFW}}(u) = \begin{cases} \dfrac{2r_{200}\delta_{\mathrm{c}}\rho_{\mathrm{c}}}{c_{\mathrm{NFW}}(u^2-1)\Sigma_{\mathrm{c}}}\left[1 - \dfrac{2}{\sqrt{1-u^2}}\,\mathrm{arctanh}\left(\sqrt{\dfrac{1-u}{1+u}}\right)\right] & (u<1) \\ \dfrac{2r_{200}\delta_{\mathrm{c}}\rho_{\mathrm{c}}}{3c_{\mathrm{NFW}}\Sigma_{\mathrm{c}}} & (u=1) \\ \dfrac{2r_{200}\delta_{\mathrm{c}}\rho_{\mathrm{c}}}{c_{\mathrm{NFW}}(u^2-1)\Sigma_{\mathrm{c}}}\left[1 - \dfrac{2}{\sqrt{u^2-1}}\,\arctan\left(\sqrt{\dfrac{u-1}{1+u}}\right)\right] & (u>1) \end{cases} \quad . \tag{6.9}$$

[11] While Navarro et al. (1997) originally designed their profile as a single-parameter model, we follow the usual approach in weak lensing studies of expressing the NFW profile in terms of two independent parameters.

Table 6.7: Parameters resulting from NFW modelling of CL 0030+2618 for models relying on different assumptions. Given are the radii and concentration parameters $r_{200}^{\rm min}$ and $c_{\rm NFW}^{\rm min}$ minimising $\chi^2_{\rm L}$ (Eq. 6.12). The fourth column shows the cluster mass M_{200} from Eq. (6.7), while the fifth column gives the mass $\mu = M_{200}/M_{200}^{\rm def}$ in units of the default cluster mass.

Model	$r_{200}^{\rm min}$/Mpc	$c_{\rm NFW}^{\rm min}$	$M_{200}(r_{200}^{\rm min})$	μ
default	$1.49^{+0.14}_{-0.15}$	$1.8^{+0.95}_{-0.75}$	$6.8^{+2.1}_{-1.9}\times10^{14}\mathrm{M}_\odot$	$--$
$0.5' \le \theta \le 15'$	$1.49^{+0.14}_{-0.15}$	$2.05^{+1.25}_{-0.9}$	$6.8^{+2.1}_{-1.9}\times10^{14}\mathrm{M}_\odot$	1.00
$0' \le \theta \le 4'$	$1.55^{+0.24}_{-0.27}$	$1.5^{+0.8}_{-0.75}$	$7.7^{+4.2}_{-3.4}\times10^{14}\mathrm{M}_\odot$	1.13
$\max(\lvert\varepsilon\rvert) = 1.0$	$1.41^{+0.15}_{-0.17}$	$1.7^{+1.0}_{-0.8}$	$5.8^{+2.0}_{-1.9}\times10^{14}\mathrm{M}_\odot$	0.85
$\max(\lvert\varepsilon\rvert) = 10^4$	$1.29^{+0.19}_{-0.22}$	$1.4^{+1.3}_{-0.85}$	$4.4^{+2.3}_{-1.9}\times10^{14}\mathrm{M}_\odot$	0.65
centred on BCG	$1.49^{+0.14}_{-0.16}$	$1.6^{+0.9}_{-0.7}$	$6.8^{+2.1}_{-2.0}\times10^{14}\mathrm{M}_\odot$	1.00
no contam. corr.	$1.46^{+0.14}_{-0.15}$	$1.65^{+0.9}_{-0.7}$	$6.4^{+2.0}_{-1.8}\times10^{14}\mathrm{M}_\odot$	0.94
$f_0 = 0.91$	$1.40^{+0.13}_{-0.14}$	$1.75^{+0.9}_{-0.75}$	$5.7^{+1.7}_{-1.5}\times10^{14}\mathrm{M}_\odot$	0.83
$f_0 = 1.13$	$1.52^{+0.14}_{-0.16}$	$1.85^{+0.9}_{-0.8}$	$7.3^{+2.2}_{-2.1}\times10^{14}\mathrm{M}_\odot$	1.06
$\langle D_{\rm ds}/D_{\rm s}\rangle = 0.324$	$1.55^{+0.14}_{-0.16}$	$1.9^{+0.9}_{-0.8}$	$7.7^{+2.3}_{-2.1}\times10^{14}\mathrm{M}_\odot$	1.13
$\langle D_{\rm ds}/D_{\rm s}\rangle = 0.372$	$1.44^{+0.14}_{-0.14}$	$1.75^{+0.9}_{0.75}$	$6.2^{+2.0}_{-1.6}\times10^{14}\mathrm{M}_\odot$	0.90

and

$$\gamma_{\rm NFW}(u) = \begin{cases} \dfrac{r_{200}\delta_{\rm c}\rho_{\rm c}}{c_{\rm NFW}\Sigma_{\rm c}}\left[\dfrac{4(3u^2-2)}{u^2(u^2-1)\sqrt{1-u^2}}\,\mathrm{arctanh}\left(\sqrt{\dfrac{1-u}{1+u}}\right) + \dfrac{4}{u^2}\ln\left(\dfrac{u}{2}\right) + \dfrac{2}{1-u^2}\right] & (u<1) \\ \dfrac{r_{200}\delta_{\rm c}\rho_{\rm c}}{c_{\rm NFW}\Sigma_{\rm c}}\left[\dfrac{10}{3} - 4\ln 2\right] & (u=1) \\ \dfrac{r_{200}\delta_{\rm c}\rho_{\rm c}}{c_{\rm NFW}\Sigma_{\rm c}}\left[\dfrac{4(3u^2-2)}{u^2(u^2-1)\sqrt{u^2-1}}\,\arctan\left(\sqrt{\dfrac{u-1}{1+u}}\right) + \dfrac{4}{u^2}\ln\left(\dfrac{u}{2}\right) + \dfrac{2}{1-u^2}\right] & (u<1) \end{cases} , \tag{6.10}$$

Note that $\langle D_{\rm ds}/D_{\rm s}\rangle$ enters into Eqs. (6.9) and (6.10) via the critical surface mass density $\Sigma_{\rm c}$.

6.4.3 Fits to the Ellipticity Profile

In Fig. 6.12, there is a discernible positive tangential alignment signal extending out to $\sim 10'$ (or ~ 3.5 Mpc) from the cluster centre. (The solid line and dots in all panels give the shear averaged in bins of $90''$ width.) In order to validate that this tangential alignment is indeed caused by gravitational shear of a cluster-like halo, we fit the NFW reduced shear profile given in Eq. (6.8) to the measured shear estimates, probing the range $0' < \theta < 15'$. To avoid binning effects, the fit is done on individual shear estimates, not on the filled circles shown in Fig. 6.12.

We define a *default model* using the preferred parameter values presented in Table 6.6. The table also lists references to the sections where these values are justified. In order to determine r_{200} and $c_{\rm NFW}$, we fit an NFW model to the shear estimates of the *lensing catalogue* galaxies, defined by the parameters above the vertical line in Table 6.6. We repeat that there are two changes to the default model compared to Israel et al. (2010): first, the improved estimate of $\langle D_{\rm ds}/D_{\rm s}\rangle$; second, the correction to the cluster member decontamination. The differences in the best fit values of the model parameters obtained for CL 0030+2618 are caused by these modifications.

The fitting is done by minimising χ^2 using an `IDL` implementation of the Levenberg-Marquardt algorithm (Moré 1978; Markwardt 2009) and returning $r_{200}^{\rm fit} = 1.62 \pm 0.16$ Mpc and $c_{\rm NFW}^{\rm fit} = 1.9 \pm 1.0$

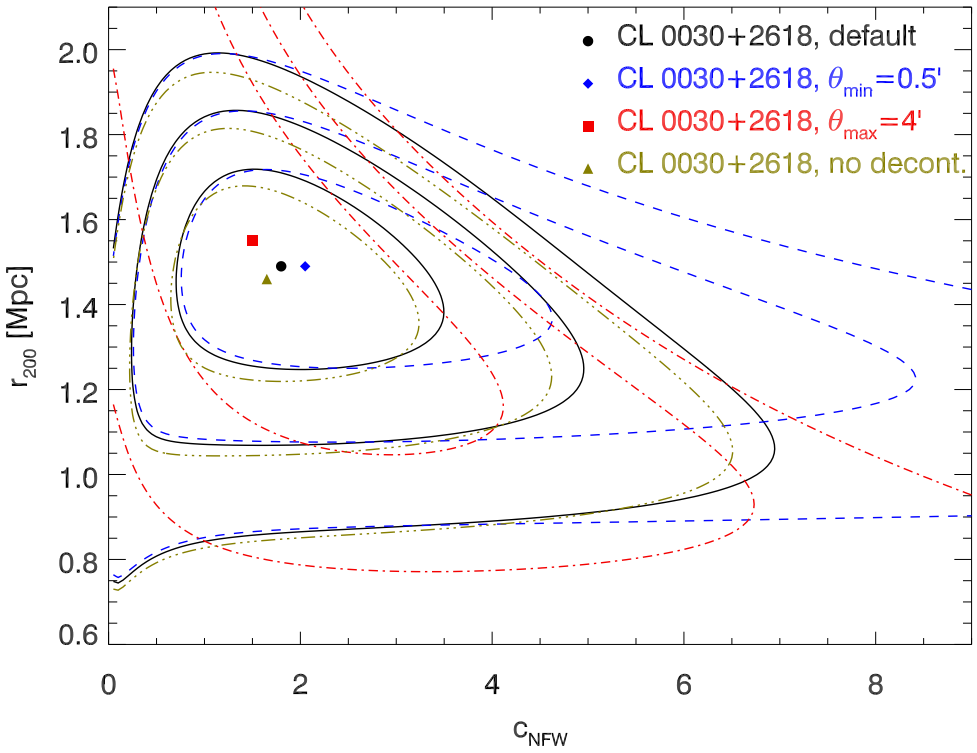

Figure 6.13: Confidence contours in the NFW parameter space spanned by the virial radius r_{200} and concentration $c_{\rm NFW}$, corresponding to confidence levels of 99.73%, 95.4%, and 68.3% for two interesting parameters. Also given as symbols are the cluster parameters minimising $\chi^2_{\rm L}$ (Eq. 6.12) for four different cases. They are: the default model, using data in the complete range $0' \leq \theta \leq 15'$ (solid contours and dot); a model where the central $30''$ are excised from the analysis (dashed contours and diamond); and a model considering only data inside $0' \leq \theta \leq 4' \approx r_{200}$ (dash-dotted contours and square). The triple-dot dashed curve and triangle show a model without correction for cluster members ("decontamination").

for the free parameters of the model. Note that the superscript "fit" always refers to results from the Levenberg-Marquardt fitting. Comparing the best-fitting NFW model (dashed curves in the two upper and lower left panels of Fig. 6.12) to the data, we find the shear profile to be reasonably well-modelled by an NFW profile: we measure $\chi^2/\nu_{\rm dof} = 13399/13636 \approx 0.98$, assuming an error

$$\sigma_{\rm fit} = f_1(\theta)\sigma_{\rm gt} \quad , \quad \sigma_{\rm gt} = f_0\sigma_\varepsilon/\sqrt{2} \approx 0.29 \tag{6.11}$$

for the individual shear estimate. We assigned the same weight to each galaxy in our analysis. *Shear weighting* is discussed in Sect. 5.4.2. This overall agreement with NFW is consistent with shear profiles of clusters with comparable redshift and data quality (Clowe et al. 2006b). We discuss the NFW parameter values obtained by the fit and the radial range over which the NFW fit is valid (the lower left and lower right panels of Fig. 6.12) in Sect. 6.5.

Gravitational lensing by a single axially symmetric deflector causes tangential alignment of the resulting ellipticities. Thus, the ellipticity cross-component $\langle\varepsilon_\times(\theta)\rangle$ corresponding to a pure curl field around the centre – assuming axial symmetry – should be consistent with zero at all θ. The dotted line and diamonds in the upper panel of Fig. 6.12 show that $\varepsilon_\times$ is indeed consistent or

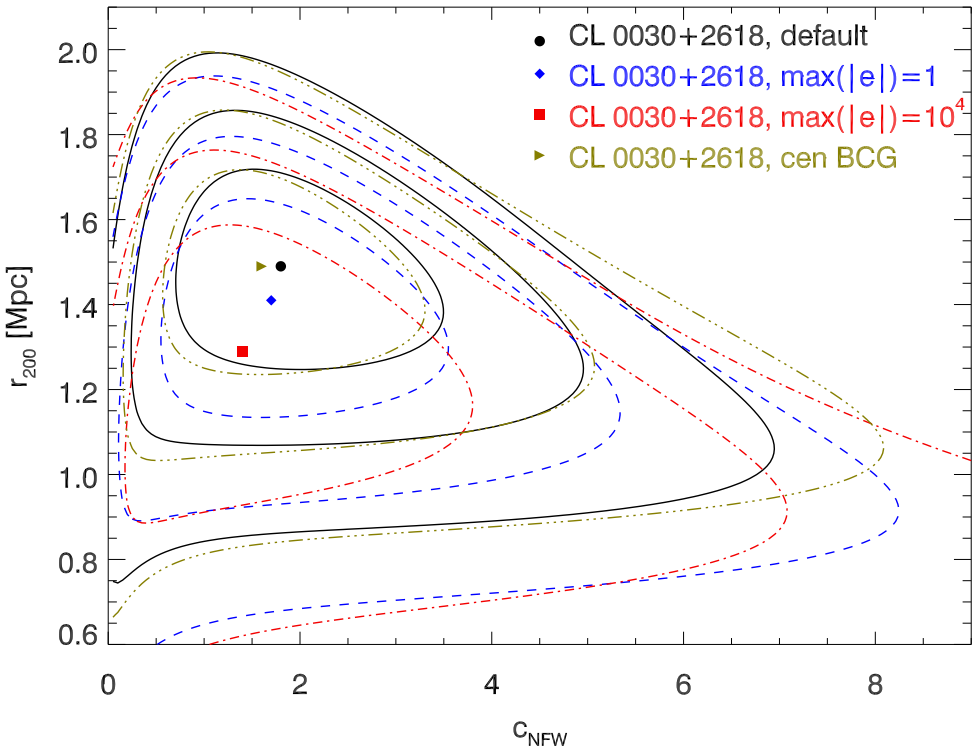

Figure 6.14: Confidence contours and values of r_{200} and $c_{\rm NFW}$ minimising $\chi^2_{\rm L}$ (Eq. 6.12) in dependence of the maximum shear estimator max($|\varepsilon|$) permitted in the catalogue: Given are the default case (max($|\varepsilon|$) = 0.8, solid contours and dot, see Sect. 6.1.4); max($|\varepsilon|$) = 1.0 (dashed contours and diamond); and max($|\varepsilon|$) = 10^4, equivalent to no cut (dot-dashed contours and square). Triple dot-dashed contours and the triangle denote the results for an otherwise default model centred on the BCG of CL 0030+2618.

nearly consistent with zero in its error bars in all bins but the innermost 90″. This feature is, like the general shapes of both $\varepsilon_{\rm t}$ and $\varepsilon_\times$, quite robust against the choice of binning.

To investigate the role of lensing by the foreground mass associated with the $z \approx 0.25$ galaxies (cf. Sect. 6.2.5), centred to the East of CL 0030+2618, we split up the ellipticity catalogue into an eastern ($\alpha_{\rm J2000} > \alpha_{\rm CL0030}$) and western ($\alpha_{\rm J2000} < \alpha_{\rm CL0030}$) subset (with 50.0 % of the galaxies in each). We repeat the profile fitting for both of them separately, as the influence of a possible perturber at the position of G2 should be small compared to the eastern sub-catalogue. We show the results in the upper right panel of Fig. 6.12, where left-facing triangles and the long-dashed fit curve denote the western subset, and right-facing triangles and the triple-dot dashed fit curve the eastern subset. In accordance with the mass distribution displayed in Fig. 6.9, in which a higher and more extended surface mass density can be found west of the centre of CL 0030+2618 than east of it, the $g_{\rm t}$ signal is more significant in the sources lying to the West of the cluster than to the East. We find $r^{\rm fit}_{200,{\rm W}} = 1.80 \pm 0.21$ Mpc, $c^{\rm fit}_{\rm NFW,W} = 2.1 \pm 1.1$, and $r^{\rm fit}_{200,{\rm E}} = 1.44 \pm 0.24$ Mpc, $c^{\rm fit}_{\rm NFW,E} = 1.5 \pm 1.5$. The cross components in the central bins of both subsets are similarly high than in the complete catalogue with the eastern half also showing a high $g_\times$ in the second bin. As the values for r_{200} from the two sub-catalogues are consistent given their uncertainties, we find

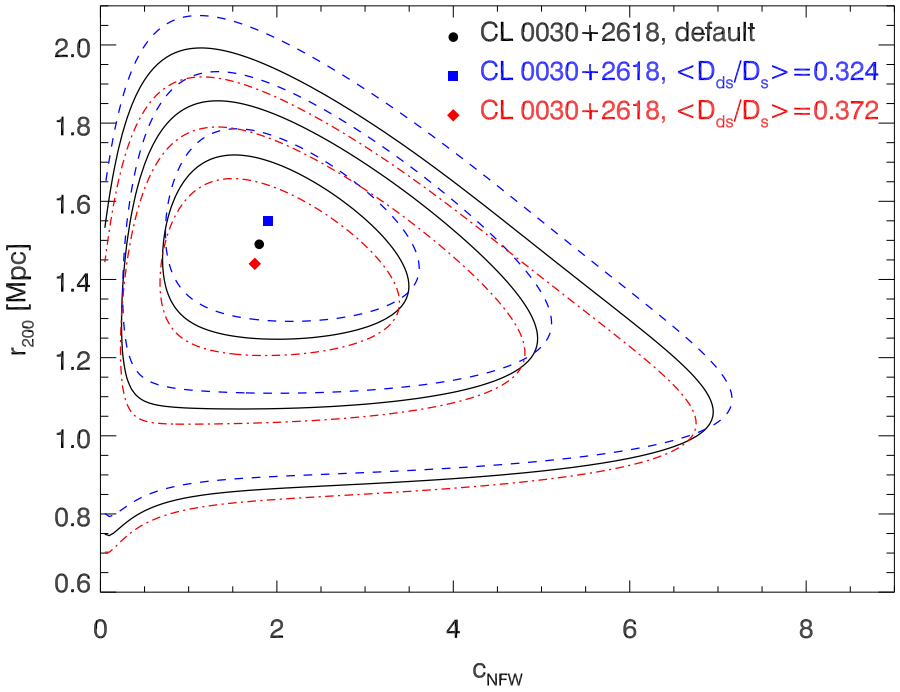

Figure 6.15: Confidence contours and values of r_{200} and $c_{\rm NFW}$ minimising $\chi^2_{\rm L}$ (Eq. 6.12) for models of different geometric factors: The default case, $\langle D_{\rm ds}/D_{\rm s}\rangle$ = 0.348 (solid contours and dot) is compared to the low ($\langle D_{\rm ds}/D_{\rm s}\rangle = 0.324$, dashed contours and square) and high cases ($\langle D_{\rm ds}/D_{\rm s}\rangle =$ 0.372, dot-dashed contours and diamond) derived from the CFHTLS Deep fields in Sect. 6.2.4.

no clear indications for a significant impact of the foreground structure. Its inconspicuous lensing signal is consistent with the inconspicuous X-ray signal at its position.

The deviation of $g_\times$ from zero by $\sim 1.5\sigma$ in the central bin, out of the 10 bins we probe, is not unexpected and does thus not pose a severe problem for the interpretation of our results with respect to $c_{\rm NFW}$ (Sect. 6.5.1). In a further test, we repeated the analysis centred on G1, the brightest cluster galaxy and found very similar results in terms of shapes of $\varepsilon_{\rm t}$ and $\varepsilon_\times$ and fit parameters.

6.4.4 The Mass of CL 0030+2618

The merit function χ^2 using the error model given by $\sigma_{\rm fit}$ (Eq. 6.11) provides a usable first guess for the cluster parameters. However, Schneider et al. (2000) showed that a better estimator of the uncertainty in the individual shear estimate exists. This more accurate noise model $\sigma^2_{\rm SKE} = \sigma^2_{\rm fit}(1-|g_{{\rm t},i}|^2)^2$ takes into account the dependence of the noise on the shear value itself, as expected by the model. Thus, for our default mass estimate, we evaluate the consistency between the tangential reduced shear $g_{{\rm t},i}(r_{200}, c_{\rm NFW})$ predicted by an NFW model for the i-th sample galaxy and the tangential ellipticity component $\varepsilon_{{\rm t},i}$ from the data by considering the function

$$\chi^2_{\rm L} = \sum_{i=1}^{N_{\rm gal}} \frac{\left|g_{{\rm t},i}(r_{200}, c_{\rm NFW}) - \varepsilon_{{\rm t},i}\right|^2}{\sigma^2_{\rm fit}\left(1-\left|g_{{\rm t},i}(r_{200}, c_{\rm NFW})\right|^2\right)^2} \quad . \tag{6.12}$$

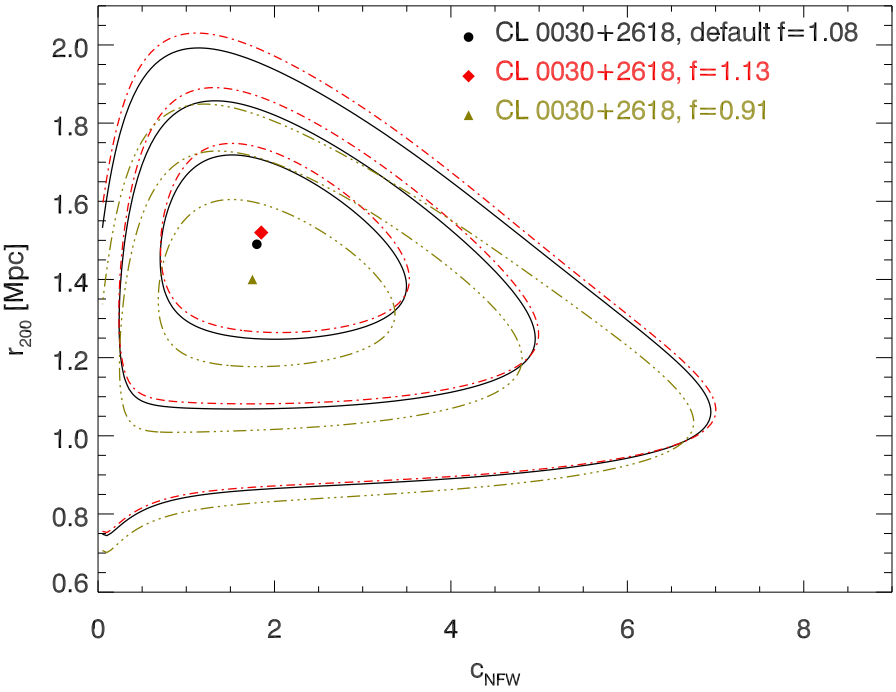

Figure 6.16: Confidence contours and values of r_{200} and $c_{\rm NFW}$ minimising $\chi^2_{\rm L}$ (Eq. 6.12) for models of different geometric factors, assuming an error of $\sigma_{f_0} = 0.05$ on the shear calibration and a fraction of 15.2 % foreground sources in the lensing catalogue. The default case, $f_0 = 1.08$ (solid contours and dot) is compared to the cases $f_0 = 1.13$ (dot-dashed contours and diamond) and $f_0 = 0.91$ (triple-dot dashed contours and triangle) resulting from the error modelling.

We denote the use of this modified merit function by writing $\chi^2_{\rm L}$ instead of χ^2. Computing Eq. (6.12) for a suitable grid of test parameters r_{200} and $c_{\rm NFW}$, we determine the values $r^{\rm min}_{200}$ and $c^{\rm min}_{\rm NFW}$ for which $\chi^2_{\rm L}$ becomes minimal. This approach allows us to better quantify the uncertainties in the model parameters given the data and – an important advantage over the Levenberg-Marquardt method – also their interdependence.

In Fig. 6.13, we present the regions corresponding to confidence intervals of 68.3%, 95.4%, and 99.73% in the r_{200}-$c_{\rm NFW}$-parameter space for three radial ranges in which data galaxies are considered. The solid curves denote the default model with the complete $0' \leq \theta \leq 15'$ range, giving $r^{\rm min}_{200} = 1.49^{+0.14}_{-0.15}$ Mpc and $c^{\rm min}_{\rm NFW} = 1.8^{+0.95}_{-0.75}$. We will adopt these as the default results of our analysis (see Table 6.7), yielding a cluster mass of $M_{200}(r^{\rm min}_{200}) = 6.8^{+2.1}_{-1.9} \times 10^{14} {\rm M}_\odot$ (statistical uncertainties) by applying Eq. (6.7). Figures 6.14, 6.15 and 6.16 show the confidence contours for modifications to our default model. We discuss these cases in Sect. 6.5, leading to an estimate of the systematic errors of the mass determination.

6.5 Discussion for CL 0030+2618

6.5.1 The Concentration Parameter

While our resulting r_{200} seems reasonable for a galaxy cluster of the redshift and X-ray luminosity of CL 0030+2618, its concentration, despite the fact that it is not well constrained by our data and cluster weak lensing in general, seems low compared to the known properties of galaxy clusters:

Bullock et al. (2001) established a relation between mass and concentration parameter from numerical simulations of dark matter haloes, using a functional form:

$$c_{\rm NFW} = \frac{c_{\rm NFW,0}}{1+z}\left(\frac{M_{\rm vir}}{M_*}\right)^{\alpha} \tag{6.13}$$

with $c_{\rm NFW,0} = 9.0$ and $\alpha = -0.13$ for a pivotal mass $M_* = 1.3 \times 10^{13}\,h^{-1}{\rm M}_\odot$. Bullock et al. (2001) find a 1σ scatter of 0.18 in $\log(c_{\rm NFW})$ about the mean value. This, for $z = 0.50$ and $M_{\rm vir} = 6.7 \times 10^{14}\,{\rm M}_\odot$ gives $c_{\rm NFW} = 3.7^{+1.9}_{-1.3}$. Comerford & Natarajan (2007), analysing a sample of 62 galaxy clusters for which virial masses and concentration parameters have been determined, and using the same relation Eq. (6.13), find $c_{\rm NFW,0} = 14.5 \pm 6.4$ and $\alpha = -0.15 \pm 0.13$, yielding $c_{\rm NFW} = 5.6^{+7.4}_{-3.6}$ for the virial mass and redshift of CL 0030+2618.

This large interval is consistent within the error bars with our default $c_{\rm NFW} = 1.8^{+1.65}_{-1.05}$ with $\chi^2_{\rm L}/\nu_{\rm dof} = 13413/13636 \approx 0.98$, but as the value itself remains unusually small, we investigate it further. First, we test $c_{\rm NFW} = 4.0$, close to the value suggested by Bullock et al. (2001), by fixing $r^{\rm fit}_{200} = 1.62$ Mpc and find $\chi^2_{\rm L}/\nu_{\rm dof} = 13426/13637$ and the shear profile of the resulting model (dash-dotted line in the lower left panel of Fig. 6.12) to be clearly outside the error margin for the innermost bin, demanding a significantly higher shear in the inner $90''$ than consistent with the measurements. With changes in $c_{\rm NFW}$ mainly affecting the modelling of the cluster centre, there is no such tension in the other bins. In the next step, we repeat the fit to the profile, now with $c_{\rm NFW} = 4.0$ fixed and r_{200} as the only free parameter. The resulting best-fitting model yields $r^{\rm fit4}_{200} = 1.46$ Mpc (triple-dot dashed in the lower left panel of Fig. 6.12), still outside but close to the measured 1σ-margin of the data. As this fit gives $\chi^2_{\rm L}/\nu_{\rm dof} = 13420/13637$, we conclude that more strongly concentrated models than the default are indeed disfavoured.

Residual contamination by cluster galaxies reduces the measured $c_{\rm NFW}$, as can be seen when "switching off" the contamination correction factor (see Table 6.7). This is expected as contamination suppresses the signal most strongly in the cluster centre. Removing all galaxies at separations $\theta < 0.5'$ from the analysis of Eq. (6.12), we indeed measure a higher $c^{\rm min}_{\rm NFW} = 2.05^{+2.55}_{-1.25}$, but for the price of larger error bars, as the same galaxies close to the cluster centre have the highest constraining power on $c_{\rm NFW}$. As can be seen from the dashed contours and the diamond in Fig. 6.13, excising the $\theta < 0.5'$ galaxies just stretches the confidence contours towards higher $c_{\rm NFW}$, leaving $r^{\rm min}_{200} = 1.49^{+0.22}_{-0.24}$ Mpc, and thus the inferred cluster mass unchanged (see also Table 6.7).

Replacing the contamination correction with a background selection down to the faintest magnitudes ($m_{\rm faint} = 29$), removing a large fraction of the "red sequence-like" galaxies in Fig. 6.11, also yields a slightly higher $c^{\rm fit}_{\rm NFW} = 3.0 \pm 1.5$ in the shear profile fit, together with a slightly larger $r^{\rm fit}_{200} = 1.65 \pm 0.18$ Mpc (compared to the default $c^{\rm fit}_{\rm NFW} = 1.9 \pm 1.0$ and $r^{\rm fit}_{200} = 1.62 \pm 0.16$ Mpc) and a less significant detection $S(\boldsymbol{\theta}_{\rm c}) = 5.10$ than the default case. We note that these values are consistent within their mutual error bars. A further possible explanation for the low $c_{\rm NFW}$ due to additional lensing by the $z \approx 0.25$ foreground structure is rather unlikely (cf. Sect. 6.4.3). We notice that existing literature puts more emphasis on clusters showing *excessive* concentration parameters; see e.g., Oguri et al. (2009) who find concentration higher than predicted in a WL analysis of four strong lensing clusters.

Except for the extraordinary cases of CL 1701+6414 and CL 1641+4001 (Sects. 7.3.7 and 7.3.8), CL 0030+2618 exhibits the lowest concentration parameter out of our eight clusters. We discuss the mass-concentration relation for the subsample of eight MEGACAM clusters in Sect. 8.2.2. Concerning CL 0030+2618, the higher $c_{\rm NFW}$ measured with the same method add credit to our measured $c_{\rm NFW} = 1.8^{+1.65}_{-1.05}$ being caused by a physical effect in the cluster rather than a bias in the analysis. Some indications from simulations exist that link scatter and biases in $c_{\rm NFW}$ to cluster triaxiality (Corless & King 2007) and merging (Clowe et al. 2004). However, further investigation is needed to confirm whether low measured $c_{\rm NFW}$, both in the case of CL 0030+2618 and generally, correlate with indicators of cluster merging.

6.5.2 The Extent of the NFW Profile

Navarro et al. (1997) designed their profile to represent the mass distribution of galaxy clusters in numerical simulations within the virial radius. Thus, as theory provides no compelling argument to use it out to larger radii, this practice has to be justified empirically.

In the lower right panel of Fig. 6.12, we show results for a toy model profile in which the shear signal drops faster than NFW outside r_{200}. For simplicity, we chose the shear profile of a point mass, i.e.

$$g_{\rm t,ext}(\theta) = g_{\rm t,NFW}(\theta_{200}) \left(\frac{\theta_{200}}{\theta}\right)^2 \tag{6.14}$$

for $\theta > \theta_{200}$, the separation corresponding to r_{200}. As in the lower left panel of Fig. 6.12, dashed, dot-dashed, and triple dot dashed lines denote the fit to both r_{200} and $c_{\rm NFW}$, setting $c_{\rm NFW} = 4.0$ for the same r_{200}, and fitting to r_{200} for a fixed $c_{\rm NFW} = 4.0$, respectively. The truncation points θ_{200} are marked by squares in Fig. 6.12. For the usual two-parameter model with $\chi^2_{\rm L,trunc} - \chi^2_{\rm L,NFW} = 0.47$, as for the other two models, the difference in goodness-of-fit between the truncated and pure NFW profiles is marginal.

Additionally, we repeat the evaluation of Eq. (6.12) on the parameter grid for galaxies $0' \leq \theta \leq 4' \approx \theta_{200}$ only. The dash-dotted contours and the square in Fig. 6.13 for the resulting optimal parameters show the corresponding values. Here, $r^{\rm min}_{200} = 1.55^{+1.76}_{-0.50}$ Mpc and $c^{\rm min}_{\rm NFW} = 1.5^{+2.6}_{-1.5}$ are more degenerate than in the default case (cf. Table 6.7). We conclude that there is no evidence in the CL 0030+2618 data for a deviation of the shear profile from NFW at $r > r_{200}$. Applying Occam's razor, we use this profile for the whole radial range, but stress cautiously that we cannot preclude an *underestimation* of the errors and, to a lesser extent, a bias in the virial mass here.

6.5.3 Shear Calibration

As already pointed out in Sect. 6.1.4, the maximum shear estimator $\max(|\varepsilon|)$ considered in the catalogue strongly affects averaged shear observables. In Fig. 6.14, we quantify this dependence by comparing the confidence contours and best values for r_{200} and $c_{\rm NFW}$ from the default $\max(|\varepsilon|) = 0.8$ catalogue (solid contours and dot) to cases with $\max(|\varepsilon|) = 1.0$ (dashed contours and diamond) and $\max(|\varepsilon|) = 10^4$ (dot-dashed contours and square). The latter includes even the most extreme shear estimates[12]. The $\max(|\varepsilon|)$ cut, via the amplitude of the shear signal, mainly influences $r^{\rm min}_{200}$, reducing[13] it by 5 % and 13 % for the frequently used $\max(|\varepsilon|) = 1.0$ and the extreme $\max(|\varepsilon|) = 10^4$, respectively. In turn, the mass estimate would be reduced by 15 % and 35 %, as can be seen from Table 6.7.

[12] Note that, although unphysical, shear estimates $\varepsilon > 1$ in KSB are to some extent justified when averaging over large ensembles.

[13] The sign here is likely due to a statistical fluke; theory expects $r^{\rm min}_{200}$ to increase with a less strict $\max(|\varepsilon|)$. We return to this question in Sect. 8.2.1.

The influence on the mass estimate by the choice of max($|\varepsilon|$) is compensated by the shear calibration $f_0 \neq 1$; and we account for this effect by considering different f_0. Given the uncertainty $\sigma_{f_0} = 0.05$ (Sect. 6.1.4), we repeat the analysis of Eq. (6.12) with $f_0 = 1.13$. For the negative sign, the signal dilution by foreground galaxies has to be taken into account. Combining in quadrature the 15.2 % foreground dilution estimated from the CFHTLS D1 field (Sect. 6.2.3) with σ_{f_0}, we arrive at $f_0 = 0.91$ as the lower bound of the error margin. The +5 % (−17 %) variation in f_0 translates into +2.0 % (−6.0 %) in $r_{200}^{\rm min}$, yielding again $\approx +6$ % (≈ -17 %) variation in M_{200} (see Table 6.7).

6.5.4 Combined Mass Error Budget

Replacing the weak lensing centre in our default model by the cluster's BCG as the centre of the NFW profile, we find the resulting differences in $r_{200}^{\rm min}$ and $c_{\rm NFW}^{\rm min}$ returned by minimising $\chi^2_{\rm L}$, and hence in M_{200}, to be small (cf. triple dot-dashed contours and triangle in Fig 6.14; Table 6.7). We conclude the error on the chosen centre to be subdominant.

Variations in the geometric factor $\langle D_{\rm ds}/D_{\rm s}\rangle$ induce a similar scaling in $r_{200}^{\rm min}$ and $c_{\rm NFW}^{\rm min}$ as shear calibration does. Using the error margin from the determination of the distance ratios from the CFHTLS Deep fields (Sect. 6.2.4), we produce confidence contours for $\langle D_{\rm ds}/D_{\rm s}\rangle = 0.30$ (dashed lines and square in Fig. 6.15) and $\langle D_{\rm ds}/D_{\rm s}\rangle = 0.36$ (dot-dashed contours and diamond). Comparing to the default model (solid contours and dot), we find an increase in $r_{200}^{\rm min}$ by 4.0 % and by 13 % in M_{200} for $\langle D_{\rm ds}/D_{\rm s}\rangle = 0.324$ (a more massive lens is needed for the same shear if the source galaxies are closer on average) and a decrease by 3.4 % in $r_{200}^{\rm min}$ and 10 % in M_{200} for $\langle D_{\rm ds}/D_{\rm s}\rangle = 0.372$ (cf. Table 6.7). The confidence contours for these cases are shown in Fig. 6.16.

An additional source of uncertainty in the mass estimate not discussed so far are triaxiality of galaxy cluster dark matter haloes and projection of the large-scale structure (LSS) onto the image. King & Corless (2007) and Corless & King (2007) showed with simulated clusters that masses of prolate haloes tend to get their masses overestimated in weak lensing while masses of oblate haloes are underestimated.

Again owing to cosmological simulations, Kasun & Evrard (2005) devised a fitting formula for the largest-to-smallest axis ratio η of a triaxial haloes as a function of redshift and mass

$$\eta(M_{200}, z) = \eta_0 (1+z)^{\epsilon} \left(1 - \zeta \ln\left(\frac{M_{200}}{h\, 10^{15}\,{\rm M}_\odot}\right)\right) \tag{6.15}$$

with $\epsilon = 0.086$, $\zeta = 0.023$, and $\eta_0 = 0.633$. Inserting the values for CL 0030+2618, we find $\eta = 0.61$ and, like Dietrich et al. (2009) whose lines we are following, derive the following maximal biases from Corless & King (2007): for a complete alignment of the major cluster axis with the line of sight mass is overestimated by 16 %, while complete alignment with the minor axis results in a 10 % underestimation.

The projection of physically unrelated large scale structure can lead to a significant underestimation of the statistical errors in M_{200} and $c_{\rm NFW}$ (Hoekstra 2003, 2007). The simulations of Hoekstra (2003) yield an additional error of $\pm 1.2\, h^{-1} \times 10^{14} {\rm M}_\odot = \pm 1.67 \times 10^{14} {\rm M}_\odot$ for a cluster in the mass range of CL 0030+2618, and little redshift dependence for $z > 0.2$. Thus, we adopt this value as the systematic uncertainty due to large scale structure. The impact of LSS projections on WL cluster number counts and the cluster mass function was studied by, e.g., Marian et al. (2010).

We define the systematic mass uncertainty $\sigma_{\rm sys}$ as the quadratic sum of the errors $\sigma_{\rm cali}$ from shear calibration, $\sigma_{\rm geom}$ from the geometric factor, $\sigma_{\rm proj}$ from projection, and $\sigma_{\rm LSS}$ from large-

scale structure.[14] The total error, used in Fig. 8.2, is then defined as the quadratic sum also including $\sigma_{\rm stat}$, evaluated independently for the positive and negative error contributions:

$$\sigma^2_{\rm tot} = \sigma^2_{\rm stat} + \sigma^2_{\rm sys} = \sigma^2_{\rm stat} + \sigma^2_{\rm LSS} + \sigma^2_{\rm proj} + \sigma^2_{\rm geom} + \sigma^2_{\rm cali} \tag{6.16}$$

We note that the statistical errors are already quite large and the dominating factor in Eq. (6.16). As its main result, this study arrives at a mass estimate of $M_{200} = 6.8^{+2.1+2.2}_{-1.9-2.2} \times 10^{14} {\rm M}_\odot$ for CL 0030+2618, quoting the statistical and statistical error as the first and second uncertainty. Concerning the total uncertainty, we find $M_{200} = 6.8^{+3.0}_{-2.9} \times 10^{14} {\rm M}_\odot$. Because the uncertainties to due to triaxiality, shear calibration, and the uncertainty in the geometric factor are multiplicative rather than additive errors, the error margin yielded by Eq. (6.16) are misleading when compared to detection significances. Multiplicative uncertainties do not affect the S-statistics cluster detection. Therefore, comparing the cluster mass estimate to the lower boundary of its 1σ total error margin does not give its detection significance.

[14] We remark, however, that strictly speaking $\sigma_{\rm LSS}$ qualifies as a statistical error, because it leads to an increase in the uncertainties rather than a scaling of the mass estimate.

Chapter 7

MMT Analysis of Seven *400d* Clusters

7.1 Photometric Analysis

7.1.1 Number Counts and Redshift Distribution

In Sect. 6.2.2, we found that the r'-band source count histogram of the CL 0030+2618 data analysed in the pilot study closely matches the distribution in the CFHTLS *Deep* fields. Noting that the net exposure times for the r'-band of the seven further MEGACAM clusters are shorter than for CL 0030+2618, we now compare the MEGACAM number counts in these images to CFHTLS *Deep* as well as the shallower COSMOS photo-z catalogue.

The r'-band magnitude distributions in all eight cluster fields we analysed are shown in Fig. 7.1. In analogy to Fig. 6.6, we compare the galaxy shape catalogues obtained with MEGACAM to the histograms of r^+- and r'-band magnitudes from the COSMOS (Ilbert et al. 2006) and CFHTLS *Deep 1* (Ilbert et al. 2009) photo-z catalogues. We note that only the r'-band data set of CL 1641+4001 matches the depth of the CL 0030+2618 field, as we would expect from the limiting magnitudes given in Table 4.2. The brightest $r'_{\rm lim}$ and consequently the largest deviation from the CFHTLS *Deep 1* histogram coinciding with the two deepest MEGACAM fields can be found for CL 1357+6232 and, unfortunately, for the most distant of the eight clusters, CL 0230+1836. We further note that in the CL 0809+2811 field, showing the same $r'_{\rm lim} = 25.4$ measured in a $2''$ aperture (Eq. 4.3) as CL 1357+6232 but a considerably better seeing, the catalogue extends to fainter r'-magnitudes. Thus, all MEGACAM cluster fields reach deeper than the COSMOS photo-z catalogue. The two deepest fields reach the depth of the CFHTLS *Deep* fields, and exceed them in the case of the nominal 7500 s exposure we plan to obtain in future *400d* WL observations.

In the CL 0030+2618 analysis, we used the CFHTLS *Deep* fields' photo-zs as a proxy for the unknown redshift distribution of our background sources. In order to test for a possible bias in $\langle D_{\rm ds}/D_{\rm s}\rangle$ for the more shallow cluster fields, we repeat the fit of Eq. (6.2) to the photo-z catalogues from the four *Deep* fields with the following modification: Introducing a magnitude cut, we remove all galaxies with $r' > r'_{\rm max}$ from the CFHTLS catalogues. Vertical lines in Fig. 7.1 indicate the corresponding cut-offs in the histogram for the cases $r'_{\rm max} = 26.0$ and $r'_{\rm max} = 25.0$.

The effect of the magnitude cut for the relevant $r'_{\rm max}$ interval is presented in Fig. 7.2, where solid lines and shaded areas denote the mean values and standard deviations of $\langle D_{\rm ds}/D_{\rm s}\rangle$, resp., averaged over the D1 to D4 fields, in dependence of $r'_{\rm max}$. For three deflector redshifts $z_{\rm d}$ spanning the range of our MEGACAM clusters, we compare to $\langle D_{\rm ds}/D_{\rm s}\rangle$ calculated from the complete catalogues. We note that at $r'_{\rm max} = 27.0$, the difference is negligible, because few sources are removed from the catalogue. Virtually independent of $z_{\rm d}$, we find the $\langle D_{\rm ds}/D_{\rm s}\rangle$ for the cases with and without magnitude cut to agree within mutual error bars for $r'_{\rm max} \approx 25.2$. In other words, at $r'_{\rm max} = 25.2$ – for which the faintest 1/3 of galaxies is cut from the D1 catalogue – the variation

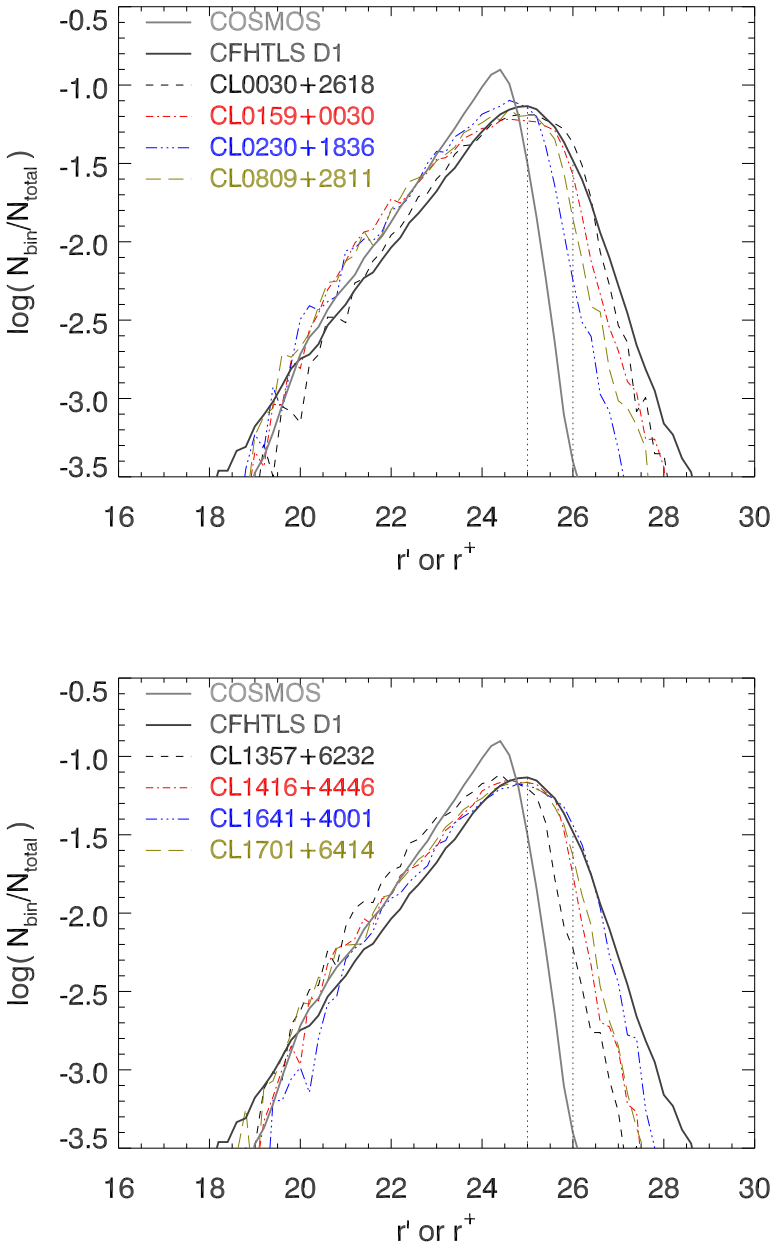

Figure 7.1: Comparison of the r'-band source count histograms for all eight clusters discussed in this thesis with the COSMOS r^+-band (thick, light-grey line) and CFHTLS *Deep 1* r'-band (thick, dark-grey line) data from the photo-z catalogues of Ilbert et al. (2006, 2009). Plotted are the source counts in bins of 0.2 mag width and scaled by the total number of sources in the respective catalogue, on a logarithmic axis. The upper panel shows the MEGACAM galaxy shape catalogues for CL 0030+2618 (black, dashed line), CL 0159+0030 (red, dash-dotted), CL 0230+1836 (blue, triple dot-dashed), and CL 0809+2811 (green, long-dashed). Vertical dotted lines indicate the effects of magnitude cuts at $r'_{\rm max} = 26.0$ and $r'_{\rm max} = 25.0$. The lower panel is the same, but for CL 1357+6232 (black, dashed), CL 1416+4446 (red, dash-dotted), CL 1641+4001 (blue, triple dot-dashed), and CL 1701+6414 (green, long-dashed). For CL 0030+2618, compare also Fig. 6.6.

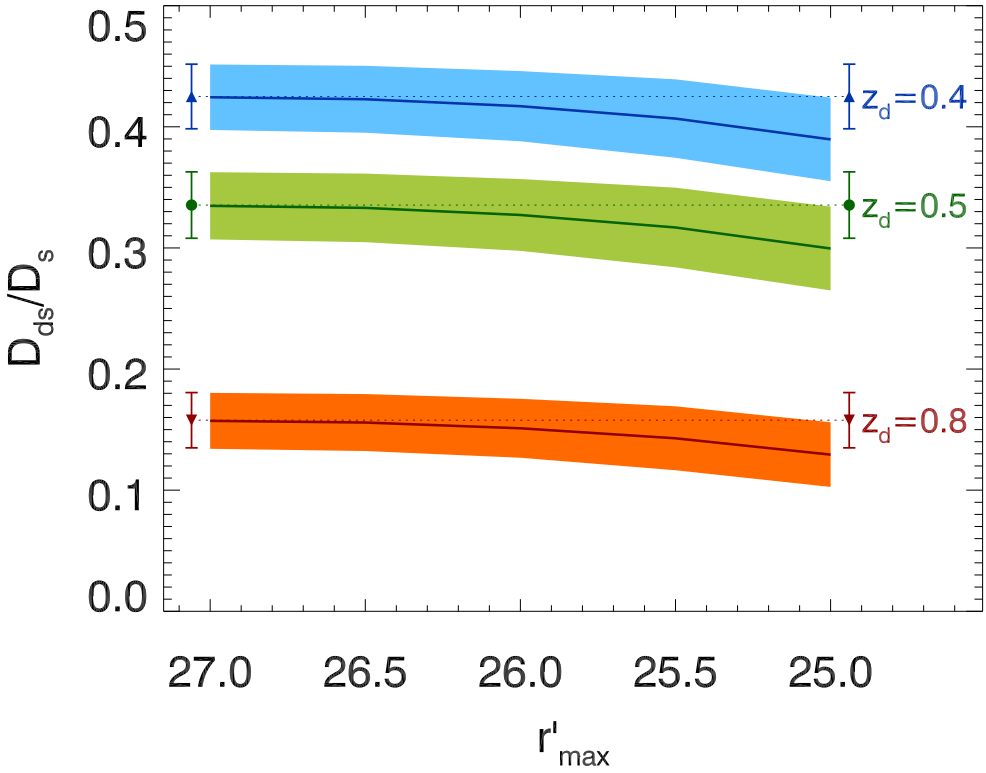

Figure 7.2: Change in $\langle D_{\rm ds}/D_{\rm s}\rangle$ introduced by applying a magnitude cut at $27.0 > r'_{\rm max} > 25.0$ to the CFHTLS D1 to D4 photo-z catalogues. Solid lines and shaded areas give the mean values and standard deviations of $\langle D_{\rm ds}/D_{\rm s}\rangle$, resp., calculated from the four *Deep* fields as a function of $r'_{\rm max}$ at $z_{\rm d} = 0.4$, $z_{\rm d} = 0.5$, and $z_{\rm d} = 0.8$. For comparison, symbols with error bars, connected by horizontal dotted lines, show $\langle D_{\rm ds}/D_{\rm s}\rangle$ for the full catalogue, i.e. up to the faintest source at $r' = 30.57$.

within the four *Deep* fields has the same amplitude as the effect of removing the faintest sources. In our shallowest field, CL 0230+1836, we measure a *limiting magnitude* of $r'_{\rm lim} = 25.1$, with 52 % of the sources in the KSB catalogue and still 15 % of galaxies in the galaxy shape catalogue (cf. Fig. 7.1) showing $r' > 25.2$. We thus conclude that no significant bias in $\langle D_{\rm ds}/D_{\rm s}\rangle$ is introduced by using the full D1 to D4 catalogues for all *400d* MEGACAM fields. For the average $\langle D_{\rm ds}/D_{\rm s}\rangle$ values and standard deviations computed with the individual cluster redshifts, we refer to Table 6.4.

7.1.2 Background Selection

Contrary to the expectations, the background selection applied for CL 0030+2618 was not very efficient in removing foreground and cluster galaxies on the CFHTLS *Deep* photo-z catalogues. Therefore, for the analysis of CL 0159+0030, CL 0230+1836, and CL 0809+2811 (for which data in three bands are available), we aim at improving the background selection by investigating the relations between photo-zs and galaxy colours in the CFHTLS *Deep* fields.

In Fig. 7.3, we present the galaxy numbers and the fraction of $z_{\rm ph} \leq 0.40$ sources in the CFHTLS D1 photo-z catalogue in dependence of the r' magnitude and g'–r' and r'–i' colours. The layout is the same as for Fig. 6.7, with the red, green, and blue contours in Fig. 7.3 marking regions

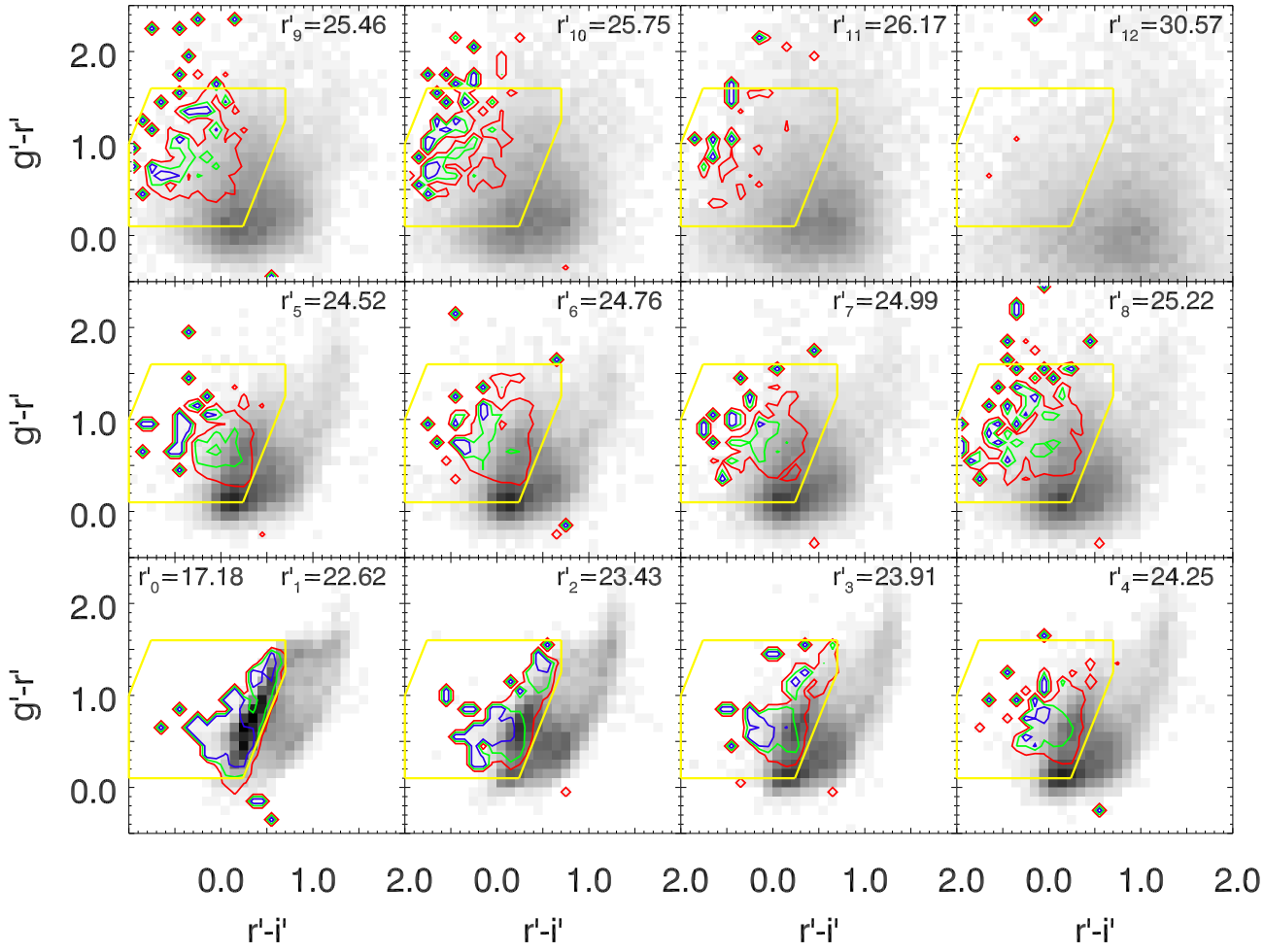

Figure 7.3: The same as Fig. 6.7, but showing the fraction $f_{\rm fg}$ of galaxies with $z_{\rm ph} \leq 0.40$ in the CFHTLS D1 field as a function of their $g'-r'$ and $r'-i'$ colours and r' magnitude. Red, green and blue contours correspond to $f_{\rm fg} = 25$ %, 50 %, and 75 %. Based on the distribution of $z_{\rm ph} \leq 0.40$ galaxies in the three brightest dodeciles, we define the yellow polygon (see Table 7.1), in order to remove foreground galaxies from the CL 0159+0030 and CL 0809+2811 fields.

of the colour–colour space populated by fractions $f_{\rm fg}$ of 25 %, 50 %, and 75 % of foreground galaxies compared to the $z_{\rm d} = 0.40$ clusters, CL 0159+0030 and CL 0809+2811. The contours are defined such that $f_{\rm fg}$ exceeds the respective threshold in all grid cells enclosed by the contour.

As expected, $f_{\rm fg}$ generally decreases towards fainter magnitudes, with only a few $z_{\rm ph} \leq 0.40$ sources at $r' > 26.0$. For all magnitudes, foreground sources with r'–$i' > 0.5$ are rare. In the brightest three dodeciles, a well-defined region with a distinctive edge towards redder $r'-i'$ colours exists[1], confirming our similar results for the $z_{\rm ph} \leq 0.50$ sources from Israel et al. (2010) and Sect. 6.2.3.

[1]Towards very blue $r'-i'$ colours, few galaxies are found in the CFHTLS D1 catalogue, basically all of them at low $z < 0.4$ redshift. This can be seen from the contours in Fig. 7.3 which follow the irregular shape of the point cloud. We choose a conservative $\min(r'-i') = -1.0$ limit for the selection polygons (Table 7.1), both at $z = 0.40$ and $z = 0.80$.

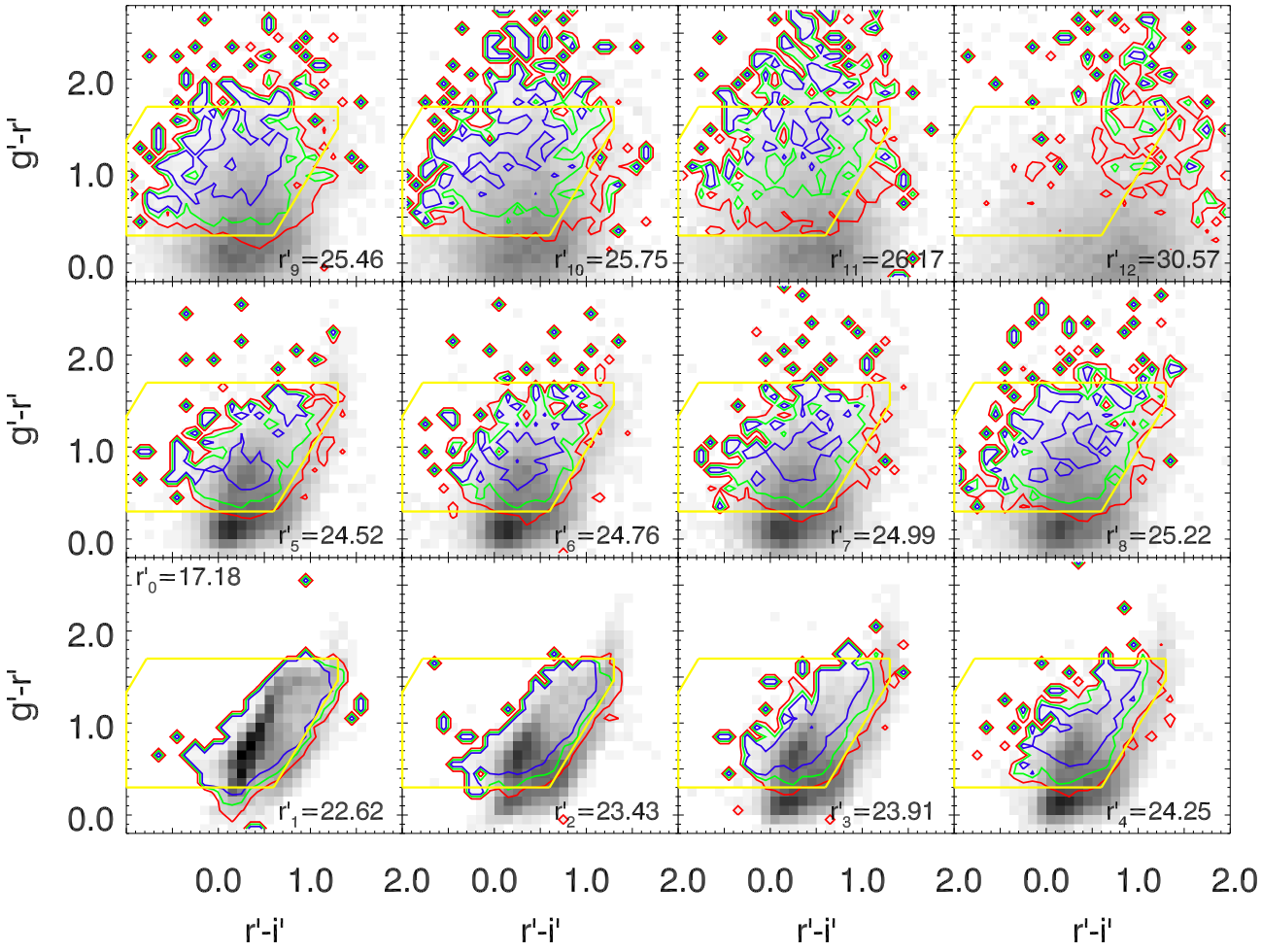

Figure 7.4: The same as Fig. 6.7, but showing the fraction of galaxies $z_{\rm ph} \leq 0.80$. Applying the cuts given in Table 7.1, we define the yellow polygon in order to remove foreground galaxies from the CL 0230+1836 field.

Although the preferred locus of $z_{\rm ph} \leq 0.40$ galaxies depends little on the r' magnitude, the zone populated by low-z objects becomes more diffuse for fainter sources. Finding little significance in the $f_{\rm fg}$-distribution at $r' > 25.0$, dominated by small-number Poisson noise, we find our background selection method justified, which includes all sources fainter than $m_{\rm faint}$ and selects brighter galaxies based on their $g'-r'$ and $r'-i'$. Furthermore, the secondary role of $m_{\rm bright}$ compared to $m_{\rm faint}$ in the CL 0030+2618 analysis (Sect. 6.1.2) becomes clear from Fig. 6.7, corresponding to Fig. 7.3 at $z_{\rm d} = 0.50$, noticing the small number of $r' < 20$ galaxies.

Calculating $f_{\rm fg}$ for a cluster redshift of $z_{\rm d} = 0.80$, we show the regions preferentially inhabited by galaxies in the foreground of a cluster like CL 0230+1836 in Fig. 7.4. For the higher cluster redshift $z_{\rm d}$, the regions in colour–colour space where a given value of $f_{\rm fg}$ is exceeded extend as well towards fainter r' as towards redder $g'-r'$ and $r'-i'$ colours. For $z_{\rm d} = 0.80$, only a small

Table 7.1: Cuts defining the polygons used for background selection for the $z \approx 0.40$ and $z = 0.80$ clusters, based on the colours of foreground galaxies (Figs. 7.3 and 7.4). We specify the values of $g'-r$, $r'-i'$, and $s_\beta = \beta(r'-i') - (g'-r')$ at the edges of the polygons. Compare to Table 6.2 for CL 0030+2618, where $s = s_{\beta=1.5}$ was used.

Redshift	$\min(r'-i')$	$\max(r'-i')$	$\min(g'-r')$	$\max(g'-r')$	β	$\min(s_\beta)$	$\max(s_\beta)$
$z=0.4$	-1.0	0.7	0.1	1.6	2.5	-3.5	0.5
$z=0.8$	-1.0	1.2	0.3	1.7	1.5	-3.0	0.7

number of *background* sources remain in the first dodecile, while there are significant foreground objects even in the $r'_{10} < r' < r'_{11}$ bin.

We adjust our background selection polygon to $z_d = 0.40$ and $z_d = 0.80$ by using the polygons (plotted in yellow in Figs. 7.3 and 7.4) based on $f_{fg} > 0.25$ contours in the three brightest dodeciles ($r' < 23.91$) of the CFHTLS D1 photo-z catalogue and defined by the cuts given in Table 7.1.

7.2 Lensing Detections

7.2.1 The Three–Band Clusters

Adaptations to the Background Selection In this section, we present the lensing detections for the clusters CL 0159+0030, CL 0230+1836, and CL 0809+2811. The preparation of catalogues and KSB analysis for these objects for which we have $g'r'i'$ data (cf. Table 4.2) has been performed in complete analogy to CL 0030+2618. Parameter values determining the galaxy shape catalogues are summarised in Table 5.3. We now focus on the optimisation of the lensing signal, determined by $m_{\rm bright}$ and $m_{\rm faint}$. Based on the knowledge obtained by analysing the photo-z distribution in the *Deep 1* field (Sect. 7.1.2), we construct the background selection polygons for the $z \approx 0.40$ and $z = 0.80$ cases (Figs. 7.3 and 7.4). Table 7.1 lists the parameter values defining the polygons.

The relations between galaxy colours and photo-z measured in the CFHTLS *Deep 1* field (Figs. 7.3 and 7.4) show that $m_{\rm faint}$ is the more important parameter for constructing an effective background selection than $m_{\rm bright}$: Even for the brightest magnitudes in the *Deep 1* field, and at $z_d = 0.80$, a distinction between foreground and background sources is possible based on $g'-r'$ and $r'-i'$. This is also consistent with our experience from CL 0030+2618 (Fig. 6.3), where including all galaxies up to the saturation limit $m_{\rm bright} = r'_{\rm min}$ (cf. Sect. 5.4) does not significantly lower the shear signal compared to its maximum. Hence, we focus on $m_{\rm faint}$ in the following analysis.

We determine the S-statistics (Eq. 3.29) for the three cluster fields, using a grid of 15″ mesh size and testing several cases of the parameters defining the lensing catalogues. Beside $m_{\rm faint}$ and $m_{\rm bright}$, we vary the "polygon parameters", $\min(r'-i')$, $\max(r'-i')$, $\min(g'-r')$, $\max(g'-r')$, $\min(s_\beta)$, $\max(s_\beta)$, and β from their default values given in Table 7.1. Optimising the lensing catalogue is an iterative process, of which we present the final result for CL 0159+0030 and CL 0809+2811 in Fig. 7.5, and for CL 0230+1836 in Fig. 7.6. Using preliminary values for $m_{\rm faint}$ and $m_{\rm bright}$, we determine the optimal value for the filter scale $\theta_{\rm out}$ in Eq. (3.29), which depends on the mass and z of the cluster. The results are visualised in the upper panel of Fig. 7.7, which shows $S(\theta_{out})$ for the final lensing catalogues. We find $\theta_{\rm out}^{\rm opt} = 10\farcm5$ for CL 0159+0030, $\theta_{\rm out}^{\rm opt} = 8\farcm5$ for CL 0230+1836, and $\theta_{\rm out}^{\rm opt} = 13\farcm5$ for CL 0809+2811. Based on the preliminary analysis, we also determine the position of the S-peak for the three clusters. We discuss the lensing centres and the spatial distribution of the aperture mass signal in Sect. 7.3.

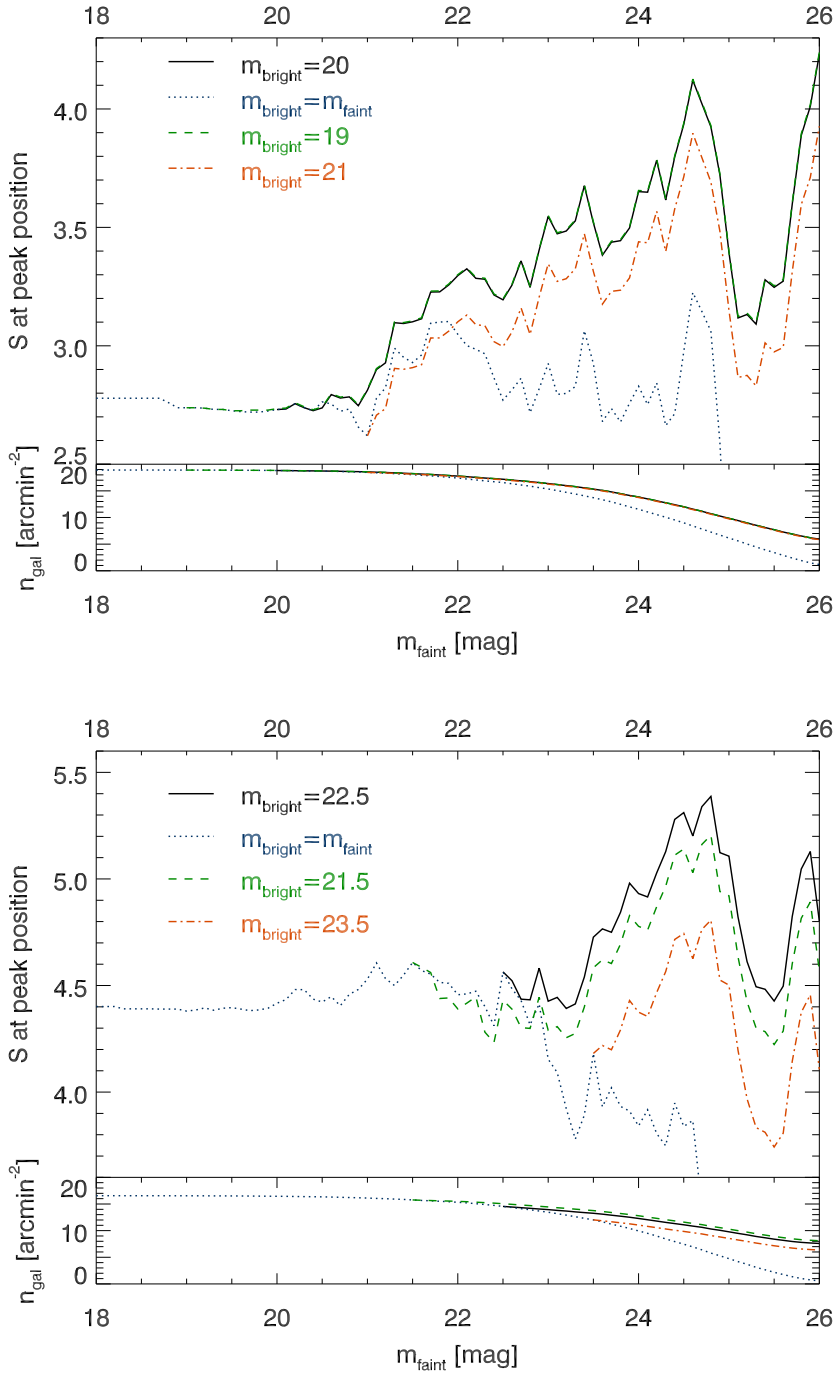

Figure 7.5: The S-statistics detections of CL 0159+0030 (*upper plot*) and CL 0809+2811 (*lower plot*) for different background selection models. Shown in the *upper panels* of both plots is the significance level of the lensing signal as a function of $m_{\rm faint}$, at the position of the lensing peak for filter scales of $\theta_{\rm out}^{\rm opt} = 10\farcm5$ (CL 0159+0030) and $\theta_{\rm out}^{\rm opt} = 13\farcm5$ (CL 0809+2811). In both plots, the solid line denotes the case for the value of $m_{\rm bright}$ which we adopted. For comparison, the dashed and dot-dashed lines show the variations if $m_{\rm bright}$ is chosen 1.0 mag brighter or fainter; and the dotted lines give the results of a magnitude cut. For the same cases, the *lower panels* of both plots show the cumulative number density of sources in the lensing catalogue as a function of $m_{\rm faint}$.

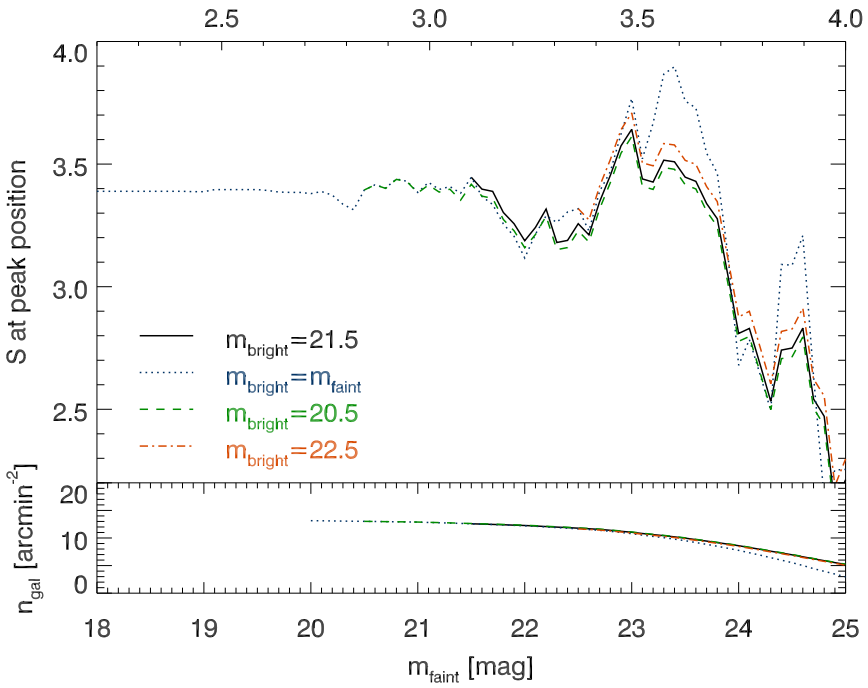

Figure 7.6: The same as Fig. 7.5, but showing the S-statistics detection of CL 0230+1836 for different background selection models and a filter scale of $\theta_{\rm out}^{\rm opt} = 8\farcm5$.

Results for CL 0159+0030 and CL 0809+2811 Figures 7.5 and 7.6 show the aperture mass signal-to-noise ratio in the respective peak pixels and for $\theta_{\rm out} = \theta_{\rm out}^{\rm opt}$ as a function of $m_{\rm faint}$. Of the two $z \approx 0.40$ clusters, CL 0809+2811 with $S_{\rm max} = 5.39$ for the final lensing catalogue shows a stronger shear signal than CL 0159+0030 with $S_{\rm max} = 4.12$. As solid lines in Fig. 7.5, we plot $S(m_{\rm faint})$ for the default value of $m_{\rm bright}$, which we adopted based on the preliminary analysis. We compare to the cases where $m_{\rm bright}$ is varied by 1.0 mag to brighter (dashed line) or fainter (dot-dashed line) magnitudes, and to a magnitude cut at $m_{\rm bright} = m_{\rm faint}$ (dotted curve). Note that the curves for $m_{\rm faint} > m_{\rm bright}$ set off from the dotted curve as the differences between the corresponding lensing catalogues grow with larger $m_{\rm faint}$. For both CL 0159+0030 and CL 0809+2811, the default case shows a more pronounced peak than the best magnitude cut, corresponding to an increase of $\Delta S \approx 1$ in the significance level owed to the background selection using three bands. In the case of CL 0809+2811, we observe the peak at an $m_{\rm faint}$ for which a magnitude cut already gives a significantly smaller S than including all galaxies fainter than $r'_{\rm min}$.

Qualitatively, we observe similar behaviours of $S(m_{\rm faint})$ in the upper and lower plot of Fig. 7.5, arriving at $m_{\rm faint} = 24.6$ for CL 0159+0030 and $m_{\rm faint} = 24.8$ for CL 0809+2811. As shown in the lower panels of Fig. 7.5, we count $n_{\rm gal} = 11.58$ galaxies/arcmin^2 and $n_{\rm gal} = 10.36$ galaxies/arcmin^2 in the respective lensing catalogues. By choosing $m_{\rm faint} = 24.6$ for CL 0159+0030, we take the source number density into account: Noticing the very small $n_{\rm lc} \sim 5$ galaxies/arcmin^2, we consider the $S > 4$ we measure for $m_{\rm faint} = 26$ in CL 0159+0030 as a likely statistical fluke, and the match with a similar peak in CL 0809+2811 as mere coincidence. Considering $m_{\rm bright}$, the value of 22.5 found for CL 0809+2811 indeed gives a higher $S_{\rm max}$ than $m_{\rm bright} = 21.5$ or 23.5 (dashed and dot-dashed curves in the lower plot of Fig. 7.5). For CL 0159+0030, the default $m_{\rm bright} = 20.0$ is slightly better than $m_{\rm bright} = 21.0$ (dot-dashed curve) and indistinguishable from $m_{\rm bright} = 19.0$.

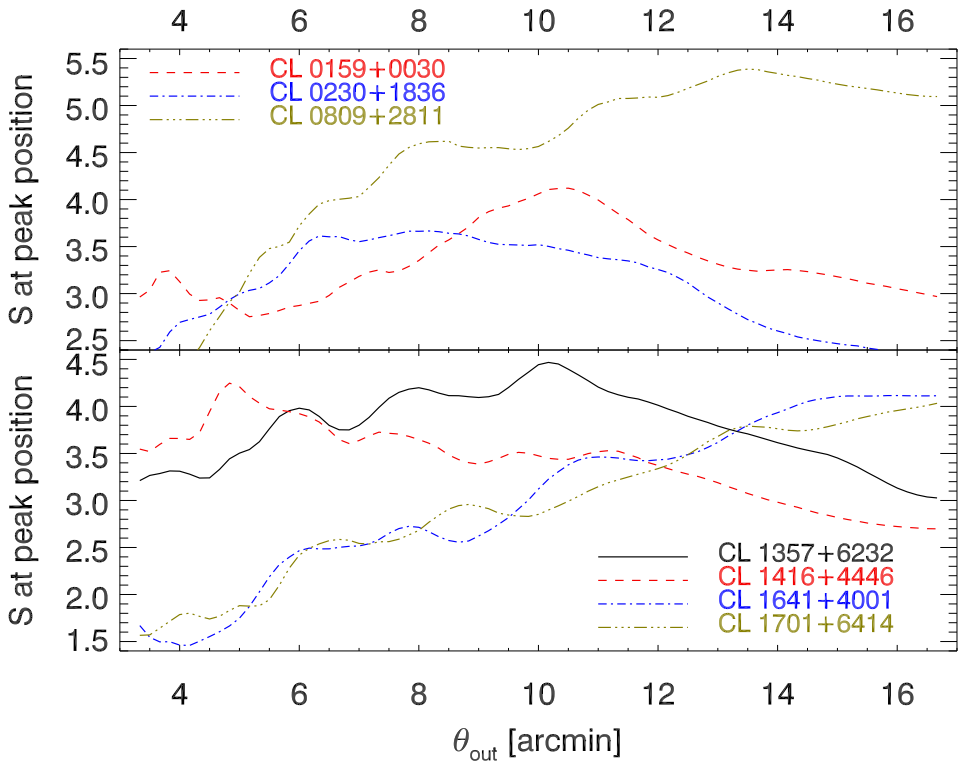

Figure 7.7: The S-statistics detections of the three-band clusters (*upper panel*) discussed in Sect. 7.2.1 and the single-band clusters (*lower panel*, Sect. 7.2.2) as a function of the filter scale $\theta_{\rm out}$. Shown are the values for S at the maxima of the shear peaks for CL 0159+0030 (dashed curve), CL 0230+1836 (dot-dashed curve), and CL 0809+2811 (triple-dot dashed curve) in the upper panel; and for CL 1357+6232 (solid curve), CL 1416+4446 (dashed curve), CL 1641+4001 (dot-dashed curve), and CL 1701+6414 (triple-dot dashed curve) in the lower panel. For all clusters, the final lensing catalogues are used.

Slight variations in the polygon parameters induce only small changes in the $S(m_{\rm faint})$ we measure for the $z \approx 0.40$ clusters. We present the corresponding plots in Figs. B.6 and B.7 in Appendix B.2. In some cases, changes in these parameters result in a more significant detection (e.g., for $\min(s_\beta) = 0.4$ instead of $\min(s_\beta) = 0.3$ for CL 0159+0030) or lead to a small shift in the value of $m_{\rm faint}$ giving the maximum S (with $\min(g'-r') = 0.0$ instead of $\min(g'-r') = 0.1$ for CL 0809+2811). Nevertheless, the differences in the significance levels are generally small, and our choices for the polygon from Fig. 7.3 are justified by the MMT data. We list the specifications of the detections in Table 7.2.

Results for CL 0230+1836 Interestingly, for CL 0230+1836, the most distant of the observed clusters, we do not find a higher $S_{\rm max}$ using the $g'r'i'$-based background selection (see the solid curve in Fig. 7.6 for the default case) compared to a magnitude cut (dotted curve). Given the cluster redshift of $z_{\rm d} = 0.8$, we expected the background selection to play an important role, especially considering the colour-colour-diagram down to fainter magnitudes than for the more nearby clusters (cf. Fig. 7.4). On the contrary, we find a magnitude cut at $m_{\rm faint} = 23.4$ to provide a more significant detection ($S_{\rm max} = 3.90$) than the default lensing catalogue based on the $g'-r'$ and $r'-i'$ colours ($S_{\rm max} = 3.64$ for $m_{\rm faint} = 23.0$ and $m_{\rm bright} = 21.5$). We note that the improvement in S compared to taking the complete galaxy shape catalogue is small in all cases, resembling the situation

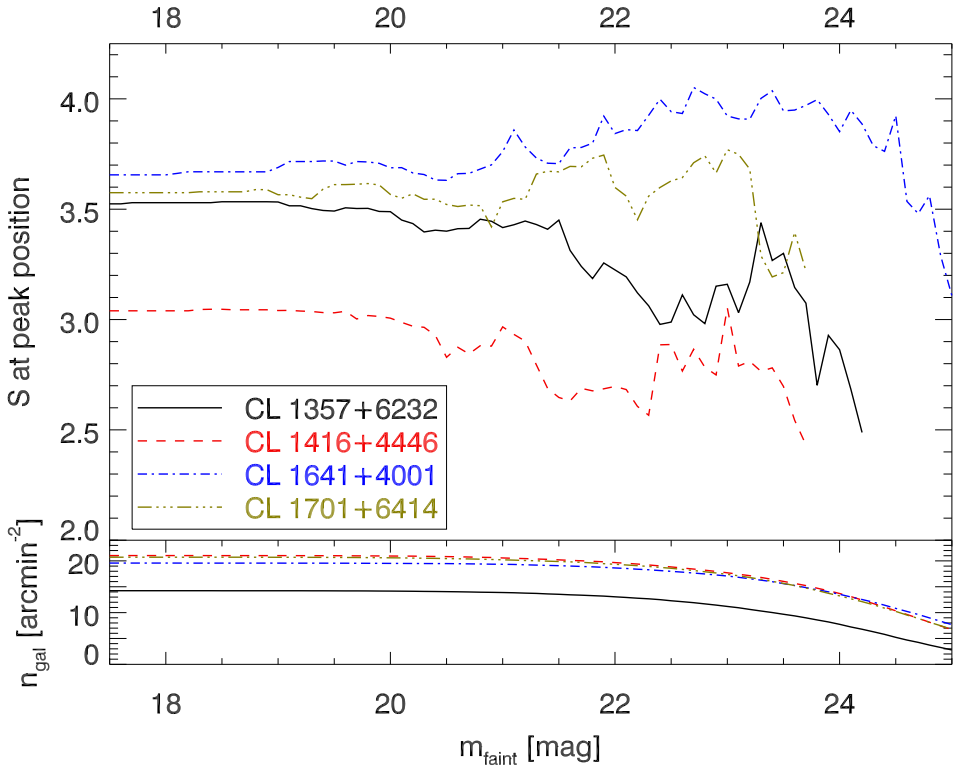

Figure 7.8: *Upper panel:* Dependence of the S-statistics on the magnitude cut $m_{\rm faint}(=m_{\rm bright})$ for the four clusters observed in *Run C* for which only lensing band data exist: CL 1357+6232 (solid curve), CL 1416+4446 (dashed curve), CL 1641+4001 (dot-dashed curve), at CL 1701+6414 (triple dot-dashed curve). Shown are results for the grid cells identified as the lensing centres and at $\theta_{\rm out} = 15\farcm5$. *Lower panel*: The number density of objects in the lensing catalogue as a function of the magnitude cut, for the same fields.

for CL 0030+2618 (Sect. 6.1.2), and that the best range for $m_{\rm faint}$ is located at *brighter* magnitudes than the one for the $z \approx 0.40$ clusters. Concerning $m_{\rm bright}$, we observe small changes in the maximum S for a broad range $20 \lesssim m_{\rm bright} \lesssim 23$. We adopt a value in the middle, $m_{\rm bright} = 21.5$, as our preferred case (solid line in Fig. 7.6), but note the higher S for fainter $m_{\rm bright}$ (e.g. $m_{\rm bright} = 22.5$, the dot-dashed line in Fig. 7.6). In synopsis, the results for CL 0230+1836 hint towards little contribution to the lensing signal by $r' \lesssim 23.5$ galaxies. Thus, a possible explanation is that the existing imaging ($T_{\rm exp} = 2700$ s in r', 4200 s in g', and 3600 s in i', Table 4.2) could be too shallow for the background selection to become relevant.

Consequently, we find a very small influence of variations in the polygon parameters (Fig. B.8 in Appendix B.2) on the peak value of S and the optimal value for $m_{\rm faint}$. Despite the lower $S_{\rm max}$, we prefer the default ($m_{\rm faint} = 23.0$, $m_{\rm bright} = 21.5$) background selection in the further analysis over the $m_{\rm faint} = 23.4$ magnitude cut, because the number density of lensing catalogue galaxies is higher: 11.04 galaxies/arcmin^2 (cf. Table 7.2) compared to only 9.79 galaxies/arcmin^2.

7.2.2 The Single–Band Clusters

In the following, we discuss the preparation of lensing catalogues for the clusters CL 1357+6232, CL 1416+4446, CL 1641+4001, and CL 1701+6414, for which we have r'-band data but no g'-

Table 7.2: Lensing catalogues and lensing detections using the S-statistics for all eight clusters we analysed. Shown are the values for $m_{\rm bright}$ and $m_{\rm faint}$, and the source number densities in galaxies/arcmin^2 in the second to fourth column. Columns five and six contain the optimal S-statistics filter scale $\theta_{\rm out}^{\rm opt}$ and the maximum $S_{\rm max}$ obtained with that scale on a 15″ grid. If not stated otherwise, the coordinates of that grid cell are given as the lensing centre in the seventh and eighth column. Finally, we show the separation between lensing and ROSAT centres.

Cluster	$m_{\rm bright}$	$m_{\rm faint}$	$n_{\rm lc}$	$\theta_{\rm out}^{\rm opt}$	$S_{\rm max}$	$\alpha_{\rm J2000}^{\rm wl}$	$\delta_{\rm J2000}^{\rm wl}$	$\Delta\theta$
CL 0030+2618	20.0	22.5	21.28	15.′5	5.84	$00^{\rm h}30^{\rm m}34\overset{\rm s}{.}0$	+26°17′54″	23″[†]
CL 0159+0030	20.0	24.6	11.58	10.′5	4.12	$01^{\rm h}59^{\rm m}23\overset{\rm s}{.}0$	+00°29′37″	79″[‡,§]
CL 0230+1836	21.5	23.0	11.04	8.′5	3.64	$02^{\rm h}30^{\rm m}27\overset{\rm s}{.}0$	+18°36′03″	20″
CL 0809+2811	22.5	24.8	10.36	13.′5	5.39	$08^{\rm h}09^{\rm m}30\overset{\rm s}{.}4$	+28°10′08″	178″[§]
CL 1357+6232	–	18.5	14.23	10.′17	4.47	$13^{\rm h}57^{\rm m}13\overset{\rm s}{.}5$	+62°32′13″	50″[†]
CL 1416+4446	–	18.5	21.02	4.′83	4.25	$14^{\rm h}16^{\rm m}29\overset{\rm s}{.}9$	+44°46′38″	19″[†]
CL 1641+4001	–	22.7	17.65	16.′0	4.12	$16^{\rm h}41^{\rm m}55\overset{\rm s}{.}3$	+40°02′56″	95″
CL 1701+6414	–	21.9	19.47	(15.′5)	3.75	$17^{\rm h}01^{\rm m}12\overset{\rm s}{.}4$	+64°15′14″	66″

[†] Lensing centre determined by bootstrapping of lensing catalogue.
[‡] Lensing centre not used in further analysis because of large mask near the cluster centre.
§ Accuracy of lensing centre diminished by large mask in centre.

or i'-band observations. As a direct consequence, we can not attempt a selection of background galaxies and a correction for cluster members in the same way we did for the other clusters. Note that a large number of foreground and cluster galaxies has already been removed during the construction of the galaxy shape catalogue, in particular very extended sources (Sect. 5.3.1).

As a background selection, we apply a magnitude cut to the galaxy shape catalogues defined by the cuts in Table 4.2. In the same way as for the three-band clusters, we compute the S-statistics on a grid of 15″ mesh size. For each cluster, we define the shear peak to be located in the grid cell in which the highest S is measured in the majority of the tested lensing catalogues resulting from the magnitude cut at $m_{\rm faint}$. We note that this step is a bit more complicated for CL 1701+6414 and CL 1641+4001, which show multiple strong shear peaks. The CL 1701+6414 field contains four galaxy clusters identified in the *160d* X-ray survey (Vikhlinin et al. 1998). We detail the determination of lensing centres for these clusters in Sects. 7.3.7 and 7.3.8.

Figure 7.8 shows how the detection significance varies with $m_{\rm faint}$ at the shear peaks we determined for the four clusters. For none of them, the magnitude cut leads to a significant improvement in S. In fact, for CL 1357+6232 (solid curve) and CL 1416+4446 (dashed curve), the strongest detections are achieved by choosing values of $m_{\rm faint} = 18.5$, basically cutting no galaxies from the galaxy shape catalogues. In CL 1641+4001 (dot-dashed curve) and CL 1701+6414 (triple-dot dashed curve), slightly better detections than with the complete galaxy shape catalogues can be achieved, but the $S(m_{\rm faint})$ curves are rather flat. Note that the curves in Fig. 7.8 are continued to higher $m_{\rm faint}$ as long as a local maximum is observed in the chosen shear peak grid cell. We measure the highest value for S at $m_{\rm faint} = 22.7$ for CL 1641+4001 and at $m_{\rm faint} = 21.9$ for CL 1701+6414. The fractions of foreground galaxies remaining in the lensing catalogues are discussed in Sect. 8.2.1 and considered in the error analysis.

In a second step, we determine the optimal filter scale $\theta_{\rm out}^{\rm opt}$ for the single-band cluster, keeping $m_{\rm faint}$ fixed to the values we determined from Fig. 7.8, where $\theta_{\rm out} = 15.'5$ was used. The resulting curves $S(\theta_{\rm out})$ are depicted in the lower panel of Fig. 7.7. We find $\theta_{\rm out}^{\rm opt} = 10.'17$ for CL 1357+6232,

yielding a detection of $S_{\max} = 4.47$, a small[2] $\theta_{\rm out}^{\rm opt} = 4\farcm83$ for CL 1416+4446, giving $S_{\max} = 4.25$ and an optimal detection of $S_{\max} = 4.12$ for CL 1641+4001 at $\theta_{\rm out}^{\rm opt} = 16\farcm0$. In the CL 1701+6414 field, the aperture mass filter unavoidably contains signal from more than one cluster. Therefore, we do not attempt to define a $\theta_{\rm out}^{\rm opt}$ here and use the wide ($\theta_{\rm out} = 15\farcm5$) default scale found for CL 0030+2618. We notice a qualitatively different behaviour of $S(\theta_{\rm out})$ for CL 1641+4001 and CL 1701+6414 than in all other clusters (Fig. 7.7): For these two fields, no significant decrease in S is measured up to the largest scale we tested, $\theta_{\rm out} = 16\farcm67''$. Regarding the dependence of S on the filter scale for CL 1357+6232 and CL 1416+4446 where the detection significance can be increased by $\Delta S > 1$ by choosing a smaller $\theta_{\rm out}$, we point out that the peak in $S(m_{\rm faint})$ might be located at different values of $m_{\rm faint}$. We are going to determine the optimal values of $m_{\rm faint}$ and $\theta_{\rm out}$ *simultaneously* in a future, more detailed analysis of the four clusters. Given the flat $S(m_{\rm faint})$ curves for both the single-band clusters at $\theta_{\rm out} = 15\farcm5$ (Fig. 7.8) and also the three-band clusters with magnitude cuts and at their respective, *different* $\theta_{\rm out}^{\rm opt}$, we expect the differences in the resulting best $m_{\rm faint}$ and lensing catalogues to be small. We summarise the detections in Table 7.2.

Comparing to lensing catalogues defined by magnitude cuts for the three-band clusters (solid line in Fig. 6.3 and dotted lines in Figs. 7.5 and 7.6), we conclude that for all eight clusters we analysed so far, only small improvements can be achieved by introducing a magnitude cut as background selection. Background selections based on $g'-r'$ and $r'-i'$ could lead to improved lensing catalogues for the four single-band clusters, if additional observations were performed. This is demonstrated by the examples of CL 0159+0030, CL 0809+2811, and, to a lesser degree, CL 0030+2618. A better understanding of the catalogue and, probably, deeper r'-band data in equally good seeing are necessary to understand why a magnitude cuts gives a more significant detection of CL 0230+1836 than the three-band background selection.

7.2.3 Significance Testing

Do the values for the S-statistics we obtained represent the correct significance levels, i.e. is the chance to find a $S \geq 3$ peak 0.27 %? In order to test the interpretation of S-values as significances, we conducted the following test: For each of the cluster detections, we consider the lensing catalogue for the peak grid cell, i.e. all galaxies with a separation $\theta < \theta_{\rm out}$. For each galaxy in the catalogue, we add to the phase φ of the complex ellipticity estimator $\varepsilon = |\varepsilon| \exp(2{\rm i}\varphi)$ an additional term $\varphi_{\rm rnd}$ drawn randomly from a uniform distribution in the interval $0 \leq \varphi_{\rm rnd} < \pi$. This procedure should completely remove the lensing signal from the data such that the resulting value of S be normally distributed around zero, with a standard deviation $\sigma = 1$.

We produced 10^6 realisations of such a randomised catalogue for each cluster and present the distributions of the resulting S-statistics in the upper panels of the sub-plots in Figs. 7.9 and B.9 in Appendix B.2. For illustrative purposes, we plot the distributions as histograms $H(S)$ with a bin size of $\Delta S = 0.01$. The results we discuss in the following do not depend on the choice of the (arbitrary) bin size. We find the S-distributions for all eight cluster detection to be well represented by a Gaussian distribution (solid lines in Figs. 7.9 and B.9, note that logarithmic scales of the ordinates). In all cases, the absolute of the mean value μ of the fitted Gaussian is $|\mu| < 0.002$, and of the same order of magnitude as the uncertainty in μ derived from the fit. We do not find a bias to either positive or negative S. For six of the eight clusters, we find $|1-\sigma| < 0.01$ for the standard deviations σ of the fitted Gaussians, although none of them is consistent with $\sigma = 1$ considering the fitting errors. For CL 1416+4446 and CL1641+4001, however, we find $\sigma = 0.962$ and $\sigma = 0.978$, respectively, for the standard deviations of the best-fit Gaussian distributions. The dashed lines in Figs. 7.9 and B.9 show the expected Gaussian G with mean $\mu = 0$ and standard deviation $\sigma = 1$, for comparison.

[2] We stress that CL 1416+4446 is detected at the $> 3\sigma$ level also for significantly larger $\theta_{\rm out}$, up to $\theta_{\rm out} = 14'$.

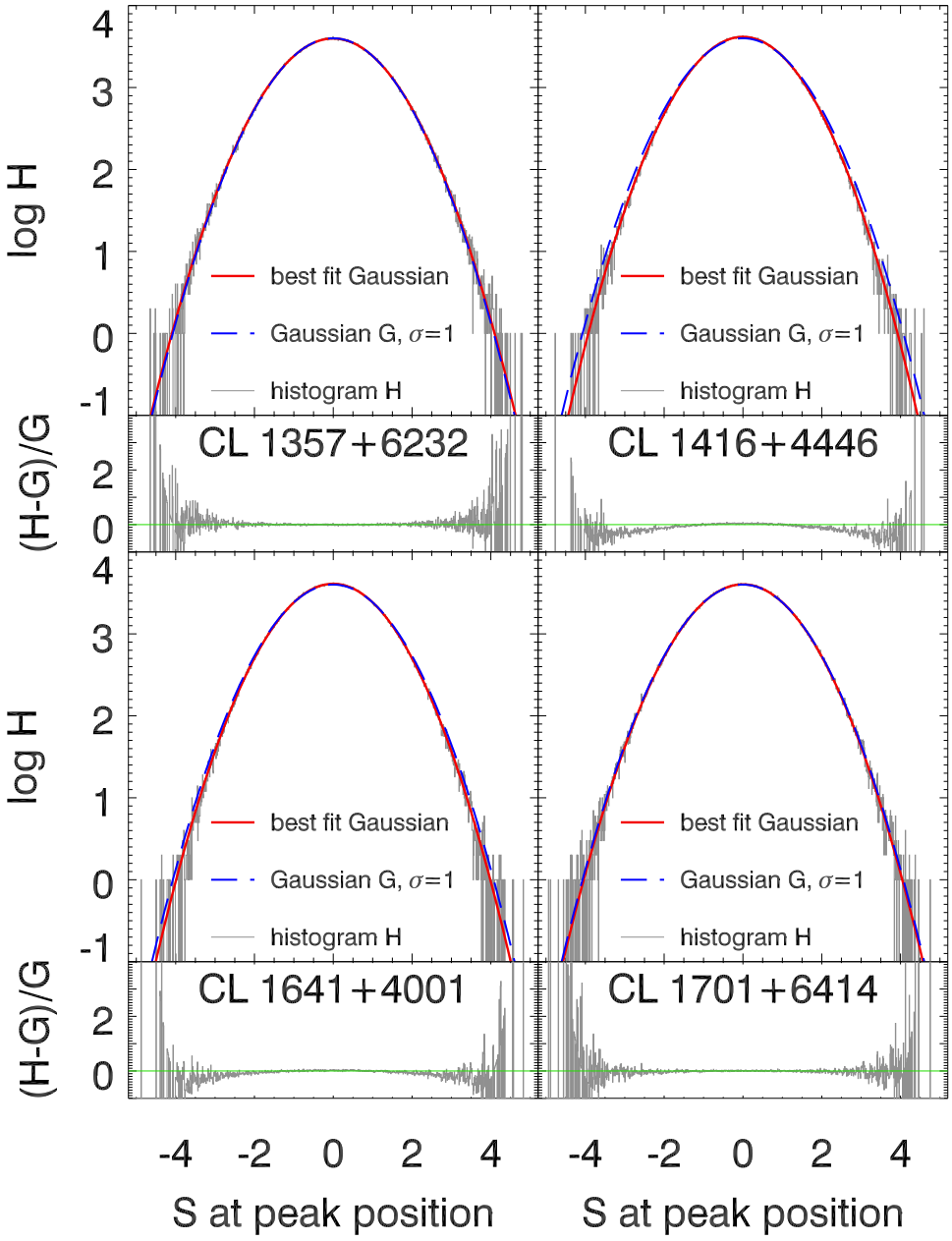

Figure 7.9: *Upper panels:* Histograms $H(S)$ of the S-statistics measured in 10^6 randomised lensing catalogues of CL 1357+6232, CL 1416+4446, CL 1641+4001, and CL 1701+6414. A random phase is added to all ellipticities considered for the shear peak grid cell. The solid line shows the Gaussian best-fit to $H(S)$, while the dashed lines shows the Gaussian distribution G with mean $\mu = 0$ and standard deviation $\sigma = 1$. *Lower panels:* The relative deviations $(H-G)/G$ of the measured from the expected S-distribution, for the same four clusters. Corresponding plots for the other four clusters are presented in Fig. B.9 in Appendix B.2.

In the lower panels of the sub-plot in Figs. 7.9 and B.9, the relative deviations $(H-G)/G$ of the measured histograms from the expected distribution G, are presented. With the exceptions of CL 1416+4446 and CL1641+4001, these deviations are negligible over the whole range in S-values which occur more than a few times in the 10^6 randomised catalogues. Only for the very rare $|S|>4$ events, the relative deviations seem to differ from the expectation, with a large scatter. This is likely to be an artefact of the small-number Poisson statistics in the extreme wings of the distribution function. Only for one cluster, we find one $|S|>5$ event in the 10^6 realisations, consistent with the expectation of one such events in 1.7×10^6 realisations of the expected Gaussian distribution G. Therefore, we conclude that this randomisation test does not find indications for an overestimation of the significance of our cluster detections, as inferred from the S-statistics. On the contrary, the small standard deviations measured from the fits to the CL 1416+4446 and CL1641+4001 correspond to slightly *underestimated* significances of these two cluster detections.

7.3 Lensing Analysis

7.3.1 Contamination Correction for Three–Band Clusters

By considering the colour indices available with $g'r'i'$ data, we search for the best colour index to perform the contamination correction (Sect. 6.4.1) for CL 0159+0030, CL 0230+1836, and CL 0809+2811. In Fig. 7.10, we present the colour indices of the Coleman et al. (1980, CWW) "Elliptical/S0" template galaxy as a function of redshift. The template magnitudes were calculated in the MMT/MEGACAM filters using routines from the `HyperZ` photo-z code (Bolzonella et al. 2000), by placing the same template at different redshifts, i.e. ignoring evolution in the underlying stellar population. An ideal colour index for distinguishing cluster galaxies from background, but also foreground galaxies should show a monotonic behaviour with z and a steep gradient around the cluster redshift.

The $g'-i'$ colour index matches our requirements in the $0.35<z<0.80$ interval better than $g'-r'$ or $r'-i'$ (thick lines in Fig. 7.10). We thus confirm the choice made for CL 0030+2618 in Israel et al. (2010). Adding a near-infrared z' filter to the $g'r'i'$-bands (thin lines in Fig. 7.10) results in a small improvement for the most distant ($z\approx0.8$) *400d* clusters, where the $g'-z'$ colour continues to increase with z while $g'-i'$ shows a plateau for $0.8<z<1.0$. We stress that if we had $g'r'i'z'$ data, a significantly better selection of cluster galaxies would be possible with photometric redshifts.

The left panels of Fig. 7.11 present the colour-magnitude diagrams of CL 0159+0030 ($z=0.39$), CL 0809+2811 ($z=0.40$), and CL 0230+1836 ($z=0.80$). Plotted are the $g'-i'$ colours in dependence of the i' magnitude for galaxies in the galaxy shape catalogue with $<4'$ separation to the respective ROSAT cluster centre. Sources with $<3'$ and $<2'$ cluster-centric distance are indicated by symbols of increasing size, in analogy to the lower panel of Fig. 6.5. Black dots and solid lines mark the $g'-i'$ colours of the CWW "Elliptical/S0" template at the cluster redshifts, fixing $i'=20.0$. We find the most prominent red sequence in the CL 0809+2811 field, where the brightest sources in the galaxy shape catalogue cluster around $g'-i'=2.6$, predicted using the CWW template. CL 0159+0030, at nearly the same z, shows only a very weak concentration of galaxies at $g'-i'=2.6$. We point out that in this field the masked area in the coadded image, necessary due to the presence of a bright star (Sect. 5.1), is larger than for the two other clusters discussed here, leading to a very small number of $\theta<2'$ sources in the CL 0159+0030 catalogue.

In the CL 0230+1836 field, we observe a clustering of galaxies with separations $\theta<2'$ from the cluster centre at very red ($g'-i'>2.5$) colours. Although these galaxies are spread out in $g'-i'$, they appear to be consistent with the expected g'–$i'=3.7$ for an elliptical cluster member. Possibly, for CL 0230+1836 we see a red cluster sequence in the process of formation.

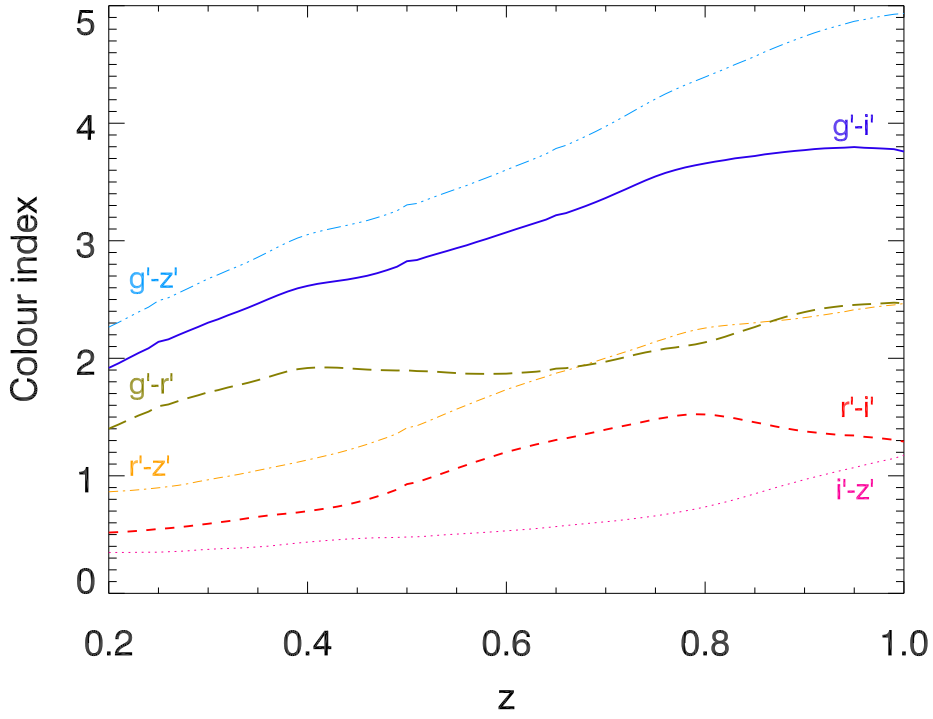

Figure 7.10: Colour indices of the CWW80 elliptical galaxy template as a function of redshift z. Thick lines show colour indices available from $g'r'i'$ data computed with `HyperZ` in the MMT/Megacam passbands. The solid, long-dashed and short-dashed lines give $g'-i'$, $g'-r'$, and r'–i' colours, respectively. With an additional z' filter, the i'–z' (dotted line), r'–z' (dot-dashed line), and $g'-z'$ (triple dot-dashed line) could be computed.

Based on the distribution of galaxies in the colour-magnitude diagrams, we define all galaxies $2.0 < g'-i' < 3.0$ in the CL 0159+0030 and CL 0809+2811 fields to be "red sequence-like" galaxies, as well as those with $2.5 < g'-i' < 5.0$ for CL 0230+1836. In all three fields we find the "red sequence-like" galaxies to be more concentrated around the cluster centre than around a random position. The right panels of Fig. 7.11 present the fractions $f_{\rm cg}$ of "red sequence-like" galaxies in the galaxy shape (open symbols) and lensing (filled symbols) catalogues as a function of the distance θ to the Rosat cluster centre. We observe a strong increase of $f_{\rm cg}$ towards small θ for CL 0230+1836 and CL 0809+2811, and a very weak one for CL 0159+0030. Again, as for CL 0030+2618 (Fig. 6.11), the influence of background selection on $f_{\rm cg}$ is small in all cases. In the same way as for CL 0030+2618, we fit Eq. (6.4) to the measured $f_{\rm cg}(\theta)$ and determine the contamination correction factors $f_1(\theta)$ for the three clusters from these fits. No such correction is applied for the single-band clusters (Sect. 7.2.2). Noticing that the fits in Fig. 6.11 do not give a very good representation of the data, we plan to revise the functional form Eq. (6.4) for future analyses. We repeated this step using the lensing centres instead of the Rosat centres and come to similar results.

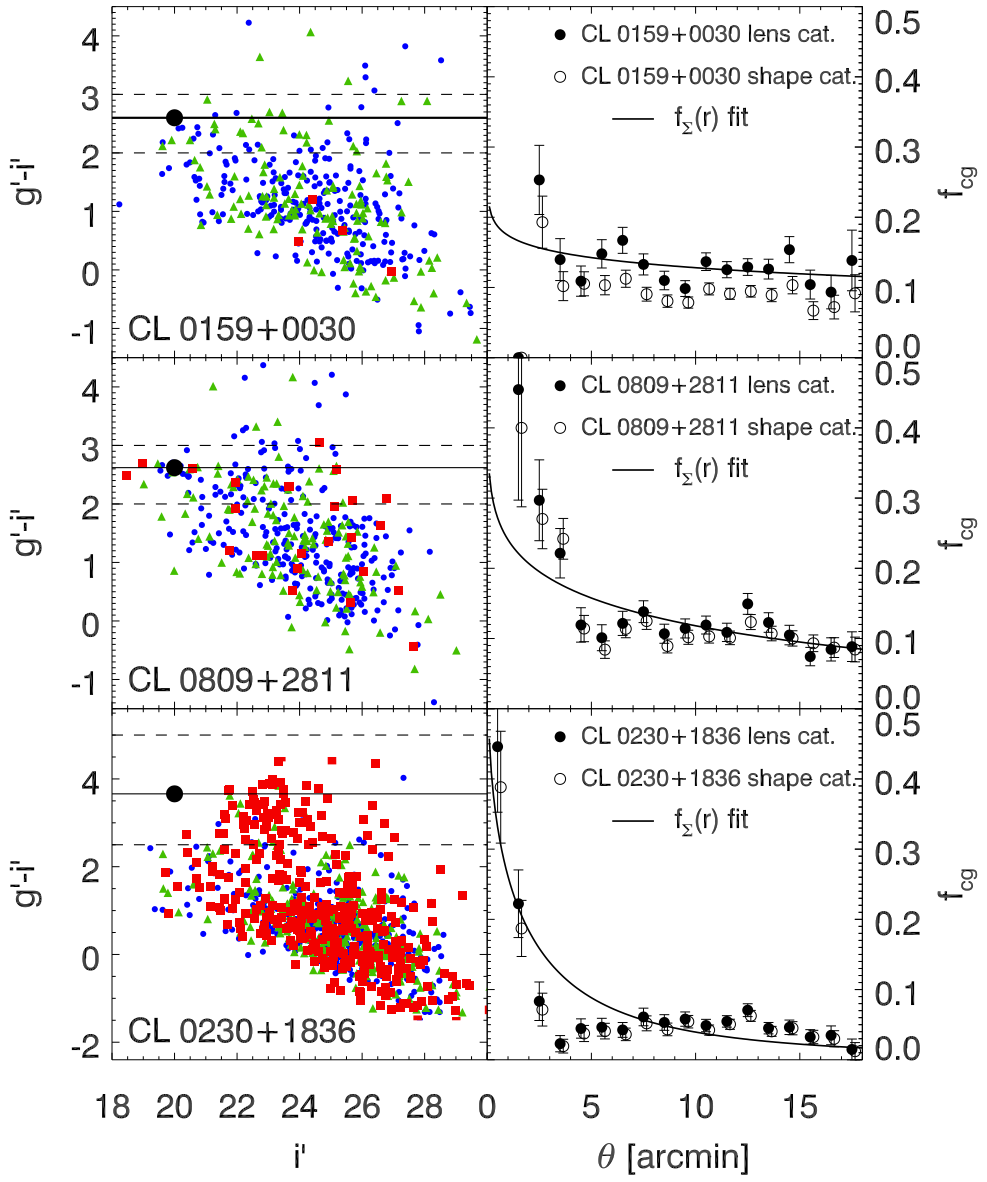

Figure 7.11: Correction for dilution by cluster members ("decontamination") for the clusters CL 0159+0030, CL 0230+1836, and CL 0809+2811. *Left panels:* In analogy to Fig. 6.5, the $g' - i'$ versus i' colour-magnitude diagrams for the galaxy shape catalogues of the three fields are shown. Galaxies within 4′, 3′, and 2′ separation from the ROSAT cluster centres are indicated by filled circles, triangles and squares. The solid line and big filled circle denote the $g' - i'$ colour calculated for the CWW80 elliptical galaxy template at the cluster redshift. Dashed lines mark the regions in which we define the respective samples of "red sequence-like" galaxies. *Right panels:* The fractions $f_{\rm cg}$ of "red sequence-like" galaxies as a function of separation θ in the galaxy shape (open symbols) and lensing catalogues (filled symbols). As in Fig. 6.11, the solid lines denote the best-fit of Eq. (6.4) to the lensing catalogues. The decontamination factors f_1 for the three data sets are determined from these fits.

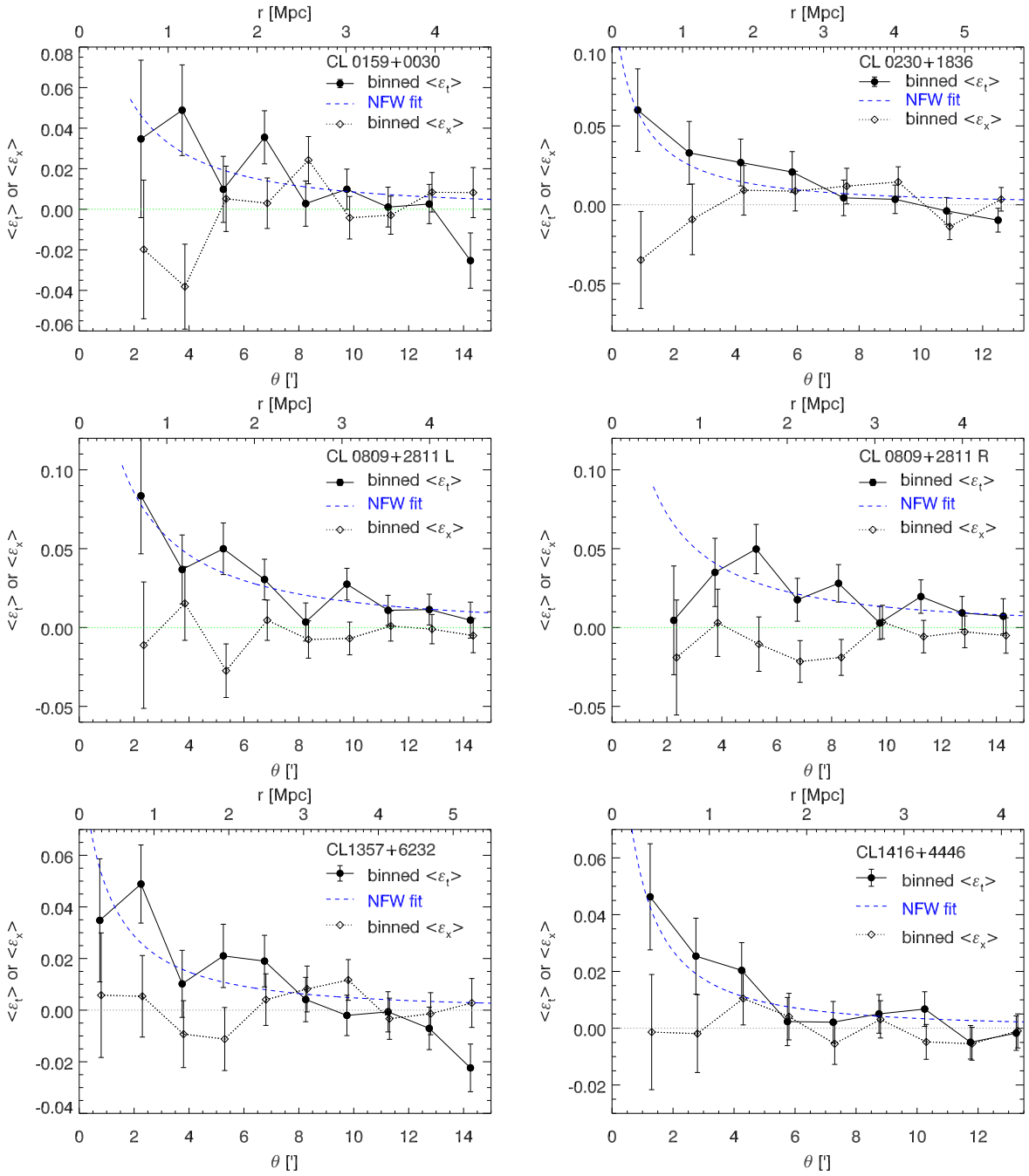

Figure 7.12: Shear profiles measured in five clusters: Shown are, from top left to bottom right, CL 0159+0030 (centred on ROSAT peak), CL 0230+1836, CL 0809+2811, CL 0809+2811 (centred on ROSAT peak), CL 1357+6232, and CL 1416+4446. If not stated otherwise, the S-statistics centres are assumed. Within each plot, filled circles with error bars give the mean and standard deviation of the measured shear $\langle\varepsilon_t(\theta)\rangle$ in bins. Diamonds with error bars show the same for the cross component $\langle\varepsilon_\times(\theta)\rangle$. Dashed curves present the best NFW fits to the unbinned shear data of the respective cluster.

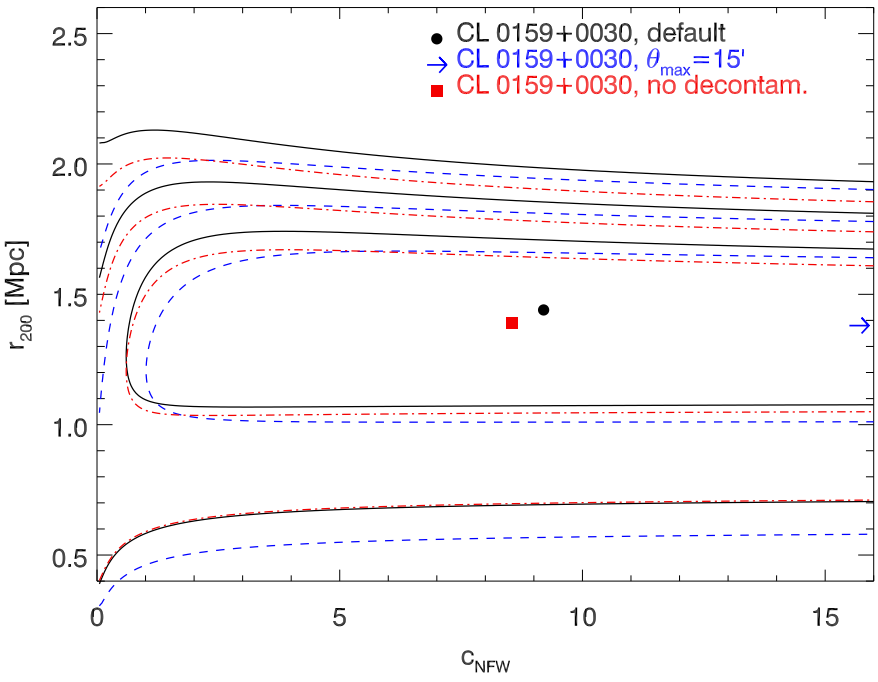

Figure 7.13: Confidence contours (99.73%, 95.4%, and 68.3%) and cluster parameters minimising $\chi^2_{\rm L}$ (Eq. 6.12) for three models of CL 0159+0030. Shown are the default model, including lensing catalogues sources at $\theta < 13\farcm33$ (solid contours and filled circle), the same model for $\theta < 15\farcm0$ (dashed contours and arrow), and a model without correction for the shear dilution by cluster members (dot-dashed contours and square).

7.3.2 Mass Modelling for CL 0159+0030

The lensing analysis of CL 0159+0030 is determined and limited by the fact that this field has the largest masks near the cluster centre, due to a bright star at less than 2′ separation (Table 5.1). In our lensing catalogue defined in Sect. 7.2.1, we measure a smallest separation of $\theta = 112''$ for a background galaxy to the ROSAT centre of CL 0159+0030. This corresponds to a distance of 580 kpc at the cluster redshift of $z = 0.39$.

The masks resulting from the detection of over- and underdense regions (Sect. 5.1.3), using the default settings applied to all our cluster fields, can be seen in Fig. 7.23 in Sect. 7.4. The BCG of CL 0159+0030, just right to the ROSAT centre of CL 0159+0030 marked by a star symbol, resides in a region of the image strongly affected by stray light of the bright star. Orange contours in Fig. 7.23 give the S-statistics measured from the lensing catalogue, starting at $S = 0.5$ and with an increment of $\Delta S = 0.5$. Despite the large masks, the strongest S-peak in the field can be attributed to CL 0159+0030. Note that, due to the filter scale of $\theta_{\rm out} = 10\farcm5$ we applied in Fig. 7.23, we measure S also in grid cells which are centred within masks. Indeed, the highest S-value is found in such a grid cell whose position and size of 15″ are indicated by a green square with error bars in Fig. 7.23.

Nevertheless, due to the masking, there is little variation between neighbouring grid cells in the masked area near the cluster. As a consequence, the position of the peak is less robust against variations in $m_{\rm faint}$ or $\theta_{\rm out}$ than the S-peaks of the other clusters. Hence, we use the ROSAT centre of CL 0159+0030 instead of the S-centre in subsequent analyses. We interpret the rather large

separation of $\Delta\theta = 79''$ between the two peaks as being mainly caused by the poor accuracy in the determination of the lensing centre.

The upper left panel of Fig. 7.12 shows the tangential shear profile $\langle\varepsilon_t(\theta)\rangle$ of CL 0159+0030, using the ROSAT centre, in analogy to Fig. 6.12 for CL 0030+2618: We consider the weighted shear estimator $f_0 f_1(\theta)\varepsilon(\theta)$, where $f_0 = 1.08$ is the global shear calibration factor and $f_1(\theta)$ the correction for cluster members determined in Sect. 7.3.1. This is done consistently for all three-band clusters. The measured $\langle\varepsilon_t(\theta)\rangle$ (black symbols, shown in bins of 1.′5 width) agrees well with an NFW profile (dashed curve), we fit using the same method as for CL 0030+2618 (Sect. 6.4.3), but keeping $c_{\rm NFW} = 4.0$ fixed, as it is poorly constrained by our data set with few points near the cluster centre. Our fit assumes $\langle D_{\rm ds}/D_{\rm s}\rangle = 0.447$, estimated for $z_{\rm d} = 0.39$ in Table 6.4. We measure $\chi^2/\nu_{\rm dof} = 6302/6229 \approx 1.01$ and obtain $r_{200}^{\rm fit} = 1.50 \pm 0.24\,$Mpc. Noting a coincidence between the highest value of $\langle\varepsilon_t(\theta)\rangle$ found in the $3.'0 \le \theta < 4.'5$ bin with the value of the cross-component $\langle\varepsilon_\times(\theta)\rangle$ (open diamonds in Fig. 7.12) which is least consistent with zero, we emphasise that $\varepsilon_\times = 0$ lies within the 1σ margin for seven of nine bins.

To determine the mass of CL 0159+0030, we evaluate the merit function (Eq. 6.12) for a grid of points in r_{200} and $c_{\rm NFW}$, following the method of Sect. 6.4.4. The confidence contours resulting from the default model including all sources at $\theta < 13.'33$ and otherwise assuming the same parameter values as for the fit to $\langle g_t(\theta)\rangle$ are presented in Fig. 7.13 (solid contours and filled circle). The minimum of $\chi^2_{\rm L}$ (Eq. 6.12) is found for $r_{200}^{\rm min} = 1.44^{+0.18}_{-0.22}\,$Mpc. All quoted errors are statistical 1σ uncertainties for *one* interesting parameter. The corresponding concentration parameter $c_{\rm NFW}^{\rm min} = 9.2$ is hardly constrained by the data: In the default case, the upper 1σ limit of $c_{\rm NFW}^{\rm min} = 9.2$ is outside the range $0.05 \le c_{\rm NFW} < 16.00$ we probe. The same holds for the best value if all sources $\theta < 15.'0$ are included in the analysis (dashed contours and diamond in Fig. 7.13). From the confidence contours, that for $c_{\rm NFW} \gtrsim 3$ are basically parallel to the $c_{\rm NFW}$-axis in Fig. 7.13, we conclude that our data cannot constrain it because of missing information at small θ. We therefore give only a lower limit to $c_{\rm NFW}$ in Table 7.3 (Sect. 7.3.9), where we compile the results for the default model of CL 0159+0030 and all variations to it that we tested. For example, "switching off" the correction for cluster members ($f_1(\theta) = 1$, dot-dashed contours and square in Fig. 7.13) has a small effect, insignificant compared to the statistical mass errors (Table 7.3). From $r_{200}^{\rm min}$ for the default model, we compute $M_{200} = 5.4^{+2.3}_{-2.1} \times 10^{14}\,{\rm M}_\odot$ for CL 0159+0030. We discuss this mass estimate and its uncertainties, estimated from the different models listed in Table 7.3, in Sect. 8.2. Confidence contours for these alternative models are presented in Fig. B.10 Appendix B.3.

7.3.3 Mass Modelling for CL 0809+2811

Concerning the large masks, CL 0809+2811 bears similarity to CL 0159+0030 and thus provides an interesting comparison. Here, the bright star is even closer to the ROSAT coordinates of the cluster (1.′5, Table 5.1), but relative to the stronger shear signal (Table 7.2), the masking is not as extensive as for CL 0159+0030. This is visualised in Fig. 7.24, showing the S-contours and masks for CL 0809+2811 the same way Fig. 7.23 does for CL 0159+0030. The smallest separation of a source galaxy to the ROSAT coordinates of CL 0809+2811 we measure is $\theta = 83''$, or 430 kpc at the cluster redshift of $z = 0.40$.

Being the second-strongest detection in our MEGACAM data set, the shear peak of CL 0809 +2811 is by far the most prominent in its field. However, probably due to the loss of positional accuracy caused by the masking, the S-peak is separated by $178''$ from the ROSAT centre. In contrast to CL 0159+0030, it makes a bigger difference for CL 0809+2811 whether the S-peak or the ROSAT centre is chosen as the centre of the shear profile.

The resulting tangential shear profiles are shown in the middle left ("L" as in lensing) and middle right ("R" as in ROSAT) plot of Fig. 7.12, respectively. Centred on the lensing peak, we

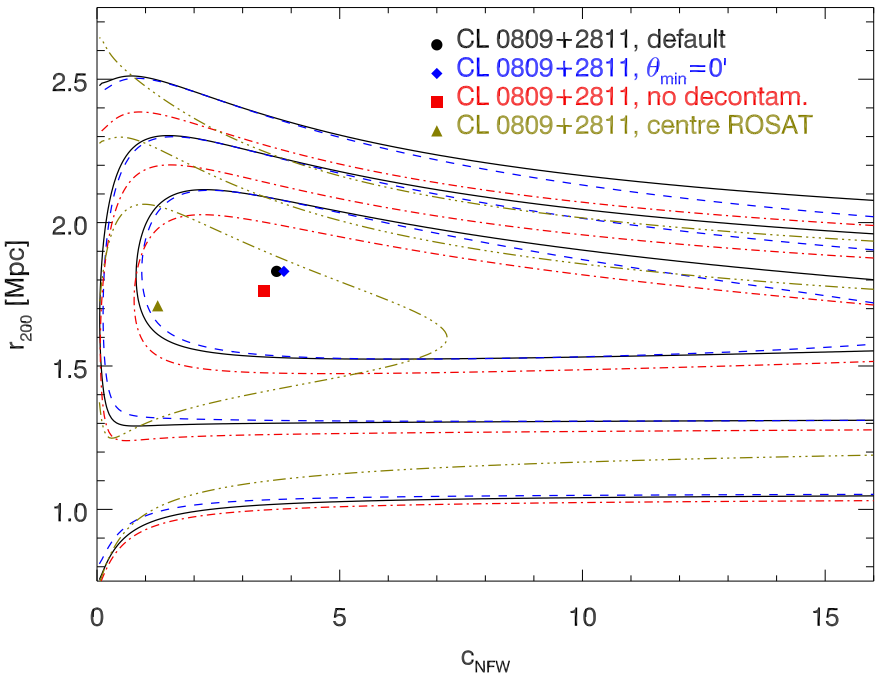

Figure 7.14: Confidence contours (99.73%, 95.4%, and 68.3%) and cluster parameters minimising $\chi^2_{\rm L}$ (Eq. 6.12) for four models of CL 0809+2811. Shown are the default model, centred on the S-peak and including lensing catalogues sources at $1\farcm5 < \theta < 15\farcm0$ (solid contours and filled circle), the same model for $0' < \theta < 15\farcm0$ (dashed contours and diamond), and a model without correction for shear dilution by cluster members (dot-dashed contours and square). The triple-dot dashed contours and diamond show the results of an analysis using the Rosat centre of CL 0809+2811.

measure a high $\langle\varepsilon_{\rm t}\rangle = 0.084 \pm 0.036$ in the innermost ($1\farcm5 < \theta < 3\farcm0$) bin, compared to the $\langle\varepsilon_{\rm t}\rangle = 0.005 \pm 0.034$ if the centre is set to the Rosat centre. Note that each of these bins contains only ≈ 1.4 % of the lensing catalogue. Concerning the NFW fit to the $\langle\varepsilon_{\rm t}(\theta)\rangle$ profile, the resulting values of $r^{\rm fit}_{200} = 1.98 \pm 0.18$ Mpc for the "L" case and $r^{\rm fit}_{200} = 1.81 \pm 0.20$ Mpc for the "R" case are in marginal agreement. Again, $c_{\rm NFW} = 4.0$ was held fixed. We point out that the visual impression of binned shear profiles as in Fig. 7.12 can be misleading: The fits in the "L" case with $\chi^2/\nu_{\rm dof} = 5818/5784 \approx 1.01$ and the "R" case with $\chi^2/\nu_{\rm dof} = 5439/5408 \approx 1.01$ are statistically equally good. In both shear profiles, the factor $f_1(\theta)$ correcting for cluster members (Sect. 7.3.1) was obtained w.r.t. the correct centre, because we find a noticeable difference between the two cases. At $z_{\rm d} = 0.40$, we assume $\langle D_{\rm ds}/D_{\rm s}\rangle = 0.447$ for the NFW shear model. The cross-component $\langle\varepsilon_\times(\theta)\rangle$ is overall consistent with zero for the "L" profile and slightly biased to negative values for the "R" profile.

We base the default model for the evaluation of the r_{200}–$c_{\rm NFW}$–grid on the S-peak of CL 0809 +2811 and compute Eq. (6.12) from all source galaxies at separations $1\farcm5 < \theta < 15\farcm0$. The resulting confidence contours are shown by the solid curves in Fig. 7.14. A filled circle represents cluster parameters minimising Eq. (6.12), $r^{\rm min}_{200} = 1.83^{+0.16}_{-0.19}$ Mpc and $c^{\rm min}_{\rm NFW} = 3.7^{+5.1}_{-2.2}$. The concentration parameter is not well constrained by the data, but better as in CL 0159+0030. Table 7.4 (Sect. 7.3.9) summarises the cluster parameters for all models we tested for CL 0809+2811. Noting that the 1σ contour seems to close not too far outside the highest value $c_{\rm NFW} = 16.0$ we tested, we plan

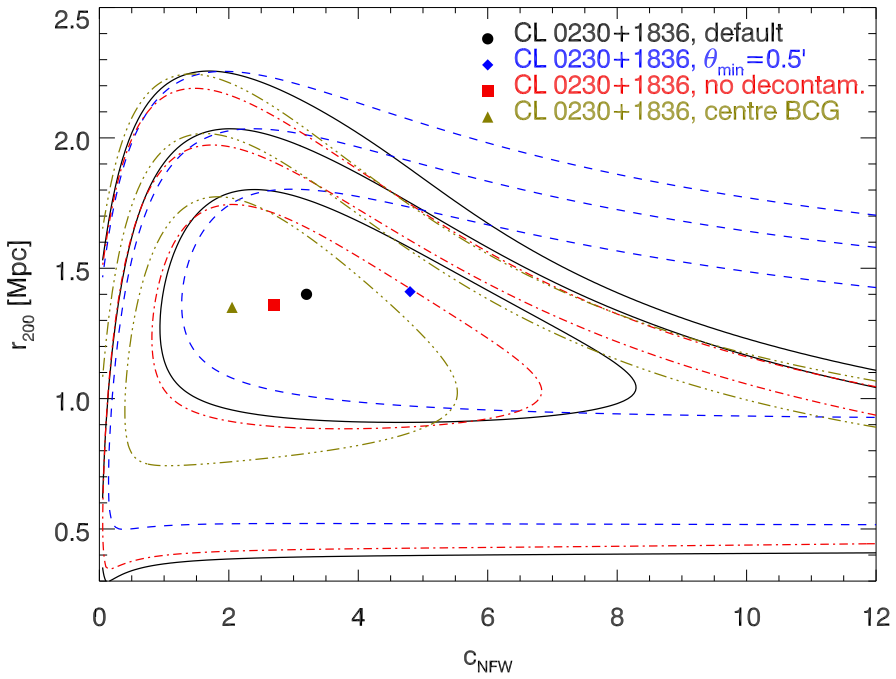

Figure 7.15: Confidence contours (99.73%, 95.4%, and 68.3%) and cluster parameters minimising $\chi^2_{\rm L}$ (Eq. 6.12) for four models of CL 0230+1836. Symbols and line-styles have the same meaning as in Fig. 7.14, except that the default includes all sources $0' < \theta < 13.'33$ and the dashed contours and diamond denote the case where sources $0.'5 < \theta < 13.'33$ are considered.

to explore higher concentrated models of CL 0809+2811 in the future. We constrain the mass of CL 0809+2811 to $M_{200} = 11.2^{+3.2}_{-3.2} \times 10^{14}\,{\rm M}_\odot$.

Repeating the analysis of the r_{200}–$c_{\rm NFW}$–grid centred on the RosAT centre of CL 0809+2811, the results differ somewhat, although within the statistical uncertainty (triple-dot dashed contours and triangle in Fig. 7.14): We obtain a smaller $r^{\rm min}_{200} = 1.71^{+0.23}_{-0.24}$ Mpc, but with larger uncertainties, leading to a mass estimate of $M_{200} = 9.2^{+4.7}_{-3.3} \times 10^{14}\,{\rm M}_\odot$. The corresponding concentration parameter is at $c^{\rm min}_{\rm NFW} = 1.25^{+2.3}_{-0.9}$ better constrained to high values, but very small $c_{\rm NFW} \approx 0$ are not ruled out. Changing the default, S-peak centred model of CL 0809+2811 by also including sources at separations $< 1.'5$ (dashed contours and diamond in Fig. 7.14; note that the smallest separation is $64''$ in this case) or applying no correction for shear dilution by cluster members (dot-dashed contours and square in Fig. 7.14) result in smaller differences in the returned cluster parameters than using the RosAT centre. We refer to Table 7.4 for the values of $r^{\rm min}_{200}$, $c_{\rm NFW}$, and M_{200} for those and other models we discuss in the error analysis in Sect. 8.2. Confidence contours for these alternative models are presented in Fig. B.12 in Appendix B.3.

7.3.4 Mass Modelling for CL 0230+1836

For our most distant and therefore most difficult cluster in terms of shear signal detection, CL 0230+1836 at $z_{\rm d} = 0.80$, the masking poses a less severe problem than for CL 0159+0030 and CL 0809+2811. As shown in the overlay of the optical image (Fig. 7.25) with the masks (thin red lines) and the S-contours (thick orange lines, starting at $S = 0.5$ and increasing in steps of $\Delta S = 0.5$), the RosAT centre of CL 0230+1836 is located safely outside the masked region. In this case, the

separation between the bright star and the ROSAT centre is larger ($\theta = 3\farcm59$) than for the other two clusters. Besides the shear peak close to the ROSAT centre and the likely BCG of CL 0230+1836, we observe several less significant shear peaks in the CL 0230+1836 field.[3] We discuss these in Sect. 8.1.3. Searching for the shear peak using our usual grid of 15″ mesh size, we find the ROSAT centre (star symbol in Fig. 7.25) to be separated by 20″ from the centre of the grid cell with the maximum S, and just outside this grid cell (green square with error bars in Fig. 7.25).

The upper right plot in Fig. 7.12 presents the tangential shear profile $\langle\varepsilon_\mathrm{t}(\theta)\rangle$ of CL 0230+1836. We measure a positive tangential alignment within $\sim 7'$ from the (lensing) cluster centre. There is no significant cross component $\langle\varepsilon_\times(\theta)\rangle$. Assuming $\langle D_\mathrm{ds}/D_\mathrm{s}\rangle = 0.168$ (Table 6.4), we fit an NFW shear profile to $\langle\varepsilon_\mathrm{t}(\theta)\rangle$ and find good agreement with $\chi^2/\nu_\mathrm{dof} = 5488/5547 \approx 0.99$. The best-fit results for the cluster parameters are $r_{200}^\mathrm{fit} = 1.51 \pm 0.32\,\mathrm{Mpc}$ and $c_\mathrm{NFW}^\mathrm{fit} = 3.4 \pm 2.5$. Note that because of the less extensive masking, we are able to constrain the concentration parameter better than for CL 0159+0030 and CL 0809+2811.

The high value for r_{200} returned by the Levenberg-Marquardt method with the σ_fit error model points to CL 0230+1836 being a very massive cluster, given its large redshift. We provide a more thorough mass estimation by applying the method introduced in Sect. 6.4.4. For our default model, we evaluate Eq. (6.12) for all source galaxies $0' < \theta < 13\farcm33$ and measure its minimum for $r_{200}^\mathrm{min} = 1.40^{+0.24}_{-0.29}\,\mathrm{Mpc}$ and $c_\mathrm{NFW}^\mathrm{min} = 3.2^{+1.9}_{-1.6}$. These results are illustrated by the filled circle and the solid confidence contours in Fig. 7.15. Via Eq. (6.7), our r_{200}^min corresponds to a mass of $8.1^{+4.0}_{-4.9}\times10^{14}\,\mathrm{M}_\odot$ for CL 0230+1836.

Excluding sources at separation $\theta < 0\farcm5$ from the analysis does not alter the radius estimate significantly ($r_{200}^\mathrm{min} = 1.41^{+0.22}_{-0.27}\,\mathrm{Mpc}$), but leads to a loss of constraining power for $c_\mathrm{NFW}^\mathrm{min} = 4.8^{+4.4}_{-2.65}$ (see Table 7.5 in Sect. 7.3.9 and the dashed contours and diamond in Fig. 7.15). The cluster parameters for further models, e.g. centred on the BCG position instead of the shear peak (dot-dashed contours and square in Fig. 7.15), or without correction for cluster members (triple-dot-dashed contours and triangle in Fig. 7.15) are summarised in Table 7.5. We return to these results for the error analysis in Sect. 8.2. Here, we point out that repeating the analysis of the r_{200}–c_NFW–grid with the lensing catalogue derived from the magnitude cut at $m_\mathrm{faint} = 23.4$ that, as we saw in Sect. 7.2.1, results in a more significant detection of CL 0230+1836 than the default lensing catalogue, we obtain $r_{200}^\mathrm{min} = 1.51^{+0.24}_{-0.29}\,\mathrm{Mpc}$ and $c_\mathrm{NFW}^\mathrm{min} = 3.2^{+1.65}_{-1.45}$, resulting in a higher mass estimate of $10.2^{+5.7}_{-4.8}\times10^{14}\,\mathrm{M}_\odot$ for CL 0230+1836, but within the statistical uncertainty. The confidence contours for these models are shown in Fig. B.11 in Appendix B.3.

7.3.5 Mass Modelling for CL 1357+6232

Figure 7.26 shows an overlay of the r'-band image of CL 1357+6232 with the S-statistics contours measured using the lensing catalogue we defined in Sect. 7.2.2. Despite being one of the two fields with the shallowest exposure ($T_\mathrm{exp} = 2700\,\mathrm{s}$) and having the poorest seeing of $0\farcs90$ in our sample, we clearly detect CL 1357+6232 at a significance level of $\approx 4.5\sigma$ (Table 7.2) as the most significant shear peak in the field. Performing 10^5 bootstrap resamples of the CL 1357+6232 lensing catalogue using the same method as for CL 0030+2618 (Sect. 6.3.1), we determine the lensing centre of CL 1357+6232 and its uncertainty (shown as a green filled circle with error bars in Fig. 7.26). We find the centre obtained by bootstrapping to lie inside the 15″ wide grid cell giving the highest S value, which we used as a preliminary lensing centre. The separation of the final lensing centre from the ROSAT centre is $\theta = 50''$; the one from the BCG candidate $\theta = 44''$. We measure $\theta = 19''$ separation between the ROSAT centre and the BCG candidate (which is hardly visible in Fig. 7.26 because of the contour lines).

[3] We identify as the likely BCG of CL 0230+1836 an elliptical galaxy at $\alpha_\mathrm{J2000} = 02^\mathrm{h}30^\mathrm{m}28\fs7$ and $\delta_\mathrm{J2000} = +18°36'11''$, based on its extended light distribution. This galaxy is separated by 32″ from the lensing centre.

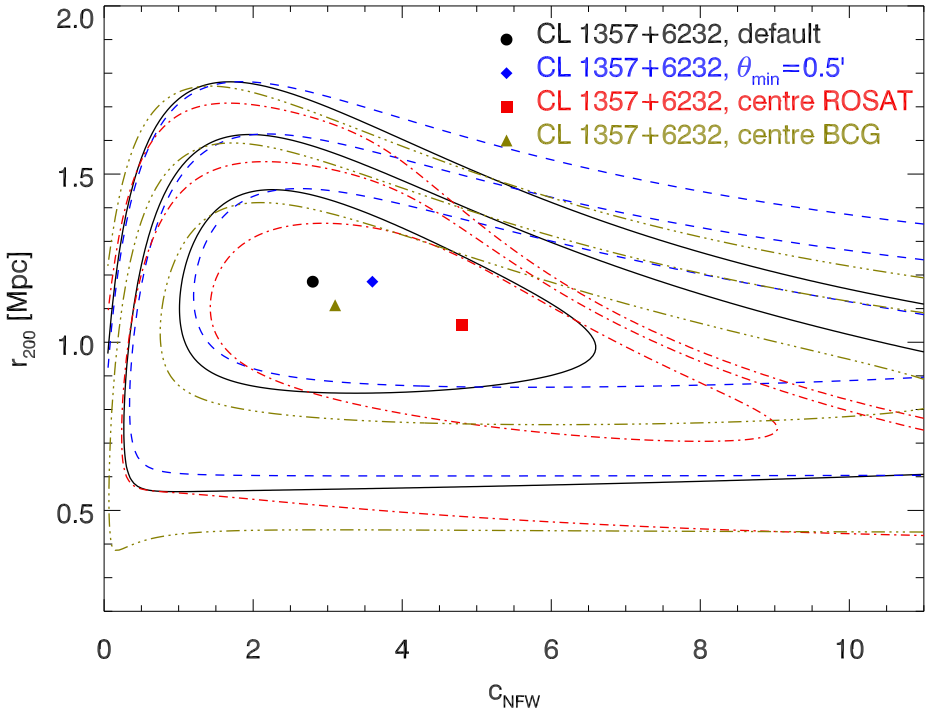

Figure 7.16: Confidence contours (99.73%, 95.4%, and 68.3%) and cluster parameters minimising $\chi^2_{\rm L}$ (Eq. 6.12) for four models of CL 1357+6232. Solid contours and the filled circle denote the default model, including all sources within $0' < \theta < 15'$ around the lensing centre. Dashed contours and a diamond mark the model with a range $0\farcm5 < \theta < 15'$. Models centred on the ROSAT centre and the BCG are given by dot-dashed contours and a square, and triple-dot dashed contours and a triangle, respectively.

As presented in the lower left plot of Fig. 7.12, CL 1357+6232 exhibits a positive tangential alignment $\langle\varepsilon_{\rm t}(\theta)\rangle$ of source galaxies until $\sim 7'$ separation, and insignificant cross component $\langle\varepsilon_{\times}(\theta)\rangle$. Note that, for CL 1357+6232 and the other single-band clusters (Sect. 7.2.2) *no correction for contamination by cluster members is applied* to the shear estimates. Fitting an NFW profile to the $\varepsilon_{\rm t}(\theta)$ with the Levenberg-Marquardt method gives a goodness-of-fit of $\chi^2/\nu_{\rm dof} = 7670/7761 \approx 0.99$ and a virial radius estimate $r^{\rm fit}_{200} = 1.26 \pm 0.22$ Mpc and concentration parameter $c^{\rm fit}_{\rm NFW} = 2.9 \pm 2.1$ for CL 1357+6232, making it less massive than CL 0030+2618 at a similar redshift ($z_{\rm d} = 0.53$ compared to $z_{\rm d} = 0.50$ for the latter). We assume $\langle D_{\rm ds}/D_{\rm s}\rangle = 0.324$ (Table 6.4).

Computing the merit function (Eq. 6.12) for the same grid in r_{200} and $c_{\rm NFW}$ that we used for the three-band clusters, we obtain the following parameters minimising $\chi^2_{\rm L}$ for CL 1357+6232: $r^{\rm min}_{200} = 1.18^{+0.17}_{-0.20}$ Mpc and a concentration of $c^{\rm min}_{\rm NFW} = 2.8^{+1.65}_{-1.25}$. Thus, we infer a mass of $3.5^{+1.7}_{-1.5} \times 10^{14} {\rm M}_{\odot}$. In this default model (filled circle and solid confidence contours in Fig. 7.16), all sources at $0' < \theta < 15\farcm0$ have been included. Table 7.6 in Sect. 7.3.9 lists the cluster parameters and masses for all models tested for CL 1357+6232. Removing sources $\theta < 0\farcm5$ close to the cluster centre from the analysis (dashed contours and diamond in Fig. 7.16) leaves $r^{\rm min}_{200}$ unchanged – indicating that the uncorrected dilution by cluster members is small – but leads to a larger uncertainty in $c_{\rm NFW}$,

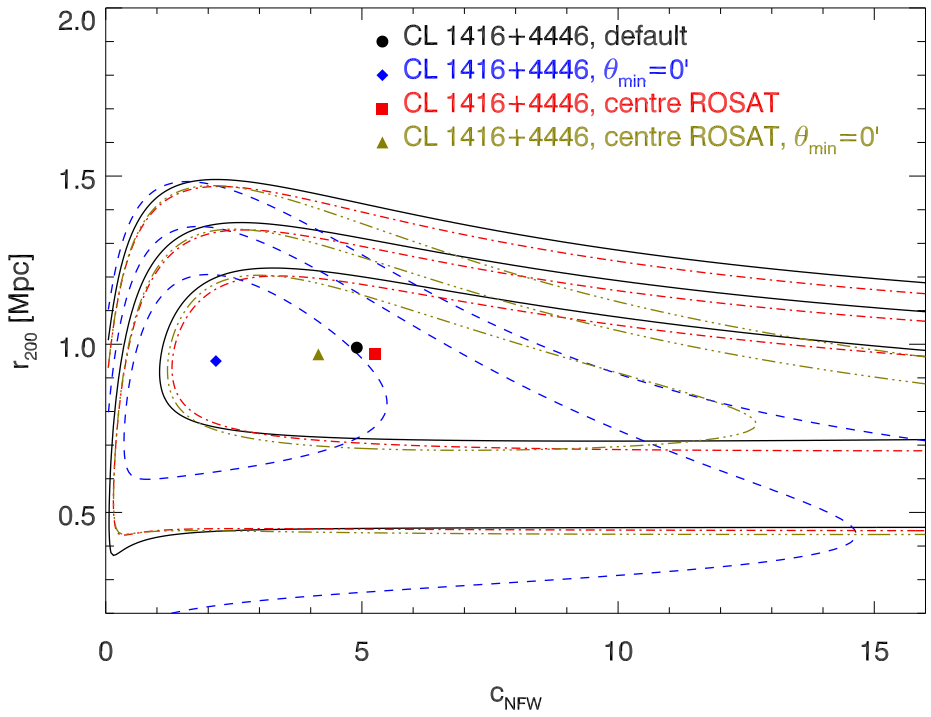

Figure 7.17: Confidence contours (99.73%, 95.4%, and 68.3%) and cluster parameters minimising $\chi^2_{\rm L}$ (Eq. 6.12) for four models of CL 1416+4446. The default model (solid contours and filled circle) includes all sources in a range $0\farcm5 < \theta < 12'$ around the lensing centre. A model with range $0' < \theta < 12'$ is given by dashed contours and a diamond. The dot-dashed contours and square, and the triple-dot dashed contours and triangle mark cases with the same two ranges, but centred on the ROSAT centre.

such that the 1σ contours close beyond the largest value of $c_{\rm NFW} = 16$ we tested.[4] Models centred on the ROSAT centre (dot-dashed contours and square in Fig. 7.16) or the BCG candidate (triple-dot dashed contours and triangle in Fig. 7.16) give slightly lower values for $r_{200}^{\rm min}$ and, hence, the cluster mass (Table 7.6). Confidence contours for the further cases considered for the error analysis in Sect. 8.2 can be found in Fig. B.13 in Appendix B.3.

7.3.6 Mass Modelling for CL 1416+4446

At most filter scales $\theta_{\rm out}$ in the S-statistics (Eq. 3.29), CL 1416+4446 is the weakest detection among the *400d* clusters we analysed. Only at small filter scales $\theta_{\rm out} \approx 5'$, it is detected at a $> 4\sigma$ significance level. This gives a first hint of its low mass. Figure 7.27 shows the S-contours of CL 1416+4446 at the best filter scale, $\theta_{\rm out} = 4\farcm83$, overlaid on the r'-band MEGACAM image. The overall pattern of the shear signal in Fig. 7.27 is robust also at larger $\theta_{\rm out}$, meaning more smoothing: From the highest S-peak close to the ROSAT centre of CL 1416+4446 (big star symbol in Fig. 7.27, also covering the BCG at $6''$ separation), the signal extends to a south-eastern direction. There exist two other shear peaks at $> 3\sigma$ significance to the west and southwest of CL 1416+4446. As we will detail in Sec. 8.1.3, these peaks correspond to known clusters (small star symbols)

[4] We will extend the exploration of the parameter space to stronger concentrated models in the future.

at redshifts similar to $z_d = 0.40$ measured for CL 1416+4446. For the time being, we investigate CL 1416+4446 as a single cluster of galaxies.

Due to the morphology of the shear signal, the 1σ uncertainty in the shear centre derived from 10^5 bootstrap resamples of the lensing catalogue (filled green circle with error bars in Fig. 7.27) is rather large: $43''$ in the x- or α_{J2000}-direction and $56''$ in the y- or δ_{J2000}-direction. We note that the bootstrapping lensing centre is south of the most significant grid cell (indicated in Fig. 7.27 by the 4σ contour) and the ROSAT centre, which both are covered by its error ellipse.

The tangential shear profile of CL 1416+4446 in the lower right plot of Fig 7.12 shows a positive tangential component $\langle\varepsilon_t(\theta)\rangle$ in the inner $\sim 5'$ around the shear centre. The cross component is consistent with zero. As for CL 1357+6232 no correction for cluster members could be applied to this single-band cluster. The $\langle\varepsilon_t(\theta)\rangle$ profile is well represented by an NFW fit (fitting the range $0.'5 < \theta < 14.'0$ and assuming $\langle D_{ds}/D_s\rangle = 0.437$ from Table 6.4), with $\chi^2/\nu_{dof} = 12639/12453 \approx 1.01$. We obtain the parameters $r_{200}^{fit} = 1.06 \pm 0.18$ Mpc and $c_{NFW}^{fit} = 4.9 \pm 4.7$ for CL 1416+4446.

Evaluating χ^2_L on the r_{200}–c_{NFW}-grid, the default model with the above-mentioned range yields a radius estimate $r_{200}^{min} = 0.99^{+0.14}_{-0.16}$ Mpc (filled circle and solid confidence contours in Fig. 7.17). This results in a mass estimate of $1.8^{+0.9}_{-0.7}\times10^{14}M_\odot$ for CL 1416+4446. The 1σ confidence contours of the concentration parameter $c_{NFW}^{min} = 4.9^{+5.65}_{-2.95}$ in the default model extend beyond $c_{NFW} = 16$, the largest tested value, as Table 7.7 in Sect. 7.3.9 shows.[5] Including all sources $0' < \theta < 14.'0$ to the analysis, c_{NFW} is constrained better, with a slightly lower r_{200}^{min} (see Table 7.7 and diamond and dashed confidence contours in Fig. 7.17). Using the ROSAT centre in the analysis of χ^2_L returns higher values for c_{NFW}, both in the case $\theta_{min} = 0.'5$ (square and dotted contours in Fig. 7.17) and for $\theta_{min} = 0'$ (triangle and triple-dot dashed contours in Fig. 7.17). This does not come unexpected, because the ROSAT centre lies closer to the highest S grid cell than the bootstrapping lensing centre. Table 7.7 includes the results for all models tested for CL 1416+4446. The confidence contours for the cases discussed in the error analysis (Sect. 8.2) are presented in Fig. B.14 in Appendix B.3.

7.3.7 Mass Modelling for CL 1701+6414

A weak lensing analysis of CL 1701+6414 has to deal with shear by multiple structures. At first glance, the MEGACAM image (shown in Fig. 7.28 overlaid with S-contours and masks) not only shows CL 1701+6414 – the five-pointed star symbol marks the ROSAT centre – but also a rich cluster of galaxies $\sim 4.'5$ to the west. Abell 2246 (big four-pointed star symbol in Fig. 7.28, masked due to the high concentration of galaxies) was detected as BVH 210 in the *400d* survey (Burenin et al. 2007) with a luminosity $L_X = 6.10 \times 10^{43}\,\mathrm{erg\,s^{-1}}$ in the ROSAT 0.5–2.0 keV band and a redshift of $z = 0.225$. Thus, it is not part of the distant cosmological subsample (Sect. 4.1.2), but a likely cluster lens. Both CL 1701+6414 and A 2246 are also included in the *160d* survey (Vikhlinin et al. 1998), as VMF 190 and VMF 189. This ROSAT catalogue lists two further clusters in the field, VMF 191 at $z = 0.220$ and VMF 192 at $z = 0.224$ (small star symbols in Fig. 7.28).

Also from an analysis of ROSAT data, Donahue et al. (2002) detect these same four clusters and a further one (RX J1702+6407) which we do not detect. Applying the Postman et al. (1996) matched filter technique to KPNO 4 m data, they assign optical counterparts to the four clusters included in the *160d* survey. The redshift of $z = 0.7$ found for the Donahue et al. (2002) optical counterpart of CL 1701+6414 deviates from the redshift of $z = 0.45$ measured by Burenin et al. (2007) and all other references. CL 1701+6414 is further listed as RX J1701.3+6414 in the *Bright Serendipitous High-Redshift Archival* ROSAT *Cluster* sample (Bright SHARC, Romer et al. 2000).

As the S-contours in Fig. 7.28 show, all four known clusters correspond to regions of high M_{ap}-significance. The strongest shear peak $S = 4.3\sigma$ is located at the position of A 2246, whereas

[5] Note that that all errors given, e.g. in Table 7.7 are calculated for *one* interesting parameter.

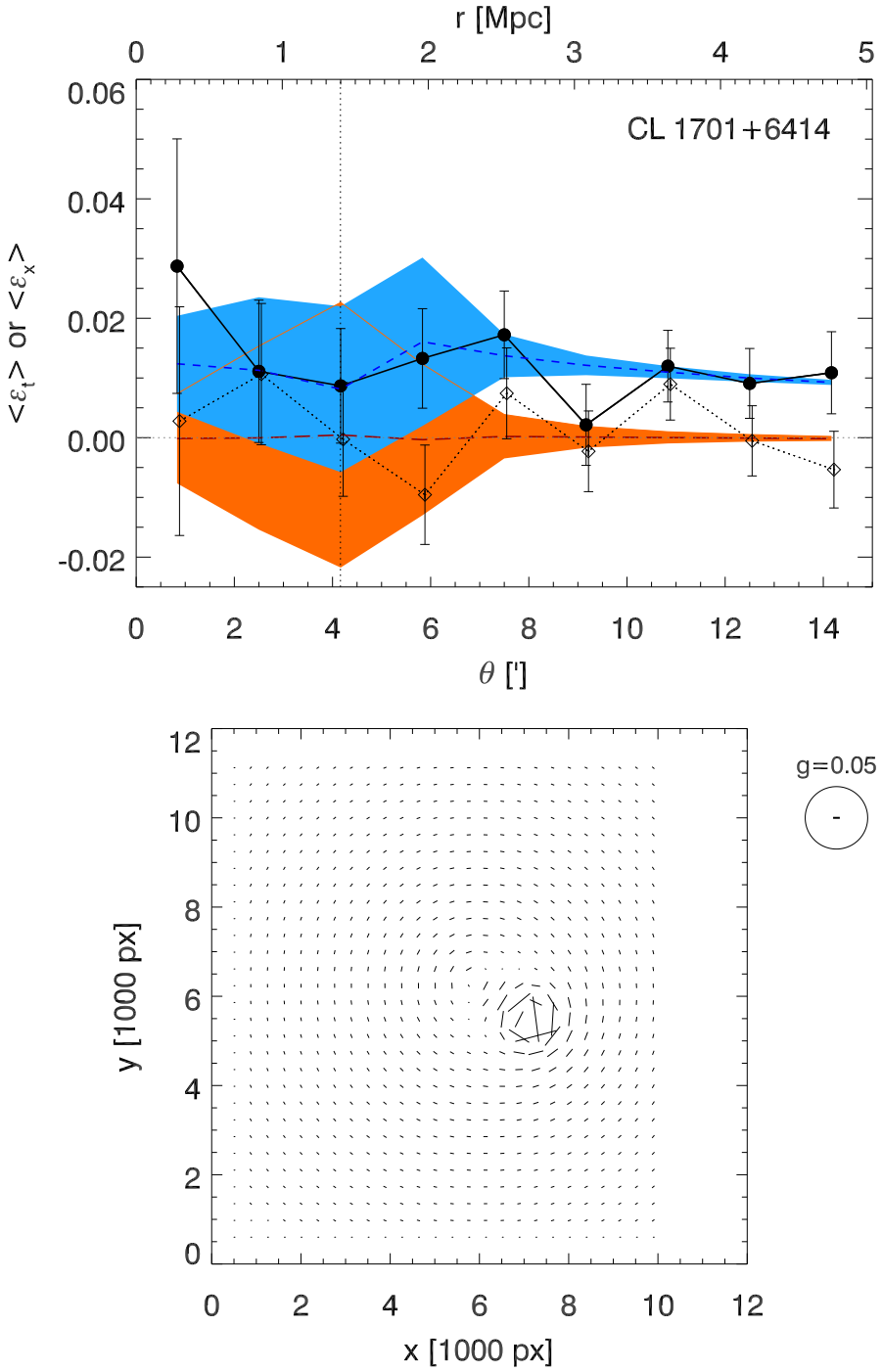

Figure 7.18: Modelling the shear distribution around CL 1701+6414 and A 2246. *Upper plot:* Shown are the binned tangential ($\langle g_t(\theta)\rangle$, filled circles with error bars) and cross components ($\langle g_\times(\theta)\rangle$, diamonds with error bars) of the shear w.r.t. the CL 1701+6414 lensing centre. The blue dashed line shows $\langle g_t^{\rm fit}(\theta)\rangle$ for the best-fit two-cluster model, while the orange long-dashed lines gives $\langle g_\times^{\rm fit}(\theta)\rangle$ as expected for this model. Both model profiles are computed by averaging over the same annuli around the cluster centre as done for the data. Blue and orange shaded regions show the 1σ dispersions of the *model* values in these annuli. *Lower plot:* The orientations and amplitudes of the shear as expected from the best-fit two-cluster model, on a regular grid.

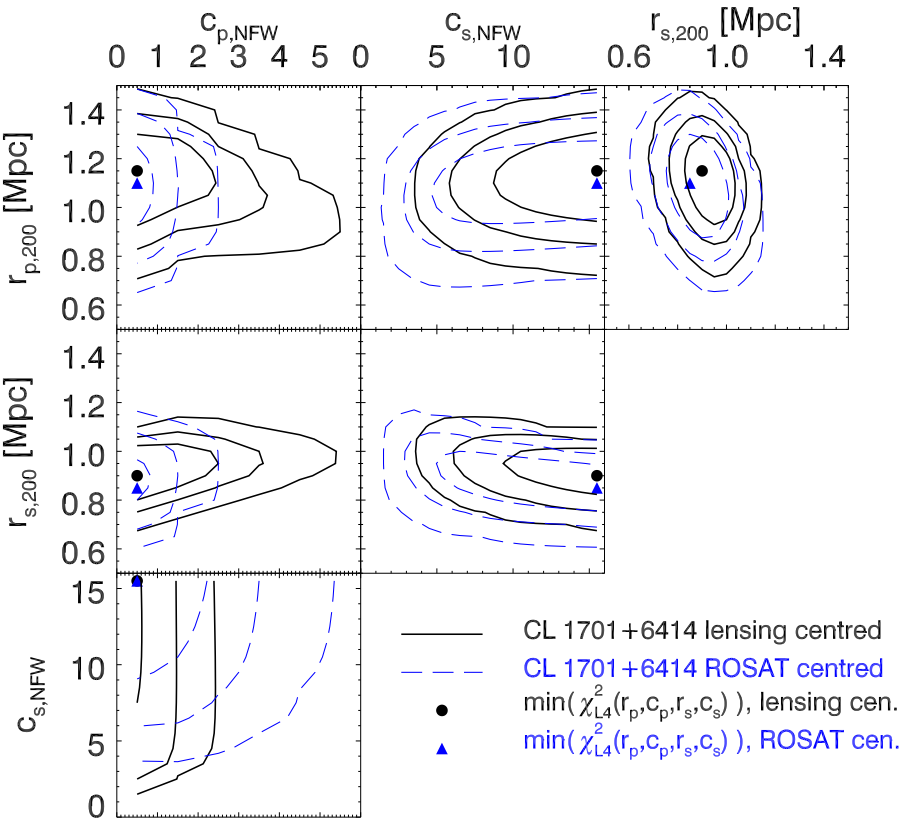

Figure 7.19: Confidence contours (99.73%, 95.4%, and 68.3%) and cluster parameters from the simultaneous modelling of CL 1701+6414 and A 2246. Each panel shows the dependencies between two of the four parameters, with the other two marginalised. Solid contours denote the default case, centred on the shear peaks; dashed contours denote a model using ROSAT centres. The parameters minimising $\chi^2_{\rm L4}$ for the two models are indicated by a filled circle and a triangle.

CL 1701+6414 is detected at the 3.7σ level. We stress that the lensing catalogue was optimised for the detection of CL 1701+6414 (Sect. 7.2.2). The smaller shear peaks at the coordinates of VMF 191 and VMF 192 measure 2.9σ and 2.7σ, respectively, with another 3.1σ S-peak close-by. The shear signal we measure forms an extended band of $>20'$ extent, reaching from the north-east of VMF 192 to a 3.6σ shear peak south-west of A 2246, which does not correspond to a known cluster.[6] Noticing the very similar redshifts of A 2246, VMF 191, and VMF 192, we might observe a physical filament at $z=0.22$, through whose centre we observe CL 1701+6414 in projection. We plan to perform a mass reconstruction of our lensing catalogue in the future, to provide further insight into the mass distribution.

Luckily, there exists direct proof that CL 1701+6414 does act as a gravitational lens, and thus contributes to the lensing signal: We observe a likely strong lensing arc, $10''$ to the west of

[6] Inspection of the ROSAT image does not show any obvious, strong extended emission at this position.

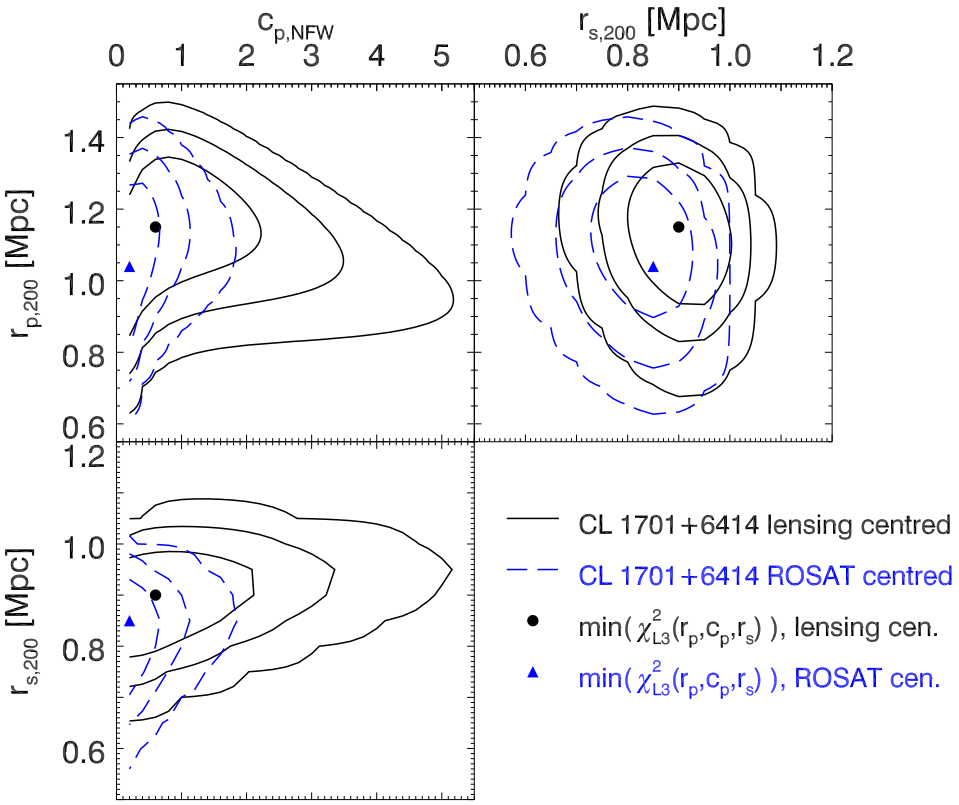

Figure 7.20: The same as Fig. 7.19, but for $c_{\rm s,NFW} = 20$ held fixed such that two out of three parameters are shown, and we marginalise over the third parameter. In addition, we used a finer grid than for Fig. 7.19.

the BCG of CL 1701+6414 ($z = 0.44 \pm 0.01$, Reimers et al. 1997). We show a zoomed version of Fig. 7.28, detailing the centre of CL 1701+6414 in Fig. 7.29. This arc candidate was found already by Reimers et al. (1997), who detected CL 1701+6414 and A 2246 using ROSAT *PSPC* data and optical imaging and spectroscopy with the Calar Alto 3.5 m and 2.2 m telescopes. Reimers et al. (1997) suggest that the very luminous QSO HS 1700+6414 at $z' = 2.72$ might be magnified by the combined lensing effects of the two clusters.

As the lensing centre, we define the grid cell with the highest S-value in the shear peak we attribute to CL 1701+6414, located 66″ off the ROSAT centre. Plotting the binned tangential shear around this lensing centre (filled circles in the upper plot of Fig. 7.18), we find a flat profile whose average $\langle \varepsilon_{\rm t}(\theta) \rangle > 0$ is consistent with the extended shear signal in the S-map. The cross-component $\langle \varepsilon_{\times}(\theta) \rangle$ is consistent with zero. Attempts to fit $\langle \varepsilon_{\rm t}(\theta) \rangle$ with our usual NFW profile (Eq. 6.8) produce nonsensical results because there is no preferred radial scale in a flat profile. Therefore, we modify our approach and, in a cautious step towards more complexity, model the shear of CL 1701+6414 and A 2246, the strongest shear peak, simultaneously.

In the two-cluster model, we assume an NFW shear profile originating from each deflector. We assume both the shear g_p of the primary and g_s of the secondary component to be small. In this case the superposition (Eq. 3.21) of the two polars becomes a simple addition. Thus, we expect the following shear components at a position $\boldsymbol{\theta}$ in the image plane:

$$g_{\mathrm{add},\alpha}(\boldsymbol{\theta}) = g_{\mathrm{p},\alpha}(\boldsymbol{\theta}; r_{\mathrm{p},200}, c_{\mathrm{p,NFW}}) + g_{\mathrm{s},\alpha}(\boldsymbol{\theta}; r_{\mathrm{s},200}, c_{\mathrm{s,NFW}}) \quad , \quad \alpha = 1,2 \quad . \tag{7.1}$$

Here, $r_{\mathrm{p},200}$, $r_{\mathrm{s},200}$, $c_{\mathrm{p,NFW}}$, and $c_{\mathrm{s,NFW}}$ are the radii and concentration parameters of the primary and secondary component, resp. Note that $g_{\mathrm{add},\alpha}(\boldsymbol{\theta})$ explicitly depends on the two-dimensional coordinate vector $\boldsymbol{\theta}$; the shear field of two clusters no longer has radial, but only axial symmetry. This is illustrated in the lower panel of Fig. 7.18, showing the best-fit two-cluster model for the CL 1701+6414 lensing catalogue evaluated on a regular grid.

For this best-fit model with the Levenberg-Marquardt method, we assume the lensing peaks of CL 1701+6414 at $z = 0.45$ and A 2246 at $z = 0.225$ as the centres of the two clusters; further $\langle D_\mathrm{ds}/D_\mathrm{s}\rangle = 0.381$ for CL 1701+6414 (Table 6.4) and $\langle D_\mathrm{ds}/D_\mathrm{s}\rangle = 0.640$ for A 2246, calculated analogously. With a goodness-of-fit of $\chi^2/\nu_\mathrm{dof} = 26469/26502 \approx 1.00$, we obtain $r^\mathrm{fit}_{\mathrm{p},200} = 1.26 \pm 0.27\,\mathrm{Mpc}$ and $c^\mathrm{fit}_\mathrm{p,NFW} = 0.3 \pm 0.5$ for CL 1701+6414 and $r^\mathrm{fit}_{\mathrm{s},200} = 0.85 \pm 0.16\,\mathrm{Mpc}$.[7] The concentration $c_\mathrm{s,NFW}$ of A 2246 is unconstrained by the result of the Levenberg-Marquardt fit. Based on this model, we compute the tangential and cross-component of the shear expected at each source galaxy and present the resulting profile in the upper plot of Fig. 7.18. The equivalent to the radial bin in the radially symmetric shear profile are concentric annuli within which the *model* shear g_t varies also azimuthally. For each annulus, we show the average and 1σ dispersion of g_t as the blue dashed line and blue-shaded region. The orange long-dashed line and orange shaded region display the same quantities for $g_\times$. Note that the fitted shear components $\langle g_{\mathrm{t},\times}\rangle$ are directly comparable to the measured $\langle \varepsilon_{\mathrm{t},\times}\rangle$. Figure 7.18 shows the good agreement between the measured and fitted tangential shear. A vertical dotted line denotes the separation of CL 1701+6414 and A 2246. For similar separations, the dispersion in the fitted shear components is largest, because we average over points with vastly different separations to the two clusters. Finally, we note that although the cross-component can be large at some points in the image plane, $\langle g_\times\rangle$ cancels out nearly completely when averaging over the annuli.

While the values for r_{200} returned in the fit seem reasonable, the concentration parameters for both clusters are ill-constrained, formally consistent with unphysical negative values. This problem is avoided using the method based on the parameter grid, which allows for asymmetric error margins. We consider a modification of the merit function given by Eq. (6.12):

$$\chi^2_\mathrm{L4} = \sum_{i=1}^{N_\mathrm{gal}} \frac{\left|g_{\mathrm{add},i}(r_{\mathrm{p},200}, c_\mathrm{p,NFW}, r_{\mathrm{s},200}, c_\mathrm{s,NFW}) - \varepsilon_i\right|^2}{\sigma^2_\mathrm{fit}\left(1 - \left|g_{\mathrm{add},i}(r_{\mathrm{p},200}, c_\mathrm{p,NFW}, r_{\mathrm{s},200}, c_\mathrm{s,NFW})\right|^2\right)^2} \quad . \tag{7.2}$$

The symbol χ^2_L4 highlights the dependence on four parameters, the radii and concentrations of the two clusters. We denote by $(r^\mathrm{min}_{\mathrm{p},200}, c^\mathrm{min}_\mathrm{p,NFW}, r^\mathrm{min}_{\mathrm{s},200}, c^\mathrm{min}_\mathrm{s,NFW})$ the cluster parameters minimising χ^2_L4. Note that χ^2_L4 models the measured ε_i directly, without recursion to the tangential component.

Figure 7.19 presents the confidence contours and parameters minimising Eq. (7.2) for the default model which is centred on the lensing peaks and uses no separation limit (filled circle and solid contours). The panels of Fig. 7.19 show all combinations of two parameters, where we marginalised over the two remaining parameters. Owing to the 4-dimensional parameter space, we tested a coarse grid of points to avoid excessive computing time. The picture emerges that

[7] This formal error range can be interpreted as $c_\mathrm{p,NFW}$ being consistent with zero. The unphysically negative lower limit points to the limitations of the Markwardt (2009) Levenberg-Marquardt implementation.

$r_{\rm p,200}$ and $r_{\rm s,200}$ are relatively independent of each other (top right panel). Hence, the presence of the respective other cluster does not seem to affect the accuracy with which we can determine the masses of the two clusters strongly. Consistent with the Levenberg-Marquardt fit results, the data favour the smallest tested value, $c_{\rm p,NFW} = 0.5$ for the concentration of CL 1701+6414, and the largest tested value, $c_{\rm s,NFW} = 15.5$ for the one of A 2246. Using ROSAT cluster centres (dashed contours and triangle in Figure 7.19), high $c_{\rm p,NFW}$ are ruled out even more.

We notice that $c_{\rm s,NFW}$ seems not to be well constrained by the data, which might explain the very high $c^{\rm fit}_{\rm s,NFW}$ we obtained. A possible explanation is the masking of the immediate surroundings of A 2246 (see Fig. 7.28), barring the region in which $c_{\rm s,NFW}$ can be constrained best from the analysis. Shear contribution of the BCG of A 2246 could mimic a strongly concentrated cluster. In an extended analysis, we plan to test if including a galaxy lens on top of the A 2246 profile improves the modelling.

Given the mask around A 2246 and the fact that the value of $c_{\rm s,NFW}$ has little influence on $r_{\rm p,200}$, the parameter important for determining the mass of CL 1701+6414, we fix $c_{\rm s,NFW} = 20$ to a high, but reasonable value and repeat the analysis with a finer parameter grid for a 3-dimensional parameter space and $\chi^2_{\rm L3}(r_{\rm p,200}, c_{\rm p,NFW}, r_{\rm s,200})$. Now marginalising over only one parameter, the confidence contours in Fig. 7.20 confirm the results of Fig. 7.19. The best model is found for $r^{\rm min}_{\rm p,200} = 1.15^{+0.18}_{-0.20}$ Mpc, $c^{\rm min}_{\rm p,NFW} = 0.6^{+1.6}_{-0.6}$ and $r^{\rm min}_{\rm s,200} = 0.9^{+0.05}_{-0.1}$ Mpc. Apart from the larger 1σ uncertainty ranges due to the more complex models compared to the other clusters, the degeneracies between the parameters are relatively small. The low concentration of CL 1701+6414 seems inherent in the data and not to be a direct artifact of the presence of A 2246. Using the default model, we compute masses of $3.0^{+1.7}_{-1.3}\times10^{14}\,{\rm M}_\odot$ for CL 1701+6414 and $1.1^{+0.2}_{-0.3}\times10^{14}\,{\rm M}_\odot$ for A 2246. Table 7.8 in Sect. 7.3.9 summarises all models we tested (see Sect. 8.2 for the error analysis) with $\chi^2_{\rm L3}$ depending on three parameters. The corresponding confidence contours are presented in Fig. B.16 in Appendix B.3.

7.3.8 Mass Modelling for CL 1641+4001

The S-statistics map of CL 1641+4001 – presented in Fig. 7.30 overlaid on the MEGACAM image – bears some resemblance to the CL 1701+6414 field. Here too, we observe several shear peaks, forming a connected structure of $> 20'$ extent. The ROSAT centre of CL 1641+4001 (big star symbol) is located within a plateau of $> 3\sigma$ significance in the S-statistics, as well as its BCG, 24″ north-east of the ROSAT centre. Within this plateau, the 15″ mesh size grid cell giving the highest S-value is found 95″ north of the ROSAT coordinates (green square with error bars in Fig. 7.30).

Beside CL 1641+4001, the only other known galaxy cluster in the vicinity of the shear peaks is SDSS-C4-DR3 3628 at $z = 0.032$. This object was identified in the SDSS Data Release 3 (DR3), using the "C4" cluster detection algorithm (Miller et al. 2005). However, it was published by von der Linden et al. (2007) who, in their studies of BCGs, also included DR3 objects not published by Miller et al. (2005). Our MEGACAM r'-band image shows two bright galaxies at the coordinates of SDSS-C4-DR3 3628 (small star symbol in Fig. 7.30) but gives no indication of a nearby cluster of galaxies. We notice that NED, at the same coordinates, also lists CGCG 224-092, a *galaxy pair*, at the same $z = 0.032$. Nevertheless, inspection of the CHANDRA image shows extended X-ray emission at these coordinates, indicative of a deep gravitational potential.

Both plots in Fig. 7.21 show the shear profile around the lensing centre of CL 1641+4001. The $\langle\varepsilon_{\rm t}(\theta)\rangle$ profile is flat, with a positive average in all bins and the most significant positive signal at $\sim 9'$ distance from the cluster centre. In the innermost two bins ($\theta < 3\farcm33$), $\langle\varepsilon_\times(\theta)\rangle$ is of similar amplitude as the tangential component, but consistent with zero at the 1σ level. In the upper plot of Fig. 7.21, we present the best-fit one-cluster model, assuming $z = 0.46$, implying $\langle D_{\rm ds}/D_{\rm s}\rangle = 0.381$ (Table 6.4). We obtain a goodness-of-fit of $\chi^2/\nu_{\rm dof} = 10988/10889 \approx 1.01$ and

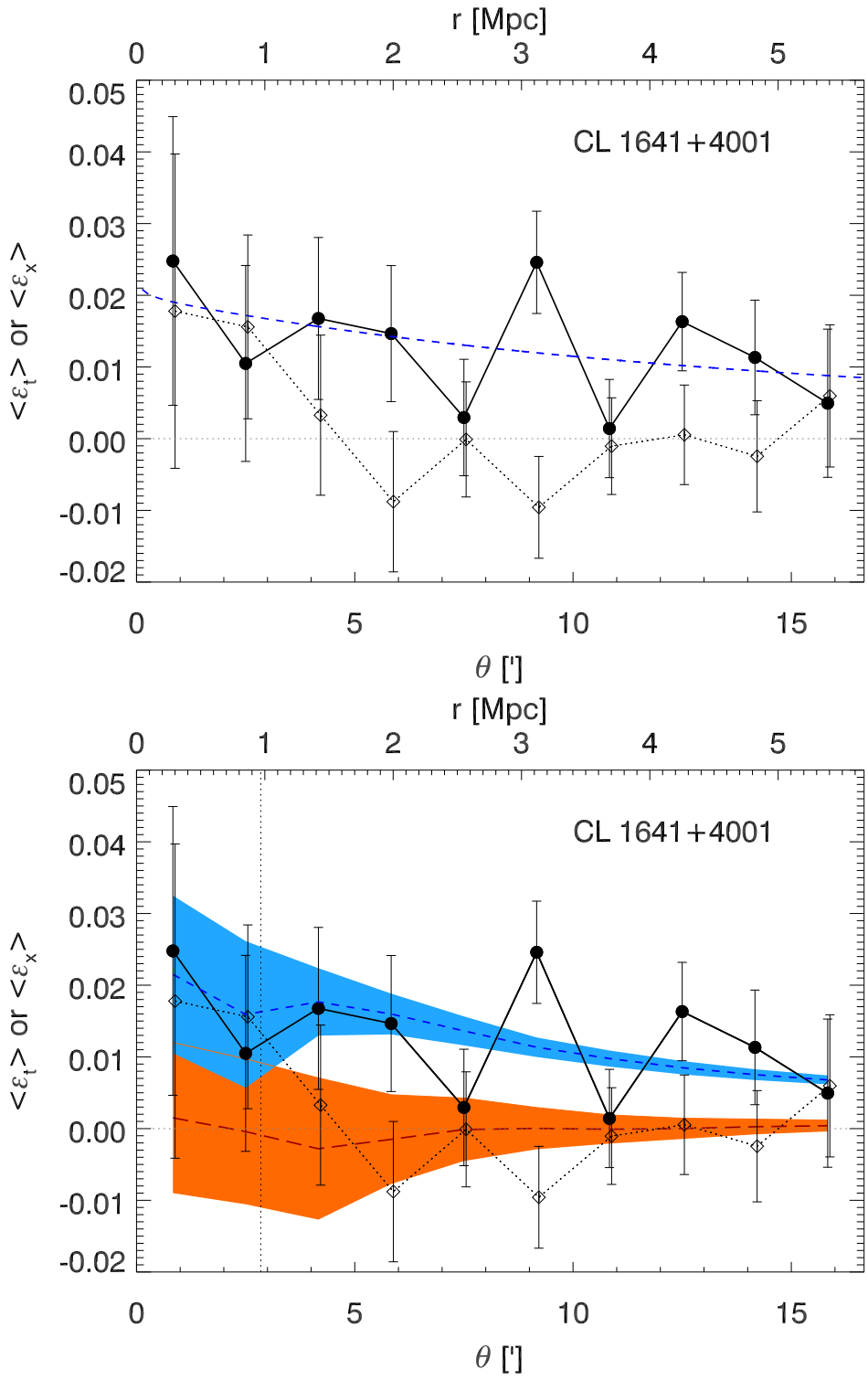

Figure 7.21: Tangential shear profile around CL 1641+4001 assuming a single cluster at $z = 0.46$ (upper panel) and two clusters at $z = 0.46$ and $z = 0.032$, respectively (lower panel). The symbols in the upper panel are the same as in Fig. 7.12, the ones in the lower panel the same as in Fig. 7.18.

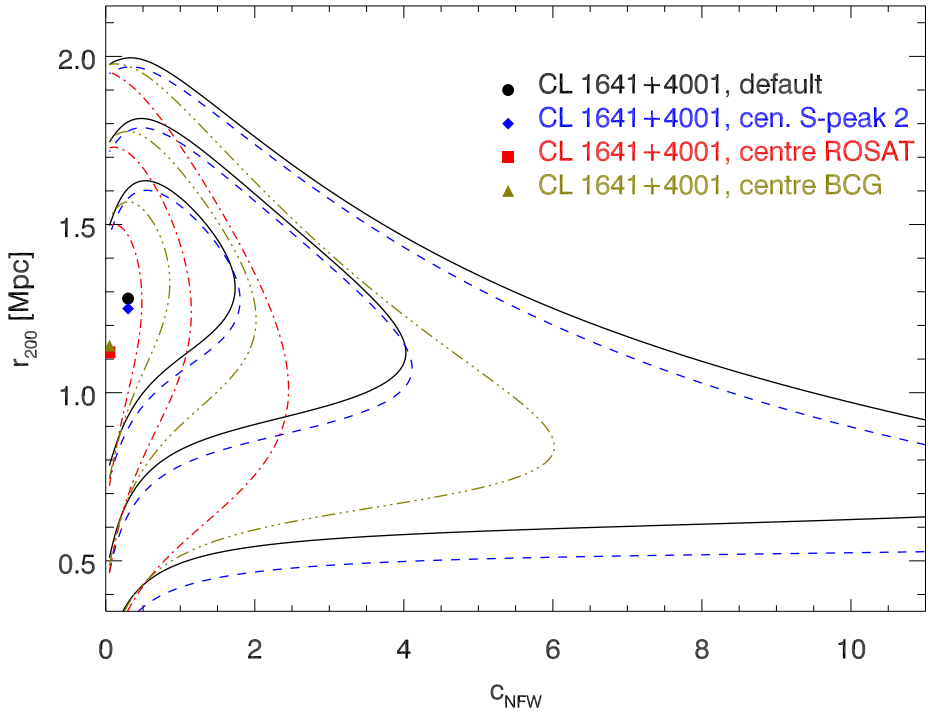

Figure 7.22: Confidence contours (99.73%, 95.4%, and 68.3%) and cluster parameters minimising $\chi^2_{\rm L}$ (Eq. 6.12) for four models of CL 1641+4001. Solid contours and the filled circle denote the default model, centred on the strongest lensing peak. Dashed contours and a diamond mark the model centred on the second-strongest lensing peak. Models centred on the ROSAT centre and the BCG are given by dot-dashed contours and a square, and triple-dot dashed contours and a triangle, respectively.

$r^{\rm fit}_{200} = 1.44 \pm 0.26$ Mpc and $c^{\rm fit}_{\rm NFW} = 0.3 \pm 0.5$. Similar to the single-cluster fit of CL 1701+6414, the very low $c^{\rm fit}_{\rm NFW}$ is consistent with zero, reflecting the flat shear profile.

Therefore, we test a two-cluster model, introducing a second component at the redshift of SDSS-C4-DR3 3628, with $\langle D_{\rm ds}/D_{\rm s}\rangle = 0.940$ calculated in the same way as the other geometric factors. We choose the position of the second-highest shear peak ($S = 3.95$; green triangle in Fig. 7.30) as the centre of the secondary component. The offset of $\sim 3'$ to the coordinates of SDSS-C4-DR3 3628 is justified by the large mask at the latter position. The two-cluster fit yields $\chi^2/\nu_{\rm dof} = 22640/22658 \approx 1.00$ and cluster parameters $r^{\rm fit}_{\rm p,200} = 1.10 \pm 0.33$ Mpc and $c^{\rm fit}_{\rm p,NFW} = 1.2 \pm 1.7$ for CL 1641+4001 and $r^{\rm fit}_{\rm s,200} = 0.88 \pm 0.35$ Mpc and $c^{\rm fit}_{\rm s,NFW} = 6.4 \pm 1.0$ for the secondary. The best-fit shear profiles for the two-cluster model are shown in the lower plot of Fig. 7.21, in the same way as the two-cluster model in Fig. 7.18. The modelled tangential component $\langle g_{\rm t}\rangle$ around CL 1641+4001 for the inner bins agrees well with the data $\langle \varepsilon_{\rm t}\rangle$. The problem with the two-cluster model lies in the mass estimate of $8.5 \times 10^{13}\,{\rm M}_\odot$ given by Eq. (6.7) for SDSS-C4-DR3 3628, the mass of a fully fledged cluster. This estimate is in stark disagreement with the absence of a massive, nearby cluster from our MEGACAM image. Which, against all odds, would have had to be missed by all but one cluster surveys hitherto! Hence, we deem it unlikely that the complex structure in the S-map of CL 1641+4001 bears a significant contribution from the $z = 0.032$ structure: In order for it to

cause the observed shear, the necessary mass would have to be too large to be consistent with the observed light.

We prefer the hypothesis that the shear is caused by a complex structure at the redshift of CL 1641+4001, although its X-ray morphology does not hint at a merger (Vikhlinin et al. 2009a). Being aware of the shortcomings of a single NFW model in this case, we return to the model presented in the upper panel of Fig. 7.21. We plan to conduct a more detailed analysis of CL 1641+4001, including a κ reconstruction.

In our default model for the analysis of the r_{200}–$c_{\rm NFW}$–grid, we consider all sources at separation $\theta < 16\farcm67$ from the shear peak of CL 1641+4001. We obtain a minimum of $\chi^2_{\rm L}$ for $r_{200}^{\rm min} = 1.28^{+0.21}_{-0.22}$ Mpc and $c_{\rm NFW}^{\rm min} = 0.3^{+0.7}_{-0.3}$. These results are illustrated by the filled circle and solid contours in Fig. 7.22. The very low concentration parameter is consistent with the one-cluster fit result. Cautioning the limitations of our model, we obtain a mass estimate of $4.1^{+2.4}_{-1.8}\times10^{14}\,{\rm M}_\odot$. Interestingly, choosing the secondary shear peak as a centre yields similar cluster parameters (Table 7.9 in Sect. 7.3.9 and diamond and dashed contours in Fig. 7.22). Models centred on the ROSAT centre (square and dot-dashed contours) or BCG (triangle and triple-dot dashed contours) give lower cluster masses and also even lower values for $c_{\rm NFW}$. Table 7.9 compiles the parameters obtained in all tested cases. Confidence contours for the models evaluated in the error analysis (Sect. 8.2) are given in Fig. B.15 in Appendix B.3.

7.3.9 Tabular Overview of Cluster Parameters

Tables 7.3 to 7.9 summarise the cluster parameters $r_{200}^{\rm min}$ and $c_{\rm NFW}^{\rm min}$ for all tested models of the seven clusters presented in this Chapter. Following the layout of Table 6.7 for CL 0030+2618, we show the mass M_{200} (Eq. 6.7) for each model and also list the ratio μ to the mass $M_{200}^{\rm def}$ obtained for the default model. See Tables 7.2 and 8.1 for comparisons between the cluster detections and masses.

Table 7.3: Like Table 6.7, but for CL 0159+0030 (Sect. 7.3.2). The default model includes all sources at separations $0' < \theta < 13\farcm33$ around the ROSAT centre, offset by $23''$ from the lensing centre. The default model includes correction for contamination by cluster members. (Sect. 7.3.1).

Model	$r_{200}^{\rm min}$/Mpc	$c_{\rm NFW}^{\rm min}$	$M_{200}(r_{200}^{\rm min})$	μ
default	$1.44^{+0.18}_{-0.22}$	$9.2^{+>6.8}_{-7.5}$	$5.4^{+2.3}_{-2.1}\times10^{14}\,{\rm M}_\odot$	–
$\theta_{\rm max} = 15'$	$1.38^{+0.17}_{-0.22}$	>16	$4.8^{+2.0}_{-1.9}\times10^{14}\,{\rm M}_\odot$	0.88
no contam. corr.	$1.39^{+0.17}_{-0.21}$	$8.55^{+>7.45}_{-6.9}$	$4.9^{+2.0}_{-1.9}\times10^{14}\,{\rm M}_\odot$	0.90
$\max(\lvert\varepsilon\rvert) = 1.0$	$1.51^{+0.17}_{-0.20}$	$11.9^{+>4.1}_{-9.7}$	$6.3^{+2.4}_{-2.2}\times10^{14}\,{\rm M}_\odot$	1.15
$\max(\lvert\varepsilon\rvert) = 10^4$	$1.51^{+0.20}_{-0.24}$	>16	$6.3^{+2.8}_{-2.5}\times10^{14}\,{\rm M}_\odot$	1.15
$f_0 = 0.97$	$1.40^{+0.17}_{-0.21}$	$9.05^{+>6.95}_{-7.35}$	$5.0^{+2.0}_{-1.9}\times10^{14}\,{\rm M}_\odot$	0.92
$f_0 = 1.13$	$1.45^{+0.19}_{-0.22}$	$9.45^{+>6.55}_{-7.8}$	$5.5^{+2.5}_{-2.2}\times10^{14}\,{\rm M}_\odot$	1.02
$\langle D_{\rm ds}/D_{\rm s}\rangle = 0.424$	$1.47^{+0.18}_{-0.22}$	$9.45^{+>6.55}_{-7.75}$	$5.8^{+2.3}_{-2.2}\times10^{14}\,{\rm M}_\odot$	1.06
$\langle D_{\rm ds}/D_{\rm s}\rangle = 0.470$	$1.41^{+0.17}_{-0.22}$	$9.0^{+>7.0}_{-7.35}$	$5.1^{+2.1}_{-2.0}\times10^{14}\,{\rm M}_\odot$	0.94

Table 7.4: Like Table 6.7, but for CL 0809+2811 (Sect. 7.3.3). The default model includes all sources at separations $0\farcm5 < \theta < 15'$ around the lensing centre centre, offset by 79″ from the ROSAT centre. The default model includes correction for contamination by cluster members. (Sect. 7.3.1).

Model	$r_{200}^{\rm min}$/Mpc	$c_{\rm NFW}^{\rm min}$	$M_{200}(r_{200}^{\rm min})$	μ
default	$1.83^{+0.16}_{-0.19}$	$3.7^{+5.1}_{-2.2}$	$11.2^{+3.2}_{-3.2}\times10^{14}\,M_\odot$	–
$\theta_{\rm min}=0'$	$1.83^{+0.16}_{-0.18}$	$3.85^{+4.2}_{-2.2}$	$11.2^{+3.2}_{-3.0}\times10^{14}\,M_\odot$	1.00
no contam. corr.	$1.76^{+0.16}_{-0.18}$	$3.45^{+4.7}_{-2.05}$	$10.0^{+3.0}_{-2.8}\times10^{14}\,M_\odot$	0.89
centred on ROSAT peak	$1.71^{+0.25}_{-0.24}$	$1.25^{+2.3}_{-0.9}$	$9.2^{+4.7}_{-3.3}\times10^{14}\,M_\odot$	0.82
$\max(\lvert\varepsilon\rvert)=1.0$	$1.79^{+0.20}_{-0.23}$	$1.95^{+2.85}_{-1.35}$	$10.5^{+3.9}_{-3.6}\times10^{14}\,M_\odot$	0.94
$\max(\lvert\varepsilon\rvert)=10^4$	$1.87^{+0.25}_{-0.28}$	$1.2^{+1.85}_{-0.9}$	$12.0^{+5.5}_{-4.6}\times10^{14}\,M_\odot$	1.07
$f_0=0.95$	$1.75^{+0.16}_{-0.17}$	$3.7^{+5.25}_{-2.25}$	$9.8^{+3.0}_{-2.6}\times10^{14}\,M_\odot$	0.87
$f_0=1.13$	$1.85^{+0.17}_{-0.19}$	$3.8^{+5.35}_{-2.3}$	$11.6^{+4.0}_{-3.2}\times10^{14}\,M_\odot$	1.03
$\langle D_{\rm ds}/D_{\rm s}\rangle=0.414$	$1.87^{+0.17}_{-0.21}$	$3.85^{+5.2}_{-2.3}$	$12.0^{+3.6}_{-3.6}\times10^{14}\,M_\odot$	1.07
$\langle D_{\rm ds}/D_{\rm s}\rangle=0.460$	$1.78^{+0.17}_{-0.18}$	$3.7^{+5.25}_{-2.25}$	$10.4^{+3.3}_{-2.8}\times10^{14}\,M_\odot$	0.92

Table 7.5: Like Table 6.7, but for CL 0230+1836 (Sect. 7.3.4). The default model includes all sources at separations $0' < \theta < 13\farcm33$ around the lensing centre centre, offset by 20″ from the ROSAT centre, and by 32″ from the likely BCG. The default model includes correction for contamination by cluster members. (Sect. 7.3.1).

Model	$r_{200}^{\rm min}$/Mpc	$c_{\rm NFW}^{\rm min}$	$M_{200}(r_{200}^{\rm min})$	μ
default	$1.40^{+0.24}_{-0.29}$	$3.2^{+1.9}_{-1.6}$	$8.1^{+4.9}_{-4.1}\times10^{14}M_\odot$	–
$\theta_{\rm min}=0\farcm5$	$1.41^{+0.22}_{-0.27}$	$4.8^{+4.4}_{-2.65}$	$8.3^{+4.5}_{-3.9}\times10^{14}M_\odot$	1.02
$m_{\rm faint}=m_{\rm bright}=23.4$	$1.51^{+0.24}_{-0.29}$	$3.2^{+1.65}_{-1.45}$	$10.2^{+5.7}_{-4.8}\times10^{14}M_\odot$	1.26
centred on BCG	$1.35^{+0.28}_{-0.35}$	$2.05^{+1.55}_{-1.1}$	$7.3^{+5.5}_{-4.3}\times10^{14}M_\odot$	0.90
no contam. corr.	$1.36^{+0.23}_{-0.29}$	$2.7^{+1.6}_{-1.3}$	$7.4^{+4.4}_{-3.8}\times10^{14}M_\odot$	0.92
$\max(\lvert\varepsilon\rvert)=1.0$	$1.47^{+0.27}_{-0.31}$	$2.5^{+1.8}_{-1.4}$	$9.4^{+6.2}_{-4.8}\times10^{14}M_\odot$	1.16
$\max(\lvert\varepsilon\rvert)=10^4$	$1.49^{+0.28}_{-0.34}$	$2.85^{+2.05}_{-1.65}$	$9.8^{+6.6}_{-5.3}\times10^{14}M_\odot$	1.21
$f_0=0.73$	$1.22^{+0.20}_{-0.24}$	$2.9^{+1.85}_{-1.4}$	$5.4^{+3.1}_{-2.6}\times10^{14}M_\odot$	0.66
$f_0=1.13$	$1.42^{+0.25}_{-0.30}$	$3.25^{+1.9}_{-1.65}$	$8.5^{+5.3}_{-4.3}\times10^{14}M_\odot$	1.04
$\langle D_{\rm ds}/D_{\rm s}\rangle=0.148$	$1.49^{+0.25}_{-0.31}$	$3.4^{+1.95}_{-1.7}$	$9.8^{+5.8}_{-4.9}\times10^{14}M_\odot$	1.21
$\langle D_{\rm ds}/D_{\rm s}\rangle=0.188$	$1.33^{+0.23}_{-0.28}$	$3.05^{+1.85}_{-1.55}$	$6.2^{+4.3}_{-3.5}\times10^{14}M_\odot$	0.90

Table 7.6: Like Table 6.7, but for CL 1357+6232 (Sect. 7.3.5). The default model includes all sources at separations $0' < \theta < 15'$ around the lensing centre, offset by 50″ from the ROSAT centre. The default model of this single-band cluster includes *no* correction for contamination by cluster members.

Model	$r_{200}^{\min}$/Mpc	$c_{\mathrm{NFW}}^{\min}$	$M_{200}(r_{200}^{\min})$	μ
default	$1.18^{+0.17}_{-0.20}$	$2.8^{+1.65}_{-1.25}$	$3.5^{+1.7}_{-1.5}\times10^{14}\,\mathrm{M}_\odot$	–
$0\farcm5 \le \theta \le 15'$	$1.18^{+0.17}_{-0.18}$	$3.6^{+2.85}_{-1.75}$	$3.5^{+1.7}_{-1.4}\times10^{14}\,\mathrm{M}_\odot$	1.00
centred on BCG	$1.11^{+0.18}_{-0.20}$	$3.1^{+2.45}_{-1.85}$	$2.9^{+1.7}_{-1.3}\times10^{14}\,\mathrm{M}_\odot$	0.83
centred on ROSAT peak	$1.05^{+0.14}_{-0.17}$	$4.8^{+1.25}_{-1.85}$	$2.5^{+1.1}_{-1.0}\times10^{14}\,\mathrm{M}_\odot$	0.70
$\max(\lvert\varepsilon\rvert) = 1.0$	$1.11^{+0.19}_{-0.23}$	$2.65^{+2.05}_{-1.35}$	$2.9^{+1.8}_{-1.5}\times10^{14}\,\mathrm{M}_\odot$	0.83
$\max(\lvert\varepsilon\rvert) = 10^4$	$1.01^{+0.22}_{-0.29}$	$3.2^{+3.3}_{-2.0}$	$2.2^{+1.8}_{-1.4}\times10^{14}\,\mathrm{M}_\odot$	0.63
$f_0 = 0.86$	$1.08^{+0.16}_{-0.17}$	$2.65^{+1.6}_{-1.8}$	$2.7^{+1.4}_{-1.1}\times10^{14}\,\mathrm{M}_\odot$	0.77
$f_0 = 1.13$	$1.19^{+0.18}_{-0.20}$	$2.85^{+1.7}_{-1.3}$	$3.6^{+1.9}_{-1.5}\times10^{14}\,\mathrm{M}_\odot$	1.03
$\langle D_{\mathrm{ds}}/D_{\mathrm{s}}\rangle = 0.300$	$1.22^{+0.18}_{-0.21}$	$2.9^{+1.75}_{-1.3}$	$3.9^{+2.0}_{-1.7}\times10^{14}\,\mathrm{M}_\odot$	1.11
$\langle D_{\mathrm{ds}}/D_{\mathrm{s}}\rangle = 0.348$	$1.14^{+0.16}_{-0.19}$	$2.7^{+1.65}_{-1.2}$	$3.2^{+1.9}_{-1.3}\times10^{14}\,\mathrm{M}_\odot$	0.90

Table 7.7: Like Table 6.7, but for CL 1416+4446 (Sect. 7.3.6). The default model includes all sources at separations $0\farcm5 < \theta < 14'$ around the lensing centre, offset by 19″ from the ROSAT centre. The default model of this single-band cluster includes *no* correction for contamination by cluster members.

Model	$r_{200}^{\min}$/Mpc	$c_{\mathrm{NFW}}^{\min}$	$M_{200}(r_{200}^{\min})$	μ
default	$0.99^{+0.14}_{-0.16}$	$4.9^{+5.65}_{-2.95}$	$1.8^{+0.9}_{-0.7}\times10^{14}\,\mathrm{M}_\odot$	–
$\theta_{\min} = 0'$	$0.95^{+0.17}_{-0.20}$	$2.15^{+1.8}_{-1.2}$	$1.6^{+1.0}_{-0.8}\times10^{14}\,\mathrm{M}_\odot$	0.88
centred on ROSAT peak	$0.97^{+0.13}_{-0.18}$	$5.25^{+5.55}_{-3.0}$	$1.7^{+0.8}_{-0.8}\times10^{14}\,\mathrm{M}_\odot$	0.94
centred on ROSAT peak, $\theta_{\min} = 0'$	$0.97^{+0.14}_{-0.18}$	$4.15^{+2.85}_{-2.1}$	$1.7^{+0.8}_{-0.8}\times10^{14}\,\mathrm{M}_\odot$	0.94
$\max(\lvert\varepsilon\rvert) = 1.0$	$1.03^{+0.15}_{-0.17}$	$4.2^{+4.9}_{-2.55}$	$2.0^{+1.0}_{-0.8}\times10^{14}\,\mathrm{M}_\odot$	1.13
$\max(\lvert\varepsilon\rvert) = 10^4$	$1.08^{+0.16}_{-0.18}$	$4.45^{+5.05}_{-2.65}$	$2.3^{+1.2}_{-1.0}\times10^{14}\,\mathrm{M}_\odot$	1.30
$f_0 = 0.92$	$0.94^{+0.13}_{-0.15}$	$4.6^{+5.4}_{-2.7}$	$1.5^{+0.7}_{-0.6}\times10^{14}\,\mathrm{M}_\odot$	0.86
$f_0 = 1.13$	$1.01^{+0.14}_{-0.17}$	$4.9^{+5.55}_{-2.9}$	$1.9^{+0.9}_{-0.8}\times10^{14}\,\mathrm{M}_\odot$	1.06
$\langle D_{\mathrm{ds}}/D_{\mathrm{s}}\rangle = 0.414$	$1.02^{+0.14}_{-0.17}$	$4.95^{+5.5}_{-2.95}$	$2.0^{+0.9}_{-0.8}\times10^{14}\,\mathrm{M}_\odot$	1.09
$\langle D_{\mathrm{ds}}/D_{\mathrm{s}}\rangle = 0.460$	$0.97^{+0.14}_{-0.18}$	$4.75^{+5.55}_{-2.85}$	$1.7^{+0.8}_{-0.8}\times10^{14}\,\mathrm{M}_\odot$	0.94

Table 7.8: Like Table 6.7, but for the CL 1701+6414 field in which two clusters, CL 1701+6414 and A 2246, are modelled (Sect. 7.3.7). In addition to the parameters of CL 1701+6414, the radius r_{200} and the corresponding mass inferred for A 2246 are given. The two-cluster model includes the complete radial range of the lensing catalogue and is centred on the lensing peak of CL 1701+6414, separated by 66″ from its ROSAT peak. *No* correction for contamination by cluster members is applied in this single-band field.

	CL 1701+6414				ABELL 2246	
Model	$r^{\min}_{\mathrm{p},200}$/Mpc	$c^{\min}_{\mathrm{p,NFW}}$	$M_{\mathrm{p},200}(r^{\min}_{\mathrm{p},200})$	μ	$r^{\min}_{\mathrm{s},200}$/Mpc	$M_{\mathrm{s},200}(r^{\min}_{\mathrm{s},200})$
default	$1.15^{+0.19}_{-0.21}$	$0.6^{+1.6}_{-0.6}$	$3.0^{+1.7}_{-1.3}\times10^{14}\,\mathrm{M}_\odot$	–	$0.9^{+0.05}_{-0.1}$	$1.1^{+0.2}_{-0.3}\times10^{14}\,\mathrm{M}_\odot$
cent. on ROSAT peak	$1.04^{+0.20}_{-0.22}$	<0.2	$2.2^{+1.5}_{-1.1}\times10^{14}\,\mathrm{M}_\odot$	0.74	$0.85^{+0.05}_{-0.1}$	$0.9^{+0.2}_{-0.3}\times10^{14}\,\mathrm{M}_\odot$
$\max(\lvert\varepsilon\rvert)=1.0$	$1.07^{+0.21}_{-0.22}$	$0.4^{+2.0}_{-0.2}$	$2.4^{+1.7}_{-1.2}\times10^{14}\,\mathrm{M}_\odot$	0.81	$0.9^{+0.05}_{-0.1}$	$1.1^{+0.2}_{-0.3}\times10^{14}\,\mathrm{M}_\odot$
$\max(\lvert\varepsilon\rvert)=10^4$	$1.11^{+0.22}_{-0.25}$	$0.8^{1.6}_{-0.4}$	$2.7^{+1.9}_{-1.4}\times10^{14}\,\mathrm{M}_\odot$	0.90	$0.95^{+0.05}_{-0.1}$	$1.3^{+0.2}_{-0.4}\times10^{14}\,\mathrm{M}_\odot$
$f_0=0.92$	$1.03^{+0.18}_{-0.19}$	$0.4^{+1.6}_{-0.2}$	$2.1^{+1.3}_{-1.0}\times10^{14}\,\mathrm{M}_\odot$	0.72	$0.85^{+0.05}_{-0.10}$	$0.9^{+0.2}_{-0.3}\times10^{14}\,\mathrm{M}_\odot$
$f_0=1.13$	$1.18^{+0.19}_{-0.21}$	$0.6^{+1.6}_{-0.6}$	$3.2^{+1.8}_{-1.4}\times10^{14}\,\mathrm{M}_\odot$	1.08	$0.9^{+0.05}_{-0.1}$	$1.1^{+0.2}_{-0.3}\times10^{14}\,\mathrm{M}_\odot$
$\langle D_{\mathrm{ds}}/D_{\mathrm{s}}\rangle=0.357$	$1.20^{+0.19}_{-0.22}$	$0.65^{+1.6}_{-0.6}$	$3.4^{+1.9}_{-1.5}\times10^{14}\,\mathrm{M}_\odot$	1.14	$0.9^{+0.05}_{-0.1}$	$1.1^{+0.2}_{-0.3}\times10^{14}\,\mathrm{M}_\odot$
$\langle D_{\mathrm{ds}}/D_{\mathrm{s}}\rangle=0.405$	$1.11^{+0.18}_{-0.20}$	$0.6^{+1.6}_{-0.6}$	$2.7^{+1.5}_{-1.2}\times10^{14}\,\mathrm{M}_\odot$	0.90	$0.9^{+0.05}_{-0.1}$	$1.1^{+0.2}_{-0.3}\times10^{14}\,\mathrm{M}_\odot$

Table 7.9: Like Table 6.7, but for the CL 1641+4001 field (Sect. 7.3.8), in which we, despite a complicated shear field, favour a single-cluster model. The default model includes all sources at separations $0' < \theta < 16\farcm66$ around the lensing centre, offset by 95″ from the ROSAT centre. *No* correction for contamination by cluster members is applied in this single-band field.

Model	$r^{\min}_{200}$/Mpc	$c^{\min}_{\mathrm{NFW}}$	$M_{200}(r^{\min}_{200})$	μ
default	$1.28^{+0.21}_{-0.22}$	$0.3^{+0.7}_{-0.3}$	$4.1^{+2.4}_{-1.8}\times10^{14}\,\mathrm{M}_\odot$	–
$\theta_{\min}=30'$	$1.28^{+0.21}_{-0.22}$	$0.3^{+0.65}_{-0.3}$	$4.1^{+2.4}_{-1.8}\times10^{14}\,\mathrm{M}_\odot$	1.00
centred on ROSAT peak	$1.12^{+0.24}_{-0.26}$	<0.05	$2.8^{+2.2}_{-1.5}\times10^{14}\,\mathrm{M}_\odot$	0.67
centred on BCG	$1.14^{+0.25}_{-0.25}$	<0.05	$2.9^{+2.4}_{-1.5}\times10^{14}\,\mathrm{M}_\odot$	0.71
centred on 2. S-peak	$1.25^{+0.21}_{-0.23}$	$0.3^{+0.75}_{0.3}$	$3.8^{+2.3}_{-1.8}\times10^{14}\,\mathrm{M}_\odot$	0.93
$\max(\lvert\varepsilon\rvert)=1.0$	$1.33^{+0.22}_{-0.23}$	$0.3^{+0.7}_{-0.3}$	$4.6^{+2.7}_{-2.0}\times10^{14}\,\mathrm{M}_\odot$	1.12
$\max(\lvert\varepsilon\rvert)=10^4$	$1.16^{+0.25}_{-0.29}$	$0.75^{+1.65}_{-0.55}$	$3.1^{+2.5}_{-1.8}\times10^{14}\,\mathrm{M}_\odot$	0.74
$f_0=0.93$	$1.19^{+0.19}_{-0.20}$	$0.3^{+0.6}_{-0.3}$	$3.3^{+1.9}_{-1.4}\times10^{14}\,\mathrm{M}_\odot$	0.80
$f_0=1.13$	$1.31^{+0.22}_{-0.23}$	$0.3^{+0.7}_{-0.3}$	$4.4^{+2.7}_{-2.0}\times10^{14}\,\mathrm{M}_\odot$	1.07
$\langle D_{\mathrm{ds}}/D_{\mathrm{s}}\rangle=0.357$	$1.36^{+0.22}_{-0.23}$	$0.35^{+0.7}_{-0.3}$	$5.0^{+2.8}_{-2.1}\times10^{14}\,\mathrm{M}_\odot$	1.20
$\langle D_{\mathrm{ds}}/D_{\mathrm{s}}\rangle=0.405$	$1.23^{+0.20}_{-0.21}$	$0.3^{+0.65}_{-0.3}$	$3.7^{+2.1}_{-1.6}\times10^{14}\,\mathrm{M}_\odot$	0.89

7.4 Aperture Mass Significance Maps

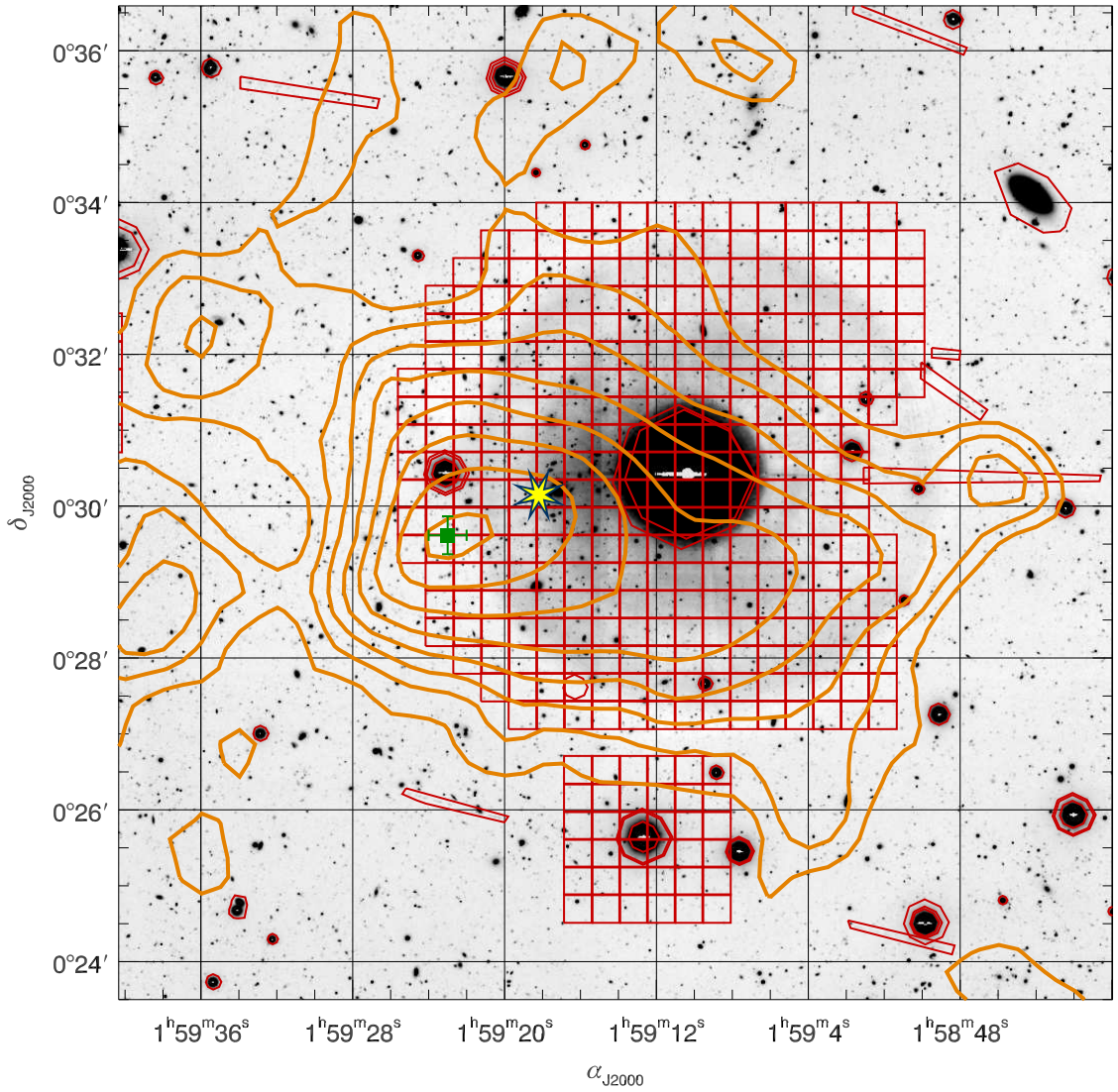

Figure 7.23: Aperture mass significance map of CL 0159+0030. The figure shows the central, most interesting region of the MEGACAM r'-band image, overlaid with excision masks (thin red lines, Sect. 5.1.3) and S-contours (thicker orange lines). Contour levels start at $S = 0.5$, with an increment of $\Delta S = 0.5$. The cell in the grid of 15″ mesh size with the highest S-value is marked by a green square with error bars showing its extent. A star symbol denotes the ROSAT centre of CL 0159+0030. Beside the square masks related to the source density counts, the figure shows examples of octagonal masks around saturated stars and manually defined masks for asteroid tracks and a saturated galaxy.

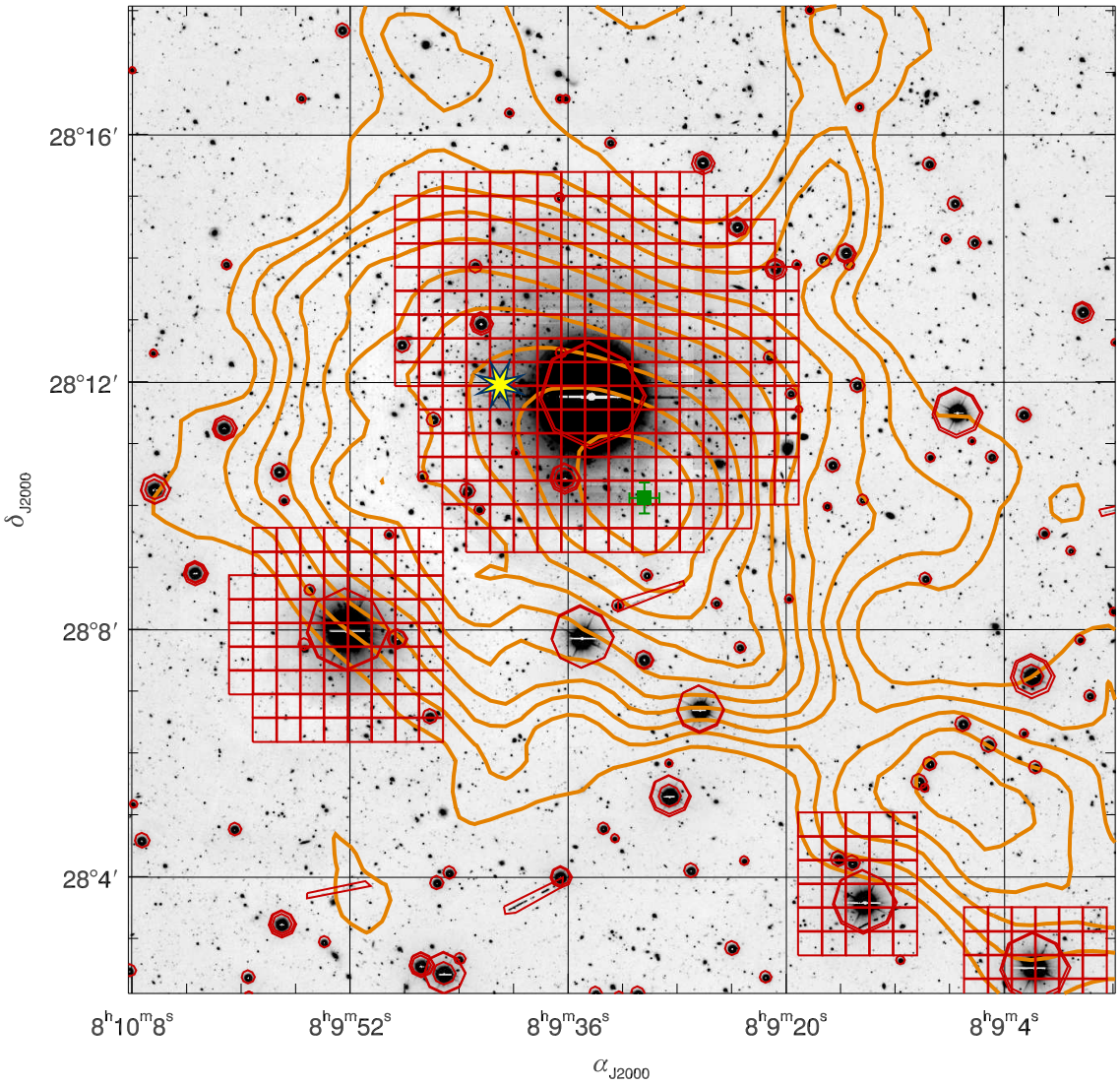

Figure 7.24: Aperture mass map of CL 0809+2811, overlaid on the central, most interesting region of the MEGACAM r'-band image. The lines and symbols are the same as in Fig. 7.23.

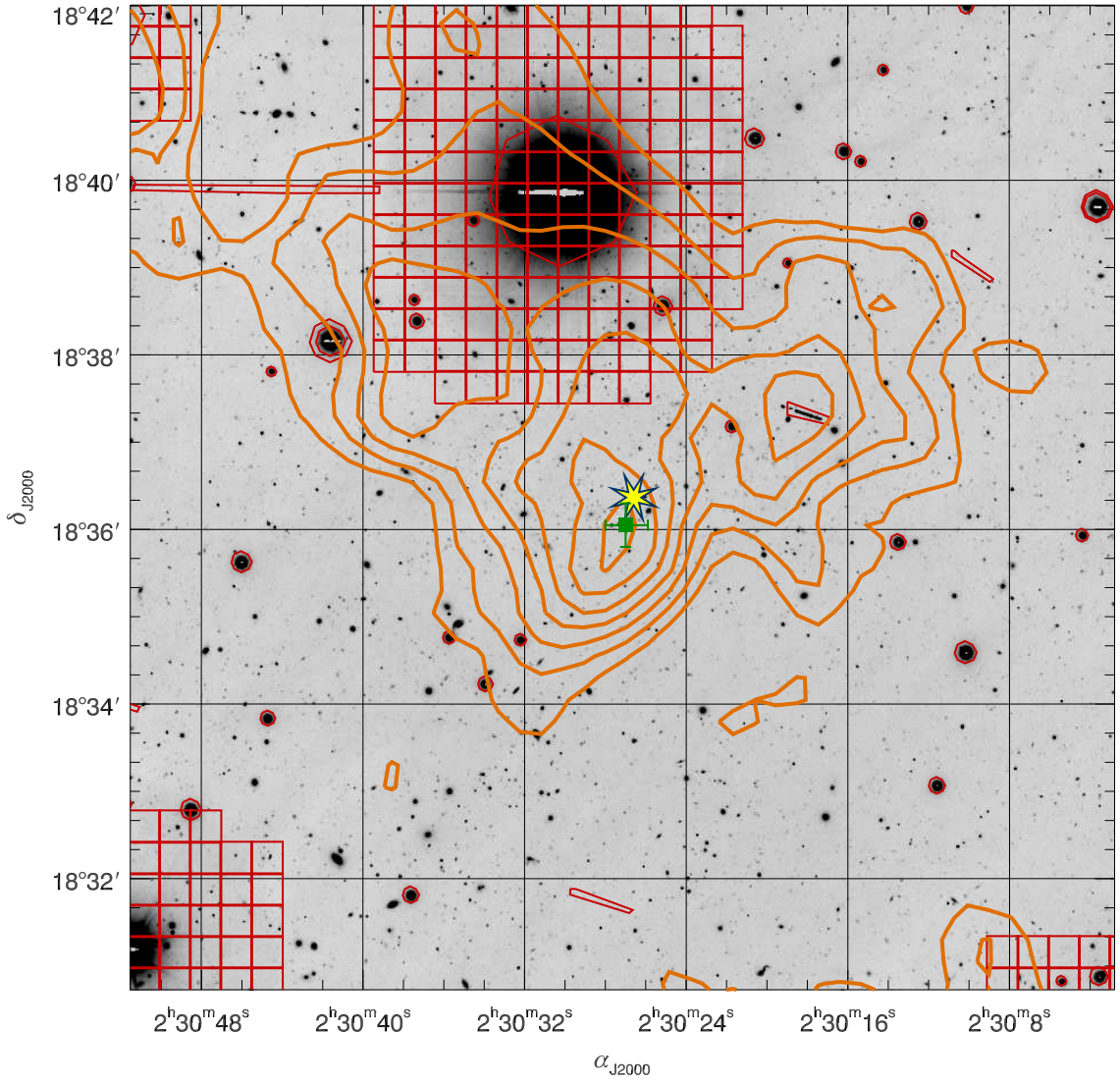

Figure 7.25: Aperture mass map of CL 0230+1836, overlaid on the central region, overlaid on the central, of the MEGACAM r'-band image. The lines and symbols are the same as in Fig. 7.23.

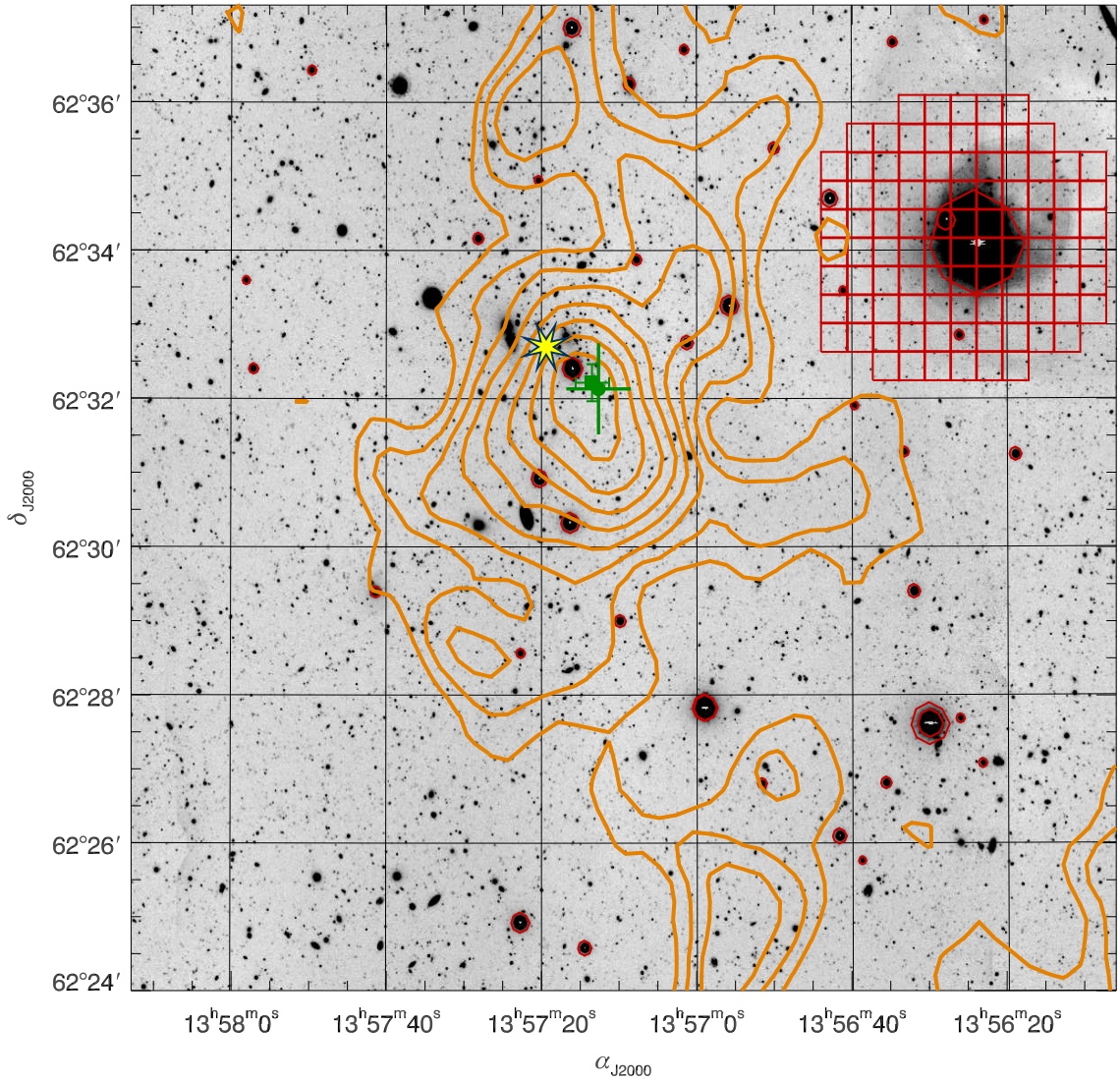

Figure 7.26: Aperture mass map of CL 1357+6232, overlaid on the most interesting region of the MEGACAM r'-band image. The lines and symbols are the same as in Fig. 7.23.

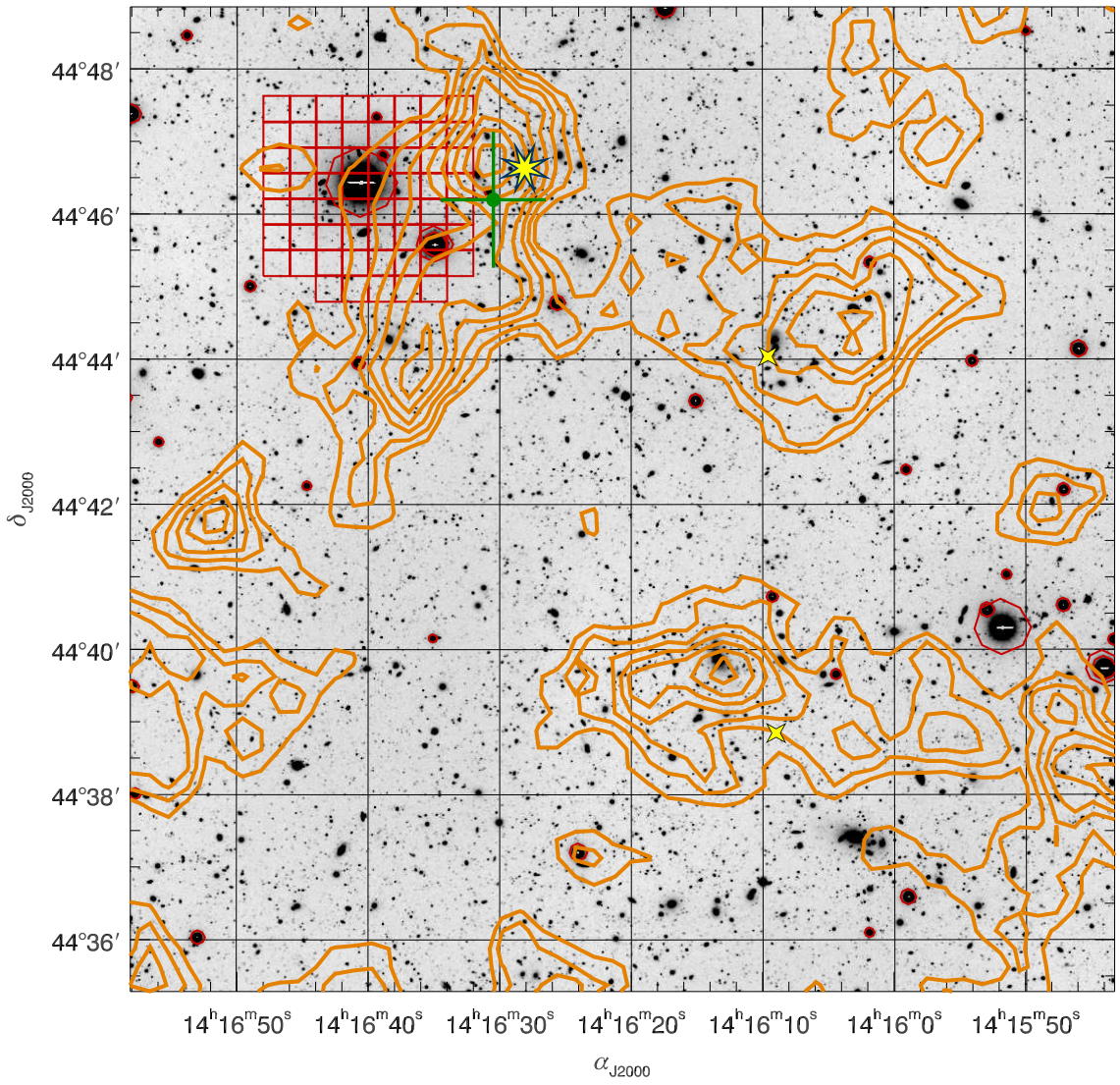

Figure 7.27: Aperture mass map of CL 1416+4446, overlaid on the most interesting region of the MEGACAM r'-band image. The lines and symbols are the same as in Fig. 7.23. In addition, two small four-pointed star symbols mark the coordinates of two further clusters, which we discuss in Sect. 8.1.3.

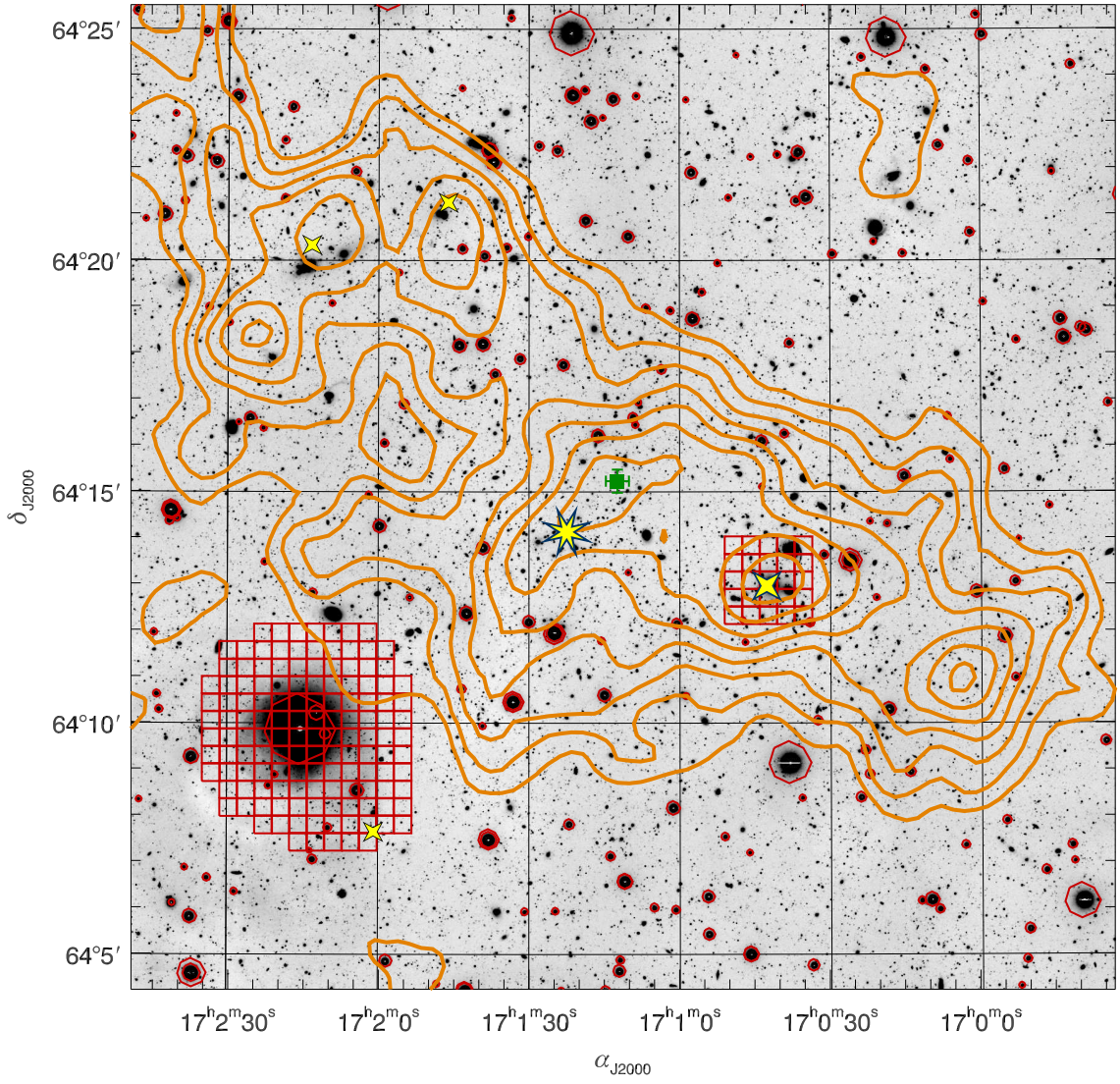

Figure 7.28: Aperture mass map of CL 1701+6414, overlaid on the central, most interesting region of the MEGACAM r'-band image. The lines and symbols are the same as in Fig. 7.23. In addition to the eight-pointed star symbol denoting the ROSAT centre of CL 1701+6414, a big four-pointed star symbol marks the position of Abell 2246, and three smaller ones the positions of VMF 191 ($\alpha_{\rm J2000} = 17^{\rm h}01^{\rm m}46^{\rm s}$, $\delta_{\rm J2000} = +64°21'15''$), VMF 192 ($\alpha_{\rm J2000} = 17^{\rm h}02^{\rm m}13^{\rm s}$, $\delta_{\rm J2000} = +64°20'20''$), and RX J1702+6407 ($\alpha_{\rm J2000} = 17^{\rm h}02^{\rm m}01^{\rm s}$, $\delta_{\rm J2000} = +64°07'39''$), respectively. All of these clusters are X-ray sources detected with ROSAT. Inspection of the ROSAT image does not show any obvious, strong extended emission at the position of the 3.6σ shear peak south-west of A 2246.

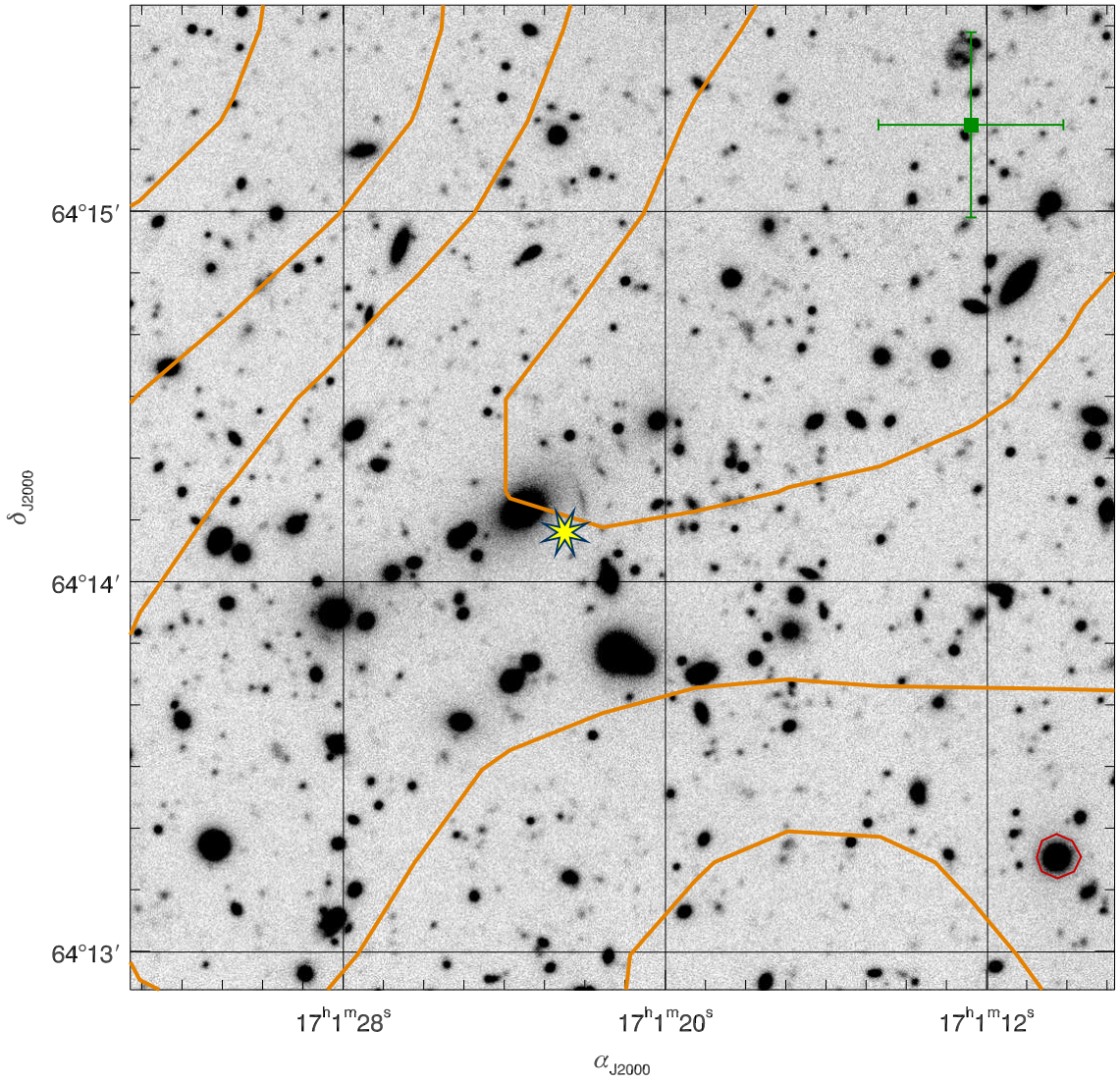

Figure 7.29: Zoomed version of Fig. 7.28, showing the BCG of CL 1701+6414, and, to the west of it and above the star symbol marking the ROSAT centre, the tentative strong lensing arc.

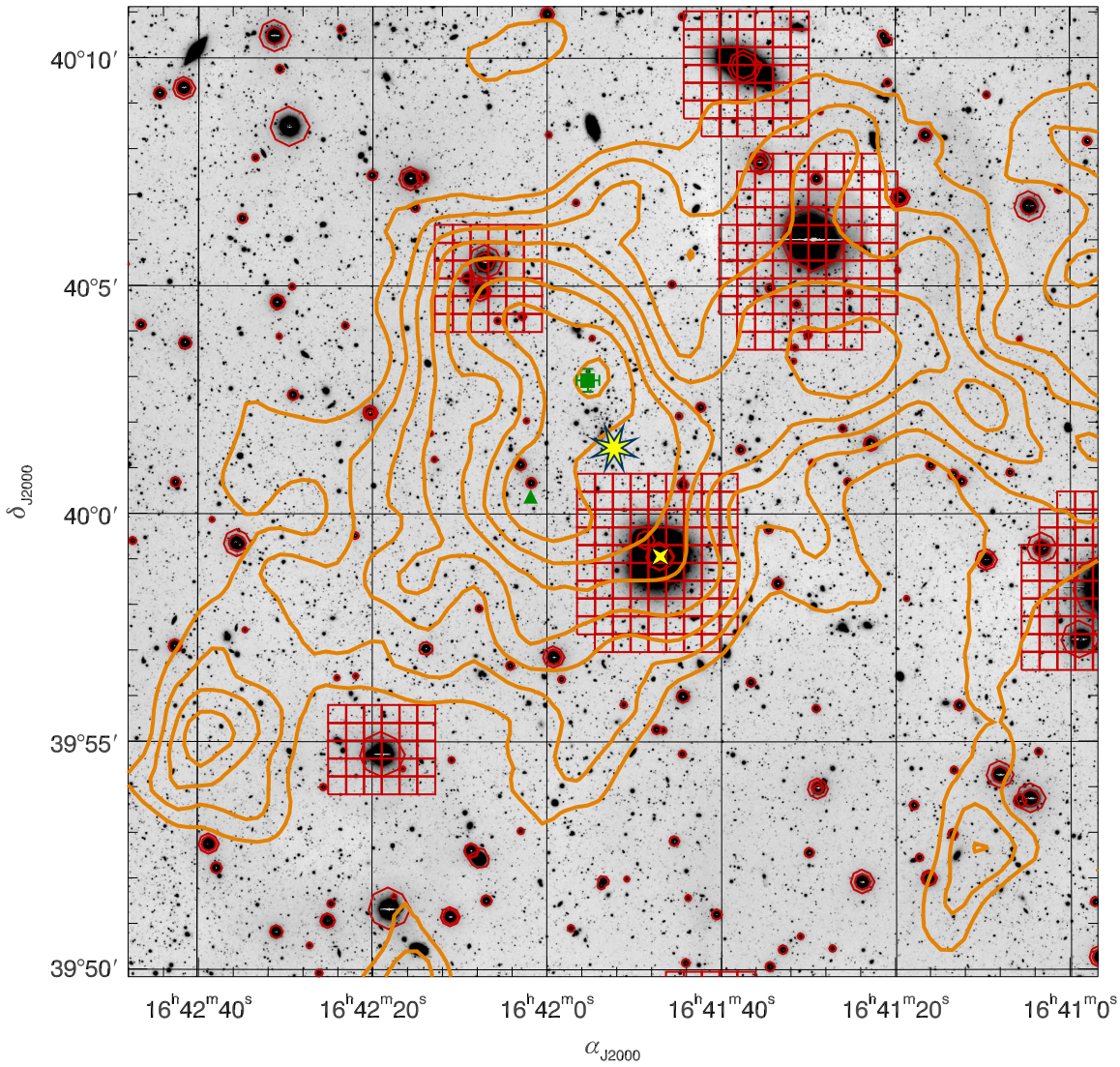

Figure 7.30: Aperture mass map of CL 1641+4001, overlaid on the central, most interesting region of the MEGACAM r'-band image. The lines and symbols are the same as in Fig. 7.23. In addition to the eight-pointed star symbol denoting the ROSAT centre of CL 1641+4001, a four-pointed star symbol marks the coordinates of SDSS-C4-DR3 3628 (Sect. 7.3.8). Inspection of the CHANDRA image shows extended X-ray emission at these coordinates of SDSS-C4-DR3 3628, indicative of a deep gravitational potential.

Chapter 8

Discussion

In this final major Chapter, we present and discuss the mass estimates for the eight clusters investigated in this thesis. Section 8.1 reviews the background selection, shear measurement, and cluster detections using the S-statics before we repeat the error analysis for the Sect. 7 clusters in Sect. 8.2. We further determine hydrostatic X-ray masses and compare them to the lensing mass estimates. In Sect. 8.3, we extend this comparisons to scaling relations including the results of Vikhlinin et al. (2009a). Finally, Sect. 8.4 presents an outlook on the further analyses we plan for these clusters for the follow-up publication to Israel et al. (2010).

8.1 Shear Estimates and Cluster Detections

8.1.1 Possible Improvements to the Background Selection Technique

We found in Sect. 7.2 that the background detection technique based on the g'–r' and r'–i' colours of galaxies improved the S-statistics detection of our clusters in three out of the four cases for which we have $g'r'i'$ imaging. The corresponding improvement is $\Delta S \approx 1$ for the best cases, CL 0159+0030 and CL 0809+2811, consistent with the expectation based on assuming all objects removed from the catalogue being shear-diluting foreground galaxies.

Given observations in the $g'r'i'$ bands only, a possible improvement of our method could be to assign to each source in the galaxy shape catalogue a probability of being in the background of a galaxy cluster at a redshift $z_{\rm d}$, by analysing the $g'r'i'$ colours of galaxies in a photo-z catalogue used as a proxy. To this end, we consider the fine grid in r', $g'-r'$, and $r'-i'$, we constructed for plotting the loci of foreground galaxies in Figs. 6.7, 7.3, and 7.4. Instead of somewhat artificially defining a sharp boundary between fore- and background sources via background selection polygons (Tables 6.2 and 7.1), the method we suggest for the future weights the shear estimate observed for each data galaxy in the grid cell by the background fraction measured in the same cell from the photo-z catalogue. Ideally, the photo-z catalogue should be observed with the same camera under similar conditions, to minimise biases induced by using this proxy.

Obviously, the priority in a WL survey is to achieve the deepest possible lensing image band in the best possible seeing. We emphasise that the *Run C* data from which we draw lensing catalogues leading to $> 3\sigma$ detections and mass estimates of four clusters, were observed in only two nights at the MMT. The instrumental problem leading to an anisotropic PSF in a significant fraction of the exposures (Sec. 5.3) prevented this as well as our other runs from achieving its full detection potential. With the caveat that the situation might be different if the nominal exposure times in the $g'r'i'$ bands were met, the outcome of our background selections suggests that more efficient observing strategies exist in terms of S-detection level per hours of telescope time than the one we used so far in the *400d* WL survey (Sect. 4.2.3).

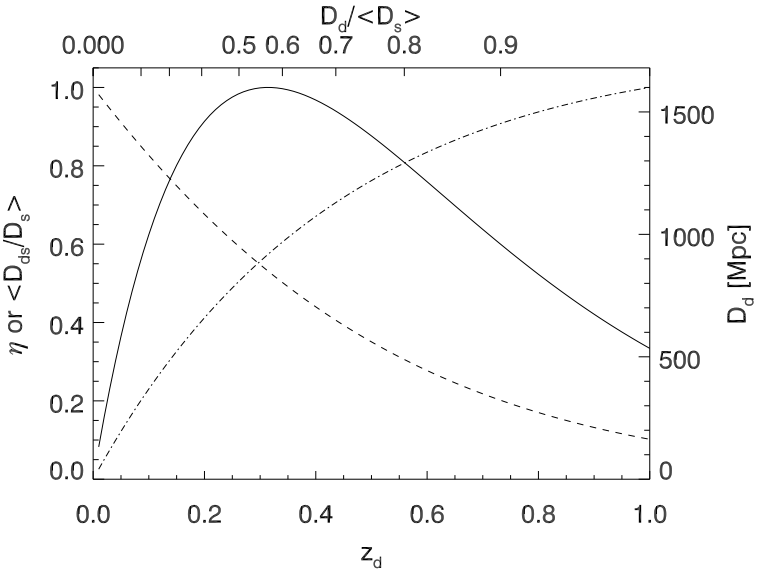

Figure 8.1: Lensing efficiency as a function of lens redshift z_d, given the CFHTLS *Deep 1* photo-*z* distribution. The solid line gives the lensing efficiency $\eta(z_d) = D_d(z_d)\,\langle D_{ds}(z_d)/D_s\rangle/\eta_{max}$ for a fixed $\langle D_s\rangle$, where $\eta_{max} = \max\,[D_d(z_d)\,\langle D_{ds}(z_d)/D_s\rangle]$. The dashed curve denotes $\langle D_{ds}(z_d)/D_s\rangle$, measured from the CFHTLS *Deep 1* photo-*z* distribution (Sect. 6.2.4); while the dot-dashed curve denotes the angular-diameter distance $D_d(z_d)$ of the lens.

Photometric redshifts with at least five bands, e.g. $u'g'r'i'z'$, provide a more accurate background selection than our method based on three bands. Given that we were able to detect our clusters with less than the nominal net exposure times, observing five bands might be feasible without spending more time per cluster. In the future, we will compare our background selection method to a background selection based on excising the red cluster sequence from the galaxy shape catalogue, similar to the one used by Okabe et al. (e.g., 2009). The most important point, however, concerning accuracy of the mass estimate is – most likely – the data quality in the lensing band, which is difficult to control given the fixed scheduling with which the existing *400d* WL runs were observed.

8.1.2 Significance of Cluster Detections

We successfully detected all observed *400d* clusters with at least 3.5σ significance and were able to derive a weak lensing mass estimate for each of the eight clusters. In Table 7.2, we summarise the maximum detection levels S and the corresponding filter scales θ_{out}. The most significant detection is CL 0030+2618 at $z = 0.50$ with $S = 5.84$; the formally least significant detection is CL 0230+1836 at $z = 0.80$ with $S = 3.64$. We note that the $S = 3.75$ measured for CL 1701+6414 has a contribution by A 2246 at $\theta \approx 270''$ separation (Sect. 7.3.7), rendering it the least secure detection. For $\theta_{out} = 220''$, we detect CL 1701+6414 at the 2.5σ level.

There are several factors influencing the strength of a cluster's lensing signal: its mass and redshift, but also the depth and quality (mainly seeing) of the data. In order to compare the detections of clusters at different *z*, we consider their relative lensing efficiencies (Sect. 3.2.2), expressed by the distances $D_d\,\langle D_{ds}/D_s\rangle$ in Eq. (3.5). By writing $\langle D_{ds}/D_s\rangle$, we already took into account our measurement of this quantity as an ensemble average. In Fig. 8.1, we present $\eta(z_d) = D_d(z_d)\,\langle D_{ds}(z_d)/D_s\rangle/\eta_{max}$ (solid curve) for a fixed $\langle D_s\rangle$ and as a function of lens redshift z_d, normalised to its maximum $\eta_{max} = \max\,[D_d(z_d)\,\langle D_{ds}(z_d)/D_s\rangle]$ at $z_d = 0.31$. The fixed source

redshift distribution in Fig. 8.1 is taken from the CFHTLS *Deep 1* field, which we used in our analysis (Sect. 6.2.4). The corresponding estimate of $\langle D_{\rm ds}/D_{\rm s}\rangle$ is shown as the dashed curve in Fig. 8.1). We note that $\eta(z_{\rm d})$ confirms the rule-of-thumb that for a given $\langle z_{\rm s}\rangle$ the maximum lensing efficiency is found for $D_{\rm d} \sim \langle D_{\rm s}\rangle/2$ (Sect. 3.2.2). In Fig. 8.1, only one $\langle z_{\rm s}\rangle$ was tested, though. Because we consider an *average* source redshift, the lensing efficiency for $z_{\rm d} = \langle z_{\rm s}\rangle = 1.04$ is still significant ($\eta \approx 0.3$).

The relative lensing efficiencies of our clusters range between $\eta = 0.97$ for CL 0159+0030 and $\eta = 0.52$ for CL 0230+1836. Correcting for the distance effect, CL 0230+1836 is the most significant detection (in terms of $S_{\rm max}/\eta(z_{\rm d})$), despite its short net exposure time, closely followed by CL 0030+2618. The smallest value for the corrected significance we find for CL 1701+6414. We observe no significant trend of $S_{\rm max}/\eta(z_{\rm d})$ with WL mass. We notice that by detecting CL 0230 +1836, we demonstrated the feasibility of MEGACAM weak lensing studies out to the highest redshifts accessible for current ground-based weak lensing.

The aperture mass S-statistics is known to produce spurious shear peaks even at high significance levels, although as simulations show, false detections above the $\sim 4\sigma$ level are rare (e.g., Hetterscheidt et al. 2005; Dietrich et al. 2007). Thus, in principle, there is a nonzero, but small chance for one or the other of our detections to be false. Spurious detections are more sensitive against changes in the lensing catalogue or $\theta_{\rm out}$. Our tests with different photometric cuts and values for $\theta_{\rm out}$ found our cluster shear peaks to be robust. Another useful check is the bootstrapping of the lensing catalogue which we performed for CL 0030+2618, CL 1357+6232, and CL 1416+4446, and plan to conduct for the remaining clusters.

The separations between the shear peaks and ROSAT centres are $< 3'$ in all cases and $< 1'$ for four of the eight clusters. This coincidence of X-ray and lensing centres adds further significance to the S-detections. Two out of the four remaining clusters, CL 0159+0030 and CL 0809+2811, have their S-peaks within larger masked areas, reducing the accuracy with which the centres can be determined.[1] The complicated shear fields in the vicinities of CL 1701+6414 and CL 1641+4001, with separations $> 1'$ between lensing and ROSAT have been discussed in Sects. 7.3.7 and 7.3.8.

We note that the ROSAT cluster centres themselves are accurate to $\sim 10''$ accuracy while CHANDRA offers higher spatial resolution, such that an order of magnitude is gained in the accuracy of the centring ($\sim 1''$). Therefore, we plan to compare the lensing centres to centres obtained with CHANDRA, as we did already for CL 0030+2618 (Sect. 6.3.1). Furthermore, we plan to conduct "mass" (κ) reconstructions for the seven clusters analysed in Sect. 7. Finally, we notice that methods exist which are less sensitive to projections of LSS at different redshifts, which can mimic the signal of a galaxy cluster in the S-statistics. In particular, we mention the optimal filter ("P-statistics"), introduced by Maturi et al. (2005, 2007), which might provide a useful tool to clarify the detections in the CL 1701+6414 and CL 1641+4001 fields.

8.1.3 Cross-Identifications

Here, we present detections of the *400d* survey clusters in surveys besides *400d*, and its precursor *160d*. Only two clusters are cross-listed in similar X-ray surveys: CL 0030+2618 in *WARPS*, the *Wide Angle Pointed* ROSAT *Survey* (Horner et al. 2008), and CL 1701+6414 in the *Bright SHARC* sample (Sect. 7.3.7, Romer et al. 2000). In the following, we also list known clusters close to our clusters of interest. For CL 0030+2618, we refer to the introduction to Sect. 6. The fields of CL 1701+6414 and CL 1641+4001 have been discussed already in Sects. 7.3.7 and 7.3.8. For CL 0230+1836, there are neither independent detections nor other galaxy clusters within a $20'$

[1] A possible route to circumvent this problem is to modify the spatial response of the filter $Q(x)$ in (Eq. 6.1), accounting for the large masks.

radius listed in NED. We notice that, generally, relying on NED, we might miss rather recent references not listed yet in their database.

CL 0159+0030 Being located in the SDSS equatorial strip, CL 0159+0030 has been detected by Goto et al. (2002) in the SDSS commissioning data, using their photometric "cut and enhance" cluster finder. Plionis et al. (2005) followed up Goto et al. (2002) cluster candidates using archival XMM-Newton observations. From the 3800 s PN observation Plionis et al. (2005) analysed, only a 3σ upper flux limit of 2.1×10^{-14} erg cm^{-2} s^{-1} in the 0.5–2.0 keV energy range could be inferred. This non-detection disagrees with the flux of $3.3\pm0.4\times10^{13}$ erg cm^{-2} s^{-1} Vikhlinin et al. (2009a) measure for CL 0159+0030 with Rosat.

CL 0809+2811 We hypothesise that CL 0809+2811 is identical to ZwCl 0806.5+2822 at $\alpha_{J2000} = 08^h09^m34^s$, $\delta_{J2000} = +28°13'.1$, a position 1'.9 off the CL 0809+2811 Rosat centre and at similar distance to the bright star in the field, where we do not see a concentration of galaxies. Neither do we observe an overdensity of galaxies at the position of a secondary shear peak with $S = 2.9$ (Fig. 7.24). It is located at $\alpha_{J2000} = 08^h09^m08^s$, $\delta_{J2000} = +28°05'22''$. No cluster within 3' of this position is known to NED.

CL 1357+6232 Lopes et al. (2004) conducted a cluster survey on digitised plates from the Second Palomar Observatory Sky Survey, using a Voronoi tesselation technique. In their catalogue, Lopes et al. (2004) quote a cluster of galaxies at $\alpha_{J2000} = 13^h57^m22^s$, $\delta_{J2000} = +62°33'11''$, where there is no source in the Megacam image. Using the relation found between r' magnitude, $g'-r'$ colour and z_{spec} for a subsample of clusters with spectroscopic redshifts, Lopes et al. (2004) assign $z = 0.19$ to their detection. (NSCS J135722+623311, their #7243). Noting that the position of NSCS J135722+623311 is only 16'' from the Rosat centre of CL 1357+6232, we speculate that it might be the result of a confusion of the *400d* cluster with two bright galaxies to its east, one of which (SDSS J135723.83+623246.1) has a measured redshift of $z = 0.078$.

CL 1416+4446 Lopes et al. (2004) list a cluster NSCS J141623+444558 in their catalogue which, by NED, is identified with CL 1416+4446. Furthermore, Lopes et al. (2004) detected a cluster of galaxies at $\alpha_{J2000} = 14^h16^m09^s$ and $\delta_{J2000} = +44°38'51''$, with a redshift of $z = 0.39$. Less than 2' north-east of these coordinates we find the south-western shear peak which coincides with the $g' = 20.1$ galaxy SDSS J141613.33+443951.3. For this source, SDSS (Adelman-McCarthy et al. 2008) quotes a spectroscopic redshift of $z = 0.397$. Note that the brighter galaxy SDSS J141603.01+443725.1, located 2' further to the south-west from the Lopes et al. (2004) cluster position has an SDSS $z_{spec} = 0.310$ and does not correspond to an S-peak.

Barkhouse et al. (2006) detected a galaxy cluster at $\alpha_{J2000} = 14^h16^m09^s.6$, $\delta_{J2000} = +44°44'02''.4$, coincident with the western shear peak, comparing archival Chandra data to optical $g'r'i'$ observations in the Chandra Multiwavelength Project. They assign a redshift $z = 0.427$ to the cluster, designated BGV 50. In the same Chandra observation, Barkhouse et al. (2006) identified another cluster, BGV 53 at $\alpha_{J2000} = 14^h16^m27^s.6$ and $\delta_{J2000} = +44°52'44''.4$ and a redshift of $z = 0.452$, which doesn't correspond to a bright galaxy in the Megacam image or a peak in the S-statistics.

Out of the three confirmed clusters in the field, CL 1416+4446 not only is the only *400d* X-ray cluster and the strongest lensing detection, but also appears to be the optically richest system in the Megacam r'-band image. Therefore, CL 1416+4446 possibly presents the most massive system in a physically interacting super-structure, indicated by the $z \approx 0.40$ redshifts of all mentioned clusters. Judging by the X-ray morphology, Vikhlinin et al. (2009a) classify CL 1416+4446 as

a relaxed system, though. We conclude that the CL 1416+4446 field qualifies as an interesting candidate for further investigation concerning the existence of a super-cluster.

8.2 Interpretation of the Mass Estimates

8.2.1 Error Analysis

Calculation of the Errors The error analysis of the seven clusters analysed in Chapter 7 follows the method described in Sect. 6.5.4, i.e. we apply Eq. (6.16) to calculate the total uncertainty for each cluster. We will now discuss how we obtain the different terms in Eq. (6.16). The statistical error $\sigma_{\rm stat}$ is taken from the computation of $\Delta\chi^2_{\rm L}$ (or $\Delta\chi^2_{\rm L3}$ for CL 1701+6414) for the respective cluster on a grid in r_{200} and $c_{\rm NFW}$ (Sect. 7.3), converting the upper and lower limits into masses by applying Eq. (6.7). Table 8.1 compares the masses of our eight clusters and their errors.

The components $\sigma_{\rm cali}$ and $\sigma_{\rm geom}$, accounting for the uncertainties in the shear calibration factor f_0 (cf. Sect. 6.5.3) and the redshift distribution of the source galaxies are likewise determined from the analysis of the parameter grid, as shown in Sects. 6.5.3 and 6.5.4 for CL 0030+2618. Assuming the redshift distribution to be well modelled by the fits to the CFHTLS *Deep 1* photo-*z* catalogue (Sect. 7.1.1), we vary $\langle D_{\rm ds}/D_{\rm s}\rangle$ by the uncertainties tabulated in Table 6.4. The parameters minimising the respective $\chi^2_{\rm L}$ and confidence contours for these models can be found in Figs. B.10 to B.16 in Appendix B.3; the resulting parameters are also listed in Tables 7.3 to 7.9. As expected, $\sigma_{\rm geom}$ increases with redshift because of the higher relative uncertainty in $\langle D_{\rm ds}/D_{\rm s}\rangle$.

As in the case of CL 0030+2618, we not only consider the uncertainty of ±0.05 we estimate for f_0, but also take into account the dilution by remaining foreground galaxies in the shear calibration error. Once again using the CFHTLS *Deep 1* photo-*z* catalogue as a proxy, we determine the fraction of galaxies at $z_{\rm ph} < z_{\rm cl}$ after applying the respective background selection. We measure this fraction $\hat{f}_{\rm d}$ to increase with z: it varies from 8.7 % for CL 0159+0030 to 32.1 % for CL 0230+1836 (Table 8.2). As can be seen for CL 0809+2811 and CL 1416+4446 at the same redshift $z = 0.40$, the background selection based on three bands results in a lower $\hat{f}_{\rm d} = 10.5$ % that the mere magnitude cut ($\hat{f}_{\rm d} = 13.6$ %) for only one band. Adding the two components of the error in quadrature, the lower limit we consider for f_0 ranges from 0.97 for CL 0159+0030 to 0.73 for CL 0230+1836. Again, the corresponding parameters minimising the respective $\chi^2_{\rm L}$ and confidence contours are presented in Figs. B.10 to B.16 in Appendix B.3 and Tables 7.3 to 7.9.

To calculate the error $\sigma_{\rm LSS}$ induced by LSS for the more general case, we need to extrapolate the findings of Hoekstra (2003), covering only the cases of $5h^{-1}$, $10h^{-1}$, and $20h^{-1} \times 10^{14}\,{\rm M}_\odot$ to lower masses. (Note that our $M^{\rm wl}$ estimate for CL 0030+2618 is very close to the first case.) The respective error contributions read from Fig. 6 of Hoekstra (2003) are $\sim 1.2h^{-1}$, $\sim 1.7h^{-1}$, and $\sim 2.7h^{-1} \times 10^{14}\,{\rm M}_\odot$. By assuming that the *relative* LSS error $\sigma_{\rm LSS}/M^{\rm wl}$ increases linearly towards smaller masses, we arrive at the following relation:

$$\sigma_{\rm LSS}/(10^{14}\,{\rm M}_\odot) = aM_{14} + bM_{14}^2 \quad , \tag{8.1}$$

where $a = 0.22h^{-1}$, $b = -0.01$, and $M_{14} = M^{\rm wl}/(10^{14}\,{\rm M}_\odot)$. We understand Eq. (8.1) as an order-of-magnitude estimate for the LSS error and stress that simulated WL measurements are required to provide a better understanding of this important source of uncertainty. In particular, we expect a larger $\sigma_{\rm LSS}$ for higher $z_{\rm d}$ clusters, for which chances are higher that significant structure is to be found between $z_{\rm d}$ and $z = 0$. We notice that the results of Hoekstra (2003) are obtained at $z = 0.3$, more nearby than our clusters.

Table 8.1: Weak lensing and X-ray masses resulting from our analysis. Given are the weak lensing masses $M_{200}^{\rm wl}(r_{200}^{\rm wl})$, their lower and upper statistical ($\sigma_{\rm stat}^{-}$ and $\sigma_{\rm stat}^{+}$), systematic ($\sigma_{\rm sys}^{-}$ and $\sigma_{\rm sys}^{+}$), and total error margins ($\sigma_{\rm tot}^{-}$ and $\sigma_{\rm tot}^{+}$). Next, the corresponding relative errors are presented. The last two columns give the ICM temperature $T_{\rm X}$ from Vikhlinin et al. (2009a) and the hydrostatic X-ray mass $M_{200}^{\rm hyd}(r_{200}^{\rm wl})$. All masses are given in units of $10^{14}\,{\rm M}_{\odot}$.

Cluster	$M_{\rm wl}(r_{200,\rm wl})$	$\sigma_{\rm stat}^{-}$	$\sigma_{\rm stat}^{+}$	$\sigma_{\rm sys}^{-}$	$\sigma_{\rm sys}^{+}$	$\sigma_{\rm tot}^{-}$	$\sigma_{\rm tot}^{+}$	$\frac{\sigma_{\rm stat}^{-}}{M^{\rm wl}}$	$\frac{\sigma_{\rm stat}^{+}}{M^{\rm wl}}$	$\frac{\sigma_{\rm sys}^{-}}{M^{\rm wl}}$	$\frac{\sigma_{\rm sys}^{+}}{M^{\rm wl}}$	$\frac{\sigma_{\rm tot}^{-}}{M^{\rm wl}}$	$\frac{\sigma_{\rm tot}^{+}}{M^{\rm wl}}$	$T_{\rm X}\,[{\rm keV}/k_{\rm B}]$	$M_{200}^{\rm hyd}(r_{200}^{\rm wl})$
CL 0030+2618	6.83	1.86	2.11	2.17	2.21	2.89	3.03	27 %	31 %	32 %	32 %	42 %	44 %	5.63 ± 1.13	6.13 ± 1.23
CL 0159+0030	5.42	2.12	2.30	1.57	1.65	2.64	2.83	39 %	42 %	29 %	30 %	49 %	52 %	4.25 ± 0.96	4.86 ± 1.10
CL 0230+1836	8.10	4.06	4.92	3.58	2.81	5.41	5.66	50 %	61 %	44 %	35 %	67 %	70 %	5.50 ± 1.02	11.76 ± 2.18
CL 0809+2811	11.25	3.15	3.22	2.96	2.94	4.33	4.36	28 %	29 %	26 %	26 %	38 %	39 %	4.17 ± 0.73	8.60 ± 1.51
CL 1357+6232	3.51	1.50	1.75	1.35	1.17	2.02	2.10	43 %	50 %	38 %	33 %	58 %	60 %	4.60 ± 0.69	4.67 ± 0.70
CL 1416+4446	1.78	0.73	0.87	0.61	0.62	0.95	1.07	41 %	49 %	34 %	35 %	53 %	60 %	3.26 ± 0.46	2.75 ± 0.39
CL 1641+4001	4.13	1.78	2.38	1.49	1.55	2.33	2.84	43 %	58 %	36 %	37 %	56 %	69 %	3.31 ± 0.62	3.87 ± 0.73
CL 1701+6414	2.96	1.34	1.72	1.24	1.05	1.83	2.02	45 %	58 %	42 %	36 %	62 %	68 %	4.36 ± 0.46	3.23 ± 0.34

Table 8.2: Components of the statistical error. We show the estimated fraction $\hat{f}_{\rm d}$ of foreground galaxies in the lensing catalogue and list all components entering (Eq. 6.16): The uncertainties $\sigma_{\rm cali}^{\pm}$ due to shear calibration, and $\sigma_{\rm geom}^{\pm}$ from $\langle D_{\rm ds}/D_{\rm s}\rangle$, the projectional uncertainty $\sigma_{\rm proj}^{\pm}$ due to cluster triaxiality, and $\sigma_{\rm LSS}^{\pm}$ from the projection of unrelated LSS. All errors are given in units of $10^{14}\,{\rm M}_{\odot}$; the numbers in parentheses present the relative uncertainties.

Cluster	$\hat{f}_{\rm d}$	$\sigma_{\rm cali}^{-}$	$\sigma_{\rm cali}^{+}$	$\sigma_{\rm geom}^{-}$	$\sigma_{\rm geom}^{+}$	$\sigma_{\rm proj}^{-}$	$\sigma_{\rm proj}^{+}$	$\sigma_{\rm LSS}^{-}$	$\sigma_{\rm LSS}^{+}$
CL 0030+2618	0.152	1.16 (17 %)	0.42 (6 %)	0.66 (10 %)	0.86 (13 %)	0.68 (10 %)	1.10 (16 %)	1.62 (24 %)	1.62 (24 %)
CL 0159+0030	0.087	0.44 (8 %)	0.11 (2 %)	0.33 (6 %)	0.35 (6 %)	0.54 (10 %)	0.87 (16 %)	1.36 (25 %)	1.36 (25 %)
CL 0230+1836	0.321	2.74 (34 %)	0.35 (4 %)	1.16 (14 %)	1.66 (20 %)	0.81 (10 %)	1.30 (16 %)	1.82 (22 %)	1.82 (22 %)
CL 0809+2811	0.105	1.41 (13 %)	0.37 (3 %)	0.90 (8 %)	0.75 (7 %)	1.12 (10 %)	1.80 (16 %)	2.17 (19 %)	2.17 (19 %)
CL 1357+6232	0.198	0.82 (23 %)	0.09 (3 %)	0.35 (10 %)	0.37 (11 %)	0.35 (10 %)	0.56 (16 %)	0.95 (27 %)	0.95 (27 %)
CL 1416+4446	0.136	0.26 (15 %)	0.11 (6 %)	0.11 (6 %)	0.17 (10 %)	0.18 (10 %)	0.28 (16 %)	0.51 (29 %)	0.51 (29 %)
CL 1641+4001	0.127	0.81 (20 %)	0.30 (7 %)	0.47 (11 %)	0.82 (20 %)	0.41 (10 %)	0.66 (16 %)	1.10 (27 %)	1.10 (27 %)
CL 1701+6414	0.134	0.83 (28 %)	0.24 (8 %)	0.30 (10 %)	0.40 (14 %)	0.30 (10 %)	0.47 (16 %)	0.82 (28 %)	0.82 (28 %)

Applying Eq. (6.15) for all our eight clusters, we find predicted largest-to-smallest axis ratios $0.60 < \eta < 0.64$. Hence, again considering the triaxiality biases of Corless & King (2007), we use $\sigma^{+}_{\rm proj} = 0.16\,M^{\rm wl}$ for the error $M^{\rm wl}$ induced by overestimation and $\sigma^{-}_{\rm proj} = 0.10\,M^{\rm wl}$ for the one induced by underestimation caused by the projection of triaxial halos.

Interpretation of the Errors The statistical, systematic, and total errors for all eight clusters are summarised in Table 8.1, both as absolute masses and as relative errors. Table 8.2 provides the details on the composition of the systematic error for the eight clusters. We note that for all our clusters, in particularly the ones with small WL masses, the statistical uncertainties are the largest component in the total error (the second largest usually being the projection of unrelated LSS). The relative statistical errors range between ≈ 30 % and ≈ 60 %. The reason for this can be twofold: First, the large statistical uncertainties *per se* are caused by the small signal-to-noise in the lensing signals and thus a consequence of the low net exposure times in the lensing-band images, once we removed frames with high PSF anisotropy (Table 4.2 and Sect. 5.3). Second, our account of the systematics might underestimate or neglect contributions to the systematic error. For instance, uncertainties in the determination of the centres and the radial fitting ranges are not considered in Eq. (6.16). A reliable quantification of these errors has to be found for future analyses. Neither does Eq. (6.16) include the contamination correction available only for clusters imaged in $g'r'i'$. However, we find its impact on the cluster parameters to be small compared to the statistical errors.

We neither consider the uncertainty in the choice of $\max(|\varepsilon|)$ in the error analysis. However, we account for its effect via the shear calibration (Sect. 6.1.4), such that we do not expect a significant systematic error. Simulations of cluster lensing (Sect. 5.4.2) will be necessary to test whether our shear calibration $f_0 = 1.08$ cancels the bias resulting from $\max(|\varepsilon|)$ completely. We mentioned in Sect. 6.5.3 the counter-intuitive decrease of $r^{\rm min}_{200}$ for CL 0030+2618 with increasing $\max(|\varepsilon|)$. Indeed, only CL 1357+6232 shows a similar relative decrease in $r^{\rm min}_{200}$. Averaging over all eight clusters, these cases are balanced by CL 0230+1836 and CL 1416+4446, for which we measure $r^{\rm min}_{200}$ to *increase* with $\max(|\varepsilon|)$. With $\max(|\varepsilon|) = 1.0$, we measure for four cases a smaller $r^{\rm min}_{200}$ than for $\max(|\varepsilon|) = 0.8$, and in four cases a larger radius. The same holds for $\max(|\varepsilon|) = 10^4$. These results suggest that even the uncorrected bias due to $\max(|\varepsilon|)$ might be small.

We notice that the roles of the shear calibration f_0, considered in Eq. (6.16) as $\sigma_{\rm cali}$ and the correction $f_1(\theta)$ (Sects. 6.4.1 and 7.3.1) for cluster members cannot be completely disentangled. On the one hand, considering the cluster member correction separately is justified by the radial dependence of $f_1(\theta)$. On the other hand, we have to stress that the uncertainty in $f_1(\theta)$ might be large due to the weak detections of the cluster red sequence. In addition, the effect of $f_1(\theta)$ on the mass estimate (6 % to 11 %, Tables 6.7 and 7.3 to 7.5) falls behind the related systematic error component $\sigma^{-}_{\rm cali}$ in three out of four cases (Table 8.2) and is significantly smaller than the statistical uncertainty in the mass. Hence, a possible plan to consider cluster membership consistently – also for single-band clusters – would be to include it into the systematic error. Also here, we suppose performing simulations of cluster WL fields to be helpful for the further investigations.

Finally, we note that total 1σ error intervals consistent with cluster masses close to zero do not mean these clusters are detected merely at the $\sim 1\sigma$ level: Shear calibration, $z_{\rm s}$-distribution, and triaxiality errors are multiplicative, such that they do not affect the detection significance.

8.2.2 Mass–Concentration Relation

In the case of a very low concentration parameter $c_{\rm NFW} \lesssim 1$, the tangential shear profile becomes flat and the r_{200} becomes difficult to constrain. We notice that the confidence contours in the extreme cases CL 1641+4001 and CL 1701+6414 become more elongated towards low r_{200}, with a cusp at small r_{200} and $c_{\rm NFW} \approx 0$ (Figs. 7.20 and 7.22).

Table 8.3: Weak lensing and hydrostatic masses under the assumption of the Bullock et al. (2001) mass–concentration relation. We compare $c_{\rm NFW}$ and r_{200} from the default cluster models to $c_{\rm B,NFW}$ expected from Bullock et al. (2001) and the corresponding cluster parameters $r_{\rm B,200}$, given in the fourth and fifth column. The sixth and seventh column give the WL mass $M^{\rm wl}_{200,\rm B}(r_{200,\rm B})$ and the ratio $\mu^{\rm wl}_{\rm B} = M^{\rm wl}_{200,\rm B}(r_{200,\rm B})/M^{\rm wl}_{200}(r_{200})$ between the inferred with the Bullock et al. (2001) and independent concentration parameters. The last column shows the hydrostatic mass $M^{\rm hyd}_{200,B}(r_{200,\rm B})$.

Cluster	$c_{\rm NFW}$	r_{200} [Mpc]	$c_{\rm B,NFW}$	$r_{\rm B,200}$ [Mpc]	$M^{\rm wl}_{200,\rm B}(r_{200,\rm B})$ [$10^{14}\,{\rm M}_\odot$]	$\mu^{\rm wl}_{200,\rm B}$	$M^{\rm hyd}_{200,\rm B}(r_{200,\rm B})$ [$10^{14}\,{\rm M}_\odot$]
CL 0030+2618	$1.8^{+0.95}_{-0.75}$	$1.49^{+0.14}_{-0.15}$	3.75	$1.36^{+0.12}_{-0.13}$	$5.19^{+1.64}_{-1.35}$	0.76	5.58 ± 1.12
CL 0159+0030	$9.2^{+>6.8}_{-7.5}$	$1.44^{+0.18}_{-0.22}$	4.00	$1.45^{+0.20}_{-0.24}$	$5.53^{+2.62}_{-2.32}$	1.02	4.90 ± 1.10
CL 0230+1836	$3.2^{+1.9}_{-1.6}$	$1.40^{+0.24}_{-0.29}$	3.80	$1.37^{+0.23}_{-0.28}$	$7.59^{+4.50}_{-3.77}$	0.94	11.36 ± 2.11
CL 0809+2811	$3.7^{+5.1}_{-2.2}$	$1.83^{+0.16}_{-0.19}$	3.65	$1.83^{+0.17}_{-0.19}$	$11.25^{+3.43}_{-3.15}$	1.00	8.60 ± 1.51
CL 1357+6232	$2.8^{+1.65}_{-1.25}$	$1.18^{+0.17}_{-0.20}$	4.20	$1.11^{+0.16}_{-0.18}$	$2.92^{+1.46}_{-1.20}$	0.83	4.36 ± 0.65
CL 1416+4446	$4.9^{+5.65}_{-2.95}$	$0.99^{+0.14}_{-0.16}$	4.55	$1.00^{+0.14}_{-0.17}$	$1.84^{+0.88}_{-0.79}$	1.03	2.80 ± 0.40
CL 1641+4001	$0.3^{+0.7}_{-0.3}$	$1.28^{+0.21}_{-0.22}$	4.15	$1.11^{+0.15}_{-0.18}$	$2.69^{+1.25}_{-1.11}$	0.65	3.34 ± 0.63
CL 1701+6414	$0.6^{+1.6}_{-0.6}$	$1.15^{+0.19}_{-0.21}$	4.40	$1.00^{+0.20}_{-0.28}$	$1.95^{+1.42}_{-1.22}$	0.66	2.79 ± 0.29

We suspect that the low $c_{\rm NFW}$ – caused by a multi-peaked shear signal – not only affects the error in r_{200} but might also influence its value, introducing a bias in the mass. Thus, we consider the one-dimensional merit function for r_{200}, where $c_{\rm NFW}$ is fixed to the value predicted by the Bullock et al. (2001) formula (6.13), given the virial mass estimates tabulated in Table 8.1. The concentrations given by Eq. (6.13) which we list in Table 8.3[2] span a relatively narrow range from $c_{\rm B,NFW} = 3.65$ for CL 0809+2811 on the high-mass end to $c_{\rm B,NFW} = 4.55$ for CL 1416+4446 on the low mass end of the spectrum. We determine the optimal $r_{200,\rm B}$ given $c_{\rm B,NFW}$ and infer $M^{\rm wl}_{200,\rm B}(r_{200,\rm B})$ by applying Eq. (6.7).

Three clusters have measured $c_{\rm NFW} > c_{\rm B,NFW}$; for these three most concentrated objects in our sample, we infer a ratio $\mu^{\rm wl}_{\rm B} = M^{\rm wl}_{200,\rm B}(r_{200,\rm B})/M^{\rm wl}_{200}(r_{200})$ between the masses obtained with fixed and free concentration parameters of $\mu^{\rm wl}_{\rm B} \geq 1$. (For CL 0809+2811, where the difference between $c_{\rm NFW}$ and $c_{\rm B,NFW}$ is small, we obtain identical masses.) Generally, we observe a correlation $\mu^{\rm wl}_{\rm B}$ and $c_{\rm NFW}$: Those clusters, for which we measure $c_{\rm NFW} \ll c_{\rm B,NFW}$, also have $r_{200,\rm B} < r_{200}$ and thus a smaller WL mass if we assume the Bullock et al. (2001) concentration–mass relation rather than determining $c_{\rm NFW}$ from the data. This correlation can be explained by the shape consistently found in the confidence contours of the clusters where $c_{\rm NFW}$ can be constrained (e.g., CL 0030+2618): Relatively high values for $c_{\rm NFW}$ only agree with the data for $r_{200} < r^{\rm min}_{200}$. The underlying reason is the absolute value of the shear signal ruling out simultaneously higher values for $c_{\rm NFW}$ and r_{200}. The masses $M^{\rm wl}_{200,\rm B}(r_{200,\rm B})$ which are by $\sim 1/3$ smaller than the default estimates $M^{\rm wl}_{200}(r_{200})$ once again point out the modelling problems for CL 1641+4001 and CL 1701+6414.

8.2.3 Comparison to X-ray Masses: The CL 0030+2618 Example

We will now compare our weak lensing masses to mass profiles drawn from the CHANDRA analysis. In this section, we demonstrate the measurement of the hydrostatic X-ray mass for our example

[2]The values given in Table 8.3 are rounded to the closest value considered in the parameter grid. Given the spacing of $\Delta c_{\rm NFW} = 0.05$, the resulting difference is < 0.025. The only exception is CL 1701+6414, where a coarser grid with $\Delta c_{\rm NFW} = 0.20$ had to be used. Hence, we pick $c_{\rm B,NFW} = 4.40$ as closest match to $c_{\rm B,NFW} = 4.31$ resulting from Eq. (6.13).

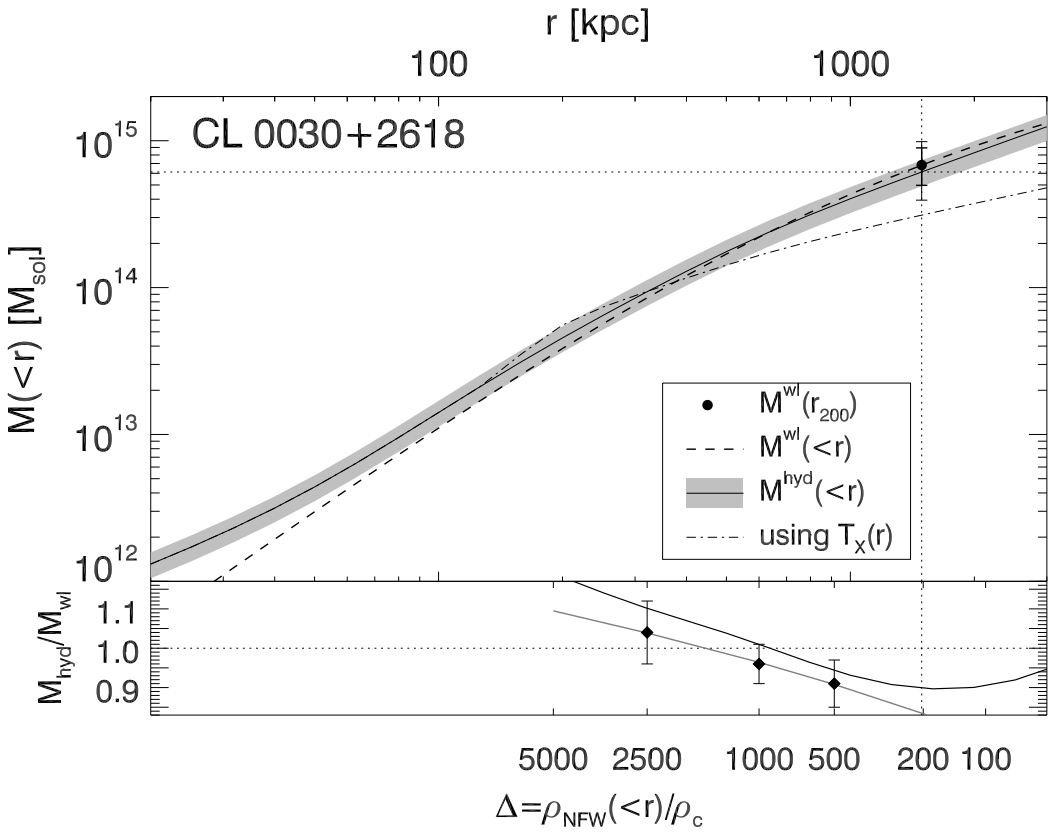

Figure 8.2: Comparison of mass profiles of CL0030+2618. *Upper panel:* The hydrostatic mass $M^{\rm hyd}(<r)$ derived from the Chandra analysis (thick solid line): A constant ICM temperature is assumed and the grey lines delineate the error margin derived from its error. The dash-dotted line gives the Chandra profile for a more realistic temperature profile. The dot with error bars and the dashed line denote the mass estimate and profile $M^{\rm wl}(<r)$ from our weak lensing analysis, assuming an NFW profile. The thick error bars show the statistical errors while thin bars include all components discussed in Sect. 6.5.4. *Lower panel:* Ratio of X-ray to lensing mass as a function of radius (black line). The symbols and grey line show the $M^{\rm hyd}/M^{\rm wl}$ found by Zhang et al. (2010) at three overdensity radii and their fitted relation.

cluster, CL 0030+2618, before we extend it to all Megacam clusters in Sect. 8.2.4. As we saw in Sect. 2.1.2, under the assumption that the ICM is in hydrostatic equilibrium, the total mass $M(<r)$ of a galaxy cluster within a radius r can be derived as (Eq. 2.4):

$$M(<r) = \frac{-k_{\rm B} T_{\rm X}(r) r}{\mu m_{\rm p} G} \left(\frac{{\rm d}\ln \rho_{\rm g}}{{\rm d}\ln r} + \frac{{\rm d}\ln T_{\rm X}}{{\rm d}\ln r} \right) \tag{8.2}$$

where $m_{\rm p}$ is the proton mass and μ the mean molecular mass. In a first step, we treat the ICM temperature to be independent of the radius and fix it to the Vikhlinin et al. (2009a) value of $k_{\rm B}\langle T_{\rm X}\rangle = 5.63 \pm 1.13\,{\rm keV}$. For the gas density $\rho_{\rm g}$, we use a Vikhlinin et al. (2006) particle density profile

$$\sqrt{n_{\rm e} n_{\rm p}} = n_0^2 \frac{(r/r_{\rm c})^{-\alpha}}{\left(1 + r^2/r_{\rm c}^2\right)^{3\beta-\alpha/2}} \frac{1}{\left(1 + r^\gamma/r_{\rm s}^\gamma\right)^{\varepsilon/\gamma}} + \frac{n_{02}^2}{\left(1 + r^2/r_{\rm c2}^2\right)^{3\beta_2}} \quad . \tag{8.3}$$

This model is motivated by observations of X-ray surface brightness profiles and represents an extension of the "β-model" (Eq. 2.2). It accounts for the observed steepening of surface brightness

Table 8.4: Parameters and best-fit values of the Vikhlinin et al. (2006) ICM model (Eq. 8.3) for all eight MEGACAM clusters (A. Vikhlinin, priv. comm.). In this modified double β-model, n_0 gives the number density of electrons, while r_c and r_s are the core and scale radii, respectively. Parameters named with Greek letters are dimensionless exponents. For all except two clusters, a second density component n_{02} with a core radius r_{c2} is modelled.

Cluster	n_0 $[10^{-3}\,\mathrm{cm}^{-3}]$	r_c [kpc]	r_s [kpc]	α	β	ϵ	n_{02} $[10^{-3}\,\mathrm{cm}^{-3}]$	r_{c2} [kpc]
CL 0030+2618	3.784	139.0	420.7	0.5867	0.4653	1.2293	0	–
CL 0159+0030	3.410	137.6	499.2	2.1467	0.5329	1.1832	247.8	0.017
CL 0230+1836	1.669	623.1	1214.5	0.3061	1.0579	4.9933	0.1968	22.296
CL 0809+2811	2.667	457.5	459.9	0	1.0579	0.1736	7.185	2.655
CL 1357+6232	1.718	365.0	2439.5	1.2342	0.8377	0.0002	0	–
CL 1416+4446	3.639	140.5	1260.0	1.9307	0.4989	5.0000	362.8	5.083
CL 1641+4001	3.836	190.9	667.6	0.5536	0.8453	0	0.6754	10.300
CL 1701+6414	1.640	233.2	372.1	2.2548	0.3333	1.5473	597.1	5.834

profiles at large radii as well as for the possibility of a distinct cluster core, to be modelled by a second β-component. The best-fit values of the parameters in Eq. 8.3 found by A. Vikhlinin (priv. comm.) for all eight MEGACAM clusters are given in Table 8.4. Note that the second "β-model" component including n_{02} has been set to zero for CL 0030+2618. The parameters $\gamma = 3$ and, where $n_{02} \neq 0$, of $\beta_2 = 1$ are held fixed. The CHANDRA images used in the Vikhlinin et al. (2009a) analyses enable good measurements of the *400d* cluster properties out to r_{500}. In the following, we extrapolate the resulting models out to r_{200}.

We apply the recipe by Vikhlinin et al. (2006) for converting the number densities of ions in the ICM into a mass density, assuming a primordial He abundance and a metallicity of $0.2\,\mathrm{Z}_\odot$, yielding $\rho_g = 1.624\, m_p \sqrt{n_e n_p}$. Inserting this ρ_g into Eq. (8.2), we arrive at a total cluster mass of $M^{hyd} = (6.13 \pm 1.23) \times 10^{14}\,\mathrm{M}_\odot$ for CL 0030+2618, at the virial radius of $r_{200} = 1.49$ Mpc obtained in the lensing analysis. We show the corresponding mass profile as the thick and its error margin as the grey lines in the upper panel of Fig. 8.2. The error is determined from the T_X uncertainty, which usually dominates over the statistical uncertainty in the gas density modelling.

This value is in very good agreement with the weak lensing mass estimate (dot with thick error bars for statistical and thin error bars for systematic plus statistical uncertainties in Fig. 8.2). The consistency between the X-ray mass profile derived from T_X and the (baryonic) ICM using Eq. (8.3) and the NFW profile describing the combined dark and luminous matter densities holds at all relevant radii $\gtrsim 50$ kpc in a wide range from the cluster core till beyond the virial radius.

Assuming an isothermal cluster profile, one likely overestimates the total hydrostatic mass, as the ICM temperature is often found to be lower at the large radii dominating the mass estimation around r_{vir} (e.g., Vikhlinin et al. 2006; Pratt et al. 2007; Zhang et al. 2008; Reiprich et al. 2009; George et al. 2009). The competing effect of the temperature gradient term in the hydrostatic equation is subdominant in most cases compared to this effect of the temperature value.

Therefore, to estimate the systematic uncertainty arising from assuming isothermality, we consider a toy model temperature profile consisting of the flat core at $\langle T_X \rangle$, a power-law decrease

at larger radii, and a minimal temperature $k_B T_0 = 0.5\,\mathrm{keV}$ in the cluster outskirts to qualitatively represent the features of an ensemble-averaged temperature profile:

$$k_B T_X(r) = \begin{cases} k_B \langle T_X \rangle & r \le r_i \\ p\, r^q & r_i \le r \le r_t \\ k_B T_0 & r \ge r_t \end{cases} \tag{8.4}$$

where we choose an inner (core) radius $r_i = r_{200}/8$ (as used in Pratt et al. 2007), a power-law slope $q = -0.4$ taken as a typical value found by Eckmiller et al. (in prep.), and fixing the truncation radius r_t and amplitude p demanding continuity of $T_X(r)$. The mass profile resulting from this temperature distribution is plotted in Fig. 8.2 (upper panel) as the dash-dotted line, giving an estimate of the systematic uncertainty in the X-ray profile. Its value at r_{200} is outside the 1σ error bar of M^{wl}, taking into account the *total* error. Another systematic factor in X-ray analysis is non-thermal pressure support, leading to an underestimation of the X-ray mass by ~ 10 % (e.g. Zhang et al. 2008). Taking into account all these effects, we conclude a very good agreement of X-ray and weak lensing mass estimates of CL 0030+2618, despite the potential perturbation by line-of-sight structure.

In the lower panel of Fig. 8.2, we show the ratio M^{hyd}/M^{wl} of hydrostatic X-ray and weak lensing mass as a function of radius. Although this quantity has a large error, our values are in good agreement with the X-ray-to-lensing mass ratios found by Zhang et al. (2010) for a sample of relaxed clusters for three radii corresponding to overdensities $\Delta = \rho_{NFW}(<r)/\rho_c = 2500$, 1000, and 500 (black line). We note that we recover well the relation $\frac{M^{hyd}}{M^{wl}}(\Delta)$ found by Zhang et al. (2010) by fitting their cluster sample data (grey line).

8.2.4 X-ray and Lensing Mass Profiles

The WL mass estimates our analysis yields for the eight *400d* clusters span a range consistent in principle with the expectations from the Chandra analysis published by Vikhlinin et al. (2009a). For all clusters, we measure WL masses $> 10^{14}\,M_\odot$, confirming that our objects are fairly massive clusters. The two most massive clusters, CL 0809+2811 and CL 0230+1836, yield masses of the order $10^{15}\,M_\odot$, which, at the redshift of $z = 0.80$ for CL 0230+1836 is exceptional, but not implausible given the currently favoured cosmological parameters.[3] Our upcoming analyses will give special emphasis to the most distant *400d* clusters like CL 0230+1836, bearing the strongest leverage on the cluster mass function.

We compare the WL masses of the eight Megacam clusters to masses inferred from the Chandra analysis by Vikhlinin et al. (2009a). For each cluster in the sample, a Vikhlinin et al. (2006) ICM particle density profile (Eq. 8.3) was fitted to the Chandra data and the resulting parameters are summarised in Table 8.4. Chandra temperatures T_X for the eight clusters are summarised in Table 8.1. By applying Eq. (8.2) in the same way as for CL 0030+2618 in Sect. 8.2.3, we infer the hydrostatic masses $M^{hyd}_{200}(r^{wl}_{200})$ listed in Table 8.1. Note that the only source of error considered for these *isothermal* mass estimates is the uncertainty in T_X. Further note that the ICM modelling is independent of the WL analysis, but the mass is computed within r_{200} determined by WL.

We repeat the comparison – shown in Fig. 8.2 for CL 0030+2618 – between the mass profile determined by Eq. 8.2 and the NFW profile given by r_{200} and c_{NFW} (Table 8.3) and present the results for the seven other clusters in Figs. 8.3 to 8.6. We emphasise that the WL profiles rely on *extrapolations* from the actual measurement at r_{200}, assuming the mass profiles following NFW

[3] Jee et al. (2009) claim the WL measurement of a similar high cluster mass at $z \approx 1.4$ which, if confirmed, would indeed ensue interesting ramifications for the cosmological model.

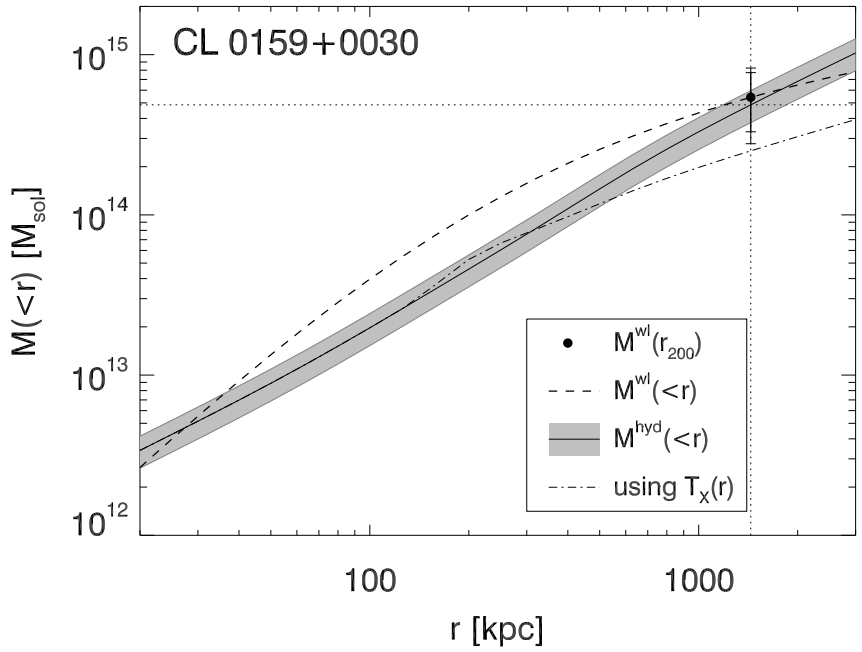

Figure 8.3: The same as Fig. 8.2, but for CL 0159+0030.

profiles with the $c_{\rm NFW}$ yielded by our analyses. Therefore, at $r < r_{200}$, we can only provide an order-or-magnitude consistency check. Extrapolations beyond r_{200} are even more speculative.

On the one hand, for all clusters, the hydrostatic mass estimate $M^{\rm hyd}_{200}(r^{\rm wl}_{200})$ lies within the range given by the statistical errors of the WL mass. On the other hand, $M^{\rm wl}_{200}(r^{\rm wl}_{200})$, the filled circle with error bars in Figs. 8.3 to 8.6, is included in the – narrower – 1σ uncertainty interval (grey lines) of the hydrostatic mass only for CL 0030+2618, CL 0159+0030, CL 1641+4001, and CL 1701+6414. Considering mass ratios, only for CL 1416+4446 a non-isothermal ICM model following Eq. (8.4) clearly provides better agreement with $M^{\rm wl}_{200}(r^{\rm wl}_{200})$ than the isothermal model. For CL 0030+2618, CL 0159+0030, and CL 0809+2811, the simple temperature gradient model is inconsistent with $M^{\rm wl}$, even considering its systematic errors.

We notice that none of the seven other clusters shows an agreement between the hydrostatic (solid lines in Figs. 8.3 to 8.6) and NFW mass profiles (dashed lines) over a wide range in $\log(r)$ within the error margin of $M^{\rm hyd}_{200}(r^{\rm wl}_{200})$ as observed for CL 0030+2618. The "best" cluster in this perspective is CL 1357+6232, where $M^{\rm wl}_{200}(r^{\rm wl}_{200})$ is a bit to the lower side of the 1σ interval of $M^{\rm hyd}_{200}(r^{\rm wl}_{200})$. By far, CL 0030+2618 provides the best agreement with the Zhang et al. (2010) $M^{\rm hyd}(\Delta)/M^{\rm wl}(\Delta)$ relation within the MEGACAM sample.

There are few qualitative changes to these results if we consider the weak lensing and hydrostatic masses $M^{\rm wl}_{200,\rm B}(r_{200,\rm B})$ and $M^{\rm hyd}_{200,\rm B}(r_{200,\rm B})$ (Table 8.3) obtained when fixing the concentration parameter to the value predicted by Eq. (6.13). We show the corresponding WL and X-ray mass profiles in Figs. B.17 to B.20 in Appendix B.4. The 1σ WL and hydrostatic masses for CL 1416+4446 disagree and $M^{\rm wl}_{200,\rm B}(r_{200,\rm B})$ for CL 1701+6414 lies outside the 1σ error interval of the hydrostatic mass. Also, the WL and hydrostatic mass profiles obtained when using $c_{\rm B,NFW} = 3.75$ for CL 0030+2618 not longer follow the Zhang et al. (2010) relation, but are still consistent at $\Delta = 1000$.

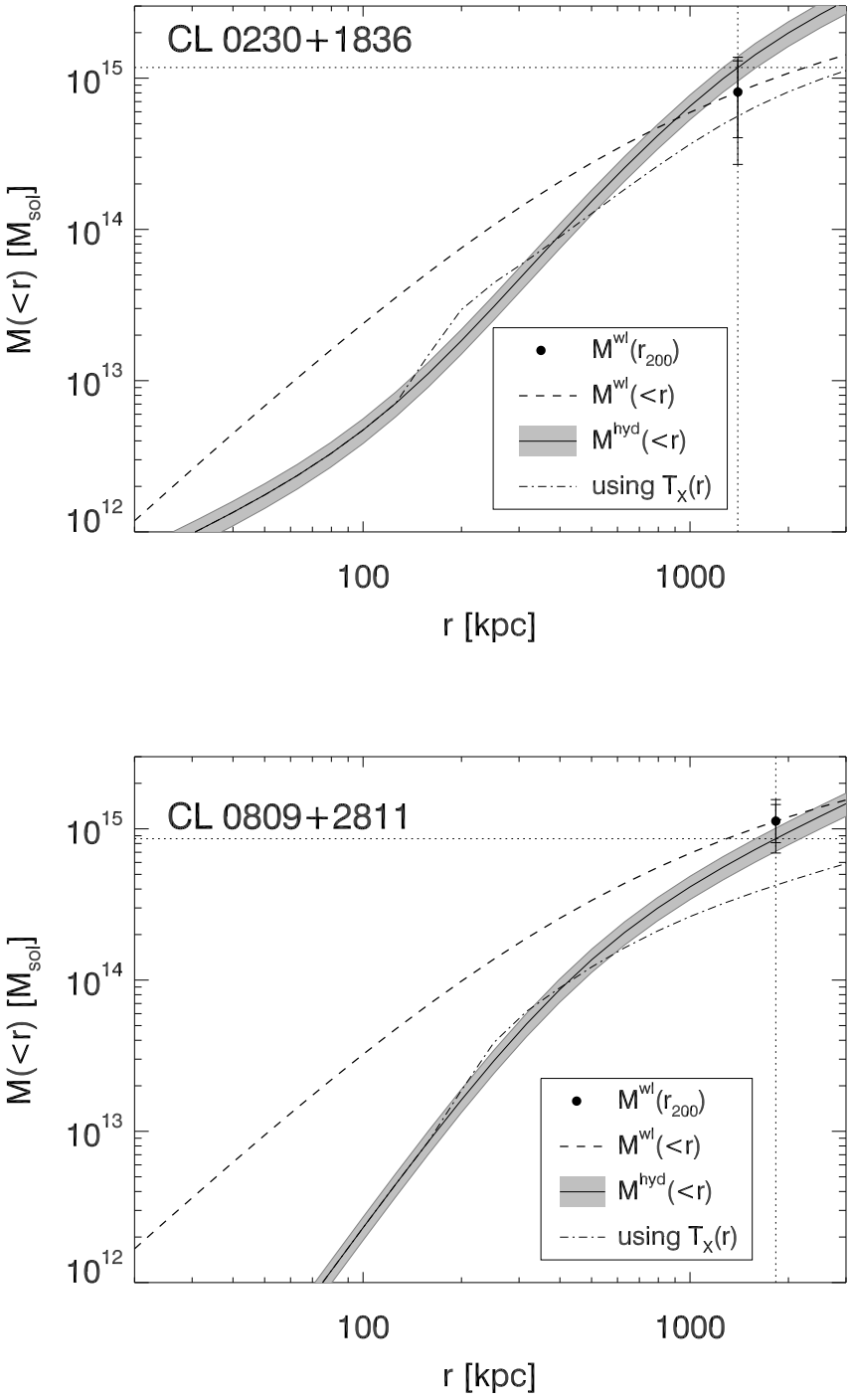

Figure 8.4: The same as Fig. 8.2, but for CL 0230+1836 (top) and CL 0809+2811 (bottom).

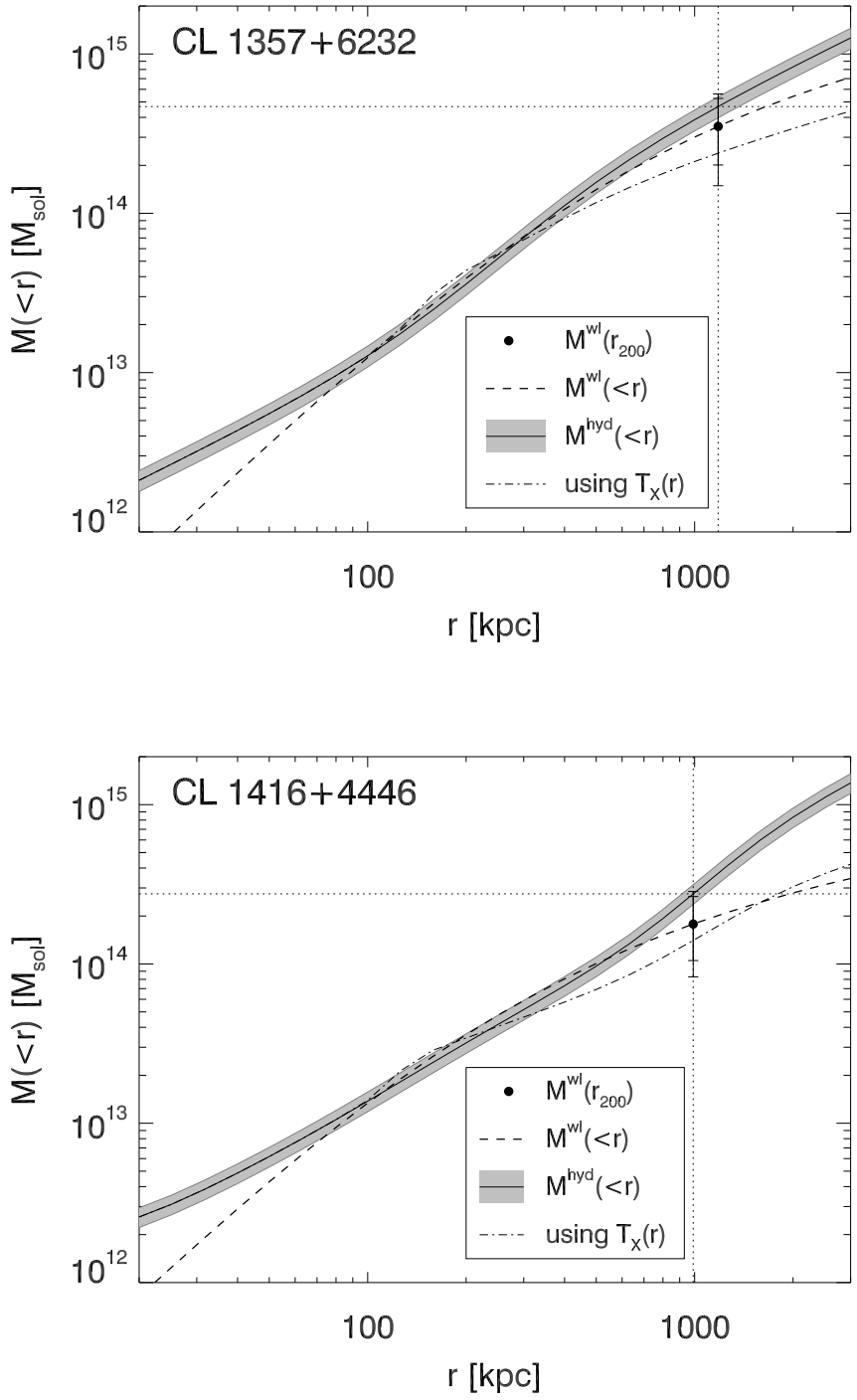

Figure 8.5: The same as Fig. 8.2, but for CL 1357+6232 (top) and CL 1416+4446 (bottom).

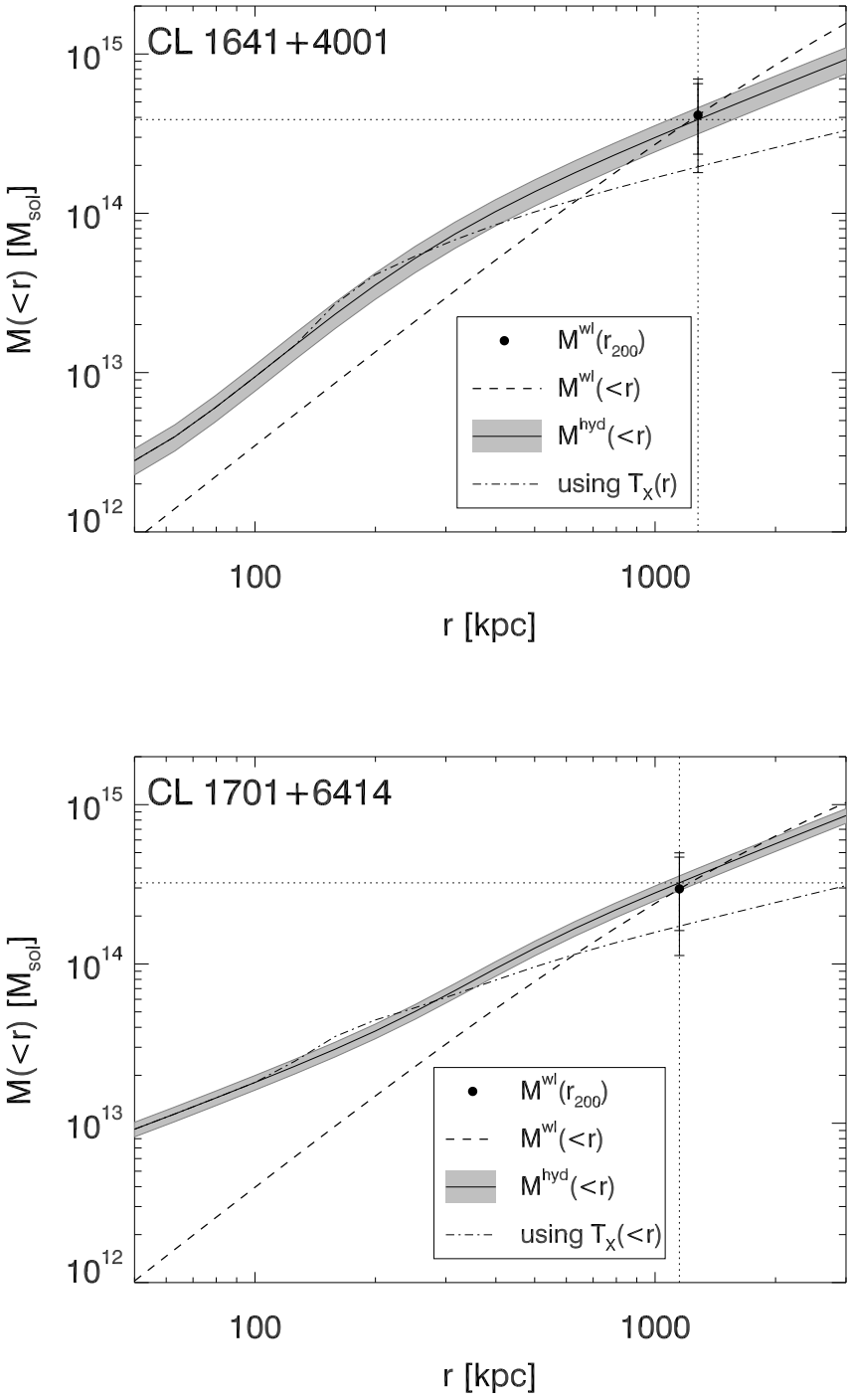

Figure 8.6: The same as Fig. 8.2, but for CL 1641+4001 (top) and CL 1701+6414 (bottom).

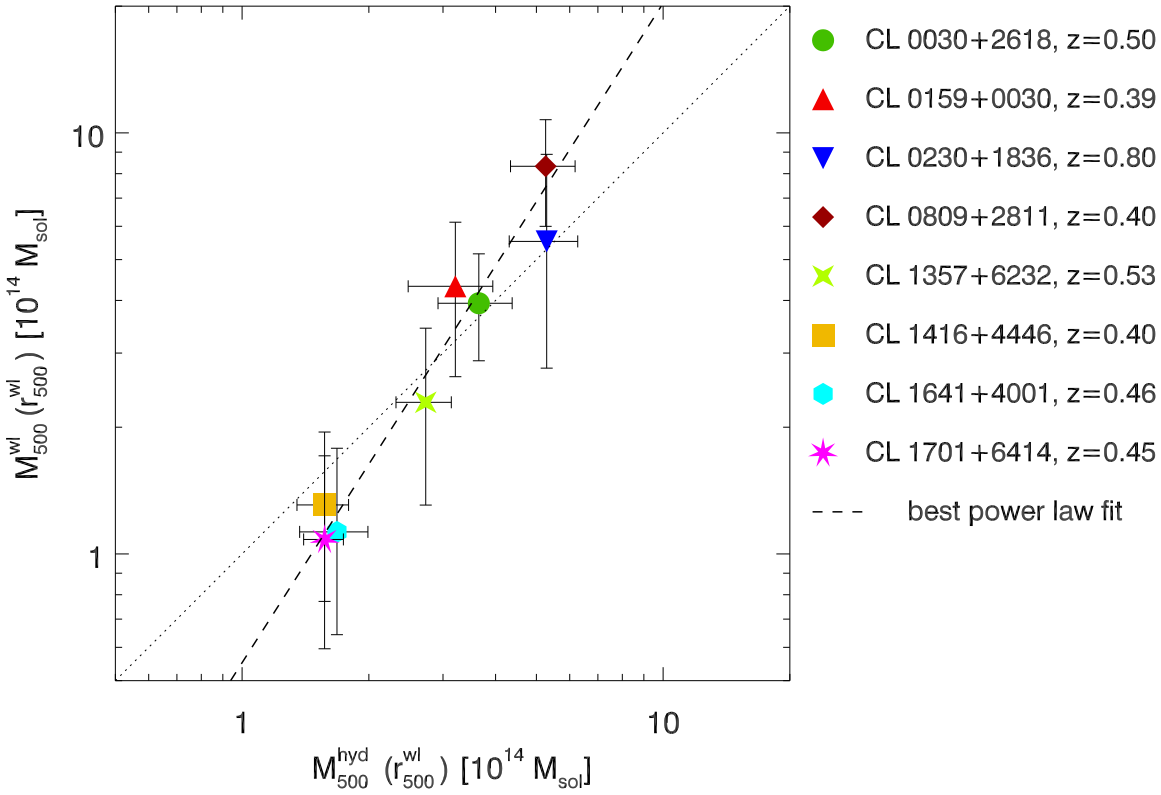

Figure 8.7: The weak lensing mass $M^{\rm wl}_{500}(r^{\rm wl}_{500})$ of the eight clusters as a function of the hydrostatic mass $M^{\rm hyd}_{500}(r^{\rm wl}_{500})$, in a double logarithmic plot. Error bars give the statistical errors to the lensing mass and the error resulting from the uncertainty in $T_{\rm X}$. On the dotted line, both masses are equal; the dashed line represents the best linear fit of $\log M^{\rm wl}_{500}(r^{\rm wl}_{500})$ to $\log M^{\rm hyd}_{500}(r^{\rm wl}_{500})$.

8.3 Weak Lensing – X-ray Scaling Relations

8.3.1 The $M^{\rm wl}$–$M^{\rm hyd}$ Relation

How do the weak lensing masses resulting from our analysis scale with the hydrostatic masses? For this purpose, we consider both WL and hydrostatic masses within the radius $r_{\Delta=500}$, for which, in general, the accuracy in both techniques its close to its optimum with respect to changes in Δ (Okabe et al. 2009; Zhang et al. 2010). Therefore, M_{500} is commonly used in the literature. Noticing that our WL masses were determined at r_{200}, we caution that the conversion to r_{500}, assuming the validity of the NFW density profile, might introduce additional errors and biases. Nevertheless, we apply the conversion to r_{500} in order to facilitate comparisons to similar studies.

Figure 8.7 presents $M^{\rm wl}_{500}(r^{\rm wl}_{500})$ in dependence of $M^{\rm hyd}_{500}(r^{\rm wl}_{500})$ in a double logarithmic scale. The quoted uncertainties in $M^{\rm wl}_{500}(r^{\rm wl}_{500})$ are first-order estimates assuming the relative errors in $M^{\rm wl}_{500}(r^{\rm wl}_{500})$ to equal the relative errors in $M^{\rm wl}_{200}(r^{\rm wl}_{200})$ presented in Table 8.2. We find the mass estimates to clearly follow a power law and generally agree with the equality $M^{\rm wl}_{500}(r^{\rm wl}_{500}) = M^{\rm hyd}_{500}(r^{\rm wl}_{500})$. The sole exception is CL 0230+1836, for which the diagonal in Fig. 8.7 (dotted line) lies slightly outside the margin given by the 1σ statistical errors of the lensing mass and the error in $M^{\rm hyd}_{500}(r^{\rm wl}_{500})$ propagated from the temperature error (Table 8.3).

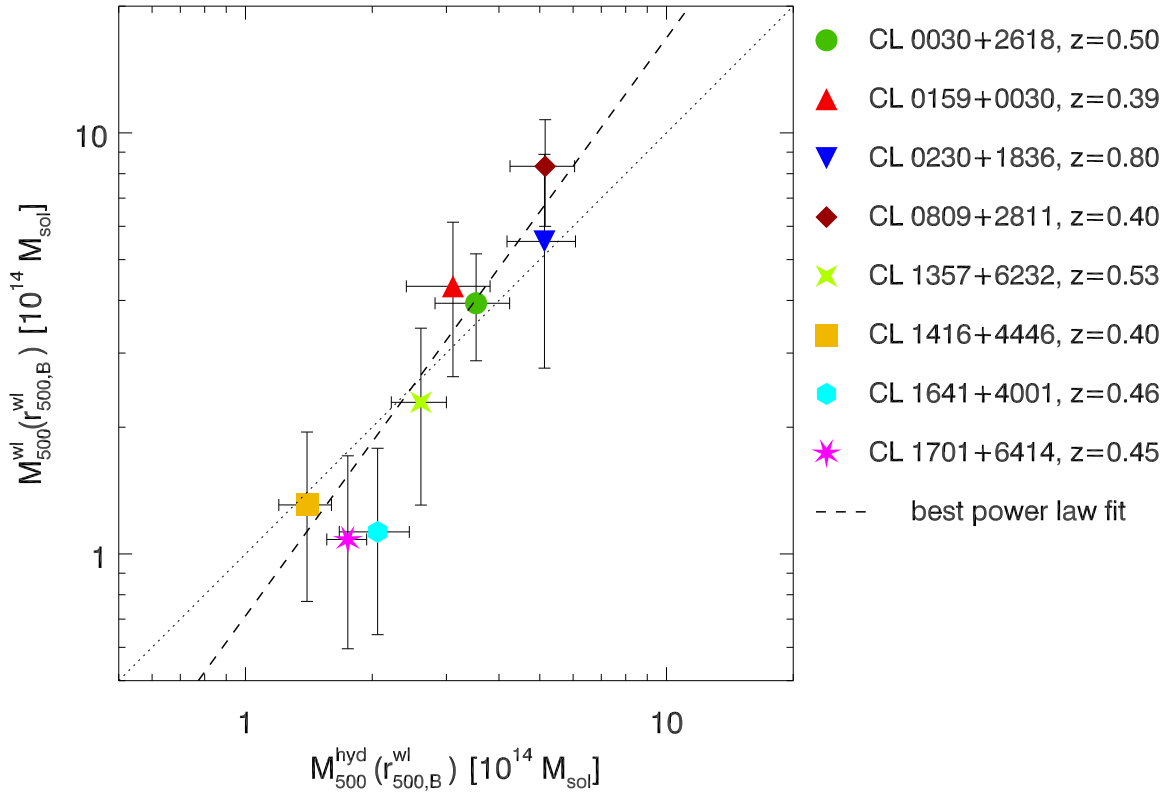

Figure 8.8: The same as Fig. 8.7, but showing $M^{\rm wl}_{500,\rm B}(r^{\rm wl}_{500,\rm B})$ as a function of $M^{\rm hyd}_{500,\rm B}(r^{\rm wl}_{500,\rm B})$ and the respective fit. The subscript "B" denotes the results with $c_{\rm NFW}$ fixed to the value predicted by the Bullock et al. (2001) relation.

Considering the WL masses, CL 0809+2811 with $M^{\rm wl}_{200} > 10^{15}{\rm M}_\odot$ is the most massive object, but not a particularly rare structure at its $z = 0.40$. Judging by the CHANDRA model, CL 0230+1836 at $z = 0.80$, the most distant cluster among the eight, marks the most massive cluster. With $M^{\rm hyd}_{200} > 10^{15}{\rm M}_\odot$, CL 0230+1836 is an outstanding object at its redshift of $z = 0.8$ and a fascinating object for further investigation. An obvious consequence of the higher redshift are the large statistical error bars. We note that our showcase cluster, CL 0030+2618, has the smallest relative statistical error in $M^{\rm wl}$, together with the more massive and more nearby CL 0809+2811. The second tentative strong lens, CL 1701+6414, suffers from large uncertainties owing to the complex shear morphology. The same holds for CL 1641+4001.

We infer the scaling relation between X-ray and WL mass by fitting a power law

$$\log\left(M^{\rm wl}/10^{14}{\rm M}_\odot\right) = A\,\log\left(M^{\rm hyd}/10^{14}{\rm M}_\odot\right) + B \tag{8.5}$$

to the data in Fig. 8.7. For the fit, a symmetrised error in $M^{\rm wl}$ is used (cf. Reiprich & Böhringer 2002). The best-fit relation, given by the dashed line in Fig. 8.7, has a slope of $A = 1.57 \pm 0.19$ and a very small $\chi^2_{\rm red} = 0.74$. We note that this best fit predicts equality between lensing and X-ray masses for $M \approx 3 \times 10^{14}{\rm M}_\odot$. Interchanging the dependent and independent variable in the fit to Eq. (8.5), we obtain a very similar relation. We notice that *all eight clusters* agree within their 1σ errors with the best-fit line. Given 1σ error bars, we would expect two or three clusters off the relation. This observation, as well as the small $\chi^2_{\rm red} < 1$ indicate an overestimation of the statistical

errors to $M_{\rm wl}$ which we have to investigate in a future analysis. Possibly, the fact that we used r_{500} (resp. r_{200}) determined from our lensing data for both $M^{\rm wl}$ and $M^{\rm hyd}$ contributes, at least partially, to this conspicuous agreement.

In order to test for the effect of the concentration parameter, implicit in Fig. 8.7 due to the conversion from r_{500} to r_{200}, we repeat the comparison of WL and hydrostatic masses based on the results using the Bullock et al. (2001) relation. Figure 8.8 shows the dependence of the weak lensing mass $M^{\rm wl}_{500,B}(r^{\rm wl}_{500,\rm B})$ on the hydrostatic mass $M^{\rm hyd}_{500,B}(r^{\rm wl}_{500,\rm B})$, for the mass models in which $c_{\rm NFW}$ is kept fixed to the value predicted by the Bullock et al. (2001) relation (Table 8.3). The most noticeable differences are the lower WL masses for the clusters where $c_{\rm NFW}$ is small, when determined from the fit. Most prominently, we measure for CL 1701+6414 the same small hydrostatic mass as for CL 1416+4446, and a WL mass just short of $2\times10^{14}{\rm M}_\odot$, with large error bars, induced by the less flexible lensing model. The power law fit (Eq. 8.5), assuming the mass-concentration relation, gives $A = 1.37 \pm 0.20$ and an again small $\chi^2_{\rm red} = 0.77$, consistent with the default fit using a free concentration parameter.

For comparison, we present diagrams equivalent to Figs. 8.7 and 8.8, but using the more direct mass estimate within r_{200}, in Figs. B.21 and B.22 in Appendix B.5. We find the scaling between $M^{\rm wl}_{200}(r^{\rm wl}_{200})$ and $\log M^{\rm hyd}_{200}(r^{\rm wl}_{200})$ to be similarly tight as the one observed for r_{500}. All data points are consistent within their 1σ error bars with the best-fit power law, for which we compute $\chi^2_{\rm red} = 0.89$ and $\chi^2_{\rm red} = 0.83$ for Figs. B.21 and B.22. The corresponding best-fit slopes, $A = 1.30 \pm 0.39$ and $A = 1.36 \pm 0.38$ are in good agreement with each other and with the slopes found using r_{500}.

The value for the slope A of Eq. (8.5) is in excellent agreement with the relation $M^{\rm wl}_{500}/M^{\rm hyd}_{500} = 1.57 \pm 0.38$ measured by Zhang et al. (2008) in the case of a free $c_{\rm NFW}$ and in good agreement when using the Bullock et al. (2001) relation for our data. The Zhang et al. (2008) cluster sample consists of 37 sources from the *Local Cluster Substructure Survey* of which 19 have measured WL masses and were considered in the determination of $M^{\rm wl}_{500}/M^{\rm hyd}_{500}$. Their redshifts range between $z = 0.15$ and $z = 0.30$, with an average of $\langle z\rangle = 0.22$. We attempted to determine the intrinsic scatter in the $M^{\rm wl}$–$M^{\rm hyd}$ distribution, using the same method as Zhang et al. (2008), but found the statistical errors in our data to be too large to measure it. The average lensing–to–hydrostatic mass ratio in our sample of eight clusters is $\langle M^{\rm wl}_{500}/M^{\rm hyd}_{500}\rangle = 1.01$, with a standard deviation of 0.32. Using a fixed slope of 1 in the $M^{\rm wl}$–$M^{\rm hyd}$ power law, equivalent to considering the weighted mean for $\langle M^{\rm wl}_{500}/M^{\rm hyd}_{500}\rangle$, Zhang et al. (2010) find $\langle M^{\rm wl}_{500}/M^{\rm hyd}_{500}\rangle = 1.01^{+0.08}_{-0.07}$. This result is perfectly consistently with our simple average, while the weighted average of our measurements yields a higher $\langle M^{\rm wl}_{500}/M^{\rm hyd}_{500}\rangle = 1.24 \pm 1.01$. We note that this weighted average is dominated by the high-mass clusters, for which we measure smaller *relative* statistical $M^{\rm wl}_{500}$ errors. For these clusters, we measure $M^{\rm wl}_{500}/M^{\rm hyd}_{500} > 1$, leading to the weighted average being significantly higher than the simple average.[4] In their Fig. 7, Zhang et al. (2008) considered the histogram of $\log\left(M^{\rm wl}_{500}/M^{\rm hyd}_{500}\right)$ and determined the mean and logarithmic standard deviation in their sample to be $\langle M^{\rm wl}_{500}/M^{\rm hyd}_{500}\rangle = 0.99 \pm 0.05$ and 0.51 ± 0.05, respectively. Despite our small number of eight objects, we performed a similar Gaussian fit to the histogram, yielding a marginally consistent $\langle M^{\rm wl}_{500}/M^{\rm hyd}_{500}\rangle = 0.93$ and logarithmic standard deviation of 0.15.

In a study of 18 galaxy clusters in the $0.17 < z < 0.43$ redshift range, with WL masses between $3\times10^{14}{\rm M}_\odot$ and $20\times10^{14}{\rm M}_\odot$, Mahdavi et al. (2008) measure $\langle M^{\rm hyd}_{500}/M^{\rm wl}_{500}\rangle = 0.78 \pm 0.09$,

[4] We further note that the three clusters with the highest weights, CL 0030+2618, CL 0230+1836, and CL 0809+2811, are the three out of our eights clusters which are flagged as "mergers" due to their X-ray morphology by Vikhlinin et al. (2009a). Our S-maps Sect. 7.4 do not hint towards merging activity in these clusters but find complex lensing signals for CL 1416+4446 and CL 1641+4001 which are flagged as non-merging by Vikhlinin et al. (2009a). Zhang et al. (2010) measure a reduced $M^{\rm wl}_{500}/M^{\rm hyd}_{500}$ for disturbed clusters, consistent with the qualitative analysis of the S-maps but at odds with the (simplistic) Vikhlinin et al. (2009a) merger flags. More thorough analysis of our data is necessary to test the role of merging for the $M^{\rm wl}_{500}/M^{\rm hyd}_{500}$ of our cluster sample.

corresponding to $\langle M^{\rm wl}_{500}/M^{\rm hyd}_{500}\rangle = 1.28^{+0.17}_{-0.13}$, applying a weighting scheme that takes into account the uncertainties in both masses. This measurement is in good agreement with our value for the weighted average $\langle M^{\rm hyd}_{500}/M^{\rm wl}_{500}\rangle$. Our present subsample of eight galaxy clusters does not provide enough statistics for more thorough investigations into the scaling between X-ray and WL masses, nor the construction of a mass function. Nevertheless, the present analysis forms the groundwork for these subsequent steps for which the tight $M^{\rm wl}$–$M^{\rm hyd}$ correlation we find is encouraging.

8.3.2 Scaling of $M^{\rm wl}$ with Masses Derived from $Y_{\rm X}$ and $M_{\rm gas}$

In the upper plot of Fig. 8.9, we present how our WL masses $M^{\rm wl}$ scale with the r_{500} cluster mass $M^{\rm Y_X}$ derived by Vikhlinin et al. (2009a) using measurements of $Y_{\rm X}$. Note that $M^{\rm Y_X}$ is the mass estimator used in constructing the Vikhlinin et al. (2009a) mass function. The lower panel of Fig. 8.9 directly compares $M^{\rm wl}$ to the proxy $Y_{\rm X}$.[5] Because of the power law relation between $M^{\rm Y_X}$ and $Y_{\rm X}$, the upper and lower plot in Fig. 8.9 are basically rescaled versions of one another. Figure 8.9 employs an estimate of the r_{500} radius computed directly from the $M^{\rm Y_X}$ data via inversion of the defining relation $M_{500} = (4\pi/3) r^3_{500} \cdot 500\rho_{\rm c}$. We denote this radius by $r^{\rm Y_X}_{500}$.

There is good agreement between the WL masses $M^{\rm wl}(r^{\rm Y_X}_{500})$, measured within $Y_{\rm X}$-derived radius, plotted against $Y_{\rm X}$, and the M_{500}–$Y_{\rm X}$–relation measured by Maughan (2007). The Maughan (2007) relation was constructed using hydrostatic X-ray masses of 12 clusters at $0.15 \lesssim z < 0.60$. We present the best-fit power law $M_{500} = C\,E(z)^A \left(Y_{\rm X}/6\times10^{14}\,{\rm M}_\odot\,{\rm keV}\right)^B$ as a dashed line for $z = 0.40$ and as a long-dashed line for $z = 0.80$ in Fig. 8.9. Out of our eight cluster masses, five are consistent with the Maughan (2007) expectation given their $Y_{\rm X}$, and two further masses (of CL 1416+4446 CL1641+4001) are marginally inconsistent with it at the 1σ level. The Maughan (2007) relation further coincides with the equality line in the $M^{\rm wl}$–$M^{\rm Y_X}$–diagram: The same five clusters agree with $M^{\rm wl}_{500}(r^{\rm Y_X}_{500}) = M^{\rm Y_X}_{500}(r^{\rm Y_X}_{500})$ at the 1σ level.

Although the clusters in the $M^{\rm wl}_{500}(r^{\rm Y_X}_{500})$ – $M^{\rm Y_X}_{500}(r^{\rm Y_X}_{500})$ plane match the expected equality relation, they inhabit a narrower interval in $M^{\rm Y_X}(r^{\rm Y_X}_{500})$ than in $M^{\rm wl}(r^{\rm Y_X}_{500})$, giving rise to a seemingly steep scaling relation. A similar behaviour can be found for the total cluster mass $M^{\rm g}$, inferred by Vikhlinin et al. (2009a) using the gas mass $M_{\rm gas}$ as a mass proxy. This can be seen in the upper panel of Fig. 8.10, showing $M^{\rm wl}(r^{\rm g}_{500})$ plotted against $M^{\rm g}(r^{\rm g}_{500})$, where the radius $r^{\rm g}_{500}$ is calculated in analogy to $r^{\rm Y_X}_{500}$. As well as for the $M^{\rm wl}_{500}(r^{\rm Y_X}_{500})$ – $M^{\rm Y_X}_{500}(r^{\rm Y_X}_{500})$ relation, we find the four least massive clusters to have $M^{\rm g}_{500}(r^{\rm g}_{500}) > M^{\rm wl}_{500}(r^{\rm g}_{500})$, and the four most massive ones to have $M^{\rm g}_{500}(r^{\rm g}_{500}) < M^{\rm wl}_{500}(r^{\rm g}_{500})$, rendering equality of the masses on average a reasonable representation for the eight cluster subsample.

The mass estimates $M^{\rm g}(r^{\rm g}_{500})$ for the eight clusters we investigated populate a quite narrow mass range between $(1.34 \pm 0.13)\times10^{14}\,{\rm M}_\odot$ for CL 1641+4001 and $(3.98 \pm 0.35)\times10^{14}\,{\rm M}_\odot$ for CL 0809+2811, a factor of $\sim$3.0. This is even more pronounced considering $M^{\rm Y_X}(r^{\rm Y_X}_{500})$, for which masses range between $(1.70 \pm 0.20)\times10^{14}\,{\rm M}_\odot$ for CL 1641+4001 and $(3.69 \pm 0.42)\times10^{14}\,{\rm M}_\odot$ for CL 0809+2811, a factor of $\sim$2.2. We note that CL 1641+4001 ranks among the least massive objects in the whole sample of 36 clusters, both in $M^{\rm Y_X}$ and $M^{\rm g}$, and, correspondingly CL 0809+2811 among the most massive clusters. Hence, our subsample discussed here does not probe a particularly small mass interval compared to the complete sample.

This is contrasted by the factor of $\sim$ 7.7 between the least massive cluster within $r^{\rm wl}_{500}$ according to our WL analysis, CL 1701+6414 with $M^{\rm wl}_{500}(r^{\rm wl}_{500}) = 1.70^{+0.63}_{-0.49}\times10^{14}\,{\rm M}_\odot$, and the most massive cluster, again CL 0809+2811, with $M^{\rm wl}_{500}(r^{\rm wl}_{500}) = 8.33^{+2.42}_{-2.33}\times10^{14}\,{\rm M}_\odot$. This factor reduces

[5] In order to obtain the values for $Y_{\rm X}$, we reversed the $M^{\rm Y_X}$–$Y_{\rm X}$ relation $M^{\rm Y_X}_{500} = M_0\,(Y_{\rm X}/3\times10^{14}\,{\rm M}_\odot\,{\rm keV})^\alpha E(z)^{-2/5}$ given by Vikhlinin et al. (2009a) in their Table 3. In this relation, $E(z) = H(z)/H_0$ accounts for the redshift evolution, while the normalisation and slope of the power law are $M_0 = \sqrt{h}\,5.78\times10^{14}\,{\rm M}_\odot$ and $\alpha = 0.60$, respectively.

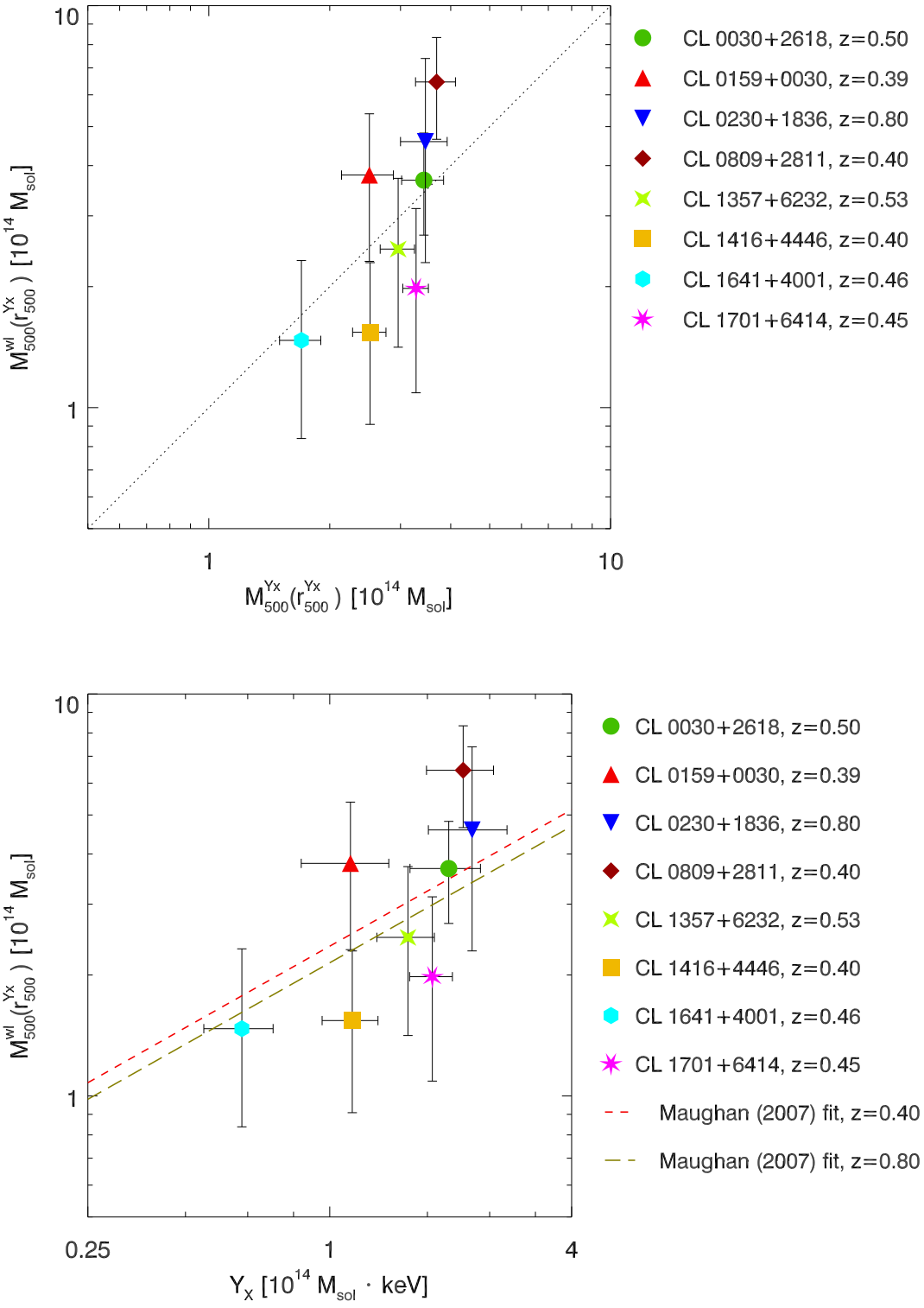

Figure 8.9: Scaling of the mass estimate M^{Y_X} (*upper plot*) and the Y_X proxy (*lower plot*) from Vikhlinin et al. (2009a) with M^{wl}. The symbols and lines follow the layout of Fig. 8.7. In the lower plot, a short and long dashed line present the Maughan (2007) M_{500}–Y_X–relation for redshifts of $z = 0.40$ and $z = 0.80$, respectively.

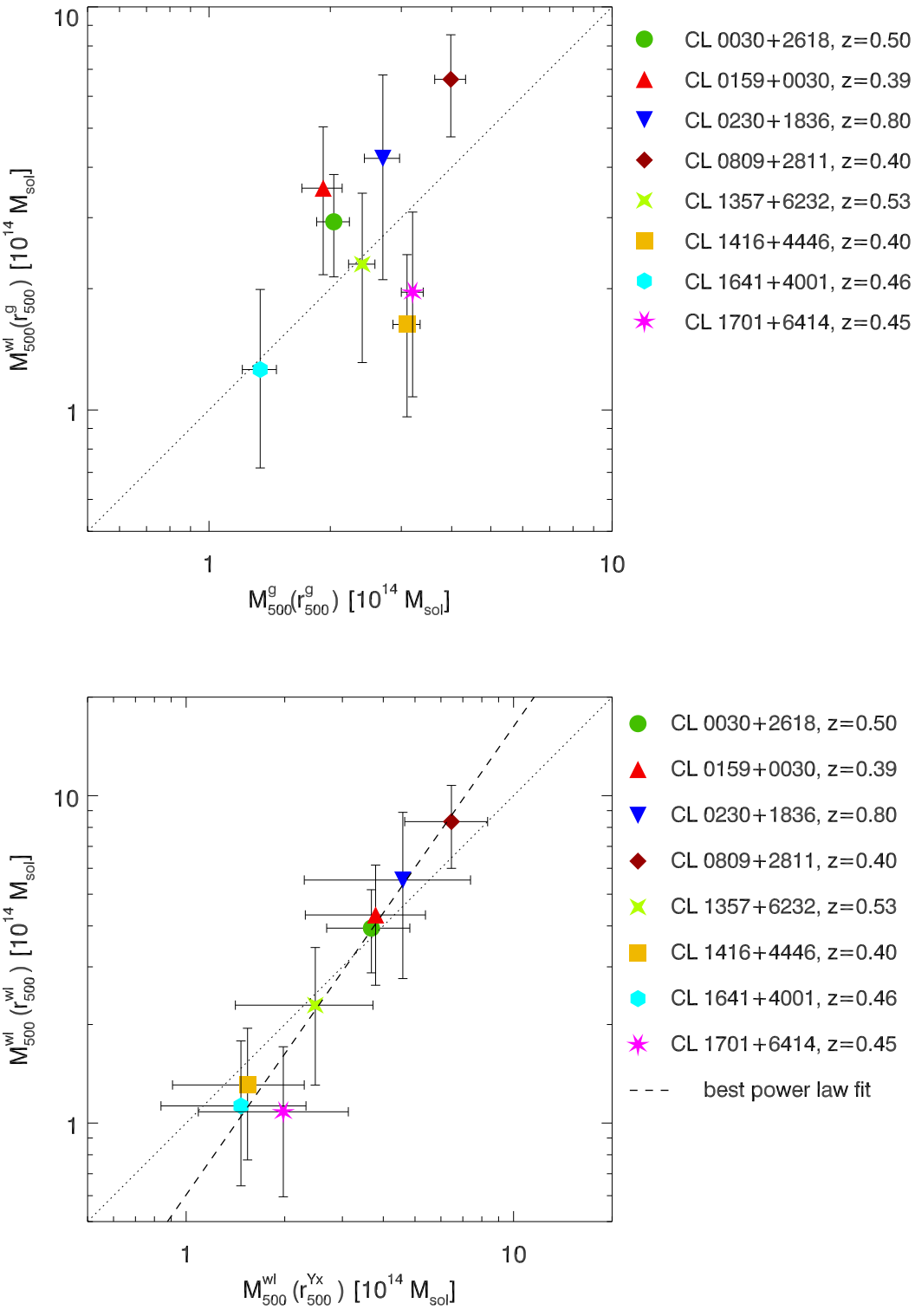

Figure 8.10: *Lower plot:* Scaling of the mass estimate M^{g} (*lower plot*) from Vikhlinin et al. (2009a) from Vikhlinin et al. (2009a) with M^{wl}. The symbols and lines follow the layout of Fig. 8.7. *Upper plot:* Comparison of the WL masses evaluated at two different estimates of r_{500}: Plotted is M^{wl} measured inside r^{wl}_{500} inferred from the best-fit NFW profile against r^{Yx}_{500} obtained from the CHANDRA analysis.

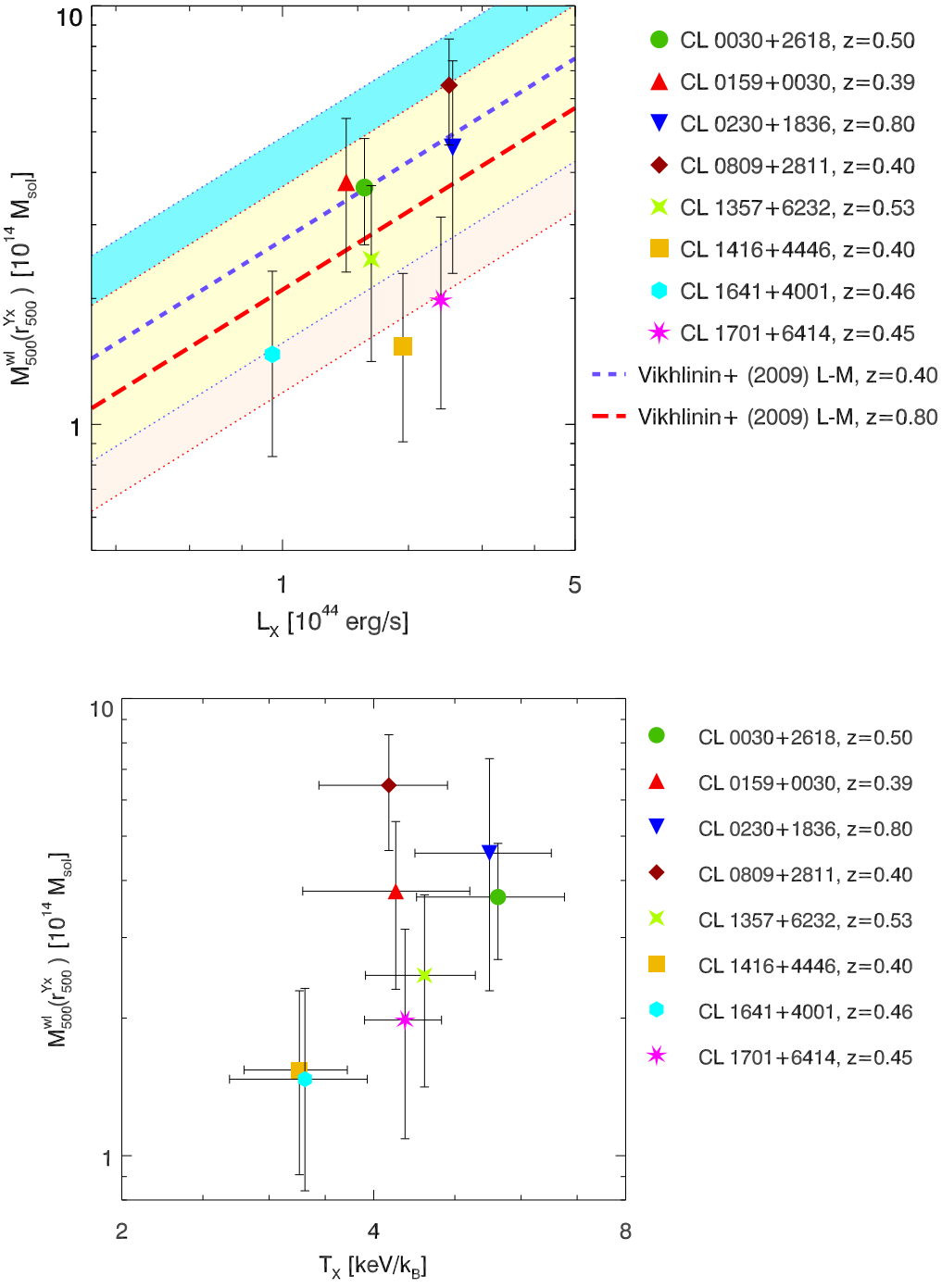

Figure 8.11: Scaling of the X-ray luminosity L_X (*upper plot*) and the ICM temperature T_X (*lower plot*) from Vikhlinin et al. (2009a) with M^{wl}. Vikhlinin et al. (2009a) quote as L_X the total luminosity in the 0.5–2 keV object frame, and T_X to be integrated from $0.15\,r_{500}$ and r_{500}. The symbols follow the layout of Fig. 8.7. Thick dashed and long-dashed line show the Vikhlinin et al. (2009a) L_X–M relation at $z = 0.40$ and $z = 0.80$, together with the respective 1σ uncertainties (dotted lines). The region consistent with the measured 1σ scatter of the $z = 0.40$ L_X–M relation is shaded blue, the corresponding region for $z = 0.80$ is shaded pink, and the overlap is shaded yellow.

to 4.4 considering $M^{\rm wl}_{500}(r^{\rm Y_X}_{500})$ and to 5.2 for $M^{\rm wl}_{500}(r^{\rm g}_{500})$. In both these cases, the lowest mass is measured for CL 1641+4001.

Because of the narrow intervals in $M^{\rm g}$ and $M^{\rm Y_X}$, we do not attempt to fit power laws to the distributions in the upper panels of Figs. 8.9 and 8.10. The resulting power law slopes would exhibit large uncertainties and unphysically high values, given that we compare two estimators of the *same* quantity, the cluster mass. Notice that CL 0809+2811, with its high $M^{\rm wl}$, marks the most discrepant object from both $M^{\rm wl}_{500} = M^{\rm Y_X}_{500}$ and $M^{\rm wl}_{500} = M^{\rm g}$. are not known to us at this early stage of the WL–X-ray mass comparison.

We investigate the differences between these two relations and the scaling of $M^{\rm wl}$ with $M^{\rm hyd}$ (Fig. 8.7) by comparing $M^{\rm wl}$ at $r^{\rm Y_X}_{500}$ and $r^{\rm wl}_{500}$. We find a tight power-law relation between $M^{\rm wl}(r^{\rm wl}_{500})$ and $M^{\rm wl}(r^{\rm Y_X}_{500})$ (Fig. 8.10, lower plot). All points are consistent with equality (dotted line) given their 1σ errors, as we expect for the same mass proxy at the same overdensity. Nevertheless the slope of the best-fit power law, $A = 1.43 \pm 0.50$ demonstrates that low-mass cluster are biased low when considering $r^{\rm wl}_{500}$ as opposed to $r^{\rm Y_X}_{500}$, while high-mass clusters are biased high. The best-fit power law is presented as a dashed line in the lower plot of Fig. 8.10. This effect can, to some degree, explain the observed larger mass range in $M^{\rm wl}$ than in $M^{\rm Y_X}_{500}$ and $M^{\rm g}$. Its cause is not clear to us at the moment; also the question of which mass estimate is the most reliable remains to be answered by further investigations.

8.3.3 Scaling of $M^{\rm wl}$ with X-ray Luminosity and Temperature

The upper plot of Fig. 8.11 presents the relation between the X-ray luminosity $L_{\rm X}$ quoted from the Vikhlinin et al. (2009a) CHANDRA analysis, with $M^{\rm wl}_{500}(r^{\rm Y_X}_{500})$. The X-ray luminosity is given for the 0.5–2 keV object frame. Interestingly, we find the distribution of our eight clusters to resemble the $M^{\rm wl}_{500}$–$M^{\rm g}$ distribution in Fig. 8.10. In particular, the luminosities span a factor of ~ 2.7, similar to $M^{\rm g}$ or $M^{\rm Y_X}$, although the most X-ray luminous cluster in the *complete* sample, CL 1226+3332 at $z = 0.89$, exceeds the most luminous MEGACAM cluster, CL 0230+1836 at $z = 0.80$, by another factor of ~ 3.3. The thick dashed and long-dashed lines in the upper plot of Fig. 8.11 show the Vikhlinin et al. (2009a) $L_{\rm X}$–$M^{\rm Y_X}$ relation at $z = 0.40$ and $z = 0.80$, respectively:

$$\ln L_{\rm X} = A_{\rm LM} + B_{\rm LM} \ln M_{500} + C_{\rm LM} \ln E(z) \pm S_{\rm LM} \quad , \tag{8.6}$$

where Vikhlinin et al. (2009a) find $A_{\rm LM} = 47.392 \pm 0.085$, $B_{\rm LM} = 1.61 \pm 0.14$, and $C_{\rm LM} = 1.85 \pm 0.42$. Taking into account the intrinsic 1σ scatter $S_{\rm LM} = 0.396 \pm 0.039$ in the relation, indicated by the shaded areas (blue shading for the $z = 0.40$ relation, pink shading for the $z = 0.80$ relation, and yellow shading for their overlap), five of the eight clusters are consistent with the $L_{\rm X}$–$M^{\rm Y_X}$ relation. In addition there is substantial overlap in the 1σ margins of $M^{\rm wl}_{500}(r^{\rm Y_X}_{500})$ of CL 1641+4001 and the Vikhlinin et al. (2009a) relation, interpolating to the cluster redshift of $z = 0.46$. The WL masses of CL 1416+4446 and CL 1701+6414 are too small, given their X-ray luminosities. Nevertheless, even for the most extreme case of CL 1416+4446, the upper boundary of the 1σ margin in $M^{\rm wl}_{500}$ lies not more than one standard deviation below the $z = 0.40$ $L_{\rm X}$–$M^{\rm Y_X}$ relation. We note that that among the three mentioned clusters with low $M^{\rm wl}_{500}$ given $L_{\rm X}$, we find the two clusters with the most complicated shear fields. Thus we conclude that, overall, our WL mass estimates, measured using $r^{\rm Y_X}_{500}$ match well the predictions using their $L_{\rm X}$.

In the lower plot of Fig. 8.11, we plot $M^{\rm wl}_{500}$ against $T_{\rm X}$, determined by Vikhlinin et al. (2009a) integrating the X-ray spectrum between $0.15 r_{500}$ and r_{500}. Even more than in the previous cases, the $T_{\rm X}$ measured for the eight clusters populate a narrow interval between $3.26 \pm 0.46\,{\rm keV}/k_{\rm B}$ for CL 1416+4446 and $5.63 \pm 1.13\,{\rm keV}/k_{\rm B}$ for CL 0030+2618, differing at the $\sim 2\sigma$ level. Thus, we refrain from fitting a $T_{\rm X}$–$M^{\rm wl}$ relation to our measurements and conclude that further investigations are necessary to reconcile our results with the Vikhlinin et al. (2009a) X-ray observables.

8.4 Conclusions and Outlook

In order to achieve the ultimate goal of the *400d* WL survey, the weak lensing mass function of all 36 clusters, a large number of analyses and several observing runs are still needed. We emphasise that this task is progressing with a wealth of already existing data, both from the dedicated observing runs by our team and from the archives. In addition, more observations are scheduled.

The most important conclusion to be drawn for the short- and medium term perspective of the project is that its feasibility has been demonstrated by analysing a significant subsample of eight clusters with MMT/MEGACAM. Building on the experiences and results presented in this thesis, we can evaluate the performance of our techniques so far, in order to better understand our measurements and improve the constraints on the cluster masses.

From a practical perspective, we identify the open questions concerning the analysis of the seven clusters presented in Sect. 7. First, we plan to complete the analysis of these seven clusters to a homogeneous level, by e.g., running bootstrap resamplings where this hasn't been done. Also, we plan to perform two-dimensional mass reconstructions and compare the resulting κ-maps with the CHANDRA centres and X-ray morphology.

We mention three particularly interesting lines of investigation we are going to pursue: On the more technical side, we-will re-run analyses of the clusters fields hampered by bright stars with reduced and without masking in order to determine the optimal level of prudence in avoiding bright stars. Second, we are going to test an alternative background selection model based on removing the galaxies consistent with the (probable) red sequences (Sects. 6.4.1 and 7.3.1). This will provide an interesting comparison to our default background selection.

Third, we will attempt a direct comparison of shear catalogues form MMT/MEGACAM and CFHT/MEGACAM for the CL 1701+6414 field, for which deep public archival observation exist in the r'-band and shorter ones in $g'i'z'$. Next to a detailed analysis of the shear measured using the same pipeline and from the same cluster but with different cameras/telescopes, we hope to shed more light on the mass distribution in this field containing at least four galaxy clusters. The obvious near-future goal is to improve the constraints on the WL mass of CL 1701+6414, for which, as we saw, the uncertainties are still large.

In the cases where a single NFW model provides obviously not a good representation of the mass distribution, we should consider alternative methods to infer the WL mass, as a medium term project. For instance, Mandelbaum et al. (2010) recently suggested a technique to infer cluster masses from WL data, specifically designed to yield accurate mass estimates by avoiding biases due to assumptions of a cluster profile, e.g. NFW, and including a correction for cluster members. Comparing different mass determination methods can also be seen in a wider context of improving cluster weak lensing based on both observations and simulations. The current state of the *400d* WL survey enables us to ask - and hopefully answer in the future - these and other questions related to the cosmology of galaxy clusters.

Chapter 9

Summary

This thesis reports first results of the largest weak lensing survey of X-ray selected, high-redshift clusters, the *400d cosmological sample* defined by Vikhlinin et al. (2009a) . We determined weak lensing masses for eight clusters of galaxies at redshifts $0.39 \leq z \leq 0.80$. None of these clusters had been studied with gravitational lensing before, and for seven of them the MMT/MEGACAM observations our team performed for this project represents the first deep imaging with a large optical telescope. Applying the aperture mass S-statistics, we detected weak lensing (WL) signals of our eight clusters at $> 3.5\sigma$ significance. Modelling these shear signals with a profile (Bartelmann 1996; Wright & Brainerd 2000) resulting from the Navarro et al. (1997) universal cluster density profile, we found good overall agreement between the WL and hydrostatic X-ray masses of our eight clusters.

The objects studied in this thesis were selected from the *400d cosmological sample*, from which Vikhlinin et al. (2009a) inferred the cluster mass function which was used to constrain cosmological parameters, in particular $\Omega_{\rm DE}$ and $w_{\rm DE}$ (Vikhlinin et al. 2009a,b). The work presented here shows the first results of an effort to follow up the complete 36 cluster sample with weak lensing. The ultimate goal of this project is to perform a detailed comparison of the clusters's X-ray and weak lensing properties with good statistics at high redshifts and to construct a robust mass function in the sense of having two completely independent mass estimates.

As the initial phase of this project, we obtained and analysed observations of eight clusters with the MEGACAM $\sim 24' \times 24'$ imager at the MMT. For four clusters, we observed deep $g'r'i'$ exposures, while for the other four clusters only the r'-band exists. We use the r'-band for the lensing analysis in all clusters. Employing an adaptation of the Erben et al. (2005) pipeline, `THELI`, and the "TS" KSB shape measurement pipeline (Heymans et al. 2006; Schrabback et al. 2007), we have measured weak gravitational shear with MEGACAM for the first time, demonstrating its PSF properties are well suited for weak lensing analyses.

These results were published as part of the pilot study of our project, demonstrating its feasibility and detailing our analysis methods for the example of CL 0030+2618 (Israel et al. 2010). The lensing catalogue of background galaxies was selected by a photometric method, using $g'r'i'$ colour information. We found the number count statistics in our MEGACAM data to be similar to the CFHTLS deep fields which we then used to estimate the redshift distribution of the lensed galaxies. MEGACAM $g'r'i'$ photometry established the galaxy we name G1, for which Boyle et al. (1997) determined a redshift $z = 0.516$, as the BCG of CL 0030+2618, ruling out as the BCG a slightly brighter source found inconsistent in its colours with the cluster redshift $z = 0.50$. We find additional evidence of a foreground structure at $z \approx 0.25$ (Horner et al. 2008) from photometry but find that it significantly affects neither the lensing nor the X-ray mass estimate of CL 0030+2618.

Having applied several consistency checks to the lensing catalogue, we detect CL 0030+2618 with optimal 5.84σ significance. The WL centre obtained by bootstrapping this map is in good agreement with the BCG position and the X-ray detections by ROSAT, CHANDRA, and XMM-NEWTON. Two tentative strong lensing arcs are detected in CL 0030+2618. The tangential shear profile of CL 0030+2618 is well modelled by an NFW profile out to $> 2r_{200}$. The low concentration parameter found by least squares fitting to the shear profile is confirmed by an analysis of the r_{200}–$c_{\rm NFW}$ parameter space with which we determine CL 0030+2618 to be parametrised by $r_{200}^{\rm min} = 1.49^{+0.14}_{-0.15}$ Mpc and $c_{\rm NFW}^{\rm min} = 1.8^{+0.95}_{-0.75}$. Modifying the default cluster model, we estimate the systematic errors caused by shear calibration, the redshift distribution of the background galaxies, and the likely non-sphericity of the cluster. We obtain a WL mass for CL 0030+2618 with statistical and systematic uncertainties of $M_{200}^{\rm wl}(r_{200}^{\rm wl}) = 6.8^{+2.1+2.2}_{-1.9-2.2}\times10^{14}{\rm M}_\odot$, in good agreement with $M_{200}^{\rm hyd}(r_{200}^{\rm wl}) = (6.13 \pm 1.23)\times10^{14}{\rm M}_\odot$, obtained using CHANDRA and the hydrostatic equation.

Next, we analysed MEGACAM data of seven further *400d* clusters, CL 0159+0030, CL 0230+1836, CL 0809+2811, CL 1357+6232, CL 1416+4446, CL 1641+4001, and CL 1701+6414. Based on the CFHTLS *Deep* photo-*z* catalogue, we revised the background selection based on MEGACAM $g'r'i'$ photometry, where three bands are available. We find the background selection to improve the lensing detection significance of CL 0159+0030 and CL 0809+2811 by $\Delta S \approx 1$. Surprisingly, no such improvement was found for the most distant tested cluster, CL 0230+1836 at $z = 0.80$. For CL 0030+2618 also, the gain in lensing signal by $\Delta S \approx 0.1$ was found insignificant.

Despite drastic reductions of usable exposure time in some cases, due to the removal of observations with highly anisotropic point spread function, all eight *400d* clusters are detected at the $S > 3.5\sigma$ significance level. For the clusters observed only in r', a magnitude cut was applied to select background galaxies. We note that several galaxy clusters exist in the CL 1416+4446 and CL 1701+6414 fields, while CL 1641+4001 exhibits a multi-peaked shear signal. Modelling of the latter two clusters is difficult, returning a concentration parameter consistent with zero for our standard NFW shear model. CL 1701+6414 at $z = 0.45$, which is a likely strong lensing cluster, is separated by $4\farcm5$ from the $z = 0.225$ cluster A 2246, which shows a higher S-signal. The S-map suggests that CL 1701+6414 might be seen through a filament connecting A 2246 with two structures at similar redshifts. The only known cluster candidate besides CL 1641+4001 can be ruled out to cause the disturbed lensing signal of CL 1641+4001. We consider our models of CL 1641+4001 and CL 1701+6414 starting points for further investigation. Our most massive objects are CL 0809+2811 with $M_{200}^{\rm wl}(r_{200}^{\rm wl}) = 11.2^{+3.2+2.9}_{-3.2-3.0}\times10^{14}\,{\rm M}_\odot$, and CL 0230+1836, for which we obtain $M_{200}^{\rm wl}(r_{200}^{\rm wl}) = 8.1^{+4.0+2.8}_{-4.9-3.6}\times10^{14}\,{\rm M}_\odot$. This is an impressively high mass for a cluster at $z = 0.80$, close to the limits of current ground-based WL. We notice the difference between mass uncertainties and detection significances, due to multiplicative systematic error components.

The agreement between $M_{\rm wl}$ and hydrostatic masses $M_{\rm hyd}$ is good: seven of eight $M_{\rm hyd}$ are consistent with the 1σ statistical lensing uncertainties, and lensing masses of four clusters are consistent with the (smaller) errors in $M^{\rm hyd}$. We find a linear $\log M^{\rm wl}$–$\log M^{\rm hyd}$ relation with remarkably small scatter. This is consistent with other $M^{\rm hyd}$– $M^{\rm wl}$ comparison, but extending the results to higher redshifts. A first, simple comparison with the X-ray observables and resulting masses derived for the same clusters by Vikhlinin et al. (2009a) shows the spread in $M^{\rm wl}$ to be significantly larger than in all Vikhlinin et al. (2009a) quantities.

The statistical errors in the lensing mass remain high, and we conclude that high-quality data and well-calibrated analysis techniques are essential to exploit the full available cosmological information from the mass function of galaxy clusters with weak lensing. Nevertheless, once lensing masses for all the 36 clusters are available, these statistical errors will be averaged out and reduced by a factor of 6 compared to the individual estimate, when measuring cosmological parameters. Thus, the understanding and controlling of systematic errors remain important.

Appendix A

Observing Runs

Here we give an overview of observations of galaxy clusters at optical telescopes for the *400 Square Degree* Weak Lensing Follow-up Survey. Note that we cover only those clusters for which optical observations have been made with the purpose of contributing to the *400d* WL project. Existing archival observations are not included here.

In Table A.1, the main data table, all observations made with respect to the *400d* WL project are listed. Note that the frames reported here are the **raw science frames**, not the frames contributing to the final coadded images.

The first three columns give the cluster name, and the filter and instrument with which it has been observed. Throughout this document, "Megacam" refers to the MMT instrument. The fourth column gives the UT date of observation. The fifth to seventh columns give the exposure time $t_{\rm exp}$, the number $n_{\rm exp}$ of such exposures, and their product $t_{\rm tot} = n_{\rm exp} t_{\rm exp}$. Total exposure times for the respective cluster and filter are given in bold face in separate lines. Column eight contains the abbereviated names of the observers. These abbreviations are detailed in Table A.2. The ninth column gives the unambiguous designation of the *Run* in which the data were taken while the tenth and last column states the completeness of observations. Note that data from "Run F" (MMT, June/July 2006) and "Run M" (WFI, Oct. 2009) will very probably not be usable and are therefore not considered in this table. Text in italics for CL0030+2618 refers to experimental observations in MEGACAM 1×1 binning mode which are not considered in $t_{\rm tot}$.

Table A.1: Overview of the weak lensing raw data of *400d* clusters existing as of January 1st, 2010. See text for explanations of its columns.

Galaxy Clusters Observed for the *400d* WL Project									
Cluster	Filter	Instrument	Date	$t_{\rm exp}$ [s]	$n_{\rm exp}$	$t_{\rm tot}$ [s]	Observer	Run ID	Complete?
CL0030+2618	g	Megacam	2005-10-30	600	7	4200	mc, mc, tp	E	
		Megacam	2005-10-30	300	7	2100	mc, mc, tp	E	
		Megacam	2005-10-31	300	2	600	Er, Hi	E	
		Megacam	2005-11-01	450	5	2250	Er, Hi	E	
						9150			yes
	r	Megacam	2004.10-06	300	26	7800	Re, mo	B	
		Megacam	2004.10-07	300	25	7500	Re, mo, mh	B	
		Megacam	*2005-11-08*	*300*	*14*	*4200*	*Er, Hi*	*E*	
						15300			yes
	i	Megacam	2005-10-31	300	20	**6000**	Er, Hi	E	yes

Continued on next page

Cluster	Filter	Instrument	Date	t_{exp} [s]	n_{exp}	t_{tot} [s]	Observer	Run ID	Complete?
CL0141-3034	B	WFI	2007-12-03	480	5	2400	Co, Mi	I	
		WFI	2007-12-07	480	10	4800	Co, Mi	I	
		WFI	2007-12-08	480	5	2400	Co, Mi	I	
		WFI	2007-12-09	480	5	2400	Co, Mi	I	
						12000			yes
	V	WFI	2007-12-05	300	15	**4500**	Co, Mi	I	yes
	R	WFI	2008-10-04	500	1	500	Mi, Ec	K	
		WFI	2008-10-05	500	31	15500	Mi, Ec	K	
		WFI	2008-11-21	500	10	5000	Gr	L	
						21000			no[1]
	I	WFI	2008-09-28	300	15	4500	Mi, Ec	K	
		WFI	2008-09-29	300	15	4500	Mi, Ec	K	
		WFI	2008-09-30	300	15	4500	Mi, Ec	K	
		WFI	2008-10-04	300	10	3000	Mi, Ec	K	
		WFI	2008-11-17	300	12	3600	Gr	L	
		WFI	2008-11-29	300	10	3000	Co, Te	L	
		WFI	2008-12-02	300	10	3000	Co, Te	L	
		WFI	2008-12-03	300	10	3000	Co, Te	L	
		WFI	2008-12-04	300	5	1500	Co, Te	L	
						30600			yes
CL0159+0030	g	Megacam	2005-11-01	600	10	**6000**	Er, Hi	E	yes
	r	Megacam	2005-10-30	300	26	7800	Er, Hi	E	
		Megacam	2005-10-31	300	2	600	Er, Hi	E	
		Megacam	2005-11-01	300	5	1500	Er, Hi	E	
						9900			yes
	i	Megacam	2005-10-31	300	17	5100	Er, Hi	E	
		Megacam	2005-11-01	300	10	3000	Er, Hi	E	
						8100			yes
CL0216-1747	g	IMACS/2	2007-11-09	600	10	**6000**	Is, Zh	H	yes
	r	IMACS/2	2007-11-08	300	15	**4500**	Is, Zh	H	no
	I	WFI	2007-12-12	300	5	**1500**	Co, Mi	I	no
CL0230+1836	g	Megacam	2005-11-08	600	10	**6000**	Er, Hi	E	yes
	r	Megacam	2004-10-06	300	7	2100	Re, mo	B	
		Megacam	2004-10-07	300	20	6000	Re, mo, mh	B	
		Megacam	2005-11-08	300	5	1500	Er, Hi	E	
						9600			yes
	i	Megacam	2005-10-31	300	12	3600	Er, Hi	E	
		Megacam	2005-11-01	300	10	3000	Er, Hi	E	
		Megacam	2005-11-08	300	12	3600	Er, Hi	E	
						9600			yes
	I	IMACS	2005-10-31	100	2	**200**	Vi, Kr	D	–

Continued on next page

[1] rescheduled on WFI for data quality

Cluster	Filter	Instrument	Date	t_{exp} [s]	n_{exp}	t_{tot} [s]	Observer	Run ID	Complete?
CL0302-0423	B	WFI	2007-12-07	480	5	2400	Co, Mi	I	
		WFI	2007-12-08	480	5	2400	Co, Mi	I	
		WFI	2008-10-01	480	9	4320	Mi, Ec	K	
		WFI	2008-10-03	480	10	4800	Mi, Ec	K	
		WFI	2008-10-07	480	3	1440	Mi, Ec	K	
		WFI	2008-10-07	115	1	115	Mi, Ec	K	
		WFI	2008-11-27	480	5	2400	Co, Te	L	
		WFI	2008-12-01	480	10	4800	Co, Te	L	
		WFI	2008-12-02	480	2	960	Co, Te	L	
						23635			yes
	V	WFI	2008-10-06	300	10	3000	Mi, Ec	K	
		WFI	2008-10-07	300	5	1500	Mi, Ec	K	
						4500			yes
	R	WFI	2008-10-06	500	5	2500	Mi, Ec	K	
		WFI	2008-11-21	500	15	7500	Gr	L	
		WFI	2008-11-27	500	5	2500	Co, Te	L	
		WFI	2008-11-30	500	10	5000	Co, Te	L	
		WFI	2008-12-01	500	2	1000	Co, Te	L	
		WFI	2008-12-03	500	1	500	Co, Te	L	
						19000			no[2]
	r	Megacam	2008-01-09	300	7	**2100**	Is	J	-
CL0318-0302	B	WFI	2008-10-03	480	1	480	Mi, Ec	K	
		WFI	2008-10-01	480	15	7200	Mi, Ec	K	
		WFI	2008-11-28	480	10	4800	Co, Te	L	
						12480			no[3]
	V	WFI	2008-11-29	300	1	300	Co, Te	L	
		WFI	2008-11-30	300	5	1500	Co, Te	L	
		WFI	2008-12-02	300	5	1500	Co, Te	L	
		WFI	2008-12-03	300	10	3000	Co, Te	L	
		WFI	2008-12-04	300	7	2100	Co, Te	L	
						8400			yes
	R	WFI	2008-11-27	500	5	2500	Co, Te	L	
		WFI	2008-11-30	500	5	2500	Co, Te	L	
		WFI	2008-12-01	500	8	4000	Co, Te	L	
		WFI	2008-12-03	500	3	1500	Co, Te	L	
		WFI	2008-12-04	500	15	7500	Co, Te	L	
						16000			no
CL0328-2140	V	IMACS	2005-10-30	300	11	**3300**	Vi, Kr	D	no
	R	IMACS	2005-10-29	300	1	300	Vi, Kr	D	
		IMACS	2005-10-30	300	17	5100	Vi, Kr	D	
						5400			no/?
	I	IMACS	2005-10-30	600	3	**1800**	Vi, Kr	D	no

Continued on next page

[2]rescheduled on WFI for data quality
[3]rescheduled on WFI for data quality

Cluster	Filter	Instrument	Date	t_{exp} [s]	n_{exp}	t_{tot} [s]	Observer	Run ID	Complete?
CL0333-2456	V	IMACS	2006-12-12	600	5	3000	Co, Is	G	
		IMACS	2006-12-13	600	6	3600	Co, Is	G	
						6600			yes
	R	IMACS	2005-10-31	300	23	6900	Vi, Kr	D	
		IMACS	2005-10-31	270	1	270	Vi, Kr	D	
						7170			yes
	I	IMACS	2006-12-12	300	5	1500	Co, Is	G	
		IMACS	2006-12-13	300	11	3300	Co, Is	G	
						4800			yes
CL0350-3801	B	WFI	2007-12-08	480	10	4800	Co, Mi	I	
		WFI	2007-12-09	480	10	4800	Co, Mi	I	
		WFI	2007-12-14	480	5	2400	Co, Mi	I	
						12000			yes
	V	WFI	2007-12-04	300	11	3300	Co, Mi	I	
		WFI	2007-12-05	300	5	1500	Co, Mi	I	
						4800			yes
	R	WFI	2007-12-04	500	5	2500	Co, Mi	I	
		WFI	2007-12-07	500	10	5000	Co, Mi	I	
		WFI	2007-12-10	500	10	5000	Co, Mi	I	
		WFI	2007-12-11	500	11	5500	Co, Mi	I	
						18000			yes
CL0355-3741	B	WFI	2007-12-05	480	10	4800	Co, Mi	I	
		WFI	2007-12-06	480	10	4800	Co, Mi	I	
		WFI	2007-12-08	480	5	2400	Co, Mi	I	
						12000			yes
	V	WFI	2007-12-15	300	15	**4500**	Co, Mi	I	yes
	R	WFI	2007-12-06	500	5	2500	Co, Mi	I	
		WFI	2007-12-12	500	20	10000	Co, Mi	I	
		WFI	2008-10-04	500	1	500	Mi, Ec	K	
		WFI	2008-10-05	500	5	2500	Mi, Ec	K	
		WFI	2008-10-07	500	1	500	Mi, Ec	K	
		WFI	2008-11-26	500	10	5000	Co, Te	K	
		WFI	2008-11-30	500	3	1500	Co, Te	K	
						22500			yes
	I	WFI	2008-09-28	300	30	9000	Mi, Ec	K	
		WFI	2008-09-30	300	25	7500	Mi, Ec	K	
		WFI	2008-10-06	300	5	1500	Mi, Ec	K	
		WFI	2008-10-07	300	5	1500	Mi, Ec	K	
		WFI	2008-11-28	300	15	4500	Co, Te	L	
		WFI	2008-11-29	300	10	3000	Co, Te	L	
		WFI	2008-12-02	300	10	3000	Co, Te	L	
		WFI	2008-12-03	300	10	3000	Co, Te	L	
						33000			yes

Continued on next page

Cluster	Filter	Instrument	Date	t_{exp} [s]	n_{exp}	t_{tot} [s]	Observer	Run ID	Complete?
CL0405-4100	g	IMACS/2	2007-11-09	600	10	**6000**	Is, Zh	H	yes
	r	IMACS/2	2007-11-08	300	22	6600	Is, Zh	H	
		IMACS/2	2007-11-09	300	5	1500	Is, Zh	H	
						8100			yes
	i	IMACS/2	2007-11-08	300	15	4500	Is, Zh	H	
		IMACS/2	2007-11-10	300	3	900	Is, Zh	H	
						5400			yes
	R	IMACS	2005-10-29	300	2	**600**	Vi, Kr	D	–
CL0521-2530	g	IMACS/2	2007-11-09	600	10	**6000**	Is, Zh	H	yes
	r					**0**			no
	i					**0**			no
CL0522-3624	B	WFI	2007-12-03	480	5	2400	Co, Mi	I	
		WFI	2007-12-04	480	5	2400	Co, Mi	I	
		WFI	2007-12-05	480	5	2400	Co, Mi	I	
		WFI	2007-12-06	480	5	2400	Co, Mi	I	
		WFI	2007-12-08	480	5	2400	Co, Mi	I	
						12000			yes
	V	WFI	2007-12-03	300	10	3000	Co, Mi	I	
		WFI	2007-12-05	300	5	1500	Co, Mi	I	
						4500			yes
	R	WFI	2007-12-10	500	5	2500	Co, Mi	I	
		WFI	2007-12-11	500	26	13000	Co, Mi	I	
						15500			yes
	I	WFI	2008-11-29	300	15	4500	Co, Te	L	
		WFI	2008-12-02	300	20	6000	Co, Te	L	
		WFI	2008-12-03	300	15	4500	Co, Te	L	
		WFI	2008-12-04	300	24	7200	Co, Te	L	
		WFI	2008-12-05	300	25	7500	Co, Te	L	
						29700			yes
CL0542-4100	V					**0**			no
	R	IMACS	2005-10-29	300	1	300	Vi, Kr	D	
		IMACS	2006-12-12	300	10	3000	Co, Is	G	
		IMACS	2006-12-13	300	19	5700	Co, Is	G	
						9000			yes
	I	IMACS	2006-12-12	300	11	3300	Co, Is	G	
		IMACS	2006-12-13	300	10	3000	Co, Is	G	
						6300			yes
CL0809+2811	g	Megacam	2005-10-31	400	5	2000	Er, Hi	E	
		Megacam	2005-11-08	400	10	4000	Er, Hi	E	
						6000			yes
	r	Megacam	2005-11-08	300	5	1500	Er, Hi	E	
		Megacam	2008-01-09	300	26	7800	Is	J	
						9300			yes

Continued on next page

Cluster	Filter	Instrument	Date	t_{exp} [s]	n_{exp}	t_{tot} [s]	Observer	Run ID	Complete?
		Megacam	2005-10-31	300	10	3000	Er, Hi	E	
	i	Megacam	2005-11-01	300	15	4500	Er, Hi	E	
						7500			yes
CL0853+5759	g	Megacam	2008-01-05	600	5	**3000**	Is	J	no
	r					**0**			no
		Megacam	2008-01-05	300	5	1500	Is	J	
	i	Megacam	2008-01-09	300	10	3000	Is	J	
						4500			yes
CL0958+4702	g	Megacam	2008-01-05	600	4	**2400**	Is	J	no
	r	Megacam	2008-01-09	300	12	**3600**	Is	J	no
	i	Megacam	2008-01-05	300	4	**1200**	Is	J	no
		Megacam	2008-01-05	600	4	2400	Is	J	
CL1357+6232	g	Megacam	2008-01-09	600	5	3000	Is	J	
						5400			no
	r	Megacam	2005-06-07	300	24	**7200**	Hu	C	yes
	i	Megacam	2008-01-09	300	15	**4500**	Is	J	yes?
	g					**0**			no
CL1416+4446	r	Megacam	2005-06-08	300	25	**7500**	Hu	C	yes
	i					**0**			no
CL1641+4001	r	Megacam	2005-06-07	300	27	**8100**	Hu	C	yes
CL1701+6414	r	Megacam	2005-06-08	300	25	**7500**	Hu	C	yes[4]

[4]Covered in three bands with archival data

Table A.2: List of observers. The following abbreviations are used in Table A.1.

Abbreviation	Name of Observer	Abbreviation	Name of Observer
Co	Oliver Cordes	mh	unknown MMTO staff member
Ec	Helen Eckmiller	Mi	Rupal Mittal
Er	Thomas Erben	mo	unknown MMTO staff member
Fu	César Fuentes	Pi	Jennifer Piel
Gr	Jochen Greiner	Re	Thomas Reiprich
Hi	Hendrik Hildebrandt	Sc	Tim Schrabback-Krahe
Hu	Daniel Hudson	Te	Ismael Tereno
Is	Holger Israel	tp	unknown MMTO staff member
Kl	Matthias Klein	Vi	Alexey Vikhlinin
Kr	Andrey Kravtsov	Zh	Yu-Ying Zhang

Appendix B

Additional Figures

B.1 PSF Anisotropy Plots

Here we present the correction of PSF anisotropies as a function of position on the MEGACAM array surface for the seven clusters CL 0159+0030, CL 0230+1836, CL 0809+2811, CL 1357+6232, CL 1416+4446, CL 1641+4001, and CL 1701+6414. We observe a qualitatively similar behaviours as for CL 0030+2618, shown in Fig. 5.12.

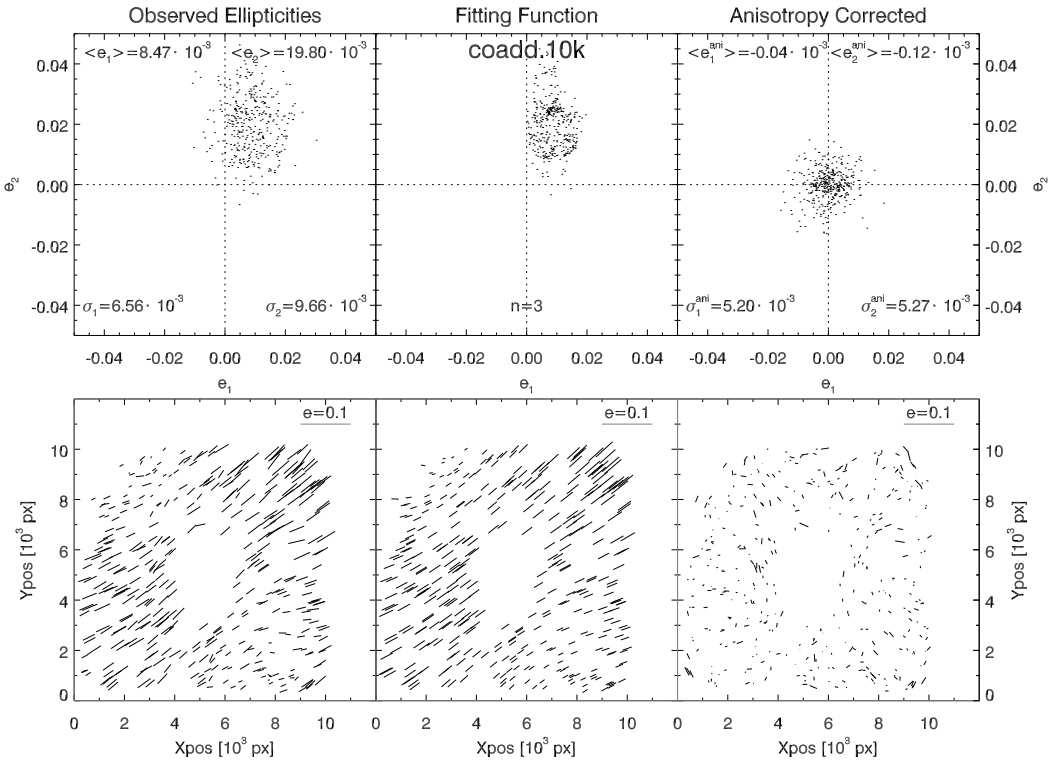

Figure B.1: Same as Fig. 5.12, but for the r'-band of CL 0159+0030.

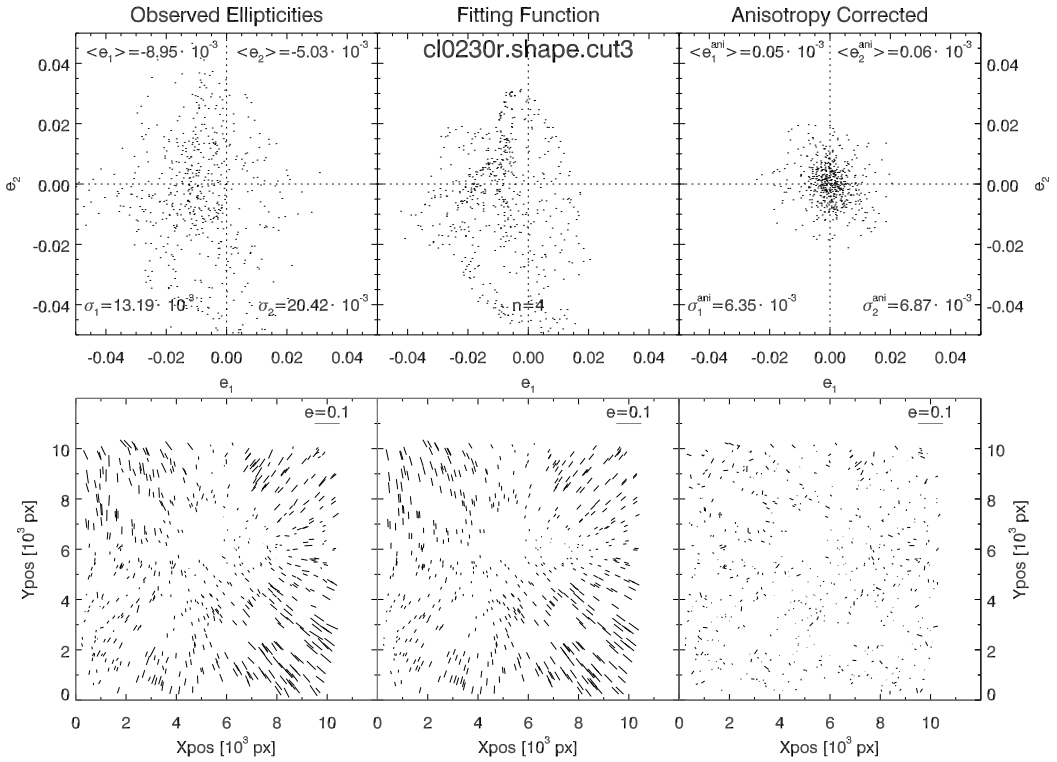

Figure B.2: Same as Fig. 5.12, but for the r'-band of CL 0230+1836.

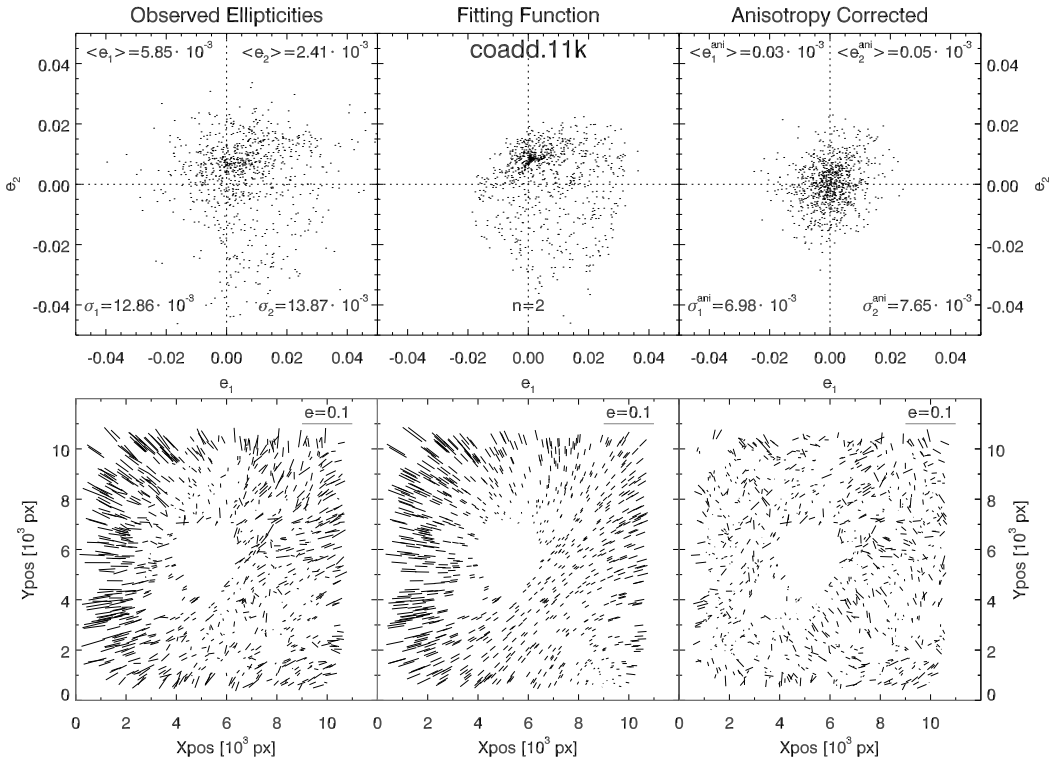

Figure B.3: Same as Fig. 5.12, but for the r'-band of CL 0809+2811.

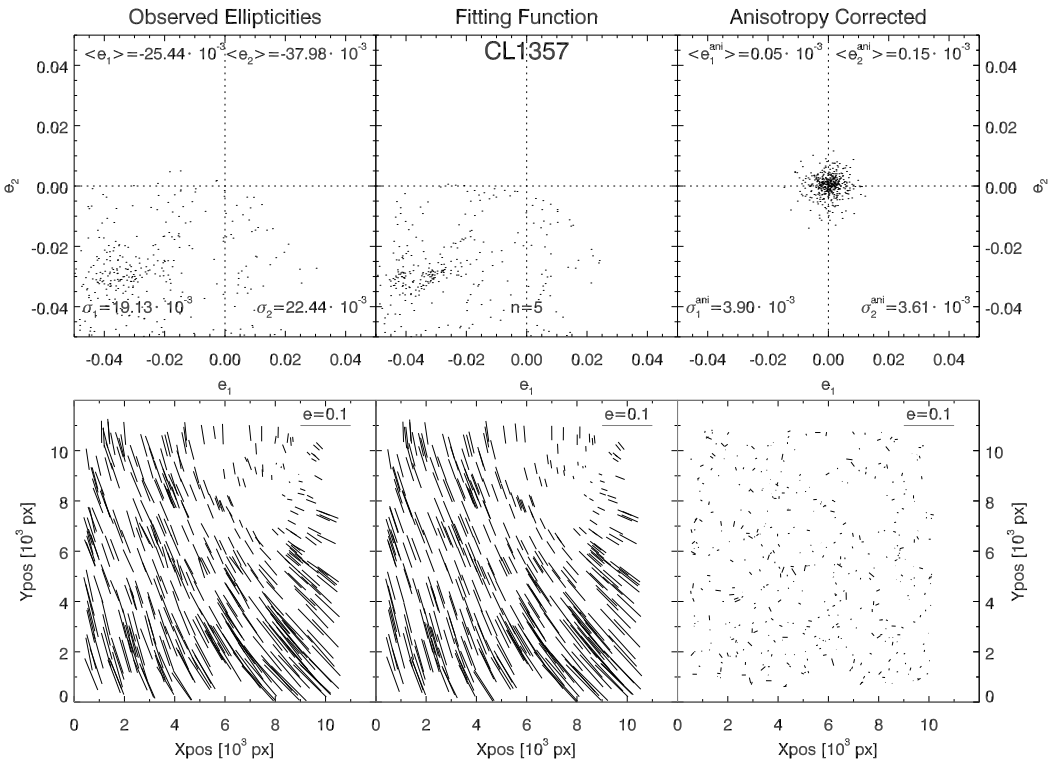

Figure B.4: Same as Fig. 5.12, but for the r'-band of CL 1357+6232.

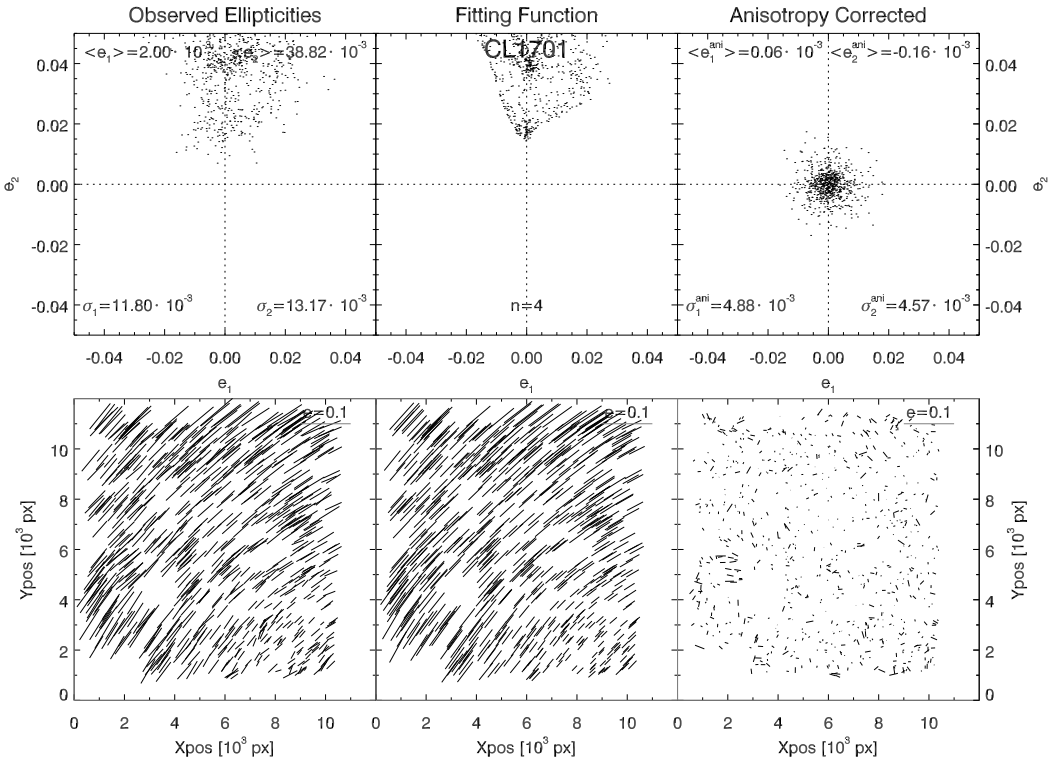

Figure B.5: Same as Fig. 5.12, but for the r'-band of CL 1701+6414.

B.2 Shear Signal Significance

In the following diagrams we show the influence of variation in the parameters defining the background selection polygons (Table 7.1) on the S-statistics measured at the shear peaks of CL 0159+0030, CL 0809+2811, and CL 0230+2811.

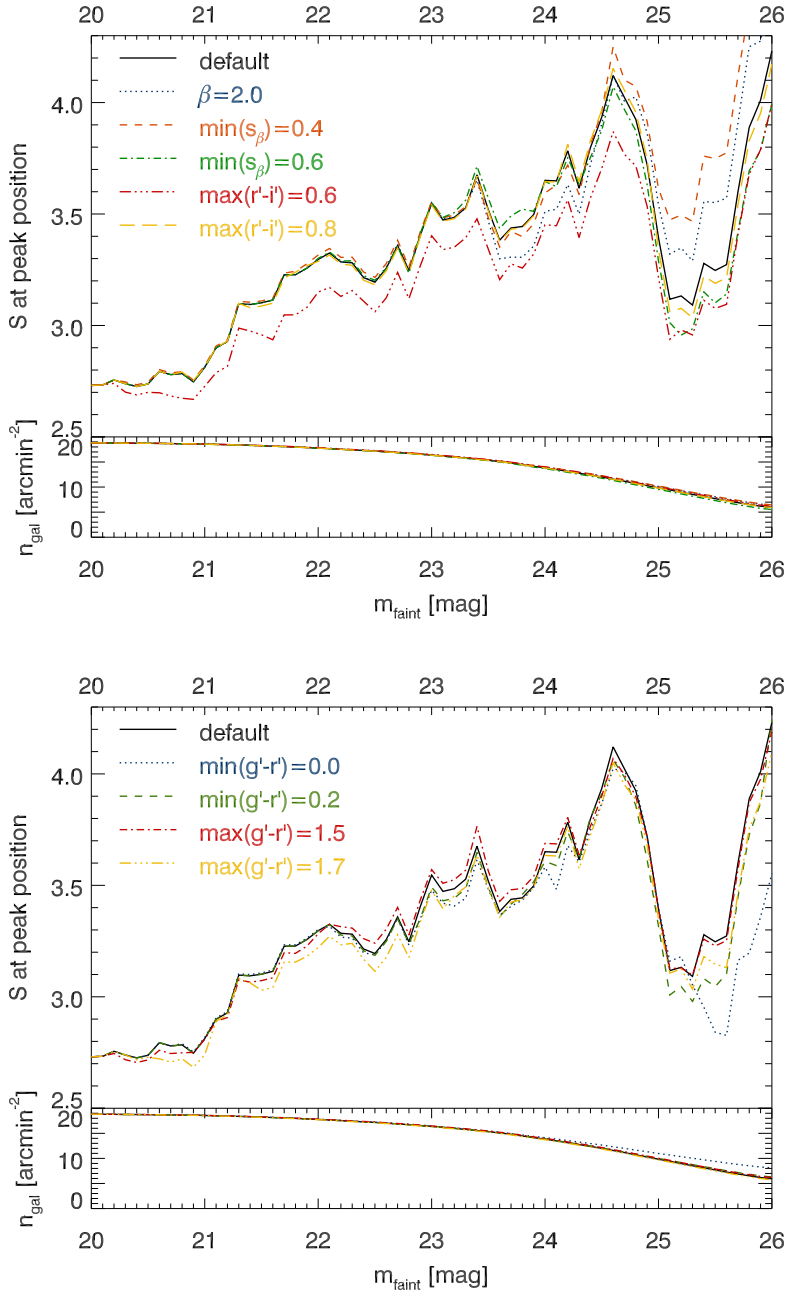

Figure B.6: The same as Fig. 7.5, but comparing the default case for CL 0159+0030 (solid lines) to these cases: *Upper plot:* $\beta = 2.0$ (dotted), $\min(s_\beta) = 0.4$ (dashed), $\min(s_\beta) = 0.6$ (dot-dashed line), $\max(r'-i') = 0.6$ (triple dot-dashed), and $\max(r'-i') = 0.8$ (long dashed). *Lower plot:* $\min(g'-r') = 0.0$ (dotted), $\min(g'-r') = 0.2$ (dashed), $\max(g'-r') = 1.5$ (dot-dashed), and $\max(g'-r') = 1.7$ (triple dot-dashed).

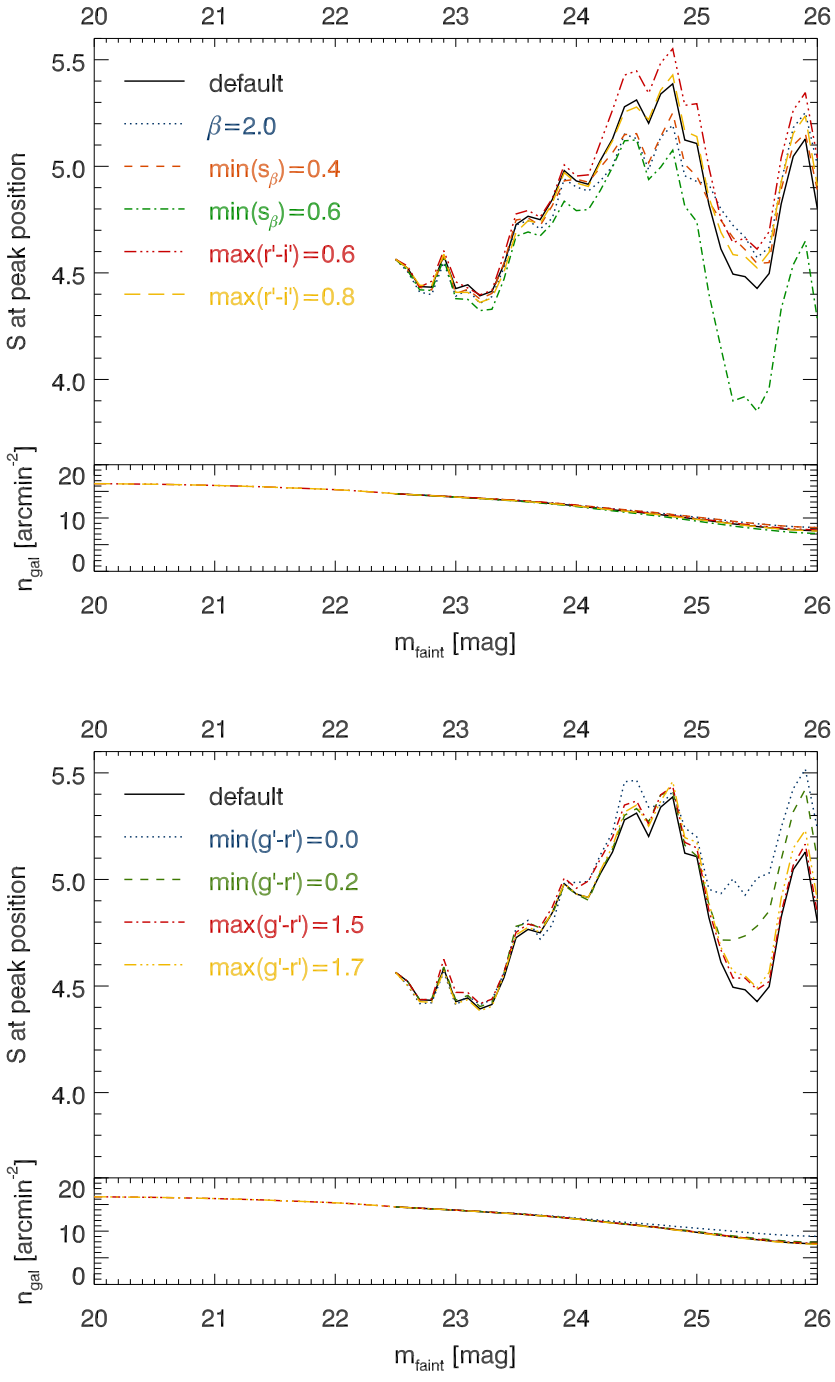

Figure B.7: The same as Fig. B.6, but showing the effects of the same cuts for CL 0809+2811.

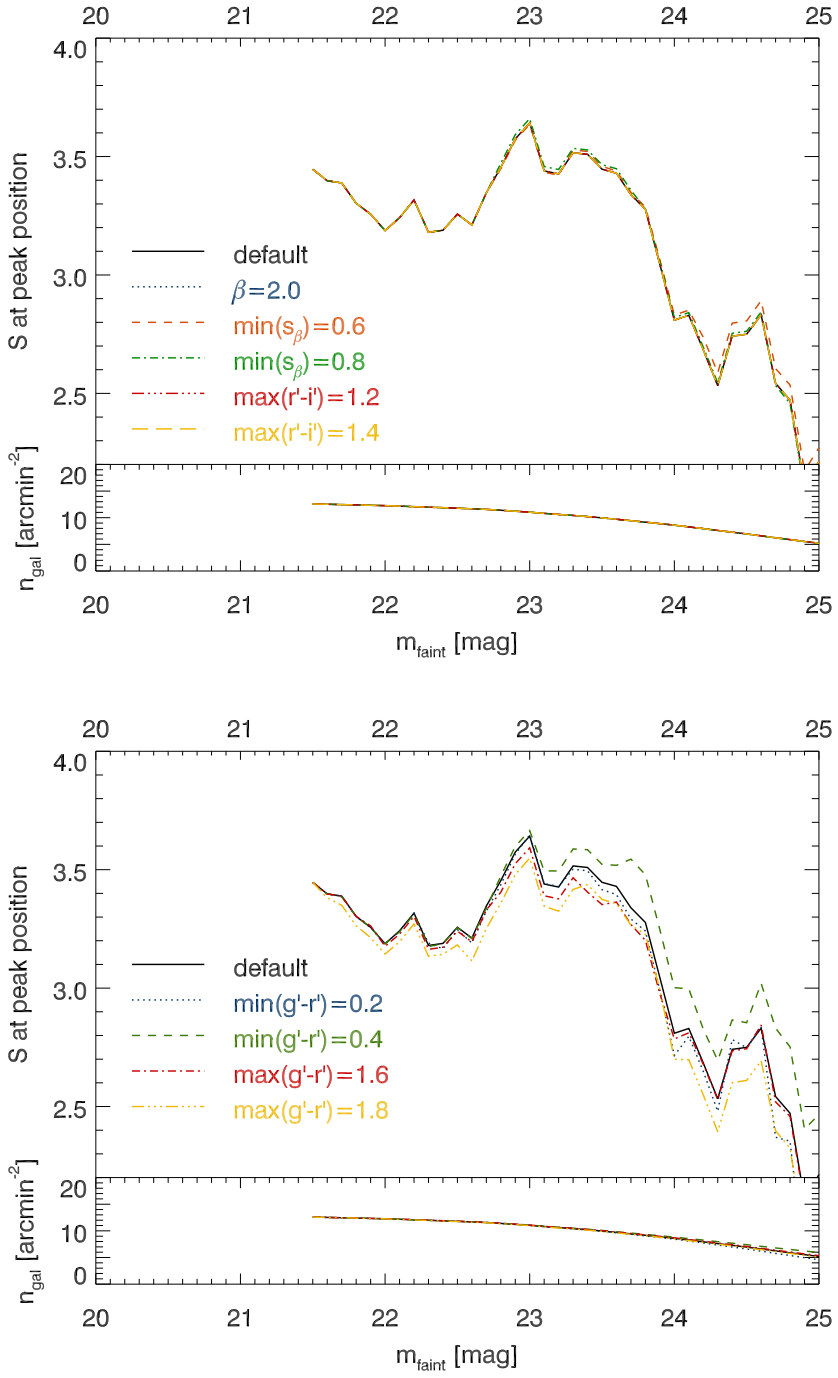

Figure B.8: The same as Fig. 7.6, but comparing the default case for CL 0230+2811 (solid lines) to these cases: *Upper plot:* $\beta = 2.0$ (dotted), $\min(s_\beta) = 0.6$ (dashed), $\min(s_\beta) = 0.8$ (dot-dashed line), $\min(r'-i') = 1.2$ (triple dot-dashed), and $\min(r'-i') = 1.4$ (long dashed). *Lower plot:* $\min(g'-r') = 0.2$ (dotted), $\min(g'-r') = 0.4$ (dashed), $\max(g'-r') = 1.6$ (dot-dashed), and $\max(g'-r') = 1.8$ (triple dot-dashed).

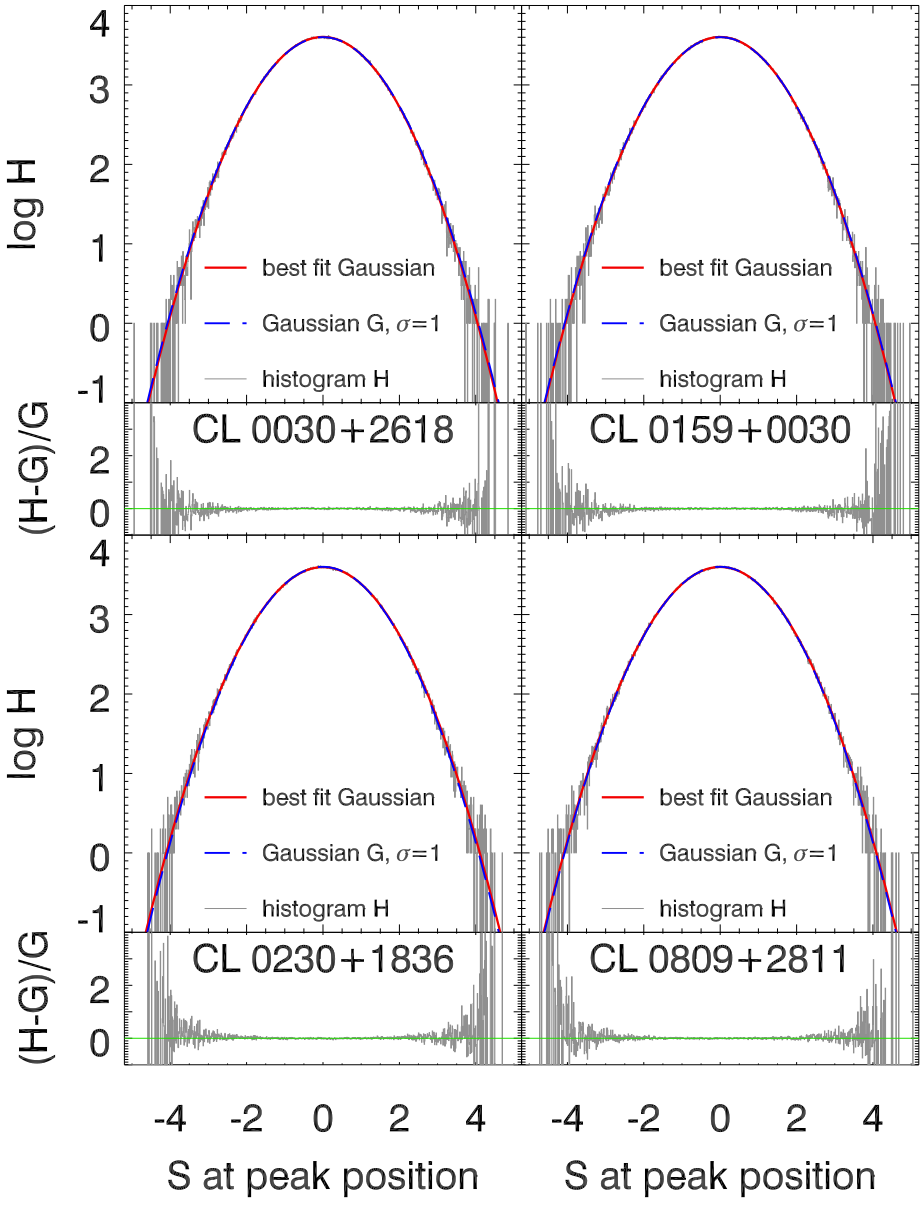

Figure B.9: The same as Fig. 7.9, but for CL 0030+2618, CL 0159+0030, CL 0230+1836, and CL 0809+2811.

B.3 Confidence Contours

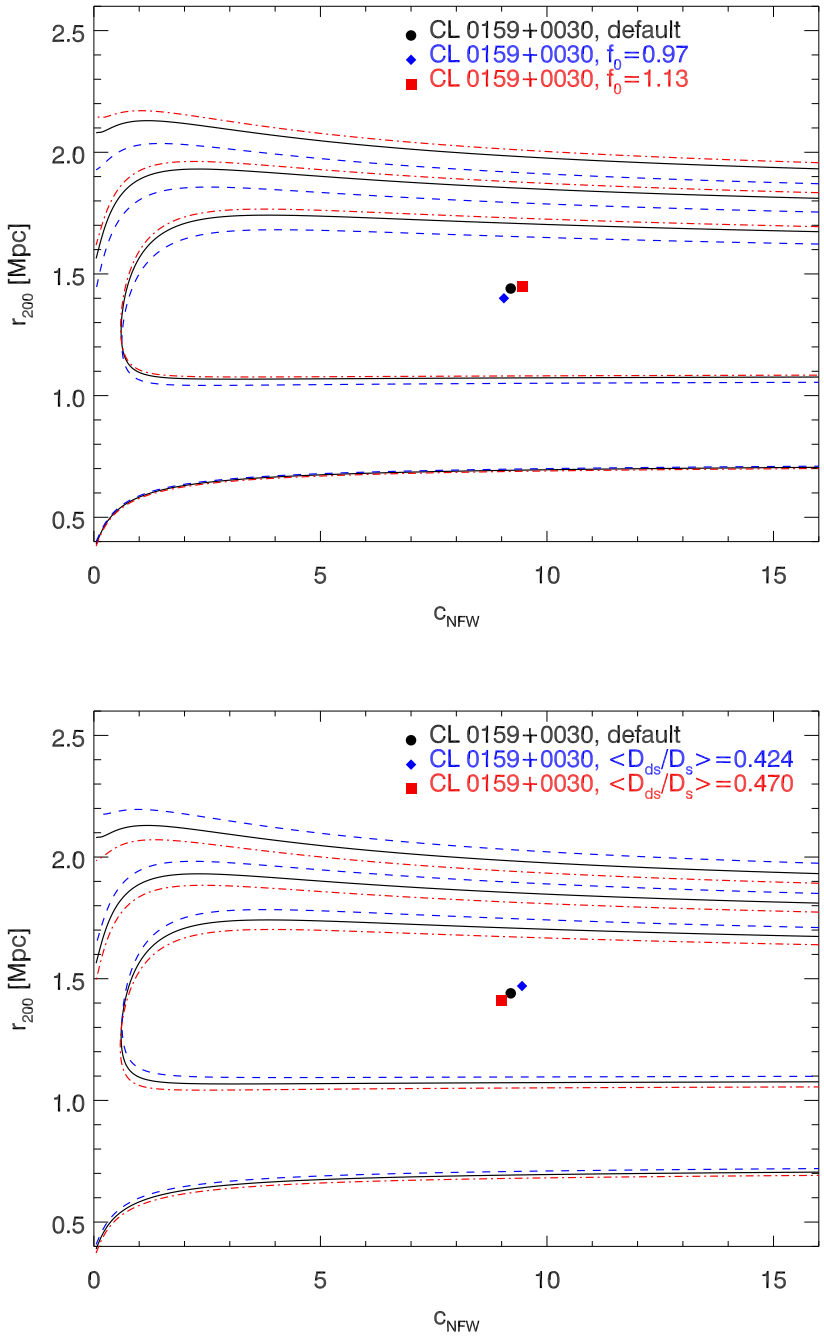

Figure B.10: Confidence contours (99.73%, 95.4%, and 68.3%) and cluster parameters minimising $\chi^2_{\rm L}$ (Eq. 6.12) for models of CL 0159+0030 considered in the error analysis. The fiducial model (solid contours and filled circle) is the same as in Fig. 7.13. In the *upper plot*, dashed contours and a diamond denote a model with shear calibration factor $f_0 = 0.97$; dot-dashed contours and a square stand for $f_0 = 1.13$. In the *lower plot*, the same contours and symbols denote geometric factors of $\langle D_{\rm ds}/D_{\rm s}\rangle = 0.424$ and $\langle D_{\rm ds}/D_{\rm s}\rangle = 0.470$, respectively.

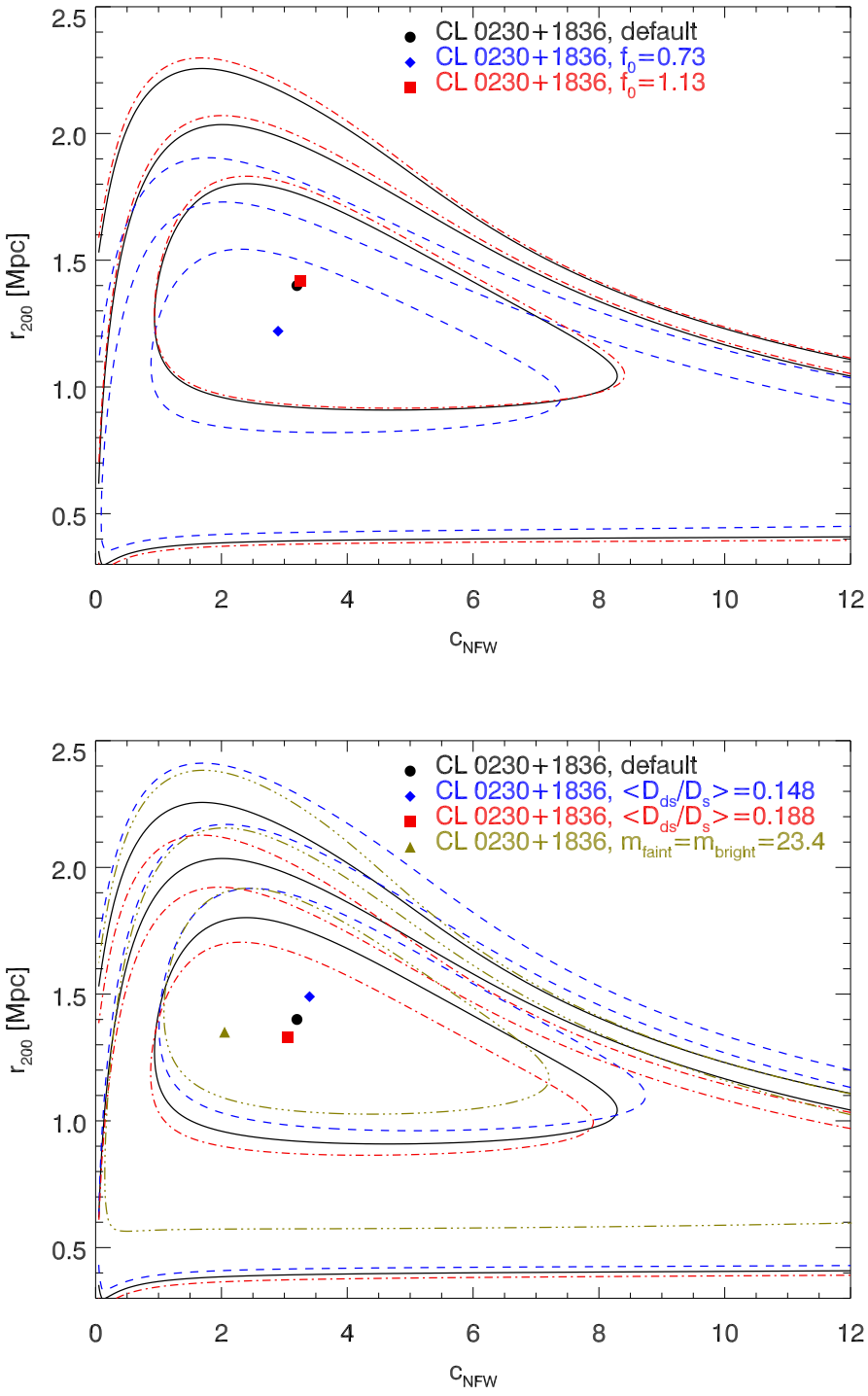

Figure B.11: The same as Fig. B.10, but for CL 0230+1836 and with different values for f_0 and $\langle D_{\rm ds}/D_{\rm s}\rangle$ (see legend in plots and Sect. 8.2). The fiducial model (solid contours and filled circle) is the same as in Fig. 7.15. In addition, the lower plot shows a model based on the lensing catalogue derived from a magnitude cut at $r' = 23.4$ (triple-dot dashed contours and triangle; see Sect. 7.2.1).

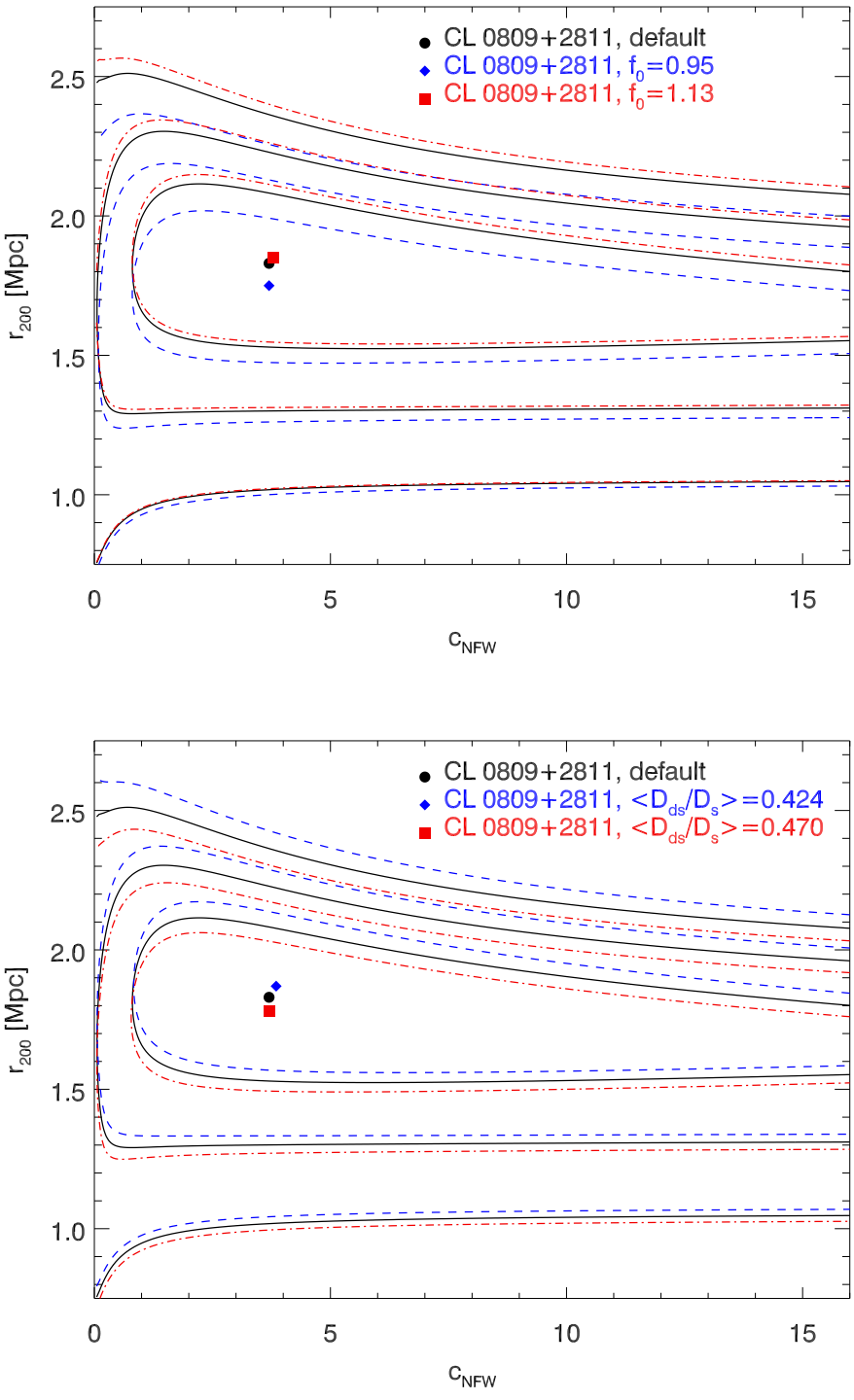

Figure B.12: The same as Fig. B.10, but for CL 0809+2811 and with different values for f_0 and $\langle D_{\rm ds}/D_{\rm s}\rangle$ (see legend in plots and Sect. 8.2). The fiducial model (solid contours and filled circle) is the same as in Fig. 7.14.

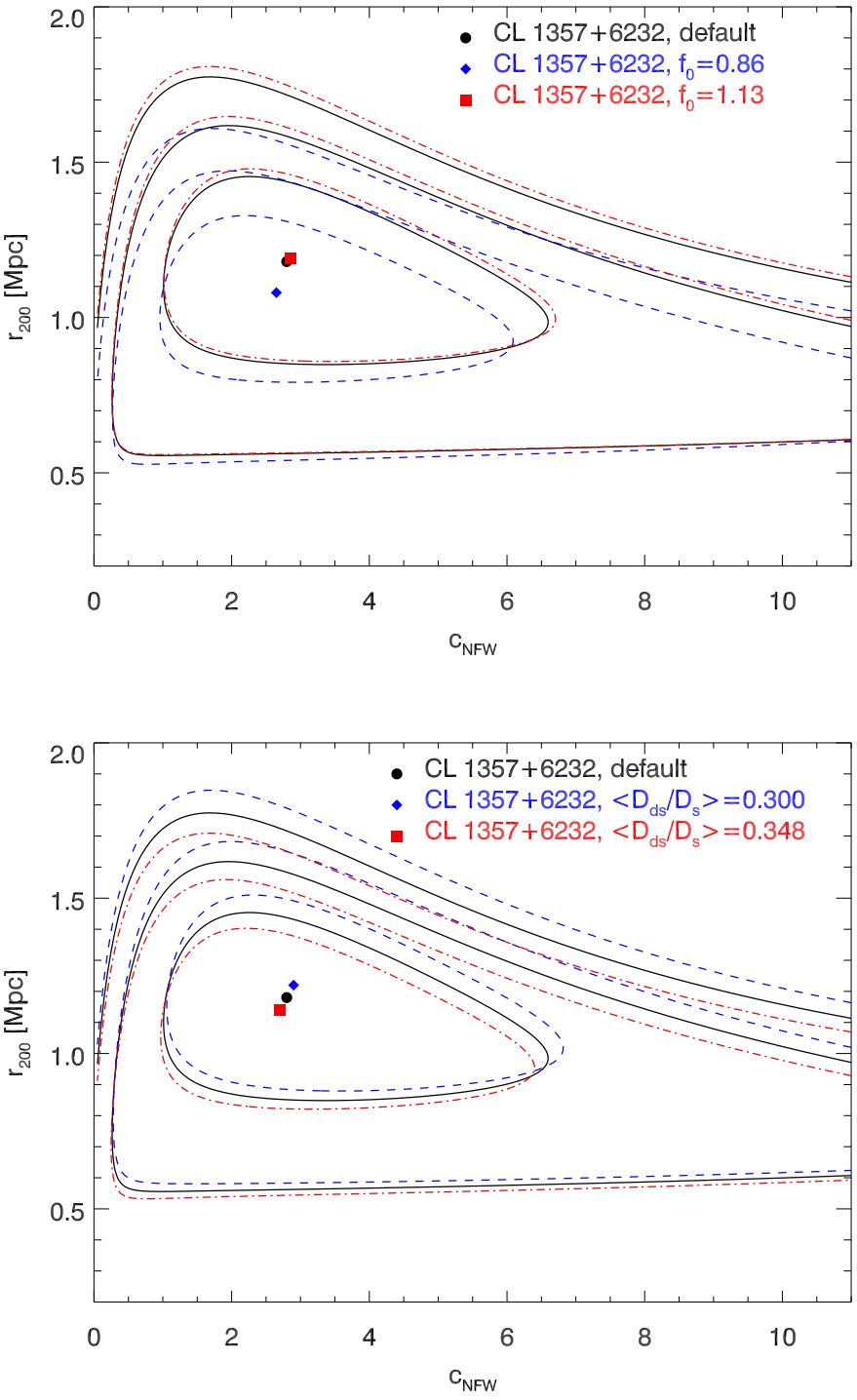

Figure B.13: The same as Fig. B.10, but for CL 1357+6232 and with different values for f_0 and $\langle D_{\rm ds}/D_{\rm s}\rangle$ (see legend in plots and Sect. 8.2). The fiducial model (solid contours and filled circle) is the same as in Fig. 7.16.

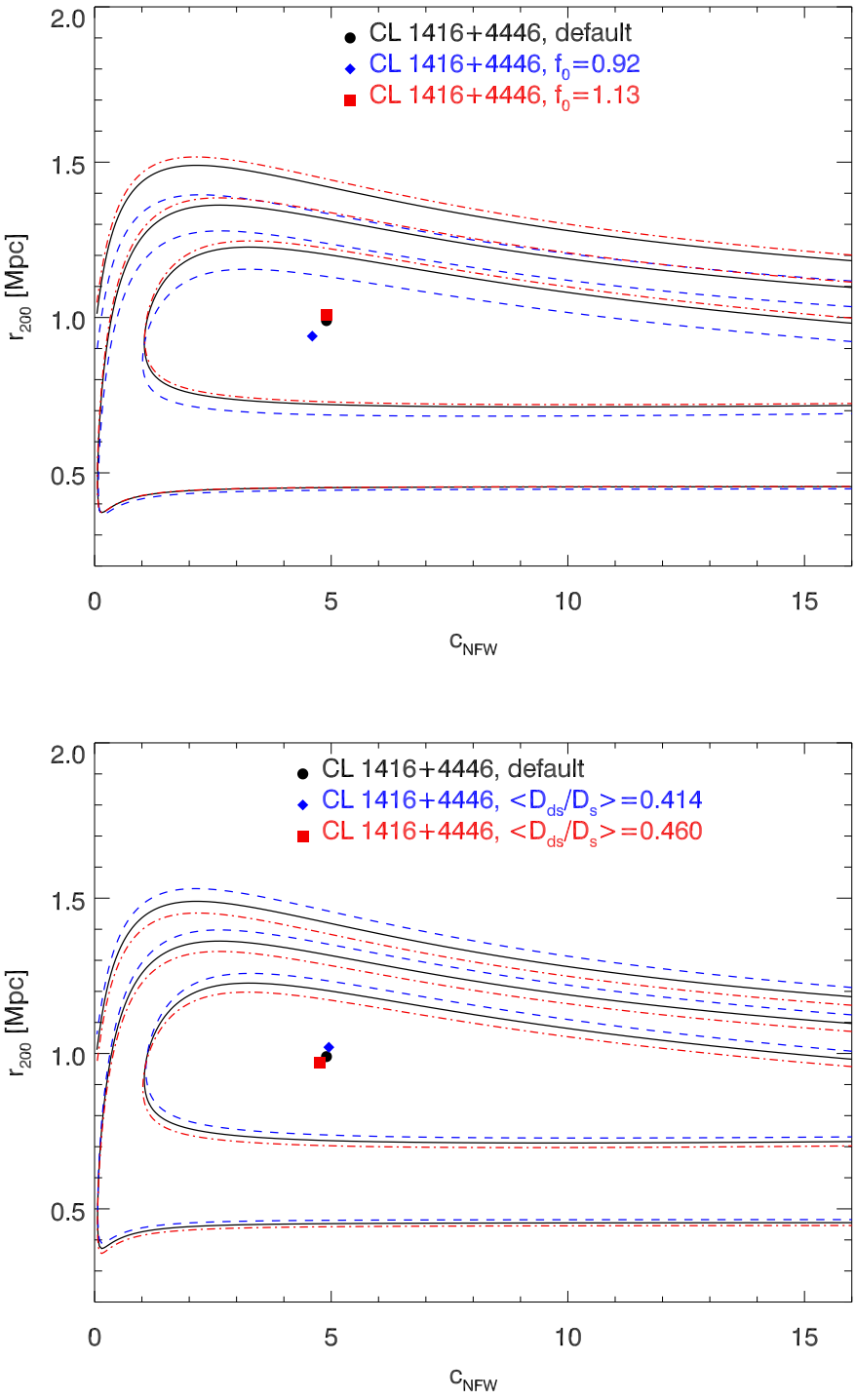

Figure B.14: The same as Fig. B.10, but for CL 1416+4446 and with different values for f_0 and $\langle D_{\rm ds}/D_{\rm s}\rangle$ (see legend in plots and Sect. 8.2). The fiducial model (solid contours and filled circle) is the same as in Fig. 7.17.

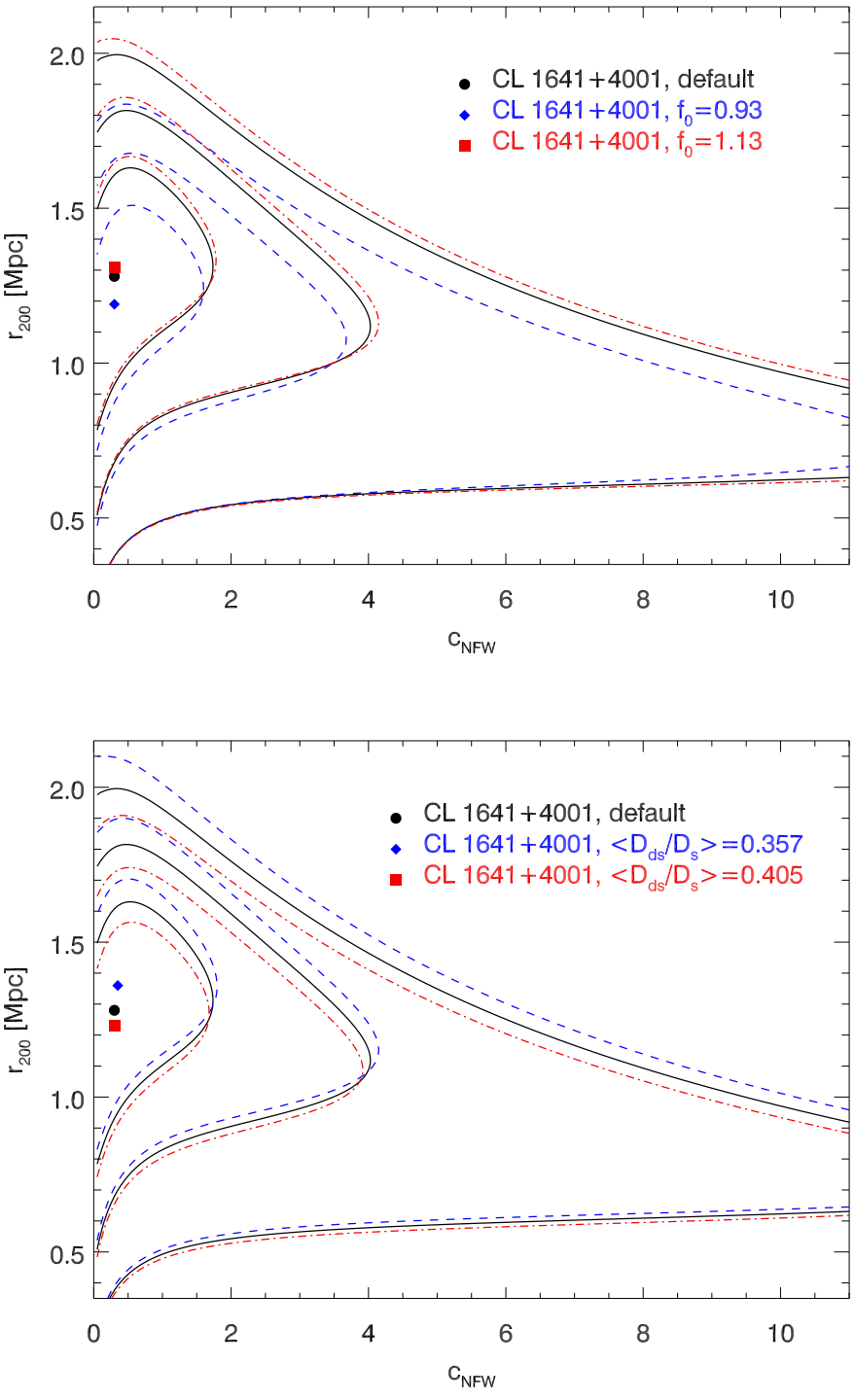

Figure B.15: The same as Fig. B.10, but for CL 1641+4001 and with different values for f_0 and $\langle D_{\rm ds}/D_{\rm s}\rangle$ (see legend in plots and Sect. 8.2). The fiducial model (solid contours and filled circle) is the same as in Fig. 7.22.

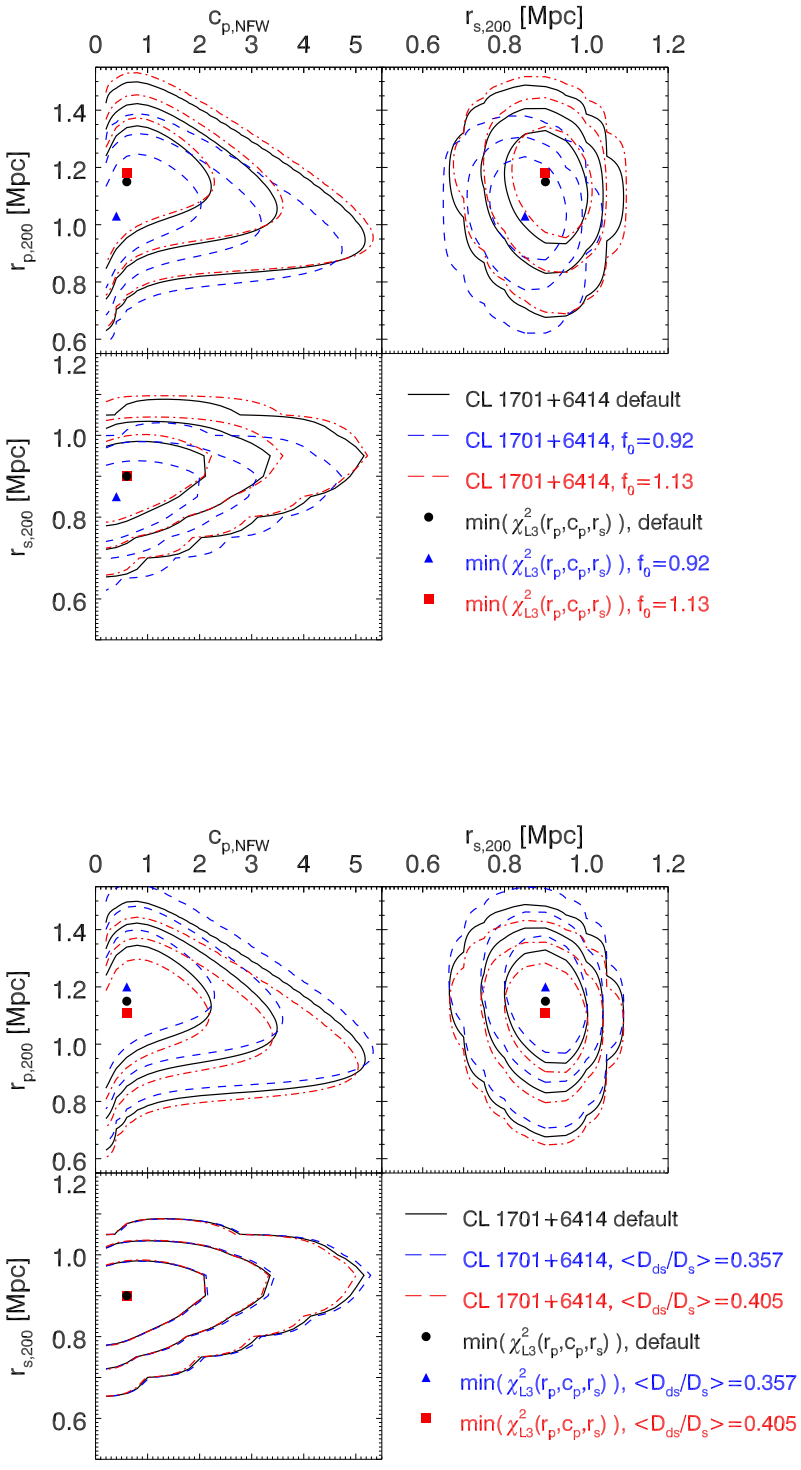

Figure B.16: Analogous to Fig. B.10, but for CL 1701+6414 and with different values for f_0 and $\langle D_{\rm ds}/D_{\rm s}\rangle$ (see legend in plots and Sect. 8.2). The fiducial model (solid contours and filled circle) and layout of the plots are the same as in Fig. 7.20.

B.4 Mass Profiles

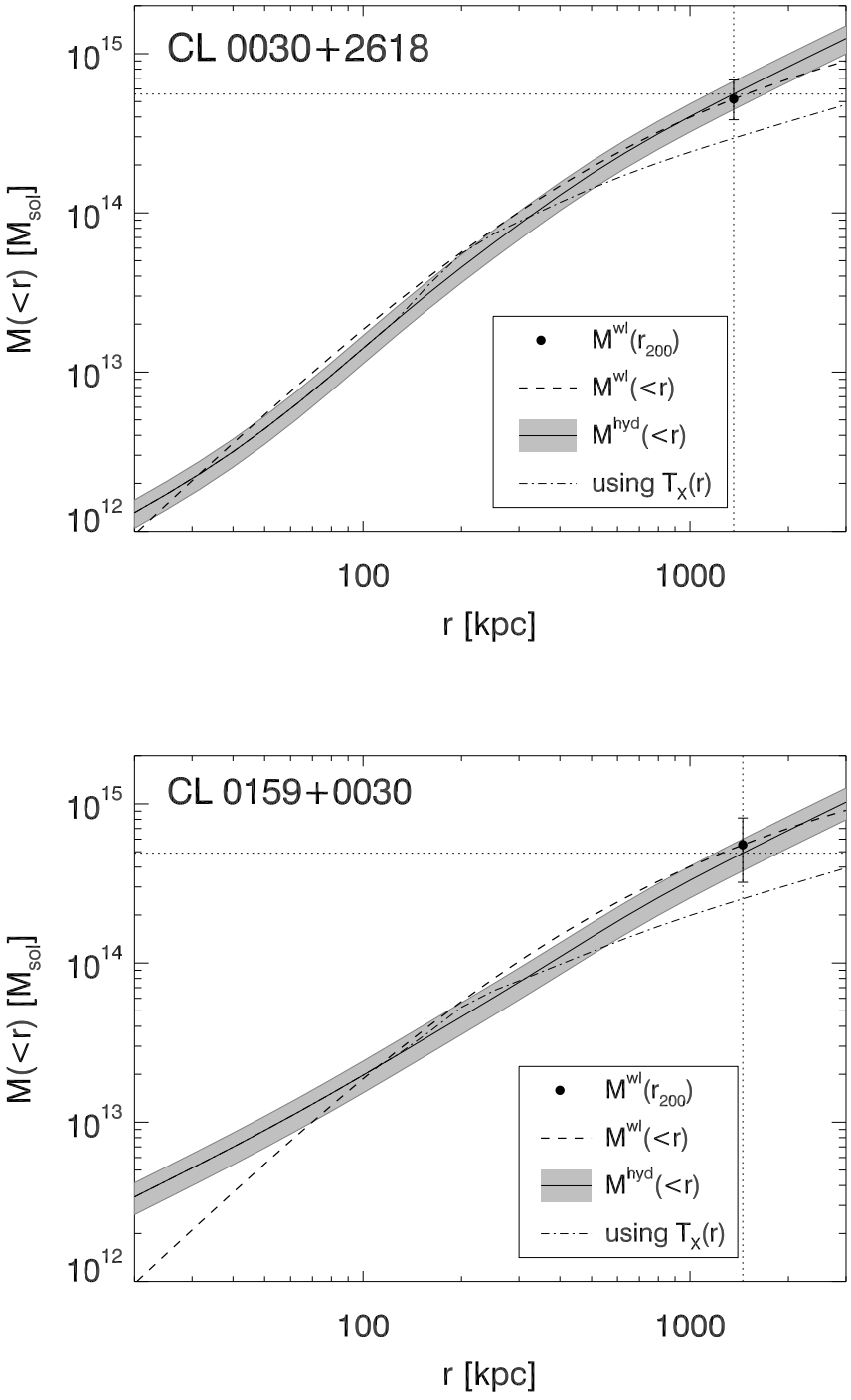

Figure B.17: The same as Fig. 8.2 (upper plot) and Fig. 8.3 (lower plot), but assuming the value predicted by Bullock et al. (2001) for $c_{\rm NFW}$ (Table 8.3).

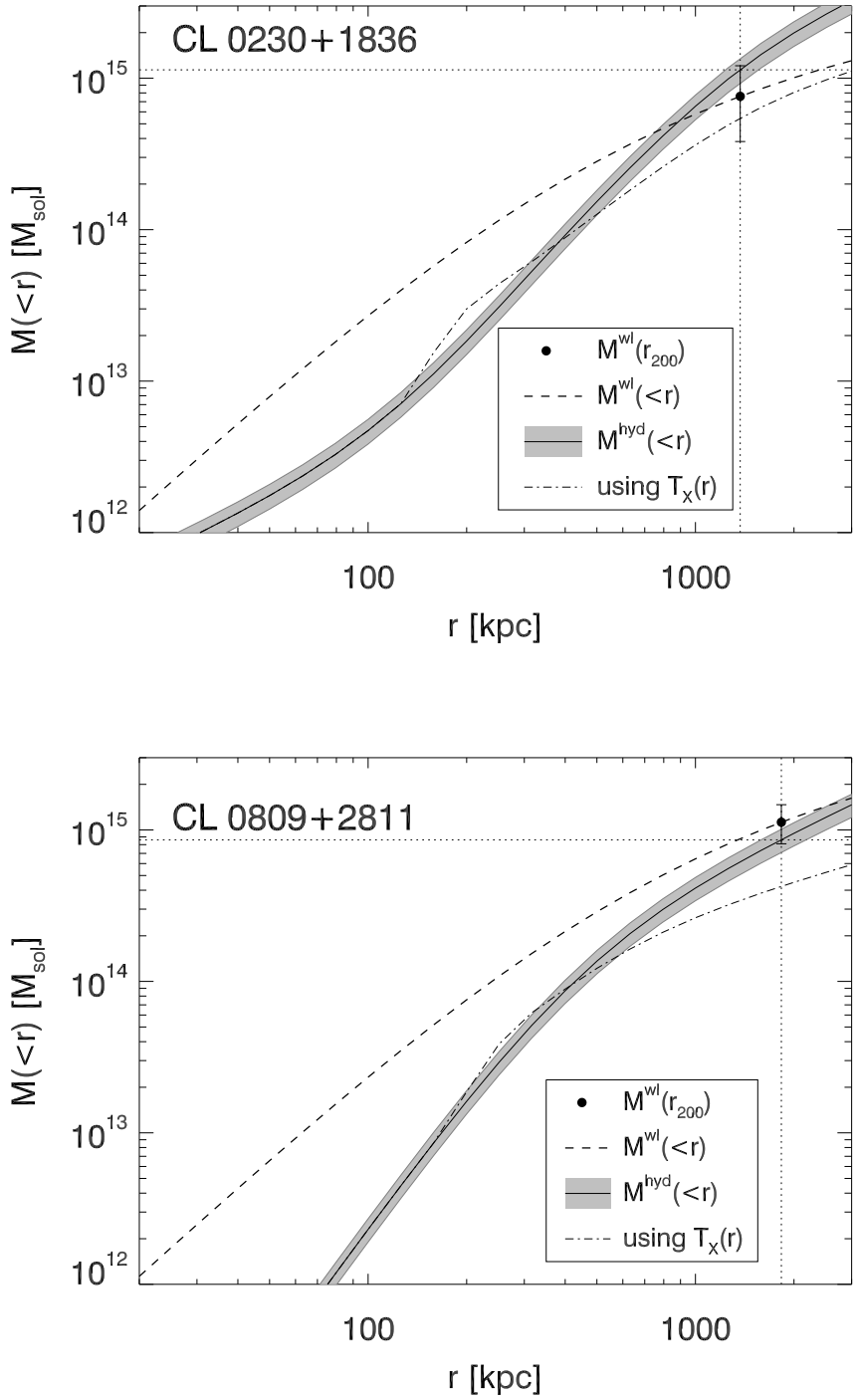

Figure B.18: The same as Fig. 8.4, but assuming the value predicted by Bullock et al. (2001) for $c_{\rm NFW}$ (Table 8.3).

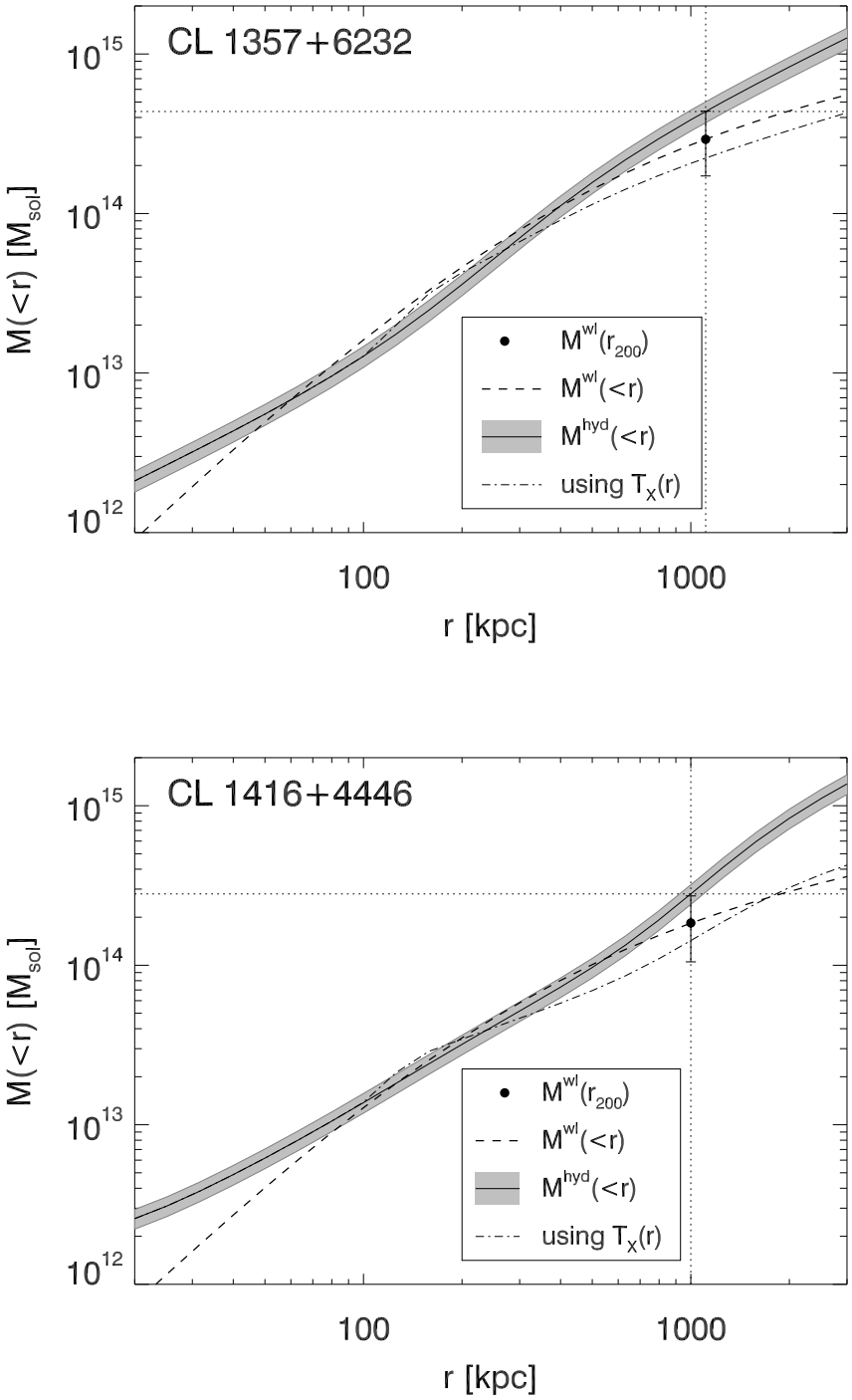

Figure B.19: The same as Fig. 8.5, but assuming the value predicted by Bullock et al. (2001) for $c_{\rm NFW}$ (Table 8.3).

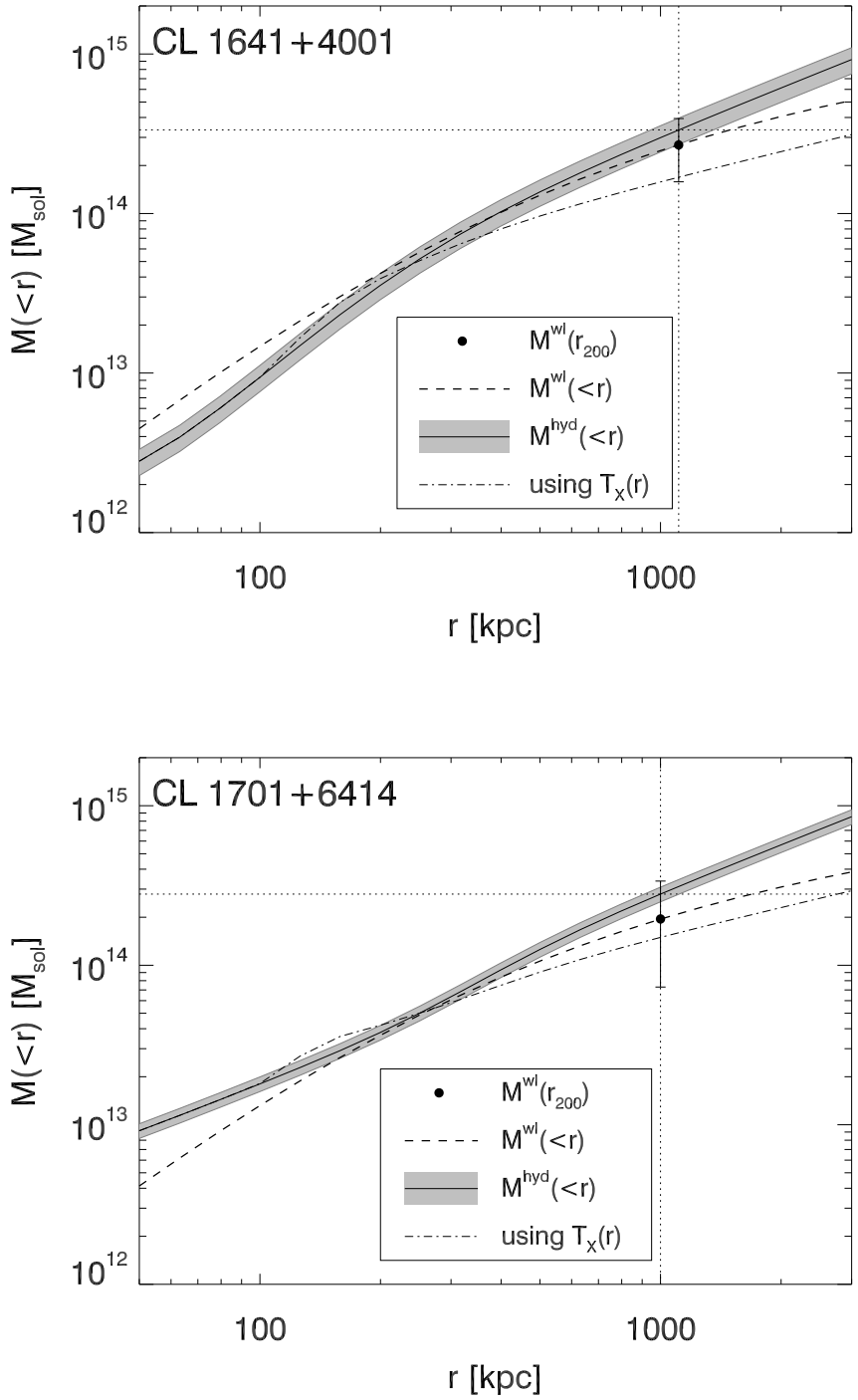

Figure B.20: The same as Fig. 8.6, but assuming the value predicted by Bullock et al. (2001) for $c_{\rm NFW}$ (Table 8.3).

B.5 Scaling of WL and X-ray Masses

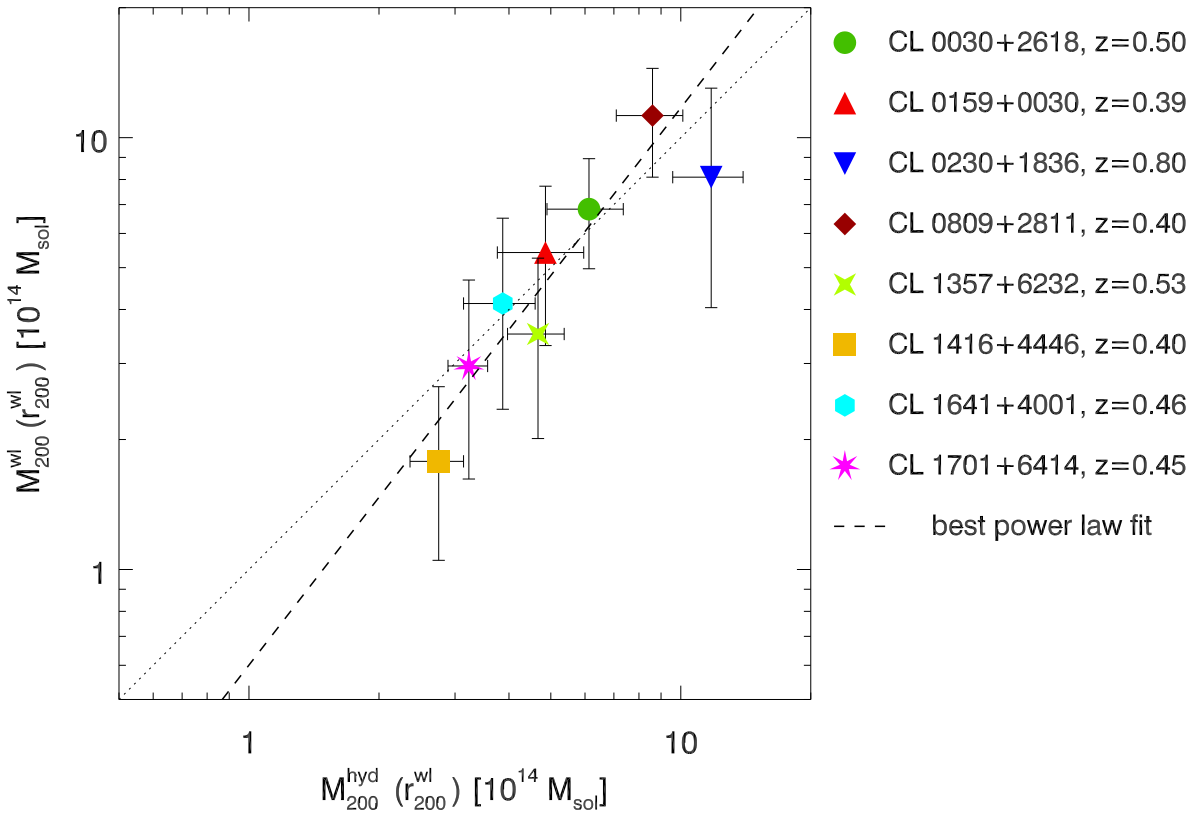

Figure B.21: The same as Fig. 8.7, but for r_{200}. Shown are the weak lensing mass $M_{200}^{\rm wl}(r_{200}^{\rm wl})$ of the eight clusters as a function of the hydrostatic mass $M_{200}^{\rm hyd}(r_{200}^{\rm wl})$, in a double logarithmic plot. Error bars give the statistical errors to the lensing mass and the error resulting from the uncertainty in $T_{\rm X}$. On the dotted line, both masses are equal; the dashed line represents the best linear fit of $\log M_{200}^{\rm wl}(r_{200}^{\rm wl})$ to $\log M_{200}^{\rm hyd}(r_{200}^{\rm wl})$.

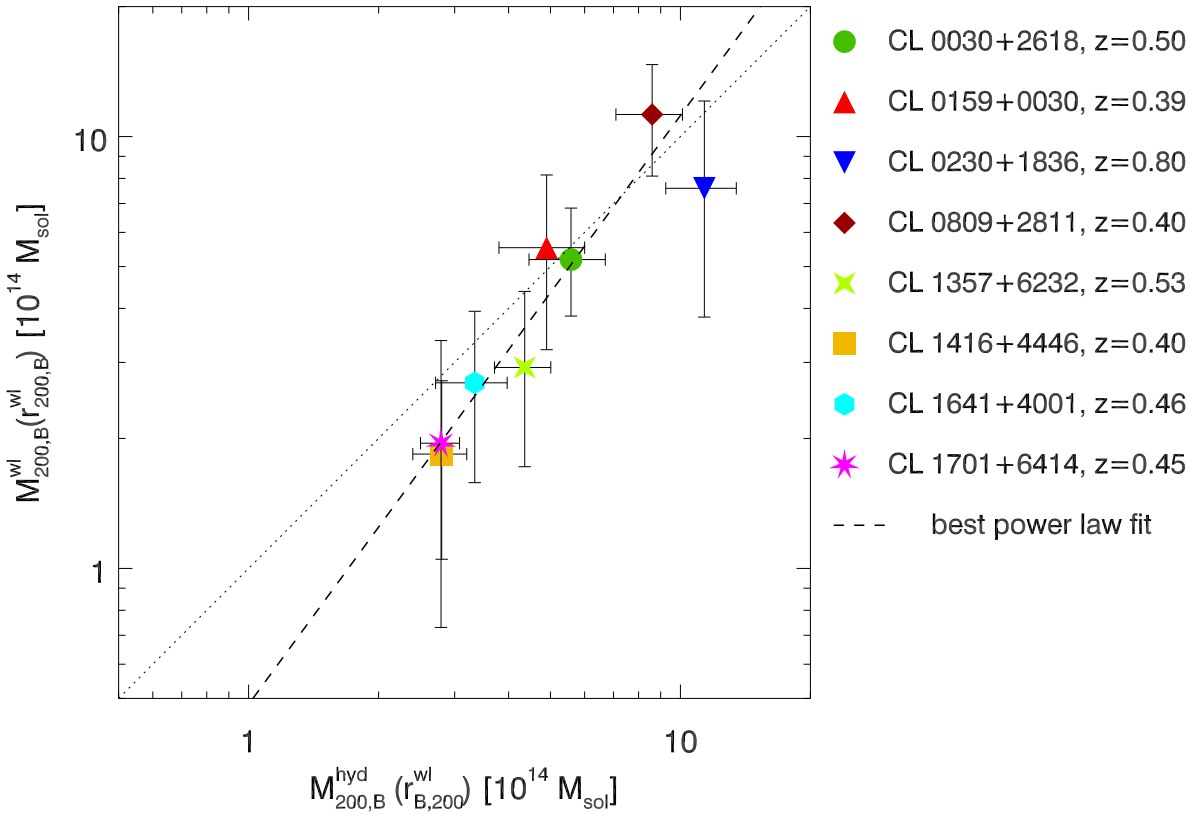

Figure B.22: Analogous to Figs. 8.8 and B.21, but showing $M^{wl}_{200,B}(r^{wl}_{200,B})$ as a function of $M^{hyd}_{200,B}(r^{wl}_{200,B})$ and the respective fit. The subscript "B" denotes the results with c_{NFW} fixed to the value predicted by the Bullock et al. (2001) relation.

Bibliography

Abell, G. O. 1958, ApJS, 3, 211

Abell, G. O., Corwin, Jr., H. G., & Olowin, R. P. 1989, ApJS, 70, 1

Adelman-McCarthy, J. K., Agüeros, M. A., Allam, S. S., et al. 2008, ApJS, 175, 297

Afonso, C., Albert, J. N., Andersen, J., et al. 2003, A&A, 400, 951

Albrecht, A., Bernstein, G., Cahn, R., et al. 2006, ArXiv astro-ph/0609591

Alcock, C., Allsman, R. A., Alves, D. R., et al. 2000, ApJ, 542, 281

Arnaud, M., Pointecouteau, E., & Pratt, G. W. 2007, A&A, 474, L37

Bardeau, S., Soucail, G., Kneib, J., et al. 2007, A&A, 470, 449

Barkhouse, W. A., Green, P. J., Vikhlinin, A., et al. 2006, ApJ, 645, 955

Bartelmann, M. 1995, A&A, 303, 643

Bartelmann, M. 1996, A&A, 313, 697

Bartelmann, M. & Schneider, P. 2001, Phys. Rep., 340, 291

Bekenstein, J. D. 2004, Phys. Rev. D, 70, 083509

Benítez, N. 2000, ApJ, 536, 571

Bennett, D. P., Bond, I. A., Udalski, A., et al. 2008, ApJ, 684, 663

Bernstein, G. M. & Jarvis, M. 2002, AJ, 123, 583

Bertin, E. 2006, in ASP Conference Series, Vol. 351, Astronomical Data Analysis Software and Systems XV, ed. C. Gabriel, C. Arviset, D. Ponz, & S. Enrique, 112

Bertin, E. & Arnouts, S. 1996, A&AS, 117, 393

Birkinshaw, M. 1999, Phys. Rep., 310, 97

Birkinshaw, M., Hughes, J. P., & Arnaud, K. A. 1991, ApJ, 379, 466

Böhringer, H., Schuecker, P., Guzzo, L., et al. 2004, A&A, 425, 367

Böhringer, H., Voges, W., Huchra, J. P., et al. 2000, ApJS, 129, 435

Bolzonella, M., Miralles, J., & Pelló, R. 2000, A&A, 363, 476

Bonamente, M., Joy, M. K., LaRoque, S. J., et al. 2006, ApJ, 647, 25

Bond, I. A., Udalski, A., Jaroszyński, M., et al. 2004, ApJ, 606, L155

Borgani, S. & Guzzo, L. 2001, Nature, 409, 39

Boschin, W. 2002, A&A, 396, 397

Bower, R. G., Lucey, J. R., & Ellis, R. S. 1992, MNRAS, 254, 601

Boyle, B. J., Wilkes, B. J., & Elvis, M. 1997, MNRAS, 285, 511

Bradač, M., Allen, S. W., Treu, T., et al. 2008a, ApJ, 687, 959

Bradač, M., Erben, T., Schneider, P., et al. 2005, A&A, 437, 49

Bradač, M., Schrabback, T., Erben, T., et al. 2008b, ApJ, 681, 187

Brandt, W. N., Hornschemeier, A. E., Schneider, D. P., et al. 2000, AJ, 119, 2349

Bridle, S., Balan, S. T., Bethge, M., et al. 2010, MNRAS, 405, 2044

Bryan, G. L. & Norman, M. L. 1998, ApJ, 495, 80

Bullock, J. S., Kolatt, T. S., Sigad, Y., et al. 2001, MNRAS, 321, 559

Burenin, R. A., Vikhlinin, A., Hornstrup, A., et al. 2007, ApJS, 172, 561

Butcher, H. & Oemler, Jr., A. 1978, ApJ, 226, 559

Cappi, M., Mazzotta, P., Elvis, M., et al. 2001, ApJ, 548, 624

Carlstrom, J. E., Holder, G. P., & Reese, E. D. 2002, ARA&A, 40, 643

Carlstrom, J. E., Joy, M., Grego, L., et al. 2001, in Constructing the Universe with Clusters of Galaxies. IAP Conference 2000, astro-ph/0103480

Cavaliere, A. & Fusco-Femiano, R. 1978, A&A, 70, 677

Chen, Y., Reiprich, T. H., Böhringer, H., Ikebe, Y., & Zhang, Y.-Y. 2007, A&A, 466, 805

Clowe, D., Bradač, M., Gonzalez, A. H., et al. 2006a, ApJ, 648, L109

Clowe, D., De Lucia, G., & King, L. 2004, MNRAS, 350, 1038

Clowe, D. & Schneider, P. 2002, A&A, 395, 385

Clowe, D., Schneider, P., Aragón-Salamanca, A., et al. 2006b, A&A, 451, 395

Cohn, J. D. & White, M. 2005, Astroparticle Physics, 24, 316

Coleman, G. D., Wu, C.-C., & Weedman, D. W. 1980, ApJS, 43, 393

Comerford, J. M. & Natarajan, P. 2007, MNRAS, 379, 190

Corless, V. L. & King, L. J. 2007, MNRAS, 380, 149

Corless, V. L. & King, L. J. 2009, MNRAS, 396, 315

Dahle, H. 2006, ApJ, 653, 954

Davis, T. M., Mörtsell, E., Sollerman, J., et al. 2007, ApJ, 666, 716

Dietrich, J. P., Biviano, A., Popesso, P., et al. 2009, A&A, 499, 669

Dietrich, J. P., Erben, T., Lamer, G., et al. 2007, A&A, 470, 821

Donahue, M., Scharf, C. A., Mack, J., et al. 2002, ApJ, 569, 689

Dunkley, J., Spergel, D. N., Komatsu, E., et al. 2009, ApJ, 701, 1804

Ebeling, H., Edge, A. C., Allen, S. W., et al. 2000, MNRAS, 318, 333

Ebeling, H., Edge, A. C., Mantz, A., et al. 2010, ArXiv astro-ph/1004.4683

Edge, A. C. 2004, in Clusters of Galaxies: Probes of Cosmological Structure and Galaxy Evolution, ed. J. S. Mulchaey, A. Dressler, & A. Oemler, 58

Eisenstein, D. J., Zehavi, I., Hogg, D. W., et al. 2005, ApJ, 633, 560

Eke, V. R., Cole, S., & Frenk, C. S. 1996, MNRAS, 282, 263

Erben, T., Hildebrandt, H., Lerchster, M., et al. 2009, A&A, 493, 1197

Erben, T., Schirmer, M., Dietrich, J. P., et al. 2005, Astronomische Nachrichten, 326, 432

Erben, T., van Waerbeke, L., Bertin, E., Mellier, Y., & Schneider, P. 2001, A&A, 366, 717

Freedman, W. L., Madore, B. F., Gibson, B. K., et al. 2001, ApJ, 553, 47

Frieman, J. A., Turner, M. S., & Huterer, D. 2008, ARA&A, 46, 385

Fu, L., Semboloni, E., Hoekstra, H., et al. 2008, A&A, 479, 9

Fukugita, M., Ichikawa, T., Gunn, J. E., et al. 1996, AJ, 111, 1748

Gavazzi, R. & Soucail, G. 2007, A&A, 462, 459

George, M. R., Fabian, A. C., Sanders, J. S., Young, A. J., & Russell, H. R. 2009, MNRAS, 395, 657

Gladders, M. D., Lopez-Cruz, O., Yee, H. K. C., & Kodama, T. 1998, ApJ, 501, 571

Gladders, M. D. & Yee, H. K. C. 2000, AJ, 120, 2148

Gladders, M. D. & Yee, H. K. C. 2005, ApJS, 157, 1

Goto, T., Sekiguchi, M., Nichol, R. C., et al. 2002, AJ, 123, 1807

Gott, III, J. R., Jurić, M., Schlegel, D., et al. 2005, ApJ, 624, 463

Grego, L., Carlstrom, J. E., Reese, E. D., et al. 2001, ApJ, 552, 2

Gull, S. F. & Northover, K. J. E. 1976, Nature, 263, 572

Halkola, A., Hildebrandt, H., Schrabback, T., et al. 2008, A&A, 481, 65

Halverson, N. W., Lanting, T., Ade, P. A. R., et al. 2009, ApJ, 701, 42

Hartlap, J., Schrabback, T., Simon, P., & Schneider, P. 2009, ArXiv astro-ph/0901.3269

Hartman, J. D., Gaudi, B. S., Holman, M. J., et al. 2008, ApJ, 675, 1233

Hetterscheidt, M., Erben, T., Schneider, P., et al. 2005, A&A, 442, 43

Hetterscheidt, M., Simon, P., Schirmer, M., et al. 2007, A&A, 468, 859

Heymans, C., van Waerbeke, L., Bacon, D., et al. 2006, MNRAS, 368, 1323

Hildebrandt, H., Bomans, D. J., Erben, T., et al. 2005, A&A, 441, 905

Hildebrandt, H., Erben, T., Dietrich, J. P., et al. 2006, A&A, 452, 1121

Hildebrandt, H., Pielorz, J., Erben, T., et al. 2007, A&A, 462, 865

Hildebrandt, H., Wolf, C., & Benítez, N. 2008, A&A, 480, 703

Hoekstra, H. 2003, MNRAS, 339, 1155

Hoekstra, H. 2007, MNRAS, 379, 317

Hoekstra, H., Franx, M., & Kuijken, K. 2000, ApJ, 532, 88

Hoekstra, H., Franx, M., Kuijken, K., & Squires, G. 1998, ApJ, 504, 636

Horner, D. J., Perlman, E. S., Ebeling, H., et al. 2008, ApJS, 176, 374

Hu, W. & Dodelson, S. 2002, ARA&A, 40, 171

Hudson, D. S., Mittal, R., Reiprich, T. H., et al. 2010, A&A, 513, A37

Ilbert, O., Arnouts, S., McCracken, H. J., et al. 2006, A&A, 457, 841

Ilbert, O., Capak, P., Salvato, M., et al. 2009, ApJ, 690, 1236

Israel, H., Erben, T., Reiprich, T. H., et al. 2010, A&A, in press

Jee, M. J., Rosati, P., Ford, H. C., et al. 2009, ApJ, 704, 672

Jee, M. J. & Tyson, J. A. 2009, ApJ, 691, 1337

Jee, M. J., White, R. L., Benítez, N., et al. 2005, ApJ, 618, 46

Jeltema, T. E., Hallman, E. J., Burns, J. O., & Motl, P. M. 2008, ApJ, 681, 167

Jenkins, A., Frenk, C. S., White, S. D. M., et al. 2001, MNRAS, 321, 372

Joachimi, B. & Schneider, P. 2009, A&A, 507, 105

Kaiser, N. & Squires, G. 1993, ApJ, 404, 441

Kaiser, N., Squires, G., & Broadhurst, T. 1995, ApJ, 449, 460

Kasun, S. F. & Evrard, A. E. 2005, ApJ, 629, 781

Kausch, W., Gitti, M., Erben, T., & Schindler, S. 2007, A&A, 471, 31

King, L. & Corless, V. 2007, MNRAS, 374, L37

Kitching, T. D., Miller, L., Heymans, C. E., van Waerbeke, L., & Heavens, A. F. 2008, MNRAS, 390, 149

Kochanek, C. S. 2006, "Strong Gravitational Lensing" in: Gravitational Lensing: Strong, Weak and Micro: Saas-Fee Advanced Courses, Vol. 33 (Springer-Verlag Berlin Heidelberg), 91 ff.

Koester, B. P., McKay, T. A., Annis, J., et al. 2007, ApJ, 660, 221

Komatsu, E., Dunkley, J., Nolta, M. R., et al. 2009, ApJS, 180, 330

Komatsu, E., Smith, K. M., Dunkley, J., et al. 2010, ArXiv astro-ph/1001.4538

Kowalski, M., Rubin, D., Aldering, G., et al. 2008, ApJ, 686, 749

Kravtsov, A. V., Vikhlinin, A., & Nagai, D. 2006, ApJ, 650, 128

Laganá, T. F., de Souza, R. S., & Keller, G. R. 2010, A&A, 510, A76

LaRoque, S. J., Bonamente, M., Carlstrom, J. E., et al. 2006, ApJ, 652, 917

Larson, D., Dunkley, J., Hinshaw, G., et al. 2010, ArXiv astro-ph/1001.4635

Leith, B. M., Ng, S. C. C., & Wiltshire, D. L. 2008, ApJ, 672, L91

Liddle, A. 2003, An Introduction to Modern Cosmology, Second Edition (Wiley-VCH)

Limousin, M., Cabanac, R., Gavazzi, R., et al. 2009, A&A, 502, 445

Limousin, M., Richard, J., Jullo, E., et al. 2007, ApJ, 668, 643

Lopes, P. A. A., de Carvalho, R. R., Gal, R. R., et al. 2004, AJ, 128, 1017

Mahdavi, A., Hoekstra, H., Babul, A., Balam, D. D., & Capak, P. L. 2007, ApJ, 668, 806

Mahdavi, A., Hoekstra, H., Babul, A., & Henry, J. P. 2008, MNRAS, 384, 1567

Mandelbaum, R., Hirata, C. M., Ishak, M., Seljak, U., & Brinkmann, J. 2006, MNRAS, 367, 611

Mandelbaum, R., Seljak, U., Baldauf, T., & Smith, R. E. 2010, MNRAS, 405, 2078

Mantz, A., Allen, S. W., Ebeling, H., & Rapetti, D. 2008, MNRAS, 387, 1179

Mantz, A., Allen, S. W., Ebeling, H., Rapetti, D., & Drlica-Wagner, A. 2009a, ArXiv astro-ph/0909.3099

Mantz, A., Allen, S. W., Rapetti, D., & Ebeling, H. 2009b, ArXiv astro-ph/0909.3098

Margoniner, V. E., Lubin, L. M., Wittman, D. M., & Squires, G. K. 2005, AJ, 129, 20

Marian, L., Smith, R. E., & Bernstein, G. M. 2010, ApJ, 709, 286

Markwardt, C. B. 2009, in ASP Conference Series, Vol. 411, Astronomical Data Analysis Software and Systems XVIII, ed. D. A. Bohlender, D. Durand, & P. Dowler, 251–255

Massey, R., Heymans, C., Bergé, J., et al. 2007, MNRAS, 376, 13

Massey, R., Kitching, T., & Richard, J. 2010, ArXiv astro-ph/1001.1739

Maturi, M., Meneghetti, M., Bartelmann, M., Dolag, K., & Moscardini, L. 2005, A&A, 442, 851

Maturi, M., Schirmer, M., Meneghetti, M., Bartelmann, M., & Moscardini, L. 2007, A&A, 462, 473

Maughan, B. J. 2007, ApJ, 668, 772

Maughan, B. J., Jones, C., Forman, W., & Van Speybroeck, L. 2008, ApJS, 174, 117

McInnes, R. N., Menanteau, F., Heavens, A. F., et al. 2009, MNRAS, 399, L84

McLeod, B., Geary, J., Ordway, M., et al. 2006, in Scientific Detectors for Astronomy 2005, ed. J. E. Beletic, J. W. Beletic, & P. Amico, 337

McLeod, B. A., Conroy, M., Gauron, T. M., Geary, J. C., & Ordway, M. P. 2000, in Further Developments in Scientific Optical Imaging, ed. M. B. Denton, 11

Melchior, P., Böhnert, A., Lombardi, M., & Bartelmann, M. 2010, A&A, 510, A75

Meneghetti, M., Rasia, E., Merten, J., et al. 2009, ArXiv astro-ph/0912.1343

Merten, J., Cacciato, M., Meneghetti, M., Mignone, C., & Bartelmann, M. 2009, A&A, 500, 681

Milgrom, M. 1983, ApJ, 270, 365

Milkeraitis, M., van Waerbeke, L., Heymans, C., et al. 2009, ArXiv astro-ph/0912.0739

Miller, C. J., Nichol, R. C., Reichart, D., et al. 2005, AJ, 130, 968

Miller, L., Kitching, T. D., Heymans, C., Heavens, A. F., & van Waerbeke, L. 2007, MNRAS, 382, 315

Mittal, R., Hudson, D. S., Reiprich, T. H., & Clarke, T. 2009, A&A, 501, 835

Mohr, J. J. 2005, in Astronomical Society of the Pacific Conference Series, Vol. 339, Observing Dark Energy, ed. S. C. Wolff & T. R. Lauer, 140

Monet, D. G., Levine, S. E., Canzian, B., et al. 2003, AJ, 125, 984

Moré, J. J. 1978, in Lecture Notes in Mathematics, Vol. 630, Numerical Analysis (Springer-Verlag Berlin Heidelberg), 105–116

Mullis, C. R., McNamara, B. R., Quintana, H., et al. 2003, ApJ, 594, 154

Nagai, D., Kravtsov, A. V., & Vikhlinin, A. 2007a, ApJ, 668, 1

Nagai, D., Vikhlinin, A., & Kravtsov, A. V. 2007b, ApJ, 655, 98

Navarro, J. F., Frenk, C. S., & White, S. D. M. 1995, MNRAS, 275, 720

Navarro, J. F., Frenk, C. S., & White, S. D. M. 1996, ApJ, 462, 563

Navarro, J. F., Frenk, C. S., & White, S. D. M. 1997, ApJ, 490, 493

Newberg, H. J. & Sloan Digital Sky Survey Collaboration. 2003, in Bulletin of the American Astronomical Society, Vol. 35, Bulletin of the American Astronomical Society, 1385

Nord, M., Basu, K., Pacaud, F., et al. 2009, A&A, 506, 623

Oguri, M., Hennawi, J. F., Gladders, M. D., et al. 2009, ApJ, 699, 1038

Okabe, N., Takada, M., Umetsu, K., Futamase, T., & Smith, G. P. 2009, ArXiv astro-ph/0903.1103

Okabe, N. & Umetsu, K. 2008, PASJ, 60, 345

Pace, F., Maturi, M., Bartelmann, M., et al. 2008, A&A, 483, 389

Peacock, J. A., Cole, S., Norberg, P., et al. 2001, Nature, 410, 169

Peacock, J. A., Schneider, P., Efstathiou, G., et al. 2006, ESA-ESO Working Group on "Fundamental Cosmology", Tech. rep., ESA-ESO Working Group on "Fundamental Cosmology"

Percival, W. J., Cole, S., Eisenstein, D. J., et al. 2007, MNRAS, 381, 1053

Percival, W. J., Reid, B. A., Eisenstein, D. J., et al. 2010, MNRAS, 401, 2148

Perlmutter, S., Aldering, G., Goldhaber, G., et al. 1999, ApJ, 517, 565

Pickles, A. J. 1998, PASP, 110, 863

Pillepich, A., Porciani, C., & Hahn, O. 2010, MNRAS, 402, 191

Plionis, M., Basilakos, S., Georgantopoulos, I., & Georgakakis, A. 2005, ApJ, 622, L17

Postman, M., Lubin, L. M., Gunn, J. E., et al. 1996, AJ, 111, 615

Pratt, G. W., Böhringer, H., Croston, J. H., et al. 2007, A&A, 461, 71

Press, W. H. & Schechter, P. 1974, ApJ, 187, 425

Press, W. H., Teukolsky, S. A., Vetterling, W. T., & Flannery, B. P. 1992, Numerical recipes in C. The art of scientific computing (Cambridge: University Press, 2nd ed.)

Rasia, E., Ettori, S., Moscardini, L., et al. 2006, MNRAS, 369, 2013

Rasia, E., Mazzotta, P., Borgani, S., et al. 2005, ApJ, 618, L1

Refregier, A. 2003, MNRAS, 338, 35

Refregier, A. & Bacon, D. 2003, MNRAS, 338, 48

Reimers, D., Toussaint, F., Hagen, H., Hippelein, H., & Meisenheimer, K. 1997, A&A, 326, 489

Reiprich, T. H. 2006, A&A, 453, L39

Reiprich, T. H. 2009a, Introduction to Galactic and Extragalactic X-Ray Astronomy (Argelander-Institut für Astronomie, Bonn)

Reiprich, T. H. 2009b, Radio and X-ray Observations of Dark Matter and Dark Energy (Argelander-Institut für Astronomie, Bonn)

Reiprich, T. H. & Böhringer, H. 2002, ApJ, 567, 716

Reiprich, T. H., Hudson, D. S., Zhang, Y., et al. 2009, A&A, 501, 899

Rephaeli, Y. 1995, ARA&A, 33, 541

Riess, A. G., Filippenko, A. V., Challis, P., et al. 1998, AJ, 116, 1009

Riess, A. G., Macri, L., Casertano, S., et al. 2009, ApJ, 699, 539

Rines, K. & Diaferio, A. 2010, AJ, 139, 580

Rines, K., Diaferio, A., & Natarajan, P. 2007, ApJ, 657, 183

Romer, A. K., Nichol, R. C., Holden, B. P., et al. 2000, ApJS, 126, 209

Rosati, P., Borgani, S., & Norman, C. 2002, ARA&A, 40, 539

Rosati, P., Tozzi, P., Gobat, R., et al. 2009, A&A, 508, 583

Rowe, B. 2010, MNRAS, 404, 350

Sarazin, C. L. 1988, X-ray emission from clusters of galaxies (Cambridge University Press)

Schirmer, M., Erben, T., Hetterscheidt, M., & Schneider, P. 2007, A&A, 462, 875

Schneider, P. 1996, MNRAS, 283, 837

Schneider, P. 2006a, Einführung in die extragalaktische Astronomie und Kosmologie (Springer-Verlag Berlin Heidelberg)

Schneider, P. 2006b, ”Introduction to Gravitational Lensing and Cosmology” in: Gravitational Lensing: Strong, Weak and Micro, Saas-Fee Advanced Courses, Volume 33 (Springer-Verlag Berlin Heidelberg), 1ff.

Schneider, P. 2006c, ”Weak Gravitational Lensing” in: Gravitational Lensing: Strong, Weak and Micro: Saas-Fee Advanced Courses, Volume 33 (Springer-Verlag Berlin Heidelberg), 269 ff.

Schneider, P., Ehlers, J., & Falco, E. E. 1992, Gravitational Lenses (Springer-Verlag Berlin Heidelberg New York)

Schneider, P., Eifler, T., & Krause, E. 2010, ArXiv astro-ph/1002.2136

Schneider, P. & Er, X. 2008, A&A, 485, 363

Schneider, P., King, L., & Erben, T. 2000, A&A, 353, 41

Schrabback, T., Erben, T., Simon, P., et al. 2007, A&A, 468, 823

Schrabback, T., Hartlap, J., Joachimi, B., et al. 2009, ArXiv astro-ph/0911.0053

Schuecker, P. 2005, in Reviews in Modern Astronomy, Vol. 18, Reviews in Modern Astronomy, ed. S. Röser, 76–105

Schuecker, P., Böhringer, H., Collins, C. A., & Guzzo, L. 2003, A&A, 398, 867

Seitz, C. & Schneider, P. 1997, A&A, 318, 687

Seitz, S. & Schneider, P. 1996, A&A, 305, 383

Seitz, S. & Schneider, P. 2001, A&A, 374, 740

Semboloni, E., Mellier, Y., van Waerbeke, L., et al. 2006, A&A, 452, 51

Sheldon, E. S., Johnston, D. E., Scranton, R., et al. 2009, ApJ, 703, 2217

Sheth, R. K. & Tormen, G. 1999, MNRAS, 308, 119

Sijacki, D., Pfrommer, C., Springel, V., & Enßlin, T. A. 2008, MNRAS, 387, 1403

Springel, V., White, S. D. M., Jenkins, A., et al. 2005, Nature, 435, 629

Stanek, R., Evrard, A. E., Böhringer, H., Schuecker, P., & Nord, B. 2006, ApJ, 648, 956

Stanek, R., Rasia, E., Evrard, A. E., Pearce, F., & Gazzola, L. 2010, ApJ, 715, 1508

Stanford, S. A., Romer, A. K., Sabirli, K., et al. 2006, ApJ, 646, L13

Staniszewski, Z., Ade, P. A. R., Aird, K. A., et al. 2009, ApJ, 701, 32

Sunyaev, R. A. & Zel'dovich, Y. B. 1970, Comments on Astrophysics and Space Physics, 2, 66

Suyu, S. H., Marshall, P. J., Auger, M. W., et al. 2010, ApJ, 711, 201

Tegmark, M., Blanton, M. R., Strauss, M. A., et al. 2004, ApJ, 606, 702

Tereno, I. 2006, PhD thesis: Cosmological Parameters Estimation with Cosmic Shear (Universidade de Lisboa)

Tinker, J., Kravtsov, A. V., Klypin, A., et al. 2008, ApJ, 688, 709

Tully, R. B. & Fisher, J. R. 1977, A&A, 54, 661

Tytler, D., O'Meara, J. M., Suzuki, N., & Lubin, D. 2000, Phys. Rep., 333, 409

van Waerbeke, L., Mellier, Y., Radovich, M., et al. 2001, A&A, 374, 757

Vanderlinde, K., Crawford, T. M., de Haan, T., et al. 2010, ArXiv astro-ph/1003.0003

Ventimiglia, D. A., Voit, G. M., Donahue, M., & Ameglio, S. 2008, ApJ, 685, 118

Vikhlinin, A., Burenin, R. A., Ebeling, H., et al. 2009a, ApJ, 692, 1033

Vikhlinin, A., Kravtsov, A., Forman, W., et al. 2006, ApJ, 640, 691

Vikhlinin, A., Kravtsov, A. V., Burenin, R. A., et al. 2009b, ApJ, 692, 1060

Vikhlinin, A., McNamara, B. R., Forman, W., et al. 1998, ApJ, 502, 558

Voevodkin, A., Borozdin, K., Heitmann, K., et al. 2010, ApJ, 708, 1376

Voigt, L. M. & Bridle, S. L. 2010, MNRAS, 404, 458

Voit, G. M. 2005, Reviews of Modern Physics, 77, 207

von der Linden, A., Best, P. N., Kauffmann, G., & White, S. D. M. 2007, MNRAS, 379, 867

Vuissoz, C., Courbin, F., Sluse, D., et al. 2008, A&A, 488, 481

Walsh, S. M., Willman, B., Sand, D., et al. 2008, ApJ, 688, 245

Wambsganss, J. 2006, "Gravitational Microlensing" in: Gravitational Lensing: Strong, Weak and Micro, Saas-Fee Advanced Courses, Vol. 33 (Springer-Verlag Berlin Heidelberg), 453 ff.

White, M. 2001, A&A, 367, 27

White, S. D. M., Navarro, J. F., Evrard, A. E., & Frenk, C. S. 1993, Nature, 366, 429

Wiltshire, D. L. 2007, New Journal of Physics, 9, 377

Wolf, C., Meisenheimer, K., & Röser, H. 2001, A&A, 365, 660

Wright, C. O. & Brainerd, T. G. 2000, ApJ, 534, 34

Zhang, Y.-Y., Finoguenov, A., Böhringer, H., et al. 2008, A&A, 482, 451

Zhang, Y.-Y., Okabe, N., Finoguenov, A., et al. 2010, ApJ, 711, 1033

Acknowledgements

I like to thank my supervisors, Prof. Dr. Thomas Reiprich and Prof. Dr. Peter Schneider, for giving me the opportunity to write this thesis at the Argelander-Institut für Astronomie. Both of them motivated me many times with their great and continuing interest in the advance of my project, the Weak Lensing follow-up of the *400d* survey.

Becoming a member of Thomas Reiprich's research group "Studying the Nature of Dark Energy with Galaxy Clusters" acquainted me with the large-scale view of the known Universe and extended my perception of it beyond the visible wavelength regime, which I work with on a regular basis. Thomas's patient supervision and constructive criticism helped a lot and continues to help shaping my work and the *400d* Weak Lensing Programme as such. Thank you, especially for the open atmosphere in the group, and for the opportunity to continue my work on the *400d* clusters as a post-doc.

Peter Schneider advanced my insights into cosmology, via his lectures and textbooks, but also in the framework of the Tuesday "Lens Seminar", explaining the "great picture" of cosmology and how to achieve scientific progress in this field. His interest in my work, from the cosmological phenomena it probes to the layout of individual figures, like once discussed in a long session one Saturday afternoon, provided this thesis with momentum. Thank you for your support.

Thanks to Prof. Dr. Ian Brock and Prof. Dr. Andreas Bott for agreeing to join the thesis committee.

During the course of my thesis I could draw from the accumulated expertise in gravitational lensing at AIfA, very directly from its present, and less directly from its former members. Thomas Erben deserves to be mentioned first, for supervising my daily work and answering countless questions ranging from the meaning of tangential shear components to technical aspects of programming. Numerous people helped me consider and re-consider my work by offering their advice: Tim Schrabback, back in 2006, provided me with an introduction to the subtle workings of KSB and the parameters and levers of the pipeline he wrote and which I used extensively. Later, I could rely on Hendrik Hildebrandt's expertise in photometric redshift and multi-band photometry. There were many helpful discussions with Mischa Schirmer, Daniela Wuttke, Karianne Holhjem, Jörg Dietrich and Marco Hetterscheidt on various aspects of the handling of optical imaging data. Daniel Hudson and Yu-Ying Zhang acquainted me with their respective viewing angles towards galaxy clusters. Thanks to the "cluster group", a special substructure of AIfA, and in particular Helen Eckmiller for discussing many cluster-related but also other topics. Furthermore, I acknowledge Patrick Simon for his help dealing with statistics.

My office mates, Ismael Tereno, Rupal Mittal, and Vera Jaritz deserve and receive[1] particularly cordial thanks for continuously making our office a pleasant space to work but also for countless good discussions and diversions. I am more than grateful for your friendship and the many inspirations and motivations I owe to you!

[1] Keeping in mind the important difference between giving to somebody a bottle of wine or a wine bottle.

The work presented here was supported by Deutsche Forschungsgemeinschaft through project B6 “Gravitational Lensing and X-ray Emission by Non-Linear Structures” of Transregional Collaborative Research Centre TRR 33 – “The Dark Universe”. The *400d* Weak Lensing Survey would have hardly been possible without the support by Alexey Vikhlinin and Craig Sarazin, who have been principal investigators on several of the observing runs conducted by our team. Our MMT observations were supported in part by a donation from the F. H. Levinson Fund of the Silicon Valley Community Foundation to the University of Virginia. In addition, MMT observations used for this project were granted by the Smithsonian Astrophysical Observatory and by NOAO, through the Telescope System Instrumentation Program (TSIP). TSIP is funded by NSF.

I owe thanks to all observers who contributed to the collection of data on which this thesis builds. Over the past years, starting even before my involvement in the *400d* survey, an impressive number of people travelled to the MMT, La Silla, and Las Campanas to record a few of the photons emitted by distant galaxies more than 10^9 years ago. Having experienced the gravitational lensing by a galaxy cluster, these photons were eventually noticed by Oliver Cordes, Helen Eckmiller, Thomas Erben, César Fuentes, Jochen Greiner, Hendrik Hildebrandt, Daniel Hudson, Matthias Klein, Andrey Kravtsov, Rupal Mittal, Jennifer Piel, Thomas Reiprich, Tim Schrabback-Krahe, Alexey Vikhlinin, or Yu-Ying Zhang. Of course, this would not have been possible without the work of the helpful staff at the different observations, whom I like to thank on this occasion. Four of the observing runs gave me the opportunity to visit the MMT and Las Campanas observatories, to conduct observations for the project. On the first of these runs, Tim Schrabback-Krahe provided me with a nice introduction to the practicalities of optical observations.

In preparing the observing runs, but also in the everyday life at the Argelander-Institut, the secretaries, in particular Kathy Schrüfer and Christina Stein-Schmitz always offered help and good advice. Thank you. I owe thanks to the AIfA “Rechnergruppe”, especially Oliver Cordes and the deceased Günther Lay, for fixing various small and not so small problems.

Several people helped to improve this thesis by proofreading it. I acknowledge the suggestions of Philipp Bett, Helen Eckmiller, Thomas Erben, Jennifer Piel, Donate Weghorn, Daniela Wuttke, and Yu-Ying Zhang.

I would like to thank all members of AIfA for the good atmosphere I have encountered there during the last four years! I can not mention everyone here, but like to point out the efforts of the AIfA “Social Committee”. In particular, I recall interesting coffee breaks with Elisabeth Krause during my first year at AIfA. Throughout my PhD time, I much enjoyed the quiz nights at “Fiddler’s” with Ismael Tereno, Donate Weghorn, and all the others who responded to my recurrent calls for attendance.

The life of a cosmologist does not take place in an empty Universe. Thank you to all my friends for my life down here on planet Earth, especially to the Amnesty International Hochschulgruppe people for reminding me of important tasks outside physics. Thanks to my family for supporting me throughout my studies. Finally, I would like to state my gratefulness for all the people worldwide who produced the coffee without which my work would have been unthinkable.